frontiers | Research Topics

Inhibitory interneuron classification, function and dysfunction in neural network

Edited by
Thomas Claude Bienvenu, Norbert Hajos and Frederic Lanore

Published in
Frontiers in Cellular Neuroscience
Frontiers in Aging Neuroscience
Frontiers in Psychiatry

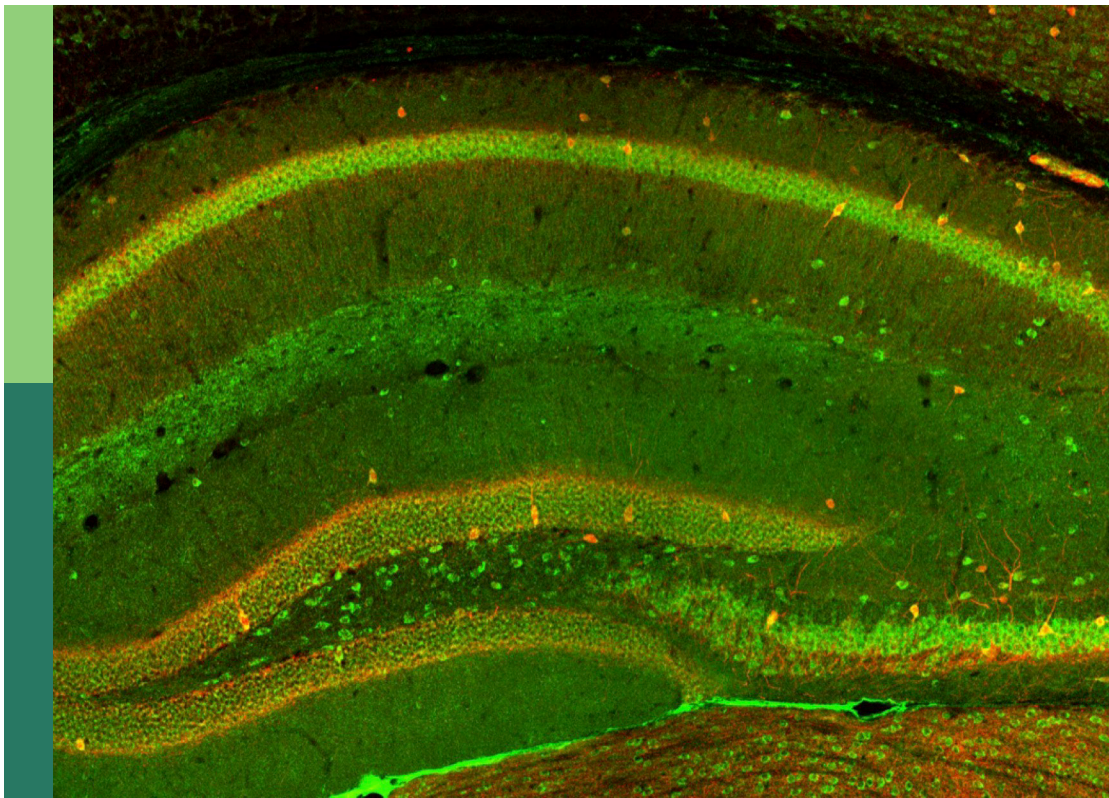

ISSN 1664-8714
ISBN 978-2-8325-4737-3
DOI 10.3389/978-2-8325-4737-3

About Frontiers

Frontiers is more than just an open access publisher of scholarly articles: it is a pioneering approach to the world of academia, radically improving the way scholarly research is managed. The grand vision of Frontiers is a world where all people have an equal opportunity to seek, share and generate knowledge. Frontiers provides immediate and permanent online open access to all its publications, but this alone is not enough to realize our grand goals.

Frontiers journal series

The Frontiers journal series is a multi-tier and interdisciplinary set of open-access, online journals, promising a paradigm shift from the current review, selection and dissemination processes in academic publishing. All Frontiers journals are driven by researchers for researchers; therefore, they constitute a service to the scholarly community. At the same time, the *Frontiers journal series* operates on a revolutionary invention, the tiered publishing system, initially addressing specific communities of scholars, and gradually climbing up to broader public understanding, thus serving the interests of the lay society, too.

Dedication to quality

Each Frontiers article is a landmark of the highest quality, thanks to genuinely collaborative interactions between authors and review editors, who include some of the world's best academicians. Research must be certified by peers before entering a stream of knowledge that may eventually reach the public - and shape society; therefore, Frontiers only applies the most rigorous and unbiased reviews. Frontiers revolutionizes research publishing by freely delivering the most outstanding research, evaluated with no bias from both the academic and social point of view. By applying the most advanced information technologies, Frontiers is catapulting scholarly publishing into a new generation.

What are Frontiers Research Topics?

Frontiers Research Topics are very popular trademarks of the *Frontiers journals series*: they are collections of at least ten articles, all centered on a particular subject. With their unique mix of varied contributions from Original Research to Review Articles, Frontiers Research Topics unify the most influential researchers, the latest key findings and historical advances in a hot research area.

Find out more on how to host your own Frontiers Research Topic or contribute to one as an author by contacting the Frontiers editorial office: frontiersin.org/about/contact

Inhibitory interneuron classification, function and dysfunction in neural network

Topic editors

Thomas Claude Bienvenu — Université de Bordeaux, France
Norbert Hajos — Indiana University Bloomington, United States
Frederic Lanore — UMR5297 Institut Interdisciplinaire de Neurosciences (IINS), France

Citation

Bienvenu, T. C., Hajos, N., Lanore, F., eds. (2024). *Inhibitory interneuron classification, function and dysfunction in neural network*. Lausanne: Frontiers Media SA.
doi: 10.3389/978-2-8325-4737-3

Table of contents

frontiers in Cellular Neuroscience

ORIGINAL RESEARCH
published: 17 June 2020
doi: 10.3389/fncel.2020.00118

Homogeneous and Narrow Bandwidth of Spike Initiation in Rat L1 Cortical Interneurons

Stefano Borda Bossana[1†], *Christophe Verbist*[1†] *and Michele Giugliano*[1,2*]

[1]*Molecular, Cellular, and Network Excitability Laboratory, Department of Biomedical Sciences, Faculty of Pharmaceutical, Biomedical and Veterinary Sciences, Institute Born-Bunge, Universiteit Antwerpen, Wilrijk, Belgium,* [2]*Neuroscience Area, Scuola Internazionale Superiore di Studi Avanzati (SISSA), Trieste, Italy*

The cortical layer 1 (L1) contains a population of GABAergic interneurons, considered a key component of information integration, processing, and relaying in neocortical networks. In fact, L1 interneurons combine top–down information with feed-forward sensory inputs in layer 2/3 and 5 pyramidal cells (PCs), while filtering their incoming signals. Despite the importance of L1 for network emerging phenomena, little is known on the dynamics of the spike initiation and the encoding properties of its neurons. Using acute brain tissue slices from the rat neocortex, combined with the analysis of an existing database of model neurons, we investigated the dynamical transfer properties of these cells by sampling an entire population of known "electrical classes" and comparing experiments and model predictions. We found the bandwidth of spike initiation to be significantly narrower than in L2/3 and 5 PCs, with values below 100 cycle/s, but without significant heterogeneity in the cell response properties across distinct electrical types. The upper limit of the neuronal bandwidth was significantly correlated to the mean firing rate, as anticipated from theoretical studies but not reported for PCs. At high spectral frequencies, the magnitude of the neuronal response attenuated as a power-law, with an exponent significantly smaller than what was reported for pyramidal neurons and reminiscent of the dynamics of a "leaky" integrate-and-fire model of spike initiation. Finally, most of our *in vitro* results matched quantitatively the numerical simulations of the models as a further contribution to independently validate the models against novel experimental data.

Keywords: noise, spike-triggered average, interneuron, layer 1 cortex, dynamical transfer function

OPEN ACCESS

Edited by:
Jonathan Mapelli, Università degli Studi di Modena e Reggio Emilia, Italy

Reviewed by:
Thierry Ralph Nieus, Luigi Sacco Hospital, Italy
Charles J. Wilson, University of Texas at San Antonio, United States

***Correspondence:**
Michele Giugliano
michele.giugliano@sissa.it

[†]*These authors have contributed equally to this work*

Specialty section:
This article was submitted to Cellular Neurophysiology, a section of the journal Frontiers in Cellular Neuroscience

Received: *04 March 2020*
Accepted: *14 April 2020*
Published: *17 June 2020*

Citation:
Borda Bossana S, Verbist C and Giugliano M (2020) Homogeneous and Narrow Bandwidth of Spike Initiation in Rat L1 Cortical Interneurons. Front. Cell. Neurosci. 14:118. doi: 10.3389/fncel.2020.00118

INTRODUCTION

Layer 1 (L1) is the most superficial neocortical layer and holds a key role in the hierarchy of information processing within neocortical networks. It contains a resident population of interneurons, which are solely GABAergic in the mature neocortex (Hestrin and Armstrong, 1996; Gentet, 2012). They receive afferents from a variety of brain areas, including primary and higher-order thalamic relays, cortico-cortical projections, as well as neuromodulatory afferents from subcortical structures. Thanks to this convergence, it was suggested that L1 interneurons might integrate top–down information with feedforward sensory inputs, filter out the noise in the incoming signals, and convert them into local inhibition (Larkum, 2013; Schuman et al., 2019). From L1, information is then transferred to pyramidal cells (PCs)

of layer 2/3 (L2/3) and of layer 5 (L5) *via* two distinct microcircuits, which can either promote or inhibit the generation of dendritic spikes (Jiang et al., 2013). Hence, L1 interneurons may play a pivotal role in modulating, in a state-dependent manner, the coincidence detection mechanism that ensures the amplification and the further processing of attentional signals by PCs (Larkum and Zhu, 2002; Zhu and Zhu, 2004; D'Souza and Burkhalter, 2017).

However, as opposed to L2/3 and L5 PCs, the excitable properties of interneurons have not yet been examined systematically in terms of dynamical firing regimes (but see Linaro et al., 2019; Merino et al., 2019). Within neocortical networks of L2/3 and L5, we already know that information encoding and transfer feature wide-bandwidth dynamics. These performances are ensured by the rapid-onset dynamics of action potentials (APs), which allow neuronal populations to collectively phase-lock their instantaneous firing rate to the fast-varying Fourier components of the input signals (200–1,000 cycle/s; Goriounova et al., 2018; Linaro et al., 2018). In analogy to electrical filters, the upper limit to such broad neuronal bandwidth is referred to as *cut off frequency* (Brunel et al., 2001; Fourcaud-Trocmé et al., 2003), which has been experimentally measured in L2/3 and L5 pyramidal neurons upon identification of the *dynamical transfer function* of those cells (Kondgen et al., 2008; Boucsein et al., 2009; Ilin et al., 2013; Goriounova et al., 2018; Linaro et al., 2018).

For L1, we know that several subpopulations of L1 interneurons can be distinguished on the basis of their firing in response to constant amplitude currents (Muralidhar et al., 2013), displaying quite heterogeneous electrical phenotypes. Nonetheless, it is still not clear how these different electrical signatures contribute to the distinct properties in the network dynamics of information processing within L1.

In this work, by means of whole-cell patch-clamp recordings in rodent acute brain tissue slices, we examined L1 interneurons *in vitro* and identified their electrical phenotype as well as their dynamical transfer function. We quantified how L1 cells' firing output is influenced by a temporal modulation of their input, namely, described in the Fourier domain, the cells' filter properties of incoming input signals. Allowing a comparison with previous studies in principal cells, we specifically adopted a simple and established experimental protocol (Higgs and Spain, 2009; Ilin et al., 2013). This is equivalent (Tchumatchenko and Wolf, 2011) to our previous probing strategy of the dynamical excitable properties of cortical neurons (Kondgen et al., 2008; Linaro et al., 2018). Importantly, we showed earlier that cut off frequency and bandwidth are features that are independent on the parameters of the injected currents and the firing regimes (Linaro et al., 2018).

Given the impact that L1 interneurons have on the output of PCs, characterizing their dynamical response properties is highly relevant and timely to clarify how information integration, processing, and transfer take place to select behaviorally relevant signals. Finally, a set of previously released multicompartmental mathematical models of L1 interneurons (Markram et al., 2015) was studied under the same stimulation protocols *in vitro*, aiming at further validating them and at supporting the interpretation of the experimental data.

MATERIALS AND METHODS

Brain Tissue Slice Preparation

Experiments were performed as described previously (Arsiero et al., 2007; Kondgen et al., 2008) and in accordance with international and institutional guidelines on animal welfare. All procedures were approved by the Ethical Committee of the University of Antwerp (permission no. 2011_87) and licensed by the Belgian Animal, Plant, and Food Directorate-General of the Federal Department of Public Health, Safety of the Food Chain, and the Environment (license no. LA1100469).

Fourteen- to twenty-one days old Wistar rats of either sex were anesthetized using isoflurane and decapitated. The brains were rapidly extracted and immersed in bubbled ice-cold artificial cerebrospinal fluid (ACSF) containing (in mM) 125 NaCl, 25 $NaHCO_3$, 2.5 KCl, 1.25 NaH_2PO_4, 2 $CaCl_2$, 1 $MgCl_2$, and 25 glucose saturated with 95% O_2 and 5% CO_2, with pH of 7.3 and osmolarity of ∼315 mOsm. Then, 300-μm-thick parasagittal slices were cut from the primary somatosensory cortex using a vibratome (VT1000 S, Leica Microsystems GmbH, Germany) and incubated in ACSF at 36°C for 30 min.

After recovery, the slices were stored in ACSF at room temperature in a holding chamber until the recordings were started. Once placed in the recording chamber, constituting the stage of an upright microscope, the L1 cells were visualized with infrared differential interference contrast microscopy under ×40 magnification. All experiments were performed in submerged conditions at a temperature of 32°C under continuous perfusion with oxygenated ACSF.

Electrophysiology

Layer 1 cells were selected on the basis of their distance from the pia mater and from the border with L2/3, which was identified as an increase in the density of cell somata, located approximately 100 μm away from the pia mater. Within this region, the whole-cell patch-clamp configuration was established from the cell soma and the neuronal response properties were probed in the current-clamp mode. Filamented borosilicate glass pipettes were prepared using a micropipette horizontal puller (P-97, Sutter Instruments, Novato, CA, USA) and had a resistance of 4–7 MΩ when filled with an intracellular solution containing (in mM) 115 K-gluconate, 20 KCl, 10 4-(2-hydroxyethyl)-1-piperazineethanesulfonic acid, 4 adenosine triphosphate-Mg, 0.3 Na_2-guanosine triphosphate, and 10 Na_2-phosphocreatine, with the pH adjusted to 7.3 with KOH and osmolarity of ∼290 mOsm. Recordings and intracellular current stimulation were performed using an Axon Multiclamp 700B Amplifier (Molecular Devices, San Jose,CA, USA) controlled by a personal computer running a real-time Linux operating system (Linaro et al., 2014). For more information on how to install our real-time software, see Linaro et al. (2015). The recorded voltage waveforms were sampled at a frequency of 30 kHz and digitized at 16 bit. In order to compensate for

the glass pipette electrical resistance and capacitance, a digital non-parametric model was repeatedly identified throughout the recording sessions by a computer-aided technique, known as *active electrode compensation* (Brette et al., 2008). This allowed us to digitally separate the electrode and the membrane contributions to the recorded traces, requiring neither the bridge balance nor the capacitance neutralization circuits of the amplifier. The adoption of such a technique became a routine procedure in our laboratory for both conventional and real-time experiments (Couto et al., 2015; Linaro et al., 2018, 2019). However, while for the dynamic clamp online accurate "active" electrode compensation is necessary to avoid recording instabilities (Brette et al., 2008; Linaro et al., 2019), for the current-clamp—in the context of the present work—it is not strictly required. In fact, on one hand, we focused here on probing the dynamical transfer function of neurons in the current-clamp mode by spike-triggered averaging (see below) so that accurate *active electrode compensation* was not imperative. Indeed despite using a single electrode for both stimulation and recordings, only the times of AP occurrence must be detected for further analysis (see below). Such detection occurs, by definition, with a very high signal-to-noise ratio and it usually does not represent a problem, even with imperfect electrode compensation. On the other hand, estimating the features of AP waveforms definitely benefits of a more accurate (non-parametric) compensation procedure than the (parametric) one allowed by the electronic amplifier controls. Finally, postponing the compensation of all acquired traces to an offline automated procedure ultimately offered us an efficient management of time during each experiment, while only requiring to periodically run a "calibration" protocol (Linaro et al., 2015).

Electrical Phenotype Identification

The recorded voltage traces were processed and analyzed offline in MATLAB (The MathWorks, Natick, MA, USA). Data from $N = 65$ L1 interneurons were included in this study, which were selected on the basis of a healthy cell resting membrane potential ($\leq$65 mV) and AP peak amplitude (>50 mV). These criteria were considered to be indicative of a good patch stability and proper electrical access to the cell. The membrane input resistance, capacitance, and time constant were estimated by standard procedures (Kondgen et al., 2008). Briefly, hyperpolarizing current steps of decreasing amplitudes [i.e., (−200; 0) *pA* lasting 1 s each] were repeatedly applied and the voltage response was recorded. The membrane input resistance was then identified as the slope of the best-fit straight line to the steady-state data points in the voltage vs. current plane. The membrane time constant was instead extracted as the slowest time constant of the best-fit bi-exponential function, describing the recovery of the membrane potential from 10–ms -long hyperpolarizing pulses of amplitude −150 pA. The cell capacitance was finally estimated as the ratio between the time constant and the input resistance of the membrane.

Each recorded neuron was classified in one of the five identified subtypes on the basis of their response to depolarizing current pulses (Muralidhar et al., 2013). Briefly, a *frequency–current* curve was first computed upon injecting current steps of increasing depolarizing amplitudes [i.e., in the range (0; 300) pA, lasting 1 s]. The voltage responses containing a train of APs, corresponding to a mean firing rate of 20 spike/s, were compared to each other as the sequence of successive inter-spike intervals (ISIs) was plotted (**Figure 1A**). Sorting each cell into one of the five classes (i.e., cAC, continuous accommodating; cNAC, continuous non-accommodating; bNAC, bursting non-accommodating; cSTUT, continuous stuttering; and cIR, continuous irregular firing) was performed manually, following closely (Muralidhar et al., 2013) and according to the following criteria: cAC, if the slope of the best-fit straight line over the ISI sequence was larger than 1 ms; cNAC, if the best-fit line was mostly horizontal (i.e., slope smaller than 1 ms); bNAC, if the initial 1 to 2 ISIs were shorter than 20 ms and followed by a train of APs showing no accommodation; cSTUT, if at least one ISI was equal or larger than 100 ms; and cIR, if the ISI sequence was irregular, with individual values shorter than 100 ms. The above criteria led to classifying 11 cells as cAC, 13 as cNAC, 10 as bNAC, 17 as cSTUT, and 14 as cIR (**Figure 1A**).

Spike-Triggered Average and Dynamical Transfer Function

Wide-band input current waveforms $i(t)$ were injected into the cell soma in order to probe their first-order dynamical transfer properties, following closely (Ilin et al., 2013; see also Higgs and Spain, 2009). Under these conditions, neuronal firing is irregular and subthreshold membrane potential fluctuations resemble the activity recorded *in vivo* (Destexhe et al., 2003). The injected current was defined as the sum of a DC and of a fluctuating component (**Figure 1B**):

$$i(t) = i_0 + \sigma\eta(t) \quad (1)$$

with $\eta(t)$ being an independent realization of an Ornstein–Uhlenbeck stochastic process (Cox and Miller, 1965) with zero mean, unitary variance, and correlation time $\tau = 5$ ms. $\eta(t)$ was generated offline, iterating an algebraic expression (Gillespie, 1996).

By such a definition, σ represents the standard deviation of the noisy fluctuation in $i(t)$, while i_0 is its expected value. In each experiment, σ was adjusted to obtain membrane potential fluctuations with 4 mV standard deviation and ≈15 mV peak-to-peak changes. The value of i_0 was instead chosen to maintain the mean firing rate of the neurons in the range of 3–6 spike/s. Each stimulation trial lasted 60 s and was preceded by brief current steps, monitoring over time the stability of the recording, i.e., in terms of resting potential, input resistance, and mean firing rate as in Kondgen et al. (2008). The stimulation was repeated several times, with distinct realizations of $\eta(t)$, until at least 3,500 APs in total were collected, while allowing sufficient inter-stimulus recovery intervals of up to 60–100 s, depending on the cell. This resulted in 18–20 repetitions, corresponding to approximately 40–45 min of recording in total.

We recorded the train of APs fired by the cell in response to the injected stimulus $i(t)$, evaluating offline the spike-triggered average $sta(t)$ of such a stimulus waveform. This analysis allows an estimate of the dynamical transfer function

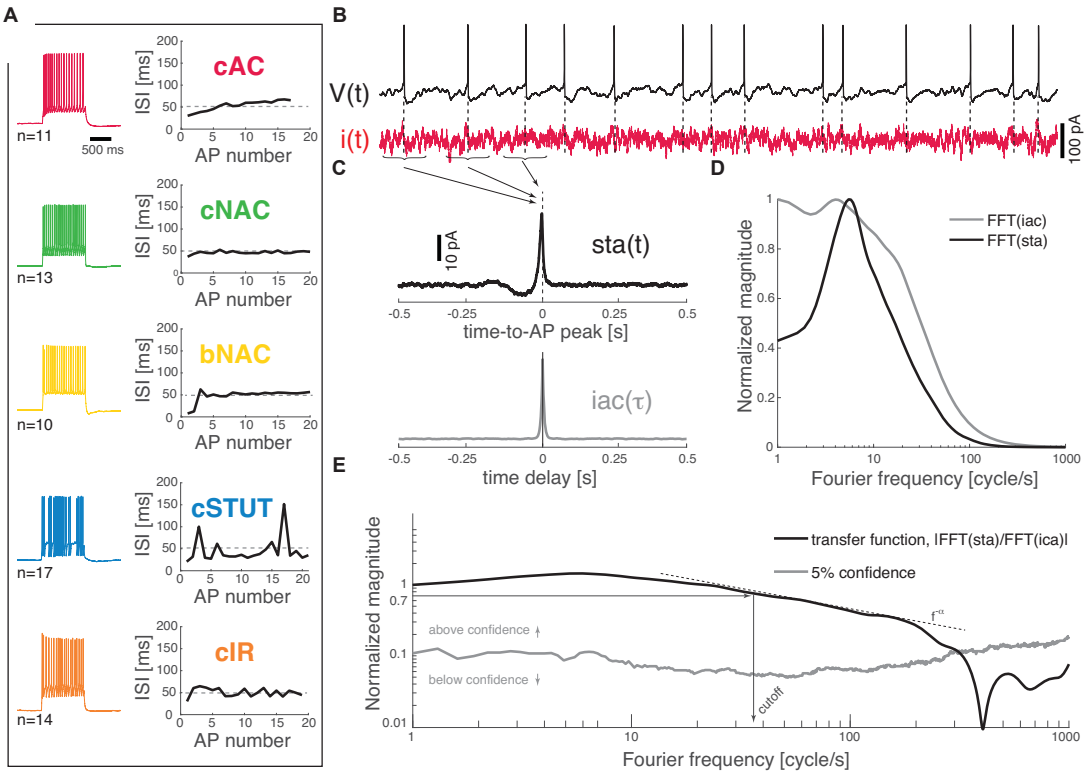

FIGURE 1 | Dynamical transfer function identification in L1 cortical interneurons. Distinct subtypes of L1 interneurons can be distinguished **(A)** from their electrical response pattern by the sequence of interspike intervals in a 20 spike/s train. These are continuous accommodating, c. non-accommodating, bursting non-accommodating, c. stuttering, and c. irregular. Regardless of their identity, the neurons were stimulated by a fluctuating current $i(t$; **B**) while recording their voltage response $V(t)$. The spike-triggered average [i.e., $sta(t)$] of the stimulus and its autocorrelation function [i.e., $iac(\tau)$] were computed **(C)** and fast Fourier-transformed **(D)** to estimate the neuron dynamical transfer function **(E)**. As in electronic filters, the magnitude of this function expresses the intensity of the output firing rate of the cell across temporal modulations or Fourier components of an input signal, thus revealing the bandwidth of spike initiation dynamics. The cut off was characterized—above significance (see "Materials and Methods" section)—as the frequency corresponding to a 70% decrease of the response magnitude of the value taken at 1 cycle/s. The high-frequency profile was finally described as a $f^{-\alpha}$ power-law.

(Kondgen et al., 2008) in biological neurons as well as model neurons and was performed following closely Ilin et al. (2013). Briefly, $sta(t)$ was evaluated as the ensemble average of the data points of $i(t)$ that shortly preceded and followed the peak of each AP fired, i.e., over the times t_1, t_2, t_3, …, t_N of AP occurrences (**Figures 1B,C**):

$$sta(t) = < \sum_{k=1}^{N} i(t_k - t) > \quad t \in [-T; T] \tag{2}$$

where T = 500 ms is the chosen time interval preceding and following each AP. This expression can be equivalently rewritten as an ensemble average of the convolution between $i(t)$ and a train of Dirac's delta functions $s(t)$; (i.e., one for each AP):

$$\begin{aligned} sta(t) &= < \int_{-\infty}^{+\infty} s(\tau) i(\tau - t) d\tau > \\ s(t) &= \sum_{k=1}^{N} \delta(t - t_k) \end{aligned} \tag{3}$$

Invoking linearity and swapping integral and average operators, we may derive another expression (Dayan and Abbott, 2005) linking $sta(t)$ to the instantaneous firing rate $r(t)$ associated to the AP train $s(t)$:

$$sta(t) = \int_{-\infty}^{+\infty} r(\tau) < i(\tau - t) > d\tau \tag{4}$$

In the Fourier domain, this convolution integral simplifies the product of the firing rate transform $R(f)$ and the average (complex conjugate) of the input transform $I^*(f)$:

$$STA(f) = R(f) < I*(f) > \tag{5}$$

Finally, as $R(f)$ is also the product of the first-order dynamical transfer function $H(f)$ (Marmarelis and Naka, 1972) times the average input $< I(f) >$ (Brunel et al., 2001),

$$R(f) = H(f) < I(f) > \tag{6}$$

the transfer function $H(f)$ (**Figure 1E**) can be computed as the ratio between the $sta(t)$ (fast) Fourier transform and the power spectral density of $i(t)$ (**Figures 1C,D**):

$$H(f) = STA(f) / <I(f) I*(f) > \tag{7}$$

where the power spectral density of $i(t)$ is the (fast) Fourier transform of its autocorrelation function $iac(\tau) = < i(t)i(t-\tau) >$.

The profile of the transfer function was considered above the 5% confidence threshold (**Figure 1E**) generated by a bootstrap method on surrogate data (Press, 2007). Briefly, these were obtained upon generating 500 times a random shuffling of the original interspike intervals and repeating each time the $sta(t)$ analysis in the Fourier domain. The confidence threshold was then computed at each frequency as the sum of the mean (surrogate) transfer function (i.e., over the 500 surrogate trials) and its (surrogate) standard deviation.

The *cut off* frequency was then defined as the frequency at which the magnitude of the transfer function $||H(f)||$ (above the confidence threshold) decreases down to 70% of the value it takes at 1 Hz (**Figure 1E**).

For very large Fourier frequencies f, the magnitude of the transfer functions decayed as a negative power-law, i.e., $f^{-\alpha}$ (Fourcaud-Trocmé et al., 2003; Kondgen et al., 2008; Linaro et al., 2018). In order to best describe the input–output transformation of the neurons in this high spectral domain, the part of the transfer curves going from the cut off frequency down to 20% of the cut off value was fitted by a power-law $y = bx^{-\alpha}$ where α describes the slope of the decay in log–log coordinates.

Rapidness of the Action Potential at Its Onset

The average waveform of the AP was examined for each cell by averaging the APs fired during the steady-state response regime of the recorded voltage responses. The threshold for AP initiation (in mV) was conventionally calculated as the potential where the change in voltage over time is 20 mV/ms (Naundorf et al., 2006). When plotted in the plane dV_m/dt vs. V_m, each AP described a closed trajectory. The AP speed at onset (expressed in ms^{-1}) was then measured in this plane as the slope of the tangent line to the AP trajectory at the voltage coordinate corresponding to the AP threshold.

The *dynamic IV curve* method was also employed to quantify the AP waveforms, relating the upstroke phase of an AP to the best-fit equation of a non-linear (i.e., exponential) relationship between dV_m/dt and V_m (Brette et al., 2008; Badel et al., 2008a,b). From the resulting fit, the spike–slope factor Δ_T was extracted to further quantify the rapidness of the AP.

Computer Simulations

The simulation of 69 distinct L1 interneuron models was performed in NEURON (Hines and Carnevale, 2001; Carnevale and Hines, 2006) using the publicly available Blue Brain Project (BBP) database (Markram et al., 2015). Each model was originally built from experimental data collected from L1 neurons classified into the same electrical response phenotypes employed in this work (see also Ascoli et al., 2008).

As close as possible, we mimicked *in silico* the very same stimulation protocols and analysis employed *in vitro*. For the spike-triggered average estimate, we chose the parameters of the injected current $i(t)$ by means of an iterative procedure based on the bisection method (Press, 2007). Given the increased reproducible character of simulated neuronal responses compared to experiments, by selecting i_0 we could set the firing rate of the models with higher precision. We then chose three regimes (3, 5, and 7 spikes/s) to cover the entire range obtained in our experiments (3–6 spike/s) with increased confidence. We repeated 60 s-long stimulations *in silico* until a minimum of 5,000 APs were collected, and we followed closely the analysis methods described in the previous sections (**Figure 2**).

Statistical Analysis

All numerical data are presented as mean ± standard deviation. A statistical analysis of all correlations between parameters was performed using the Pearson correlation test (Press, 2007), thus reporting the values of the correlation coefficient ρ and its p-value. The one-way analysis of variance by Kruskal–Wallis was employed [i.e., the MATLAB kruskalwallis() command] to reject the hypothesis, at 1% significance, that the observables extracted from distinct electrical phenotypes originate from the same probability density distribution. Finally, qualitative comparison between the distribution densities of cut off frequencies, among different electrical phenotypes (**Figure 3**), were performed, normalizing the peak amplitudes of smoothed histograms by the kernel smoothing method [i.e., the MATLAB histfit() command].

RESULTS

We describe the firing response properties of L1 cortical interneurons based on a set of whole-cell patch-clamp recordings in $N = 65$ cells from slices of the rat somatosensory cortex. We studied systematically both passive and active membrane properties, revealing that cells had an input resistance of 184.40 ± 51.15 MΩ a membrane capacitance of 201.51 ± 62.95 nF, and a membrane time constant of 35.77 ± 10.23 ms (see "Materials and Methods" section). When active response properties were studied, we identified distinct electrical phenotypes and sorted the cells into five separate classes (Muralidhar et al., 2013). Such a classification was based on the analysis of the time course of the ISIs sequence, during ≈ 20 spike/s trains of APs in response to a current step lasting 1 s (**Figure 1A**).

Encoding Properties of L1 Interneurons

We studied the encoding properties of L1 interneurons by measuring their *dynamical transfer function* in the Fourier domain (**Figures 1B–E**). Following closely Ilin et al. (2013), we injected randomly fluctuating current stimuli into the soma of the cells, mimicking the irregular and intense synaptic activity present *in vivo* in an intact cortex. A DC offset was also superimposed to the injected current, with its amplitude adapted so that the output mean firing rate was in the range 3–6 spike/s. Under these conditions (see "Materials and Methods" section), cells fired irregularly (**Figure 1B**) with a coefficient of variation of 0.53 ± 0.09 for their distribution of ISIs. This stimulation protocol enabled us to measure the spike-triggered average waveform of the injected current $sta(t)$ and compare it to its autocorrelation function $iac(t)$ in the

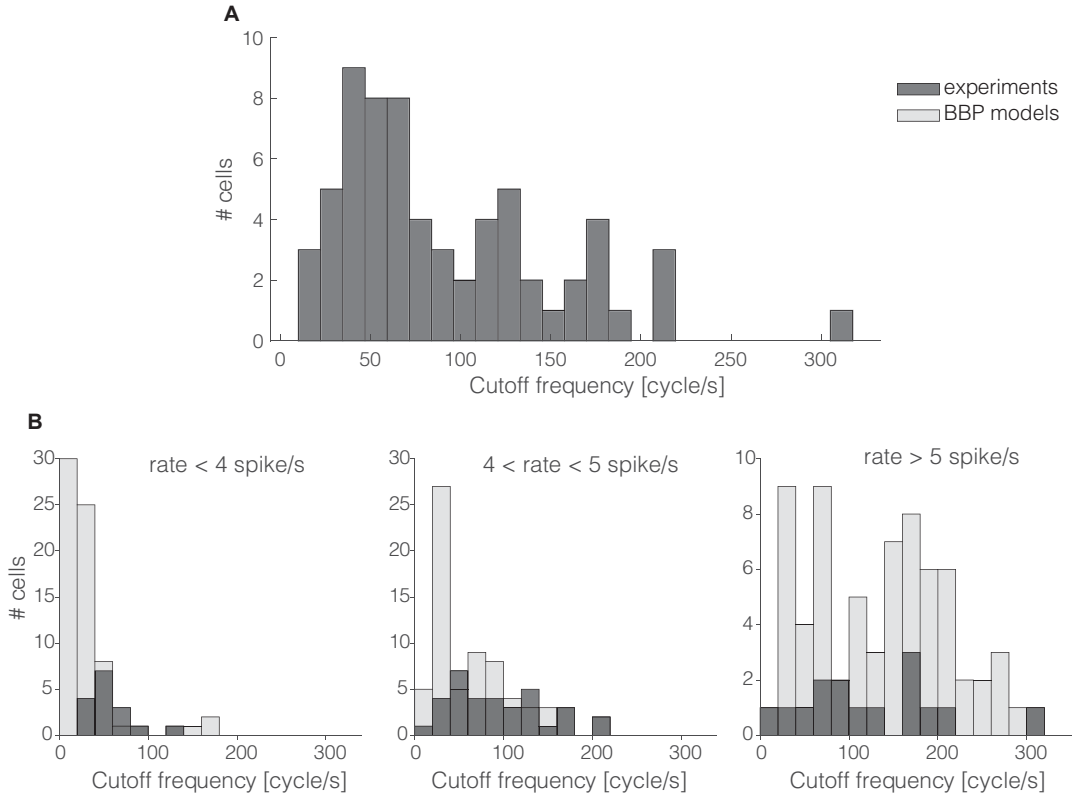

FIGURE 2 | The cells' cutt off frequency distribution. More than 60% of the 65 interneurons recorded in this work had their cut off frequencies markedly below 100 cycle/s **(A)**. The same trend was quantitatively confirmed *in silico* by repeating the same protocol as that of **Figures 1B–E** in 69 L1 neuron models **(B)** as released by the Blue Brain Project (BBP). Numerical simulations and experimental data were compared over three distinct ranges of experimental firing rates, where models were set to fire at precisely 3, 5, and 7 spike/s (**B**; from left to right). The histogram overlay displays the rather good model predictions of the horizontal span of cut off frequencies over the three distinct firing rates.

Fourier domain (**Figures 1C,D**). In fact, the ratio of the two quantities in the transformed domain immediately leads to an estimate of the dynamical transfer function (**Figure 1E**; see "Materials and Methods" section) arising from the cell's spike initiation mechanisms.

The magnitude and the phase of the transfer function, especially for large spectral frequencies, allow one to predict the collective dynamics of a neuronal population in response to rapid external inputs (Fourcaud-Trocmé et al., 2003; Kondgen et al., 2008) as well as to interpret oscillatory regimes (Wang, 2010). Here, we quantified the bandwidth of the neuronal transfer function, expressing the numerical value of the conventional high-frequency *cut off* limit (see "Materials and Methods" section). The distribution of the *cut off* frequencies demonstrates that, in general, L1 interneurons can encode fast-varying input signals up to 200 cycles/s (**Figure 2A**). However, differently from L2/3 and L5 PCs (Testa-Silva et al., 2014; Linaro et al., 2018), the majority (i.e., ≈65%) of L1 neurons unexpectedly display a *cut off* below 100 cycles/s.

These observations were confirmed *in silico* by applying the experimental protocol of **Figures 1B–E** on a large public database of 69 detailed multicompartmental models of rat cortical L1 interneurons (see "Materials and Methods" section). At a reference mean firing rate of 5 spikes/s, around 78% of the models display a *cut off* frequency below 100 cycles/s. **Figure 2B** compares experimental and simulated data when the computer models were set to fire on average at (from left to right) 3, 5, and 7 spikes/s. Under these conditions, the coefficients of variation of their respective ISI distributions were 0.74 ± 0.12, 0.65 ± 0.12, and 0.58 ± 0.12, respectively, for 3, 5, and 7 spikes/s mean firing rates. Real cells were thus found to be in good agreement with the range of *cut off* frequencies displayed by the models when their firing rate was sorted in close intervals.

Electrical Classes and Encoding Properties

When the cells' electrical classes were explicitly taken into consideration, we found no preference in the *cut off* frequency distributions (**Figures 3A,B**). Indeed the probability distribution densities for each group of continuous accommodating (cAC), c. non-accommodating (cNAC), bursting non-accommodating (bNAC), c. stuttering (cSTUT), and c. irregular (cIR) showed a substantial overlap (**Figure 3A**) and no significant differences were found (**Figure 3B**).

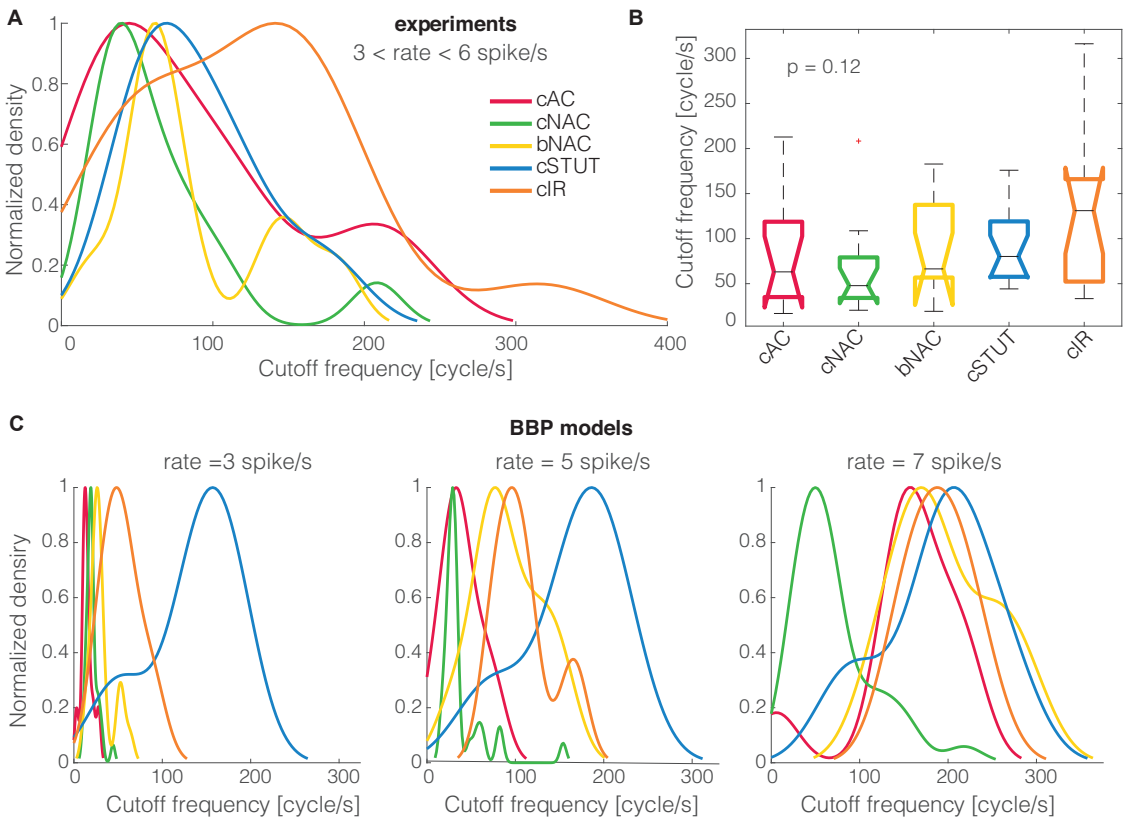

FIGURE 3 | The cells' electrical phenotype and cut off frequency distributions. When the five distinct electrical classes of L1 interneurons were compared to each other, their (smoothed) probability density distributions of the cut off frequencies, normalized by their peak values, showed no major differences **(A)**. Quantitatively, the Kruskal–Wallis statistical test failed to reject, at 1% significance level, the null hypothesis that the cut off frequencies come from the same distribution **(B)**. A similar trend was largely reproduced *in silico* for the BBP models **(C)**.

The same analysis was repeated *in silico*, where the diversity of electrical (as well as morphological) phenotype is made explicit *a priori* by a distinct set of electrotonic and excitable properties (Markram et al., 2015). The model's electrical identity played a role in shaping, to some extent, the probability distribution densities of the cSTUT and the cNAC classes in particular.

Dependency of *Cut Off* on the Mean Firing Rate

Previous theoretical investigations on the dynamical properties of spike initiation reported that, in integrate-and-fire neuron models, the *cut off* frequency is sensitive to the mean firing rate. Thus, the higher the rate, the wider the bandwidth (Brunel et al., 2001; Fourcaud-Trocmé et al., 2003). This was examined experimentally in L5 PCs but failed to be confirmed as the mean firing rate altered the dynamical transfer function at low, not high, spectral frequencies (Linaro et al., 2018). Despite the small range of our experimental firing rates, we asked whether L1 interneurons behave differently than PCs. We thus studied the correlation between *cut off* frequency and the mean firing rate and found it to be very significantly correlated ($\rho = 0.48$ and $p < 0.001$), as also exemplified in **Figure 4A**. This implies that the boundary in the Fourier domain, where fast input signal components get filtered out, increases considerably even with a moderate increase in the neuronal firing rate.

When the analysis was repeated *in silico*, a similar phenomenon was replicated for the entire population of multicompartmental neuron models. There we found a similar correlation with a much stronger significance ($\rho = 0.58$ and $p < 10^{-20}$; **Figure 4B**). This effect is very apparent in the simulated experiment reported in **Figure 4B** as most electrical types progressively shift their *cut off* frequency upwards for increasing firing rates. Such a susceptibility was further quantified by linear fitting the simulated data points at different firing rates for each firing type. The slope of this fit was 34.57 cycles/spike for cAC, 11.96 for cNAC, 41.16 for bNAC, 11.43 for cSTUT, and 32.78 for cIR. This indicates that cSTUT and cNAC models were the least sensitive to their firing rate, while cAC, bNAC, and cIR were the most sensitive.

Action Potential Rapidity at Onset

The broad bandwidth of the AP initation dynamics has been related, in both theoretical (Fourcaud-Trocmé et al., 2003) and experimental works (Testa-Silva et al., 2014; Linaro et al., 2018),

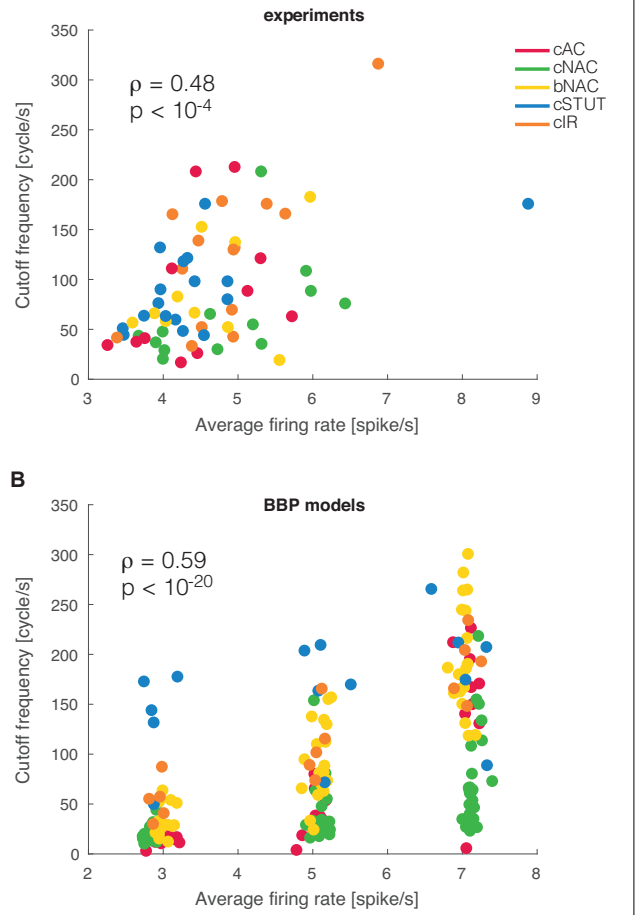

FIGURE 4 | Mean firing rate modulation of the cut off frequencies. As suggested by earlier theoretical studies, a significant correlation was observed between the mean firing rate of a cell and the cut off frequency of its dynamical transfer function **(A)**. The very same result was reproduced *in silico* for the BBP models **(B)**.

to the rapidity of APs at their onset. Thus, neurons with fast AP onset dynamic keep track of the most rapid spectral components in the input signals, as demonstrated for L2/3 and L5 PCs (see also Gorionova et al., 2018). However, when we examined the correlation between AP rapidity and *cut off* frequency in L1 inteneurons, we failed to confirm the previous reports. In fact, correlations were not significant ($\rho = 0.13$ and $p = 0.32$).

As we repeated the analysis *in silico* for all L1 model neurons available, we also observed a lack of significant correlations as in the experiments ($\rho = 0.15$ and $p = 0.22$, $\rho = 0.08$ and $p = 0.32$, and $\rho = 0.16$ and $p = 0.20$ at firing rates of 3, 5, and 7 spikes/s, respectively). Moreover, no clear separation of AP rapidity at onset was found across the electrical classes of the model cells. Even when the impact of some morphological features was considered (as in Eyal et al., 2014; Gorionova et al., 2018), we found no significant correlations between the AP onset rapidity and the total dendritic length of the model cells over a broad range of total dendritic lengths 500–5,400 μm ($\rho = 0.11$ and $p = 0.38$, $\rho = 0.10$ and $p = 0.40$, and $\rho = 0.11$ and $p = 0.35$ at firing rates of 3, 5, and 7 spikes/s, respectively). However, unexpectedly, we found slightly significantly negative correlations between the total dendritic length and the *cut off* frequency ($\rho = -0.3$ and $p = 0.011$, $\rho = -0.31$ and $p = 0.011$, and $\rho = 0.10$ at a firing rate of 3, 5, and 7 spikes/s, respectively).

As the last result was neither anticipated in simulation studies (Eyal et al., 2014) nor matched with others experimental reports, we further characterized *in vitro* and *in silico* the AP initiation employing the *dynamic IV curve* (Badel et al., 2008a,b). This allowed us to extract an additional quantitative parameter for AP initiation, known as the slope factor Δ_T (see "Materials and Methods" section). Across all our experiments, Δ_T took values smaller than 2.5 mV (1.51 ± 0.73 mV), a range that was confirmed and replicated *in silico*, consistently with the larger spike *sharpness* of interneurons compared to PCs (Badel et al., 2008a).

While Δ_T and the AP onset rapidity showed correlations *in silico* ($\rho = 0.26$ and $p = 0.03$ at 5 spike/s), their values *in vitro* had no significant correlation ($\rho = -0.11$ and $p = 0.37$). Importantly, as the values of Δ_T and the *cut off* frequency were compared across cells, a significant correlation was finally observed in our experimental data ($\rho = -0.31$ and $p = 0.012$), but not *in silico* ($\rho = -0.06$ and $p = 0.06$ at 5 spike/s).

Transfer at High Spectral Frequencies

For high spectral frequencies f (i.e., above the *cut off*), the dynamical transfer function is known to decay as $f^{-\alpha}$ (Kondgen et al., 2008), where the numerical value of the exponent has been linked to the precise dynamics of AP initiation at threshold (Fourcaud-Trocmé et al., 2003). In comparison with standard simplified models of excitability, such as the integrate-and-fire units (Tuckwell, 1988), previous results in pyramidal neurons [i.e., $\alpha \in (1;1.5)$] consistently pointed towards an *exponential* or *polynomial* dependency of the AP initiation on the membrane potential (Kondgen et al., 2008; Linaro et al., 2018). Unexpectedly, as we analyzed the transfer properties of L1 neuron at high spectral frequencies, we found values of α in the range from 0 to 1.4, with the largest majority (i.e., 94%) smaller than 1 (0.57 ± 0.26; **Figure 5A**). The distribution of α across different electrical cell types displayed largely overlapping features (**Figure 5A**) with no significant differences, thus hinting at similar transfer behaviors.

These observations were confirmed *in silico*, where L1 interneuron models were characterized by α in the range 0.2–1.5, with the majority below 1 (0.51 ± 0.14, 0.44 ± 0.24, and 0.74 ± 0.43 at firing rates of 3, 5, and 7 spike/s, respectively), matching the values obtained in the experiments (**Figure 5B**).

DISCUSSION

In this work, we have examined the dynamical signal transfer properties of L1 cortical interneurons. These cells are likely to play a major role in cortical computation as they receive several afferents from a variety of brain regions while establishing synapses downstream in several cortical columns. Their function

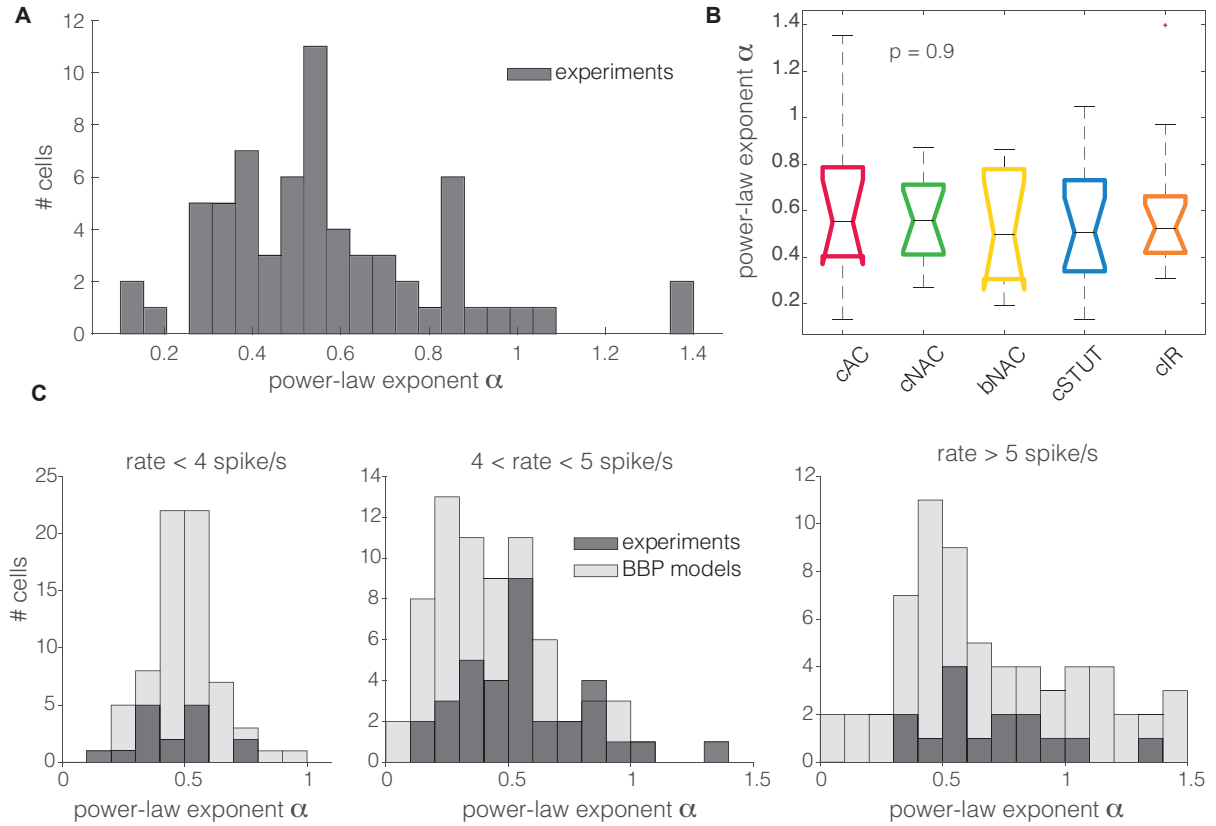

FIGURE 5 | The distribution of the power-law exponent at high spectral frequencies. Almost all the cells recorded in this work had a power-law exponent lower than 1 for high spectral frequencies **(A)**. Concerning the cell subtypes, the same as for **Figure 3B**, the Kruskal–Wallis statistical test failed to reject at, 1% significance level, the null hypothesis that the cut off frequencies come from the same distribution **(B)**. The same trend was quantitatively confirmed *in silico* for the BBP models **(C)**. Numerical simulations and experimental data were compared over three distinct ranges of experimental firing rates, where the models were set to fire at precisely 3, 5, and 7 spike/s (**C**; from left to right). The histogram overlay displays the model predictions of the horizontal span of the cut off frequencies over the three distinct firing rates.

of gating and filtering the output spike trains of PCs in other layers appears clear, although its careful spectral characterization remained so far unexplored. When an established protocol (**Figure 1**) was used to quantify the encoding properties of L1 interneurons, a markedly lower bandwidth (**Figure 2**) and a gentler attenuation at high spectral frequencies were observed (**Figure 5**), compared to L2/3 and L5 PCs. Thus, while the rapidly varying frequency component of their inputs can be tracked, i.e., up to 200–300 cycle/s, the large majority of L1 interneurons possesses much lower *cut off* values, below 100 cycle/s. This might indicate that L1 outputs may be well suited to filter incoming information and relay it to PCs, especially in the center of their own bandwidth (Ilin et al., 2013; Goriounova et al., 2018; Linaro et al., 2018), particularly where the phase delay introduced by the PCs transfer function is minimal (Linaro et al., 2018).

The markedly lower *cut off* frequencies and smaller power-law attenuation coefficient α in L1 interneurons might therefore indicate their specialization at keeping track of slower *top–down* input modulations (Jiang et al., 2013; Larkum and Phillips, 2016) compared to *bottom–up* inputs reaching directly PCs in L2/3 and L5, while attenuating less rapidly the components at higher spectral frequencies. Despite the limited size of our data set, we successfully sampled all the known electrical subtypes of L1 cells and found no significant differences in their spectral responses (**Figure 3**). This finding is backed up by an extensive database of accurate multicompartmental models (Markram et al., 2015) that contains *a priori* an extensive diversity in cell response properties.

Our choice of the *in vitro* protocol and the limited cell viability during long experimental conditions did not allow us a systematic exploration of the modulatory effect of the cell's mean firing rate on the neuronal bandwidth. Nonetheless, we could establish that a significant correlation exists between the *cut off* frequency and the cell's firing rate (**Figure 4**), as anticipated by the theory (Brunel et al., 2001; Fourcaud-Trocmé et al., 2003) but not previously reported for PCs (Linaro et al., 2018). This suggests that an increase in the mean firing rate of L1 interneurons can expand their filtering capabilities, perhaps relaying to the

dendritic compartment of PCs distinct spectral information during different cortical firing regimes. The simulations also suggest that some neuronal types should be more susceptible for the firing rate modulation, such as cAC, bNAC, and cIR types.

As opposed to previous reports in PCs, when we characterized the AP waveform and its relevance for the tracking of fast-input spectral components, we did not observe any correlation with the values of the *cut off* frequency, both *in vitro* and *in silico*. Therefore, we suggest that the emerging mechanisms for spike initiation of L1 interneurons might have some quantitative differences when compared to those of excitatory neurons (Ilin et al., 2013; Linaro et al., 2018). In contrast with other studies (Goriounova et al., 2018), we found a negative correlation between the total dendritic length and the cut off frequency *in silico*. This might be a consequence of the smaller dendritic length in L1 models than L5 PCs (i.e., 500–5,400 vs. 8,000 μm and up to 15,000–20,000 μm), although the values of AP onset speed were in a similar range as for L5 PCs, both in experiments and in simulations. No correlation was found between the AP onset speed and the total dendritic length in the models. However, as the AP slope factor Δ_T was measured, we found similar values as those obtained for other neocortical types. *In silico*, an (expected) negative correlation was found between Δ_T and the AP onset rapidity (Badel et al., 2008a,b), but not *in vitro*. A correlation between Δ_T and the *cut off* frequency clearly was detected *in vitro*, but not *in silico*. We speculate that such a mismatch between theory and experiments might be a consequence of the reduced repertoire of active membrane mechanism models (i.e., sodium and potassium currents kinetics), which are shared by all BBP cortical model neurons (Markram et al., 2015). While using the same biophysical models for describing all cell types is a convenient strategy for constraining automated parameters (Druckmann et al., 2007), we wonder whether L1 interneurons might be even better described with "custom" kinetic parameters for sodium and potassium currents. In addition, we think that the excitability of L1 interneurons has been investigated partially and in less detail when compared to L5 PCs. The latter have been widely studied as a "reference" cortical neuron by many investigators over the last decades. Lastly, BBP L1 models have been identified automatically while extracting only a limited set of features from the experimental data (e.g., time-to-first AP, width of the AP, AP frequency, etc.) (Druckmann et al., 2008), and we wonder whether the use of additional protocols, such as the probing of the dynamical transfer function, might have increased the faithfulness of theory–experiments matching. Taken together, all these results call for further investigation of the AP initiation mechanisms in L1 interneurons, both experimentally and numerically.

Finally, as we characterized the transfer properties at high spectral frequencies, we observed a power-law decay, although with unexpectedly low absolute values of the exponent α, both *in vitro* and *in silico*. According to Fourcaud-Trocmé et al. (2003), different reduced models of excitability are associated to distinct characteristic values of α. In particular, while the exponential integrate-and-fire unit seems to be more appropriate to describe PCs, the leaky integrate-and-fire excitability (i.e., $\alpha = 0.5$) seems closer to explain the data, both *in vitro* (i.e., $\alpha = 0.57$ on average) and *in silico* (i.e., in the range $\alpha = 0.44$–0.74). This suggests that L1 interneurons indeed might have distinct spike initiation dynamics when compared to PCs.

In conclusion, we believe that our results contribute with timely and relevant observations to the series of efforts, worldwide, to describe and classify the excitable properties of neocortical neurons. The spectral characterization of the bandwidth of spike initiation thus revealed to be more informative than the standard methods to quantify neuronal excitability, and the present study extends such characterization to the population of L1 interneurons.

DATA AVAILABILITY STATEMENT

Relevant datasets and analysis scripts are available at FigShare.com (https://dx.doi.org/10.6084/m9.figshare.12091047).

ETHICS STATEMENT

The animal study was reviewed and approved by Ethical Committee of the University of Antwerpen (permission n. 2011_87) and Belgian Animal, Plant, and Food Directorate-General of the Federal Department of Public Health, Safety and Food Chain and the Environment (license n. LA1100469).

AUTHOR CONTRIBUTIONS

MG conceived and designed the research. SB performed the experiments. CV performed the simulations. SB and CV analyzed the data. SB, CV, and MG wrote the article.

FUNDING

Financial support by the European Union's ERASMUS program and the Horizon 2020 Framework Program for Research and Innovation, under the Specific Grant Agreement n. 785907 (Human Brain Project SGA2), the Research Foundation—Flanders (Grant No. G0F1517N), is kindly acknowledged. Access to high-performance computing was generously provided by the VSC (Flemish Supercomputer Center), funded by the Research Foundation—Flanders (Fonds Wetenschappelijk Onderzoek; FWO) and the Flemish Government—Department EWI. The funders had no role in the study design, data collection, and analysis, decision to publish, or preparation of the manuscript.

ACKNOWLEDGMENTS

We thank Mrs. G. Van de Vijver for her valuable technical assistance.

REFERENCES

Arsiero, M., Lüscher, H. R., Lundstrom, B. N., and Giugliano, M. (2007). The impact of input fluctuations on the frequency-current relationships of layer 5 pyramidal neurons in the rat medial prefrontal cortex. *J. Neurosci.* 27, 3274–3284. doi: 10.1523/JNEUROSCI.4937-06.2007

Ascoli, G. A., Alonso-Nanclares, L., Anderson, S. A., Barrionuevo, G., Benavides-Piccione, R., Burkhalter, A., et al. (2008). Petilla terminology: nomenclature of features of GABAergic interneurons of the cerebral cortex. *Nat. Rev. Neurosci.* 9, 557–568. doi: 10.1038/nrn2402

Badel, L., Lefort, S., Berger, T. K., Petersen, C. C. H., Gerstner, W., and Richardson, M. J. E. (2008a). Extracting non-linear integrate-and-fire models from experimental data using dynamic i–v curves. *Biol. Cybern.* 99, 361–370. doi: 10.1007/s00422-008-0259-4

Badel, L., Lefort, S., Brette, R., Petersen, C. C. H., Gerstner, W., and Richardson, M. J. E. (2008b). Dynamic i-v curves are reliable predictors of naturalistic pyramidal-neuron voltage traces. *J. Neurophysiol.* 99, 656–666. doi: 10.1152/jn.01107.2007

Boucsein, C., Tetzlaff, T., Meier, R., Aertsen, A., and Naundorf, B. (2009). Dynamical response properties of neocortical neuron ensembles: multiplicative versus additive noise. *J. Neurosci.* 29, 1006–1010. doi: 10.1523/JNEUROSCI.3424-08.2009

Brette, R., Piwkowska, Z., Monier, C., Rudolph-Lilith, M., Fournier, J., Levy, M., et al. (2008). High-resolution intracellular recordings using a real-time computational model of the electrode. *Neuron* 59, 379–391. doi: 10.1016/j.neuron.2008.06.021

Brunel, N., Chance, F. S., Fourcaud, N., and Abbott, L. F. (2001). Effects of synaptic noise and filtering on the frequency response of spiking neurons. *Phys. Rev. Lett.* 86, 2186–2189. doi: 10.1103/physrevlett.86.2186

Carnevale, N., and Hines, M. (2006). *The Neuron Book*. Cambridge, MA: Cambridge University Press.

Couto, J., Linaro, D., De Schutter, E., and Giugliano, M. (2015). On the firing rate dependency of the phase response curve of rat Purkinje neurons *in vitro*. *PLoS Comput. Biol.* 11:e1004112. doi: 10.1371/journal.pcbi.1004112

Cox, D., and Miller, H. (1965). *The Theory of Stochastic Processes*. Chapman: Hall.

D'Souza, R. D., and Burkhalter, A. (2017). A laminar organization for selective cortico-cortical communication. *Front. Neuroanat.* 11:71. doi: 10.3389/fnana.2017.00071

Dayan, P., and Abbott, L. F. (2005). *Theoretical Neuroscience*. Cambridge, MA: MIT Press.

Destexhe, A., Rudolph, M., and Paré, D. (2003). The high-conductance state of neocortical neurons *in vivo*. *Nat. Rev. Neurosci.* 4, 739–751. doi: 10.1038/nrn1198

Druckmann, S., Banitt, Y., Gidon, A., Schüermann, F., Markram, H., and Segev, I. (2007). A novel multiple objective optimization framework for constraining conductance-based neuron models by experimental data. *Front. Neurosci.* 1, 7–18. doi: 10.3389/neuro.01.1.1.001.2007

Druckmann, S., Berger, T., Hill, S., Schüermann, F., Markram, H., and Segev, I. (2008). Evaluating automated parameter constraining procedures of neuron models by experimental and surrogate data. *Biol. Cybern.* 99, 371–379. doi: 10.1007/s00422-008-0269-2

Eyal, G., Mansvelder, H. D., de Kock, C. P., and Segev, I. (2014). Dendrites impact the encoding capabilities of the axon. *J. Neurosci.* 34, 8063–8071. doi: 10.1523/JNEUROSCI.5431-13.2014

Fourcaud-Trocmé, N., Hansel, D., van Vreeswijk, C., and Brunel, N. (2003). How spike generation mechanisms determine the neuronal response to fluctuating inputs. *J. Neurosci.* 23, 11628–11640. doi: 10.1523/JNEUROSCI.23-37-11628.2003

Gentet, L. J. (2012). Functional diversity of supragranular GABAergic neurons in the barrel cortex. *Front. Neural Circuits* 6:52. doi: 10.3389/fncir.2012.00052

Gillespie, D. T. (1996). Exact numerical simulation of the Ornstein-Uhlenbeck process and its integral. *Phys. Rev. E* 54, 2084–2091. doi: 10.1103/physreve.54.2084

Goriounova, N. A., Heyer, D. B., Wilbers, R., Verhoog, M. B., Giugliano, M., Verbist, C., et al. (2018). Large and fast human pyramidal neurons associate with intelligence. *eLife* 7:e41714. doi: 10.7554/eLife.41714

Hestrin, S., and Armstrong, W. E. (1996). Morphology and physiology of cortical neurons in layer I. *J. Neurosci.* 16, 5290–5300. doi: 10.1523/JNEUROSCI.16-17-05290.1996

Higgs, M. H., and Spain, W. J. (2009). Conditional bursting enhances resonant firing in neocortical layer 2-3 pyramidal neurons. *J. Neurosci.* 29, 1285–1299. doi: 10.1523/JNEUROSCI.3728-08.2009

Hines, M. L., and Carnevale, N. T. (2001). NEURON: a tool for neuroscientists. *Neuroscientist* 7, 123–135. doi: 10.1177/107385840100700207

Ilin, V., Malyshev, A., Wolf, F., and Volgushev, M. (2013). Fast computations in cortical ensembles require rapid initiation of action potentials. *J. Neurosci.* 33, 2281–2292. doi: 10.1523/JNEUROSCI.0771-12.2013

Jiang, X., Wang, G., Lee, A. J., Stornetta, R. L., and Zhu, J. J. (2013). The organization of two new cortical interneuronal circuits. *Nat. Neurosci.* 16, 210–218. doi: 10.1038/nn.3305

Kondgen, H., Geisler, C., Fusi, S., Wang, X. J., Lüscher, H. R., and Giugliano, M. (2008). The dynamical response properties of neocortical neurons to temporally modulated noisy inputs *in vitro*. *Cereb. Cortex* 18, 2086–2097. doi: 10.1093/cercor/bhm235

Larkum, M. E. (2013). The yin and yang of cortical layer 1. *Nat. Neurosci.* 16, 114–115. doi: 10.1038/nn.3317

Larkum, M. E., and Phillips, W. A. (2016). Does arousal enhance apical amplification and disamplification? *Behav. Brain Sci.* 39:e215. doi: 10.1017/s0140525x15001867

Larkum, M. E., and Zhu, J. J. (2002). Signaling of layer 1 and whisker-evoked Ca^{2+} and Na^{+} action potentials in distal and terminal dendrites of rat neocortical pyramidal neurons *in vitro* and *in vivo*. *J. Neurosci.* 22, 6991–7005. doi: 10.1523/JNEUROSCI.22-16-06991.2002

Linaro, D., Biro, I., and Giugliano, M. (2018). Dynamical response properties of neocortical neurons to conductance-driven time-varying inputs. *Eur. J. Neurosci.* 47, 17–32. doi: 10.1111/ejn.13761

Linaro, D., Couto, J., and Giugliano, M. (2014). Command-line cellular electrophysiology for conventional and real-time closed-loop experiments. *J. Neurosci. Methods* 230, 5–19. doi: 10.1016/j.jneumeth.2014.04.003

Linaro, D., Couto, J., and Giugliano, M. (2015). Real-time electrophysiology: using closed-loop protocols to probe neuronal dynamics and beyond. *J. Vis. Exp.* 100:e52320. doi: 10.3791/52320

Linaro, D., Ocker, G. K., Doiron, B., and Giugliano, M. (2019). Correlation transfer by layer 5 cortical neurons under recreated synaptic inputs *in vitro*. *J. Neurosci.* 39, 7648–7663. doi: 10.1523/JNEUROSCI.3169-18.2019

Markram, H., Muller, E., Ramaswamy, S., Reimann, M. W., Abdellah, M., Sanchez, C. A., et al. (2015). Reconstruction and simulation of neocortical microcircuitry. *Cell* 163, 456–492. doi: 10.1016/j.cell.2015.09.029

Marmarelis, P. Z., and Naka, K. (1972). White-noise analysis of a neuron chain: an application of the Wiener theory. *Science* 175, 1276–1278. doi: 10.1126/science.175.4027.1276

Merino, R. M., Leon-Pinzon, C., Stühmer, W., Möck, M., Staiger, J. F., Wolf, F., et al. (2019). Background correlations selectively boost the γ-sensitivity of cortical gabaergic neurons. *bioArxiv* [Preprint]. doi: 10.1101/2019.12.19.882639

Muralidhar, S., Wang, Y., and Markram, H. (2013). Synaptic and cellular organization of layer 1 of the developing rat somatosensory cortex. *Front. Neuroanat.* 7:52. doi: 10.3389/fnana.2013.00052

Naundorf, B., Wolf, F., and Volgushev, M. (2006). Unique features of action potential initiation in cortical neurons. *Nature* 440, 1060–1063. doi: 10.1038/nature04610

Press, W. H. (2007). *Numerical Recipes 3rd Edition: The Art of Scientific Computing*. Cambridge, MA: Cambridge University Press.

Schuman, B., Machold, R. P., Hashikawa, Y., Fuzik, J., Fishell, G. J., and Rudy, B. (2019). Four unique interneuron populations reside in neocortical layer 1. *J. Neurosci.* 39, 125–139. doi: 10.1523/JNEUROSCI.1613-18.2018

Tchumatchenko, T., and Wolf, F. (2011). Representation of dynamical stimuli in populations of threshold neurons. *PLoS Comput. Biol.* 7:e1002239. doi: 10.1371/journal.pcbi.1002239

Testa-Silva, G., Verhoog, M. B., Linaro, D., de Kock, C. P. J., Baayen, J. C., Meredith, R. M., et al. (2014). High bandwidth synaptic communication and frequency tracking in human neocortex. *PLoS Biol.* 12:e1002007. doi: 10.1371/journal.pbio.1002007

Tuckwell, H. C. (1988). *Introduction to Theoretical Neurobiology: Volume 2, Nonlinear and Stochastic Theories (Cambridge Studies in Mathematical Biology)*. Cambridge, MA: Cambridge University Press.

Wang, X.-J. (2010). Neurophysiological and computational principles of cortical rhythms in cognition. *Physiol. Rev.* 90, 1195–1268. doi: 10.1152/physrev.00035.2008

Zhu, Y., and Zhu, J. J. (2004). Rapid arrival and integration of ascending sensory information in layer 1 nonpyramidal neurons and tuft dendrites of layer 5 pyramidal neurons of the neocortex. *J. Neurosci.* 24, 1272–1279. doi: 10.1523/JNEUROSCI.4805-03.2004

Conflict of Interest: The authors declare that the research was conducted in the absence of any commercial or financial relationships that could be construed as a potential conflict of interest.

frontiers in Cellular Neuroscience

ORIGINAL RESEARCH
published: 28 May 2021
doi: 10.3389/fncel.2021.688905

Chemogenetic Activation of Feed-Forward Inhibitory Parvalbumin-Expressing Interneurons in the Cortico-Thalamocortical Network During Absence Seizures

*Sandesh Panthi and Beulah Leitch**

Department of Anatomy, School of Biomedical Sciences, Brain Health Research Centre, University of Otago, Dunedin, New Zealand

OPEN ACCESS

Edited by:
Victor Anggono, The University of Queensland, Australia

Reviewed by:
Arne Ittner, Flinders University, Australia
Robert C. Wykes, University College London, United Kingdom

***Correspondence:**
Beulah Leitch
beulah.leitch@otago.ac.nz

Specialty section:
This article was submitted to Cellular Neurophysiology, a section of the journal Frontiers in Cellular Neuroscience

Received: *31 March 2021*
Accepted: *04 May 2021*
Published: *28 May 2021*

Citation:
Panthi S and Leitch B (2021) Chemogenetic Activation of Feed-Forward Inhibitory Parvalbumin-Expressing Interneurons in the Cortico-Thalamocortical Network During Absence Seizures. Front. Cell. Neurosci. 15:688905. doi: 10.3389/fncel.2021.688905

Parvalbumin-expressing (PV+) interneurons are a subset of GABAergic inhibitory interneurons that mediate feed-forward inhibition (FFI) within the cortico-thalamocortical (CTC) network of the brain. The CTC network is a reciprocal loop with connections between cortex and thalamus. FFI PV+ interneurons control the firing of principal excitatory neurons within the CTC network and prevent runaway excitation. Studies have shown that generalized spike-wave discharges (SWDs), the hallmark of absence seizures on electroencephalogram (EEG), originate within the CTC network. In the stargazer mouse model of absence epilepsy, reduced FFI is believed to contribute to absence seizure genesis as there is a specific loss of excitatory α-amino-3-hydroxy-5-methyl-4-isoxazolepropionic acid receptors (AMPARs) at synaptic inputs to PV+ interneurons within the CTC network. However, the degree to which this deficit is directly related to seizure generation has not yet been established. Using chemogenetics and *in vivo* EEG recording, we recently demonstrated that functional silencing of PV+ interneurons in either the somatosensory cortex (SScortex) or the reticular thalamic nucleus (RTN) is sufficient to generate absence-SWDs. Here, we used the same approach to assess whether activating PV+ FFI interneurons within the CTC network during absence seizures would prevent or reduce seizures. To target these interneurons, mice expressing Cre recombinase in PV+ interneurons (PV-Cre) were bred with mice expressing excitatory Gq-DREADD (hM3Dq-flox) receptors. An intraperitoneal dose of pro-epileptic chemical pentylenetetrazol (PTZ) was used to induce absence seizure. The impact of activation of FFI PV+ interneurons during seizures was tested by focal injection of the "designer drug" clozapine N-oxide (CNO) into either the SScortex or the RTN thalamus. Seizures were assessed in PV^{Cre}/Gq-DREADD animals using EEG/video recordings. Overall, DREADD-mediated activation of PV+ interneurons provided anti-epileptic effects against PTZ-induced seizures. CNO activation of FFI either prevented PTZ-induced absence seizures or suppressed their severity. Furthermore, PTZ-induced

tonic-clonic seizures were also reduced in severity by activation of FFI PV+ interneurons. In contrast, administration of CNO to non-DREADD wild-type control animals did not afford any protection against PTZ-induced seizures. These data demonstrate that FFI PV+ interneurons within CTC microcircuits could be a potential therapeutic target for anti-absence seizure treatment in some patients.

Keywords: cortico-thalamocortical, parvalbumin, GABAergic interneurons, feed-forward inhibition, DREADDs, absence seizures, pentylenetetrazol

INTRODUCTION

Childhood absence epilepsy (CAE) is the most common form of pediatric epilepsy, which is characterized by synchronous 3–4 Hz generalized spike-wave discharges (SWDs) associated with impaired awareness. Absence seizures are known to arise from altered dynamics within the cortico-thalamocortical (CTC) network (McCormick and Contreras, 2001; Crunelli and Leresche, 2002; Maheshwari and Noebels, 2014; Lüttjohann and van Luijtelaar, 2015; Crunelli et al., 2020) but the precise cellular and molecular mechanisms are not fully understood and appear to be multifactorial. Within the CTC network, feed-forward inhibition (FFI) is essential to prevent runaway excitation and is mediated by fast-spiking parvalbumin-expressing (PV+) inhibitory interneurons. Studies conducted using the well-established stargazer mouse model of absence epilepsy have shown defects in α-amino-3-hydroxy-5-methyl-4-isoxazolepropionic acid receptor (AMPAR) expression at excitatory synapses in feed-forward inhibitory PV+ interneurons in the somatosensory cortex (SScortex) (Maheshwari et al., 2013; Adotevi and Leitch, 2016, 2017, 2019) and reticular thalamic nuclei (RTN) (Menuz and Nicoll, 2008; Barad et al., 2012) of the CTC network. The loss of synaptic AMPARs is the result of a genetic mutation in stargazin, a transmembrane AMPAR regulatory protein (TARP) (Noebels et al., 1990; Letts et al., 1998) that traffics AMPARs to the synapse. However, the extent to which this defect weakens FFI within the CTC network and whether this directly contributes toward the generation and maintenance of absence seizures had not been previously established. We recently reported that acute selective silencing of PV+ interneurons in the CTC network (either in the SScortex or the RTN thalamus) impairs FFI and generates absence-like SWDs in normal non-epileptic mice (Panthi and Leitch, 2019). In the current study, the goal was to determine the impact of selectively activating PV+ inhibitory interneurons within the CTC network during absence seizures, to determine if this was sufficient to prevent or reduce seizure activity.

To investigate the consequences of activating feed-forward inhibitory PV+ interneurons *in vivo*, we used Designer Receptors Exclusively Activated by Designer Drugs (DREADD) based technology (Armbruster et al., 2007). DREADDs are mutationally modified muscarinic acetylcholine (ACh) receptors, which can be specifically expressed in a targeted cell population and exclusively activated by the designer drug clozapine N-oxide (CNO), but not by their endogenous ligand ACh (Armbruster et al., 2007; Rogan and Roth, 2011). In this study, we used excitatory Gq-DREADDs inserted into PV+ interneurons to selectively activate FFI (Alexander et al., 2009). Cre-dependent excitatory Gq-DREADD mice (i.e., hM3Dq-flox mice) were crossed with PV-Cre mice to express Gq-DREADDs in PV+ interneurons (Zhu et al., 2016). Selective activation of FFI within the CTC network was achieved by focal injection of CNO into cortical or thalamic regions of interest (Panthi and Leitch, 2019).

To induce absence seizure in PV^{Cre}/Gq-DREADD mice we used pentylenetetrazol (PTZ). This chemical is routinely used in epileptic studies to induce both absence and generalized tonic-clonic seizures (Snead, 1992; Velíšková et al., 2017) and has been used in the screening of antiepileptic drugs since 1970s (see reviews by Krall et al., 1978 and Löscher, 2011). PTZ impairs GABA mediated inhibition by antagonizing $GABA_A$ receptors (Huang et al., 2001). The severity of PTZ induced seizures is dose dependent. Low dose PTZ administration (i.e., ∼20 mg/kg) is an established experimental method to pharmacologically induce generalized absence seizures involving thalamocortical mechanisms whereas high doses (>40 mg/kg) induce spike trains with tonic-clonic seizures (Snead, 1992; Snead et al., 2000; Cortez et al., 2016).

To date, there have been relatively few studies investigating the impact of activating PV+ interneurons during PTZ-induced seizures. Clemente-Perez et al. (2017) used PTZ treatment combined with optogenetic activation of PV+ interneurons to selectively modulate PV+ neurons in the RTN thalamus during free behavior. They found that unilateral optical stimulation of RTN PV+ interneurons during PTZ-induced seizures disrupts bilateral generalized seizures in PV-Cre mice injected with channelrhodopsin-2 (ChR2). Another recent DREADD-based study indicated that global activation of PV+ interneurons increases the latency and decreases the susceptibility of PTZ-induced tonic-clonic and myoclonic seizures (Johnson et al., 2018). Other studies have used different chemicals to study the impact of activating PV+ interneurons during pharmacologically induced seizures. For example, Assaf and Schiller (2016) demonstrated that optogenetic activation of cortical PV+ interneurons causes the termination of 4-aminopyridine (4-AP) induced spontaneous electrographic seizures. Activating hippocampal PV+ interneurons, on the other hand, attenuates temporal lobe seizures induced by kainic acid (KA) (Krook-Magnuson et al., 2013; Wang et al., 2018). Additionally, parvalbumin knockout ($PV^{-/-}$) mice have higher susceptibility to chemically induced seizures and these animals experience more severe seizures compared to wild-type ($PV^{+/+}$) controls

(Schwaller et al., 2004). However, there have been no published studies to date reporting the impact of activating PV+ interneurons within the CTC network during absence seizures using DREADD technology.

Hence, the aim of the current study was to test the impact of activating feed-forward inhibitory PV+ interneurons within the CTC network of PV^{Cre}/Gq-DREADD mice during PTZ-induced absence seizures, using simultaneous video/electroencephalogram (EEG) recording. We hypothesized that activating PV+ interneurons within the SScortex or the RTN thalamus would prevent or reduce PTZ-induced absence seizures.

MATERIALS AND METHODS

Animals and Breeding Paradigm

Experiments were performed on adult male and female double-transgenic mice expressing excitatory Gq-DREADD receptors in PV+ interneurons. Cre-recombinase conditional excitatory Gq-DREADD (i.e., hM3Dq-flox mice) and PV-Cre knockin mice were obtained from Jackson Laboratories, United States. Both transgenic mice were created on the background of C57BL/6 strain (Zhu et al., 2016). Detailed descriptions of hM3Dq-flox and PV-Cre knockin mouse lines can be found in Jackson laboratories datasheets stock no. 026220[1] and stock no. 008069[2], respectively. Homozygous female PV-Cre mice were crossed with heterozygous hM3Dq-floxed males to generate litters with PV^{Cre}/Gq-DREADD and non-DREADD expressing wild-type (WT) control littermates, as illustrated in **Supplementary Figure 1A**. The hM3Dq-floxed mice have a *loxP*-flanked STOP cassette designed to prevent transcription of the downstream HA-hM3Dq-pta-mCitrine coding region (**Supplementary Figure 1A**). Mating these strains (PV-Cre and hM3Dq-floxed) removes the *loxP*-flanked STOP cassette only in the cell type specified by the Cre-recombinase system (Zhu et al., 2016). This allows the strong expression of hemagglutinin (HA)-tag only in PV+ interneurons. In this study, only female PV-Cre mice were crossed with male hM3Dq-flox mice to avoid unwanted germline recombination. Mice were bred and housed at the University of Otago Animal Facility at a controlled room temperature (22–24°C) with *ad libitum* access to food and water.

Genotyping

Genotyping was performed to verify the mouse genotype. Ear notches were collected from offspring of PV-Cre × hM3Dq-flox mice. They were mixed in DNA lysis buffer and proteinase K (Roche, Basel) and digested overnight at 55°C. The following day samples were centrifuged and DNA was obtained to process for PCR. Genotyping was performed separately to confirm Cre knockin and hM3Dq-flox using the following Cre, hM3Dq mutant and wild-type primers (Integrated DNA technologies, United States): CCT GGA AAA TGC TTC TGT CCG Cre-forward; CAG GGT GTT ATA AGC AAT CCC reverse for Cre allele; CGC CAC CAT GTA CCC ATA C hM3Dq-flox forward; GTG GTA CCG TCT GGA GAG GA reverse for hM3Dq-flox allele; AAG GGA GCT GCA GTG GAG TA wild-type forward; CCG AAA ATC TGT GGG AAG TC reverse for wild-type allele. PCR product was allowed to run in agarose gel at 70–80 V for around 2 h. The gel was then placed in a UV light source to view and photograph bands. **Supplementary Figure 1B** is a representative image of gel electrophoresis blot for the PV-Cre knockin and hM3Dq-flox for three separate mice. Bands at 300 and 350 bp confirmed the PV-Cre knockin whereas bands at 204 and 300 bp indicated heterozygous hM3Dq-flox, and a band around 300 bp confirmed wild-type mice (**Supplementary Figure 1B**).

Immunofluorescence Confocal Microscopy

Adult mice from PV-Cre × hM3Dq-flox colony were deeply anesthetized with an intraperitoneal (i.p.) injection of 60 mg/kg of sodium pentobarbital. Transcardial perfusion was performed with 5% heparin in 0.1 M phosphate buffered saline (PBS) followed by 4% paraformaldehyde (PFA) in 0.1 M Sorensen's phosphate buffer. Brains were extracted and post-fixed in 4% PFA overnight at 4°C. After post-fixation, brains were washed three times in 0.1 M PBS. This was followed by cryoprotection of the brains in increasing concentration of sucrose in PBS i.e., 10% for 30 min, 20% for 30 min, and 30% at 4°C until fully infiltrated with sucrose. The cerebellum was dissected from the rest of the brain, which was then sectioned into 30 μm coronal sections. The cerebellum was also sectioned into 30 μm sagittal sections. Sectioning was performed on a freezing cryostat (Leica CM1950, Wetzlar, Germany). Sections were collected into 12-well plates containing PBS.

For immunolabelling, sections were first submerged in blocking buffer [4% Normal Goat Serum (NGS), 0.1% Bovine Serum Albumin (BSA), 0.1% Triton X-100 in PBS] for 2 h at room temperature. All sections were then incubated in a mixture of primary antibodies for 48 h at 4°C. Primary and secondary antibodies used for immunofluorescence confocal microscopy in this study are listed in **Table 1**. Primary antibody solution was prepared in PBS with 0.1% BSA and 0.3% Triton X-100. After incubation in primary antibodies, tissue sections were washed in PBS for 45 min (15 min × 3 times). Sections were then labeled

TABLE 1 | Primary and secondary antibodies used in this study for immunofluorescence confocal microscopy.

Product	Antibody/Type	Source/Catalog No.	Dilution
Parvalbumin	Primary/Mouse monoclonal	Swant/235	1:2000
HA-tag	Primary/Rabbit polyclonal	Cell Signaling/3724S	1:500
Goat anti-rabbit	Secondary/Alexa Fluor 488	Life Technologies/11008	1:1000
Goat anti-mouse	Secondary/Alexa Fluor 568	Life Technologies/11031	1:1000

[1]https://www.jax.org/strain/026220

[2]https://www.jax.org/strain/008069

with secondary antibodies for 12 h at 4°C. After labeling the tissues with secondary antibodies, they were washed in PBS for 30 min (10 min × 3 times). Sections were then mounted on polysine-coated glass slides and cover-slipped with mounting medium (1,4 diazabicyclo (2.2.2) octane DABCO-glycerol). Slides were left to air-dry in the dark at room temperature.

Image Acquisition and Analysis

Images were acquired using Nikon A1+ inverted confocal laser scanning microscope. Channel configurations were set for HA-tag (magenta channel, 488 nm laser excitation) and PV (cyan channel, 568 nm laser excitation). During confocal imaging, the detector offset for each channel was kept at zero; the detector gain and laser power were optimized accordingly. Scan speed and image pixel size were also set accordingly. Images were taken of the region of interest (ROI) in the SScortex, RTN thalamus and cerebellum. All immunolabelled cells in the SScortex and cerebellum sections were counted at 10× confocal images whereas those in RTN thalamus were counted using 40× confocal images. Cell counting and analysis were performed using ImageJ (Fiji) software (version 1.51, NIH, United States).

Surgical Implantation of Prefabricated Head Mounts and Microcannulas for EEG Recordings

Twelve-week old PV^{Cre}/Gq-DREADD mice were single-housed and were handled once daily for 2 days before performing surgical manipulation. Surgery was performed after subcutaneous injection of 5 mg/kg of Carprofen (for pain control) and 2 mg/kg of Marcaine (for local anesthesia). Animals were fully anesthetized with a continuous flow of isoflurane during surgical procedures. Animals were provided with supplementary heat during surgery by placing them on a heat pad. The head of the animal was fixed with a stereotaxic frame (David Kopf Instruments, Tujunga, CA, United States). After shaving the scalp to expose the skin, a sagittal incision was made. Two pairs of holes were carefully drilled in the skull, each pair located 1.5 mm on either side of the longitudinal fissure. The first pair was located 3.5 mm anterior to bregma and the second pair 1 mm anterior to bregma. Four stainless steel screws with lead wires attached (Pinnacle Technologies, Austin, TX, United States) were inserted through these burr holes. The screw wires were then soldered to their respective channels on a prefabricated head mount (Pinnacle Technologies, Austin, TX, United States). Dental acrylic cement (Vertex Dental, Netherlands) was used to secure soldered regions.

In this study, a guide cannula (26 gauge) was implanted for focal CNO injections, based on the stereotaxic coordinates either for the SScortex (AP: −1.22 to −2.06 mm, ML: 2.8 mm) or the RTN thalamus (AP: −1.34 to −1.94 mm, ML: 2.1–2.3 mm) (Mouse Brain Atlas, Paxinos and Franklin, 3rd Edition). A dummy cannula was inserted inside the guide cannula to prevent blood or any other fluid clogging it. During CNO injections, the dummy cannula was replaced with an internal cannula (33 gauge). CNO was delivered via a Hamilton microinjection syringe attached to polythene tubing (Microtube Extrusions, Australia) and internal cannula. Guide (C315GS-2/SPC), dummy (C315IDCS-2/SPC), and internal (C315IS-2/SPC) cannulae were obtained from Plastics One Inc., Roanoke, VA, United States. Cannulae were made of stainless steel with short pedestals.

EEG Recording

After the full recovery of animals from surgical manipulation (at least 7 days after surgery), EEG recordings were made from the subdural space over the cerebral cortex using the Pinnacle mouse system (Pinnacle Technologies, Austin, TX, United States) with simultaneous video recording. The head-mount was attached to a pre-amplifier to amplify and filter the EEG waveforms. EEG signals were filtered at 0.5 Hz high pass and 50 Hz low pass. Before each recording, animals were acclimatized in the testing environment and equipment for 1 h.

Before performing the main experiments, a pilot study was conducted to determine the dose of PTZ necessary to induce absence seizures. Briefly, a cohort of animals ($n = 6$) was injected intraperitoneally with three different doses of PTZ (10, 20, and 30 mg/kg). Based on simultaneous video/EEG data, a dose of 20 mg/kg was selected as the lowest dose that produced absence seizures in all pilot animals tested.

For experimental tests, PV^{Cre}/Gq-DREADD ($n = 14$) and non-DREADD WT control ($n = 10$) animals were allocated to two different treatment groups: either SScortex cannula-implanted group (DREADD animals $n = 7$; WT controls $n = 5$) or RTN thalamus implanted group (DREADD animals $n = 7$; WT controls $n = 5$). Experiments were performed on two consecutive days. On day 1, seizures were induced in all animals (PV^{Cre}/Gq-DREADD mice and non-DREADD WT control mice) by injection (i.p.) of 20 mg/kg PTZ. After 24 h, on day 2, the same cohort of animals was treated with the same dose of PTZ (i.p.) and 5 mg/kg CNO (into either the SScortex or the RTN thalamus). The timing and dose of CNO was based on our previous work (Panthi and Leitch, 2019) where 5 mg/kg CNO was lowest effective dose that activated inhibitory Gi-DREADD receptors and generated absence-like seizures in PV^{Cre}/Gi-DREADD animals.

Preparation and Delivery of CNO and PTZ

Clozapine N-oxide and PTZ were freshly prepared before every scheduled experiment. 1.5 mg of CNO (Advanced Molecular Technologies, Australia) was dissolved in 75 µl of dimethyl sulfoxide (DMSO). The volume was then adjusted to 3 ml by addition of 0.9% sterile saline to prepare CNO of 0.5 mg/ml concentration. PTZ doses of 3, 2, and 1 mg/ml concentration were prepared in 0.9% sterile saline for 30, 20, and 10 mg/kg dosage groups, respectively. PTZ was injected intraperitoneally based on the calculated dose for the body weight of the animal. On day 2, CNO (5 mg/kg) was injected focally (either into SScortex or RTN thalamus). After 10 min of baseline EEG recording, 0.3 µl of CNO was infused into the regional areas at a rate of 0.1 µl/min via Hamilton microinjection syringe. On conclusion of the experiments, mice were anesthetized and

methylene blue dye was injected at the same volume and rate as CNO into the focal region of the brain under investigation to verify the CNO diffusion and localization of cannula tip and histology was performed (**Supplementary Figure 2**).

Analysis of EEG Traces

Sirenia® software was used for acquisition of video/EEG traces (Panthi and Leitch, 2019). Traces were manually analyzed by an investigator blind to the experimental conditions using Seizure Pro® software. Bursts of oscillations were counted as absence-like SWDs if they had a spike-wave structure (spike, positive transient, and slow wave pattern), frequency of 3–8 Hz, an amplitude at least two times higher than baseline and lasted >1 s. Video was analyzed for concomitant behavioral arrest or motionless staring. EEG waveforms due to muscle activity, walking or scratching and grooming were considered as artifacts after confirmation of the behavior via simultaneous video analysis. Tonic-clonic seizures were characterized by high amplitude polyspikes lasting >1 s. Behavioral expressions for tonic-clonic seizures ranged from clonic jerking with or without loss of balance to wild jumping in some cases (Lüttjohann et al., 2009; Van Erum et al., 2019). Other types of epileptic events (such as brief generalized myoclonic jerks) different from above mentioned criteria for SWDs and tonic-clonic seizures were categorized as other types of seizures.

Data Analysis

Statistical analyses of significant differences in the onset of seizures between PV^{Cre}/Gq-DREADD and non-DREADD WT control animals were calculated using Mantel-Cox log-rank test. Comparison within the same treatment group was performed using Wilcoxon matched-pairs signed-rank test. Comparison between treatment groups was performed using Mann Whitney unpaired rank test. Data were presented as mean ± standard error of the mean (SEM). All statistical analysis was performed in GraphPad Prism 8.0 with statistical significance set at $p < 0.05$ (asterisks for p value: $^{*}p < 0.05$, $^{**}p < 0.01$, $^{***}p < 0.001$, and $^{****}p < 0.0001$).

RESULTS

Excitatory Gq-DREADD Receptors Are Expressed in Feed-Forward Inhibitory PV+ Interneurons

To confirm the expression of excitatory Gq-DREADD receptors in PV+ interneurons of PV^{Cre}/Gq-DREADD mice, we first performed double-labeled immunohistochemistry with antibodies against HA-tag and PV (**Figure 1**). HA-tag (identified by pseudo color magenta **Figure 1**, panel 1) was only expressed in the brain sections from PV^{Cre}/Gq-DREADD mice but not non-DREADD WT control animals. PV+ interneurons (identified by pseudo color cyan **Figure 1**, panel 2) were highly expressed in SScortical layers II-VI, in the RTN thalamus and in the cerebellar cortex of all genotypes (**Figure 1**). Co-localization of HA-tag and PV (**Figure 1**. white arrows) was above 90% in the SScortex (**Figures 1A,B**), the RTN thalamus (**Figures 1C,D**) and the cerebellar cortex (**Figures 1E,F**). In the cerebellum, HA-tag was highly expressed in PV+ Purkinje soma (**Figure 1E** white arrows). The percentage of co-localization of HA-tag in PV+ inhibitory Purkinje cell soma was also above 90% (**Figure 1F**). The pattern of staining and levels of co-localization between HA-tag and PV in all three brain regions of PV^{Cre}/Gq-DREADD animals were very similar to the results obtained in PV^{Cre}/Gi-DREADD animals in our previous published report (Panthi and Leitch, 2019).

20 mg/kg IP PTZ Is Required to Induce Absence-SWDs

To establish the dose of PTZ required to induce absence seizures, an EEG pilot study was first conducted on a cohort of animals ($n = 6$) that had not been surgically implanted with cannulae for focal delivery of CNO (**Figure 2A**). According to the literature, absence-SWDs can be induced in different mice and rat models using i.p. injections of PTZ at doses between 10 and 40 mg/kg (Marescaux et al., 1984; Snead et al., 2000; Girard et al., 2019; Van Erum et al., 2019). In this study, simultaneous video/EEG data showed that 10 mg/kg of PTZ did not induce seizures in any of the mice tested (**Figure 2B**), whereas doses of ≥30 mg/kg PTZ induced severe tonic-clonic seizures (**Figure 2D**). In contrast, a dose of 20 mg/kg consistently produced absence-SWDs (**Figure 2C** asterisks); although these were mixed with some tonic-clonic seizures (**Figure 2C**). As 20 mg/kg PTZ was the lowest dose that produced primarily absence seizures, it was selected as the dose injected into mice surgically implanted with either a cortical or thalamic cannula for subsequent experiments to test the impact of focally activating FFI within the CTC network during PTZ-induced absence seizures.

Activating Feed-Forward Inhibitory PV+ Interneurons via Focal CNO Injection Suppressed PTZ-Induced Absence Seizures

The protocol and timeline for testing the impact of activating PV+ interneurons during PTZ-induced absence seizures is shown in **Figures 3**, **4**. Experimental animals (implanted with either a cortical or thalamic cannula and scalp EEG electrodes) were injected with 20 mg/kg (i.p.) on day 1 to establish baseline seizure EEG profile; then the same cohort of animals were injected on day 2 with both PTZ (20 mg/kg) and CNO (5 mg/kg) focally delivered to ROI to activate FFI microcircuits within the CTC network during seizures.

PTZ Injection on Day 1 Induced Absence-Like Seizures and Other Types of Generalized Seizures in Both DREADD and Non-DREADD Mice

Pentylenetetrazol (20 mg/kg) i.p. injection on day 1 induced epileptic seizures in all surgically implanted test animals. However, not all animals exhibited absence seizures. Tonic-clonic and other types of seizure were also seen in EEG (**Figures 5**, **6**). In the SScortex group, 20 mg/kg PTZ induced absence seizures in 5 out of 7 PV^{Cre}/Gq-DREADD and 3 out of 5 non-DREADD WT controls (**Table 2**). Six of the 7 DREADD mice and all 5

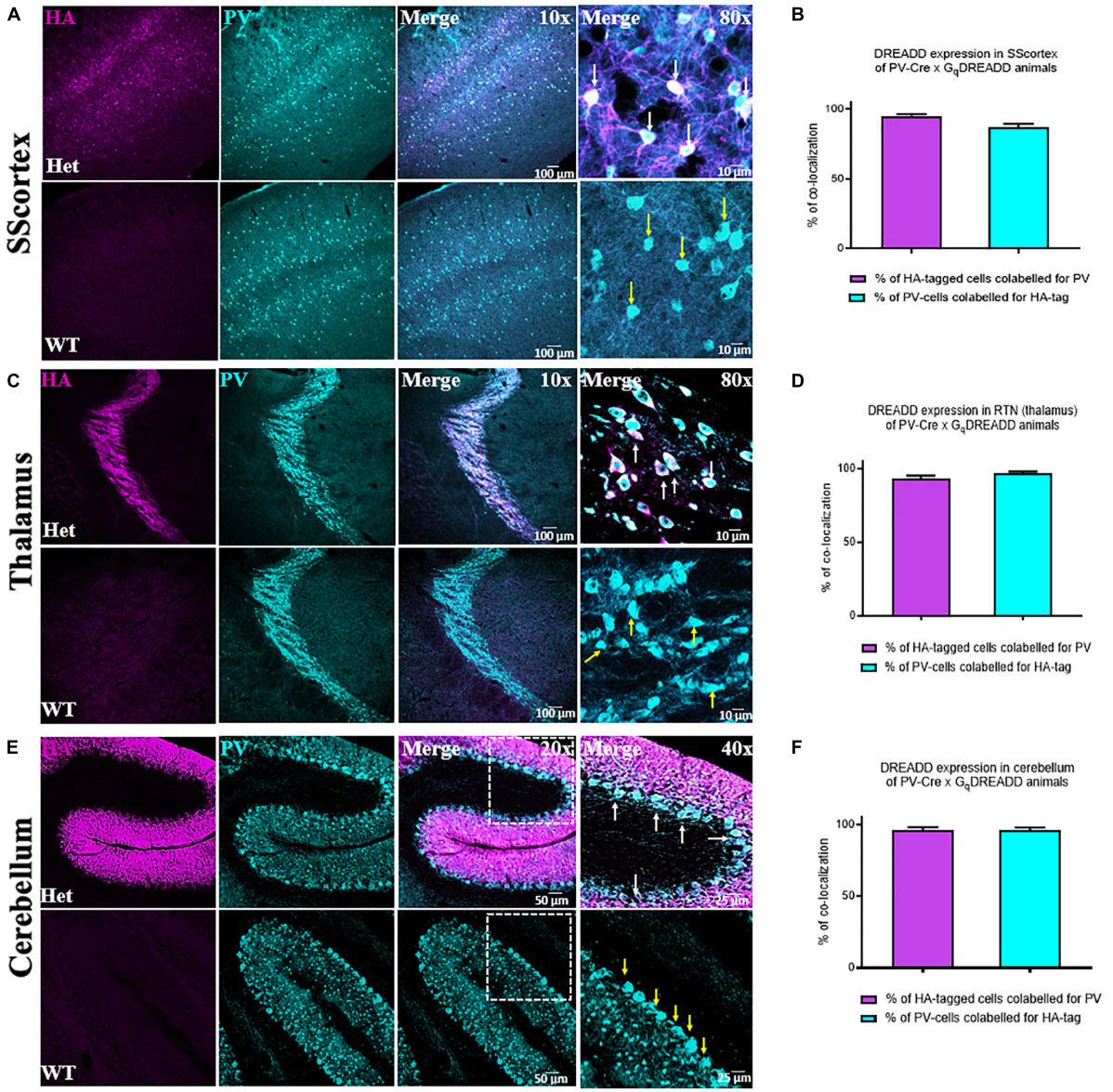

FIGURE 1 | (A,C,E) Confocal images showing the expression of HA-tag in PV+ interneurons in the SScortex, the RTN thalamus and the cerebellum of PV^{Cre}/Gq-DREADD animals, respectively. White arrows in merged images represent co-localized cells. Yellow arrows indicate PV positive neurons, which are immunonegative for HA. **(B,D,F)** Percentage of co-localization of HA-tag and PV in neurons in the SScortex, the RTN thalamus, and the cerebellum, respectively. Immunolabelled cells in the SScortex and the cerebellum were counted at 10× magnified confocal images whereas in the RTN thalamus cells were counted using 40× images (Het = PV^{Cre}/Gq-DREADD offspring from homozygous PV-Cre female and heterozygous hM3Dq-flox male; WT = Non-DREADD wild type control animals).

non-DREADD WT controls experienced tonic-clonic seizures. In the RTN thalamus cohort, absence seizures were observed in all DREADD mice (n = 7) and in 3 out of the 5 non-DREADD WT controls (**Table 2**). Tonic-clonic seizures occurred in only 3 out of 7 DREADD animals whereas all non-DREADD WT animals of this treatment group experienced tonic-clonic seizures.

Analysis of EEG data after PTZ administration on day 1, showed that the first incident of an epileptic seizure (of any type) was very consistent (**Figure 3B**). In the SScortex group mean onset of seizures was 3.65 ± 0.63 min in PV^{Cre}/Gq-DREADD mice (n = 7) and 3.59 ± 0.62 min in the non-DREADD WT control animals (n = 5). Similarly, in the RTN thalamus group seizures were induced 3.82 ± 0.74 min and 3.87 ± 1.03 min after PTZ injection in PV^{Cre}/Gq-DREADD (n = 7) and non-DREADD WT control animals (n = 5), respectively. The time at which seizures terminated was also similar between the treatment groups (**Figure 3C**). The last seizure burst in SScortex group was 20.50 ± 7.87 min and 14.41 ± 6.03 min after PTZ injection in the PV^{Cre}/Gq-DREADD (n = 7) and non-DREADD WT control animals (n = 5), respectively. Similarly, in the RTN

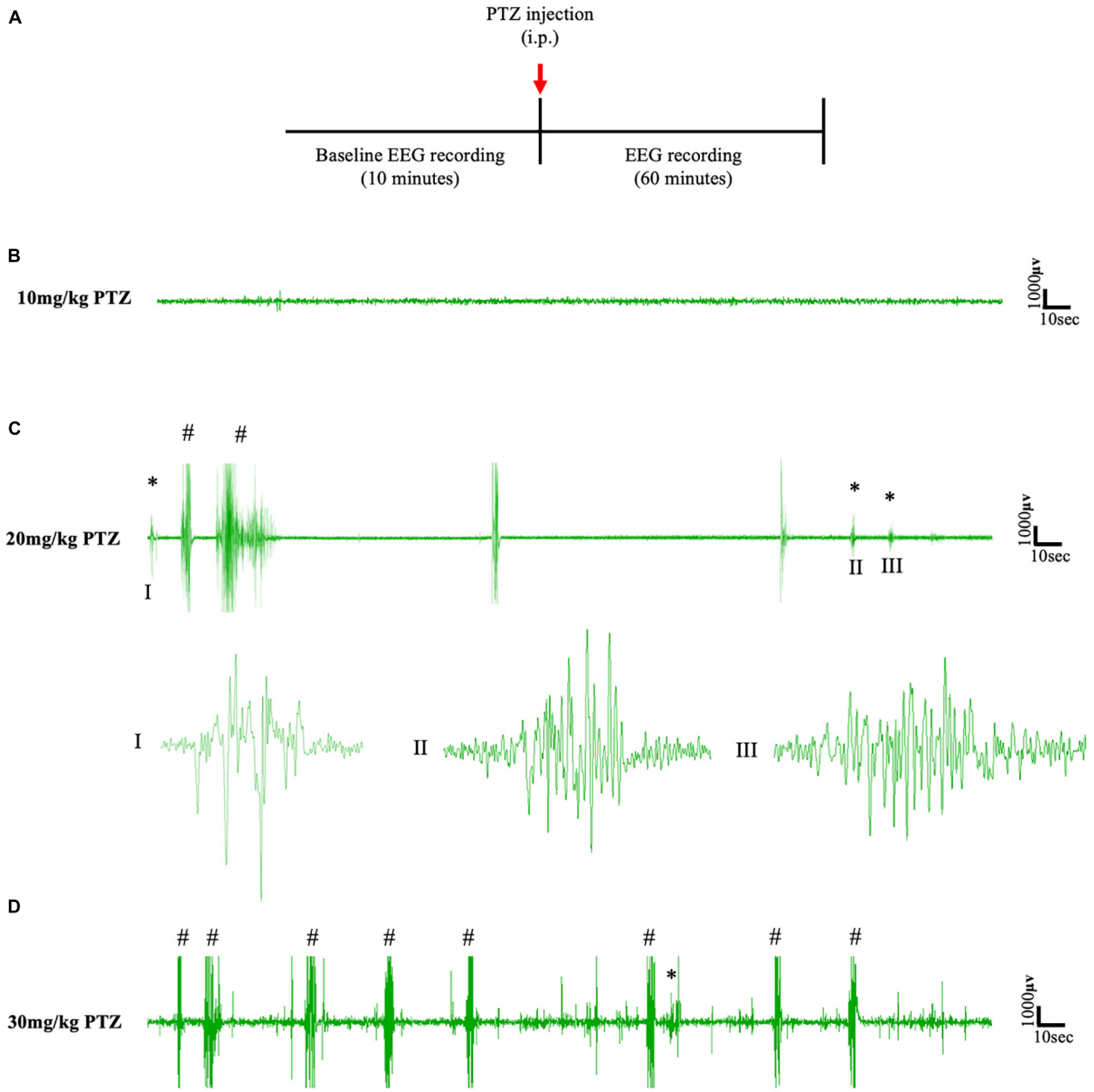

FIGURE 2 | (A) Schematic protocol for EEG recordings before and after IP PTZ injection in the pilot study. Representative EEG traces from animals after **(B)** 10 mg/kg **(C)** 20 mg/kg **(D)** 30 mg/kg of PTZ injection. Asterisks (*) and hash signs (#) represent absence-like seizures and tonic-clonic seizures, respectively. Each trace represents 5 min of EEG recording. All representative EEG traces were obtained from different animals.

thalamus group, last seizure burst was seen 13.07 ± 2.83 min and 14.27 ± 5.00 min after PTZ injection in DREADD (n = 7) and non-DREADD WT control animals (n = 5), respectively. So, in summary, there were no significant differences in the latency to the onset of first seizure or time of seizure termination between treatment groups and genotypes (**Figures 3B,C**) following a single injection of 20 mg/kg i.p. PTZ on day 1.

The relative time spent in PTZ-induced seizures during the 1 h EEG recording period on day 1 represented ≤2% of the total EEG test period (**Figures 4A,B**). The mean duration spent by DREADD SScortex group (n = 7) having absence-like seizures and tonic-clonic seizures was 17.85 ± 9.32 and 26.04 ± 11.15 s, respectively. Thus DREADD mice in the SScortex treatment group spent 36.13% of the overall seizure period having absence-like seizures and 52.70% experiencing tonic-clonic seizures (**Figure 4C**). Likewise, non-DREADD WT control animals spent 48.10% of total seizure period in absence seizures and 42.71% having tonic-clonic seizures (**Figure 4C**). The RTN thalamus group, DREADD animals (n = 7) displayed absence seizures for 31.11 ± 13.64 s and tonic-clonic seizures for 7.65 ± 2.96 s,

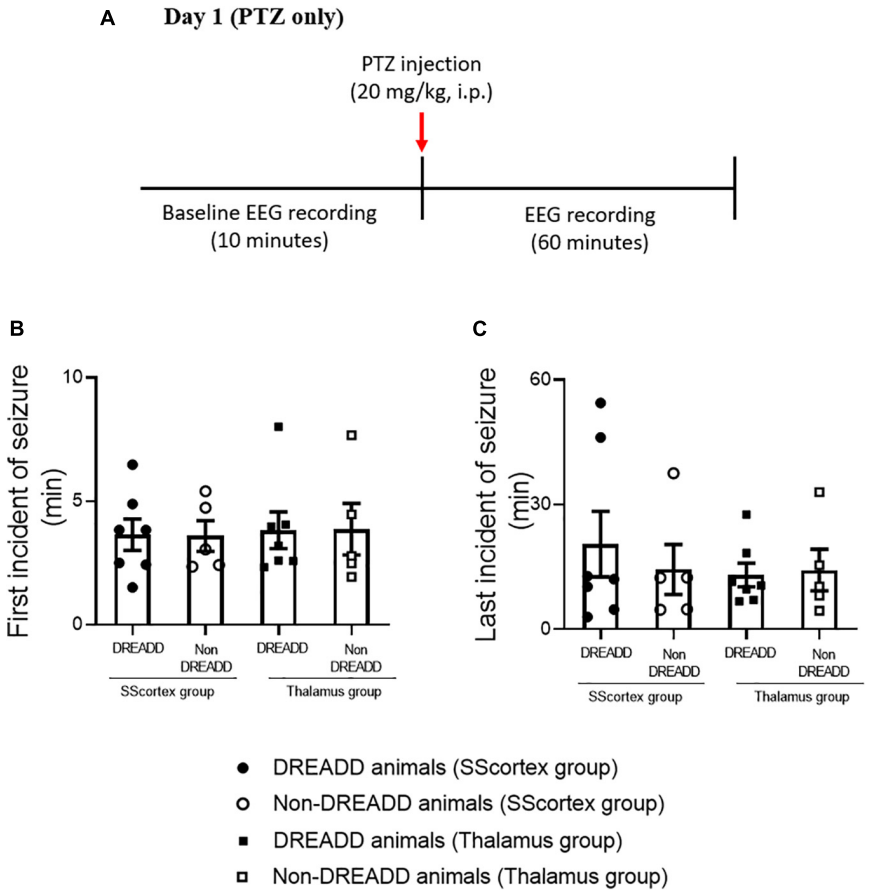

FIGURE 3 | (A) Schematic of protocol for EEG recordings before and after PTZ injection on day 1 in experimental animals. Comparison of **(B)** onset of seizure and **(C)** last incident of seizure during 1 h of EEG recording in PV^{Cre}/Gq-DREADD (DREADD) (n = 7) and non-DREADD (n = 5) WT control animals of the SScortex group and the RTN thalamus group after PTZ treatment on day 1. All values in graphs represent mean ± SEM. Comparison between treatment groups was performed using Mann Whitney unpaired rank test.

representing 51.05 and 12.56%, respectively of the overall seizure period (**Figure 4C**). Non-DREADD WT animals in the thalamic group spent 30.92% of total seizure period displaying absence seizures and 49.23% having tonic-clonic seizures (**Figure 4C**). Overall, there were no significant differences in type and duration of seizures displayed by DREADD and non-DREADD cohorts on day 1 after PTZ administration (**Figure 4C**).

CNO Injection Into the SScortex or Thalamus on Day 2 Changed the Time Spent in Seizures by DREADD Mice but Not Non-DREADD Controls

Next we injected the same cohort of mice on day 2 with both PTZ and CNO to test the impact of activating feed-forward inhibitory PV+ interneurons during PTZ-induced seizures. Having established from day 1 baseline data that the seizure onset in PV^{Cre}/Gq-DREADD and non-DREADD WT animals was approximately 5 min post-PTZ (20 mg/kg i.p.) injection, we first delivered CNO (5 mg/kg) focally into either the SScortex or the RTN thalamus 10 min prior PTZ (**Figure 4C**). The timing and dose of CNO were chosen based on data from our previous published report (Panthi and Leitch, 2019), which had established that 5 mg/kg CNO was the lowest effective dose that activated Gi-DREADD receptors and consistently generated absence-like seizures in PV^{Cre}/Gi-DREADD mice ∼15 min post-CNO injection. Simultaneous video/EEG recordings were made according to the protocol outlined in schematic **Figure 4C**. The percentage of time spent in each of the different seizure types during 1 h of EEG recording on day 2 following CNO and PTZ administration, compared to day 1 data (PTZ only administration), is shown in **Figures 4B,D**.

On day 2, CNO activation of feedforward PV+ inhibitory interneurons in DREADD mice (both cortical and thalamic treatment groups), substantially changed the relative time spent having seizures. On day 1, PTZ-injected DREADD animals of the SScortex group (n = 7) spent 17.85 ± 9.32 and 26.04 ± 11.15 s in absence and tonic-clonic seizures, respectively. On day 2 after CNO and PTZ co-administration, animals spent less time in absence seizures (1.88 ± 1.87 s) and tonic-clonic seizures (2.88 ± 2.0 s) compared to day 1 (**Figure 4D**). Similarly, DREADD animals of the RTN thalamus group (n = 7) also spent less time in absence seizures on day 2 compared to that of day 1 (**Figures 4B,D**). During 1 h of EEG recording, these animals

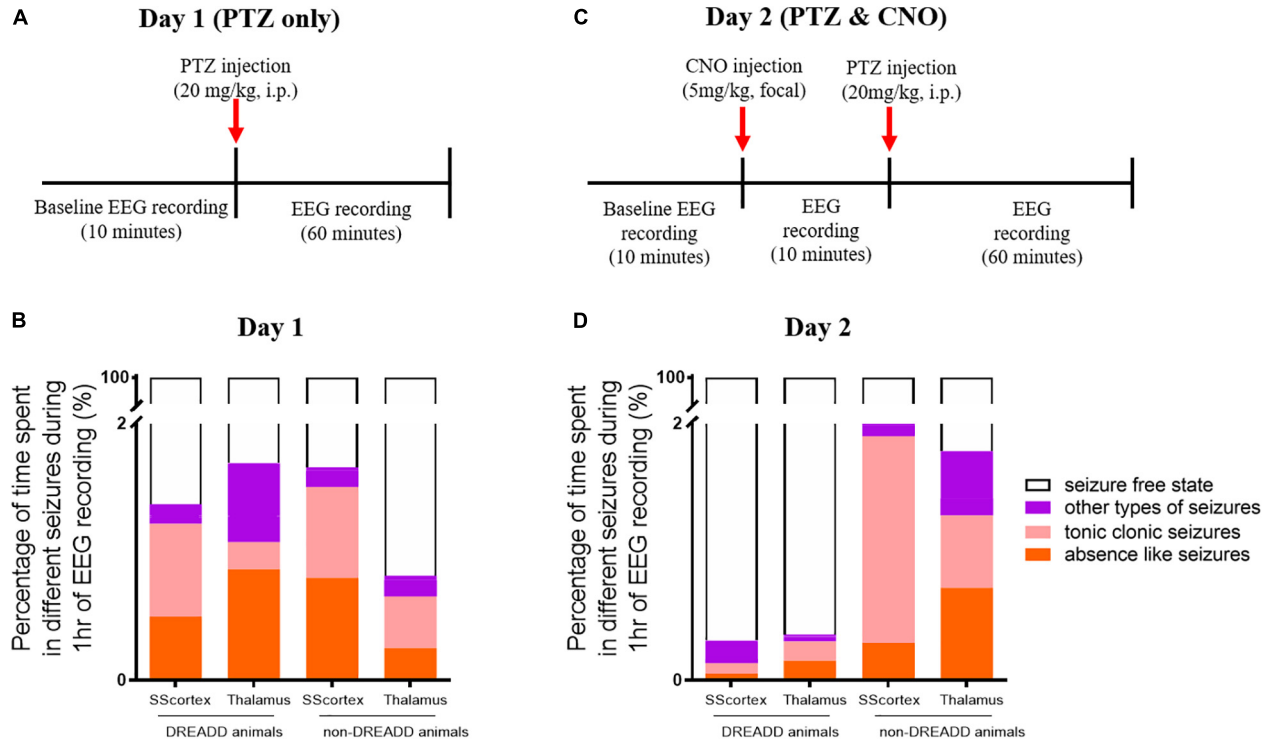

FIGURE 4 | Schematic of protocol for EEG recordings before and after **(A)** PTZ injection on day 1 and **(C)** PTZ and CNO injection on day 2. Comparison of the percentage of different types of seizures in PV^{Cre}/Gq-DREADD (DREADD) (n = 7) and non-DREADD WT control (n = 5) animals of the SScortex and the RTN thalamus group after **(B)** PTZ injection on day 1 and **(D)** PTZ and CNO injection on day 2.

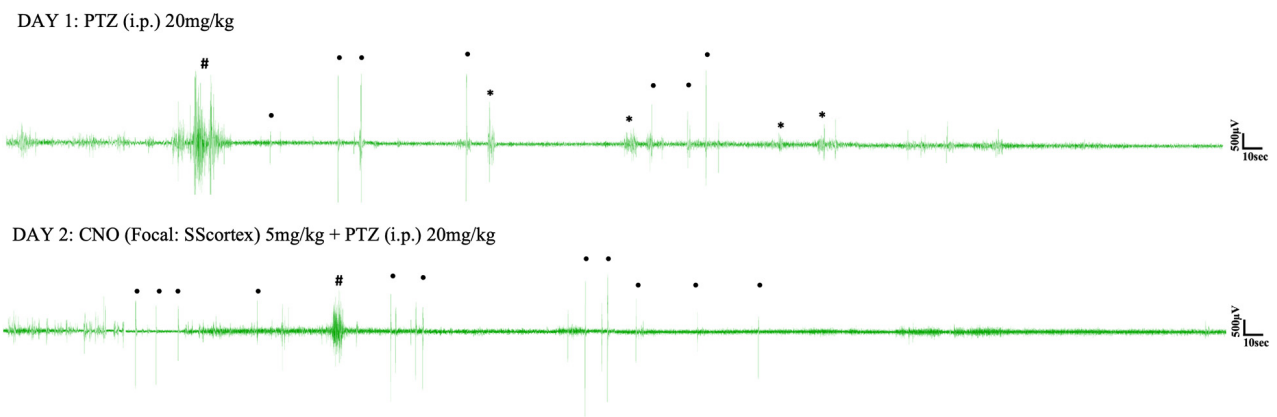

FIGURE 5 | Representative EEG traces from a PV^{Cre}/Gq-DREADD animal after i.p. PTZ injection on day 1 and focal (SScortex) CNO and i.p. PTZ injection on day 2. Asterisks (*), hash signs (#), and dot signs (•) represent absence-like, tonic-clonic and other types of seizures, respectively. Each trace represents 10 min of EEG recording.

spent 31.11 ± 13.64 s in absence seizures on day 1 after PTZ administration. On day 2 after co-administration of CNO and PTZ, they spent only 5.49 ± 3.4 s in absence seizures (**Figure 4D**). Tonic-clonic seizures in this treatment group was also changed (day 1: 7.65 ± 2.96 s, day 2: 5.37 ± 3.53 s). Overall, DREADD animals spent significantly less time having either absence or tonic clonic seizures on day 2 compared to day 1 after activation of FFI. In the SScortex group, the duration spent in other types of seizures remained almost unchanged on both days, whereas in RTN thalamus group, the percentage time spent in other types of seizures was also substantially decreased on day 2 (**Figures 4B,D**).

In non-DREADD WT controls, CNO activation of feedforward PV+ inhibitory interneurons on day 2 did not reduce the overall time spent having mixed seizures; rather the percentage time spent having seizures was increased compared to day 1 (**Figures 4C,D**). However, the profile of individual

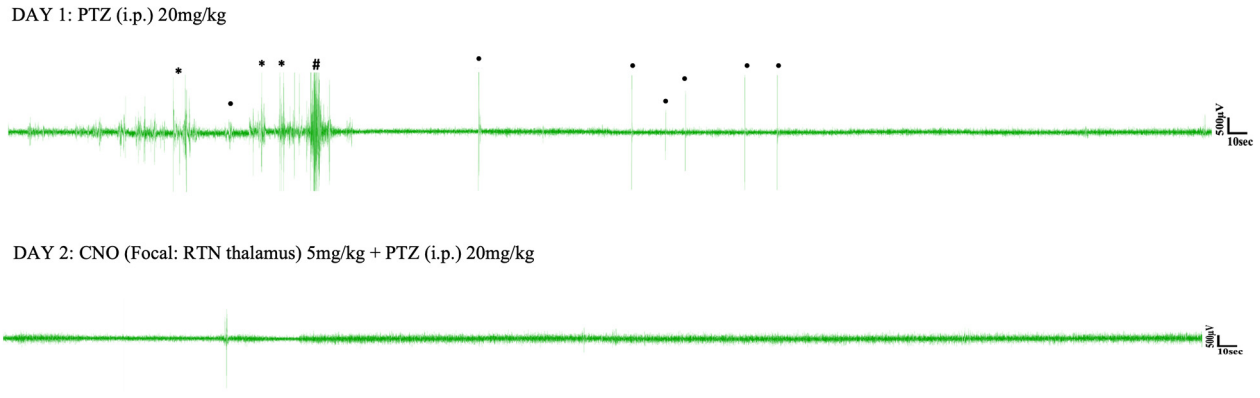

FIGURE 6 | Representative EEG traces from a PV^{Cre}/Gq-DREADD animal after i.p. PTZ injection on day 1 and focal (RTN thalamus) CNO and i.p. PTZ injection on day 2. Asterisks (*), hash signs (#), and dot signs (•) represent absence-like, tonic-clonic and other types of seizures, respectively. Each trace represents 10 min of EEG recording.

TABLE 2 | Number of animals exhibiting different seizure types on day 1 after PTZ administration.

Treatment group/Genotype (*n*)	No. of animals experiencing seizure types on day 1	
	Absence seizure	Tonic-clonic seizure
SScortex/DREADD (*n* = 7)	5	6
SScortex/non-DREADD (*n* = 5)	3	5
RTN thalamus/DREADD (*n* = 7)	7	3
RTN thalamus/non-DREADD (*n* = 5)	3	5

seizure types varied. In the thalamus group, the percentage time animals spent in absence and tonic clonic seizures was increased compared to day 1; whereas, in the SScortex group tonic clonic seizures were increased compared to absence seizures. While it is unclear why the seizure profile changed with respect to this group, nevertheless, the overall impact of CNO and PTZ co-administration on day 2 had no antiepileptic effects in non-DREADD WT control mice (**Figures 4B,D**).

Activating PV+ interneurons with CNO either prevented or delayed the onset of PTZ-induced seizures in all DREADD mice tested but had no impact on non-DREADD controls

Activating PV+ interneurons in the SScortex with CNO on day 2 prevented seizures in 2 out of 7 DREADD animals in this group i.e., 29% did not experience any type of seizure during 1 h of EEG recording (**Figure 7A**, solid red line). Likewise, in the RTN thalamus group, CNO activation of PV+ interneurons suppressed seizures in 3 out of 7 (42%) DREADD mice (**Figure 7B** solid red line). In the remaining PV^{Cre}/Gq-DREADD animals of both groups, the latency to first seizure was delayed. In the SScortex group, mean latency to first seizure was 4.32 ± 0.55 min (*n* = 5) on day 1 (**Figure 7A**, dashed red line), which increased to 8.43 ± 31 min (*n* = 5) on day 2 (**Figure 7A**, solid red line). Likewise, in the RTN thalamus group on day 1, mean onset of seizure was 3.24 ± 0.34 min (*n* = 4; **Figure 7B**, dashed red line), which increased to 10.08 ± 3.19 min (*n* = 4) on day 2 (**Figure 7B**, solid red line). In contrast, activation of PV+ interneurons did not delay the latency to first seizure in non-DREADD WT control animals [SScortex group, day 1: 3.59 ± 0.62 min (*n* = 5), day 2: 4.03 ± 1.56 min (*n* = 5); RTN thalamus, day 1; 3.87 ± 1.03 min (*n* = 5), day 2: 3.51 ± 1.09 min (*n* = 5); **Figures 7A,B** black lines]. A log-rank test was performed to statistically compare the latency to the first seizure between treatment groups (**Figures 7A,B**). This test indicated that the latency to first seizure (of any type) was significantly delayed in PV^{Cre}/Gq-DREADD animals of both SScortex and RTN thalamus groups on day 2 compared to that of day 1 but not in the non-DREADD WT controls (**Figures 7A,B**).

Latency to first absence and tonic-clonic is delayed in DREADD mice

We further analyzed the EEG data to determine the latency to onset of each type of seizure. Latency to first absence or tonic-clonic seizure in PTZ injected PV^{Cre}/Gq-DREADD animals pre-treated with CNO (in either of the brain regions of CTC network) on day 2 was delayed compared to that of day 1 (**Figures 8–10**).

Absence seizures. First, we compared the latency to first absence seizure on day 2 in those mice that had EEG evidence of absence seizures on day 1 (**Figure 8A**); and then in all tested animals (**Figure 8B**). In the SScortex group on day 1, PTZ induced absence seizures in 5 PV^{Cre}/Gq-DREADD animals. All 5 animals (100%) were completely absence seizure free when CNO and PTZ were co-administered on day 2 (**Figure 8A**, solid red line). Of the remaining 2 mice in this cohort that didn't have absence seizures on day 1, one had absence seizures on day 2 but delayed (i.e., 20.15 min post-PTZ and CNO co-administration compared to mean latency to first absence seizures on day 1 i.e., 13.52 ± 6.04 min) and the other had no absence seizures either on day 1 or day 2 (**Figure 8B**). In DREADD animals of RTN thalamus group, 4 out of 7 (57%) animals did not experience absence seizure on day 2 (**Figure 8A** solid red line); whereas all seven had displayed SWDs on EEG on day 1 (**Figure 8A** dashed red line). In the remaining three animals, mean latency to first

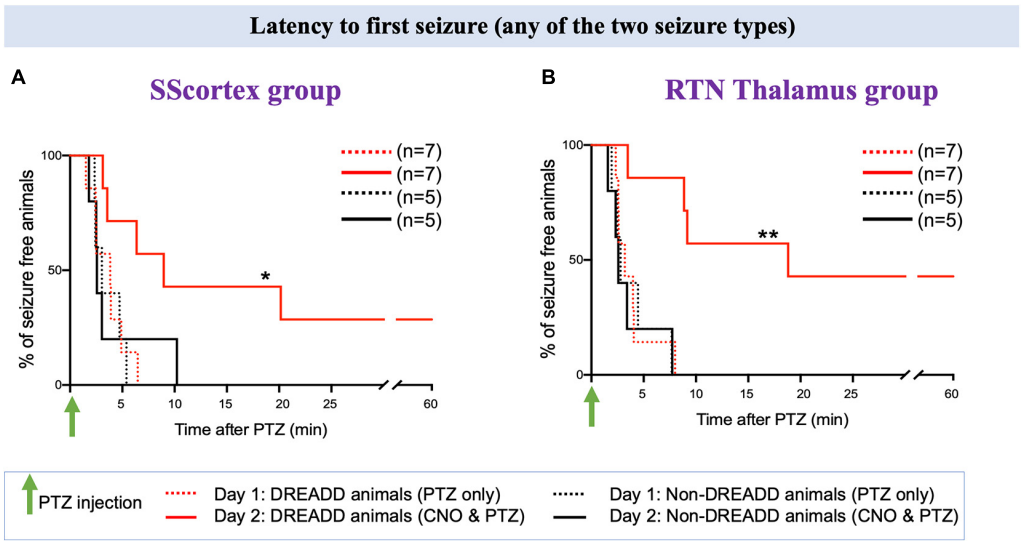

FIGURE 7 | Comparison of the latency to first seizure (any of the two seizure type) in PV^{Cre}/Gq-DREADD and non-DREADD WT controls of the **(A)** SScortex group and the **(B)** RTN thalamus group between day 1 (PTZ only treated) and day 2 (CNO and PTZ treated). Comparisons between the treatment groups were made using log-rank test. **(A)** $*p = 0.0477$; **(B)** $**p = 0.0019$.

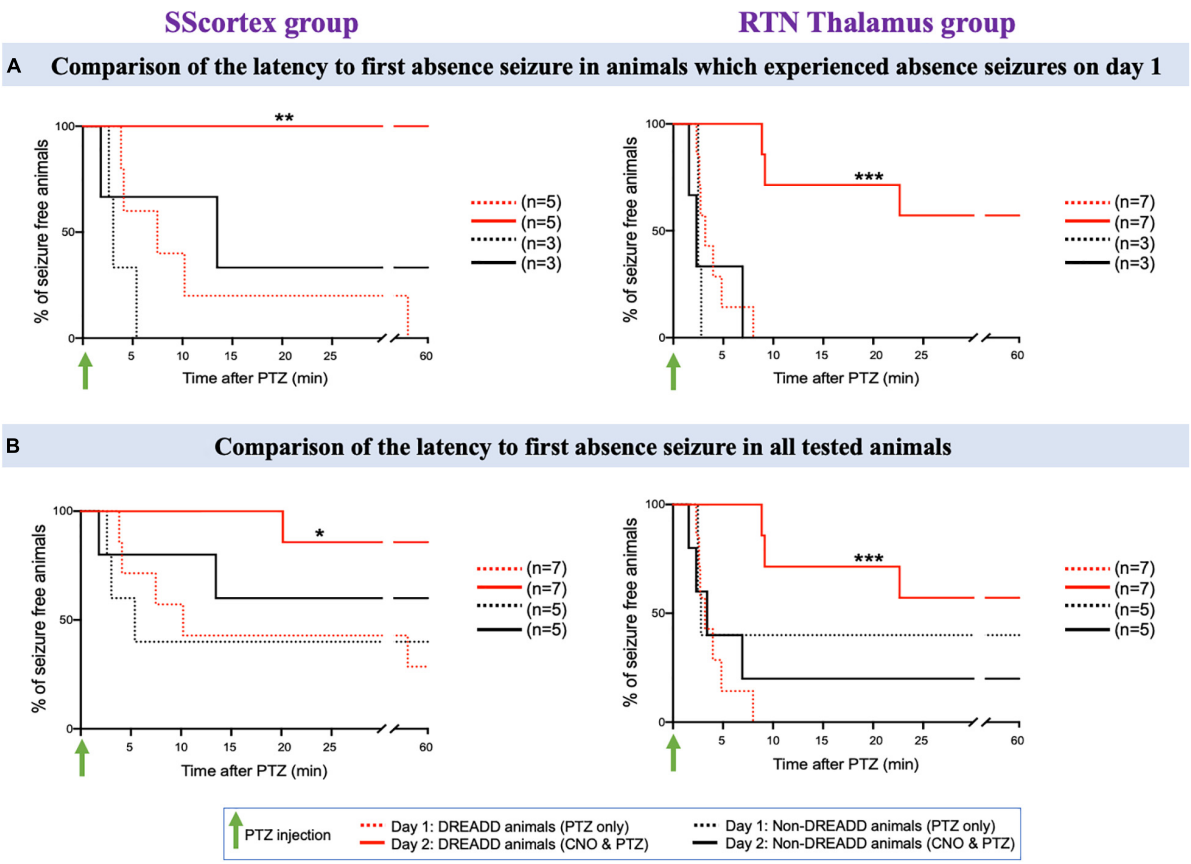

FIGURE 8 | (A) Comparison of the latency to first absence seizure in animals which experienced absence seizures on day 1. **(B)** Comparison of the latency to first absence seizure in all tested PV^{Cre}/Gq-DREADD and non-DREADD WT controls of the SScortex group and the RTN thalamus group between day 1 (PTZ only treated) and day 2 (CNO and PTZ treated). Comparisons between the treatment groups were made using log-rank test. **(A)** $**p = 0.0024$, $***p = 0.0002$; **(B)** $*p = 0.0268$, $***p = 0.0001$.

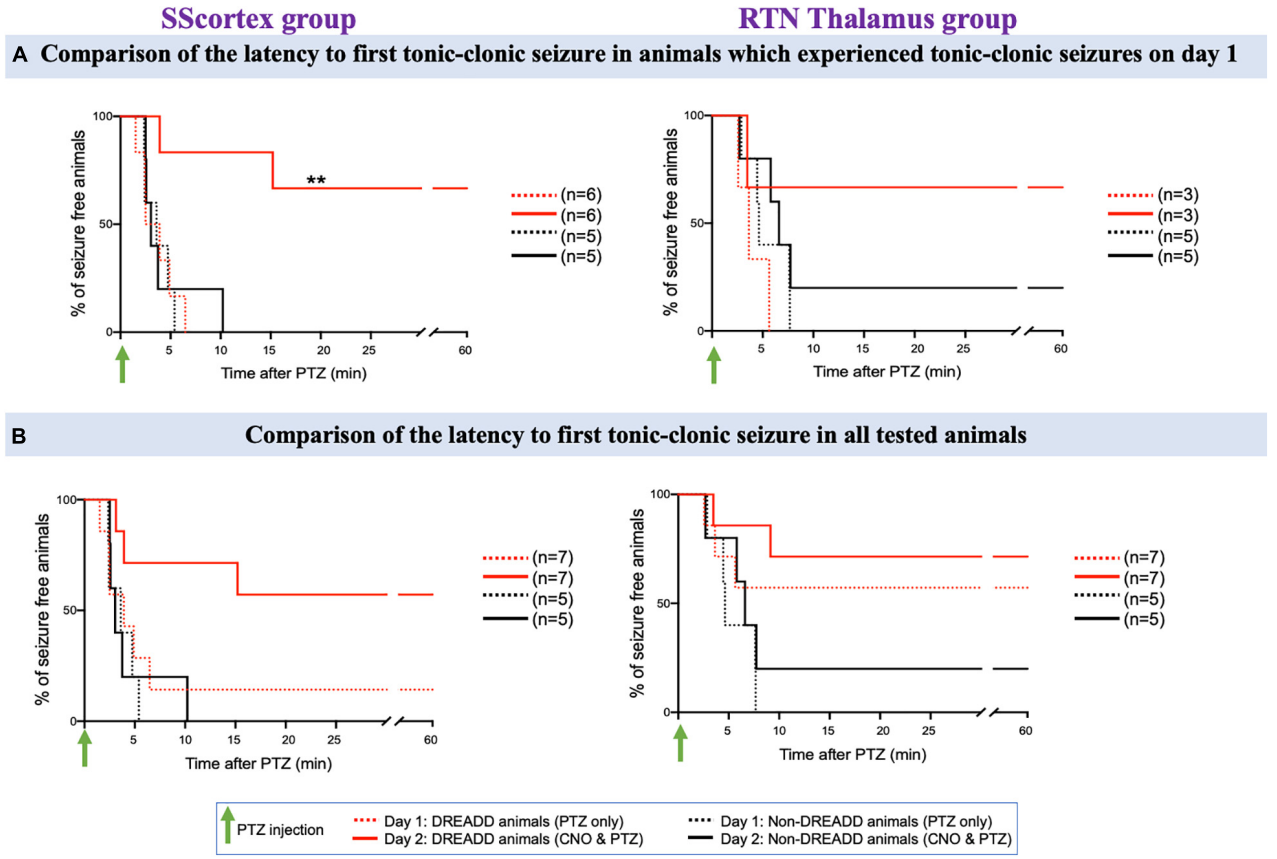

FIGURE 9 | (A) Comparison of the latency to first tonic-clonic seizure in animals, which experienced tonic-clonic seizures on day 1. **(B)** Comparison of the latency to first tonic-clonic seizure in all tested PV^{Cre}/Gq-DREADD and non-DREADD WT controls of the SScortex group and the RTN thalamus group between day 1 (PTZ only treated) and day 2 (CNO and PTZ treated). Comparisons between the treatment groups were made using log-rank test. $^{**}p = 0.0067$.

absence burst on day 2 was also delayed compared to that of day 1 i.e., day 1: 3.71 ± 0.73 min; day 2: 13.55 ± 4.54 min. Overall, there was a significant reduction in absence seizures and also latency to first absence seizure in DREADD animals treated with CNO to activate FFI in both the SScortex and thalamus (**Figures 8A,B** asterisks). In contrast no significant difference in absence seizures was evident in non-DREADD controls treated with CNO.

Tonic-clonic seizures. The latency to first tonic-clonic seizure in animals, which experienced this type of seizure on day 1, is shown in **Figure 9A** and the latency to first tonic-clonic seizure in all tested animals is shown in **Figure 9B**. PTZ treatment induced tonic-clonic seizures in 6 DREADD animals of the SScortex group on day 1; activation of feed-forward inhibitory PV+ interneurons on day 2 prevented tonic-clonic seizures in 4 (67%) of these mice (**Figure 9A**, solid red line). The remaining animals showed a delayed onset of tonic clonic-seizures compared to that of day 1 i.e., day 1: 3.69 ± 1.19 min; day 2: 9.56 ± 5.64 min (**Figure 9A**). In contrast CNO activation of FFI in the SScortex of non-DREADD controls had no impact on tonic-clonic seizures with all mice in this cohort experiencing tonic-clonic seizures within ∼10 min on both days mice (**Figures 9A,B**; black line). In the RTN thalamus group, PTZ treatment produced tonic-clonic seizures in 3 out of 7 DREADD animals on day 1. Upon co-administration of CNO and PTZ, on day 2, 67% animals did not experience any tonic-clonic seizures (**Figure 9A**). In the non-DREADD controls treated with CNO (n = 5), only one animal was free of tonic-clonic seizures on day 2.

Activating PV+ interneurons reduced total number of discharges and mean length of epileptic bursts

Analysis of the EEG data showed that total number of discharges (absence and tonic-clonic bursts) in PV^{Cre}/Gq-DREADD mice of both SScortex group and the RTN thalamus group was reduced on day 2 compared to that of day 1 (**Figure 10**). PV^{Cre}/Gq-DREADD animals of SScortex group (n = 7) treated with PTZ exhibited 4.57 ± 2.24 absence discharges, which was reduced to 0.85 ± 0.85 discharges on day 2 (**Figure 10A**). Similarly, these animals experienced 2.71 ± 1.28 tonic-clonic discharges on day 1, which were reduced to 0.42 ± 0.205 tonic-clonic discharges on day 2 (**Figure 10A**). Similar effects were seen in RTN thalamus group. PV^{Cre}/Gq-DREADD animals of this group (n = 7) treated with PTZ displayed 7.42 ± 2.58 absence-like discharges on day 1, which was reduced to 2.42 ± 1.41 discharges on day 2 (**Figure 10B**). Those animals also displayed 0.57 ± 0.20 tonic-clonic discharges on day 1, which were reduced

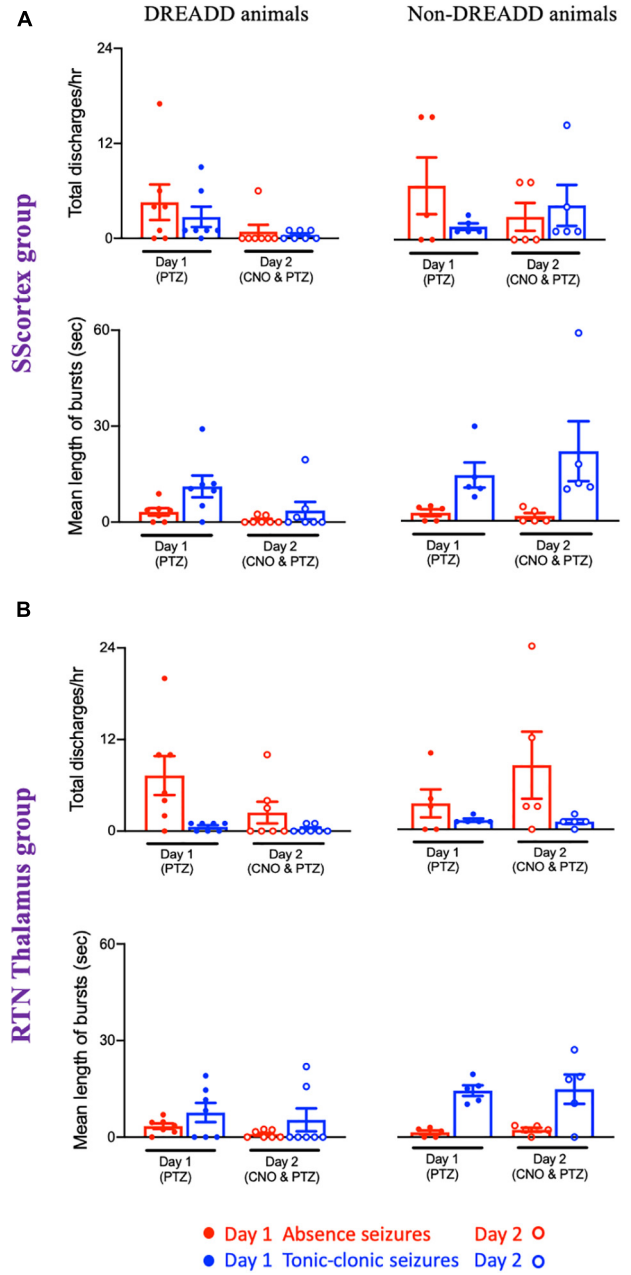

FIGURE 10 | Comparison of mean number of epileptic bursts (discharges/h) and mean length of bursts between PV^{Cre}/Gq-DREADD (DREADD) (n = 7) and non-DREADD WT (n = 5) animals of **(A)** the SScortex and **(B)** the RTN thalamus group after PTZ treatment on day 1 and CNO and PTZ treatment on day 2. All values represent mean ± SEM. Comparisons were performed using Wilcoxon matched-pairs signed-rank test.

to 0.28 ± 0.18 tonic-clonic discharges on day 2 (**Figure 10B**). In contrast, no reduction in total number of discharges was evident in non-DREADD WT control animals (**Figures 10A,B**).

Analysis of the EEG data also showed that, there was a reduction in mean duration of each epileptic bursts in PV^{Cre}/Gq-DREADD animals on day 2 compared to that of day 1 (**Figures 10A,B**). In the SScortex group, the mean length of absence and tonic-clonic seizures was 3.21 ± 1.15 and 11.18 ± 3.40 s, respectively, which decreased to 0.66 ± 0.43 and 3.60 ± 2.71 s on day 2 (**Figure 10A**). Similar reductions were also seen in the PV^{Cre}/Gq-DREADD animals of RTN thalamus group. PV^{Cre}/Gq-DREADD animals of the RTN thalamus group on day 1 displayed absence and tonic-clonic seizures spanning 3.42 ± 0.86 and 7.65 ± 2.96 s, which was reduced to 0.90 ± 0.43 and 5.37 ± 3.53 s on day 2 (**Figure 10B**). Overall, PV^{Cre}/Gq-DREADD animals of both treatment groups experienced a reduction in the number of epileptic discharges and mean length of such discharges on day 2, whereas non-DREADD WT control animals of both treatment groups did not show reductions in either number or duration of epileptic bursts (**Figures 10A,B**).

DISCUSSION

In this study, we used DREADD technology to investigate the impact of activating FFI within the CTC network during chemically (PTZ) induced seizures. We show that excitation of feed-forward inhibitory PV+ interneurons within the SScortex and RTN (via CNO activation of Gq-DREADD receptors) during PTZ-induced seizures has antiepileptic effects. Analysis of the individual seizure types revealed that activation of FFI was effective against PTZ-induced absence seizures and also other forms of generalized seizures evoked by PTZ i.p. administration. Such activation either prevented or delayed the latency to first seizure, decreased total number of discharges and their mean duration, and reduced the overall time spent in seizures. In contrast, focal injection of CNO into either the SScortex or RTN thalamus of non-DREADD WT control animals, had no effect on PTZ-induced seizures. These data demonstrate a potential for using PV+ interneurons as a therapeutic target to control absence seizures in some cases of human absence epilepsy.

Excitatory Gq-DREADD Receptors Are Highly Expressed in Feed-Forward Inhibitory PV+ Interneurons in PVCre/Gq-DREADD Mice

Confocal immunofluorescence microscopy confirmed the expression of excitatory (Gq) DREADD receptors in PV+ interneurons in PV^{Cre}/Gq-DREADD animals. DREADD HA-tag was highly expressed in all cells known to contain PV. The levels of co-localization were greater than 90% in PV+ cells in the SScortex, RTN thalamus and the Purkinje cells of the cerebellum in PV^{Cre}/Gq-DREADD mice. In contrast, none of the non-DREADD WT control animals showed any HA-tag label in PV+ cells. The labeling of PV+ cells in this study was consistent with that of other published studies (del Río and DeFelipe, 1994; Tamamaki et al., 2003; Dávid et al., 2007; Fishell, 2007; Xu et al., 2010). The efficacy and specificity of this double transgenic approach for expressing DREADD receptors in feed-forward inhibitory PV+ interneurons was higher than that reported for viral-mediated DREADD expression in PV-Cre animals. Studies have shown that the infection efficiency and specificity of labeling

vary between 70 and 95% in viral-mediated delivery of DREADD constructs into brain regions (Zou et al., 2016; Xia et al., 2017; Hijazi et al., 2019; Bicks et al., 2020). In our current study, the percentage of co-labeling of HA-tagged Gq-DREADD receptors and PV was always above 90% in all brain regions analyzed. This is similar to the results in our previous published report (Panthi and Leitch, 2019) for inhibitory Gi-DREADD receptor expression in PV+ cells.

Activation of Feed-Forward Inhibitory PV+ Interneurons in the CTC Network Suppressed PTZ-Induced Absence Seizures

Pentylenetetrazol is one of the chemicals that is widely used to induce generalized absence seizures in animals. Other chemicals such as γ-hydroxybutyrate (GHB), bicuculline, picrotoxin, penicillin are also routinely used to induce absence seizures (Snead, 1992; Cortez et al., 2016; Kostopoulos, 2017), but PTZ has been preferentially used for testing new drugs against absence seizures for more than 70 years (see reviews by Krall et al., 1978; Löscher, 2011). Moreover, use of low dose of PTZ is an established method to induce generalized seizures within the thalamocortical circuit (Snead, 1992; Snead et al., 2000; Cortez et al., 2016).

In the pilot study, a single 20 mg/kg (i.p.) dose of PTZ was needed to induce absence seizures in PV^{Cre}/Gq-DREADD and non-DREADD mice. However, a dose of 20 mg/kg also induced tonic-clonic seizures. Higher doses of PTZ (30 mg/kg and above) induced severe tonic-clonic seizures. Other studies have also reported that the severity and behavioral features of PTZ-induced seizures vary with the concentration/dose of PTZ, also genotype and age of mouse (Van Erum et al., 2020). Similar dose/response variability have also been reported in rats (Klioueva et al., 2001; Lüttjohann et al., 2009). In our study seizures were categorized on the basis of their EEG waveform profile and behavioral features during simultaneous EEG/video recordings; notably SWD and behavioral arrest were classified as absence seizures. Administration of 20 mg/kg PTZ has been reported to induce SWDs with behavioral arrest in Tau58/4 transgenic mice (Van Erum et al., 2019). Likewise, i.p. administration of 25 mg/kg PTZ into leptin-deficient mice and their wild-type counterparts induced absence seizures, myoclonic seizures, generalized clonic and clonic–tonic seizures but the proportion of absence seizures were higher (Erbayat-Altay et al., 2008). Importantly, in our current study, the proportion of absence and tonic-clonic seizures after PTZ treatment (i.p., 20 mg/kg, on day 1) in PV^{Cre}/Gq-DREADD and non-DREADD WT control animals was not significantly different. Thus, it can be concluded that injection of low dose PTZ (20 mg/kg) in our study was optimum for inducing absence seizures (albeit mixed with some other seizure types) in both PV^{Cre}/Gq-DREADD and non-DREADD mice to test the impact of FFI on absence seizure generation and severity.

The latency to first seizure after PTZ treatment (on day 1) was within 5 min in PV^{Cre}/Gq-DREADD and non-DREADD mice, which is consistent with other published studies in mice (Keskil et al., 2001; Medina et al., 2001; Ilhan et al., 2006; Erbayat-Altay et al., 2008; Nassiri-Asl et al., 2009; Koutroumanidou et al., 2013; Faghihi and Mohammadi, 2017; de Freitas et al., 2018). These studies have shown that irrespective of dose of PTZ (20–80 mg/kg, i.p.), the latency of seizure onset is within 5 min. However, some other studies have reported that increasing the concentration of PTZ from 40 to 70 mg/kg, substantially decreases the time of onset of first observed seizure from ∼5 min to ∼1 min (Medina et al., 2001; Schwaller et al., 2004). Likewise, Girard et al. (2019) found that latency to seizure was decreased in mice injected with 60 mg/kg compared to animals injected with PTZ doses of 30–50 mg/kg. Van Erum et al. (2020) recently reported genotype and age-related differences in susceptibility and onset of PTZ-induced seizures in mice. However, in the current study, regardless of genotype, first and last incident of seizure after 20 mg/kg PTZ administration on day 1, was very consistent in all animals of both treatment groups (PV^{Cre}/Gq-DREADD and non-DREADD mice surgically implanted with either cortical or thalamic cannulae).

On day 2, PTZ (20 mg/kg, i.p.) was tested after pre-treatment with CNO (5 mg/kg, into either the SScortex or the RTN thalamus). The timing of CNO treatment was based on the evidence from previous published reports where activating PV+ interneurons during pre-ictal stage provided anti-epileptic effects but activating them during the interictal phase induced epileptic events (Yekhlef et al., 2015; Assaf and Schiller, 2016). The exact timing and dose of CNO is previously explained in section "CNO Injection Into the SScortex or Thalamus on Day 2 Changed the Time Spent in Seizures by DREADD Mice but Not Non-DREADD Controls." In this study, focal activation of PV+ interneurons in either cortical or thalamic microcircuits on day 2 either prevented or significantly delayed the latency to first absence seizure (and another seizure type) compared to day 1 seizure onset in PTZ treated PV^{Cre}/Gq-DREADD animals. Furthermore, there was a reduction in the number of SWDs and mean duration of each burst of discharges and the total time spent having seizures, on day 2. However, co-administration of CNO and PTZ in non-DREADD WT control animals of both treatment groups (SScortex and RTN thalamus) on day 2 did not decrease total time spent in seizures compared to day 1. Other parameters such as total discharges and mean length of bursts in non-DREADD WT control animals also did not remarkably change upon co-administration of CNO and PTZ on day 2, compared to day 1. Thus is can be concluded that unilateral activation of FFI, within the CTC network (by CNO activation of Gq-DREADD receptors in PV+ interneurons) during PTZ-induced seizures suppresses or reduces the severity of absence seizures and other types of generalized seizure. These findings are in agreement with those from a study by Clemente-Perez et al. (2017) who found that optogenetic activation of PV+ interneurons, but not somatostatin expressing inhibitory neurons, in the RTN thalamus suppressed PTZ-induced (35–60 mg/kg) spike-and-wave seizures seen in EEG and spiking seizure episodes observed in thalamic local field potential (LFP) recordings.

Activation of PV+ interneurons in other brain regions has also been shown to afford protection against different types of chemically induced seizures. DREADD-mediated activation of hippocampal PV+ interneurons suppressed 4-AP induced *in vivo* convulsive behavior and also *in vitro* epileptiform discharges

in PV-Cre mice (Călin et al., 2018), Similarly, activation of hippocampal PV+ interneurons provided antiepileptic effects against KA-induced temporal lobe seizures in mice (Krook-Magnuson et al., 2013; Wang et al., 2018). In another study, Ledri et al. (2014) found that simultaneous optogenetic activation of several subpopulation of interneurons in the hippocampus [PV, SOM, Cholecystokinin (CCK), Neuropeptide Y (NPY)-expressing] was more effective in inhibiting 4-AP induced epileptiform activity in brain slices compared to activation of individual classes of interneurons. However, it should be noted that, in some studies, activation of PV+ interneurons did not stop or shorten chemically induced seizures as expected. For example, activation of PV+ interneurons increased epileptic discharges induced by 4-AP (Yekhlef et al., 2015). In another study by Khoshkhoo et al. (2017) it was found that silencing PV+ interneurons in the primary motor cortex was effective in reducing the duration of optogenetically induced electrographic seizures (Khoshkhoo et al., 2017). Nevertheless, global activation of PV+ interneurons (using DREADD technology) has been shown to reduce the severity of PTZ (50 mg/kg) induced tonic-clonic and myoclonic seizures in transgenic PV-Cre × LSL-hM3Dq mice (Johnson et al., 2018). Furthermore, the protective role played by inhibitory feedforward PV+ interneurons in preventing runaway excitation and seizures is confirmed by studies in PV knockout ($PV^{-/-}$) mice. These $PV^{-/-}$ mice had more severe PTZ-induced seizures compared to their wild-type ($PV^{+/+}$) genotype controls (Schwaller et al., 2004). Collectively, these findings indicate that PV+ interneurons might serve as a therapeutic target to control seizures.

Functional recordings from PV+ interneurons of stargazer animals would be highly beneficial to determine the degree to which the impaired AMPA receptor might have been involved in the alteration of activity of PV+ interneurons, as previous studies conducted in epileptic stargazers showed abnormal expression of AMPA receptors particularly at input synapses of CTC PV+ neurons (Barad et al., 2012; Maheshwari et al., 2013; Adotevi and Leitch, 2016, 2017, 2019). However, there is a technical limitation. The distance between the stargazin locus to parvalbumin locus in chromosome 15 is very close (separated by only 0.01 cM) and if stargazers are bred with parvalbumin promoter-driven animals, double crossover is very unlikely and identification of these cells during physiological study would be technically challenging (Maheshwari et al., 2013). Use of viral vector mediated delivery of the DREADD receptors into the CTC regions in other genetic rodent models of absence epilepsy (e.g., GAERS or WAG/Rij rats) is however possible and potentially could be helpful to interrogate the role of PV+ interneurons on absence seizures in future studies.

PV+ Interneurons–A Potential Target for Anti-Epileptic Therapy?

In our previous published report (Panthi and Leitch, 2019), we demonstrated that selective silencing of feed-forward inhibitory PV+ interneurons in the CTC network via regional injection of CNO into either the SScortex or the RTN thalamus of PV^{Cre}/Gi-DREADD mice, generated absence-like SWDs. In the current study, we further demonstrate that selectively activating these interneurons, during PTZ-induced seizures, prevents or suppresses the severity of absence seizures. Furthermore, PTZ-induced tonic-clonic seizures are also reduced in severity by activation of feed-forward inhibitory PV+ interneurons within the CTC network. PV+ interneurons account for ∼40% of the GABAergic population (Xu et al., 2010). Most PV+ neurons in the cortex are basket and chandelier cells; they are found throughout cortical layers 2–6. PV+ interneurons, typically have fast-spiking, low input resistance, and high-amplitude rapid after-hyperpolarization characteristics (Kawaguchi et al., 1987; Kawaguchi and Kubota, 1997), which enables them to fire a rapid train of action potentials unlike any other neuron in the cortex. They are therefore likely to have a profound impact on the spiking output of their targets (for review see Ferguson and Gao, 2018).

In the SScortex, PV+ interneurons synapse on to soma/proximal dendrites/axon initial segment of excitatory pyramidal cells (Inan and Anderson, 2014; Tremblay et al., 2016). PV+ interneurons are densely connected to pyramidal cells across cortical layers and areas influencing their excitability (Packer and Yuste, 2011; Hu et al., 2014). A single PV interneuron contacts nearly every local pyramidal neuron (Ferguson and Gao, 2018). Packer and Yuste (2011) estimated that a typical PV+ interneuron in the cortex makes contact with hundreds to thousands of post-synaptic targets (both pyramidal cells and other PV+ interneurons) and each excitatory pyramidal cell is contacted by ∼50–200 inhibitory PV+ interneurons. Thus activating them may generate widespread post-synaptic inhibitory currents in pyramidal neurons, thereby preventing cortical hyper-excitation and attenuating PTZ-induced absence seizures.

On the other hand, PV+ interneurons in the RTN project onto excitatory thalamocortical relay neurons of VP thalamus and provide powerful feedforward inhibition (Fogerson and Huguenard, 2016); thus activating them may have prevented the firing of excitatory relay neurons of VP thalamus, thereby disrupting generalized absence-SWDs induced by systemic PTZ injection.

It is important to note that a number of different molecular mechanisms are capable of switching CTC network from normal oscillations to pathological absence-SWD oscillations. There is a long-standing debate over the site of initiation of absence-SWDs within the CTC network. However, the current general consensus is that rhythmic epileptic discharges are initiated in the cortex (for reviews see Meeren et al., 2005; Crunelli et al., 2020). Meeren et al. (2002) were the first researchers to clearly demonstrate the initiation of absence seizures in the perioral region of primary SScortex of (WAG/Rij) rats. They showed that the SScortex always leads all other cortical and thalamic sites during the first ∼500 ms of absence seizures; but after cortical initiation, the activity of either thalamic or cortical neurons may precede the other during subsequent paroxysmal cycles. Later studies on GAERS rats confirmed the primary SScortex (Studer et al., 2018) and specifically layer 5/6 excitatory pyramidal neurons (Polack et al., 2007), as the originators of the initial paroxysmal activity. It is now accepted that a cortical initiation network (CIN) contributes to the pre-ictal changes of absence seizure.

Notwithstanding, once initiated both the cortex and thalamus are intimately involved in the generation and maintenance of SWDs. McCafferty et al. (2018) have demonstrated that both cortex and thalamus consistently receive a robust burst of action potentials from the other region (in correlation with EEG spikes) at each and every SWD cycle. The critical role played by the thalamus is also indicated by the fact that SWD and absence seizures can be induced experimental by activation of different thalamic regions in non-epileptic animals (Avoli, 2012; Lüttjohann and van Luijtelaar, 2015; Sorokin et al., 2017). Numerous experimental studies have demonstrated that changes in neuronal excitability limited to a restricted cortical or thalamic region can lead to generalized SWD-like activity throughout the CTC network (Tan et al., 2007; Rossignol et al., 2013; Crunelli et al., 2020). In this context it is interesting to note that in our previous study (Panthi and Leitch, 2019), acute unilateral silencing of PV+ interneurons in either cortical or thalamic regions was sufficient to illicit SWDs; likewise the current study shows that activation of these same PV+ interneurons (either cortical or thalamic) during chemically induced seizures, profoundly decreases SWDs expression and the generation and severity of absence seizure.

CONCLUSION

Collectively, our data indicate that DREADD-mediated activation of feed-forward inhibitory PV+ interneurons, in either somatosensory cortical or thalamic microcircuits of the CTC network, yields antiepileptic effects against chemically induced absence seizures. Thus, these interneurons might serve as targets for anti-seizure therapy for some forms of absence epilepsy. The findings from this study could be highly significant in developing new targeted approaches for the treatment of childhood absence epilepsy in patients from different genetic backgrounds.

DATA AVAILABILITY STATEMENT

The raw data supporting the conclusions of this article will be made available by the authors, without undue reservation.

ETHICS STATEMENT

All experiments were performed in accordance with the University of Otago Animal Ethics Committee under the AEC no. D94/16 and AUP-19-98.

AUTHOR CONTRIBUTIONS

BL was responsible for conception, hypothesis development and design of the research, also secured the funding, and wrote the manuscript. SP conducted the experiments and data analyses. Both authors conducted the interpretation of the results, contributed to draft versions of the manuscript, and approved the final version.

FUNDING

This work was supported by grants from the University of Otago and Deans Bequest Fund awarded to BL. The authors acknowledge the University of Otago Doctoral Scholarship and publishing bursary and the Brain Health Research Centre Roche Hanns Möhler awarded to SP.

ACKNOWLEDGMENTS

The authors thank Greg Anderson (University of Otago) for sharing male Gq-DREADD mice. The authors also thank the staff of the Otago Centre for Confocal Microscopy (OCCM) for technical support.

SUPPLEMENTARY MATERIAL

The Supplementary Material for this article can be found online at: https://www.frontiersin.org/articles/10.3389/fncel.2021.688905/full#supplementary-material

Supplementary Figure 1 | (A) Schematic showing breeding paradigm to generate PV-Cre × hM3Dq-flox offspring and WT (non-DREADD) control mice by crossing a female homozygous PV-Cre mouse with heterozygous hM3Dq-floxed mice. **(B)** Representative gel electrophoresis blot showing the homozygous (Homo) PV-Cre knockin (350 and 300 bp) and the hM3Dq-flox [heterozygous (Het) 300 and 204 bp and wild-type (WT) 300 bp] for three mice to verify PV-Cre knockin and hM4Di-flox. For the confirmation of PV-Cre knockin and hM3Dq-flox in the same mouse, genotyping was performed separately.

Supplementary Figure 2 | Representative coronal slices of mouse brain showing histological localization of methylene blue dye injected via a cannula located in either **(A)** SScortex and **(B)** thalamus, verifying CNO site of diffusion within those regions. Coronal slice drawings were adapted from Mouse Brain Atlas.

REFERENCES

Adotevi, N. K., and Leitch, B. (2016). Alterations in AMPA receptor subunit expression in cortical inhibitory interneurons in the epileptic stargazer mutant mouse. *Neuroscience* 339, 124–138. doi: 10.1016/j.neuroscience.2016.09.052

Adotevi, N. K., and Leitch, B. (2017). Synaptic changes in AMPA receptor subunit expression in cortical parvalbumin interneurons in the stargazer model of absence epilepsy. *Front. Mol. Neurosci.* 10:434. doi: 10.3389/fnmol.2017.00434

Adotevi, N. K., and Leitch, B. (2019). Cortical expression of AMPA receptors during postnatal development in a genetic model of absence epilepsy. *Int. J. Dev. Neurosci.* 73, 19–25. doi: 10.1016/j.ijdevneu.2018.12.006

Alexander, G. M., Rogan, S. C., Abbas, A. I., Armbruster, B. N., Pei, Y., Allen, J. A., et al. (2009). Remote control of neuronal activity in transgenic mice expressing evolved G protein-coupled receptors. *Neuron* 63, 27–39. doi: 10.1016/j.neuron.2009.06.014

Armbruster, B. N., Li, X., Pausch, M. H., Herlitze, S., and Roth, B. L. (2007). Evolving the lock to fit the key to create a family of G protein-coupled

receptors potently activated by an inert ligand. *Proc. Natl. Acad. Sci. U.S.A.* 104, 5163–5168. doi: 10.1073/pnas.0700293104

Assaf, F., and Schiller, Y. (2016). The antiepileptic and ictogenic effects of optogenetic neurostimulation of PV-expressing interneurons. *J. Neurophysiol.* 116, 1694–1704. doi: 10.1152/jn.00744.2015

Avoli, M. (2012). A brief history on the oscillating roles of thalamus and cortex in absence seizures. *Epilepsia* 53, 779–789. doi: 10.1111/j.1528-1167.2012.03421.x

Barad, Z., Shevtsova, O., Arbuthnott, G. W., and Leitch, B. (2012). Selective loss of AMPA receptors at corticothalamic synapses in the epileptic stargazer mouse. *Neuroscience* 217, 19–31. doi: 10.1016/j.neuroscience.2012.05.011

Bicks, L. K., Yamamuro, K., Flanigan, M. E., Kim, J. M., Kato, D., Lucas, E. K., et al. (2020). Prefrontal parvalbumin interneurons require juvenile social experience to establish adult social behaviour. *Nat. Commun.* 11:1003. doi: 10.1038/s41467-020-14740-z

Călin, A., Stancu, M., Zagrean, A. M., Jefferys, J. G., Ilie, A. S., and Akerman, C. J. (2018). Chemogenetic recruitment of specific interneurons suppresses seizure activity. *Front. Cell. Neurosci.* 12:293. doi: 10.3389/fncel.2018.00293

Clemente-Perez, A., Makinson, S. R., Higashikubo, B., Brovarney, S., Cho, F. S., Urry, A., et al. (2017). Distinct thalamic reticular cell types differentially modulate normal and pathological cortical rhythms. *Cell Rep.* 19, 2130–2142. doi: 10.1016/j.celrep.2017.05.044

Cortez, M. A., Kostopoulos, G. K., and Snead, O. C. (2016). Acute and chronic pharmacological models of generalized absence seizures. *J. Neurosci. Methods* 260, 175–184. doi: 10.1016/j.jneumeth.2015.08.034

Crunelli, V., and Leresche, N. (2002). Childhood absence epilepsy: genes, channels, neurons and networks. *Nat. Rev. Neurosci.* 3, 371–382. doi: 10.1038/nrn811

Crunelli, V., Lőrincz, M. L., McCafferty, C., Lambert, R. C., Leresche, N., Di Giovanni, G., et al. (2020). Clinical and experimental insight into pathophysiology, comorbidity and therapy of absence seizures. *Brain* 143, 2341–2368. doi: 10.1093/brain/awaa072

Dávid, C., Schleicher, A., Zuschratter, W., and Staiger, J. F. (2007). The innervation of parvalbumin-containing interneurons by VIP-immunopositive interneurons in the primary somatosensory cortex of the adult rat. *Eur. J. Neurosci.* 25, 2329–2340. doi: 10.1111/j.1460-9568.2007.05496.x

de Freitas, M. L., Mello, F. K., de Souza, T. L., Grauncke, A. C. B., Fighera, M. R., Royes, L. F. F., et al. (2018). Anticonvulsant-like effect of thromboxane receptor agonist U-46619 against pentylenetetrazol-induced seizures. *Epilepsy Res.* 146, 137–143. doi: 10.1016/j.eplepsyres.2018.08.003

del Río, M. R., and DeFelipe, J. (1994). A study of SMI 32-stained pyramidal cells, parvalbumin-immunoreactive chandelier cells, and presumptive thalamocortical axons in the human temporal neocortex. *J. Comp. Neurol.* 342, 389–408. doi: 10.1002/cne.903420307

Erbayat-Altay, E., Yamada, K. A., Wong, M., and Thio, L. L. (2008). Increased severity of pentylenetetrazol induced seizures in leptin deficient ob/ob mice. *Neurosci. Lett.* 433, 82–86.

Faghihi, N., and Mohammadi, M. T. (2017). Anticonvulsant and antioxidant effects of pitavastatin against pentylenetetrazol-induced kindling in mice. *Adv. Pharm. Bull.* 7:291. doi: 10.15171/apb.2017.035

Ferguson, B. R., and Gao, W.-J. (2018). PV interneurons: critical regulators of E/I balance for prefrontal cortex-dependent behaviour and psychiatric disorders. *Front. Neural Circ.* 12:37. doi: 10.3389/fncir.2018.00037

Fishell, G. (2007). Perspectives on the developmental origins of cortical interneuron diversity. *Novartis Found. Symp.* 288, 21–35. doi: 10.1002/9780470994030.ch3

Fogerson, P. M., and Huguenard, J. R. (2016). Tapping the brakes: cellular and synaptic mechanisms that regulate thalamic oscillations. *Neuron* 92, 687–704. doi: 10.1016/j.neuron.2016.10.024

Girard, B., Tuduri, P., Moreno, M. P., Sakkaki, S., Barboux, C., Bouschet, T., et al. (2019). The mGlu7 receptor provides protective effects against epileptogenesis and epileptic seizures. *Neurobiol. Dis.* 129, 13–28. doi: 10.1016/j.nbd.2019.04.016

Hijazi, S., Heistek, T. S., Scheltens, P., Neumann, U., Shimshek, D. R., Mansvelder, H. D., et al. (2019). Early restoration of parvalbumin interneuron activity prevents memory loss and network hyperexcitability in a mouse model of Alzheimer's disease. *Mol. Psychiatry* 26, 3380–3398. doi: 10.1038/s41380-019-0483-4

Hu, H., Gan, J., and Jonas, P. (2014). Fast-spiking, parvalbumin+ GABAergic interneurons: from cellular design to microcircuit function. *Science* 345:6196. doi: 10.1126/science.1255263

Huang, R. Q., Bell-Horner, C. L., Dibas, M. I., Covey, D. F., Drewe, J. A., and Dillon, G. H. (2001). Pentylenetetrazole-induced inhibition of recombinant γ-aminobutyric acid type A (GABAA) receptors: mechanism and site of action. *J. Pharmacol. Exp. Ther.* 298, 986–995.

Ilhan, A., Iraz, M., Kamisli, S., and Yigitoglu, R. (2006). Pentylenetetrazol-induced kindling seizure attenuated by Ginkgo biloba extract (EGb 761) in mice. *Prog. Neuro Psychopharmacol. Biol. Psychiatry* 30, 1504–1510. doi: 10.1016/j.pnpbp.2006.05.013

Inan, M., and Anderson, S. A. (2014). The chandelier cell, form and function. *Curr. Opin. Neurobiol* 26, 142–148. doi: 10.1016/j.conb.2014.01.009

Johnson, E., Gurani, S., Dhamne, S., Lee, H., Hensch, T., and Rotenberg, A. (2018). "*Attenuation of seizure susceptibility through chemo-genetic mobilization of parvalbumin interneuron inhibitory reserve," in Abstract Retrieved from Abstracts in 72nd Annual Meeting of American Epilepsy Scoiety (Abst. 3.049)*. https://cms.aesnet.org/abstractslisting/attenuation-of-seizure-susceptibility-through-chemo-genetic-mobilization-of-parvalbumin-interneuron-inhibitory-reserve

Kawaguchi, Y., and Kubota, Y. (1997). GABAergic cell subtypes and their synaptic connections in rat frontal cortex. *Cereb. Cortex* 7, 476–486. doi: 10.1093/cercor/7.6.476

Kawaguchi, Y., Katsumaru, H., Kosaka, T., Heizmann, C. W., and Hama, K. (1987). Fast-spiking cells in rat hippocampus (CA1 region) contain the calcium-binding protein parvalbumin. *Brain Res.* 416, 369–374. doi: 10.1016/0006-8993(87)90921-8

Keskil, ÝS., Keskil, Z. A., Canseven, A. G., and Seyhan, N. (2001). No effect of 50 Hz magnetic field observed in a pilot study on pentylenetetrazol-induced seizures and mortality in mice. *Epilepsy Res.* 44, 27–32. doi: 10.1016/S0920-1211(00)00193-5

Khoshkhoo, S., Vogt, D., and Sohal, V. S. (2017). Dynamic, cell-type-specific roles for GABAergic interneurons in a mouse model of optogenetically inducible seizures. *Neuron* 93, 291–298. doi: 10.1016/j.neuron.2016.11.043

Kliouneva, I. A., van Luijtelaar, E. L. J. M., Chepurnova, N. E., and Chepurnov, S. A. (2001). PTZ-induced seizures in rats: effects of age and strain. *Physiol. Behav.* 72, 421–426. doi: 10.1016/S0031-9384(00)00425-X

Kostopoulos, G. K. (2017). "Pharmacologically induced animal models of absence seizures," in *Models of Seizures and Epilepsy*, eds A. Pitkanen, P. Buckmaster, and S. Galanopoulou (Cambridge: Academic Press). doi: 10.1016/B978-0-12-804066-9.00038-9

Koutroumanidou, E., Kimbaris, A., Kortsaris, A., Bezirtzoglou, E., Polissiou, M., Charalabopoulos, K., et al. (2013). Increased seizure latency and decreased severity of pentylenetetrazol-induced seizures in mice after essential oil administration. *Epilepsy Res. Treat.* 2013:532657. doi: 10.1155/2013/532657

Krall, R. L., Penry, J. K., White, B. G., Kupferberg, H. J., and Swinyard, E. A. (1978). Antiepileptic drug development: II. anticonvulsant drug screening. *Epilepsia* 19, 409–428. doi: 10.1111/j.1528-1157.1978.tb04507.x

Krook-Magnuson, E., Armstrong, C., Oijala, M., and Soltesz, I. (2013). On-demand optogenetic control of spontaneous seizures in temporal lobe epilepsy. *Nat. Commun.* 4:2376. doi: 10.1038/ncomms2376

Ledri, M., Madsen, M. G., Nikitidou, L., Kirik, D., and Kokaia, M. (2014). Global optogenetic activation of inhibitory interneurons during epileptiform activity. *J. Neurosci.* 34, 3364–3377. doi: 10.1523/JNEUROSCI.2734-13.2014

Letts, V. A., Felix, R., Biddlecome, G. H., Arikkath, J., Mahaffey, C. L., Valenzuela, A., et al. (1998). The mouse stargazer gene encodes a neuronal Ca 2+-channel γ subunit. *Nat. Genet.* 19, 340–347. doi: 10.1038/1228

Löscher, W. (2011). Critical review of current animal models of seizures and epilepsy used in the discovery and development of new antiepileptic drugs. *Seizure* 20, 359–368. doi: 10.1016/j.seizure.2011.01.003

Lüttjohann, A., and van Luijtelaar, G. (2015). Dynamics of networks during absence seizure's on-and offset in rodents and man. *Front. Physiol.* 6:16. doi: 10.3389/fphys.2015.00016

Lüttjohann, A., Fabene, P. F., and van Luijtelaar, G. (2009). A revised Racine's scale for PTZ-induced seizures in rats. *Physiol. Behav.* 98, 579–586. doi: 10.1016/j.physbeh.2009.09.005

Maheshwari, A., and Noebels, J. L. (2014). Monogenic models of absence epilepsy: windows into the complex balance between inhibition and excitation in

thalamocortical microcircuits. *Prog. Brain Res.* 213, 223–252. doi: 10.1016/B978-0-444-63326-2.00012-0

Maheshwari, A., Nahm, W., and Noebels, J. (2013). Paradoxical proepileptic response to NMDA receptor blockade linked to cortical interneuron defect in stargazer mice. *Front. Cell. Neurosci.* 7:156. doi: 10.3389/fncel.2013.00156

Marescaux, C., Micheletti, G., Vergnes, M., Depaulis, A., Rumbach, L., and Warter, J. M. (1984). A model of chronic spontaneous petit mal-like seizures in the rat: comparison with pentylenetetrazol-induced seizures. *Epilepsia* 25, 326–331. doi: 10.1111/j.1528-1157.1984.tb04196.x

McCafferty, C. P., David, F., Venzi, M., Lorincz, M. L., Delicata, F., Atherton, Z., et al. (2018). Cortical drive and thalamic feed-forward inhibition control thalamic output synchrony during absence seizures. *Nat. Neurosci.* 21, 744–756. doi: 10.1038/s41593-018-0130-4

McCormick, D. A., and Contreras, D. (2001). On the cellular and network bases of epileptic seizures. *Annu. Rev. Physiol.* 63, 815–846. doi: 10.1146/annurev.physiol.63.1.815

Medina, A. E., Manhães, A. C., and Schmidt, S. L. (2001). Sex differences in sensitivity to seizures elicited by pentylenetetrazol in mice. *Pharmacol. Biochem. Behav.* 68, 591–596. doi: 10.1016/S0091-3057(01)00466-X

Meeren, H. K., Pijn, J. P. M., Van Luijtelaar, E. L., Coenen, A. M., and da Silva, F. H. L. (2002). Cortical focus drives widespread corticothalamic networks during spontaneous absence seizures in rats. *J. Neurosci.* 22, 1480–1495.

Meeren, H., van Luijtelaar, G., da Silva, F. L., and Coenen, A. (2005). Evolving concepts on the pathophysiology of absence seizures: the cortical focus theory. *Arch. Neurol.* 62, 371–376.

Menuz, K., and Nicoll, R. A. (2008). Loss of inhibitory neuron AMPA receptors contributes to ataxia and epilepsy in stargazer mice. *J. Neurosci.* 28, 10599–10603.

Nassiri-Asl, M., Zamansoltani, F., and Torabinejad, B. (2009). Antiepileptic effects of quinine in the pentylenetetrazol model of seizure. *Seizure* 18, 129–132.

Noebels, J. L., Qiao, X., Bronson, R. T., Spencer, C., and Davisson, M. T. (1990). Stargazer: a new neurological mutant on chromosome 15 in the mouse with prolonged cortical seizures. *Epilepsy Res.* 7, 129–135.

Packer, A. M., and Yuste, R. (2011). Dense, unspecific connectivity of neocortical parvalbumin-positive interneurons: a canonical microcircuit for inhibition? *J. Neurosci.* 31, 13260–13271.

Panthi, S., and Leitch, B. (2019). The impact of silencing feed-forward parvalbumin-expressing inhibitory interneurons in the cortico-thalamocortical network on seizure generation and behaviour. *Neurobiol. Dis.* 132:104610.

Polack, P. O., Guillemain, I., Hu, E., Deransart, C., Depaulis, A., and Charpier, S. (2007). Deep layer somatosensory cortical neurons initiate spike-and-wave discharges in a genetic model of absence seizures. *J. Neurosci.* 27, 6590–6599.

Rogan, S. C., and Roth, B. L. (2011). Remote control of neuronal signalling. *Pharmacol. Rev.* 63, 291–315.

Rossignol, E., Kruglikov, I., Van Den Maagdenberg, A. M., Rudy, B., and Fishell, G. (2013). CaV2.1 ablation in cortical interneurons selectively impairs fast-spiking basket cells and causes generalized seizures. *Ann. Neurol.* 74, 209–222.

Schwaller, B., Tetko, I. V., Tandon, P., Silveira, D. C., Vreugdenhil, M., Henzi, T., et al. (2004). Parvalbumin deficiency affects network properties resulting in increased susceptibility to epileptic seizures. *Mol. Cell. Neurosci.* 25, 650–663.

Snead, O. C. (1992). "Pharmacological models of generalized absence seizures in rodents," in *Generalized Non-Convulsive Epilepsy: Focus on GABA-B Receptors*, eds C. Marescaux, M. Vergnes, and R. Bernasconi (Vienna: Springer).

Snead, O. C., Banerjee, P. K., Burnham, M., and Hampson, D. (2000). Modulation of absence seizures by the GABAA receptor: a critical role for metabotropic glutamate receptor 4 (mGluR4). *J. Neurosci.* 20, 6218–6224.

Sorokin, J. M., Davidson, T. J., Frechette, E., Abramian, A. M., Deisseroth, K., Huguenard, J. R., et al. (2017). Bidirectional control of generalized epilepsy networks via rapid real-time switching of firing mode. *Neuron* 93, 194–210. doi: 10.1016/j.neuron.2016.11.026

Studer, F., Laghouati, E., Jarre, G., David, O., Pouyatos, B., and Depaulis, A. (2018). Sensory coding is impaired in rat absence epilepsy. *J. Physiol.* 597:J277297. doi: 10.1113/JP277297

Tamamaki, N., Yanagawa, Y., Tomioka, R., Miyazaki, J. I., Obata, K., and Kaneko, T. (2003). Green fluorescent protein expression and colocalization with calretinin, parvalbumin, and somatostatin in the GAD67-GFP knock-in mouse. *J. Compar. Neurol.* 467, 60–79. doi: 10.1002/cne.10905

Tan, H. O., Reid, C. A., Single, F. N., Davies, P. J., Chiu, C., Murphy, S., et al. (2007). Reduced cortical inhibition in a mouse model of familial childhood absence epilepsy. *Proc. Natl. Acad. Sci. U.S.A.* 104, 17536–17541. doi: 10.1073/pnas.0708440104

Tremblay, R., Lee, S., and Rudy, B. (2016). GABAergic interneurons in the neocortex: from cellular properties to circuits. *Neuron* 91, 260–292. doi: 10.1016/j.neuron.2016.06.033

Van Erum, J., Valkenburg, F., Van Dam, D., and De Deyn, P. P. (2020). Pentylenetetrazole-induced seizure susceptibility in the Tau58/4 transgenic mouse model of tauopathy. *Neuroscience* 425, 112–122. doi: 10.1016/j.neuroscience.2019.11.007

Van Erum, J., Van Dam, D., and De Deyn, P. P. (2019). PTZ-induced seizures in mice require a revised Racine scale. *Epilepsy Behav.* 95, 51–55. doi: 10.1016/j.yebeh.2019.02.029

Velíšková, J., Shakarjian, M. P., and Velíšek, L. (2017). "Systemic chemoconvulsants producing acute seizures in adult rodents," in *Models of Seizures and Epilepsy*, eds A. Pitkanen and P. Buckmaster (Cambridge: Academic Press). doi: 10.1016/B978-0-12-804066-9.00035-3

Wang, Y., Liang, J., Chen, L., Shen, Y., Zhao, J., Xu, C., et al. (2018). Pharmacogenetic therapeutics targeting parvalbumin neurons attenuate temporal lobe epilepsy. *Neurobiol. Dis.* 117, 149–160. doi: 10.1016/j.nbd.2018.06.006

Xia, F., Richards, B. A., Tran, M. M., Josselyn, S. A., Takehara-Nishiuchi, K., and Frankland, P. W. (2017). Parvalbumin-positive interneurons mediate neocortical-hippocampal interactions that are necessary for memory consolidation. *Elife* 6:e27868. doi: 10.7554/eLife.27868.020

Xu, X., Roby, K. D., and Callaway, E. M. (2010). Immunochemical characterization of inhibitory mouse cortical neurons: three chemically distinct classes of inhibitory cells. *J. Compar. Neurol.* 518, 389–404. doi: 10.1002/cne.22229

Yekhlef, L., Breschi, G. L., Lagostena, L., Russo, G., and Taverna, S. (2015). Selective activation of parvalbumin-or somatostatin-expressing interneurons triggers epileptic seizure like activity in mouse medial entorhinal cortex. *J. Neurophysiol.* 113, 1616–1630. doi: 10.1152/jn.00841.2014

Zhu, H., Aryal, D. K., Olsen, R. H., Urban, D. J., Swearingen, A., Forbes, S., et al. (2016). Cre-dependent DREADD (designer receptors exclusively activated by designer drugs) mice. *Genesis* 54, 439–446. doi: 10.1002/dvg.22949

Zou, D., Chen, L., Deng, D., Jiang, D., Dong, F., McSweeney, C., et al. (2016). DREADD in parvalbumin interneurons of the dentate gyrus modulates anxiety, social interaction and memory extinction. *Curr. Mol. Med.* 16, 91–102.

Conflict of Interest: The authors declare that the research was conducted in the absence of any commercial or financial relationships that could be construed as a potential conflict of interest.

frontiers in Cellular Neuroscience

ORIGINAL RESEARCH
published: 22 July 2021
doi: 10.3389/fncel.2021.703407

Membrane Resonance in Pyramidal and GABAergic Neurons of the Mouse Perirhinal Cortex

Noemi Binini[1†], Francesca Talpo[1†], Paolo Spaiardi[1‡], Claudia Maniezzi[1‡], Matteo Pedrazzoli[1], Francesca Raffin[1], Niccolò Mattiello[1], Antonio N. Castagno[1], Sergio Masetto[2], Yuchio Yanagawa[3], Clayton T. Dickson[4], Stefano Ramat[5], Mauro Toselli[1] and Gerardo Rosario Biella[1*]*

[1] Department of Biology and Biotechnology Lazzaro Spallanzani, University of Pavia, Pavia, Italy, [2] Department of Brain and Behavioral Sciences, University of Pavia, Pavia, Italy, [3] Department of Genetic and Behavioral Neuroscience, Gunma University, Maebashi, Japan, [4] Department of Psychology, University of Alberta, Edmonton, AB, Canada, [5] Department of Industrial and Information Engineering, University of Pavia, Pavia, Italy

OPEN ACCESS

Edited by:
Sonia Gasparini,
Louisiana State University,
United States

Reviewed by:
Rishikesh Narayanan,
Indian Institute of Science (IISc), India
Rory McQuiston,
Virginia Commonwealth University,
United States

***Correspondence:**
Francesca Talpo
francesca.talpo01@universitadipavia.it
Gerardo Rosario Biella
gerardo.biella@unipv.it

[†]These authors share first authorship

[‡]These authors have contributed equally to this work

Specialty section:
This article was submitted to Cellular Neurophysiology, a section of the journal Frontiers in Cellular Neuroscience

Received: 30 April 2021
Accepted: 16 June 2021
Published: 22 July 2021

Citation:
Binini N, Talpo F, Spaiardi P, Maniezzi C, Pedrazzoli M, Raffin F, Mattiello N, Castagno AN, Masetto S, Yanagawa Y, Dickson CT, Ramat S, Toselli M and Biella GR (2021) Membrane Resonance in Pyramidal and GABAergic Neurons of the Mouse Perirhinal Cortex. Front. Cell. Neurosci. 15:703407. doi: 10.3389/fncel.2021.703407

The perirhinal cortex (PRC) is a polymodal associative region of the temporal lobe that works as a gateway between cortical areas and hippocampus. In recent years, an increasing interest arose in the role played by the PRC in learning and memory processes, such as object recognition memory, in contrast with certain forms of hippocampus-dependent spatial and episodic memory. The integrative properties of the PRC should provide all necessary resources to select and enhance the information to be propagated to and from the hippocampus. Among these properties, we explore in this paper the ability of the PRC neurons to amplify the output voltage to current input at selected frequencies, known as membrane resonance. Within cerebral circuits the resonance of a neuron operates as a filter toward inputs signals at certain frequencies to coordinate network activity in the brain by affecting the rate of neuronal firing and the precision of spike timing. Furthermore, the ability of the PRC neurons to resonate could have a fundamental role in generating subthreshold oscillations and in the selection of cortical inputs directed to the hippocampus. Here, performing whole-cell patch-clamp recordings from perirhinal pyramidal neurons and GABAergic interneurons of GAD67-GFP$^+$ mice, we found, for the first time, that the majority of PRC neurons are resonant at their resting potential, with a resonance frequency of 0.5–1.5 Hz at 23°C and of 1.5–2.8 Hz at 36°C. In the presence of ZD7288 (blocker of HCN channels) resonance was abolished in both pyramidal neurons and interneurons, suggesting that I_h current is critically involved in resonance generation. Otherwise, application of TTx (voltage-dependent Na^+ channel blocker) attenuates the resonance in pyramidal neurons but not in interneurons, suggesting that only in pyramidal neurons the persistent sodium current has an amplifying effect. These experimental results have also been confirmed by a computational model. From a functional point of view, the resonance in the PRC would affect the reverberating activity between neocortex and hippocampus, especially during slow wave sleep, and could be involved in the redistribution and strengthening of memory representation in cortical regions.

Keywords: membrane resonance, pyramidal neuron, GABAergic interneuron, perirhinal cortex, patch-clamp

INTRODUCTION

The perirhinal cortex (PRC) is a polymodal associative ventral region of the temporal lobe located laterally to the rhinal sulcus. It is connected with many sensory and polymodal areas, reward-related cortices, and other structures of the medial temporal lobe (MTL) such as the entorhinal and postrhinal (or parahippocampal in primates) cortices, the amygdala (Pinto et al., 2006; Biella et al., 2010), and the hippocampus (Witter et al., 2000; Kealy and Commins, 2011; Suzuki and Naya, 2014). In recent years, there has been an increasing interest in the role played by the perirhinal cortex in cognitive functions such as declarative learning and memory, as well as interest in its susceptibility during the initial stages of specific neurodegenerative diseases like Alzheimer's. More specifically, PRC is involved in recognition memory, visual perception, and associative processes. Our current understanding of the role of PRC has been primarily based on lesion experiments, but the underlying functional mechanisms determining how it executes these tasks remain to be uncovered. Based on cytoarchitectonic properties and anatomical connections, PRC should play a crucial role in processing information directed from and to the hippocampal formation. The key role of the perirhinal region, that is not simply a passive relay station, is underscored. Indeed, PRC has a robust inhibitory system (de Curtis and Paré, 2004) that acts as an active gate to selectively allow information to propagate from other cortical regions to the hippocampus and vice versa. In the PRC, in fact, excitatory neocortical inputs undergo a powerful inhibitory block maintained by local GABAergic interneurons (Martina et al., 2001; Biella et al., 2002; Garden et al., 2002; Willems et al., 2018). Moreover, PRC importantly retains integrative properties that are essential for different memory and perceptual tasks (Biella et al., 2001; Murray and Richmond, 2001; Davachi, 2006; Staresina and Davachi, 2008; Suzuki and Naya, 2014).

According to this state of the art, we suggest that the inhibitory barrier in the PRC could allow a selection of relevant inputs directed to and from the hippocampus. To this purpose, namely the ability to select and enhance specific inputs, different cellular and network strategies could be applied, like for example to enhance synaptic plasticity (Perugini et al., 2012) as well as to generate oscillatory patterns in neuronal networks. Furthermore, it has been shown that subpopulations of neurons in many cerebral areas, such as neocortex (Hutcheon et al., 1996, Sun et al., 2014), entorhinal cortex (Lampl and Yarom, 1997; Hutcheon and Yarom, 2000; Haas and White, 2002; Erchova et al., 2004; Engel et al., 2008), and hippocampus (Leung and Yu, 1998; Pike et al., 2000; Hu et al., 2002; Erchova et al., 2004; Narayanan and Johnston, 2007), are able to amplify the output voltage to current input at selected frequencies. This property is called membrane resonance. Within cerebral circuits the resonance of different types of neurons operates as a filter toward inputs signals at certain frequencies, to coordinate network activity in the brain by affecting the rate of neuronal firing (Hutcheon and Yarom, 2000), to influence the precision of spike timing (Desmaisons et al., 1999; Haas and White, 2002; Schaefer et al., 2006), and to cause spike clustering (Chen and Shepherd, 1997; Desmaisons et al., 1999; Pedroarena et al., 1999; Wu et al., 2001; Izhikevich et al., 2003). Resonant behavior emerges as a result of an interplay between membrane passive and active properties due to the frequency-dependent increase of membrane impedance produced by voltage-dependent ion channels (Hutcheon and Yarom, 2000). Several voltage-dependent ion currents are critical for the genesis of the resonance such as M-type potassium current, T-type calcium current, h-type hyperpolarized-activated cationic current, whereas other ones such as the persistent sodium current or the potassium inward rectifier current can act as amplifying currents that facilitate membrane resonance. The ability of perirhinal neurons to resonate could have a fundamental role in generating subthreshold oscillations and in the selection of cortical inputs directed to the hippocampus. At present, there is no report about a possible resonant behavior of neurons located in the PRC.

Shay et al. (2012) demonstrated that, among the different areas of the parahippocampal region, the neurons of the medial entorhinal cortex (EC) show a maximum resonant frequency ranging from 4 to 8 Hz (theta wave) suggesting that these properties could contribute to the generation of the firing dynamics of grid cells in the medial EC that are related to the processing of spatial information. Neurons recorded from the lateral EC that is strongly connected to the PRC (Burke et al., 2018) showed a lower resonant frequency, between 1 and 2 Hz, very similar to that observed in neocortical neurons (0.7–2.5 Hz) (Hutcheon et al., 1996). Furthermore, resonant behavior has been observed in different subregions of the hippocampus. Hippocampal pyramidal neurons showed a resonant frequency ranging among 2–8 Hz (Pike et al., 2000; Hu et al., 2002) whereas two subpopulations of GABAergic interneurons showed either a lower (1–3 Hz, the horizontal interneuron) or higher (10–50 Hz, fast-spiking interneurons) resonant frequency bandwidth. Likely, the resonance properties of neurons and their synaptic interactions within the different areas of the hippocampal region underlie state-dependent network oscillations that may serve as a temporal modality to associate linked and distant neural networks. In this way, by binding different neural networks, resonance could act as a potential cellular mechanism to temporally coordinate information directed to and from the hippocampus.

A systematic study of the resonance properties in the perirhinal neurons has not been performed yet. In this study, we report for the first time that a sizeable subpopulation of both pyramidal cells and GABAergic interneurons of the PRC are able to resonate in a selected range of frequencies (1–2.5 Hz).

MATERIALS AND METHODS

Animals and Brain Slice Preparation

Juvenile (P17–P27) heterozygous GAD67-GFP knock-in mice (Tamamaki et al., 2003) were used for all experiments. Experimental handling of the animals was performed in accordance with EU directive 86/609/EEC, approved by the National Ministry of Health, and designed to minimize the number of the animals and their suffering.

Animals were anesthetized by inhalation of isoflurane and decapitated. The whole brain was removed and submerged in cold (∼4°C) carboxygenated (95% O_2, 5% CO_2) cutting solution (Sucrose 70 mM, NaCl 80 mM, KCl 2.5 mM, $NaHCO_3$ 26 mM, Glucose 15 mM, $MgCl_2$ 7 mM, $CaCl_2$ 1 mM, NaH_2PO_4 1.25 mM; pH 7.3). Coronal 350 μm-thick slices containing the rhinal sulcus were prepared using a vibratome (DTK-1000, Dosaka EM). Following cutting, the slices were allowed to equilibrate for at least 1 h in a recovery chamber filled with carboxygenated artificial cerebrospinal fluid (aCSF) medium (NaCl 125 mM, KCl 2.5 mM, $NaHCO_3$ 26 mM, Glucose 15 mM, $MgCl_2$ 1.3 mM, $CaCl_2$ 2.3 mM, NaH_2PO_4 1.25 mM; pH 7.3).

Electrophysiological Recordings

Recordings were performed at room temperature (∼23°C) on submerged slices perfused at 1.4 ml/min with aCSF, unless otherwise stated. The recording chamber was mounted on an E600FN microscope connected to a near-infrared CCD camera. Data were derived from perirhinal pyramidal neurons and GAD67-GFP-expressing GABAergic interneurons using the whole-cell patch-clamp technique in voltage- and current-clamp modes. Pipettes were produced from borosilicate glass capillary tubes (Hilgenberg GmbH) using a horizontal puller (P-97, Sutter instruments) and filled with the following intracellular solution: K-gluconate 130 mM, NaCl 4 mM, $MgCl_2$ 2 mM, EGTA 1 mM, creatine phosphate 5 mM, Na_2ATP 2 mM, Na_3GTP 0.3 mM, Hepes 10 mM (pH 7.3 with KOH). Series resistance was minimized and monitored throughout the experiment (R_s initial = 9.2 ± 0.3; R_s final = 11.7 ± 0.5 for pyramidal neurons, N = 128 and R_s initial = 11.7 ± 0.5; R_s final = 13.8 ± 0.5 for GABAergic interneurons, N = 70), however, it was not compensated by using the bridge balance circuit. Recordings were made with a MultiClamp 700B amplifier (Molecular Devices) and digitized with a Digidata 1322 computer interface (Molecular Devices). Data were acquired using the software Clampex 9.2 (Molecular Devices), sampled at 20 kHz, filtered at 10 kHz, and analyzed with the software Clampfit 10.2 (Molecular Devices) and Origin 6.0 (Microcal).

Morphology of Recorded Neurons

To confirm the identity of the recorded cells by their morphology, biocytin (3 mg/ml, Sigma) was added to the intracellular solution and it diffused into the cell through the patch micropipette during electrophysiological recording. Following recordings slices were fixed in 4% paraformaldehyde for 30 min, washed with PBS (Dulbecco's phosphate buffer saline, Sigma), then incubated overnight with 10 μg/ml DAPI (4′,6-diamidino-2-phenylindole), and 5 μg/ml Alexa Fluor 568-conjugated streptavidin (Molecular Probes). Next day slices were mounted on microscope slides using DAKO Mounting Medium. Images were acquired by confocal microscopy [microscope Leica TCS SP2 equipped with three laser lines: (i) Ar/UV laser with emissions at 351 and 364 nm; (ii) Ar/Vis laser with emissions at 458 and 488 nm and (iii) HeNe laser with emissions at 543 and 633 nm] using a dedicated acquisition software (LCS software). Cells were reconstructed by using Imaris software (Bitplane).

Characterization of the Passive and the Firing Properties of the Neurons

For each recorded cell we calculated the membrane capacitance (C_m), the input resistance (R_{in}), and the resting membrane potential (V_r). C_m was estimated by integrating the capacitive current evoked by a −10 mV pulse, whereas R_{in} was calculated from the same protocol at the end of a 20 ms pulse, when the current trace reached the steady state. V_r was detected in current-clamp mode with 0pA current injection. To characterize the features of the action potentials (APs), we injected positive supra-threshold current steps. The AP threshold (AP_{Th}) is the value of the membrane potential at which a rapid upstroke of the AP starts (corresponding to the value of potential at which the action potential temporal derivative crosses 20 V/s). The AP amplitude (AP_A) was measured as the voltage difference between the top of the spike and the AP_{Th}. The AP duration (AP_D) was calculated as the spike width measured at half-maximal spike amplitude. The firing pattern of each cell was categorized through a twofold quantitative analysis. Specifically, we evaluated i) the inter-spike-intervals (ISIs) and ii) the coefficients of variation for a sequence of ISIs (CV2) (Holt et al., 1996; Shinomoto et al., 2009; Komendantov et al., 2019; Graf et al., 2020). ISIs were computed as the temporal separation of two contiguous spikes repeated for each pair of APs of the neuronal discharge. CV2 was calculated as in Holt et al. (1996) by the following Equation (1) applied for all the ISIs of the discharge:

$$CV2 = \frac{2 * |ISI_{i+1} - ISI_i|}{ISI_{i+1} + ISI_i} \quad (1)$$

Characterization of Subthreshold Resonance

To characterize the resonant behavior of the cells, the *impedance amplitude profile* (ZAP) method was used (Hutcheon et al., 1996; Hutcheon and Yarom, 2000). A sinusoidal current with constant amplitude (60 pA peak-to-peak) and linearly increasing frequency from 0 to 15 Hz (ZAP current of 50 s) was applied. The protocol was repeated 3–5 times for each cell and the voltage responses were recorded and averaged. Resonance occurs as a peak in the voltage response at a specific frequency (F_{res}). In some experiments the reproducibility of the voltage response has been demonstrated by applying modified ZAP current protocols (i.e., ZAP current with a 40 pA or a 20-pA peak-to-peak amplitude, inverted ZAP current with a 15–0 Hz declining frequency, negative ZAP current with the first peak of the stimulus oriented negatively). The impedance profile [Z(f)] was calculated by dividing the Fast Fourier Transform (FFT) of the membrane potential response (V) by the FFT of the ZAP current (I), as indicated in Equation (2).

$$Z(f) = \frac{FFT[V(t)]}{FFT[I(t)]} \quad (2)$$

Z(f) is a complex quantity (Z(f) = Z *Real*+ iZ*Imaginary*) that can be plotted as a vector whose magnitude (| Z(f)|)

and phase ($\varphi_z(f)$) are given by the expressions (3) and (4), respectively.

$$|Z(f)| = \sqrt{(Z, Real)^2 + (Z, Imaginary)^2} \quad (3)$$

$$\phi_z(f) = \tan^{-1}\left(\frac{Z, Imaginary}{Z, Real}\right) \quad (4)$$

The plot of the impedance phase as a function of frequency indicates the phase shift of the voltage wave relative to the current wave. Throughout this manuscript the term *impedance* refers to the magnitude of the impedance vector, unless otherwise stated. In the relationship between impedance and frequency, the ratio of the impedance at the resonance peak (Z_{res}) to the impedance at 0.1 Hz (Z_0) is called *Q*-value and this parameter is used to highlight the absence ($Q < 1.05$) or the presence ($Q \geq 1.05$) of resonance and its relative strength. The complex representation of the impedance integrates the information of both magnitude and phase. The impedance magnitude corresponds to the length of the vectors connecting the origin of the axes to each point of the graph, while the phase is the angle between each vector and the real axis (see **Figure 2D**). For resonant cells, the complex representation is characterized by points in both positive and negative regions of the imaginary axes whereas non-resonant neurons display a series of points limited to the negative imaginary region.

Chemicals and Drugs

All drugs were added to the aCFS medium and bath perfused at the following final concentrations: 10 μM 4-Ethylphenylamino-1,2-dimethyl-6-methylaminopyrimidin chloride (ZD7288, Abcam; HCN channel blocker), 1 μM tetrodotoxin (TTx, Alomone Labs; voltage-dependent Na^+ channel blocker), 10 μM 2,3-Dioxo-6-nitro-1,2,3,4-tetrahydrobenzo[f]quinoxaline-7-sulfonamide (NBQX, Tocris; AMPA receptors antagonist), 30 μM (RS)-3-(2-Carboxypiperazin-4-yl)-propyl-1-phosphonic acid [(RS)-CPP, Tocris; NMDA receptors antagonist] and 10 μM bicuculline methiodide (Sigma-Aldrich; $GABA_A$ receptors antagonist).

Computational Model

A conductance-based single compartment model reproducing subthreshold resonance was developed using MATLAB. It includes a passive leak current (I_{leak}), a hyperpolarization-activated cation current (I_h), and a persistent (non-inactivating) Na^+ current (I_{NaP}). In the model, these currents were described using the following equations:

$$I_{leak} = g_{leak} \times (V - E_{leak}) \quad (5)$$

$$I_h = g_h \times f \times (V - E_h) \quad (6)$$

$$I_{Nap} = g_{Nap} \times w \times (V - E_{Nap}) \quad (7)$$

with g_{leak}, g_h, and g_{NaP} being the maximal conductances of the corresponding currents and E_{leak}, E_h, and E_{NaP} their reversal potentials.

Moreover, the dynamics of the state variables $x_i = f$ were described by the following equation:

$$\frac{dx_n}{dt} = \frac{x_{n\infty}(V) - x_n}{\tau_{xn}} \quad (8)$$

where $x_{n\infty}$ were the steady-state values of x_n and τ_{xn} were the corresponding time constants.

A summary of the reversal potentials and the equations that define the steady-state variables and time constants for the different currents is shown in **Table 1**. Voltage dependence of state variables and time constants for I_h and for I_{NaP} were taken from Spain et al. (1987) and Hodgkin and Huxley (1952), respectively.

The τ value for I_h was divided by the temperature-correcting factor (Magee, 1998):

$$4.5^{(T-38)/10}$$

where T is the temperature in degree (Celsius).

The model reproduces the stimulus current used in the experiments (I_{Zap}). A holding current (I_{cmd}) was also added to the model to maintain a holding potential of −70 mV.

The output of the model is the variation of voltage vs. time, which is represented by the following equation:

$$\frac{dV}{dt} = \frac{I_{Zap} - I_{leak} - I_h - I_{Zap} + I_{Cmd}}{C} \quad (9)$$

in which C is the membrane capacitance, fixed at 1 $\mu F/cm^2$.

Statistics

Collected data are presented as all-point plots together with summary statistics [means ± standard error of the mean (SEM.)] to show them in detail and avoid misinterpretations (Marder and Taylor, 2011; Rathour and Narayanan, 2019). Statistical significance was determined, depending on data, by paired or unpaired two-tailed Student's *t*-test, One-Way ANOVA test followed by Bonferroni post-hoc, or Kruskal-Wallis test with Dunn's multiple comparisons test. To assess pairwise relationship in the parameters under investigation we analyzed the scatterplot matrices of them and computed the correspondent Pearson's correlation coefficients and significance values, as in Mishra and Narayanan (2020).

TABLE 1 | Parameters and equations used for calculation of ionic currents in the computational model.

Current	g (ms/cm^2)	V_{rev1}	V_{rev2}	State variables	τ (ms)
I_{leak}	0.03	−89	−89	–	–
I_h	0.009	−25	−25	$f_\infty = \frac{1}{1+e^{(V+70)/7}}$	38
I_{NaP}	0.23	70.6	74.2	$w_\infty = \frac{1}{1+e^{-(V+70)/5}}$	5

Summary of conductance values (g), reversal potentials, equations ruling steady-state variables, and time constants (τ) for ionic currents implemented in the model. Voltage dependence of state variables and time constants were taken from Spain et al. (1987) for I_h and from Hodgkin and Huxley (1952) for I_{NaP}.

RESULTS

Properties and Firing Patterns of Pyramidal Neurons and GABAergic Interneurons of the Mouse PRC

Targeted whole-cell patch-clamp recordings were performed on both deep and superficial layer pyramidal cells and GABAergic interneurons from coronal PRC (areas 35 and 36) brain slices obtained from young GAD67-GFP knock-in mice. In this animal model GABAergic interneurons can be easily identified because they are constitutively labeled with GFP (Tamamaki et al., 2003). In a subset of cells, confirmation of anatomical identity was obtained by biocytin labeling and imaging (**Figures 1A,F**). From a functional point of view, we found significant differences in passive membrane properties between pyramidal cells and GABAergic interneurons, as expected (Karayannis et al., 2007). Specifically, membrane capacitance (C_m) was significantly higher in pyramidal neurons than in GABAergic interneurons ($p < 0.001$), while membrane input resistance (R_{in}) was significantly higher in GABAergic interneurons as compared with pyramidal neurons ($p < 0.01$) (**Table 2**). Instead, we found no differences in resting membrane potential (V_r) (**Table 2**). Then, we analyzed the firing patterns of the PRC pyramidal neurons and GABAergic interneurons by calculating (i) the distribution of the inter-spike-intervals (ISI) (**Figure 1L**) and (ii) the coefficient of variation of the discharge (CV2), that measures the intrinsic variability of a spike train (**Figure 1M**; Holt et al., 1996; Shinomoto et al., 2009; Komendantov et al., 2019; Graf et al., 2020).

In this way, we identified 5 different types of discharge (**Figures 1B–E,G–K**).

(1) Late-spiking regular neurons (RS): At just-suprathreshold, these neurons show a slow ramp depolarization before the onset of their spike trains, with a consequent delay of the first spike. At more sustained depolarizations, they are characterized by a persistent tonic or slightly adapting firing. In line with this, their ISI distribution is linear and almost parallel to the *X*-axis (red dots in **Figure 1L**). Also, their ISI-CV2 relationship shows a cloud of dots very concentrated and close to each other at a low CV2 (about 0.1) (red dots in **Figure 1M**).

(2) Stuttering fast-spiking neurons (FS): At just-suprathreshold, these neurons fire trains of high-frequency spikes (30–50 Hz) separated by variable periods of silence. At more sustained depolarizations, they are characterized by a persistent high-frequency (50–100 Hz) tonic firing. Likewise in RS neurons, their ISI distribution is linear and almost parallel to the *X*-axis and their ISI-CV2 relationship shows a cloud of dots very concentrated and close to each other at a low CV2 (about 0.1). However, the FS dots (orange) can be distinguished from the RS dots (red) because they are shifted to lower ISI values (**Figures 1L,M**).

(3) Adapting neurons (ADP): Adapting neurons typically begin their spike trains at a short latency following onset of a depolarizing current step and accommodate strongly. Due to adaptation, their ISI distribution is linear, but with a higher angular coefficient than RS and FS neurons (blue dots in **Figure 1L**). Also, their ISI-CV2 relationship shows a quite dispersed cloud of dots (blue dots in **Figure 1M**) with a higher mean CV2 (about 0.4).

(4) Bursting neurons (BST): Bursting neurons are characterized by spikes that occur in a stereotyped pattern consisting into a cluster of 2–3 action potentials riding on a slow depolarizing wave and followed by a strong slow afterhyperpolarization. After the burst, their firing generally becomes regular. Therefore, their ISI distribution is not linear but starts with shorter ISIs (green dots in **Figure 1L**) and their ISI-CV2 relationship consists in a rather compact cloud of dots (corresponding to the regular firing) accompanied by two or three more dispersed dots (corresponding to the burst) (green dots in **Figure 1M**).

(5) Irregular neurons (IR): Irregular neurons show a random and unpredictable firing pattern. Their ISI distribution is dispersed and not linear (black dots in **Figure 1L**) and also their ISI-CV2 relationship consists in a dispersed cloud of dots (black dots in **Figure 1M**). They have a mean CV2 similar to that of adapting neurons (about 0.4), but their non-linear ISI distribution uniquely characterizes them.

This classification is similar to what is currently described in literature (Faulkner and Brown, 1999; Beggs et al., 2000; McGann et al., 2001). Accordingly, we found that 41.5% of pyramidal neurons were RS, 20.5% ADP, 26% BST, and 12% IR. The same classification indicates that 60% of GABAergic interneurons were FS, 18.5% RS, 3% ADP, 10% BST, and 8.5% IR (**Figure 1N**).

Resonant and Non-resonant Behavior in Glutamatergic Pyramidal Neurons and GABAergic Interneurons of the PRC

A regular 50sec-long ZAP current input with linearly increasing frequency from 0 to 15 Hz was applied to test for resonant behavior of pyramidal neurons (**Figures 2A,E**) and GABAergic interneurons (**Figures 2A′,E′**) at a membrane potential of −70 mV. Resonance appears as a peak in the voltage response at a specific frequency (F_{res}) (**Figures 2A,A′**), that is absent in non-resonant cells (**Figures 2E,E′**). As a consequence, resonant cells show a peak in the impedance-to-frequency relationship at F_{res} (corresponding to the dashed vertical line in **Figures 2B,B′**), whereas a clear peak is not detectable in non-resonant cells (**Figures 2F,F′**). Accordingly, the phase shift-to-frequency relationship and the complex representation of the impedance differentiates between resonant (**Figures 2C,D,C′,D′**) and non-resonant (**Figures 2G,H,G′,H′**) neurons, through clustering of positive values in resonant neurons. The percentage of the resonant pyramidal neurons and GABAergic interneurons measured in the superficial and deep layers of areas 35 (A35) and 36 (A36) of the PRC is shown in **Table 3**. Overall, the majority of perirhinal pyramidal neurons (77%) and GABAergic interneurons (54%) were resonant and were equally distributed throughout the PRC, without a clear prevalence in a specific

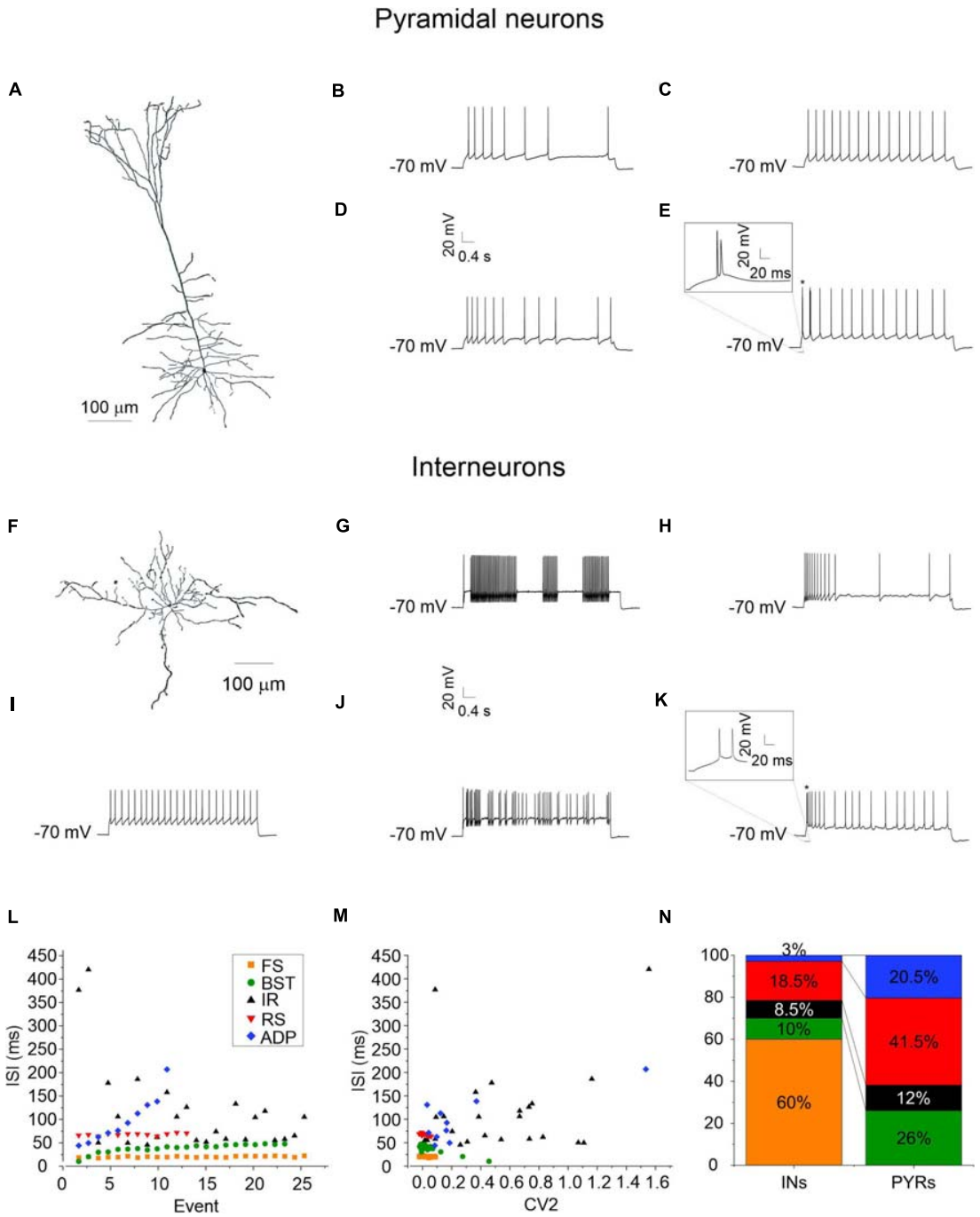

FIGURE 1 | Morphology and firing patterns of pyramidal neurons and GABAergic interneurons of the PRC. **(A)** Imaris reconstruction of a biocytin-labeled pyramidal neuron of the PRC. **(B–E)** Firing traces recorded from representative adapting (ADP) **(B)**, late- and regular-spiking (RS) **(C)**, irregular (IR) **(D)**, and bursting (BST; burst magnification in the inset) **(E)** PRC pyramidal neurons. **(F)** Imaris reconstruction of a biocytin-labeled perirhinal GABAergic interneuron. **(G–K)** Firing traces recorded from representative stuttering fast-spiking (FS) **(G)**, adapting (ADP) **(H)**, late- and regular-spiking (RS) **(I)**, irregular (IR) **(J)**, and bursting (BST; burst magnification in the inset) **(K)** PRC GABAergic interneurons. **(L,M)** Inter-spike-interval (ISI) to event plot **(L)** and inter-spike-interval (ISI) to coefficient of variation (CV2) plot **(M)** showing the behavior of five representative cells, one for each type of firing patter identified in the PRC. **(N)** Percentage of each type of discharge in PRC pyramidal cells ($N = 128$) and GABAergic interneurons ($N = 70$), respectively.

area or layer (**Table 3**), suggesting that resonance could be very important for the oscillatory synchronization and integration of the neuronal activity in this region. Also, the resonance strength (Q_{-70}) and the frequency of resonance (F_{res}) were similar in pyramidal neurons of A35 vs. A36 and of superficial vs. deep layers (**Figures 3A–D**). Comparable results were obtained also

TABLE 2 | Comparison of the principal passive electrophysiological properties of pyramidal neurons and GABAergic interneurons of the PRC.

	Number of cells (N)	C_m (pF)	R_{in} (MΩ)	V_r (mV)
Pyramidal neurons	128	92.5 ± 2.4	181 ± 5	−67.8 ± 0.5
Interneurons	70	34.4 ± 1.2 ***	210 ± 10 **	−67.9 ± 0.7

*Values of membrane capacitance, membrane input resistance, and membrane resting potential for each cell type are reported as mean ± SEM and were statistically compared (pyramidal neurons vs. GABAergic interneurons) by unpaired Student's t-test. **p < 0.01; ***p < 0.001.*

in GABAergic interneurons (**Figures 3A–D**). However, we found that the Q_{-70} was significantly different between pyramidal neurons and GABAergic interneurons regardless of their location (**Figures 3A,C**).

In a subset of cells, experiments were repeated using "inverted" ($N = 13$) and "negative" ($N = 12$) ZAP protocols without any changes in the reported resonant properties of the cells (data not shown). This demonstrates that the resonant peak depends on the frequency of stimulation and not on the timing or orientation of the ZAP input. The ZAP input was also applied before and following perfusion of the synaptic blockers NBQX (10μM), (RS)-CPP (30 μM), and bicuculline methiodide (10 μM), without any changes in resonant properties demonstrating that membrane resonance is an intrinsic property of the neurons and is not driven by synaptic input ($N = 5$; not shown).

Correlations in Firing Properties, Passive Properties, and Resonant/Non-resonant Behavior of the PRC Neurons

As already stated, PRC pyramidal neurons and GABAergic interneurons showed different firing patterns in response to the injection of suprathreshold current steps. Therefore, we tried to identify possible correlations between the firing pattern and the resonant/non-resonant behavior of these cells. To this purpose, we computed the percentage of specific firing patterns for non-resonant and resonant pyramidal (**Figures 4A,B**) and GABAergic neurons (**Figures 4A′,B′**). Furthermore, we computed the percentage of resonant vs. non-resonant cells classified for a specific firing pattern of pyramidal (**Figure 4C**) and GABAergic neurons (**Figure 4C′**). In pyramidal neurons, we found a prevalence of resonant neurons regardless of the firing pattern (**Figure 4C**). In addition, the percentage of the different types of firing pattern was quite similar in non-resonant (**Figure 4A**) and resonant (**Figure 4B**) cells. In contrast, in GABAergic interneurons we found (i) a large prevalence of resonant cells in RS, BST, and ADP neurons, (ii) an equal percentage of resonant vs. non-resonant cells in IR neurons, and iii) a prevalence of non-resonant cells in FS neurons (**Figure 4C′**). Resonant interneurons showed all the types of firing patterns, although in different percentages (**Figure 4B′**). On the contrary, a high percentage (84.5%) of non-resonant GABAergic interneurons were FS (**Figure 4A′**).

To clarify the interdependencies between passive properties, firing properties, and resonance in the neurons of the different PRC areas and layers, we plotted pairwise scatterplots of C_m (membrane capacitance), R_{in} (input resistance), V_r (membrane resting potential), AP_{Th} (spike Threshold), AP_A (spike Amplitude), AP_D (spike Duration), First ISI, Mean ISI, Mean CV2, Q_{-70} recorded from pyramidal and GABAergic neurons of A35 and A36 (**Figure 5**) and of superficial and deep layers (**Figure 6**) of the PRC. Then we computed Pearson's correlation coefficients for each of them. By examining separately pyramidal neurons or GABAergic interneurons, we found that the correlation matrices were quite similar among the different areas (**Figure 5**) and layers (**Figure 6**). As expected, we found significant correlations in pairwise comparisons of passive properties (for example inverse correlation between C_m and R_{in}) and of firing properties (for example inverse correlation between AP_{Th} and AP_A; direct correlation between Mean ISI and Mean CV2).

Focusing on Q_{-70}, in pyramidal neurons we found that this parameter was significantly correlated only with R_{in} (inverse correlation) (**Figures 5A–C**, 6A,B). Furthermore, by directly comparing R_{in} in resonant vs. non-resonant pyramidal neurons, we found a significantly lower R_{in} in resonant cells (**Table 4**). We also found a significantly more depolarized V_r in resonant pyramidal neurons (**Table 4**). Overall, we assume these results to be due to the presence of a putative cationic current expressed only in resonant cells and active at their V_r (−70 mV).

In GABAergic interneurons we found significant correlations between Q_{-70} and many other passive (direct correlations with C_m, V_r, and R_{in}) and firing (direct correlations with Mean ISI and AP_D) parameters (**Figures 5A′–C′**, **6A′,B′**). This suggested an effective correlation between the firing patterns and the resonant/non-resonant behavior of the GABAergic interneurons, as already indicated by the percentage distributions in **Figure 4**. In fact, non-resonant GABAergic interneurons were mainly FS cells characterized, compared to the other subclasses of interneurons, by higher firing rate (lower Mean ISI), lower AP_D, lower C_m, and lower R_{in} (Ma et al., 2006). Interestingly, the direct comparison of R_{in} in resonant vs. non-resonant GABAergic interneurons reinforced this hypothesis since we found a significantly lower R_{in} in non-resonant cells (**Table 4**). As in pyramidal neurons, we also found a significantly more depolarized V_r in resonant GABAergic neurons (**Table 4**), likely due to both the higher R_{in} and the expression of a resonant-specific cationic current.

Resonance Properties at Different Membrane Potentials

In resonant neurons, the voltage-dependence of Q and F_{res} was tested by applying the ZAP protocol at different membrane potentials, ranging from −55 to −90 mV. In pyramidal neurons (solid line), resonance (Q-values > 1.05) began at potential more negative than −55 mV and was preserved at more hyperpolarized potentials (**Figure 7A**). Resonance strength was maximal at −70 mV, as emphasized by the relative increase in the Q-value at this potential ($Q = 1.24 \pm 0.02$, **Figure 7A**).

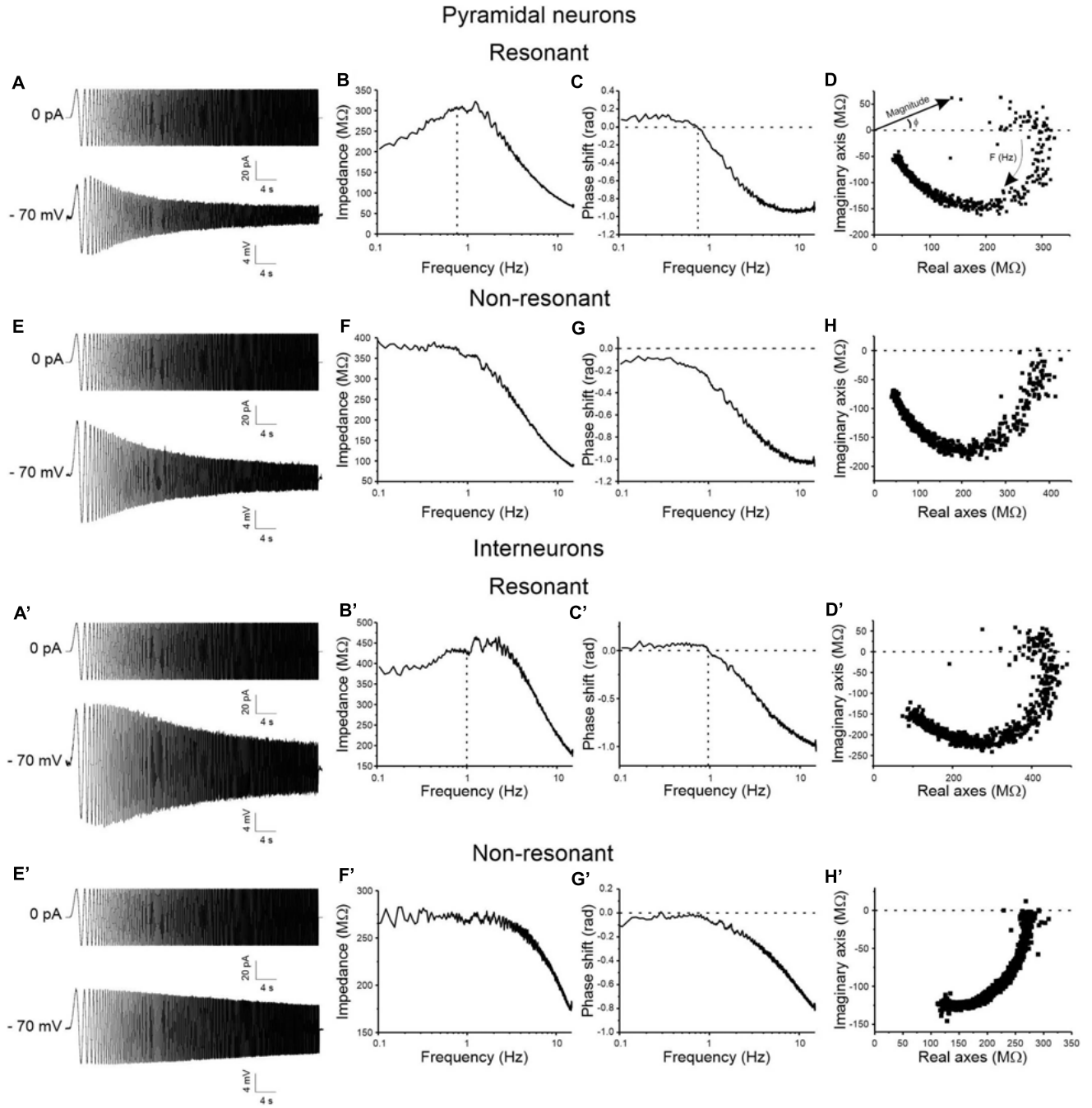

FIGURE 2 | Resonant vs. non-resonant behavior of pyramidal neurons **(A–H)** and GABAergic interneurons **(A′–H′)** of the PRC. **(A)** Representative voltage response of a resonant pyramidal neuron (lower trace) to a ZAP input of linearly increasing frequency from 0 to 15 Hz (upper trace) at membrane potential of –70 mV. **(B)** Impedance magnitude vs. frequency relationship of the same cell as in **(A)**. Dashed line in correspondence to the peak in the relationship indicates the F_{res} of the cell. **(C)** Impedance phase vs. frequency relationship of the same cell as in **(A)**. The resonant behavior of the cell determines a positive phase shift at the low frequencies, reflecting anticipation of the voltage wave relative to the current wave. Hence, F_{res} corresponds to the value of frequency at which phase shift is 0 rad (dashed lines). **(D)** Complex representation of impedance of the same neuron shown in **(A–C)**. Impedance vectors are represented as points in the complex plane: the length of the vectors connecting the origin of the axes to each point of the graph corresponds to the impedance magnitude and the angle between each vector and the real axis corresponds to the impedance phase. Note that for resonant cells the complex representation is characterized by points in both positive and negative regions of the imaginary axis. **(E–H)** Same as **(A–D)**, for a representative non-resonant pyramidal neuron. The non-resonant behavior of the cell is evidenced by the absence of the peak in the impedance-to-frequency relationship **(F)**, the negative phase shift at all investigated frequencies **(G)**, and the points limited to the negative imaginary region of the impedance locus diagram **(H)**. **(A′–H′)** Same as **(A–H)** for a representative resonant **(A′–D′)** and a representative non-resonant **(E′–H′)** GABAergic interneuron.

TABLE 3 | Distribution of the resonant pyramidal neurons and GABAergic interneurons in the superficial and deep layers of the areas 35 (A35) and 36 (A36) of the PRC.

	A35		A36		Total		Total	
	Superficial layers	Deep layers	Superficial layers	Deep layers	A35	A36	Superficial layers	Deep layers
Pyramidal neurons	10/15 (67%)	44/55 (80%)	9/17 (53%)	36/41 (88%)	54/70 (77%)	45/58 (78%)	19/32 (59%)	80/96 (83%)
Interneurons	6/12 (50%)	20/40 (50%)	4/5 (80%)	8/13 (62%)	26/52 (50%)	12/19 (63%)	10/17 (59%)	28/53 (53%)

Number of resonant cells vs. total number of recorded cells and corresponding percentages. Resonant neurons are numerous and equally distributed throughout the PRC, without a clear prevalence in a specific area or layer.

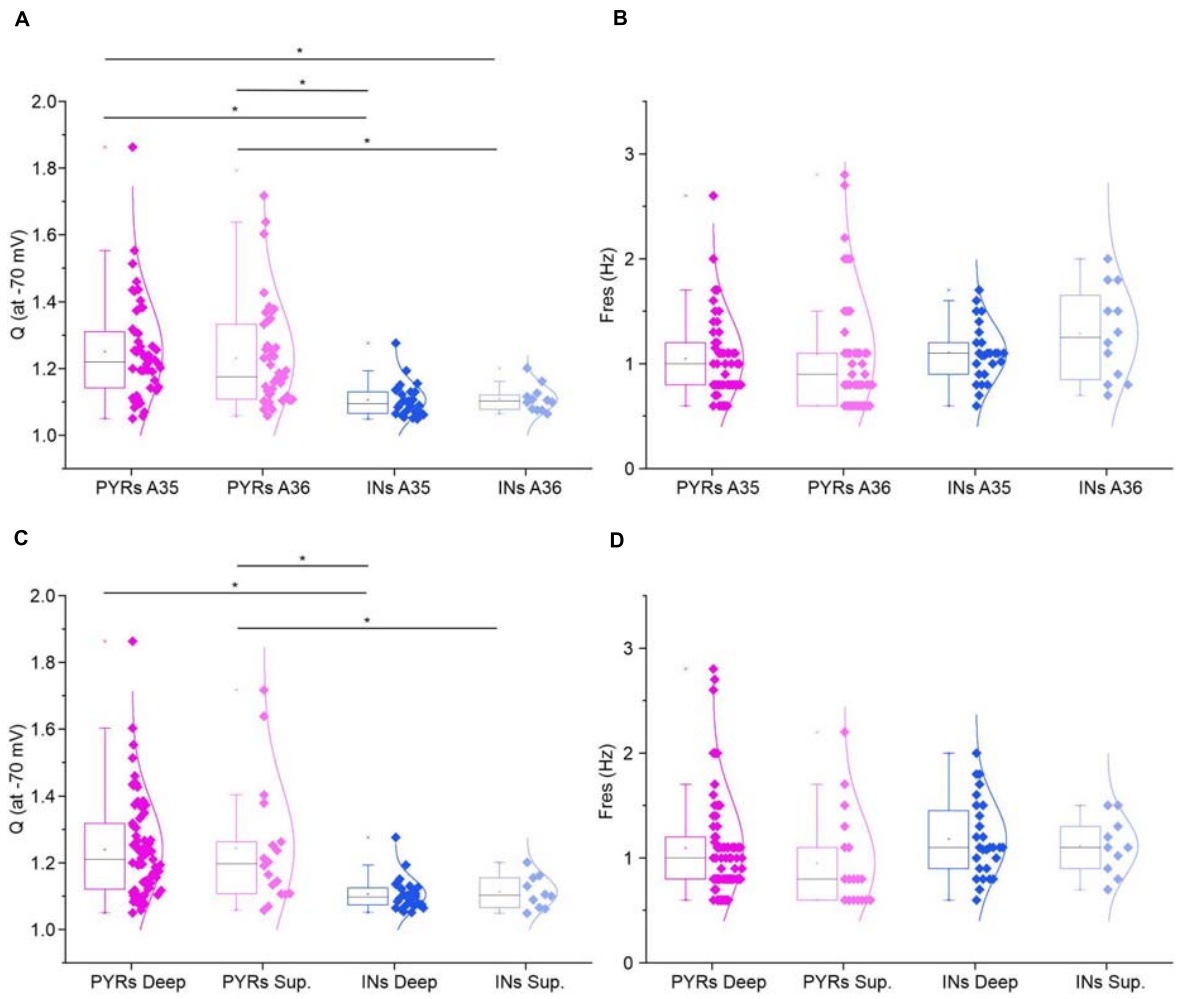

FIGURE 3 | Resonance in the different areas and layers of the PRC. **(A,B)** All-points half-violin plots flanked by summary box plots for Q **(A)** and F_{res} **(B)** at –70 mV for resonant pyramidal neurons and GABAergic interneurons of Area35 vs. Area 36. **(C,D)** Same as **(A–D)**, for superficial vs. deep layers. Data were compared by One-Way ANOVA followed by Bonferroni *post hoc*. *$p < 0.05$.

In contrast, GABAergic interneurons (dashed line) start to show resonance at potentials more negative than −60 mV and did not show a clear increase in the *Q*-value at any specific potential (**Figure 7A**). It is noteworthy that *Q*-values were significantly greater in pyramidal neurons than in GABAergic interneurons at both −60 mV ($p < 0.01$) and −70 mV ($p < 0.001$), perhaps suggesting that pyramidal neurons express an amplifying conductance that increases the *Q*-values which might be not present in interneurons.

F_{res} was similar in the two cell types and nearly constant (1–1.5 Hz) in a wide range of membrane potentials (**Figure 7B**).

Effects of the Block of HCN Channels on Resonant Behavior of the Perirhinal Neurons

As stated above, we found a more depolarized membrane resting potential in resonant compared to non-resonant neurons,

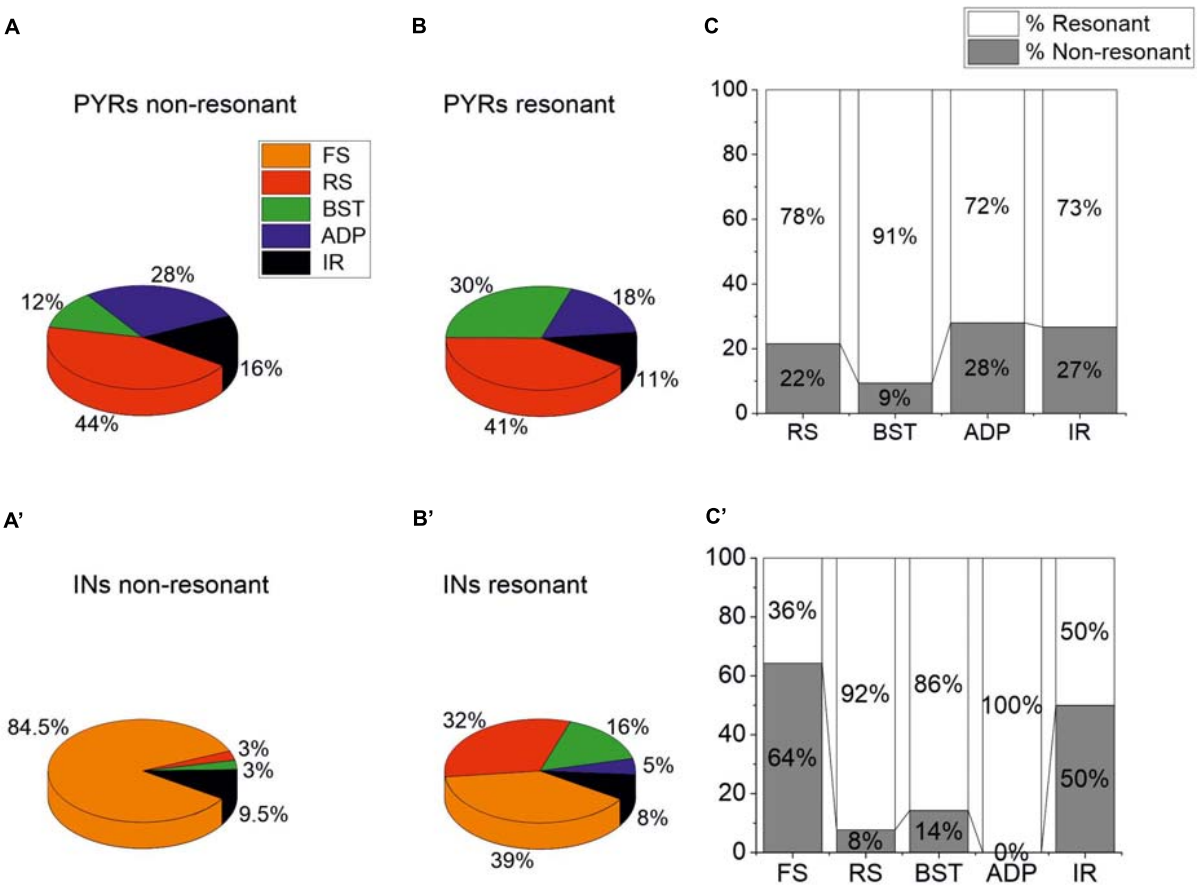

FIGURE 4 | Relationships between firing patterns and resonant or non-resonant behavior of the PRC neurons. **(A,B)** Percentage of specific firing patterns for resonant **(A)** and non-resonant **(B)** PRC pyramidal neurons. **(C)** Percentage of resonant vs. non-resonant cells classified for a specific firing pattern of pyramidal neurons. **(A′–C′)** Same as **(A–C)** for GABAergic interneurons.

suggesting the presence of a putative cationic conductance expressed only in resonant cells and active at V_r (−70 mV). Moreover, resonance behavior was preserved at hyperpolarized potentials, but disappeared at depolarized potentials. Based on this evidence and on literature (Hutcheon et al., 1996; Hu et al., 2002; Nolan et al., 2007; Biel et al., 2009; Ehrlich et al., 2012; Boehlen et al., 2013; Vera et al., 2014), we hypothesized the involvement of an I_h current in the resonance of PRC neurons. I_h is indeed a cationic subthreshold current showing biophysical properties that could cause low-frequency resonance at hyperpolarized potentials.

Consistently with the hypothesis that I_h is implicated in PRC resonance, we found a prominent "sag" in the voltage response to hyperpolarizing current steps, likely due to I_h activation, in all resonant perirhinal neurons (**Figures 8A,A′**), but not in non-resonant neurons. The "sag" was completely abolished by the administration of ZD7288 (10 μM), a specific blocker of HCN (hyperpolarization-activated cyclic nucleotide–gated) channels whose activation generate the I_h current in neurons (**Figures 8A,A′**).

Following blockage of I_h by ZD7288, the expression of resonant behavior was completely blocked (**Figures 8B–E,B′–E′**). The effect of the inhibition of I_h on the ZAP response is shown in the example traces reported in **Figures 8B,B′**. Following ZD7288 application the peak in the impedance-to-frequency relationship was abolished (**Figures 8C,C′**) and the *Q*-value decreased below the resonance threshold (**Figures 8D,D′**) for both resonant pyramidal cells and GABAergic interneurons, confirming a key role of I_h in generating resonance in PRC.

Role of Persistent Sodium Current in Amplifying the Resonant Behavior of Perirhinal Pyramidal Neurons

Given that the *Q*-value was significantly higher in resonant pyramidal neurons when compared to resonant interneurons at −60 and −70 mV (**Figure 7A**), we hypothesized that these neurons selectively express an amplifying current that is widely described in several classes of resonant cells (Traub and Miles, 1991; Gutfreund et al., 1995; Hutcheon et al., 1996; Hutcheon and Yarom, 2000; Hu et al., 2002; Vera et al., 2014; Matsumoto-Makidono et al., 2016). Since the persistent sodium current (I_{NaP}) is a typical amplifying current that has been already reported to enhance the resonant behavior at

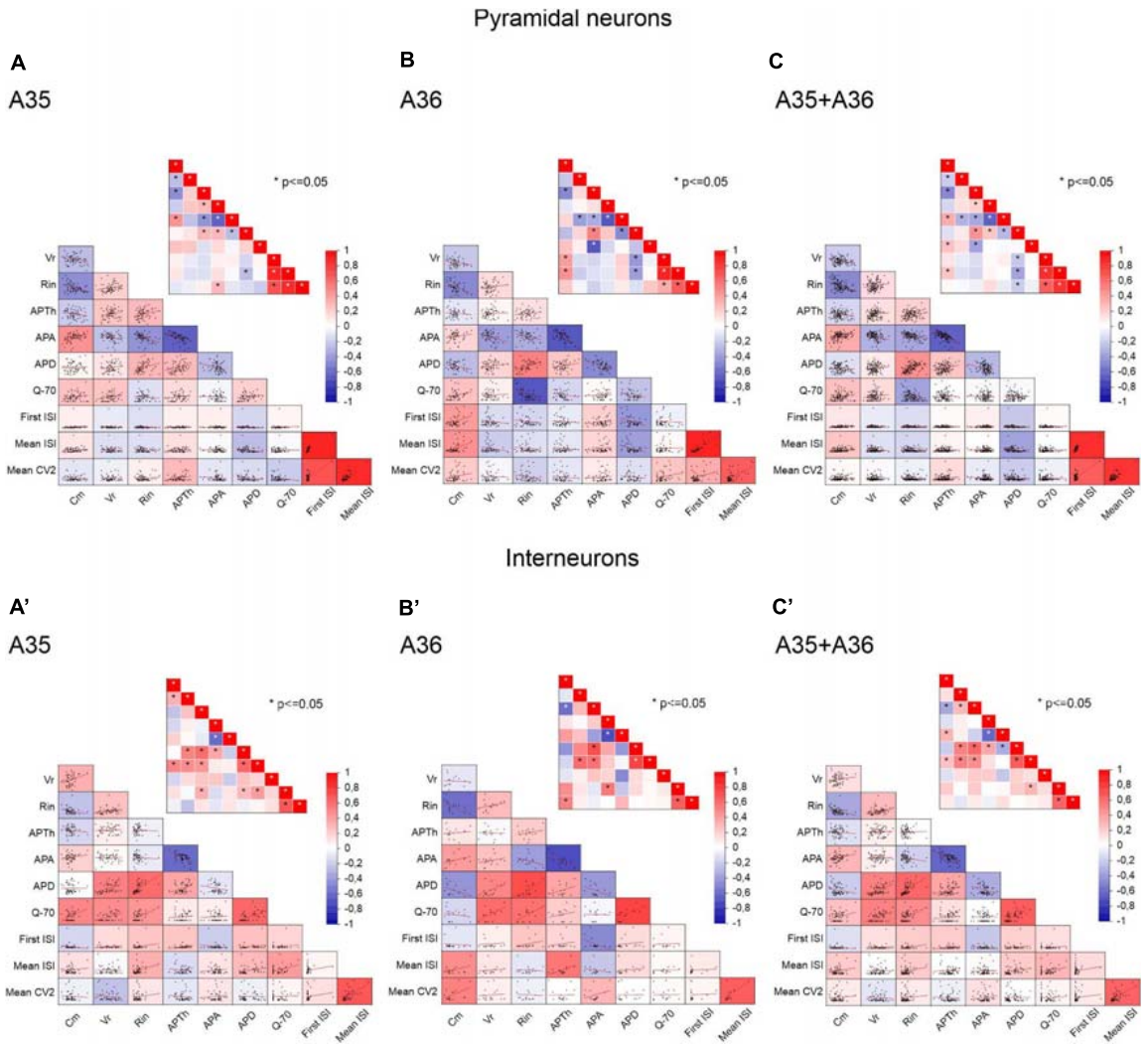

FIGURE 5 | Correlations between passive properties, firing properties, and resonance in the neurons of the different PRC areas. **(A–C)** Pairwise scatterplot matrices of C_m (membrane capacitance), V_r (membrane resting potential), R_{in} (input resistance), AP_{Th} (spike Threshold), AP_A (spike Amplitude), AP_D (spike Duration), Q_{-70}, First ISI, Mean ISI, Mean CV2 of pyramidal neurons recorded from A35 **(A)**, A36 **(B)**, and both A35+A36 **(C)**. These scatterplot matrices are overlaid on the corresponding color-coded correlation matrices and the insets in each panel represent the significance value associated with each scatterplot, computed as Pearson's correlation coefficients. **(A′–C′)** Same as **(A–C)** for GABAergic interneurons. *$p \leq 0.05$.

membrane potentials near V_r (Hutcheon et al., 1996; Vera et al., 2014), we tested the involvement of I_{NaP} on the amplification of the membrane resonance in PRC pyramidal neurons. To this purpose, we applied TTx (1μM) during the administration of the ZAP protocol. We found that TTx attenuates the resonance strength measured at −70 mV in pyramidal neurons (**Figures 9A,B**) but not in GABAergic interneurons (**Figures 9A′,B′**). Accordingly, the *Q*-value was significantly reduced from 1.3 to 1.2 in pyramidal cells ($p < 0.01$) (**Figure 9C**), whereas it remained unchanged in GABAergic interneurons (**Figure 9C′**). As expected, TTx did not alter the values of F_{res} in both cell type (**Figures 9D,D′**).

These data confirm that the persistent sodium current has an amplifying effect on the resonant behavior specifically in the pyramidal neurons of the PRC. TTx blocks also the transient Na^+ current but we excluded the involvement of this current in resonance amplification because of its fast kinetics and its more depolarized activation threshold.

Effect of Temperature on the Resonance Properties of Perirhinal Neurons

It has been shown that the resonance properties of the neurons can be affected by temperature (Hu et al., 2002; Yan et al., 2012; Vera et al., 2014). To verify whether the resonance properties of perirhinal neurons are also influenced by temperature, we performed a set of experiments at 36°C. **Figures 10A,A′** show representative impedance profiles derived at 36°C from a resonant pyramidal neuron and a resonant GABAergic interneuron, respectively. Data were obtained by

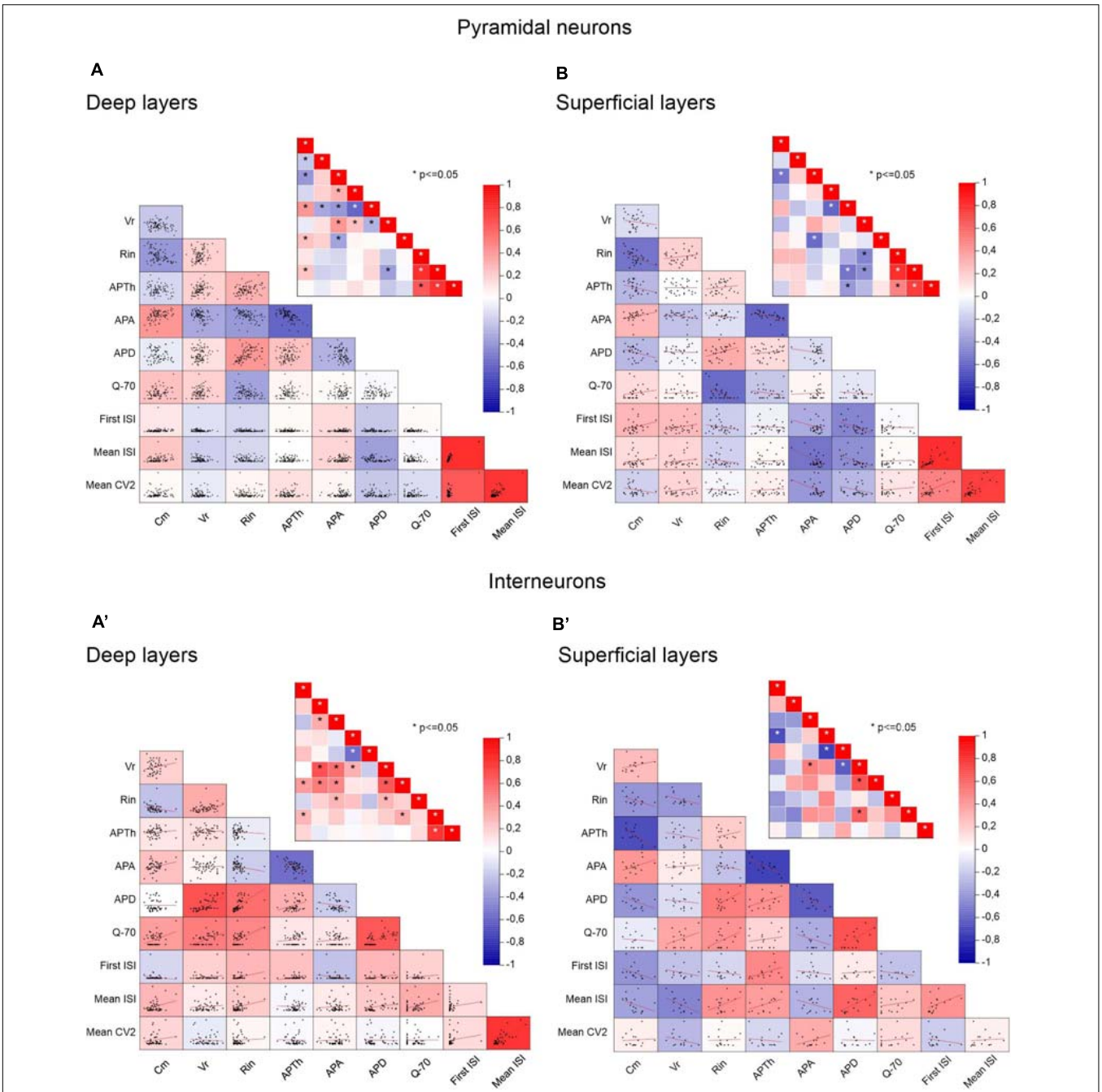

FIGURE 6 | Correlations between passive properties, firing properties, and resonance in the neurons of the different PRC layers. **(A,B)** Pairwise scatterplot matrices of C_m (membrane capacitance), V_r (membrane resting potential), R_{in} (input resistance), AP_{Th} (spike Threshold), AP_A (spike Amplitude), AP_D (spike Duration), Q_{-70}, First ISI, Mean ISI, Mean CV2 of pyramidal neurons recorded from the deep **(A)** and the superficial **(B)** layers. These scatterplot matrices are overlaid on the corresponding color-coded correlation matrices and the insets in each panel represent the significance value associated with each scatterplot, computed as Pearson's correlation coefficients. **(A′,B′)** Same as **(A,B)** for GABAergic interneurons. *$p \leq 0.05$.

applying the standard 0–15 Hz ZAP protocol at −70 mV. The analysis revealed that the *Q*-value does not change by increasing the temperature from 23 to 36° C, either in pyramidal neurons or GABAergic interneurons (**Figures 10B,B′**). On the contrary, resonant frequency significantly increased from 1.17 ± 0.04 to 2.53 ± 0.49 Hz in pyramidal neurons ($p < 0.05$) and from 1.13 ± 0.04 to 2.00 ± 0.22 Hz in GABAergic interneurons ($p < 0.05$) (**Figures 10C,C′**).

Computational Model

The resonant behavior of the perirhinal pyramidal neurons and GABAergic interneurons was reproduced by a computational

TABLE 4 | Comparison of the principal passive electrophysiological properties of resonant vs. non-resonant neurons of the PRC.

	Number of cells (N)		C_m (pF)		R_{in} (MΩ)		V_r (mV)	
	Resonant	Non-resonant	Resonant	Non-resonant	Resonant	Non-resonant	Resonant	Non-resonant
Pyramidal neurons	99	29	94.5 ± 2.5	85.8 ± 6.3	175 ± 5 *	202 ± 15	−67.1 ± 0.5 **	−70.3 ± 1.0
Interneurons	38	32	35.7 ± 1.9	32.9 ± 1.3	237 ± 15 **	177 ± 9	−65.9 ± 0.8 ***	−70.3 ± 0.9

*Values of membrane capacitance, membrane input resistance, and membrane resting potential for resonant vs. non-resonant neurons are reported as mean ± SEM and were statistically compared by unpaired Student's t-test. *$p < 0.05$; **$p < 0.01$; ***$p < 0.001$.*

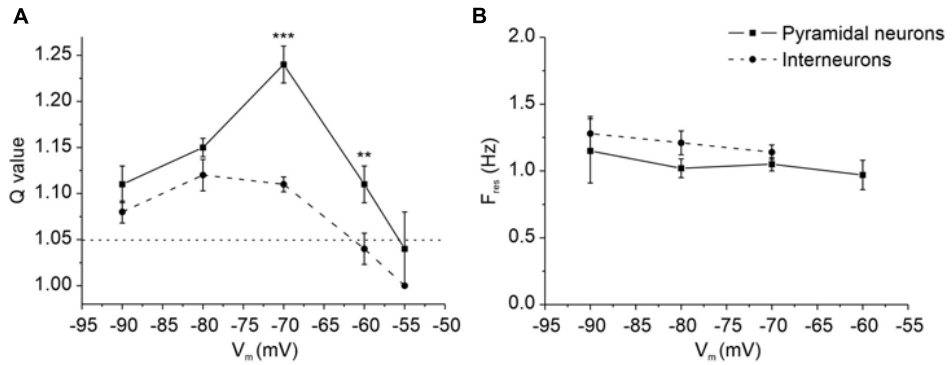

FIGURE 7 | Resonance properties of PRC pyramidal neurons and GABAergic interneurons at different membrane potentials. **(A)** Average Q values at different membrane potentials for pyramidal neurons (solid line) and GABAergic interneurons (dashed line). *Q*-value is defined as the ratio of impedance magnitude at F_{res} and 0.1 Hz and is used to highlight the strength of the resonance. Dotted line at $Q = 1.05$ discriminates between absence (*Q*-value < 1.05) and presence (*Q*-value ≥ 1.05) of resonance. On average, pyramidal neurons show a significantly higher *Q*-value at –60 and –70 mV ($N = 35$ and $N = 99$, respectively) compared to GABAergic interneurons recorded at the same membrane potentials ($N = 15$ and $N = 37$, respectively) (**$p < 0.01$; ***$p < 0.001$; unpaired Student's *t*-test). Moreover, among pyramidal neurons the mean *Q*-value was greater at –70 mV ($N = 99$) compared to the most of other tested potential [–55 mV ($p < 0.01$, $N = 5$), –60 mV ($p < 0.001$, $N = 35$), –80 mV ($p < 0.001$, $N = 40$); Kruskal-Wallis followed by Dunn's multiple comparisons test]. Among interneurons the mean *Q*-value was lower at –60 mV ($N = 15$) compared to –70 mV ($p < 0.001$, $N = 37$) and –80 mV ($p < 0.01$, $N = 12$) (Kruskal-Wallis followed by Dunn's multiple comparisons test). **(B)** Average F_{res} at different membrane potentials for pyramidal neurons (solid line) and GABAergic interneurons (dashed line). The mean values of F_{res} are similar between pyramidal neurons [–60 mV ($N = 21$), –70 mV ($N = 99$), –80 mV ($N = 38$) and –90 mV ($N = 8$)] and GABAergic interneurons [–70 mV ($N = 37$), –80 mV ($N = 12$), –90 mV ($N = 9$)] at all tested potentials (unpaired Student's *t*-test).

model in MATLAB (see section "Materials and Methods" for details) by applying the same sinusoidal ZAP input current used in the electrophysiological experiments (Origin 6.0).

At first, the model was tested with a ZAP protocol at −70 mV in its basal conditions where only the leakage current (I_{leak}) was expressed (**Figure 11A**). The corresponding impedance profile (**Figure 11B**) strongly resembled the pattern of a non-resonant neuron acting as a low-pass filter. By adding the persistent sodium current (I_{NaP}), the voltage response and the corresponding impedance profile still showed a lack of a resonant behavior (**Figures 11C,D**) indicating that I_{NaP} alone is not sufficient to generate resonance. A resonant response was obtained by simulating the expression of the h-current (I_h), as indicated by the appearance of a peak in the impedance profile ($Q = 1.1$) (**Figures 11E,F**). The F_{res} calculated from the impedance profile obtained in the model overlapped that measured during patch-clamp recording experiments. In a model simulating the presence of I_{leak}, I_h, and I_{NaP} an amplification of the resonance was observed (**Figures 11G,H**), as demonstrated by an increase of the *Q*-value ($Q = 1.2$) compared to the previous condition.

To examine whether the effect of the temperature on the resonant frequency was also reproducible in the model, the value of the simulated temperature (T) was increased up to 36°C (**Figures 11A′–H′**). As expected, F_{res} shifted toward higher values in the model simulating the presence of both I_{leak} and I_h (**Figures 7E′,F′**) and in the model simulating the contribution of all three currents $I_{leak} + I_h + I_{NaP}$ (**Figures 7G′,H′**).

In summary, by implementing a computational model with parameters obtained with patch-clamp experiments we were able to reproduce the resonant behavior observed in both pyramidal neurons and GABAergic interneurons of the PRC.

DISCUSSION AND CONCLUSION

This paper describes for the first time the membrane resonance properties of pyramidal cells and GABAergic interneurons throughout the different layers of the mouse perirhinal cortex. These findings represent a missing piece of a comprehensive puzzle designed to define the functional contribution of the parahippocampal cortical regions in the processing of information directed to and propagated from the hippocampus. In particular, by applying a 0–15 Hz ZAP protocol, we demonstrated that a substantial subpopulation (over 75% of

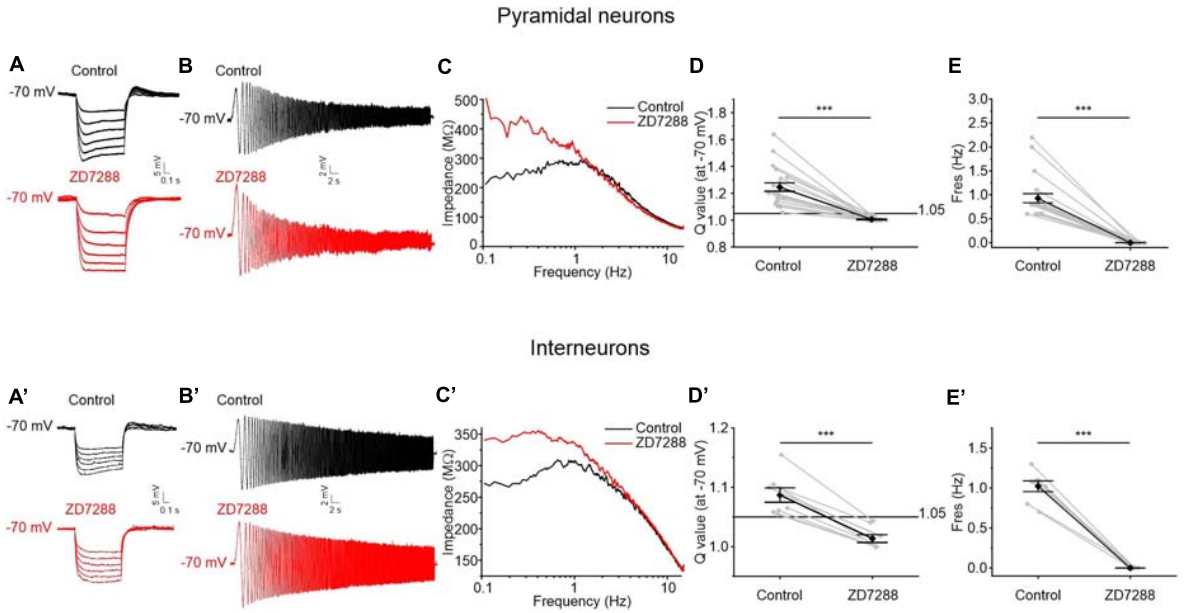

FIGURE 8 | Effects of the block of HCN channels on resonant behavior of pyramidal neurons **(A–D)** and GABAergic interneurons **(A′–D′)** of the PRC. **(A)** Representative voltage traces evoked by applying hyperpolarizing current steps to a resonant pyramidal neuron. A prominent "*sag*" appears in the voltage responses (upper traces in black) and is abolished after administration of the HCN blocker ZD7288 10 μM (lower traces in red). **(B)** Voltage responses of a representative resonant pyramidal neuron to the standard 0–15 Hz ZAP protocol at –70 mV before (upper trace in black) and after (lower trace in red) the perfusion of ZD7288 10 μM. **(C)** Impedance-to-frequency relationship of the same cell as in **(B)**, before (black line) and after (red line) ZD7288 perfusion. **(D,E)** Scatter plots comparing the *Q*-values **(C)** and F_{res} values **(D)** derived from resonant pyramidal neurons ($N = 21$) before (Control) and after (ZD7288) blocking the HCN channels (gray dots and lines). Mean ± SEM. *Q*-values are reported on the same plot in black. In ZD7288 condition, the resonant behavior is completely abolished. **(A′–D′)** Same as **(A–D)** for GABAergic interneurons ($N = 8$): also in GABAergic interneurons ZD7288 administration completely abolishes "*sag*" **(A′)** and resonant behavior **(B′–D′)**. Data in **(D,E,D′,E′)** were compared by paired Student's *t*-test. ***$p < 0.001$.

pyramidal cells and over 50% of GABAergic interneurons) of the PRC neurons showed membrane resonance in a frequency (F_{res}) ranging from 1 to 2.5 Hz. By using "inverted" and "negative" ZAP protocols, as well as by repeating the experiments before and following perfusion of synaptic blockers NBQX, (RS)-CPP, and bicuculline methiodide, we demonstrated that resonant behavior and peak are intrinsic properties of the PRC cells, not influenced by the time and the orientation of the ZAP input and not driven by synaptic input. It is worth noticing that bicuculline methiodide blocks also SK-channels (Johnson and Seutin, 1997). This is a potential caveat that needs to be considered, since SK-current could possibly be implicated in the generation of resonance (Xue et al., 2012). However, we did not observe changes in resonant properties following the perfusion of the synaptic blockers (including bicuculline methiodide). Then, we believe that SK-current is not implicated in the generation of the resonant response in the PRC cells and the results of the subset of experiments involving the administration of synaptic blockers are reliable.

We did not observed differences in the distribution of the pyramidal and GABAergic resonant neurons throughout the different areas (A35 and A36) and layers (deep and superficial) of the PRC. Furthermore, the resonance strength and the frequency of resonance seemed to be independent from the localization of the cells. The Pearson's correlation matrices of C_m (membrane capacitance), R_{in} (input resistance), V_r (membrane resting potential), AP_{Th} (spike Threshold), AP_A (spike Amplitude), AP_D (spike Duration), First ISI, Mean ISI, Mean CV2, and Q_{-70} were also similar when computed in different PRC areas and layers.

On the other hand, by analyzing possible correlations between the firing pattern and the resonant/non-resonant behavior of the PRC cells, we found interesting differences between pyramidal neurons and GABAergic interneurons. In pyramidal neurons the percentage of the different types of firing pattern (RS, ADP, BST, IR) was quite similar in non-resonant and resonant cells, with a majority of resonant cells regardless of the firing pattern. In pyramidal neurons, the Q_{-70} was inversely correlated with R_{in}. R_{in} was also significantly lower in cells that showed a resonant behavior and expressed the I_h at V_r. No others significant correlations emerged. In contrast, in GABAergic interneurons Q_{-70} significantly correlated with many other passive (direct correlations with C_m, V_r, and R_{in}) and firing (direct correlations with Mean ISI and AP_D) parameters. The high prevalence of FS cells—characterized by higher firing rate (lower Mean ISI), lower AP_D, lower C_m, and lower R_{in} (Ma et al., 2006)—in non-resonant GABAergic interneurons could support these correlations. A significantly lower R_{in} in non-resonant compared to resonant interneurons reinforced this hypothesis. Overall, these data suggested an effective correlation between the firing pattern and the resonant/non-resonant behavior in the GABAergic interneurons, but not in the pyramidal neurons of the PRC.

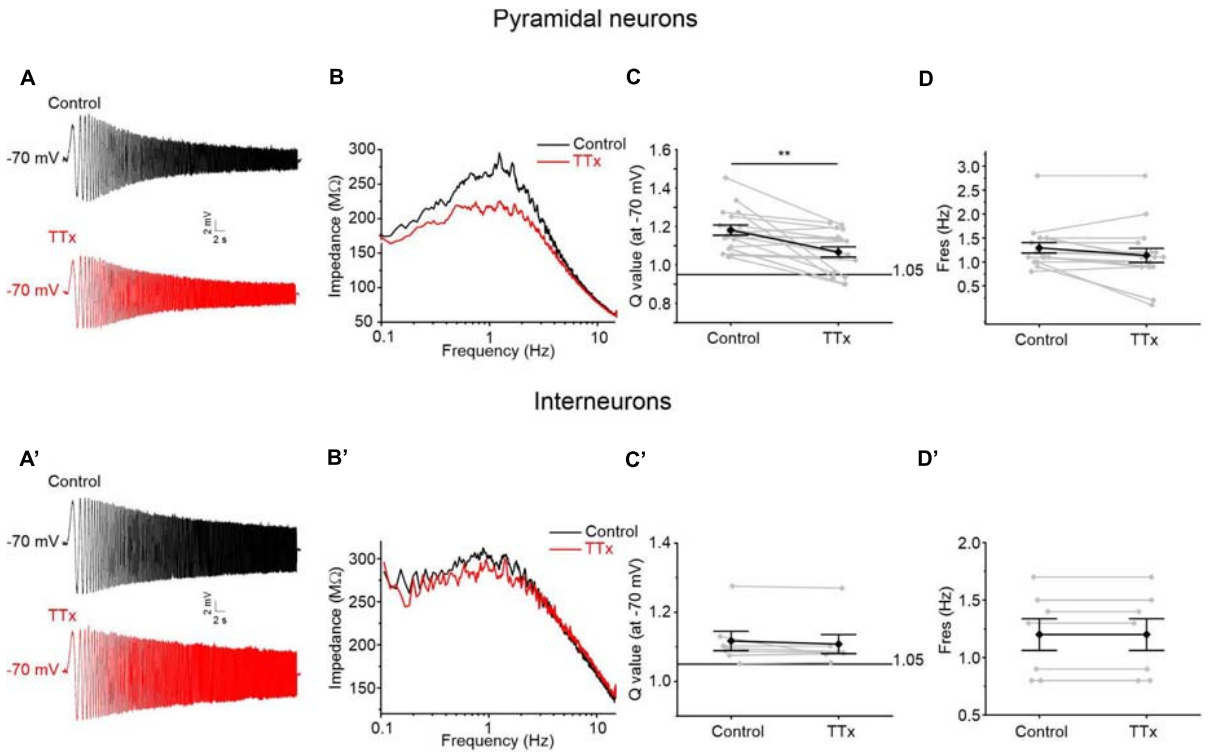

FIGURE 9 | Effects of the block of TTx-sensitive sodium channels on resonant behavior of pyramidal neurons **(A–D)** and GABAergic interneurons **(A′–D′)** of the PRC. **(A)** Voltage responses of a representative resonant pyramidal neuron to the standard 0–15 Hz ZAP protocol at –70 mV before (upper trace in black) and after (lower trace in red) the perfusion of TTx 1 μM. **(B)** Impedance-to-frequency relationship of the same cell as in **(B)**, before (black line) and after (red line) TTx perfusion. **(C,D)** Scatter plots comparing the *Q*-values **(C)** and F_{res} values **(D)** derived from resonant pyramidal neurons ($N = 17$) before (Control) and after (TTx) blocking the TTx-sensitive Sodium channels (gray dots and lines). Mean ± SEM. *Q*-values are reported on the same plot in black. In TTx condition, the *Q*-value is significantly reduced and then the resonance strength is attenuated **(C)**. The F_{res} is unaltered by TTx administration **(D)**. **(A′–D′)** Same as **(A–D)** for GABAergic interneurons ($N = 7$). In GABAergic interneurons TTx perfusion has no effect either on the *Q*-value **(C′)** or on the F_{res} **(D′)**. Data in **(C,D,C′,D′)** were compared by paired Student's *t*-test. $^{**}p < 0.01$.

Concerning voltage-dependence of resonance, the analysis of F_{res} at different membrane potential ranging from −90 to −55 mV showed very similar values. However, the characterization of the resonance strength at different holding membrane potentials, between −90 and −55 mV, indicated that the resonant neurons manifest a voltage-dependent resonance. In pyramidal neurons the *Q*-value exhibited a peak at around −70 mV, whereas in interneurons the maximum *Q*-value was measured between −80 and −70 mV. These observations indicated a prominent response at potential value at or just below resting membrane potential. The abolishment of resonance in PRC neurons following I_h current block with ZD7288 suggests that the expression of the HCN channels is mandatory for the definition of the resonant mechanism in PRC in both groups of neurons tested, confirming the important role played by HCN in the subthreshold resonance, as already demonstrated for other neocortical (Hutcheon et al., 1996) and limbic areas (Shay et al., 2012). The expression of this conductance only in resonant cells could also justify the more depolarized membrane resting potential of resonant compared to non-resonant neurons. Interestingly, the application of TTx caused a decrease in the resonant peak, but did not abolish the resonant behavior, suggesting that in pyramidal neurons of the PRC a persistent sodium current is able to amplify the resonance produced by other conductances, as demonstrated in other brain areas. Indeed, at membrane potentials ranging between −70 and −60 mV the persistent sodium current produced in pyramidal neurons a significant amplification of the resonant peak that became steeper and sharpened, whereas the F_{res} was not affected by the application of TTx. By contrast, in interneurons the amplification of the resonance mediated by persistent sodium current was not observed, probably due to a lack or to a low density of I_{NaP} channels in these cells, as shown in CA1 (Hedrich et al., 2014) and in neocortex (Aracri et al., 2006). Alternatively, it could be hypothesized, in the case of interneurons, a concurrent activation of persistent sodium current together with a current, such as the potassium inward rectifier, that attenuates resonance. The experimental data were replicated by using a MatLab model, containing I_{leak}, I_h and I_{NaP} channels. Currents' kinetics and gating properties were derived by literature (Hodgkin and Huxley, 1952; Spain et al., 1987), due to the lack of data describing these properties in the PRC pyramidal and GABAergic neurons. To overcome the limitations of the model and for a future upgrade, these parameters could be derived directly from PRC neurons. However, since these

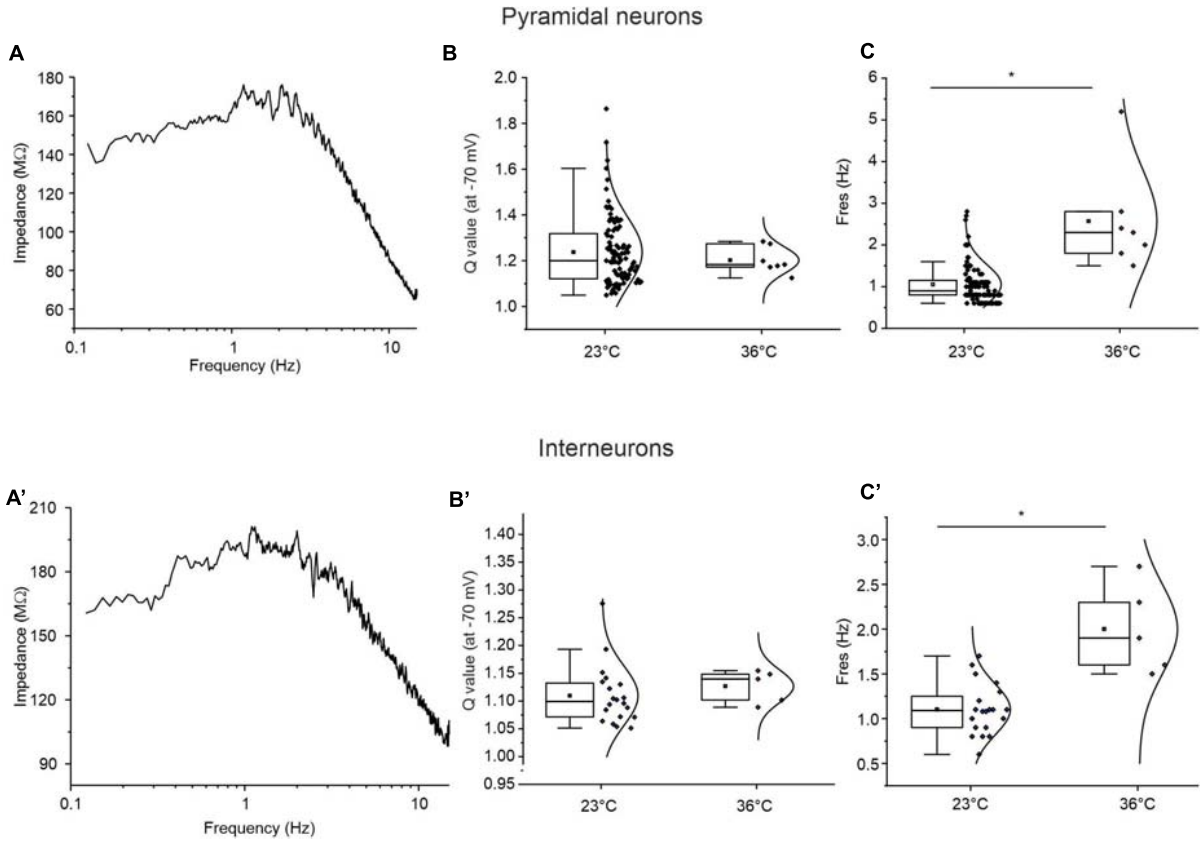

FIGURE 10 | Effect of temperature on the resonance properties of pyramidal neurons **(A–C)** and GABAergic interneurons **(A′–C′)** of the PRC.
(A) Impedance-to-frequency relationship obtained from a representative resonant pyramidal neuron at a temperature of 36°C by applying the standard 0–15 Hz ZAP protocol at –70 mV. **(B,C)** All-points half-violin plots flanked by summary box plots comparing the *Q*-values **(B)** and F_{res} values **(C)** derived from resonant pyramidal neurons at room temperature (23°C) and at physiological temperature (36°C). The increase of temperature in the 7 pyramidal neurons tested at 36°C has no influence on the *Q*-value **(B)**, while determines a significant increase of F_{res} **(C)**. **(A′–C′)** Same as **(A–C)** for resonant GABAergic interneurons ($N = 5$). Note that also in this cell type, the temperature increase does not alter the *Q*-value **(B′)**, while determines a significant increase of the F_{res} **(C′)**. Data in **(B,C,B′C′)** were compared by unpaired Student's *t*-test. $^*p < 0.05$.

electrophysiological parameters are quite conserved (Zhou and Lipsius, 1992; Kiss, 2008; Kase and Imoto, 2012), we believe that reliable results could be obtained also by using general equations. Indeed, our computational model faithfully reproduced the experimental behavior, confirming the indispensable role of I_h in the genesis of resonance and the involvement of the persistent sodium current in the amplification of the resonance peak. Furthermore, it is important to consider that temperature strongly influences the F_{res} and this happens also in PRC, as predicted by our computational model and confirmed by our experimental data. We found that the rise of temperature from 23 to 36°C significantly increased the F_{res} of both pyramidal neurons and interneurons, aligning these data to the well-known resonance frequency already observed in the brain areas functionally linked to the PRC.

The functional behavior of the individual neurons affects and defines the processing of information within neural circuits. Membrane resonance at a given frequency has already been described in many other cells across different brain areas and is strictly dependent on intrinsic membrane properties, synaptic inputs, and modulatory effects. The interaction between the passive properties of the cell and active conductances mediated by ion channels define not only membrane resonance but also action potential timing, synaptic integration, and membrane potential oscillations. Altogether these properties enable neurons to react preferentially to synaptic inputs at specific frequencies and also influence the dynamics of the neural networks of which they are part. The inhibition produced by interneurons on pyramidal neurons and other interneurons is critical for the synchronization of neural activity (Mann and Paulsen, 2007). In the PRC the resonance of interneurons at 1–3 Hz suggests that synaptic inputs at these frequencies will likely entrain the entire neuronal network of the PRC to oscillate at the range of 1–3 Hz, typical of the delta rhythm during non REM sleep.

Coherent network oscillations distributed in different brain regions are critical to achieve learning and memory and in general to process neural information. Low frequency oscillations are usually engaged to connect different cerebral regions to transfer or retrieve distributed information. On the other hand, coherent high frequency oscillations are more restricted to

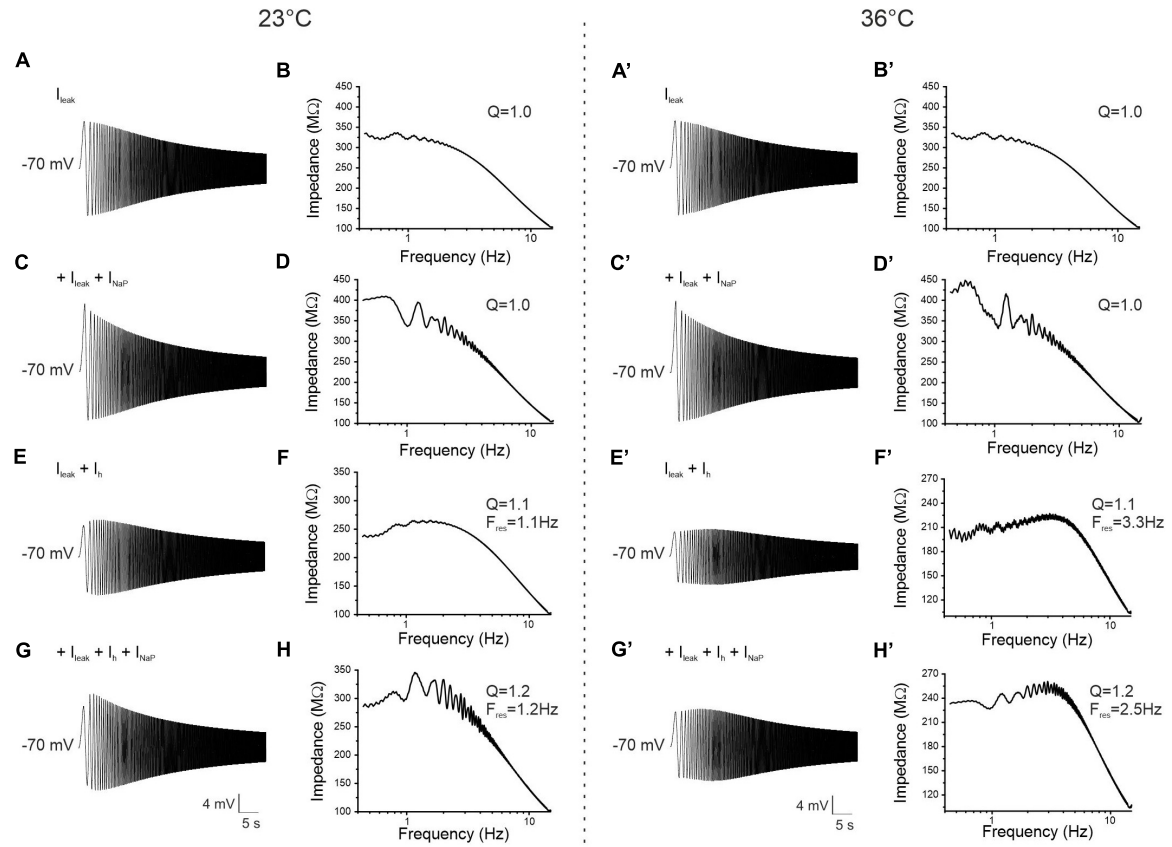

FIGURE 11 | Computational MATLAB model reflecting experimental data and simulating resonance. **(A)** Voltage response to the 0–15 Hz ZAP input at –70 mV and 23°C simulated by a model including only the leakage current (I_{leak}). **(B)** Impedance-to-frequency relationship obtained from simulation in **(A)**. The behavior strongly resembles that of an experimentally recorded non-resonant neuron. **(C,D)** Same as **(A,B)**, but with the insertion of the persistent sodium current (I_{NaP}) in the model. The voltage response **(C)** and the corresponding impedance-to-frequency relationship **(D)** still resemble that of a non-resonant neuron. **(E,F)** Same as **(A,B)**, but with the insertion of a HCN channels-mediated current (I_h) in the model. The voltage response **(E)** and the corresponding impedance-to-frequency relationship **(F)** show that in these conditions the model is able to simulate resonant behavior. **(G,H)** Same as **(A,B)** but with the insertion of both I_h and I_{NaP} in the model. The voltage response **(G)** and the corresponding impedance-to-frequency relationship **(H)** show that this model not only resonates, thanks to I_h, but it also displays a resonance amplified by I_{NaP}. **(A′–H′)** Same as **(A–H)**, but after setting the value of temperature at 36°C instead of 23°C in the model. Note that in the resonant model at the higher temperature **(E′–H′)** the *Q*-value remains constant while the F_{res} increases, as experimentally found. Model parameters are shown in **Table 1**.

localized neuronal networks and seem to be involved in encoding of sensory information, in promoting synaptic plasticity (Fries, 2005), and in the definition of the sequence of information transfer (Sejnowski and Paulsen, 2006; Fries et al., 2007).

Semantic memories are stored in different cortical areas and a still unanswered question is how these distributed memories are recalled and linked together to obtain an object representation. In the PRC, the representation of the objects learned throughout experience-dependent episodes are associated with their memorized features. The retrieving of these associations is based on the information exchange among the PRC and distributed cortical areas. The PRC, hence, via its afferent and efferent connections acts as a hub of semantic memory.

Slow frequency oscillations (0.5–4 Hz) that are widely described in different areas linked to PRC such as the neocortex, amygdala, and lateral EC (Collins et al., 2001) could subserve the pivotal role, played by the PRC, for binding the information stored sparsely in different cortical areas to obtain a coherent neural representation to be sent to the hippocampus. Similarly, but in opposite direction, short-term memory developed in hippocampus should be forwarded and stored in distributed neocortical regions throughout a consolidation process that likely use the same PRC hub and oscillatory mechanisms. The reverberating activity between neocortex and hippocampus, especially during slow wave sleep, indeed represents the mechanism by which the brain promotes the redistribution and strengthening of memory representation in cortical regions (Klinzing et al., 2019). Another aspect which worth to be considered is related with dendritic resonance. Detailed studies have characterized the spatial properties of the resonance along the dendrite-to-soma extension in hippocampal (Narayanan and Johnston, 2007; Hu et al., 2009) and prefrontal (Kalmbach et al., 2013) pyramidal neurons. In particular, recordings performed on CA1 pyramidal neurons showed that membrane resonance frequency could differ threefold between soma and apical

dendrites. These results suggest that CA1 pyramidal cells could act as stimulus-tuned filters for spatially separated synaptic inputs. The cognitive processes of the PRC strongly rely on the presence of separated synaptic inputs from piriform, entorhinal and neocortical cortices, and amygdala to the PRC and its ability to integrate them. Then, future experiments should also be addressed to investigate the resonance properties along the soma-to-dendrite extension in pyramidal neurons of the PRC.

DATA AVAILABILITY STATEMENT

The raw data supporting the conclusions of this article will be made available by the authors, without undue reservation.

ETHICS STATEMENT

The animal study was reviewed and approved by the National Ministry of Health and Local Ethical Committee of the University of Pavia (OPBA).

AUTHOR CONTRIBUTIONS

NB, FT, PS, and GB conceived the study and designed the experiments. NB, FT, PS, CM, FR, NM, and AC performed the *in vitro* experiments and data analysis. MP, SR, and MT defined and performed the computational model. YY developed and provided the GAD67-GFP mice. CD edited the manuscript. NB, FT, MT, CM, and GB wrote the manuscript. GB supervised the study. All authors contributed to the article and approved the submitted version.

FUNDING

This work was supported by the Italian Ministry of Education, University and Research (MIUR): 2005059453_003, Dipartimenti di Eccellenza Program (2018–2022)—Department of Biology and Biotechnology "Lazzaro Spallanzani," University of Pavia and Crowdfunding Campaign "La Cura in una Cellula"–University of Pavia. FT was supported by the Fondazione Umberto Veronesi.

REFERENCES

Aracri, P., Colombo, E., Mantegazza, M., Scalmani, P., Curia, G., Avanzini, G., et al. (2006). Layer-specific properties of the persistent sodium current in sensorimotor cortex. *J. Neurophysiol.* 95, 3460–3468. doi: 10.1152/jn.00588.2005

Beggs, J. M., Moyer, J. R., McGann, J. P., and Brown, T. H. (2000). Prolonged synaptic integration in perirhinal cortical neurons. *J. Neurophysiol.* 83, 3294–3298. doi: 10.1152/jn.2000.83.6.3294

Biel, M., Wahl-Schott, C., Michalakis, S., and Zong, X. (2009). Hyperpolarization-activated cation channels. from genes to function. *Physiol. Rev.* 89, 847–885. doi: 10.1152/physrev.00029.2008

Biella, G., Spaiardi, P., Toselli, M., de Curtis, M., and Gnatkovsky, V. (2010). Functional interactions within the parahippocampal region revealed by voltage-sensitive dye imaging in the isolated guinea pig brain. *J. Neurophysiol.* 103, 725–732. doi: 10.1152/jn.00722.2009

Biella, G., Uva, L., and de Curtis, M. (2001). Network activity evoked by neocortical stimulation in area 36 of the guinea pig perirhinal cortex. *J. Neurophysiol.* 86, 164–172. doi: 10.1152/jn.2001.86.1.164

Biella, G., Uva, L., and de Curtis, M. (2002). Propagation of neuronal activity along the neocortical-perirhinal-entorhinal pathway in the guinea pig. *J. Neurosci.* 22, 9972–9979. doi: 10.1523/jneurosci.22-22-09972.2002

Boehlen, A., Henneberger, C., Heinemann, U., and Erchova, I. (2013). Contribution of near-threshold currents to intrinsic oscillatory activity in rat medial entorhinal cortex layer II stellate cells. *J. Neurophysiol.* 109, 445–463. doi: 10.1152/jn.00743.2011

Burke, S. N., Gaynor, L. S., Barnes, C. A., Bauer, R. M., Bizon, J. L., Roberson, E. D., et al. (2018). Shared functions of perirhinal and parahippocampal cortices: implications for cognitive aging. *Trends Neurosci.* 41, 349–359. doi: 10.1016/j.tins.2018.03.001

Chen, W. R., and Shepherd, G. M. (1997). Membrane and synaptic properties of mitral cells in slices of rat olfactory bulb. *Brain Res.* 745, 189–196. doi: 10.1016/s0006-8993(96)01150-x

Collins, D. R., Pelletier, J. G., and Paré, D. (2001). Slow and fast (gamma) neuronal oscillations in the perirhinal cortex and lateral amygdala. *J. Neurophysiol.* 85, 1661–1672. doi: 10.1152/jn.2001.85.4.1661

Davachi, L. (2006). Item, context and relational episodic encoding in humans. *Curr. Opin. Neurobiol.* 16, 693–700. doi: 10.1016/j.conb.2006.10.012

de Curtis, M., and Paré, D. (2004). The rhinal cortices: a wall of inhibition between the neocortex and the hippocampus. *Prog Neurobiol* 74, 101–110. doi: 10.1016/j.pneurobio.2004.08.005

Desmaisons, D., Vincent, J. D., and Lledo, P. M. (1999). Control of action potential timing by intrinsic subthreshold oscillations in olfactory bulb output neurons. *J. Neurosci.* 19, 10727–10737. doi: 10.1523/jneurosci.19-24-10727.1999

Ehrlich, D. E., Ryan, S. J., and Rainnie, D. G. (2012). Postnatal development of electrophysiological properties of principal neurons in the rat basolateral amygdala. *J. Physiol.* 590, 4819–4838. doi: 10.1113/jphysiol.2012.237453

Engel, T. A., Schimansky-Geier, L., Herz, A. V., Schreiber, S., and Erchova, I. (2008). Subthreshold membrane-potential resonances shape spike-train patterns in the entorhinal cortex. *J. Neurophysiol.* 100, 1576–1589. doi: 10.1152/jn.01282.2007

Erchova, I., Kreck, G., Heinemann, U., and Herz, A. V. (2004). Dynamics of rat entorhinal cortex layer II and III cells: characteristics of membrane potential resonance at rest predict oscillation properties near threshold. *J. Physiol.* 560, 89–110. doi: 10.1113/jphysiol.2004.069930

Faulkner, B., and Brown, T. H. (1999). Morphology and physiology of neurons in the rat perirhinal-lateral amygdala area. *J. Comp. Neurol.* 411, 613–642.

Fries, P. (2005). A mechanism for cognitive dynamics. neuronal communication through neuronal coherence. *Trends Cogn. Sci.* 9, 474–480. doi: 10.1016/j.tics.2005.08.011

Fries, P., Nikolić, D., and Singer, W. (2007). The gamma cycle. *Trends Neurosci.* 30, 309–316.

Garden, D. L., Kemp, N., and Bashir, Z. I. (2002). Differences in GABAergic transmission between two inputs into the perirhinal cortex. *Eur. J. Neurosci.* 16, 437–444. doi: 10.1046/j.1460-9568.2002.02096.x

Graf, M., Nair, A., Wong, K. L. L., Tang, Y., and Augustine, G. J. (2020). Identification of mouse claustral neuron types based on their intrinsic electrical properties. *eNeuro* 7:ENEURO.0216-20.2020.

Gutfreund, Y., yarom, Y., and Segev, I. (1995). Subthreshold oscillations and resonant frequency in guinea-pig cortical neurons. physiology and modelling. *J Physiol* 483(Pt 3), 621–640. doi: 10.1113/jphysiol.1995.sp020611

Haas, J. S., and White, J. A. (2002). Frequency selectivity of layer II stellate cells in the medial entorhinal cortex. *J. Neurophysiol.* 88, 2422–2429. doi: 10.1152/jn.00598.2002

Hedrich, U. B., Liautard, C., Kirschenbaum, D., Pofahl, M., Lavigne, J., Liu, Y., et al. (2014). Impaired action potential initiation in GABAergic interneurons causes hyperexcitable networks in an epileptic mouse model carrying a human Na(V)1.1 mutation. *J. Neurosci.* 34, 14874–14889. doi: 10.1523/jneurosci.0721-14.2014

Hodgkin, A. L., and Huxley, A. F. (1952). A quantitative description of membrane current and its application to conduction and excitation in nerve. *J. Physiol.* 117, 500–544. doi: 10.1113/jphysiol.1952.sp004764

Holt, G. R., Softky, W. R., Koch, C., and Douglas, R. J. (1996). Comparison of discharge variability *in vitro* and *in vivo* in cat visual cortex neurons. *J. Neurophysiol.* 75, 1806–1814. doi: 10.1152/jn.1996.75.5.1806

Hu, H., Vervaeke, K., Graham, L. J., and Storm, J. F. (2009). Complementary theta resonance filtering by two spatially segregated mechanisms in CA1 hippocampal pyramidal neurons. *J. Neurosci.* 29, 14472–14483. doi: 10.1523/jneurosci.0187-09.2009

Hu, H., Vervaeke, K., and Storm, J. F. (2002). Two forms of electrical resonance at theta frequencies, generated by M-current, h-current and persistent Na+ current in rat hippocampal pyramidal cells. *J. Physiol.* 545, 783–805. doi: 10.1113/jphysiol.2002.029249

Hutcheon, B., Miura, R. M., and Puil, E. (1996). Subthreshold membrane resonance in neocortical neurons. *J. Neurophysiol.* 76, 683–697. doi: 10.1152/jn.1996.76.2.683

Hutcheon, B., and Yarom, Y. (2000). Resonance, oscillation and the intrinsic frequency preferences of neurons. *Trends Neurosci.* 23, 216–222. doi: 10.1016/s0166-2236(00)01547-2

Izhikevich, E. M., Desai, N. S., Walcott, E. C., and Hoppensteadt, F. C. (2003). Bursts as a unit of neural information: selective communication via resonance. *Trends Neurosci.* 26, 161–167.

Johnson, S. W., and Seutin, V. (1997). Bicuculline methiodide potentiates NMDA-dependent burst firing in rat dopamine neurons by blocking apamin-sensitive Ca2+-activated K+ currents. *Neurosci. Lett.* 231, 13–16. doi: 10.1016/s0304-3940(97)00508-9

Kalmbach, B. E., Chitwood, R. A., Dembrow, N. C., and Johnston, D. (2013). Dendritic generation of mGluR-mediated slow afterdepolarization in layer 5 neurons of prefrontal cortex. *J. Neurosci.* 33, 13518–13532. doi: 10.1523/jneurosci.2018-13.2013

Karayannis, T., Huerta-Ocampo, I., and Capogna, M. (2007). GABAergic and pyramidal neurons of deep cortical layers directly receive and differently integrate callosal input. *Cereb. Cortex* 17, 1213–1226. doi: 10.1093/cercor/bhl035

Kase, D., and Imoto, K. (2012). The role of HCN channels on membrane excitability in the nervous system. *J. Signal Transduct.* 2012:619747.

Kealy, J., and Commins, S. (2011). The rat perirhinal cortex: a review of anatomy, physiology, plasticity, and function. *Prog. Neurobiol.* 93, 522–548. doi: 10.1016/j.pneurobio.2011.03.002

Kiss, T. (2008). Persistent Na-channels: origin and function. A review. *Acta Biol. Hung.* 59(Suppl.), 1–12. doi: 10.1556/abiol.59.2008.suppl.1

Klinzing, J. G., Niethard, N., and Born, J. (2019). Mechanisms of systems memory consolidation during sleep. *Nat. Neurosci.* 22, 1598–1610. doi: 10.1038/s41593-019-0467-3

Komendantov, A. O., Venkadesh, S., Rees, C. L., Wheeler, D. W., Hamilton, D. J., and Ascoli, G. A. (2019). Quantitative firing pattern phenotyping of hippocampal neuron types. *Sci. Rep.* 9:17915.

Lampl, I., and Yarom, Y. (1997). Subthreshold oscillations and resonant behavior: two manifestations of the same mechanism. *Neuroscience* 78, 325–341. doi: 10.1016/s0306-4522(96)00588-x

Leung, L. S., and Yu, H. W. (1998). Theta-frequency resonance in hippocampal CA1 neurons *in vitro* demonstrated by sinusoidal current injection. *J. Neurophysiol.* 79, 1592–1596. doi: 10.1152/jn.1998.79.3.1592

Ma, Y., Hu, H., Berrebi, A. S., Mathers, P. H., and Agmon, A. (2006). Distinct subtypes of somatostatin-containing neocortical interneurons revealed in transgenic mice. *J. Neurosci.* 26, 5069–5082. doi: 10.1523/jneurosci.0661-06.2006

Magee, J. C. (1998). Dendritic hyperpolarization-activated currents modify the integrative properties of hippocampal CA1 pyramidal neurons. *J. Neurosci.* 18, 7613–7624. doi: 10.1523/jneurosci.18-19-07613.1998

Mann, E. O., and Paulsen, O. (2007). Role of GABAergic inhibition in hippocampal network oscillations. *Trends Neurosci.* 30, 343–349. doi: 10.1016/j.tins.2007.05.003

Marder, E., and Taylor, A. L. (2011). Multiple models to capture the variability in biological neurons and networks. *Nat. Neurosci.* 14, 133–138. doi: 10.1038/nn.2735

Martina, M., Royer, S., and Paré, D. (2001). Propagation of neocortical inputs in the perirhinal cortex. *J. Neurosci.* 21, 2878–2888. doi: 10.1523/jneurosci.21-08-02878.2001

Matsumoto-Makidono, Y., Nakayama, H., Yamasaki, M., Miyazaki, T., Kobayashi, K., Watanabe, M., et al. (2016). Ionic basis for membrane potential resonance in neurons of the inferior olive. *Cell Rep.* 16:994–1004. doi: 10.1016/j.celrep.2016.06.053

McGann, J. P., Moyer, J. R., and Brown, T. H. (2001). Predominance of late-spiking neurons in layer VI of rat perirhinal cortex. *J. Neurosci.* 21, 4969–4976. doi: 10.1523/jneurosci.21-14-04969.2001

Mishra, P., and Narayanan, R. (2020). Heterogeneities in intrinsic excitability and frequency-dependent response properties of granule cells across the blades of the rat dentate gyrus. *J. Neurophysiol.* 123, 755–772. doi: 10.1152/jn.00443.2019

Murray, E. A., and Richmond, B. J. (2001). Role of perirhinal cortex in object perception, memory, and associations. *Curr. Opin. Neurobiol.* 11, 188–193. doi: 10.1016/s0959-4388(00)00195-1

Narayanan, R., and Johnston, D. (2007). Long-term potentiation in rat hippocampal neurons is accompanied by spatially widespread changes in intrinsic oscillatory dynamics and excitability. *Neuron* 56, 1061–1075.

Nolan, M. F., Dudman, J. T., Dodson, P. D., and Santoro, B. (2007). HCN1 channels control resting and active integrative properties of stellate cells from layer II of the entorhinal cortex. *J. Neurosci.* 27, 12440–12451.

Pedroarena, C. M., Pose, I. E., Yamuy, J., Chase, M. H., and Morales, F. R. (1999). Oscillatory membrane potential activity in the soma of a primary afferent neuron. *J. Neurophysiol.* 82, 1465–1476. doi: 10.1152/jn.1999.82.3.1465

Perugini, A., Laing, M., Berretta, N., Aicardi, G., and Bashir, Z. I. (2012). Synaptic plasticity from amygdala to perirhinal cortex: a possible mechanism for emotional enhancement of visual recognition memory? *Eur. J. Neurosci.* 36, 2421–2427. doi: 10.1111/j.1460-9568.2012.08146.x

Pike, F. G., Goddard, R. S., Suckling, J. M., Ganter, P., Kasthuri, N., and Paulsen, O. (2000). Distinct frequency preferences of different types of rat hippocampal neurones in response to oscillatory input currents. *J. Physiol.* 529(Pt 1), 205–213. doi: 10.1111/j.1469-7793.2000.00205.x

Pinto, A., Fuentes, C., and Paré, D. (2006). Feedforward inhibition regulates perirhinal transmission of neocortical inputs to the entorhinal cortex: ultrastructural study in guinea pigs. *J. Comp. Neurol.* 495, 722–734. doi: 10.1002/cne.20905

Rathour, R. K., and Narayanan, R. (2019). Degeneracy in hippocampal physiology and plasticity. *Hippocampus* 29, 980–1022. doi: 10.1002/hipo.23139

Schaefer, A. T., Angelo, K., Spors, H., and Margrie, T. W. (2006). Neuronal oscillations enhance stimulus discrimination by ensuring action potential precision. *PLoS Biol.* 4:e163. doi: 10.1371/journal.pbio.0040163

Sejnowski, T. J., and Paulsen, O. (2006). Network oscillations. emerging computational principles. *J Neurosci* 26, 1673–1676. doi: 10.1523/jneurosci.3737-05d.2006

Shay, C. F., Boardman, I. S., James, N. M., and Hasselmo, M. E. (2012). Voltage dependence of subthreshold resonance frequency in layer II of medial entorhinal cortex. *Hippocampus* 22, 1733–1749. doi: 10.1002/hipo.22008

Shinomoto, S., Kim, H., Shimokawa, T., Matsuno, N., Funahashi, S., Shima, K., et al. (2009). Relating neuronal firing patterns to functional differentiation of cerebral cortex. *PLoS Comput. Biol.* 5:e1000433. doi: 10.1371/journal.pcbi.1000433

Spain, W. J., Schwindt, P. C., and Crill, W. E. (1987). Anomalous rectification in neurons from cat sensorimotor cortex *in vitro*. *J. Neurophysiol.* 57, 1555–1576. doi: 10.1152/jn.1987.57.5.1555

Staresina, B. P., and Davachi, L. (2008). Selective and shared contributions of the hippocampus and perirhinal cortex to episodic item and associative encoding. *J. Cogn. Neurosci.* 20, 1478–1489. doi: 10.1162/jocn.2008.20104

Sun, H., An, S., Luhmann, H. J., and Kilb, W. (2014). Resonance properties of GABAergic interneurons in immature GAD67-GFP mouse neocortex. *Brain Res* 1548, 1–11. doi: 10.1016/j.brainres.2013.12.032

Suzuki, W. A., and Naya, Y. (2014). The perirhinal cortex. *Annu Rev Neurosci* 37, 39–53.

Tamamaki, N., Yanagawa, Y., Tomioka, R., Miyazaki, J., Obata, K., and Kaneko, T. (2003). Green fluorescent protein expression and colocalization with calretinin, parvalbumin, and somatostatin in the GAD67-GFP knock-in mouse. *J. Comp. Neurol.* 467, 60–79. doi: 10.1002/cne.10905

Traub, R. D., and Miles, R. (1991). Multiple modes of neuronal population activity emerge after modifying specific synapses in a model of the CA3 region of the hippocampus. *Ann. N. Y. Acad. Sci.* 627, 277–290. doi: 10.1111/j.1749-6632.1991.tb25931.x

Vera, J., Pezzoli, M., Pereira, U., Bacigalupo, J., and Sanhueza, M. (2014). Electrical resonance in the θ frequency range in olfactory amygdala neurons. *PLoS One* 9:e85826. doi: 10.1371/journal.pone.0085826

Willems, J. G. P., Wadman, W. J., and Cappaert, N. L. M. (2018). Parvalbumin interneuron mediated feedforward inhibition controls signal output in the deep layers of the perirhinal-entorhinal cortex. *Hippocampus* 28, 281–296. doi: 10.1002/hipo.22830

Witter, M. P., Wouterlood, F. G., Naber, P. A., and Van Haeften, T. (2000). Anatomical organization of the parahippocampal-hippocampal network. *Ann. N. Y. Acad. Sci.* 911, 1–24. doi: 10.1111/j.1749-6632.2000.tb06716.x

Wu, N., Hsiao, C. F., and Chandler, S. H. (2001). Membrane resonance and subthreshold membrane oscillations in mesencephalic V neurons: participants in burst generation. *J. Neurosci.* 21, 3729–3739. doi: 10.1523/jneurosci.21-11-03729.2001

Xue, W. N., Wang, Y., He, S. M., Wang, X. L., Zhu, J. L., and Gao, G. D. (2012). SK- and h-current contribute to the generation of theta-like resonance of rat substantia nigra pars compacta dopaminergic neurons at hyperpolarized membrane potentials. *Brain Struct. Funct.* 217, 379–394. doi: 10.1007/s00429-011-0361-6

Yan, Z. Q., Liu, S. M., Li, J., Wang, Y., Gao, L., Xie, R. G., et al. (2012). Membrane resonance and its ionic mechanisms in rat subthalamic nucleus neurons. *Neurosci. Lett.* 506, 160–165. doi: 10.1016/j.neulet.2011.10.072

Zhou, Z., and Lipsius, S. L. (1992). Properties of the pacemaker current (If) in latent pacemaker cells isolated from cat right atrium. *J. Physiol.* 453, 503–523. doi: 10.1113/jphysiol.1992.sp019242

Conflict of Interest: The authors declare that the research was conducted in the absence of any commercial or financial relationships that could be construed as a potential conflict of interest.

frontiers in Aging Neuroscience

ORIGINAL RESEARCH
published: 23 December 2021
doi: 10.3389/fnagi.2021.782737

Effects of Aging on the Structure and Expression of NMDA Receptors of Somatostatin Expressing Neurons in the Mouse Hippocampus

*Yaiza Gramuntell[1], Patrycja Klimczak[1,2], Simona Coviello[1], Marta Perez-Rando[1,2,3] and Juan Nacher[1,2,3]**

[1] Neurobiology Unit, Program in Neurosciences and Institute of Biotechnology and Biomedicine (BIOTECMED), Universitat de València, Burjassot, Spain, [2] Spanish National Network for Research in Mental Health, Centro de Investigación Biomédica en Red de Salud Mental (CIBERSAM), Madrid, Spain, [3] Fundación Investigación Hospital Clínico de Valencia, INCLIVA, Valencia, Spain

Changes in the physiology, neurochemistry and structure of neurons, particularly of their dendritic spines, are thought to be crucial players in age-related cognitive decline. One of the most studied brain structures affected by aging is the hippocampus, known to be involved in different essential cognitive processes. While the aging-associated quantitative changes in dendritic spines of hippocampal pyramidal cells have already been studied, the relationship between aging and the structural dynamics of hippocampal interneurons remains relatively unknown. Spines are not a frequent feature in cortical inhibitory neurons, but these postsynaptic structures are abundant in a subpopulation of somatostatin expressing interneurons, particularly in oriens-lacunosum moleculare (O-LM) cells in the hippocampal CA1. Previous studies from our laboratory have shown that the spines of these interneurons are highly plastic and influenced by NMDA receptor manipulation. Thus, in the present study, we have investigated the impact of aging on this interneuronal subpopulation. The analyses were performed in 3−, 9−, and 16-month-old GIN mice, a strain in which somatostatin positive interneurons express GFP. We studied the changes in the density of dendritic spines, *en passant boutons*, and the expression of NMDA receptors (GluN1 and GluN2B) using confocal microscopy and image analysis. We observed a significant decrease in dendritic spine density in 9-month-old animals when compared with 3-month-old animals. We also observed a decrease in the expression of the GluN2B subunit in O-LM cells, but not of that of GluN1, during aging. These results will constitute the basis for more advanced studies of the structure and connectivity of interneurons during aging and their contribution to cognitive decline.

Keywords: hippocampus, interneuron, somatostatin, aging, spine, NMDA – receptor

OPEN ACCESS

Edited by:
Diego Ruano,
University of Seville, Spain

Reviewed by:
Kathy R. Magnusson,
Oregon State University,
United States
Thomas C. Foster,
University of Florida, United States

***Correspondence:**
Juan Nacher
nacher@uv.es

Specialty section:
This article was submitted to Cellular and Molecular Mechanisms of Brain-aging, a section of the journal Frontiers in Aging Neuroscience

Received: *24 September 2021*
Accepted: *23 November 2021*
Published: *23 December 2021*

Citation:
Gramuntell Y, Klimczak P, Coviello S, Perez-Rando M and Nacher J (2021) Effects of Aging on the Structure and Expression of NMDA Receptors of Somatostatin Expressing Neurons in the Mouse Hippocampus. Front. Aging Neurosci. 13:782737. doi: 10.3389/fnagi.2021.782737

INTRODUCTION

Aging is a natural process related to the gradual loss of physiological, behavioral, and social functions. Therefore, it has an essential impact on the nervous system, and it is considered a risk factor for many neurodegenerative and psychiatric illnesses (Hou et al., 2019). Thus, understanding the neurobiology underlying age-related impairment is essential given the growing

elderly population. The structural and functional brain changes observed during aging in the central nervous system are the consequence of cellular and molecular alterations, which are in turn regulated by genetic, epigenetic, lifestyle, and environmental factors (Khan et al., 2017). Interestingly, the brain is not homogeneously affected by aging; specific regions are specially altered. Such is the case of the hippocampus, which is our region of interest in the present study, and appears to be among the most affected.

During aging, the hippocampus shows a decrease in volume, which correlates with a decline in learning and memory (Driscoll et al., 2006). Aging is also associated to the presence of neuroinflammation in this region, along with an up-regulation of pro-inflammatory genes, resulting in oxidative stress (Gavilán et al., 2007; Barrientos et al., 2015). Most studies have found no evidence for the death of pyramidal neurons during aging, both in humans and mice (West et al., 1994). In the case of inhibitory neurons there is still controversy, while some studies have found loss of interneuronal markers in the hippocampus of aged animals (Potier et al., 2006; Stanley et al., 2012), others did not find it (Miettinen et al., 1993). At the cellular level, there are structural alterations in hippocampal pyramidal neurons, such as a reduction in dendritic branching (Markham et al., 2005), and reductions in the density of dendritic spines and synapses (Dickstein et al., 2013). However, little is known about the impact of aging on hippocampal inhibitory circuits. Some studies have described decreased GAD65, GAD67 and specifically, somatostatin mRNA levels in the hippocampus during aging (Vela et al., 2003; Gavilán et al., 2007), but nothing is known on the effects of aging on the structure of hippocampal inhibitory neurons.

The study of interneurons in general, and particularly in the hippocampus, represents a challenge due to the existence of several subpopulations, presenting diverse morphological, neurochemical, physiological, and synaptic characteristics (Booker and Vida, 2018). In the hippocampus, interneurons represent 10–15% of the total neuronal cell population (Pelkey et al., 2017). Particularly, the *oriens-lacunosum moleculare* (O-LM) cells, which are the subpopulation studied in the present work, represent the 4.5% of the total number of CA1 interneurons (Bezaire and Soltesz, 2013). They are characterized by the expression of the neuropeptide somatostatin (SST) (Freund and Buzsáki, 1996; Oliva et al., 2000), and are widely distributed in the different regions of the hippocampus, including CA1 (Köhler and Chan-Palay, 1982; Freund and Buzsáki, 1996). O-LM cells have their soma and main dendritic arbor in the *stratum oriens,* where they receive inputs from pyramidal neurons of the *stratum pyramidale* (Lacaille and Schwartzkroin, 1988; Blasco-Ibáñez and Freund, 1995; Katona et al., 1999). The anatomy of these cells is described in detail in Freund and Buzsáki (1996). Most of these synaptic contacts are established on dendritic spines, a peculiar characteristic of SST-expressing interneurons (Freund and Buzsáki, 1996; Guirado et al., 2014). The O-LM cells reciprocally synapse onto pyramidal and non-pyramidal neurons in the *stratum lacunosum moleculare*, through a dense axonal projection field decorated with abundant *en passant boutons* (EPB) (Sik et al., 1995; Müller and Remy, 2014). This anatomical arrangement of the O-LM cells allows them to function in a prototypical feedback inhibitory circuit (Leão et al., 2012), in which they mediate theta oscillations (Katona et al., 2016).

Because of their roles as postsynaptic and presynaptic elements, dendritic spines and synaptic boutons respectively are proper proxies for neuronal input and output; therefore, increases in their density have been correlated to increases in neuronal activity (Engert and Bonhoeffer, 1999; Becker et al., 2008). Our laboratory has previously demonstrated the structural remodeling of the dendritic arbor and dendritic spines of O-LM cells by chronic stress (Gilabert-Juan et al., 2017) and by the depletion of the polysialylated form of the neural cell adhesion molecule (PSA-NCAM), a plasticity-related molecule (Guirado et al., 2014). We also showed that the manipulation of NMDA receptors affected both the density of dendritic spines and EPB (Pérez-Rando et al., 2017a,b).

Apart from these molecular and structural changes, functional impairments are also observed during aging, such as alterations in long-term potentiation (LTP) and depression (LTD) (Lister and Barnes, 2009). Some of the most extensively studied molecules involved in these physiological mechanisms, which underlie basic cognitive processes, are the *N*-methyl-d-aspartate receptors (NMDARs). These are ionotropic glutamate receptors, which are highly expressed in the neocortex and the hippocampus, both in pyramidal and inhibitory neurons, including the O-LM cells (Alvarez et al., 2007; Oren et al., 2009; Pérez-Rando et al., 2017b). The NMDARs are assembled as tetramers composed of 4 subunits: two obligatory GluN1 subunits, along with 2 GluN2 or GluN3 subunits. There are 6 subtypes of non-obligatory subunits: 4 GluN2 (GluN2A–GluN2D) and 2 GluN3 (GluN3A and GluN3B) (Hansen et al., 2017). Alterations in NMDAR complex expression and physiology have been described during aging, especially in the hippocampus (Clayton et al., 2002; Boric et al., 2008; Foster et al., 2017). The GluN2B subunit is more affected by aging than the other GluN2 subunits, showing more significant decreases in mRNA and protein expression in aged animals (Magnusson et al., 2002). The effects of aging on hippocampal GluN1 expression have rendered conflicting results, with significant declines described in some studies, but not in others (Magnusson et al., 2005; Das and Magnusson, 2011). However, the majority of these studies have been performed using western blot or RT-PCR, which does not allow the discrimination of the expression in different hippocampal regions, layers or neuronal populations. SST-expressing interneurons are a very interesting subject to study during aging in this regard, because we know that they express NMDA receptors (Pérez-Rando et al., 2017b) in young adult animals and we have also evidence that these receptors regulate structure and connectivity of the SST-expressing interneurons (Pérez-Rando et al., 2017a,b).

Sex is a very important factor to take into account when studying the nervous system and its pathologies; the study of the female brain in preclinical research is of paramount importance, but studies using both sexes have started to appear published only recently (Shansky and Murphy, 2021). Specifically in the hippocampus, there are sex differences in the dendritic spine density of pyramidal neurons (Shors et al., 2001). These

differences are not restricted to excitatory neurons; a recent study from our laboratory has shown changes in the density of dendritic spines and EPB in the O-LM cells during the estrous cycle (Pérez-Rando et al., 2021). The expression of hippocampal NMDARs also appears to be affected by sex and levels of estrogens: Male rats express higher levels of NMDARs in the hippocampus than females, but only when females are in the estrus phase (Brandt et al., 2020). All these studies have been performed in adult-young animals. However, to our knowledge there are still no studies exploring the differential effects of sex on interneuronal morphology or NMDARs expression during aging.

The present study aimed to understand the impact of age on the structure of O-LM cells in the CA1 hippocampal region of male and female mice. We have also studied the expression of different subunits of NMDARs (GluN1 and GluN2B) in this interneuronal subpopulation.

MATERIALS AND METHODS

Animals

Thirty transgenic mice [GIN (GFP-expressing Inhibitory Neurons), Tg(GadGFP)45704Swn] (Jackson Laboratories, Bar Harbor, Maine, United States) were used in this study. They constitutively express the green fluorescent protein (GFP) in a subpopulation of SST-expressing interneurons (Oliva et al., 2000). Mice were bred and maintained in our animal facility and were divided into 3 age groups (3 months, 9 months and 16 months-old). All groups contained 5 males and 5 females. Animals were maintained under controlled conditions of temperature (25°C), humidity (50%), with food and water *ad libitum* and on a standard light/dark cycle (12 h cycle).

All animal experimentation was conducted in accordance with the Directive 2010/63/EU of the European Parliament and of the Council of 22 September 2010 on the protection of animals used for scientific purposes and was approved by the Committee on Bioethics of the Universitat de València. Every effort was made to minimize the number of animals used and their suffering.

Histological Procedures

When they reached 3, 9, or 16 months-old, mice were deeply anesthetized with pentobarbital and perfused transcardially, first for 1 min with saline (NaCl 0.9%) and then for 30 min with 4% paraformaldehyde in sodium phosphate buffer 0.1 M, pH 7.4 (PB). The left hemisphere was cut in 100 μm-thick coronal sections with a vibratome (Leica VT 1000E, Leica, Nussloch, Germany) to analyze dendritic spine and EPB density on GFP expressing interneurons. The right hemisphere was cut in 50 μm-thick coronal sections for the study of the expression of NMDARs.

Analysis of the Density of Dendritic Spines and Axonal *En Passant Boutons*

One subseries of sections from each animal was processed "free-floating" for GFP immunohistochemistry. Sections were first washed three times with phosphate buffered saline (PBS) for 10 min per washing. After that, sections were incubated for 1 min in an antigen unmasking solution (0.01 M citrate buffer, pH 6) at 100°C. Then, sections were washed as described above. To block non-specific unions, sections were treated for 1 h with 10% normal donkey serum (NDS) (Jackson ImmunoResearch Laboratories West Grove, PA, United States) in PBS with 0.2% Triton-X100 (Sigma–Aldrich, St. Louis, MO, United States). Sections were washed 3 times in PBS and were incubated for 48 h at 4°C with primary antibody (chicken anti-GFP IgY, Abcam, 1:2000) diluted in PBS 0.2% Triton-X100. After washing, sections were incubated for 2 h at room temperature with a fluorescent secondary antibody (donkey anti-chicken CF488A, Biotum, 1:800) diluted in PBS 0.2% Triton-X100. Sections were then rinsed with PB 0.1 M, mounted on slides and coverslipped using Dako fluorescent mounting medium (Agilent, United States).

For the study of GFP + interneurons, we used a laser scanning confocal microscope (Leica, SPE, Leica Microsystems, Wetzlar, Germany), obtaining 3D stacks of confocal images with 0.38 μm Z-step size. In order to be analyzed, we selected dendrites from GFP interneurons with their soma *stratum oriens* and axons in *stratum lacunosum-moleculare* of the CA1 region.

For the spine density analysis, a 63× objective with a 3.5× digital zoom was used. Dendrites had to fulfill the following features: (1) they should measure at least 150 or 200 μm from the soma; and (2) no other dendrites should be found crossing their trajectory. Furthermore, dendritic spines were defined as clear protrusions emerging from the dendritic shaft. According to these features, we randomly selected six isolated GFP-expressing interneurons per animal, in which the spines were quantified in 3 successive segments of 50 μm up to a total length of 150 μm, using ImageJ (FIJI) (Schindelin et al., 2012). Overall spine density values or densities per segment were expressed as the number of spines/150 μm or spines/50 μm, respectively.

For the EPB density analysis we used a 63× objective with a 2.5× digital zoom. EPB were considered when they fulfilled the following features: (1) they should be at least two times brighter than the axonal backbone; (2) they should be two times wider than the axonal backbone; and (3) they should not have any crossings from other axons nearby. Then, after selecting six random axonal segments per animal that measured at least 10 μm, we used ImageJ (FIJI) (Schindelin et al., 2012) to quantify the number of EPB. The EPB density values were expressed as the number of EPB/μm.

Analysis of GluN1 and GluN2B Expression

The immunohistochemical protocol employed was similar to that described above for GFP immunohistochemistry. For every subunit of NMDAR (GluN1 and GluN2B) we used different subseries of sections. In order to study the GluN1 expression, sections were incubated with rabbit anti-GluN1 (Alomone, 1:400) or GluN2B rabbit anti-GluN2B (Alomone, 1:4000) together with chicken anti-GFP IgY (Abcam, 1:500) primary antibodies for 48 h at 4°C. After washing, sections were incubated for 2 h at room temperature with donkey anti-rabbit (Biotium, A555, 1:800) and donkey anti-chicken, (Biotium, CF488A, 1:800) secondary

antibodies. Sections were then rinsed with PB 0.1 M, mounted on slides and coverslipped using Dako fluorescent mounting medium (Agilent, United States).

We used a laser scanning confocal microscope (Leica, SPE, Leica Microsystems, Wetzlar, Germany), obtaining 3D stacks of confocal images with a 63× objective, 3.5× digital zoom and 0.38 μm Z-step size for the study of GluN1 and GluN2B expression on the somata of GFP expressing interneurons. Ten isolated GFP-expressing somata per animal were selected randomly in the CA1 *stratum oriens*. Controls were performed omitting the anti-GluN1 or anti-GluN2B antibody, as well as incubating with these antibodies previously pre-absorbed overnight with an excess of its immunogenic peptide (GluN1 blocking peptide, Alomone, Jerusalem, Israel) or (GluN2B blocking peptide, Alomone, Jerusalem, Israel), respectively. No immunolabeling was observed in these controls.

Images were processed using Fiji software (Schindelin et al., 2012) as follows: the background was subtracted with a rolling value of 50, converted to 8-bit deep images and binarized using a determined threshold value. This value depended on the marker, but was kept the same for all images with the same marker. Finally, the software counted the number of puncta per cell and the percentage of area covered with these puncta. For the image analysis of GluN1, we outlined manually the profile of the cell somata and used a series of custom-made macros in Fiji, as previously described (Guirado et al., 2018). The original outline was expanded 0.5 μm from the cell body surface, obtaining two regions of interest (ROIs), the cell somata (the original outline) and the cell periphery (including the plasma membrane) (the area between both outlines). Then, ROIs were converted to 8-bit deep images and binarized using a determined size particle (larger than 0.04 μm) and threshold value. Finally, the software calculated the density of puncta and the percentage of area covered with them, both in cell somata and in the periphery. For GluN2B, we followed the same procedure, but in the 16 months-old animals, since puncta were frequently clustered into larger structures, the macro was adjusted and the threshold parameters were modified, in order to determine the percentage of area covered with these clusters of the receptor.

Statistics

The statistical analysis was based on the indications of Diester et al. (2019). We first analyzed pooled data from both sexes without considering the sex factor, and then data were segregated by sex and analyzed separately. The sex factor was not analyzed since the differences between sexes were not an objective of our study. After checking the normality and homoscedasticity of the data, one way ANOVA or Welch ANOVA tests were used to analyze the density of EPB and the density and percentage of area covered with GluN1 and GluN2B in GFP + somata during the aging process. A significant one-way ANOVA or Welch ANOVA was followed with the correspondent Tukey or Dunnett *post hoc* tests, respectively. Mean ± SEM was used in all cases. For the analysis of dendritic spine density, different generalized linear mixed models (GLMM) of the Poisson family were performed. To evaluate which variables were significant in the model, we determined the Bayesian Information Criteria (BIC). Using the non-interaction models obtained by the BIC, we determined the effect of age and segment in the density of dendritic spines performing a Wald test. A significant Wald test was followed by Tukey's *post hoc* test. In every case α was set to 0.05. All the analyses were performed using the R studio 1.3.1093 software. Graphs were generated with Graphpad Prism 8.4.3 software.

RESULTS

Dendritic Spine Density Analysis

To determine the effect of aging on the density of dendritic spines of O-LM cells (**Figures 1A,B**) in the whole (0–150 μm) dendritic segments, pooled males and females were analyzed without considering the segment factor (proximal, medial and distal). Since non-interaction models were chosen (see "Statistics" section), the effect of age in each segment (age × segment) could not be analyzed and compared; nevertheless, the results are shown in graphs **Figures 1C2–E2**. When analyzing all animals together, we observed a significant decrease in the density of dendritic spines between 3— and 9-month-old animals (**p = 0.006), but no significant differences were observed between 3— and 16-month-old animals (p = 0.22) or between 9— and 16-month-old animals (p = 0.32) (**Figure 1C1**). When females were analyzed separately, we found a significant decrease in the density of dendritic spines between 3— and 9-month-old animals (**p = 0.003), but no differences were observed between 3— and 16-month-old animals (p = 0.14) or between 9— and 16-month-old animals (p = 0.37) (**Figure 1D1**). When males were analyzed separately no significant effect of age was found (p = 0.44; **Figure 1E1**). The statistics of the correspondent test are included in the **Table 1**.

En Passant Bouton Density Analysis

No significant differences in the density of *EPB* from O-LM cells were observed between the different age groups (**Figures 2A,B**), neither when considering females and males together (p = 0.22; **Figure 2C**) nor when females (p = 0.56; **Figure 2D**) and males (p = 0.17; **Figure 2E**) were analyzed separately. The statistics of the correspondent test are included in the **Table 1**.

Analysis of GluN1 Immunoreactive Structures in Oriens-Lacunosum Moleculare Cells

We analyzed the density of GluN1 immunoreactive puncta and the area covered by these structures in the somata and the periphery (see methods) of O-LM cells (**Figures 3A,B**). The morphology and size of puncta expressing this subunit was similar in 3—, 9— and 16-month-old mice (**Figures 4A–F**). The analysis of the density of GluN1 immunoreactive puncta in the somata of O-LM cells did not show significant differences due to aging when both sexes were pooled together (p = 0.51; **Figure 4G1**), in females (p = 0.26; **Figure 4H1**) or in males (p = 0.78; **Figure 4I1**). Similar negative results were found when we analyzed the percentage of area of the somata covered with GluN1 + puncta: pooled females and males (p = 0.79;

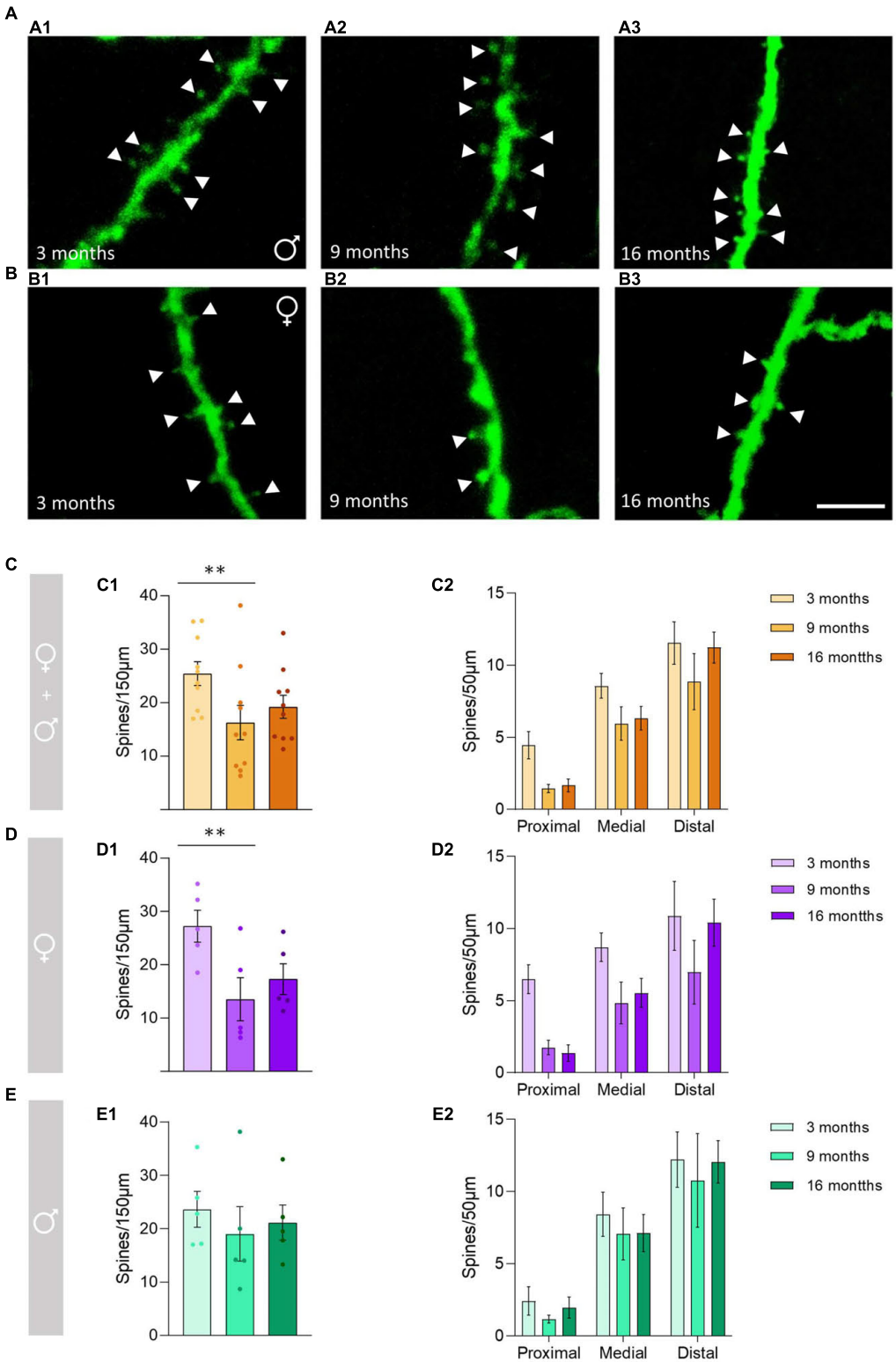

FIGURE 1 | Changes in the dendritic spine density of the *stratum oriens* O-LM cells during aging. **(A)** Segments of dendrites bearing spines (arrowheads) from 3-month-old **(A1)**, 9-month-old **(A2)**, and 16-month-old **(A3)** male mice. **(B)** Segments of dendrites bearing spines (arrowheads) from 3-month-old **(B1)**, 9-month-old **(B2)**, and 16-month-old **(B3)** female mice. **(C–E)** Graphs showing the density of the dendritic spines in pooled females and males, and animals segregated by sex in the total length of the dendrite analyzed (150 μm) **(C1–E1)** and in the proximal, medial and distal segment relative to the soma **(C2–E2)** (all graphs represent mean ± SEM., $^{**}p$-value < 0.01). Scale bar: 5 μm.

TABLE 1 | Summary of the results of the dendritic spine density and *en passant boutons*.

	Dendritic spines (150 ţm)								En passant boutons							
	Test	**DF**	**F**	***P*-value**	***Post hoc***	**3–9 months**	**9–16 months**	**3–16 months**	**Test**	**DF**	**F**	***P*-value**	***Post hoc***	**3–9 months**	**9–16 months**	**3–16 months**
Pooled females and males	Wald	2	4.77	0.008**	Tukey	0.006**	0.32	0.22	One way ANOVA	2	1.62	0.22	N/A	N/A	N/A	N/A
Females	Wald	2	5.34	0.005**	Tukey	0.003**	0.37	0.14	One way ANOVA	2	0.62	0.56	N/A	N/A	N/A	N/A
Males	Wald	2	0.82	0.44	N/A	N/A	N/A	N/A	One way ANOVA	2	2.06	0.17	N/A	N/A	N/A	N/A

$^{**}p < 0.01$.
When the test was not significant, post hoc comparisons were not applicable (N/A).

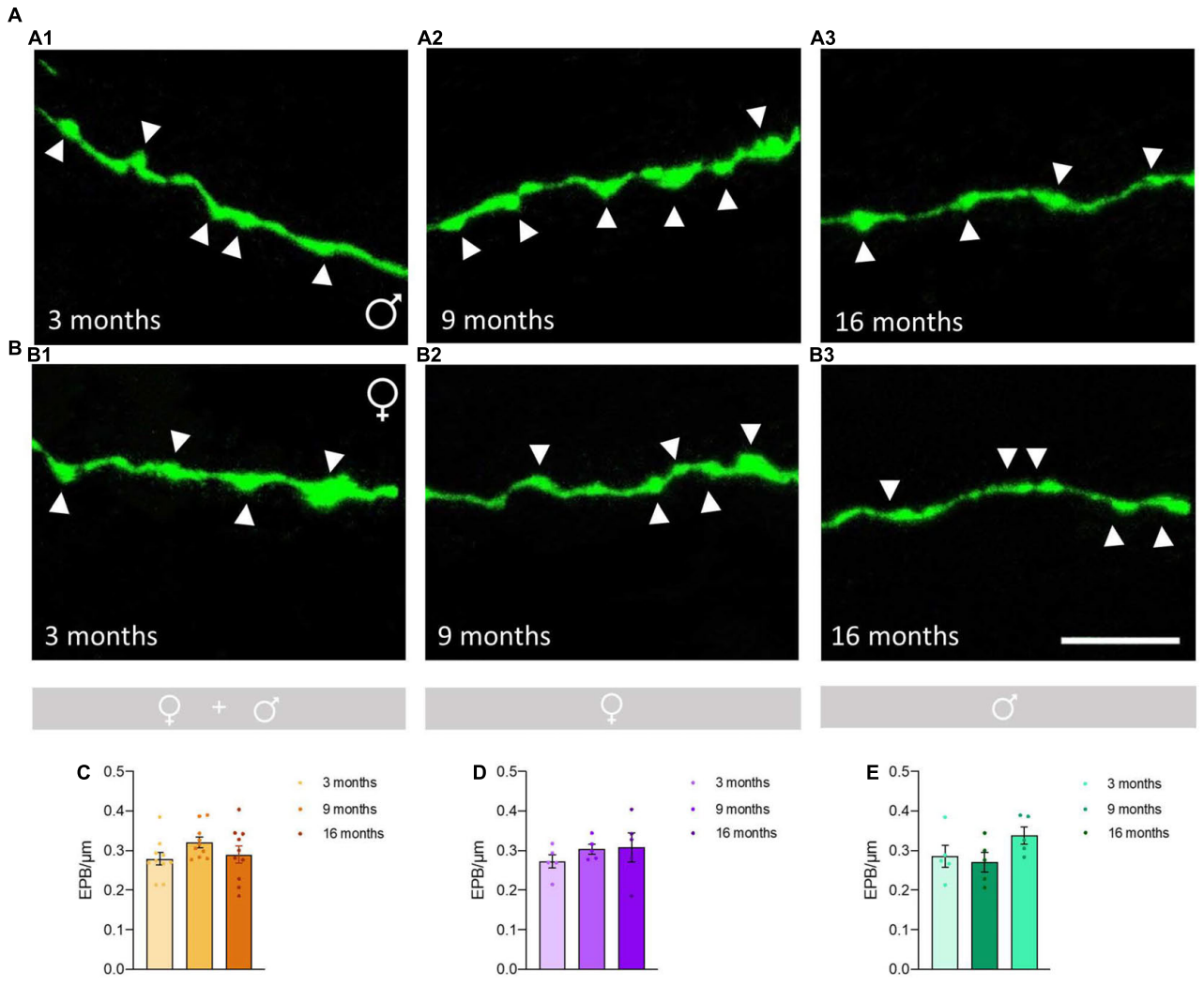

FIGURE 2 | Analysis of the effects of aging on the density of *en passant boutons* (EPB) in axons of O-LM cells in the *stratum lacunosum-moleculare*. **(A)** Axonal segments showing EPB (arrowheads) from 3-month-old **(A1)**, 9-month-old **(A2)**, and 16-month-old **(A3)** male mice. **(B)** Axonal segments showing EPB (arrowheads) from 3-month-old **(B1)**, 9-month-old **(B2)**, and 16-month-old **(B3)** female mice. **(C–E)** Graphs showing the density of EPB in animals segregated by sex **(C),** pooled females **(D)** and males **(E)** (all graphs represent mean ± SEM). Scale bar: 5 µm.

Figure 4G2), females ($p = 0.32$; **Figure 4H2**) and males ($p = 0.58$; **Figure 4I2**). In the cell periphery the density of GluN1 + puncta also did not show changes during aging: pooled females and males ($p = 0.30$; **Figure 4G3**), females ($p = 0.15$; **Figure 4H3**) and males ($p = 0.86$; **Figure 4I3**). Similarly, we did not detect significant differences in the percentage of area covered with GluN1 + puncta in the periphery of the cells: pooled males and females ($p = 0.32$; **Figure 4G4**), females ($p = 0.24$;

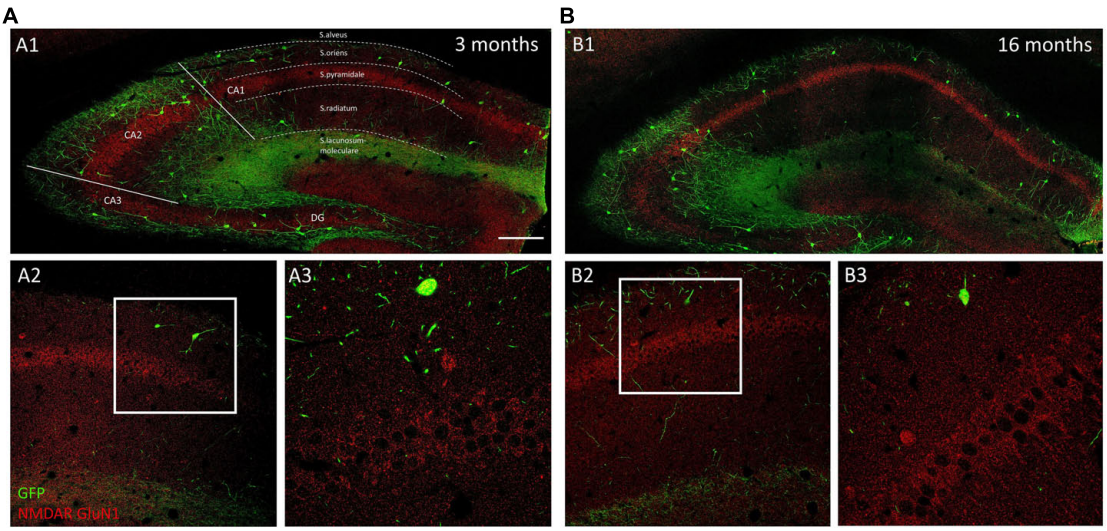

FIGURE 3 | Distribution of GluN1 immunoreactivity in young and aged GIN mice hippocampus. **(A1,B1)** Panoramic confocal planes showing the distribution of O-LM cells (green) and GluN1 immunoreactivity (red) in the hippocampus of 3-month-old **(A1)** and 16-month-old **(B1)** mice. Different regions and strata are indicated with dotted lines. **(A2,B2)** High magnification view from the different CA1 *strata* in 3-month-old **(A2)** and 16-month-old **(B2)** mice. **(A3,B3)** Enlarged view of the squared regions in panels **(A2,B2)**, showing double immunofluorescence for GFP/GluN1, in *strata oriens,* and *pyramidale.* Note the homogenous distribution of GluN1 immunoreactive puncta in pyramidal neurons in both 3-month-old **(A3)** and 16-month-old **(B3)** mice. Scale bar: 150 μm for panels **(A1,B1)**, 67 μm for panels **(A2,B2)**, and 21 μm for panels **(A3,B3)**.

Figure 4H4) and males (p = 0.91; **Figure 4I4**). The statistics of the correspondent test are included in the **Table 2**.

Analysis of GluN2B Immunoreactive Structures in Oriens-Lacunosum Moleculare Cells

We analyzed the density of GluN2B immunoreactive puncta and the area covered by these structures in the somata and the periphery of O-LM cells (**Figures 5A,B**). The morphology and size of the puncta expressing this subunit was similar to that described for GluN1 + puncta in 3− and 9-month-old mice, but in 16-month-old mice we frequently observed the presence of larger structures composed of clustered GluN2B + puncta (**Figures 6A–F**). The analysis of the density of GluN2B immunoreactive puncta in the soma showed a significant decrease between 3− and 16-month-old animals when both sexes were pooled together (****$p < 0.0001$; **Figure 6G1**) and in females (**p = 0.004; **Figure 6H1**). Additionally, we also observed a significant decrease between 9− and 16-month-old animals in pooled females and males (*p = 0.040; **Figure 6G1**), and in females (*p = 0.031; **Figure 6H1**). However, no significant differences were found between 3− and 9-month-old mice in both sexes together (p = 0.84; **Figure 6G1**) or in females (p = 0.57; **Figure 6H1**). Males did not show significant differences (p = 0.09; **Figure 6I1**). By contrast, the percentage of area covered by GluN2B + puncta in the somata of O-LM cells showed a significant increase when females and males were pooled together and in females and males separately when comparing 3− and 16− (****$p < 0.0001$) and 9− and 16-month-old mice (****$p < 0.0001$) (**Figures 6G2–I2**). However, no significant differences were found between 3− and 9-month-old individuals in pooled female and male (p = 0.55; **Figure 6G2**), female (p = 0.84; **Figure 6H2**) and male (p = 0.97; **Figure 6I2**) mice. In the cell periphery, the density of GluN2B + puncta showed a significant decrease in females and males pooled together (*p = 0.038; **Figure 6G3**) and in males (*p = 0.015; **Figure 6I3**) between 3− and 16-month-old mice. No significant differences were found in pooled females and males an in males between 3− and 9− (p = 0.88, **Figure 6G3**; p = 0.24, **Figure 6I3**) or 9− and 16-month-old mice (p = 0.10, **Figure 6G3**; p = 0.21, **Figure 6I3**). We did not detect significant differences in females (p = 0.41; 6H3). Similarly, non-significant differences were observed in the percentage of area in the periphery covered with GluN2B + immunoreactivity: females and males pooled together (p = 0.40; **Figure 6G4**), females (p = 0.26; **Figure 6H4**), and males (p = 0.45; **Figure 6I4**). The statistics of the correspondent test are included in the **Table 2**.

DISCUSSION

In the present study, we demonstrate age-dependent alterations in the structure of SST-expressing interneurons in the CA1 *stratum oriens*. There was a significant decrease in the density of the dendritic spines between 3− and 9-month-old females. However, we did not observe such changes in males. We also studied the density of the *en passant boutons* (EPB) of these interneurons in the *stratum lacunosum moleculare,* where no changes were found related to aging. We have focused our study in the *stratum oriens* of the CA1 region. It should be noted that although there is a small proportion of the GFP + cells in this

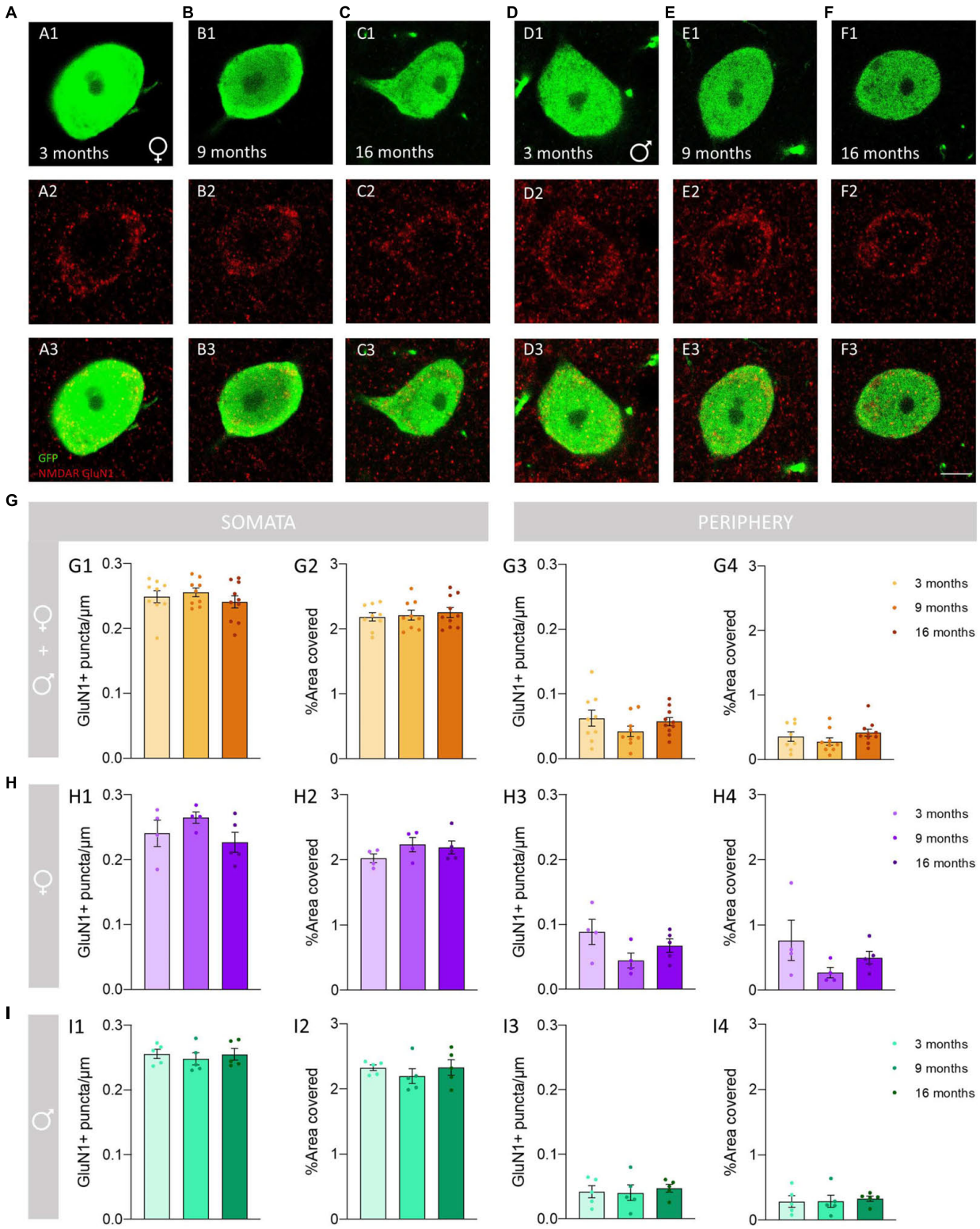

FIGURE 4 | Analysis of the density and percentage of area covered with GluN1 immunoreactive puncta in the somata and the periphery of O-LM cells during aging. **(A–F)** Double GFP/GluN1 immunohistochemistry in 3-month-old **(A)**, 9-month-old **(B)** and 16-month-old **(C)** female mice, and in 3-month-old **(D)**, 9-month-old **(E)** and 16-month-old **(F)** male mice. **(G–I)** Graphs showing the density and percentage of area covered with GluN1 immunoreactive puncta in the somata **(G1,G2–I2)** and in its periphery **(G3,G4–I4)** in animals segregated by sex **(G1–4)**, pooled females **(H1–4)** and males **(I1–4)** (all graphs represent mean ± SEM). Scale bar: 5 µm.

TABLE 2 | Summary of the results of the expression of NMDAR.

Density	Test	DF	F	*P*-value	*Post hoc*	3–9 months	9–16 months	3–16 months
				Pooled females and males				
NMDAR GluN1 cytoplasm	One way ANOVA	2	0.70	0.51	N/A	N/A	N/A	N/A
NMDAR GluN1 membrane	One way ANOVA	2	1.28	0.30	N/A	N/A	N/A	N/A
NMDAR GluN2B cytoplasm	Welch ANOVA	2	22.59	<0.0001****	Dunnet	0.84	0.040*	<0.0001****
NMDAR GluN2B membrane	One way ANOVA	2	3.93	0.033*	Tukey	0.88	0.10	0.038*
Percentage of area covered								
NMDAR GluN1 cytoplasm	One way ANOVA	2	0.24	0.79	N/A	N/A	N/A	N/A
NMDAR GluN1 membrane	One way ANOVA	2	1.21	0.32	N/A	N/A	N/A	N/A
NMDAR GluN2B cytoplasm	Welch ANOVA	2	867.00	<0.0001****	Dunnet	0.55	<0.0001****	<0.0001****
NMDAR GluN2B membrane	One way ANOVA	2	0.96	0.40	N/A	N/A	N/A	N/A
				Females				
NMDAR GluN1 cytoplasm	One way ANOVA	2	1.53	0.26	N/A	N/A	N/A	N/A
NMDAR GluN1 membrane	One way ANOVA	2	2.34	0.15	N/A	N/A	N/A	N/A
NMDAR GluN2B cytoplasm	One way ANOVA	2	9.72	0.004**	Tukey	0.57	0.031*	0.003**
NMDAR GluN2B membrane	One way ANOVA	2	0.97	0.41	N/A	N/A	N/A	N/A
Percentage of area covered								
NMDAR GluN1 cytoplasm	One way ANOVA	2	1.27	0.32	N/A	N/A	N/A	N/A
NMDAR GluN1 membrane	One way ANOVA	2	1.69	0.24	N/A	N/A	N/A	N/A
NMDAR GluN2B cytoplasm	One way ANOVA	2	570.90	<0.0001****	Tukey	0.84	<0.0001****	<0.0001****
NMDAR GluN2B membrane	Welch ANOVA	2	0.46	0.26	N/A	N/A	N/A	N/A
				Males				
NMDAR GluN1 cytoplasm	One way ANOVA	2	0.26	0.78	N/A	N/A	N/A	N/A
NMDAR GluN1 membrane	One way ANOVA	2	0.15	0.86	N/A	N/A	N/A	N/A
NMDAR GluN2B cytoplasm	One way ANOVA	2	3.11	0.09	N/A	N/A	N/A	N/A
NMDAR GluN2B membrane	One way ANOVA	2	5.86	0.018*	Tukey	0.24	0.21	0.015*
Percentage of area covered								
NMDAR GluN1 cytoplasm	One way ANOVA	2	0.57	0.58	N/A	N/A	N/A	N/A
NMDAR GluN1 membrane	One way ANOVA	2	0.09	0.91	N/A	N/A	N/A	N/A
NMDAR GluN2B cytoplasm	One way ANOVA	2	1,268.00	<0.0001****	Tukey	0.97	<0.0001****	<0.0001****
NMDAR GluN2B membrane	One way ANOVA	2	0.87	0.45	N/A	N/A	N/A	N/A

$p < 0.05$; $p < 0.01$**; $p < 0.0001$****.*
When the test was not significant, post hoc comparisons were not applicable (N/A).

stratum that project to the *striatum*, most of them are O-LM cells, which project to *stratum lacunosum moleculare* (Oliva et al., 2000; Pérez-Rando et al., 2017b). The O-LM cells are an interneuronal subpopulation characterized by the presence of abundant spines in their dendritic tree (Freund and Buzsáki, 1996) and numerous EPB in their axonal projection field in the *stratum lacunosum moleculare* (Müller and Remy, 2014). The spines and EPB of O-LM cells have been studied during aging previously, using *in vivo* two-photon imaging in GIN mice, but only from 4 to 11 months of age. The density of EPB in the *stratum lacunosum moleculare* remained constant, similar to what we have observed in fixed tissue. However, in contrast with our results, the spine density of O-LM interneurons increased by 12% from 4 to 11 months (Schmid et al., 2016). However, the big differences in methodology between the 2 experiments have to be taken into account. Ablation of neocortex covering the hippocampus, type of imaging and the age of the animals compared. It is important to note that both sexes were analyzed together in this experiment, without control over the estrous cycle, which can influence spine density in O-LM interneurons (Pérez-Rando et al., 2021). Moreover, this study examined dendritic spines in behaving animals and, consequently, spine density can be influenced by this behavior, possibly through the activation NMDA receptors. To our knowledge the present study is the first to analyze the structure of SST-expressing neurons in intact animals and to include aged animals from both sexes. Age-related structural changes have been also studied in other subpopulations of interneurons, particularly analyzing their dendritic arborization. In the visual cortex, the dendritic arbors of interneurons (in general) were simplified in aged mice (Eavri et al., 2018). However, in other specific interneuronal types, such as the vasoactive intestinal peptide/calretinin-expressing cells in the CA1 region of the hippocampus, no differences were found in dendritic length or number of intersections between young and old mice (Francavilla et al., 2020). However, it has to be noted that we have observed changes in the dendritic spine density only in 9-month females and when grouping both sexes. These results suggest that the structural changes are not the result of aging but rather of the influence of female sex hormones. The estrous cycle of female mice usually starts between the

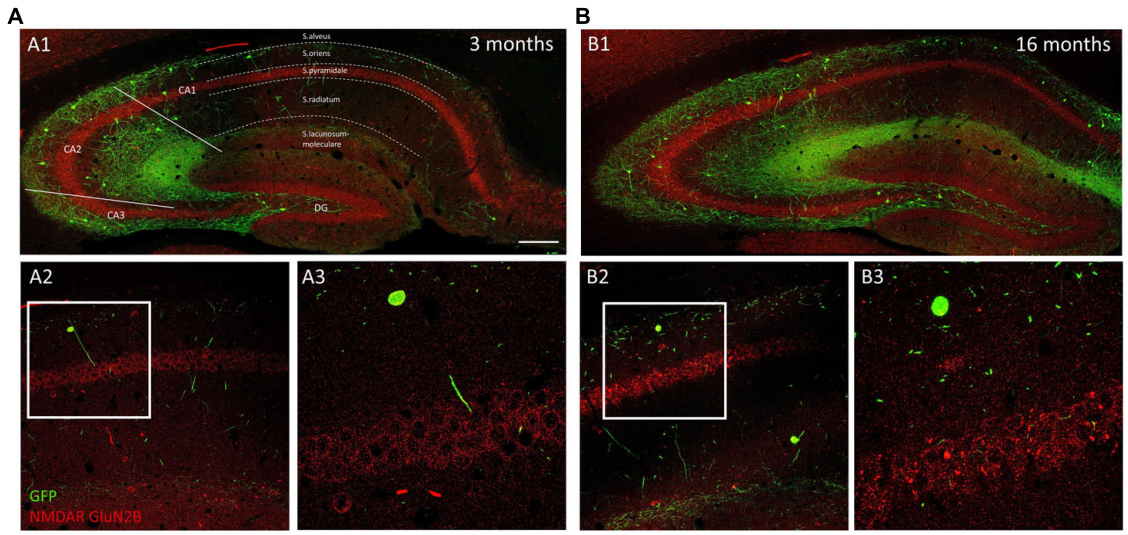

FIGURE 5 | Distribution of GluN2B immunoreactivity in young and aged GIN mice hippocampus. Panoramic confocal plane showing the distribution of O-LM cells (green) and GluN2B immunoreactivity (red) in the hippocampus of 3-month-old **(A1)** and 16-month-old **(B1)** mice. Different regions and strata are indicated with dotted lines. **(A2,B2)** High magnification view from the different CA1 *strata* in 3-month-old **(A2)** and 16-month-old **(B2)** mice. **(A3,B3)** Enlarged view of the squared regions in panels **(A2,B2)**, showing double immunofluorescence for GFP/GluN2B, in *strata oriens,* and *pyramidale*. Note the presence of GluN2B + clusters in pyramidal neurons in 16-month-old **(B3)**, but not in 3-month-old **(A3)** mice. Scale bar: 150 μm for panels **(A1,B1)**, 67 μm for panels **(A2,B2)**, and 21 μm for panels **(A3,B3)**.

6th – 8th week (White, 2007), but can be conditioned for many factors (Drickamer, 1974, 1984; Kruczek and Gruca, 1990), and prolongs itself to 14 months-old, when the animals are no longer reproductive (Flurkey et al., 2007). Furthermore, the variations we find in females, but not in males, when studying O-LM dendritic spine density are in accordance with previous findings from our laboratory studying these interneurons in intact and ovariectomized female GIN mice. We demonstrated that this parameter changes depending on the estrous phase in which the mouse is in, and the alterations seen in ovariectomized mice were also restored by 17β-Estradiol administration (Pérez-Rando et al., 2021). These structural changes had only been previously studied in pyramidal neurons (Woolley and McEwen, 1994; Luine and Frankfurt, 2013).

Interestingly, some of the effects of estrogens on hippocampal structure/connectivity appear to be mediated by NMDAR (El-Bakri et al., 2004). However, a more recent study revealed no differences in the mRNA levels of GluN1 and GluN2B in the dorsal hippocampus when comparing control and ovariectomized mice (McCarthny et al., 2018). Particularly, the study of NMDARs and hormonal levels during senescence demonstrated that NMDAR subunit mRNA levels in the hippocampus were much more prominently affected by the chronological age than by the reproductive status of the animals (Adams et al., 2001). In the present work we did not control the estrous cycle of the females, which could probably affect some parameters and constitute one of the limitations of the study.

Although we have not studied the density of SST-positive neurons, different studies have previously demonstrated a loss during aging in the hippocampus of rats, particularly in the *stratum oriens* (Potier et al., 2006; Stanley et al., 2012), although some reports did not find decreases in this cell type (Miettinen et al., 1993). Studies in mice are scarcer: one study described detrimental effects of aging on the number of these cells in the dentate gyrus (Koh et al., 2014), while another, using GIN mice, found an age-dependent decrease of O-LM interneurons from 5 to 9 months, but not from 9 to 12 months (Schmid et al., 2016). It is possible that these reductions of cell density may have an impact on the influence of SST-expressing interneurons during aging, in addition to the structural alterations that we have observed.

Interestingly, different studies have shown that aging is associated with a decrease in the excitability of hippocampal pyramidal neurons and with alterations in synaptic plasticity (LTP and LTD), which may underlie the deficits in hippocampal-dependent learning tasks (Oh and Disterhoft, 2020). These changes may be compensatory for a decrease in inhibition, because in the CA1 aging is associated with decreased GABAergic transmission (Billard et al., 1995; Potier et al., 2006), decreased number of GAD-67 + interneurons (Shetty and Turner, 1998; Stanley and Shetty, 2004), and decreased expression of GAD-67 mRNA in the CA1 (Vela et al., 2003). Specifically, the selective loss of O-LM cells in an age-dependent manner has been related to a decrease in the amplitude of evoked inhibitory postsynaptic currents (IPSCs) and a decrease in the frequency of spontaneous IPSCs in CA1 pyramidal neurons (Potier et al., 2006).

Previous studies in our laboratory have demonstrated that the structure of hippocampal SST-expressing interneurons in the *stratum oriens* of CA1 is regulated by NMDAR. Interestingly, we found that these glutamatergic receptors were expressed in the somata and dendritic spines of SST-expressing interneurons

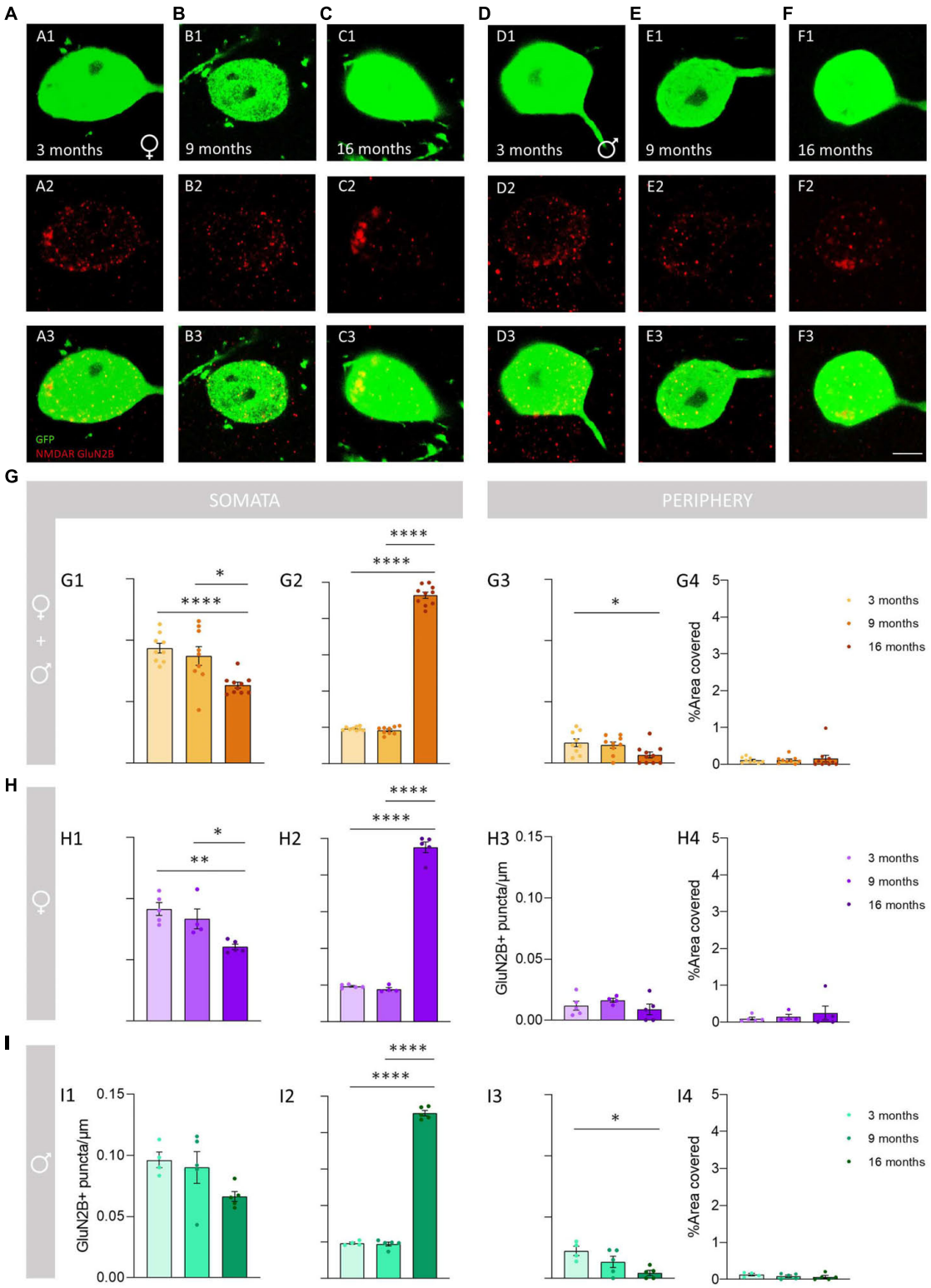

FIGURE 6 | Analysis of the density and percentage of area covered with GluN2B immunoreactive puncta in the somata and in the periphery of O-LM cells during aging. **(A–F)** Double GFP/GluN2B immunohistochemistry in 3-month-old **(A)**, 9-month-old **(B)**, 16-month-old **(C)** female mice and in 3-month-old **(D)**, 9-month-old **(E)**, 16-month-old **(F)** male mice. In panels **(C2,F2)**, a detailed view of the GluN2B clustering in aged mice can be observed. **(G–I)** Graphs showing the density and percentage of area covered with GluN2B immunoreactive puncta in the somata **(G1,G2–I2)** and in its periphery **(G3,G4–I4)** in animals segregated by sex **(G1–4)**, pooled females **(H1–4)** and males **(I1–4)** (all graphs represent mean ± SEM., **p*-value <0.05, ***p*-value <0.01, *****p*-value <0.0001). Scale bar: 5 μm.

(Pérez-Rando et al., 2017a). In our previous studies using organotypic cultures, we observed that the relative density of spines and their appearance rate increased 24 h after the NMDA infusion (Pérez-Rando et al., 2017a). By contrast, the application of an NMDAR antagonist produced opposite results (Pérez-Rando et al., 2017b).

Mounting evidence suggests that an age-associated hypofunction of the NMDAR can contribute to the impairment in spatial learning and memory, particularly affecting the Schaffer collateral pathway (Foster and Norris, 1997; Kumar and Foster, 2013). A decrease in the expression of NMDARs has been observed in the hippocampus during normal aging (Magnusson et al., 2006; Billard and Rouaud, 2007; Zhao et al., 2009), particularly in the CA1 region (Magnusson and Cotman, 1993; Wenk and Barnes, 2000). However, the response to aging was different depending on the NMDAR subunit studied (Avila et al., 2017). There are no significant changes in GluN1 protein expression in the whole hippocampus of aged mice (Zhao et al., 2009) and particularly in the expression of GluN1 mRNA in the CA1 pyramidal layer (Magnusson et al., 2005). In the present report we have studied the density of GluN1 + puncta in the O-LM cells, but we did not observe changes during aging, which is in accordance with the previous data. However, decreases in the expression of GluN1 protein (Eckles-Smith et al., 2000; Mesches et al., 2004; Liu et al., 2008) and mRNA (Adams et al., 2001) in the whole hippocampus have been reported in aged rats. By contrast with GluN1, there is a widespread agreement that the GluN2B subunit is especially affected by aging. There is a decrease of its protein (Clayton and Browning, 2001; Mesches et al., 2004; Zhao et al., 2009) and mRNA expression (Adams et al., 2001; Clayton and Browning, 2001) in the whole hippocampus, and particularly in the CA1 pyramidal layer (Magnusson, 2001), both in rats and mice. It has to be noted, however, that these studies analyzed the whole hippocampus and not specific cell types as our experiment. Notwithstanding, in concordance with these previous studies, we observed a decrease of the GluN2B + puncta in the O-LM cells in our oldest group, which is significant in females and when analyzing both sexes together. However, the area covered by GluN2B + puncta in O-LM cells is considerably larger in the oldest animals, suggesting the presence of clusters of these receptors. In fact, it has been suggested that an increased association of GluN2B receptors with scaffolding proteins in aged animals may contribute to the age-related memory impairment (Zamzow et al., 2013). Additionally, there is data supporting that the age-associated hypofunction of NMDAR may be due to decrease in the activity-dependent changes in the surface distribution of NMDAR (Clayton et al., 2002) increased association with membrane scaffolding proteins (Zamzow et al., 2013) and to decreased trafficking of GluN2B to the synapse (Kumar et al., 2019). The clustering of GluN2B subunits may be the physical manifestation of poor trafficking of NMDAR, which possibly begins in middle-age.

It is interesting to note that the genetic deletion of GluN2B in interneurons prevents the formation of glutamatergic synapses on hippocampal interneurons (Kelsch et al., 2014). Consequently, it is possible that the age-related decrease in GluN2B expression in O-LM cells also interferes with the maintenance of their glutamatergic input, affecting thus the density of dendritic spines on these cells. Our results show that alterations in NMDAR do not only affect pyramidal neurons, but also SST-expressing cells and, consequently, the inhibition that these interneurons exert on excitatory cells. In fact, SST has a potent effect on LTP in CA1 (Rostampour et al., 2002; Fan and Fu, 2014).

An important limitation of our study is the age of the oldest animals (16 months). These mice are not considered aged in most studies, although cognitive impairment starts to appear around this age in rodents (Kumar and Foster, 2013). However, in our hands, most animals of this transgenic strain died shortly after this age and many of them presented tumors and considerable hair loss. Unfortunately, we were not able to perform learning tests in these animals and there are no reports analyzing cognitive tasks in aged animals of this strain or from this genetic background (FVB).

Altogether, our results help to shed light on how aging and sex modulate the structural plasticity and the NMDARs expression of hippocampal interneurons, particularly of O-LM cells. The study of these receptors is important since changes on their expression can lead to neuronal potentiation or depression, and alterations in their physiology may underlie behavioral and cognitive dysfunctions.

DATA AVAILABILITY STATEMENT

The raw data supporting the conclusions of this article will be made available by the authors, without undue reservation.

ETHICS STATEMENT

The animal study was reviewed and approved by Committee on Bioethics of the Universitat de València.

AUTHOR CONTRIBUTIONS

JN designed the experiment. YG, PK, SC, and MP-R performed the experiments and quantifications. YG, PK, and JN wrote the manuscript and all the authors revised and edited the final version. All authors contributed to the article and approved the submitted version.

FUNDING

This work was supported by the Spanish Ministry of Science and Innovation (RTI2018− 098269−B−I00) and the Generalitat Valenciana (PROMETEU/2020/024). PK and YG were supported by predoctoral fellowships from the Generalitat Valenciana (GRISOLIAP/2020/151 and ACIF/2021/193 respectively), and MP-R was supported by a postdoctoral "Atraccio de Talent" grant from the University of Valencia.

REFERENCES

Adams, M. M., Morrison, J. H., and Gore, A. C. (2001). N-methyl-D-aspartate receptor mRNA levels change during reproductive senescence in the hippocampus of female rats. *Exp. Neurol.* 170, 171–179. doi: 10.1006/exnr.2001.7687

Alvarez, V. A., Ridenour, D. A., and Sabatini, B. L. (2007). Distinct structural and ionotropic roles of NMDA receptors in controlling spine and synapse stability. *J. Neurosci.* 27, 7365–7376. doi: 10.1523/JNEUROSCI.0956-07.2007

Avila, J., Llorens-Martín, M., Pallas-Bazarra, N., Bolós, M., Perea, J. R., Rodríguez-Matellán, A., et al. (2017). Cognitive Decline in Neuronal Aging and Alzheimer's Disease: Role of NMDA Receptors and Associated Proteins. *Front. Neurosci.* 11:626. doi: 10.3389/fnins.2017.00626

Barrientos, R. M., Kitt, M. M., Watkins, L. R., and Maier, S. F. (2015). Neuroinflammation in the normal aging hippocampus. *Neuroscience* 309, 84–99. doi: 10.1016/j.neuroscience.2015.03.007

Becker, N., Wierenga, C. J., Fonseca, R., Bonhoeffer, T., and Nägerl, U. V. (2008). LTD induction causes morphological changes of presynaptic boutons and reduces their contacts with spines. *Neuron* 60, 590–597. doi: 10.1016/j.neuron.2008.09.018

Bezaire, M. J., and Soltesz, I. (2013). Quantitative assessment of CA1 local circuits: knowledge base for interneuron-pyramidal cell connectivity. *Hippocampus* 23, 751–785. doi: 10.1002/hipo.22141

Billard, J. M., Lamour, Y., and Dutar, P. (1995). Decreased monosynaptic GABAB-mediated inhibitory postsynaptic potentials in hippocampal CA1 pyramidal cells in the aged rat: pharmacological characterization and possible mechanisms. *J. Neurophysiol.* 74, 539–546. doi: 10.1152/jn.1995.74.2.539

Billard, J.-M., and Rouaud, E. (2007). Deficit of NMDA receptor activation in CA1 hippocampal area of aged rats is rescued by D-cycloserine. *Eur. J. Neurosci.* 25, 2260–2268. doi: 10.1111/j.1460-9568.2007.05488.x

Blasco-Ibáñez, J. M., and Freund, T. F. (1995). Synaptic input of horizontal interneurons in stratum oriens of the hippocampal CA1 subfield: structural basis of feed-back activation. *Eur. J. Neurosci.* 7, 2170–2180. doi: 10.1111/j.1460-9568.1995.tb00638.x

Booker, S. A., and Vida, I. (2018). Morphological diversity and connectivity of hippocampal interneurons. *Cell Tissue Res.* 373, 619–641. doi: 10.1007/s00441-018-2882-2

Boric, K., Muñoz, P., Gallagher, M., and Kirkwood, A. (2008). Potential adaptive function for altered long-term potentiation mechanisms in aging hippocampus. *J. Neurosci.* 28, 8034–8039. doi: 10.1523/JNEUROSCI.2036-08.2008

Brandt, N., Löffler, T., Fester, L., and Rune, G. M. (2020). Sex-specific features of spine densities in the hippocampus. *Sci. Rep.* 10:11405. doi: 10.1038/s41598-020-68371-x

Clayton, D. A., and Browning, M. D. (2001). Deficits in the expression of the NR2B subunit in the hippocampus of aged Fisher 344 rats. *Neurobiol. Aging* 22, 165–168. doi: 10.1016/s0197-4580(00)00196-2

Clayton, D. A., Grosshans, D. R., and Browning, M. D. (2002). Aging and surface expression of hippocampal NMDA receptors. *J. Biol. Chem.* 277, 14367–14369. doi: 10.1074/jbc.C200074200

Das, S. R., and Magnusson, K. R. (2011). Changes in expression of splice cassettes of NMDA receptor GluN1 subunits within the frontal lobe and memory in mice during aging. *Behav. Brain Res.* 222, 122–133. doi: 10.1016/j.bbr.2011.03.045

Dickstein, D. L., Weaver, C. M., Luebke, J. I., and Hof, P. R. (2013). Dendritic spine changes associated with normal aging. *Neuroscience* 251, 21–32. doi: 10.1016/j.neuroscience.2012.09.077

Diester, C. M., Banks, M. L., Neigh, G. N., and Negus, S. S. (2019). Experimental design and analysis for consideration of sex as a biological variable. *Neuropsychopharmacology* 44, 2159–2162. doi: 10.1038/s41386-019-0458-9

Drickamer, L. C. (1974). Sexual maturation of female house mice: social inhibition. *Dev. Psychobiol.* 7, 257–265. doi: 10.1002/dev.420070310

Drickamer, L. C. (1984). Seasonal variation in acceleration and delay of sexual maturation in female mice by urinary chemosignals. *Reproduction* 72, 55–58. doi: 10.1530/jrf.0.0720055

Driscoll, I., Howard, S. R., Stone, J. C., Monfils, M. H., Tomanek, B., Brooks, W. M., et al. (2006). The aging hippocampus: a multi-level analysis in the rat. *Neuroscience* 139, 1173–1185. doi: 10.1016/j.neuroscience.2006.01.040

Eavri, R., Shepherd, J., Welsh, C. A., Flanders, G. H., Bear, M. F., and Nedivi, E. (2018). Interneuron Simplification and Loss of Structural Plasticity As Markers of Aging-Related Functional Decline. *J. Neurosci.* 38, 8421–8432. doi: 10.1523/JNEUROSCI.0808-18.2018

Eckles-Smith, K., Clayton, D., Bickford, P., and Browning, M. D. (2000). Caloric restriction prevents age-related deficits in LTP and in NMDA receptor expression. *Brain Res. Mol. Brain Res.* 78, 154–162. doi: 10.1016/s0169-328x(00)00088-7

El-Bakri, N. K., Islam, A., Zhu, S., Elhassan, A., Mohammed, A., Winblad, B., et al. (2004). Effects of estrogen and progesterone treatment on rat hippocampal NMDA receptors: relationship to Morris water maze performance. *J. Cell. Mol. Med.* 8, 537–544. doi: 10.1111/j.1582-4934.2004.tb00478.x

Engert, F., and Bonhoeffer, T. (1999). Dendritic spine changes associated with hippocampal long-term synaptic plasticity. *Nature* 399, 66–70. doi: 10.1038/19978

Fan, W., and Fu, T. (2014). Somatostatin modulates LTP in hippocampal CA1 pyramidal neurons: differential activation conditions in apical and basal dendrites. *Neurosci. Lett.* 561, 1–6. doi: 10.1016/j.neulet.2013.12.025

Flurkey, K., Currer, J. M., and Harrison, D. E. (2007). "Chapter 20 - Mouse Models in Aging Research," in *The Mouse in Biomedical Research*, 2nd Edn, eds J. G. Fox, M. T. Davisson, F. W. Quimby, S. W. Barthold, C. E. Newcomer, and A. L. Smith (Burlington: Academic Press), 637–672. doi: 10.1016/B978-012369454-6/50074-1

Foster, T. C., and Norris, C. M. (1997). Age-associated changes in Ca2 -dependent processes: Relation to hippocampal synaptic plasticity. *Hippocampus* 7, 602–612.

Foster, T. C., Kyritsopoulos, C., and Kumar, A. (2017). Central role for NMDA receptors in redox mediated impairment of synaptic function during aging and Alzheimer's disease. *Behavioural Brain Res.* 322, 223–232. doi: 10.1016/j.bbr.2016.05.012

Francavilla, R., Guet-McCreight, A., Amalyan, S., Hui, C. W., Topolnik, D., Michaud, F., et al. (2020). Alterations in Intrinsic and Synaptic Properties of Hippocampal CA1 VIP Interneurons During Aging. *Front. Cell. Neurosci.* 14:554405. doi: 10.3389/fncel.2020.554405

Freund, T. F., and Buzsáki, G. (1996). Interneurons of the hippocampus. *Hippocampus* 6, 347–470. doi: 10.1002/(sici)1098-106319966:4<347::aid-hipo1<3.0.co;2-i

Gavilán, M. P., Revilla, E., Pintado, C., Castaño, A., Vizuete, M. L., Moreno-González, I., et al. (2007). Molecular and cellular characterization of the age-related neuroinflammatory processes occurring in normal rat hippocampus: potential relation with the loss of somatostatin GABAergic neurons. *J. Neurochem.* 103, 984–996. doi: 10.1111/j.1471-4159.2007.04787.x

Gilabert-Juan, J., Bueno-Fernandez, C., Castillo-Gomez, E., and Nacher, J. (2017). Reduced interneuronal dendritic arborization in CA1 but not in CA3 region of mice subjected to chronic mild stress. *Brain Behav.* 7:e00534. doi: 10.1002/brb3.534

Guirado, R., Carceller, H., Castillo-Gómez, E., Castrén, E., and Nacher, J. (2018). Automated analysis of images for molecular quantification in immunohistochemistry. *Heliyon* 4:e00669. doi: 10.1016/j.heliyon.2018.e00669

Guirado, R., Perez-Rando, M., Sanchez-Matarredona, D., Castillo-Gómez, E., Liberia, T., Rovira-Esteban, L., et al. (2014). The dendritic spines of interneurons are dynamic structures influenced by PSA-NCAM expression. *Cereb. Cortex* 24, 3014–3024. doi: 10.1093/cercor/bht156

Hansen, K. B., Yi, F., Perszyk, R. E., Menniti, F. S., and Traynelis, S. F. (2017). NMDA Receptors in the Central Nervous System. *Methods Mol. Biol.* 1677, 1–80. doi: 10.1007/978-1-4939-7321-7_1

Hou, Y., Dan, X., Babbar, M., Wei, Y., Hasselbalch, S. G., Croteau, D. L., et al. (2019). Ageing as a risk factor for neurodegenerative disease. *Nat. Rev. Neurol.* 15, 565–581. doi: 10.1038/s41582-019-0244-7

Katona, I., Acsády, L., and Freund, T. F. (1999). Postsynaptic targets of somatostatin-immunoreactive interneurons in the rat hippocampus. *Neuroscience* 88, 37–55. doi: 10.1016/s0306-4522(98)00302-9

Katona, L., Lapray, D., Viney, T. J., Oulhaj, A., Borhegyi, Z., Micklem, B. R., et al. (2016). Sleep and Movement Differentiates Actions of Two Types of Somatostatin-Expressing GABAergic Interneuron in Rat Hippocampus. *Neuron* 91:1183. doi: 10.1016/j.neuron.2016.08.023

Kelsch, W., Li, Z., Wieland, S., Senkov, O., Herb, A., Göngrich, C., et al. (2014). GluN2B-containing NMDA receptors promote glutamate synapse development

in hippocampal interneurons. *J. Neurosci.* 34, 16022–16030. doi: 10.1523/JNEUROSCI.1210-14.2014

Khan, S. S., Singer, B. D., and Vaughan, D. E. (2017). Molecular and physiological manifestations and measurement of aging in humans. *Aging Cell* 16, 624–633. doi: 10.1111/acel.12601

Koh, M. T., Spiegel, A. M., and Gallagher, M. (2014). Age-associated changes in hippocampal-dependent cognition in Diversity Outbred mice. *Hippocampus* 24, 1300–1307. doi: 10.1002/hipo.22311

Köhler, C., and Chan-Palay, V. (1982). Somatostatin-like immunoreactive neurons in the hippocampus: an immunocytochemical study in the rat. *Neurosci. Lett.* 34, 259–264. doi: 10.1016/0304-3940(82)90185-9

Kruczek, M., and Gruca, A. (1990). Seasonal variations in male mice at the time of sexual maturation. *Lab. Anim.* 24, 36–39. doi: 10.1258/002367790780890392

Kumar, A., and Foster, T. C. (2013). Linking redox regulation of NMDAR synaptic function to cognitive decline during aging. *J. Neurosci.* 33, 15710–15715. doi: 10.1523/JNEUROSCI.2176-13.2013

Kumar, A., Thinschmidt, J. S., and Foster, T. C. (2019). Subunit contribution to NMDA receptor hypofunction and redox sensitivity of hippocampal synaptic transmission during aging. *Aging* 11, 5140–5157. doi: 10.18632/aging.102108

Lacaille, J. C., and Schwartzkroin, P. A. (1988). Stratum lacunosum-moleculare interneurons of hippocampal CA1 region. I. Intracellular response characteristics, synaptic responses, and morphology. *J. Neurosci.* 8, 1400–1410.

Leão, R. N., Mikulovic, S., Leão, K. E., Munguba, H., Gezelius, H., Enjin, A., et al. (2012). OLM interneurons differentially modulate CA3 and entorhinal inputs to hippocampal CA1 neurons. *Nat. Neurosci.* 15, 1524–1530. doi: 10.1038/nn.3235

Lister, J. P., and Barnes, C. A. (2009). Neurobiological changes in the hippocampus during normative aging. *Arch. Neurol.* 66, 829–833. doi: 10.1001/archneurol.2009.125

Liu, P., Smith, P. F., and Darlington, C. L. (2008). Glutamate receptor subunits expression in memory-associated brain structures: Regional variations and effects of aging. *Synapse* 62, 834–841. doi: 10.1002/syn.20563

Luine, V., and Frankfurt, M. (2013). Interactions between estradiol, BDNF and dendritic spines in promoting memory. *Neuroscience* 239, 34–45. doi: 10.1016/j.neuroscience.2012.10.019

Magnusson, K. R. (2001). Influence of diet restriction on NMDA receptor subunits and learning during aging. *Neurobiol. Aging* 22, 613–627. doi: 10.1016/s0197-4580(00)00258-x

Magnusson, K. R., and Cotman, C. W. (1993). Age-related changes in excitatory amino acid receptors in two mouse strains. *Neurobiol. Aging* 14, 197–206. doi: 10.1016/0197-4580(93)90001-r

Magnusson, K. R., Bai, L., and Zhao, X. (2005). The effects of aging on different C-terminal splice forms of the ζ1(NR1) subunit of the N-methyl-d-aspartate receptor in mice. *Mol. Brain Res.* 135, 141–149. doi: 10.1016/j.molbrainres.2004.12.012

Magnusson, K. R., Nelson, S. E., and Young, A. B. (2002). Age-related changes in the protein expression of subunits of the NMDA receptor. *Mol. Brain Res.* 99, 40–45. doi: 10.1016/s0169-328x(01)00344-8

Magnusson, K., Kresge, D., and Supon, J. (2006). Differential effects of aging on NMDA receptors in the intermediate versus the dorsal hippocampus. *Neurobiol. Aging* 27, 324–333. doi: 10.1016/j.neurobiolaging.2005.01.012

Markham, J. A., McKian, K. P., Stroup, T. S., and Juraska, J. M. (2005). Sexually dimorphic aging of dendritic morphology in CA1 of hippocampus. *Hippocampus* 15, 97–103. doi: 10.1002/hipo.20034

McCarthny, C. R., Du, X., Wu, Y. C., and Hill, R. A. (2018). Investigating the Interactive Effects of Sex Steroid Hormones and Brain-Derived Neurotrophic Factor during Adolescence on Hippocampal NMDA Receptor Expression. *Int. J. Endocrinol.* 2018:7231915. doi: 10.1155/2018/7231915

Mesches, M. H., Gemma, C., Veng, L. M., Allgeier, C., Young, D. A., Browning, M. D., et al. (2004). Sulindac improves memory and increases NMDA receptor subunits in aged Fischer 344 rats. *Neurobiol. Aging* 25, 315–324. doi: 10.1016/S0197-4580(03)00116-7

Miettinen, R., Sirviö, J., Riekkinen, P., Laakso, M. P., Riekkinen, M., and Riekkinen, P. (1993). Neocortical, hippocampal and septal parvalbumin- and somatostatin-containing neurons in young and aged rats: Correlation with passive avoidance and water maze performance. *Neuroscience* 53, 367–378. doi: 10.1016/0306-4522(93)90201-p

Müller, C., and Remy, S. (2014). Dendritic inhibition mediated by O-LM and bistratified interneurons in the hippocampus. *Front. Synaptic Neurosci.* 6:23. doi: 10.3389/fnsyn.2014.00023

Oh, M. M., and Disterhoft, J. F. (2020). Learning and aging affect neuronal excitability and learning. *Neurobiol. Learn. Mem.* 167:107133. doi: 10.1016/j.nlm.2019.107133

Oliva, A. A., Jiang, M., Lam, T., Smith, K. L., and Swann, J. W. (2000). Novel Hippocampal Interneuronal Subtypes Identified Using Transgenic Mice That Express Green Fluorescent Protein in GABAergic Interneurons. *J. Neurosci.* 20, 3354–3368. doi: 10.1523/jneurosci.20-09-03354.2000

Oren, I., Nissen, W., Kullmann, D. M., Somogyi, P., and Lamsa, K. P. (2009). Role of ionotropic glutamate receptors in long-term potentiation in rat hippocampal CA1 oriens-lacunosum moleculare interneurons. *J. Neurosci.* 29, 939–950. doi: 10.1523/JNEUROSCI.3251-08.2009

Pelkey, K. A., Chittajallu, R., Craig, M. T., Tricoire, L., Wester, J. C., and McBain, C. J. (2017). Hippocampal GABAergic Inhibitory Interneurons. *Physiol. Rev.* 97, 1619–1747. doi: 10.1152/physrev.00007.2017

Pérez-Rando, M., Castillo-Gómez, E., Bellés, M., Carceller, H., and Nácher, J. (2017). The activation of NMDA receptors alters the structural dynamics of the spines of hippocampal interneurons. *Neurosci. Lett.* 658, 79–84. doi: 10.1016/j.neulet.2017.08.042

Pérez-Rando, M., Castillo-Gómez, E., Guirado, R., Blasco-Ibañez, J. M., Crespo, C., Varea, E., et al. (2017). NMDA Receptors Regulate the Structural Plasticity of Spines and Axonal Boutons in Hippocampal Interneurons. *Front. Cell. Neurosci.* 11:166. doi: 10.3389/fncel.2017.00166

Pérez-Rando, M., Guirado, R., Tellez-Merlo, G., Carceller, H., and Nacher, J. (2021). Estradiol Regulates PSA-NCAM Expression and Connectivity of O-LM Interneurons in The Hippocampus of Adult Female Mice. *Neuroendocrinology* 2021:000515052. doi: 10.1159/000515052

Potier, B., Jouvenceau, A., Epelbaum, J., and Dutar, P. (2006). Age-related alterations of GABAergic input to CA1 pyramidal neurons and its control by nicotinic acetylcholine receptors in rat hippocampus. *Neuroscience* 142, 187–201. doi: 10.1016/j.neuroscience.2006.06.040

Rostampour, M., Fathollahi, Y., Semnanian, S., Hajizadeh, S., Mirnajafizadeh, J., and Shafizadeh, M. (2002). The ability of hippocampal CA1 area for induction of long-term potentiation is persistently reduced by prior treatment with cysteamine: an in vitro study. *Neuropeptides* 36, 263–270. doi: 10.1016/s0143-4179(02)00029-x

Schindelin, J., Arganda-Carreras, I., Frise, E., Kaynig, V., Longair, M., Pietzsch, T., et al. (2012). Fiji: an open-source platform for biological-image analysis. *Nat. Methods* 9, 676–682. doi: 10.1038/nmeth.2019

Schmid, L. C., Mittag, M., Poll, S., Steffen, J., Wagner, J., Geis, H.-R., et al. (2016). Dysfunction of Somatostatin-Positive Interneurons Associated with Memory Deficits in an Alzheimer's Disease Model. *Neuron* 92, 114–125. doi: 10.1016/j.neuron.2016.08.034

Shansky, R. M., and Murphy, A. Z. (2021). Considering sex as a biological variable will require a global shift in science culture. *Nat. Neurosci.* 24, 457–464. doi: 10.1038/s41593-021-00806-8

Shetty, A. K., and Turner, D. A. (1998). Hippocampal interneurons expressing glutamic acid decarboxylase and calcium-binding proteins decrease with aging in Fischer 344 rats. *J. Comparat. Neurol.* 394, 252–269. doi: 10.1002/(sici)1096-9861(19980504)394:2<252::aid-cne9<3.0.co;2-1

Shors, T. J., Chua, C., and Falduto, J. (2001). Sex differences and opposite effects of stress on dendritic spine density in the male versus female hippocampus. *J. Neurosci.* 21, 6292–6297.

Sik, A., Penttonen, M., Ylinen, A., and Buzsaki, G. (1995). Hippocampal CA1 interneurons: an in vivo intracellular labeling study. *J. Neurosci.* 15, 6651–6665. doi: 10.1523/jneurosci.15-10-06651.1995

Stanley, D. P., and Shetty, A. K. (2004). Aging in the rat hippocampus is associated with widespread reductions in the number of glutamate decarboxylase-67 positive interneurons but not interneuron degeneration. *J. Neurochem.* 89, 204–216. doi: 10.1111/j.1471-4159.2004.02318.x

Stanley, E. M., Fadel, J. R., and Mott, D. D. (2012). Interneuron loss reduces dendritic inhibition and GABA release in hippocampus of aged rats. *Neurobiol. Aging* 33, .e1–.e13. doi: 10.1016/j.neurobiolaging.2010.12.014

Vela, J., Gutierrez, A., Vitorica, J., and Ruano, D. (2003). Rat hippocampal GABAergic molecular markers are differentially affected by ageing. *J. Neurochem.* 85, 368–377. doi: 10.1046/j.1471-4159.2003.01681.x

Wenk, G. L., and Barnes, C. A. (2000). Regional changes in the hippocampal density of AMPA and NMDA receptors across the lifespan of the rat. *Brain Res.* 885, 1–5. doi: 10.1016/s0006-8993(00)02792-x

West, M. J., Coleman, P. D., Flood, D. G., and Troncoso, J. C. (1994). Differences in the pattern of hippocampal neuronal loss in normal ageing and Alzheimer's disease. *Lancet* 344, 769–772. doi: 10.1016/s0140-6736(94)92338-8

White, W. J. (2007). Management and design: breeding facilities. *Mouse Biomed. Res.* 2007, 235–269.

Woolley, C. S., and McEwen, B. S. (1994). Estradiol regulates hippocampal dendritic spine density via an N-methyl- D-aspartate receptor-dependent mechanism. *J. Neurosci.* 14, 7680–7687. doi: 10.1523/jneurosci.14-12-07680.1994

Zamzow, D. R., Elias, V., Shumaker, M., Larson, C., and Magnusson, K. R. (2013). An increase in the association of GluN2B containing NMDA receptors with membrane scaffolding proteins was related to memory declines during aging. *J. Neurosci.* 33, 12300–12305. doi: 10.1523/JNEUROSCI.0312-13.2013

Zhao, X., Rosenke, R., Kronemann, D., Brim, B., Das, S. R., Dunah, A. W., et al. (2009). The effects of aging on N-methyl-D-aspartate receptor subunits in the synaptic membrane and relationships to long-term spatial memory. *Neuroscience* 162, 933–945. doi: 10.1016/j.neuroscience.2009.05.018

Conflict of Interest: The authors declare that the research was conducted in the absence of any commercial or financial relationships that could be construed as a potential conflict of interest.

Publisher's Note: All claims expressed in this article are solely those of the authors and do not necessarily represent those of their affiliated organizations, or those of the publisher, the editors and the reviewers. Any product that may be evaluated in this article, or claim that may be made by its manufacturer, is not guaranteed or endorsed by the publisher.

frontiers | Frontiers in Psychiatry

TYPE Original Research
PUBLISHED 28 July 2022
DOI 10.3389/fpsyt.2022.946719

OPEN ACCESS

EDITED BY
Balazs Gaszner,
University of Pécs, Hungary

REVIEWED BY
Hiroyuki Hioki,
Juntendo University, Japan
Andrew Burke,
Indiana University School of Medicine, United States

*CORRESPONDENCE
Anne-Kathrin Gellner
gellner@uni-bonn.de

SPECIALTY SECTION
This article was submitted to Anxiety and Stress Disorders, a section of the journal Frontiers in Psychiatry

RECEIVED 17 May 2022
ACCEPTED 04 July 2022
PUBLISHED 28 July 2022

CITATION
Serradas ML, Stein V and Gellner AK (2022) Long-term changes of parvalbumin- and somatostatin-positive interneurons of the primary motor cortex after chronic social defeat stress depend on individual stress-vulnerability.
Front. Psychiatry 13:946719.
doi: 10.3389/fpsyt.2022.946719

Long-term changes of parvalbumin- and somatostatin-positive interneurons of the primary motor cortex after chronic social defeat stress depend on individual stress-vulnerability

Maria L. Serradas[1], Valentin Stein[1] and Anne-Kathrin Gellner[2]*

[1]Institute of Physiology II, Medical Faculty, University of Bonn, Bonn, Germany, [2]Department of Psychiatry and Psychotherapy, University Hospital Bonn, Bonn, Germany

Chronic stress is a major risk factor for developing mental illnesses and cognitive deficiencies although stress-susceptibility varies individually. In a recent study, we established the connection between chronic social defeat stress (CSDS) and impaired motor learning abilities accompanied by chronically disturbed structural neuroplasticity in the primary motor cortex (M1) of mice. In this study, we further investigated the long-term effects of CSDS exposure on M1, focusing on the interneuronal cell population. We used repeated CSDS to elicit effects across behavioral, endocrinological, and metabolic parameters in mice. Susceptible and resilient phenotypes were discriminated by symptom load and motor learning abilities were assessed on the rotarod. Structural changes in interneuronal circuits of M1 were studied by immunohistochemistry using parvalbumin (PV+) and somatostatin (SST+) markers. Stress-susceptible mice had a blunted stress hormone response and impaired motor learning skills. These mice presented reduced numbers of both interneuron populations in M1 with layer-dependent distribution, while alterations in cell size and immunoreactivity were found in both susceptible and resilient individuals. These results, together with our previous data, suggest that stress-induced cell loss and degeneration of the GABAergic interneuronal network of M1 could underlay impaired motor learning, due to their role in controlling the excitatory output and spine dynamics of principal neurons required for this task. Our study further highlights the importance of long-term outcomes of chronically stressed individuals which are translationally important due to the long timecourses of stress-induced neuropsychiatric disorders.

KEYWORDS

chronic stress, parvalbumin, motor learning, depression, somatostatin, interneuron, motor cortex

Introduction

Stress represents a major risk factor for developing mental illnesses and cognitive deficiencies in humans (1–3). Aiding neurobiological research, chronic social stress has a strong impact on affective-like behavioral responses, inducing a robust depression-like phenotype marked by anhedonia, anxiety, and social-avoidance in mice (4–6). In recent years, stress research has focused on the impact of chronic social stress in the neural circuits of limbic and prefrontal areas of the brain, due to their implications in behavior, emotions, cognition and memory. However, less attention has been given to the motor cortex and its structure and function in the context of chronic stress. The primary motor cortex (M1) is considered to be a major region for initiating and controlling voluntary movements (7, 8) and has an imperative role in contributing to motor learning (9, 10), which can be severely affected by chronic social stress. In a recent study, we have established the connection between chronic social defeat stress (CSDS) and impaired motor learning abilities accompanied by chronically disturbed structural neuroplasticity in the primary motor cortex of mice. Strikingly, long lasting cellular alterations on the level of glial cells of the motor cortex and the surrounding cerebrospinal fluid were still observed 5 weeks after cessation of the stressor (6). These findings, which were dependent on the individual stress vulnerability of the mice, open the question of whether other cellular components like interneurons of the motor cortex can get affected under chronic social stress exposure.

The motor cortex contains a vast collection of cellular components, organized by layers, including many different types of interneurons (11). The interneuronal network consists mostly of GABAergic inhibitory connections and is necessary to control output activity of principal neurons, cells that have been investigated in our previous work (6). Previous studies of limbic brain regions suggest that the interneural network is one of the most affected structures by chronic stress (12–15). GABAergic dysfunction and disturbed inhibitory/excitatory balance have been found in neuropsychiatric disorders and preclinical models, mostly investigated in the prefrontal brain regions [reviewed in (16, 17)]. The calcium-binding protein parvalbumin (PV), and the neuropeptide somatostatin (SST) define the most predominant interneuron subtypes within the motor cortex, which together comprise approximately 70% of the total GABAergic cortical interneuron population (18, 19) that control intra- and intercortical output. PV+ interneurons, contact the soma and proximal dendrites or the initial axon segment of glutamatergic pyramidal cells (19). SST+ interneurons arborize into the dendritic tuft in layer I and modulate spine dynamics (18–20). These interactions are important for intact neuroplasticity in M1 which we recently showed to be severely affected by CSDS (6).

In this study, repeated CSDS was used to induce effects depending on individual stress vulnerability across behavioral, endocrinological, and metabolic endpoints in C57BL/6J mice. Motor learning skills were assessed on the accelerating rotarod and the motor cortex studied histologically for structural changes in interneuronal circuits of M1, paying special attention to the GABAergic inhibitory network by using PV and SST markers.

Materials and methods

Animals

Twenty-four adult male mice (C57BL/6J, age 11 ± 0.75 weeks) were single housed throughout the entire experiment except for the stress period. Mice were fed *ad libitum*, maintained under a 12-h light-dark cycle and constant room temperature (22°C). Mice were weighed daily during the stress phase, the behavioral experiments and before tissue collection. All experiments were performed following the guidelines of the German Animal Protection Law and Directive 2010/63/EU of the European Commission and have been approved by the government of North Rhine Westphalia (Local Committee for Animal Health, LANUV NRW). Animal experiments have been reported in compliance with the ARRIVE guidelines.

Chronic social defeat stress

Mice were randomly assigned to either stress or control treatment with a ratio of 1.4:1 for group size. This ratio is necessary to generate sufficient numbers of the less frequently occurring resilient mice (4, 6) and avoid underpowering the analysis, in compliance with the 3R of animal research. CSDS was applied as described by Golden et al., (4). For 10 consecutive days, the experimental mouse was introduced to the home cage of an unknown, bigger and aggressive CD1 mouse (aggressor) for 5 min, where it encountered several physical attacks and threats. Afterward, both the stressed mouse and CD1 remained in the same cage for 24 h, separated by a perforated acrylic glass divider allowing continuous sensory cues. Control mice were handled daily and housed pairwise in an equally divided cage. Pairings and cages were not changed throughout the CSDS period. One mouse of the CSDS group died after 7 days without any apparent reason (such as wounding during attacks or sickness behavior) and was excluded from the analysis. In the CSDS group, the daily 5 min of physical exposure to the aggressor were recorded on video for *post-hoc* analysis of attacks. In 8 cases single sessions (randomly occurring during the

10 days and in different mice) were not recorded due to technical failure. Each attack of the CD1 toward the experimental mouse was counted and rated with a severity score from 1 (short physical contact without bite) to 3 (biting and full body contact including pinning to the ground) in score intervals of 0.5 (allowing for more nuanced scoring in cases where an attack consists of a behavioral mix).

Behavioral tests

Nestlet shredding test

Nest shredding analysis was performed as described by Deacon (21). Briefly, old nesting material was removed from the home cage. A new nestlet was placed into the animal's cage. After 3 h, the nest-building performance of the mouse was assessed on a rating scale of 1 to 5 (1 = nestlet untouched, 5 full nest and all material used).

Sucrose preference test

Mice were habituated to the smaller bottles during the CSDS phase. After the last CSDS session, all mice were single housed and received two bottles, one filled with water and one with 1% sucrose solution. Position of the bottles was switched after 24 h. Consumption of water and sucrose solution was measured by weighing the bottles at 0, after 24, and 48 h. Sucrose preference was calculated as the relative consumption of sucrose solution and averaged between the first and second day of the test.

Social avoidance test

Approximately 24 h after the last CSDS session each experimental mouse was placed in an open arena (40 cm × 40 cm) together with an empty wire cage and was left to explore for 2.5 min, which were recorded on video. The mouse was removed from the arena and the empty wire cage replaced by one filled with an unknown CD1 mouse. Exploration of the experimental mouse was again recorded for 2.5 min. Both trials were then analyzed using Anymaze software (Stoelting) and the number of entries of the mouse head interacting with the wire cage within a 4 cm zone (with and without presence of a social partner) was calculated.

Accelerating rotarod test

Mice were first habituated by placing them onto the rod at slow speed (4 rpm) until a calm and steady movement was observed for a minimum of 180 s. The motor learning was tested by accelerating the rotation speed from 4 to 20 rpm (increment of 1 rpm/s for 16 s, then remaining at 20 rpm for 74 s) for each trial. Time until the animal fell (or cut-off time of 90 s) was recorded for 15 consecutive trials and mice were allowed to rest for 60 s in-between trials. Learning curves were fitted by a sigmoid curve derived from the Hill equation and maximum time on the rod calculated.

Fecal corticosterone ELISA

All mice were moved to a fresh home cage (single-housed) after finishing the last session of CSDS or control handling. After 24 h, fecal pellets were collected from the bedding and stored at −20°C until further processing. Corticosterone (CORT) levels in feces were determined by an ELISA kit according to the manufacturer's instructions (Arbor Assays, K014- H5). All samples and standards (78.128–10,000 pg/ml) were tested in duplicates. Two samples from the control group had to be excluded due to a technical error.

Brain tissue collection

Mice were deeply anesthetized (Ketamine 240 mg/kg and Xylazine 32 mg/kg body weight) until complete loss of reflexes before transcardiac perfusion with 50 ml cold phosphate-buffered saline (PBS, pH 7.4) followed by 50 ml paraformaldehyde (4% in PBS, pH 7.4). The brain was removed and transferred to ice-cold paraformaldehyde (4% in PBS, pH 7.4) overnight before dehydration in sucrose (30% in PBS, pH 7.4), freezing in isopentane on dry ice and storage at −80°C until further processing.

Immunohistochemistry

Coronal sections of 40 μm thickness were cut through the motor cortex on a cryostat (Leica) and stored in antifreeze solution at −20°C until further processing. Sections were washed in PBS (pH 7.4) 3 × 10 min before blocking for 30 min in 0.1% Tween20 (Sigma) solution with 3% normal goat serum (Gibco). Incubation for 24 h at 4°C with primary antibodies (anti-PV 1:250, abcam ab11427; anti-SST 1:300, BMA T-4103) in blocking solution containing additional 5% bovine serum albumin (Sigma) followed. After another washing step (3 × 10 min), sections were incubated with a corresponding secondary antibody (Alexa Fluor® 568, Invitrogen A-11011) at 1:500 in 0.5% Tween20 solution for 1 h at room temperature. Specificity of both primary antibodies for their targets had already been determined elsewhere (22). As a negative secondary antibody control, randomly selected sections from different mice of the cohort were stained simultaneously using the same protocol except for the primary antibody. After washing for 3 × 20 min in PBS pH 7.4 including a nuclear counterstaining with DAPI (4′,6-diamidino-2-phenylindole 1:500, abcam) sections were mounted on slides and protected by Fluoro-Gel mounting medium (EMS).

Image acquisition

Sections containing the primary motor cortex at Bregma AP 1.7 to 0.7 mm according to Franklin and Paxinos (23) were imaged with a fluorescence microscope (BZ-X800, Keyence) equipped with a 10× objective, a DAPI and Texas Red filter cube for the DAPI and Alexa Fluor® 568 signal, respectively. Using the BZ-X800 Viewer software package, images through the entire section were acquired as stitched z-stacks with a step size of 1 µm at a xy-resolution of 1.5 µm/px. Acquisition settings were kept constant for all samples within each staining. Images were saved at the best focus plane as determined by the BZ-X800 Viewer software package.

Cell quantification, size, and intensity measurements

For all image processing and analysis, Fiji (24) was used. The area of the primary motor cortex (M1) was manually outlined according to Paxinos and Franklin (23). The layers of M1 were delimited with the aid of the Scalable Brain Atlas (25) in the DAPI channel. Images were individually thresholded based on their background in the red channel (containing the interneuronal staining) and the watershed algorithm applied to separate potential overlapping cells. Subsequently, cells located within M1 and its layers were counted using the Particle Analyzer plugin. A minimum particle size of 40 μm^2 was established and set to avoid the counting of artifacts. Size and integrated density [representing the cumulatively available PV or SST content in the cells; expressed in arbitrary units (A.U.)] were measured for each counted particle. We corrected density measurements for background fluorescence for all particles in each section individually (integrated density–background × particle area).

Statistical analysis

All behavioral tests, motor learning, microscopy, and image analysis were conducted by experimenters blinded for the treatment. The target number of mice used for the experiment was determined based on numbers in previously published studies and our experience with the model. Statistical analyses were performed in Graphpad Prism Version 8.0.1. The statistical test and group sizes are indicated in the results text. Data are presented as mean ± SEM in **Figures 1**, **2**, as median, 25th and 75th percentiles, and minimum/maximum in **Figure 3**. Validity of the statistical approach was ensured by testing all data distributions for normality (D'Agostini-Pearson test). Depending on the outcome parametric or non-parametric tests were used for group comparisons. For repeated measures ANOVA, Greenhouse-Geisser correction was applied. Significance was assumed at alpha = 0.05, with two-sided testing. Tukey's or Dunn's *post-hoc* tests were applied in case of multiple comparisons after ANOVA or Kruskal-Wallis test, respectively.

Results

Chronic social defeat stress changes affective and motor learning behavior

All mice were subjected to 10 days of CSDS, or control handling and stress-induced behavior was assessed within 2 days post stress (experimental timeline in **Figure 1A**). The average stress score based on this behavioral assessment [sucrose preference test (SPT), nestlet shredding test (NST), social avoidance test (SAT), **Supplementary Figure 1**] showed a significant increase of stressed behavior in the group of mice exposed to CSDS (t_{21} = 2.501, P = 0.021, Student's t-test, Ctrl n = 10, CSDS = 13 mice; **Figure 1B**). Each animal was classified as susceptible or resilient based on its deviation of the score from the control group. There was no difference in attack quantity and severity encountered by the resilient and susceptible subgroup during CSDS (**Supplementary Figure 2**). Cumulative CORT levels in the feces from the 24 h period after the last stress session corroborated the behavioral classification and revealed a significant increase of CORT release in resilient mice compared to controls while susceptible mice did not show this elevation post stress [$F_{(2,18)}$ = 4.309, P = 0.030, one-way ANOVA with Tukey's *post-hoc* test, Ctrl n = 8, Res n = 6, Sus n = 7 mice; **Figure 1C**]. The two stress phenotypes had markedly different weight developments throughout the first 5 days of CSDS: resilient mice gained weight compared to control and susceptible mice [time $F_{(4,80)}$ = 4.713, P = 0.002; stress $F_{(2,20)}$ = 3.896, P = 0.037; interaction $F_{(8,80)}$ = 2.404, P = 0.022, RM ANOVA with Tukey's *post-hoc* test, Ctrl n = 10, Res n = 6, Sus n = 7 mice; **Figure 1D**]. Persistence of the stress-induced phenotypes was confirmed at day 28 by a significantly reduced nest building score in susceptible mice vs. control and resilient mice (H_2 = 11.29, P = 0.004, Kruskal-Wallis test with Dunn's *post-hoc* test, Ctrl n = 10, Res n = 6, Sus n = 7 mice, **Figure 1E**) as already seen directly post CSDS (**Supplementary Figure 1**). For assessment of motor learning abilities, all mice were trained on the accelerating rotarod for 15 consecutive trials on day three post CSDS. While stress susceptible mice did not master to stay on the rod, resilient mice showed a similar learning curve as controls [maximum time: $F_{(2,20)}$ = 27.72, P < 0.0001, one-way ANOVA with Tukey's *post-hoc* test, Ctrl n = 10, Res n = 6, Sus n = 7 mice; **Figure 1F**]. This result confirmed a stress-induced change in motor skill learning in these mice, dependent on individual stress vulnerability.

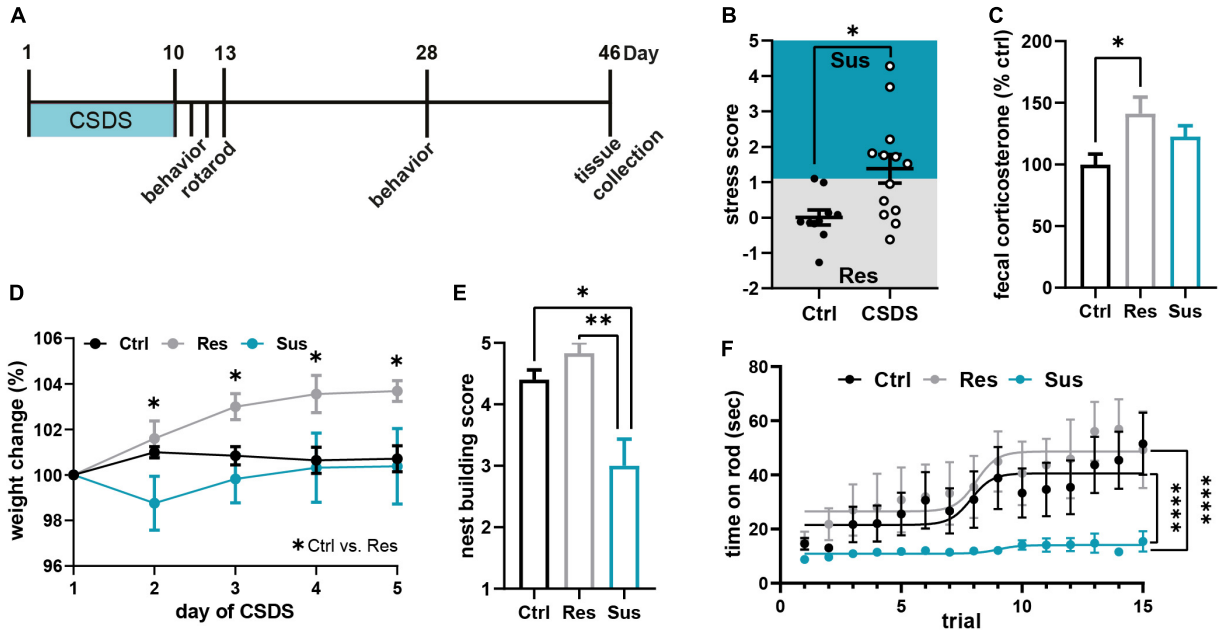

FIGURE 1
Chronic social defeat stress (CSDS) induces severe and lasting behavioral and physiological changes. **(A)** Experimental timeline. **(B)** Stress score derived from three behavioral tests [sucrose preference test (SPT), nestlet shredding test (NST), social avoidance test (SAT); **Supplementary Figure 1**] classified mice as stress susceptible or resilient. **(C)** Cumulative fecal corticosterone (CORT) levels from 24 h post CSDS normalized to the control group. **(D)** Weight development of the three behavioral groups during the first 5 days of CSDS. **(E)** Chronic stress-induced changes in the nest building test on day 28, 18 days post CSDS. **(F)** Motor learning assessed by the accelerating rotarod task 3 days post CSDS. $^{*}P < 0.05$, $^{**}P < 0.01$, $^{****}P < 0.0001$. Results are shown as mean ± SEM.

Chronic social defeat stress alters cell density in interneuronal networks in the primary motor cortex

Five weeks after CSDS, brains were collected for analysis of long-term interneuronal changes in the primary motor cortex. The density of PV positive (PV+) cells was reduced in the primary motor cortex in susceptible mice compared to controls [$F_{(2,20)} = 16.14$, $P < 0.0001$, one-way ANOVA with Tukey's *post-hoc* test, Ctrl $n = 10$, Res $n = 6$, Sus $n = 7$ mice], but not in resilient mice (**Figures 2A,D**). The stress score was not predictive of the PV+ cell density in the controls but predicted it in the CSDS group [Ctrl: $R^2 = 0.054$, $F_{(1,8)} = 0.458$, $P = 0.518$, CSDS: $R^2 = 0.416$, $F_{(1,11)} = 7.822$, $P = 0.017$, simple linear regression, **Figure 2B**]. Layer-wise analysis of the cortex revealed, that the group effect was driven by changes in PV+ cell density of layer V, which showed a significant difference between susceptible mice and both the control and resilient group [stress $F_{(2,80)} = 6.953$, $P = 0.002$, layer $F_{(3,80)} = 212.6$, $P < 0.0001$, interaction $F_{(6,80)} = 2.217$, $P = 0.05$, two-way ANOVA with Tukey's *post-hoc* test, Ctrl $n = 10$, Res $n = 6$, Sus $n = 7$ mice; **Figures 2C,D**].

The analysis of the SST positive (SST+) cells revealed a significantly reduced density in the primary motor cortex of susceptible mice compared to both control and resilient mice [$F_{(2,20)} = 6.664$, $P = 0.006$, one-way ANOVA with Tukey's *post-hoc* test, Ctrl $n = 10$, Res $n = 6$, Sus $n = 7$ mice; **Figures 2E,H**]. The individual stress score was able to predict the density of SST+ cells in stressed but not in control mice [Ctrl: $R^2 = 0.167$, $F_{(1,8)} = 1.608$, $P = 0.240$, CSDS: $R^2 = 0.417$, $F_{(1,11)} = 7.851$, $P = 0.017$, simple linear regression; **Figure 2F**]. Group differences were confirmed specifically for cortical layers II/III and V [stress $F_{(2,80)} = 14.60$, $P < 0.0001$, layer $F_{(3,80)} = 31.69$, $P < 0.0001$, interaction $F_{(6,80)} = 1.222$, $P = 0.304$, two-way ANOVA with Tukey's *post-hoc* test, Ctrl $n = 10$, Res $n = 6$, Sus $n = 7$ mice; **Figures 2G,H**].

Chronic social defeat stress alters morphological properties of motor cortical interneurons

We next sought to dissect qualitative changes in the networks of PV+ and SST+ cells of the primary motor cortex. PV+ cell size was reduced in susceptible mice compared to resilient individuals ($H_2 = 9.488$, $P = 0.009$, Kruskal-Wallis test with Dunn's *post-hoc* test, Ctrl $n = 1963$ cells/10 mice, Res $n = 1093$ cells/6 mice, Sus $n = 1109$ cells/7 mice; **Figure 3A**). This effect was driven by layers II/III and V (layer II/III $H_2 = 6.151$, $P = 0.046$, layer V $H_2 = 9.369$, $P = 0.009$, layer

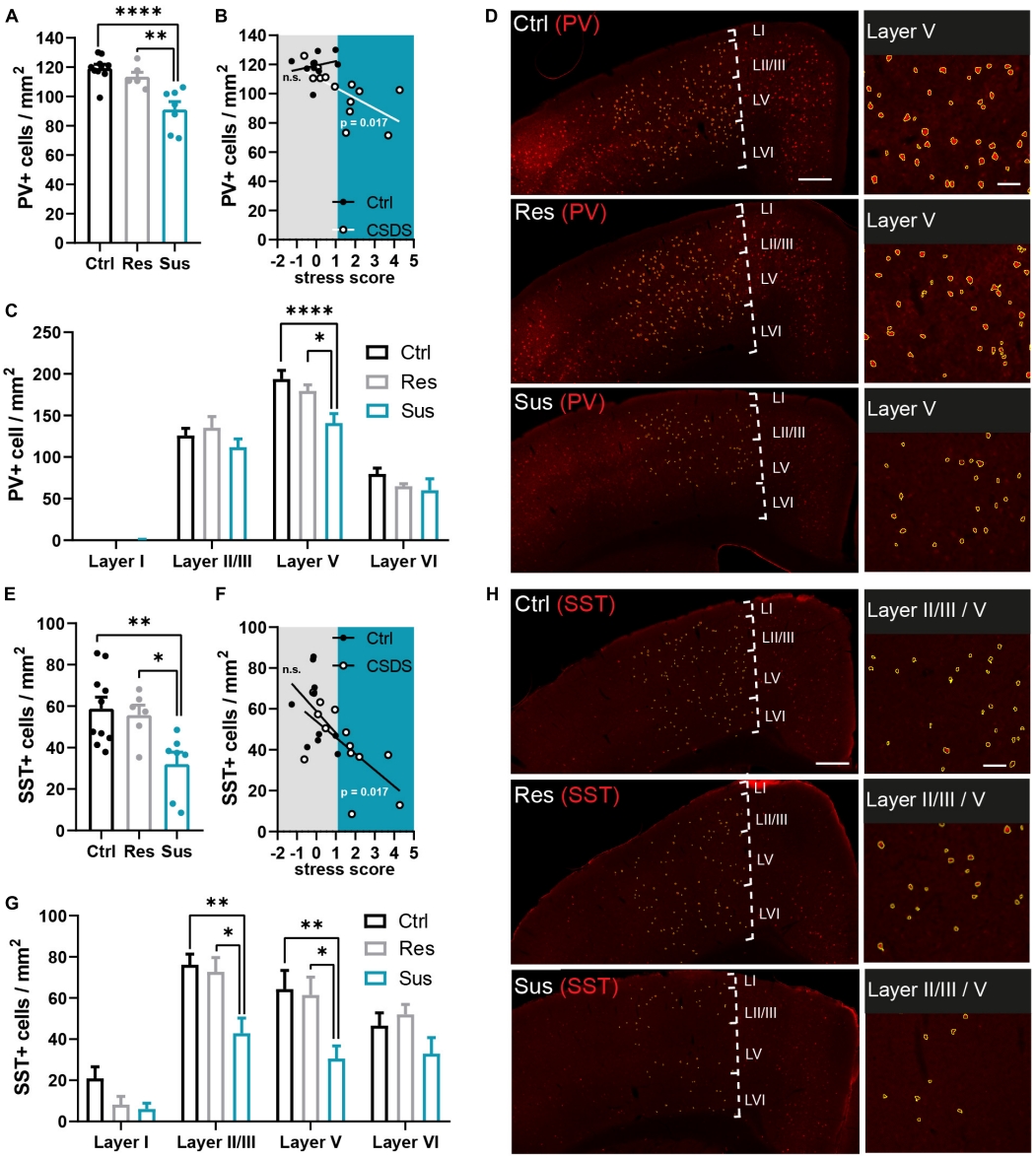

FIGURE 2
Interneuron populations are reduced in the primary motor cortex long-term after CSDS depending on stress vulnerability. **(A)** Parvalbumin (PV+) cell density in the analyzed M1 area compared between the behavioral groups. **(B)** Predictive relationship of the stress score and PV+ cell density in M1 analyzed for the stressed and unstressed group (gray area: stress score spectrum of controls and resilient mice, blue area: stress score spectrum of susceptible mice). **(C)** Layer-wise assessment of the stress effect on PV+ cell density in M1. **(D)** Examples of the PV+ cells (red = PV+ immunostaining, yellow = outlines of PV+ cells identified *via* semi-automated image analysis) in M1 and affected layers. **(E)** Somatostatin (SST+) cell density in the analyzed M1 area compared between the behavioral groups. **(F)** Predictive relationship of the stress score and SST+ cell density in M1 analyzed for the stressed and unstressed group (gray area: stress score spectrum of controls and resilient mice, blue area: stress score spectrum of susceptible mice). **(G)** Layer-wise assessment of the stress effect on SST+ cell density in M1. **(H)** Examples of the SST+ cells (red = SST+ immunostaining, yellow = outlines of SST+ cells identified *via* semi-automated image analysis yellow outlines) in M1 and affected layers. $^{*}P < 0.05$, $^{**}P < 0.01$, $^{****}P < 0.0001$. Results are shown as mean ± SEM. Left: scale bar = 500 μm, right: scale bar = 100 μm.

VI H_2 = 0.438, P = 0.804, Kruskal-Wallis tests with Dunn's *post-hoc* test, Figures 3B,C), while layer VI was not affected (Supplementary Figure 3A). For the SST+ cell population, no significant effect of CSDS in M1 overall (H_2 = 1.717, P = 0.424, Kruskal-Wallis test, Ctrl n = 877 cells/10 mice, Res n = 502 cells/6 mice, Sus n = 331 cells/7 mice; Figure 3D) or its layers (Supplementary Figures 3B–D) was detected.

The integrated density of PV+ cells was significantly altered in layers II/III and VI but not in layer V of M1: in layer II/III, the susceptible group had significantly lower values compared

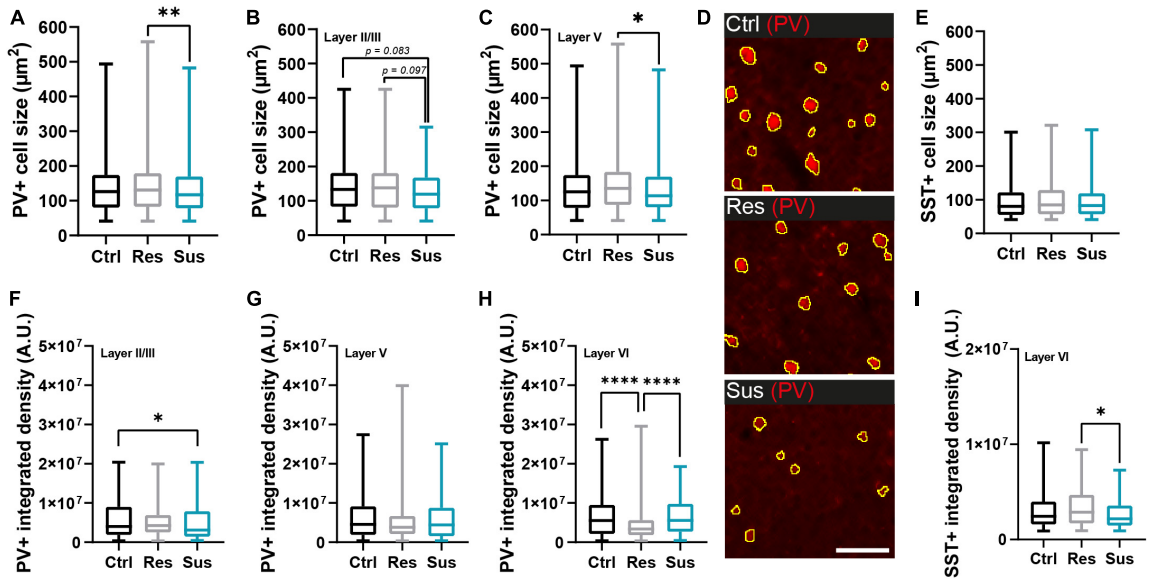

FIGURE 3
Interneuron populations are morphologically changed in the primary motor cortex (M1) long-term after CSDS depending on stress vulnerability. **(A)** Cell size changes of parvalbumin positive (PV+) cells in M1 and **(B,C)** its layers II/III and V (unchanged layer VI in **Supplementary Figure 3**). **(D)** Examples of PV+ cells from layer V in the different behavioral groups (scale bar = 100 µm). **(E)** Cell size of somatostatin positive (SST+) cells in M1. **(F–H)** Integrated density expressed as alterations of PV+ cells in the different M1 layers. **(I)** Intensity alterations of SST+ cells in layer VI (unchanged layers II/III and V in **Supplementary Figure 3**). $^{*}P < 0.05$, $^{**}P < 0.01$, $^{****}P < 0.0001$. Results are shown as median, 25th and 75th percentiles, and minimum/maximum.

to controls while in layer VI values in the resilient group were reduced compared to both controls and susceptible mice (layer II/III $H_2 = 7.844$, $P = 0.020$, layer V $H_2 = 4.904$, $P = 0.086$, layer VI $H_2 = 24.89$, $P < 0.0001$, Kruskal-Wallis tests with Dunn's *post-hoc* test when applicable **Figures 3F–H**). For SST+ cells, significant changes of integrated staining density were restricted to layer VI with a decrease in susceptible compared to resilient mice ($H_2 = 7.496$, $P = 0.024$, Kruskal-Wallis tests with Dunn's *post-hoc* test; **Figure 3I**), which exhibited a slight density increase. No significant alterations were detected in layers II/III and V (**Supplementary Figures 3E,F**).

Discussion

This study found evidence of long-term affection of the GABAergic interneural network of the primary motor cortex by CSDS, dependent on individual stress vulnerability.

Stress vulnerability determined by individual burden is linked to motor learning

We used three different behavioral tests as established previously (6) to determine individual stress burden and to classify stressed animals as susceptible or resilient. We successfully developed this approach further and transformed the outcomes into a stress score, which supports a more nuanced characterization of the animals even within stress phenotypes. As demonstrated previously, a lack of correlation between the different behavioral tests occurred (6, 26), which is an important aspect to consider since the majority of studies use the SAT as the main criterion to determine stress vulnerability (5, 27). Behavior can be influenced differently by chronic stress, leading to a heterogeneous range of responses, with variable strength and permanency (27–29). In our study, nest building behavior was found to be strongly altered by chronic stress still 2.5 weeks after CSDS, marking a persistence of stress induced symptoms in susceptible mice as demonstrated in our previous work (6). Our multimodal behavioral classification using the stress score was further validated by differences in weight development and diurnal CORT release between the two stress phenotypes. Previous studies state that a typical response to stress in rodents is decreased food intake, adiposity, and body weight, due to the appearance of anhedonic behaviors and loss of interest in palatable foods (30, 31). We did not find signs of anhedonia in the SPT, or significant weight loss in susceptible mice compared to controls. On the contrary, the resilient group exhibited a prompt increase of body weight, setting them apart from the susceptible mice. Studies using CSDS usually report weight loss in susceptible mice while resilient mice have been demonstrated to either lose or gain (26, 32). As a limitation, food intake was not measured during

A

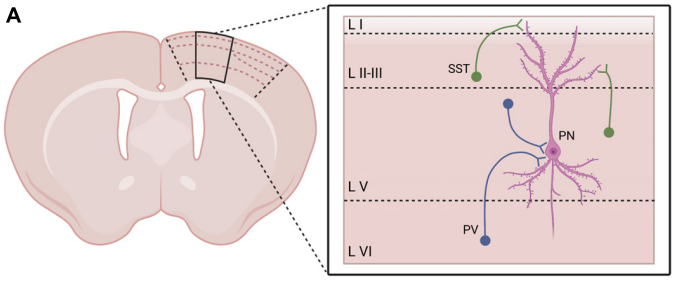

B

Parameter		Res vs. Ctrl	Sus vs. Ctrl	Sus vs. Res
Motor Learning		↔	↓	↓
PV	Cell density	↔	↓ (L V)	↓ (L V)
	Cell size	↔	↔	↓ (L II/III, V)
	Integrated density	↓ (L VI)	↓ (L II/III)	↑ (L VI)
SST	Cell density	↔	↓ (L II/III, V)	↓ (L II/III, V)
	Cell size	↔	↔	↔
	Integrated density	↔	↔	↓ (L VI)

FIGURE 4
Summary of the quantitative and qualitative changes in interneuronal networks of M1 and its layers dependent on individual stress vulnerability. **(A)** Schematic network of parvalbumin positive (PV+) and somatostatin positive (SST+) interneuron populations investigated in this study and the principal neurons (PN) of layer V of the primary motor cortex (black outline on coronal section) previously found to be affected by CSDS (6). **(B)** Comparisons between the stress phenotypes (Res, Sus) and controls (Ctrl), and between the stress phenotypes to dissect the implication of stress vulnerability for motor cortical interneurons also in relation to motor learning abilities on the rotarod.

our experiment. Glucocorticoids modulate feeding behavior but also liquid retention and can thereby promote weight gain (31, 33). Stress activates the HPA axis in order to secure homeostasis and adaptation both centrally and peripherally (5, 30, 34, 35). In our study, elevation of CORT levels was also observed solely in stress-resilient mice, which is in line with our previous data (6). Together, stress-induced HPA axis activation in resilient mice likely promotes better adaptation to chronic stress (5, 6, 30, 34). Again, we could demonstrate that motor learning on the rotarod remained intact in the resilient group whereas susceptible mice failed as shown before (6). This confirmation of the vulnerability-dependent motor learning pattern is important as the resilient phenotype was previously also accompanied by faster recovery of stress-induced spine loss of principal neurons, stability of learning-induced spine formation, and lacked the microglial and astrocytic activation in the motor cortex of susceptible mice 5 weeks post-stress (6). Although no study including ours investigated gross motor learning in such a late post-stress phase, Mizoguchi and colleagues found impaired learning on the rotarod in rats 10 days after chronic stress (36).

Interneuronal networks in M1 respond chronically to stress depending on individual vulnerability

GABAergic interneurons control (dys) regulated excitatory output and spine density of principal neurons, which in turn can influence glial activation (11). Thus, after confirmation of the behavioral and motor functional phenotypes we proceeded to analyze the two dominant populations of GABAergic interneurons, PV+ and SST+ cells, 5 weeks post-stress. We observed an overall quantitative reduction of PV+ and SST+ interneuronal networks, which was limited to stress-susceptible individuals. Several studies have investigated the effects of chronic stressors in limbic or prefrontal cortical areas of the brain, showing a decrease of GABAergic interneurons in stress-susceptible mice, especially for PV+ and SST+ interneurons (14, 15). As mentioned, the motor cortex has rarely been investigated for such stress-induced effects before. One study in rats used M1 as a control region and did not find a change in the density of GABAergic interneurons when analyzing the entire cortex area (15). These results, contradictory to ours, could be explained by several factors, limiting comparability: use of a different (non-social) stress model, different classification of stress vulnerability, and use of a different animal species according to other studies (37, 38). Moreover, we show in our data that subtle changes in interneuronal networks could potentially be revealed best by layer-wise analysis. This also takes into consideration the layer-dependent distribution and function of GABAergic interneurons. In our previous work, astrogliosis was restricted to layer I and II/III and not found in layer V of M1 of susceptible mice (6). This is in line with the now reported reduction of PV+ cells in layer V, which in turn could lead to disinhibition and glutamatergic excess in superficial layers which can lead to astrogliosis and neuronal damage (39). Consistently, we had previously found upregulation of glutamatergic proteins in the proteome analysis of the cerebrospinal fluid in the same chronic phase 5 weeks post-stress (6).

SST + interneurons can control excitatory output and spine density of pyramidal cells by reaching out into the upper layers of the cortex and playing a pivotal role in the formation and stabilization of dendritic spines upon motor learning (20, 40). The long-term marked alteration of layer V and II/III SST+ cell density we report now fits well to the protracted recovery of spine density in susceptible mice and the impaired spine dynamics we also saw recently (6). Conclusively, another study reported a reversal of drug-induced motor cortical spine loss and impaired motor learning by activation of SST+ interneurons (41). Generally, lack of SST+ signaling

underlies a depressed and anxious phenotype in mice and humans (12, 42). Although these affective behaviors are not directly linked to the motor cortex, stress burden early after CSDS was predictive of later SST+ and PV+ cell density in M1 in our study, adding new insights from an underestimated brain region regarding the stress/behavior relationship.

Changes in cell function but also decreased detectability of interneurons might be linked to alterations in morphology. Hence, we investigated soma size and staining intensity of the PV and SST markers, which can correlate with protein expression (43). PV+ cell size was altered between resilient and susceptible mice through slight up- and downregulation, respectively. Although the size reduction was not significant compared to controls, it cannot be completely ruled out that part of the decrease in cell density in susceptible mice is caused by a reduced detectability of cells slightly smaller than our determined threshold. Since the lower size threshold was carefully established using spatial correlation with nuclear DAPI staining we do not consider this as a relevant confounder. Reduced soma size could be linked to a shift in certain PV+ subpopulations (19) caused by a selective loss in susceptible mice. This could be assessed in future studies by application of co-staining techniques, high-resolution imaging of cell morphology, and electrophysiological characterization, as over 20 different subtypes of GABAergic interneurons in the cortex have been distinguished to date, which differ on the markers they express but also on firing patterns, morphology, and regional distribution (18, 19, 44).

Quantity of the PV and SST staining expressed in the integrated density was differentially altered depending on stress phenotype, cortical layer, and the marker itself. These effects were dissociated from changes in cell density or size and point to a chronic qualitative change of interneurons predominantly in layer VI. Of note, this was detected specifically in layer VI from resilient animals, a layer which had not been affected by changes in density or cell size and highlights subtle network changes induced by stress in presumably "healthy" subjects with unchanged cell numbers. Although the layer-wise connections between principal and interneuronal networks (exemplary depiction in **Figure 4A**) are still not completely understood (11, 40), layer VI exerts excitatory output into layer V (40) and thus its disinhibition can facilitate stress-induced hyperexcitability in the superficial layers of M1 in susceptible mice. Viewing quantitative and qualitative changes together (**Figure 4B**) a dissociation between reduced cell density and integrated density is notable. Hence, the reduction of detected PV+ and SST+ cells in layers II/III and V is unlikely to be caused by a general downshift of immunoreactivity. Furthermore, this is the only technique allowing for high spatial resolution and thus layer-wise analysis, which would be masked by methods using whole tissue samples.

Together with our previous data of synaptic loss, glial activation, and CSF alterations (6), the disturbance of the GABAergic interneuron network reflects another indicator of stress-induced hyperexcitability in the motor cortex, which could underly impaired motor learning. Glutamatergic excess, as mentioned above, generally promotes neurotoxicity which could be underlying cell loss and degeneration in the interneuronal networks of M1. Reduction of PV and SST has been linked to proinflammatory and neurodegenerative states (43, 45). We previously found signs of both states in M1 and the cerebrospinal fluid of mice more than 5 weeks post CSDS (6). This indicates persistent stress-induced negative effects on neuronal and non-neuronal cell populations of M1 that are likely propelling each other. Our study further highlights the importance of understanding long-term neurobiological outcomes of chronically stressed individuals considering the chronic timecourse of stress related neuropsychiatric disorders.

Data availability statement

The datasets generated during and/or analyzed during the current study are available from the corresponding author on reasonable request.

Ethics statement

The animal study was reviewed and approved by the Local Committee for Animal Health, LANUV NRW.

Author contributions

AKG: conceptualization and funding acquisition. MS and AKG: methodology and investigation and writing—original draft. MS, VS, and AKG: writing—review and editing. VS and AKG: resources and supervision. All authors contributed to the final version of the manuscript.

Funding

AKG and this study were supported by a BONFOR Funding Program grant (2019-2-07).

Acknowledgments

We thank I. Blameuser for technical support and scoring of the CSDS videos. Scientific illustrations were created using BioRender (www.biorender.com).

Conflict of interest

The authors declare that the research was conducted in the absence of any commercial or financial relationships that could be construed as a potential conflict of interest.

Publisher's note

All claims expressed in this article are solely those of the authors and do not necessarily represent those of their affiliated organizations, or those of the publisher, the editors and the reviewers. Any product that may be evaluated in this article, or claim that may be made by its manufacturer, is not guaranteed or endorsed by the publisher.

Supplementary material

The Supplementary Material for this article can be found online at: https://www.frontiersin.org/articles/10.3389/fpsyt.2022.946719/full#supplementary-material

References

1. Kirschbaum C, Wolf O, May M, Wippich W, Hellhammer D. Stress- and treatment-induced elevations of cortisol levels associated with impaired declarative memory in healthy adults. *Life Sci.* (1996) 58:1475–83. doi: 10.1016/0024-3205(96)00118-x

2. Dotson VM, Resnick SM, Zonderman AB. Differential association of concurrent, baseline, and average depressive symptoms with cognitive decline in older adults. *Am J Geriatr Psychiatry.* (2008) 16:318–30.

3. Post RM. Transduction of psychosocial stress into the neurobiology of recurrent affective disorder. *Am J Psychiatry.* (1992) 149:999–1010.

4. Golden SA, Covington HE, Berton O, Russo SJ. A standardized protocol for repeated social defeat stress in mice. *Nat Protoc.* (2011) 6:1183–91.

5. Russo SJ, Murrough JW, Han M-H, Charney DS, Nestler EJ. Neurobiology of resilience. *Nat Neurosci.* (2012) 15:1475–84.

6. Gellner A-K, Sitter A, Rackiewicz M, Sylvester M, Philipsen A, Zimmer A, et al. Stress vulnerability shapes disruption of motor cortical neuroplasticity. *Transl Psychiatry.* (2022) 12:91.

7. Kaas JH, Stepniewska I. Motor cortex. In: Ramachandran VS editor. *Encyclopedia of the Human Brain*. Amsteram: Elsevier (2002). p. 159–69.

8. Zilles K. Architecture of the human cerebral cortex. In: Paxinos G editor. *The Human Nervous System*. Amsterdam: Elsevier (2004). p. 997–1055.

9. Hallett M. The role of the motor cortex in motor learning. In: Latash ML, Lestienne F editors. *Motor Control and Learning*. Boston, MA: Kluwer Academic Publishers (2006). p. 89–95.

10. Tjia M, Yu X, Jammu LS, Lu J, Zuo Y. Pyramidal neurons in different cortical layers exhibit distinct dynamics and plasticity of apical dendritic spines. *Front Neural Circuits.* (2017) 11:43. doi: 10.3389/fncir.2017.00043

11. Papale AE, Hooks BM. Circuit changes in motor cortex during motor skill learning. *Neuroscience.* (2018) 368:283–97.

12. Gilabert-Juan J, Castillo-Gomez E, Guirado R, Moltó MD, Nacher J. Chronic stress alters inhibitory networks in the medial prefrontal cortex of adult mice. *Brain Struct Funct.* (2013) 218:1591–605. doi: 10.1007/s00429-012-0479-1

13. Czéh B, Vardya I, Varga Z, Febbraro F, Csabai D, Martis L-S, et al. Long-term stress disrupts the structural and functional integrity of GABAergic neuronal networks in the medial prefrontal cortex of rats. *Front Cell Neurosci.* (2018) 12:148. doi: 10.3389/fncel.2018.00148

14. Czéh B, Varga ZKK, Henningsen K, Kovács GL, Miseta A, Wiborg O. Chronic stress reduces the number of GABAergic interneurons in the adult rat hippocampus, dorsal-ventral and region-specific differences. *Hippocampus.* (2015) 25:393–405. doi: 10.1002/hipo.22382

15. Varga Z, Csabai D, Miseta A, Wiborg O, Czéh B. Chronic stress affects the number of GABAergic neurons in the orbitofrontal cortex of rats. *Behav Brain Res.* (2017) 316:104–14. doi: 10.1016/j.bbr.2016.08.030

16. Fogaça MV, Duman RS. Cortical GABAergic dysfunction in stress and depression: new insights for therapeutic interventions. *Front Cell Neurosci.* (2019) 13:87. doi: 10.3389/fncel.2019.00087/full

17. McKlveen JM, Moloney RD, Scheimann JR, Myers B, Herman JP. "Braking" the prefrontal cortex: the role of glucocorticoids and interneurons in stress adaptation and pathology. *Biol Psychiatry.* (2019) 86:669–81. doi: 10.1016/j.biopsych.2019.04.032

18. Kelsom C, Lu W. Development and specification of GABAergic cortical interneurons. *Cell Biosci.* (2013) 3:19.

19. Rudy B, Fishell G, Lee S, Hjerling-Leffler J. Three groups of interneurons account for nearly 100% of neocortical GABAergic neurons. *Dev Neurobiol.* (2011) 71:45–61. doi: 10.1002/dneu.20853

20. Chen SX, Kim AN, Peters AJ, Komiyama T. Subtype-specific plasticity of inhibitory circuits in motor cortex during motor learning. *Nat Neurosci.* (2015) 18:1109–15.

21. Deacon RM. Assessing nest building in mice. *Nat Protoc.* (2006) 1:1117–9.

22. Guo J, Ran M, Gao Z, Zhang X, Wang D, Li H, et al. Cell-type-specific imaging of neurotransmission reveals a disrupted excitatory-inhibitory cortical network in isoflurane anaesthesia. *EBioMedicine.* (2021) 65:103272. doi: 10.1016/j.ebiom.2021.103272

23. Franklin KBJ, Paxinos G. *Paxinos and Franklin's the Mouse Brain in Stereotaxic Coordinates*. 4th ed. Cambridge, MA: Academic Press (2012).

24. Schindelin J, Arganda-Carreras I, Frise E, Kaynig V, Longair M, Pietzsch T, et al. Fiji: an open-source platform for biological-image analysis. *Nat Methods.* (2012) 9:676–82. doi: 10.1038/nmeth.2019

25. Bakker R, Tiesinga P, Kötter R. The scalable brain atlas: instant web-based access to public brain atlases and related content. *Neuroinformatics.* (2015) 13:353–66. doi: 10.1007/s12021-014-9258-x

26. Alves-dos-Santos L, de Resende LS, Chiavegatto S. Susceptibility and resilience to chronic social defeat stress in adolescent male mice: no correlation between social avoidance and sucrose preference. *Neurobiol Stress.* (2020) 12:100221. doi: 10.1016/j.ynstr.2020.100221

27. Krishnan V, Han M-H, Graham DL, Berton O, Renthal W, Russo SJ, et al. Molecular adaptations underlying susceptibility and resistance to social defeat in brain reward regions. *Cell.* (2007) 131:391–404. doi: 10.1016/j.cell.2007.09.018

28. Toth I, Neumann ID. Animal models of social avoidance and social fear. *Cell Tissue Res.* (2013) 354:107–18.

29. Chaudhury D, Walsh JJ, Friedman AK, Juarez B, Ku SM, Koo JW, et al. Rapid regulation of depression-related behaviours by control of midbrain dopamine neurons. *Nature.* (2013) 493:532–6. doi: 10.1038/nature11713

30. Maniam J, Morris MJ. The link between stress and feeding behaviour. *Neuropharmacology.* (2012) 63:97–110.

31. Foster MT, Solomon MB, Huhman KL, Bartness TJ. Social defeat increases food intake, body mass, and adiposity in Syrian hamsters. *Am J Physiol Integr Comp Physiol.* (2006) 290:R1284–93.

32. Murra D, Hilde KL, Fitzpatrick A, Maras PM, Watson SJ, Akil H. Characterizing the behavioral and neuroendocrine features of susceptibility and resilience to social stress. *Neurobiol Stress.* (2022) 17:100437. doi: 10.1016/j.ynstr.2022.100437

33. Bartolomucci A, Pederzani T, Sacerdote P, Panerai AE, Parmigiani S, Palanza P. Behavioral and physiological characterization of male mice under chronic psychosocial stress. *Psychoneuroendocrinology.* (2004) 29:899–910. doi: 10.1016/j.psyneuen.2003.08.003

34. Liston C, Gan W-B. Glucocorticoids are critical regulators of dendritic spine development and plasticity *in vivo*. *Proc Natl Acad Sci.* (2011) 108:16074–9. doi: 10.1073/pnas.1110444108

35. Liston C, Cichon JM, Jeanneteau F, Jia Z, Chao MV, Gan W-B. Circadian glucocorticoid oscillations promote learning-dependent synapse formation and maintenance. *Nat Neurosci.* (2013) 16:698–705. doi: 10.1038/nn.3387

36. Mizoguchi K, Yuzurihara M, Ishige A, Sasaki H, Tabira T. Chronic stress impairs rotarod performance in rats: implications for depressive state. *Pharmacol Biochem Behav.* (2002) 71:79–84. doi: 10.1016/s0091-3057(01)00636-0

37. Zaletel I, Filipović D, Puškaš N. Chronic stress, hippocampus and parvalbumin-positive interneurons: what do we know so far? *Rev Neurosci.* (2016) 27:397–409. doi: 10.1515/revneuro-2015-0042

38. Rajkowska G, O'Dwyer G, Teleki Z, Stockmeier CA, Miguel-Hidalgo JJ. GABAergic neurons immunoreactive for calcium binding proteins are reduced in the prefrontal cortex in major depression. *Neuropsychopharmacology.* (2007) 32:471–82.

39. Had-Aissouni L, Ré D-B, Nieoullon A, Kerkerian-Le Goff L. Importance of astrocytic inactivation of synaptically released glutamate for cell survival in the central nervous system—are astrocytes vulnerable to low intracellular glutamate concentrations? *J Physiol.* (2002) 96:317–22. doi: 10.1016/s0928-4257(02)00022-0

40. Thomson AM. Neocortical layer 6, a review. *Front Neuroanat.* (2010) 4:13. doi: 10.3389/fnana.2010.00013/abstract

41. Chen K, Yang G, So K-F, Zhang L. Activation of cortical somatostatin interneurons rescues synapse loss and motor deficits after acute MPTP Infusion. *iScience.* (2019) 17:230–41.

42. Lin LC, Sibille E. Somatostatin, neuronal vulnerability and behavioral emotionality. *Mol Psychiatry.* (2015) 20:377–87.

43. Zachařová G, Sojka D, Paleček J. Changes of parvalbumin expression in the spinal cord after peripheral inflammation. *Physiol Res.* (2009) 58:435–42.

44. DeFelipe J, López-Cruz PL, Benavides-Piccione R, Bielza C, Larrañaga P, Anderson S, et al. New insights into the classification and nomenclature of cortical GABAergic interneurons. *Nat Rev Neurosci.* (2013) 14:202–16. doi: 10.1038/nrn3444

45. Saiz-Sanchez D, Ubeda-Bañon I, De la Rosa-Prieto C, Martinez-Marcos A. Differential expression of interneuron populations and correlation with amyloid-β deposition in the olfactory cortex of an AβPP/PS1 transgenic mouse model of Alzheimer's Disease. *J Alzheimers Dis.* (2012) 31:113–29. doi: 10.3233/JAD-2012-111889

frontiers | Frontiers in Cellular Neuroscience

TYPE Systematic Review
PUBLISHED 10 October 2022
DOI 10.3389/fncel.2022.992409

OPEN ACCESS

EDITED BY
Frederic Lanore,
UMR5297 Institut Interdisciplinaire de Neurosciences (IINS), France

REVIEWED BY
Barna Dudok,
Stanford University, United States
Ruilong Hu,
BioMarin, United States
Norbert Hajos,
Institute of Experimental Medicine (MTA), Hungary

*CORRESPONDENCE
Hyung-Bae Kwon
hkwon29@jhmi.edu

†These authors have contributed equally to this work and share first authorship

SPECIALTY SECTION
This article was submitted to Cellular Neurophysiology, a section of the journal Frontiers in Cellular Neuroscience

RECEIVED 12 July 2022
ACCEPTED 05 September 2022
PUBLISHED 10 October 2022

CITATION
Jung K, Choi Y and Kwon H-B (2022) Cortical control of chandelier cells in neural codes.
Front. Cell. Neurosci. 16:992409.
doi: 10.3389/fncel.2022.992409

Cortical control of chandelier cells in neural codes

Kanghoon Jung†, Youngjin Choi† and Hyung-Bae Kwon*

Department of Neuroscience, Johns Hopkins University School of Medicine, Baltimore, MD, United States

Various cortical functions arise from the dynamic interplay of excitation and inhibition. GABAergic interneurons that mediate synaptic inhibition display significant diversity in cell morphology, electrophysiology, plasticity rule, and connectivity. These heterogeneous features are thought to underlie their functional diversity. Emerging attention on specific properties of the various interneuron types has emphasized the crucial role of cell-type specific inhibition in cortical neural processing. However, knowledge is still limited on how each interneuron type forms distinct neural circuits and regulates network activity in health and disease. To dissect interneuron heterogeneity at single cell-type precision, we focus on the chandelier cell (ChC), one of the most distinctive GABAergic interneuron types that exclusively innervate the axon initial segments (AIS) of excitatory pyramidal neurons. Here we review the current understanding of the structural and functional properties of ChCs and their implications in behavioral functions, network activity, and psychiatric disorders. These findings provide insights into the distinctive roles of various single-type interneurons in cortical neural coding and the pathophysiology of cortical dysfunction.

KEYWORDS

chandelier cells, axo-axonic cell, interneurons, cortical network, axon initial segment (AIS) inhibitory synapse, excitatory inhibitory balance, synaptic plasticity, schizophrenia

Introduction

Various cortical processes depend on the dynamic interactions between excitation provided by glutamatergic pyramidal neurons (PyNs) and inhibition provided by interneurons (Hensch and Fagiolini, 2005). Interneurons releasing γ-aminobutyric acid (GABA) represent 10–20% of all cortical neurons in the brain (Rudy et al., 2011) and act as inhibitory nodes of neural circuits. The vast molecular diversity that exists among interneurons (Taniguchi, 2014) accounts for the variety of distinct cortical functions in the brain that collectively give rise to perception, cognition, and behavior. The chandelier cell (ChC) is a GABAergic interneuron cell type that has captured the interest of neuroscientists since its first discovery in the 1970s (Szentágothai and Arbib, 1974; Jones, 1975). The ChCs are also known as axo-axonic cells (Somogyi, 1977) due to their exclusive innervation of the axon initial segments of PyNs, a region for action potential generation.

Many discoveries have been made about the ChC's properties, functions, and implications in dysfunctional neural states, which indicate its vital role in proper cortical functioning. Distinct pathological states of ChCs are associated with neuropsychiatric disorders, such as schizophrenia (Rocco et al., 2017), epilepsy (DeFelipe, 1999), and autism spectrum disorder (Lunden et al., 2019). Although previous studies reported some controversies, such as whether the GABAergic neurotransmission of ChCs is inhibitory or excitatory (Szabadics et al., 2006; Woodruff et al., 2011) and whether its pathology in schizophrenia is contributory or compensatory (Rocco et al., 2017), recent advancements in genetic, optogenetic, and recording techniques have been applied to clarify these issues, illuminating the *in vivo* functions of ChCs in behaving animals and setting the stage for understanding its role in complex cognition.

The ChC is well-situated to mediate the balance between excitation and inhibition, given its innervation of the AIS that grants it effective, strategic inhibitory control over the excitatory activity of PyNs (Veres et al., 2014). The regulation of excitatory/inhibitory (E/I) balance by ChCs may have essential functions of preventing neuronal hyperexcitability and instantiating executive cognitive functions, as highlighted by respective pathophysiological states observed in epilepsy and schizophrenia. On one hand, dysfunctional ChCs are found in epileptic visual areas (Ribak, 1985), where seizures are generated due to unchecked propagation of excitatory activity. On the other hand, dysfunctional ChCs are found in the schizophrenic prefrontal cortex (Rocco et al., 2017), which is often associated with positive cognitive symptoms. Theoretical modeling has shown that the precise balance between inhibition and excitation in a neural network facilitates greater precision and efficiency in neural coding (Zhou and Yu, 2018). The failure of ChCs to mediate this function may underlie the disorganization of thought seen in schizophrenia.

In this review, we summarize the structural features of ChC morphology and connectivity, and neuroplasticity of axo-axonic synapses. We discuss functional features of ChC such as electrophysiological properties, synaptic effects, and neuromodulation of ChCs. We present recent discoveries about the ChC's *in vivo* functions in brain rhythms, behavioral states, and neural coding. Finally, we outline the potential pathophysiological mechanisms of ChCs in disrupted E/I balance and the corresponding implications in schizophrenia.

Diversity of GABAergic interneuron types

GABAergic interneurons comprise 10–20% of all cortical neurons in the brain (Rudy et al., 2011) and have a fundamental role in operating neural circuitry by maintaining proper levels of excitability, synchronizing the firing of neuronal ensembles, controlling precise spike timing, and integrating synaptic inputs (Isaacson and Scanziani, 2011). These multifaceted functions can originate from interneuron heterogeneity in their morphology, connectivity, electrophysiology, and chemistry. We will review three major groups of GABAergic interneurons and the heterogeneity existing within each group, which spotlights ChCs as a single cell type within the taxonomy.

First, parvalbumin-expressing interneurons (PV-INs) account for ∼40% of GABAergic interneurons (Tamamaki et al., 2003; Fogarty et al., 2007; Figure 1A). PV-INs consist mostly of basket cells (PV-BCs) that exert perisomatic inhibition targeting the soma and proximal dendrites of PyNs (Martin et al., 1983; Kawaguchi and Kubota, 1997; Figure 1B). PV-BCs share common excitatory inputs with their target PyNs that they innervate, demonstrating feedforward inhibition (Willems et al., 2018; Figure 1C; top). In addition, PV-INs neurons can be reciprocally connected with PyNs to provide feedback inhibition (Grosser et al., 2021; Figure 1C; middle). In addition to PV-BCs, cholecystokinin-expressing BCs (CCK-BCs) constitute a smaller proportion of GABAergic interneurons. Both types of BCs innervate perisomatic domains with similar GABA-A receptor subunit composition contents (Kerti-Szigeti and Nusser, 2016) and mediate similar potencies of perisomatic inhibition to control PyN firing (Andrási et al., 2017). However, these two BC cell types receive excitatory inputs from PyNs with distinct properties (Andrási et al., 2017), and CCK-BCs display slower firing rates (∼30 Hz) than PV-BCs (∼110 Hz) (Szabó et al., 2010; Barsy et al., 2017). ChCs have been traditionally considered to be PV-INs, despite evidence of little to no expression of PV (Taniguchi et al., 2013). ChCs are distinct from BCs in their exclusive connectivity to the axon initial segment (AIS) of PyNs (Somogyi, 1977; DeFelipe et al., 1985; Figure 1B). Electrophysiologically, PV-INs are fast-spiking, exhibiting high-frequency action potentials and little adaptation (Xu and Callaway, 2009). Yet, multipolar bursting (MPB) neurons, PV-INs found in the upper L2, do not display the characteristic fast-spiking firing pattern of other PV-INs (Blatow et al., 2003).

Second, somatostatin-expressing INs (SST-INs) comprise ∼30% of GABAergic interneurons (Lee et al., 2010; Figure 1A). SST-INs consist mostly of Martinotti cells (MCs) that exert dendritic inhibition targeting the distal apical dendrites of post-synaptic neurons (Karube et al., 2004; Figure 1B). Neocortical MCs project axons that horizontally bifurcate in L1 (Wang et al., 2004). MCs can be subdivided into two types, based on their expression of the calcium-binding protein calretinin (CR). CR+ and CR- MCs have been shown to exhibit differences in their dendritic morphology as well as input connectivity (Xu et al., 2006; Kapfer et al., 2007). The electrophysiology of these neurons is characterized as regular-spiking with adaptation or burst-spiking (Kawaguchi and Kubota, 1997). X94 cells are another type of SST-INs, distinct from MCs in their anatomy and electrophysiology. They are found in L4,5 and innervate

10.3389/fncel.2022.992409

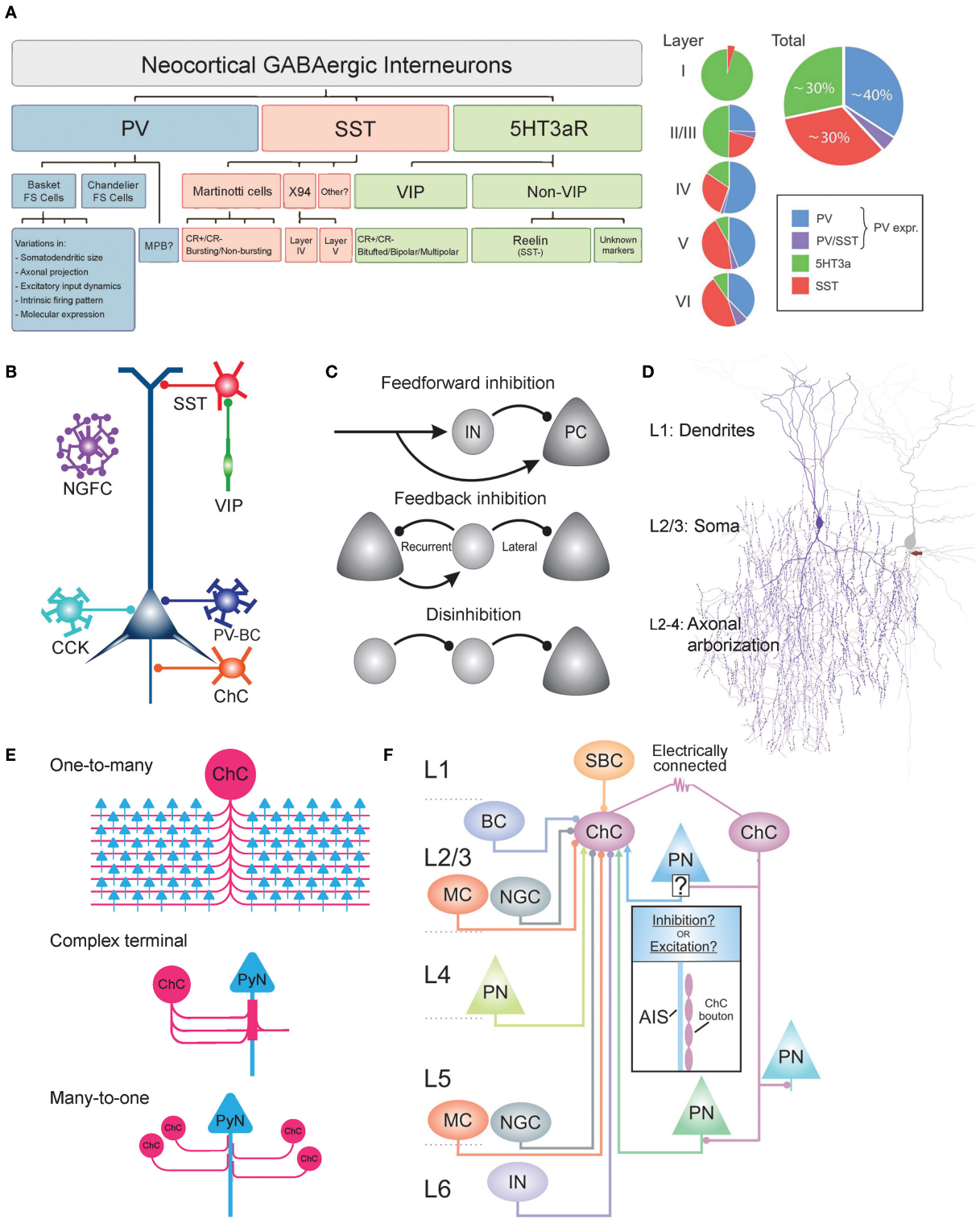

FIGURE 1
Heterogeneity of GABAergic interneurons and connectivity of ChCs. **(A)** Dendrogram and Venn diagram of neocortical GABAergic interneurons. Parvalbumin-expressing interneurons (PV-INs) account for ~40% of all GABAergic interneurons. PV-INs further divide into basket cells, chandelier cells, and multipolar bursting cells (MPBs). Somatostatin-expressing interneurons (SST-INs) account for ~30% of all GABAergic interneurons. The majority of SST-INs are Martinotti cells, which are morphological and electrophysiologically heterogeneous and can be

(Continued)

FIGURE 1 (Continued)
further classified as calretinin-positive (CR+) or calretinin-negative (CR−). 5HT3aR-expressing interneurons account for ∼30% of all GABAergic interneurons and are further divided into vasoactive intestinal peptide (VIP)-positive or VIP-negative. VIP-positive neurons display heterogeneity in their morphology and firing patterns. The majority of VIP-negative neurons express reelin. Adapted from Rudy et al. (2011). **(B)** Schematic of subcellular innervations of various GABAergic interneuron types on pyramidal neurons (PyNs). PV-expressing basket cell (PV-BC) innervates the dendrite and soma of PyNs. ChC exclusively innervates the axon initial segment of PyNs. SST-INs target the dendrites of PyNs. VIP-positive neurons commonly innervate SST-INs to disinhibit PyNs. Adapted from Taniguchi (2014). **(C)** Common circuit motifs utilized by GABAergic interneurons. In feedforward inhibition, an external source makes excitatory synapses onto both local PyNs and the GABAergic interneurons. FFI is used by ChCs and other GABAergic interneurons. Feedback inhibition occurs when GABAergic interneurons exert inhibition on local PyNs that initially provided excitation (recurrent) or other neighboring neurons that did not participate in the recruitment of the GABAergic interneuron (lateral). In disinhibition, the principal target of an interneuron is another interneuron, suppressing its inhibitory activity onto PyNs. VIP neurons inhibit SST-INs to disinhibit PyNs. Adapted from Tremblay et al. (2016). **(D)** Dendritic, somatic, and axonal morphology of neocortical ChCs. Dendrites radially arborize within a diameter of 100–150 μm, consisting of two main trunks: upper (branching to L1) and lower (branching to L4). The main axon descends 50–100 μm before profusely branching within a diameter of 100–200 μm, occupying L2–L4. The axon terminal segments consist of vertically oriented multiple boutons, which are each 1–2 μm in size and exclusively innervate the axon initial segment (AIS) of PyNs. The soma is oval in shape, found mostly in upper L2/3. Adapted from Wang et al. (2016). **(E)** Output connectivity features of ChCs. One-to-many connectivity to PyNs (top), in which a single ChC innervates many PyNs (35–50% of all PyNs that reside within the ChC's axonal field). Complex axon terminals (middle), in which multiple ChC cartridges converge onto the same region of PyN AIS to form a cylindrical-shaped axon terminal. Many-to-one connectivity to PyNs (bottom), in which multiple ChCs innervate the same PyN AIS. **(F)** Schematic of laminar distribution of inputs to cortical L2/3 ChCs. Circular and arrow tips indicate inhibitory and excitatory inputs, respectively. ChCs may be innervated by single-bouquet cells (SBC) from L1; Martinotti cells (MC), neurogliaform cells (NGC), other ChCs *via* gap junctions, basket cells (BC), and pyramidal neurons (PN) from L2/3; PN from L4; NGC and PN from L5; Unknown interneuron type from L6. Adapted from Wang et al. (2021).

L4, and they display lower input resistance along with shorter duration spikes and a stuttering firing pattern (Ma et al., 2006). In addition to the MCs and X94 cells, there are likely more subtypes of SST-INs, given observations of varying firing patterns, molecular markers, and connectivity (Xu et al., 2006; Gonchar et al., 2008).

Third, ionotropic serotonin-receptor-expressing INs (5HT3aR-INs) constitute ∼30% of INs (Lee et al., 2010; Figure 1A). 5HT3aR-INs are divided into vasoactive intestinal peptide (VIP)-expressing INs (40% of 5HT3aR-INs) and non-VIP-expressing INs (∼60% of 5HT3aR-INs) (Lee et al., 2010). Both are diverse among themselves. The majority of VIP+ INs preferentially innervate SST-INs and in turn disinhibit PyNs through the inhibition of SST-INs (Acsády et al., 1996; Pfeffer et al., 2013; Figure 1C; bottom). VIP+ INs are further classified by their morphology (bitufted, bipolar, or multipolar) (Miyoshi et al., 2010) and coexpression of calretinin (CR) (Cauli et al., 2000), which overlaps with molecular profiles of SST-IN subtypes mentioned above. VIP- INs are further classified by their expression of reelin (e.g., neurogliaform cells, ∼80% of VIP- neurons), which is also coexpressed in some SST-IN subtypes (Lee et al., 2010).

Here we have outlined the substantial heterogeneity and overlap that exist among the three major interneuron groups: PV, SST, and 5HT3aR. Such heterogeneity poses a challenge in defining single cell types, which is a prerequisite to dissecting distinct synaptic properties and functions in a cell-type-specific manner. To overcome the challenge, there has been an increasing effort to identify and classify homogeneous interneuron types. As an example of this ongoing endeavor, we spotlight the development of the various methods used to identify the ChC. In early studies of ChCs (DeFelipe et al., 1985), Golgi staining was used to visualize the fine anatomical details of the cell, which revealed its chandelier-like axonal arborization geometry ChC morphology, which allowed researchers to distinguish it from other interneuron types. Later immunohistochemical techniques revealed the immunoreactivity of ChCs to various proteins, such as GAT-1, PV, calbindin, corticotropin-releasing factor, and ankyrin-G (Howard et al., 2005). Their immunoreactivity to PV was observed in various brain regions, including the visual cortex (Lewis and Lund, 1990), sensory-motor cortex (DeFelipe et al., 1985), prefrontal cortex (Taniguchi et al., 2013), entorhinal cortex (Schmidt et al., 1993), and hippocampus (Sik et al., 1993). These widespread observations led researchers to regard ChCs as a subset of PV-expressing interneurons (Rudy et al., 2011). However, a later study showed that only ∼50 and ∼15% of ChCs in the somatosensory cortex and the medial prefrontal cortex (mPFC), respectively, were immunoreactive for PV (Taniguchi et al., 2013), demonstrating a significant heterogeneity of PV-expression among ChCs. In addition, other molecular markers of ChCs such as CRF (Lewis and Lund, 1990) and calbindin (Rio and DeFelipe, 1997) have demonstrated considerable heterogeneity among ChCs, together posing challenges in determining a homogeneous set of molecular features of the cell.

In recent years, advancements in genetics and transcriptomics have enabled a more rigorous investigation of the molecular profile of single cell types and granted genetic access to ChCs, giving way to significant discoveries about their function in synaptic inhibition and cortical processing. Using single-cell RNA sequencing (scRNA-seq) and cluster analysis, the transcriptional profile of ChCs was systematically sequenced and transcriptional differences from other GABAergic interneurons were revealed. For example, cortical ChCs showed their high expression levels of several genes, including cell adhesion molecule UNC5b, γ-subunit of GABA-A receptors,

calcium-binding protein Rasgrp1, and cGMP-dependent PKG Prkg (Paul et al., 2017). In addition, hippocampal ChCs were identified by their high expression levels of unique marker genes Ntf3 and Sntb1 (Yao et al., 2021). Furthermore, a multimodal cell census and atlas of the mammalian primary motor cortex have shown that ChCs indeed constitute a highly distinct neuronal cell type based on their transcription profiles (BICCN, 2021). Lastly, the PV-Vipr2 cell type identified by scRNA-seq data analysis was shown to correspond to the phenotypic ChC cell type, and the genetic marker Vipr2 was used to develop the transgenic mouse line Vipr2-IRES2-cre, allowing direct genetic access to ChCs (Tasic et al., 2018). The recent progress has strengthened the long-standing understanding of the ChC as a distinct single cell type with genetic profile in detail and increased accessibility to ChCs to study its functions *in vivo* in transgenic ChC specific mice. The study of ChCs thus marks a progress in detangling the complexity of GABAergic INs and serves as a platform to investigate the specific role of single IN types in brain function.

Morphology and connectivity

ChCs are identified by their unique chandelier-like axonal structures which are preserved across various species such as cats, rodents, and monkeys (Somogyi et al., 1982). ChCs are found in various neocortical regions including the dorsolateral prefrontal cortex (DLPFC) (Schoonover et al., 2020), motor cortex (Somogyi et al., 1982), visual cortex (Somogyi et al., 1982), and somatosensory cortex (Zhu et al., 2004). In the neocortex, ChCs are most abundant in cortical layer 2/3 (L2/3) (Somogyi, 1977) where ChCs account for 2% of all GABAergic interneurons (Jiang et al., 2015). ChCs are also found in subcortical regions, such as the hippocampus—CA3 (Gulyás et al., 1993), CA1 (Somogyi et al., 1983), and dentate gyrus (Soriano and Frotscher, 1989)—and the basolateral amygdala (BLA) (McDonald, 1982).

Morphology

The soma of ChCs is small and fusiform-shaped, with roughly a width of 8–10 μm and length of 16–20 μm (Somogyi et al., 1982; Figure 1D). ChC dendrites branch radially from the soma within a cylinder of 100–150 μm diameter (Somogyi et al., 1982). Two main dendritic trunks originate from the upper and lower regions of the soma, giving the ChC a bitufted morphology. In the neocortex, the upper main trunk ascends to L1 (Xu and Callaway, 2009) and the lower descends to L4 (Somogyi, 1977). On the dendritic shaft, a moderate number of drumstick-shaped spines can be found (Somogyi, 1977). The main ChC axon originates from the lower main dendritic trunk (Somogyi et al., 1982) or from the soma base (Lewis and Lund, 1990) and descends 50–100 μm before arborizing profusely and expansively, with an axonal field that covers L2/3/4 within a cylinder of 100–200 μm width (Somogyi et al., 1982). The main axons are myelinated (Somogyi et al., 1982). The axonal arbor of ChC axons consists of as many as 400 rows of horizontal collaterals (DeFelipe et al., 1985) that terminate in vertically oriented axon terminals also called "cartridges" (Szentágothai, 1975; Somogyi, 1977), which contain multiple synaptic boutons, ranging from 2∼12 in the mouse neocortex (Inan et al., 2013) and ∼8.4 in the mouse basolateral amygdala (Veres et al., 2014). The length of cartridges ranges between 10 and 50 μm, and the average synaptic bouton is 1–2 μm in size (Somogyi, 1977). These distinctive features of the ChC's axon, which resembles a chandelier, provide the basis for its name. Despite these morphological features that are largely uniform among ChCs across various brain areas and species, it is noteworthy that a recent study using high-resolution, large-volume light microscopy revealed that there are morphologically distinct subtypes based on variations in its dendritic and axonal morphology and laminar arrangement among ChCs (Wang et al., 2019). The laminar position and local geometry of dendrites and axons could determine the recruitment of different ChCs by input streams and the innervation of different PyN populations by ChCs, respectively (Wang et al., 2019). Therefore, the fine granularity of the ChC morphology and laminar distribution may indicate a potential functional heterogeneity among the ChC cell type.

Output connectivity

The most distinctive feature of ChCs is their exclusive innervation of PyNs at the axon initial segment (AIS) (Somogyi, 1977; DeFelipe et al., 1985), where action potential is generated (Stuart and Sakmann, 1994; Ogawa and Rasband, 2008). ChC cartridges vertically align themselves along the AIS of PyNs, forming multiple synaptic connections through numerous axonal boutons per AIS. The distribution of ChCs synapses is not uniform along the AIS, as they have been shown to preferentially contact a particular portion of AIS with a cross-sectional diameter of 0.5–1 μm (Vereczki et al., 2016) and distance of 20–40 μm from the PyN soma (Veres et al., 2014), which has been shown to exhibit the lowest threshold for action potential generation (Veres et al., 2014). ChC cartridges display a characteristic tendency to climb upwards along the length of the PyN AIS, with proximal boutons targeting the distal ends of the AIS (Fairén and Valverde, 1980; Peters et al., 1982; Howard et al., 2005). In these ways, ChCs cartridges strategically organize their synapses along the PyN AIS to maximize their inhibitory control. The strength of inhibition by ChCs onto PyNs has been shown to be correlated to the number of boutons contacting the AIS, with greater numbers

giving rise to more effective inhibition of PyN activity (Veres et al., 2014). Specifically, 10–12 ChC synapses onto the AIS are sufficient to reduce the firing probability of PyNs by 95% and thereby veto the generation of action potentials (Veres et al., 2014).

A single ChC densely innervates hundreds of PyNs (Figure 1E; top), specifically 35–50% of all PyNs that reside within its axonal field (Inan et al., 2013). This number ranges between 50 and 200 PyNs in the neocortex (Somogyi et al., 1982), 600–650 PyNs in the basolateral amygdala (Vereczki et al., 2016), and up to 1,200 PyNs in the hippocampus (Li et al., 1992). In some brain regions, multiple cartridges of a single ChC converge onto the same PyN AIS to create a complex cylindrical axon terminal (Fairén and Valverde, 1980; Inda et al., 2009; Figure 1E; middle). Furthermore, multiple ChCs can innervate a single PyN AIS, ranging from ∼4 ChCs in the mouse somatosensory cortex (Inan et al., 2013), ∼13 In the mouse visual cortex (Schneider-Mizell et al., 2021), and 6–7 in the mouse basolateral amygdala (Vereczki et al., 2016; Figure 1E; bottom). The convergent connections of ChCs to PyNs arise during post-natal development when the AIS is innervated by an excessive number of AIS-preferring axons of multiple ChCs, which show target preference by post-natal day 14 (P14), as well by non-AIS-preferring axons which are eliminated by P28 (Gour et al., 2021). These meticulous connectivity patterns allow ChCs to precisely and powerfully control the activities of PyN populations (Veres et al., 2014).

Input connectivity

ChCs receive excitatory and inhibitory inputs from a variety of cortical layers through synapses located primarily on the dendritic spines, less commonly on the soma, and none on the AIS (Somogyi et al., 1982). Specifically on their dendrites, ChCs receive a similar density yet fewer number of excitatory glutamatergic inputs by PyNs when compared to BCs, due to the less elaborate branching of the ChC's dendritic trees (Papp et al., 2013). As a result, ChCs display a rate of spontaneous excitatory post-synaptic current that is lower than that of BCs (Papp et al., 2013).

Various brain regions have been studied to determine the distribution of local inputs to L2/3 ChCs (Figure 1F). In the primary visual cortex (V1) of adult mice, octuple whole-cell recordings revealed that ChCs receive monosynaptic inhibitory input from single-bouquet cells (SBCs) in L1, BCs in L1, and MCs in L1 and L5 (Jiang et al., 2015). In the prelimbic cortex of adult mice, the laminar distribution of monosynaptic excitatory input to ChCs by PyNs was studied *via* optogenetic stimulation of PyNs in various layers. L2/3 ChCs receive the greatest excitatory input from more distant layers, namely L3 and L5, and significantly less input from L1 (Lu et al., 2017). Global connectivity to prelimbic ChCs was examined using trans-synaptic rabies tracing. At a network level, prelimbic ChCs receive monosynaptic excitatory input from the contralateral prelimbic cortex and mediodorsal, anteromedial, and ventromedial thalamic nuclei, and cholinergic input from the diagonal band of the basal forebrain (Lu et al., 2017). Furthermore, prelimbic ChCs were shown to receive the strongest inhibitory input from L1 (Lu et al., 2017). In the primary somatosensory cortex (S1) of adult mice, laser scanning photostimulation was used to determine the distribution of input strengths from various layers. S1 ChCs receive the strongest excitatory input from local L2/3 and L5 PyNs; no significant excitatory input from L4 PyNs; the strongest inhibitory input from L1 followed by L2/3; no significant inhibitory input from L4 and L5A; and weak inhibitory input from L5B and L6 (Xu and Callaway, 2009).

Input to ChCs is not limited to chemical synapses. Neighboring L2/3 ChCs have been shown to be electrically coupled through gap junctions which may facilitate their concerted activity (Woodruff et al., 2011; Figure 1F). Less commonly, ChCs are connected by gap junctions with adjacent BCs (Woodruff et al., 2011). In addition, in the mPFC, the firing of ChCs induced glutamatergic excitation that activated a nearby ChCs and back to itself, indicating that nearby ChCs may di-synaptically activate one another *via* an intermediate PyN (Taniguchi et al., 2013). The electrical coupling and di-synaptic excitation among local ChCs may have a role in promoting the synchronized inhibition of PyN populations, a property that has been observed in other GABAergic interneurons (Beierlein et al., 2000). Additionally, electrical coupling among ChCs *via* gap junctions may instead have a more complex role of desynchronizing the firing of ChC populations, a function that was recently shown to be possible when GABAergic interneurons coupled only *via* gap junctions evoke large, slow, inhibitory gap junction potentials with high viability in electrical connection strengths (Szoboszlay et al., 2016).

Neuroplasticity of chandelier cell

Like other neurons, ChCs undergo neuroplasticity and display substantial variability in their inhibitory synapses, depending on the developmental stage and characteristics of the post-synaptic PyN activity. Here we review molecular mechanisms related to axonal development and synaptogenesis and plasticity during the development and activity-dependent variability of ChCs.

Axo-axonic synaptic plasticity during development

The development of the ChC axon includes several key stages: Filopodia extends from axonal shafts to recognize cues

and direct the axon to its final destination. After the axon arborizes, synaptic boutons develop to form the characteristic cartridges of ChCs. Finally, ChC axons selectively establish synaptic contact with the PyN AIS. Recent studies have illuminated the various cellular and molecular components responsible for these developmental processes.

The initiation of filopodia in ChCs and resulting axonal arborization is regulated by long-range cholinergic projections from the basal forebrain (BF) (Steinecke et al., 2022). When nicotinic acetylcholine receptors (nAChRs) were blocked in ChCs of the mPFC using an antagonist selective for the α4-subunit-containing isoform of the receptor, a significant decrease in filopodia growth was observed. The spiking properties of the same ChCs were not affected, indicating that the effect of acetylcholine (ACh) signaling on axons is direct and local (Steinecke et al., 2022). Moreover, the initiation of filopodia growth was observed preferentially at axonal varicosities. Therefore, cholinergic modulation is critical for filopodia formation at axonal varicosities of ChCs (Steinecke et al., 2022). Furthermore, using electroporation and calcium imaging, it was shown that T-type voltage-gated calcium channels (VDCCs) maintain the basal calcium level range in axonal varicosities. Calcium levels were reduced in varicosities when nAChRs were blocked and increased when nicotine was rapidly administered, and an increase in calcium level was followed by filopodia initiation. As a result, the α4-nAChR–T-type VDCC signaling axis regulates filopodia initiation in ChCs (Steinecke et al., 2022). The *in vivo* function of the nAChR–T-type VDCC signaling pathway in ChC axonal arborization was tested using a loss-of-function experiment. When ChCs with mutant α4-nAChRs or mutant T-type VDCCs were transplanted in developing mice, a significant decrease in axonal branching was observed at P13 compared to the wild type, confirming that the nAChR–T-type VDCC signaling axis regulates the arborization of ChC axons.

The morphogenesis of ChC synaptic boutons has been shown to be mediated by three molecules: ErbB4, DOCK7, and FGF13. First, the depletion of a receptor tyrosine kinase ErbB4, which is expressed by PV-positive interneurons, led to a decrease in ChC bouton density without affecting the overall morphology of the ChC (Fazzari et al., 2010). Second, a guanine nucleotide exchange factor DOCK7 was shown to act as a cytoplasmic activator of ErbB4 and promote ChC bouton development by augmenting ErbB4 activation independently of its GEF activity. Indeed, defective ErbB4/DOCK7 signaling was correlated with a decrease in both size and density of ChC boutons (Tai et al., 2014). Therefore, the development of ChC boutons is understood to be controlled by DOCK7's modulation of ErbB4 activity. A recent study using RNA sequencing and whole transcriptome analyses of GABAergic interneurons during early synaptogenesis found that a non-secretory growth factor FGF13 has a critical role in regulating ChC bouton development. When FGF13 was knocked out during P2 and P14, when axonal development was mostly complete, there was a significant decrease in the density of pre-synaptic ChC boutons (Favuzzi et al., 2019). The molecules ErbB4, DOCK7, and FGF13 are involved in the development of ChC boutons.

Given the highly precise subcellular targeting of ChC axons on the AIS of PyNs in the adult brain, it is important to understand how such synaptic target preference is established during post-natal development. During development, ChCs form both AIS and off-target varicosities that undergo distinct developmental regulation and develop an excess of off-target axonal varicosities in addition to AIS-targeting varicosities (Steinecke et al., 2017). Unlike off-target varicosities, AIS-target varicosities that predominantly contain pre-synaptic markers VGAT specifically formed synapses at AIS and persisted in young adulthood (P28) whereas off-target varicosities that lack pre-synaptic markers did not form synapses and its number decreased in young adulthood. A recent study also reported that coordinated axo-axonic innervation of particular AIS *via* en passant synapses was observed already at P14 before ChC cartridges are established (Gour et al., 2021). These suggest that subcellular synapse specificity of ChCs is predetermined and such predetermined target choice possibly corresponds to the gradual removal of off-target synapses over post-natal development. It is possible that molecular cues localized at AIS provide target recognition and synapse formation by ChCs.

In vivo RNA screening revealed that the selective innervation of the PyN AIS by ChC is regulated by a pan-axonally expressed L1 family member cell adhesion molecule L1CAM. When L1CAM was depleted in the embryonic neocortex, the number of PyN AISs innervated by ChCs decreased significantly at P28 (Tai et al., 2019). Furthermore, the number of vesicular GABA transports (VGAT) and gephyrin puncta, which are, respectively, pre- and post-synaptic markers for GABAergic synapses (Micheva et al., 2010), was also decreased at the AIS but not somatic or dendritic regions of the PyN (Tai et al., 2019). In addition to being critical for establishing ChC/PyN AIS innervation, L1CAM was shown also to play an important role in maintaining these synapses during adulthood. When most axo-axonic synapses are established in adulthood, the silencing of L1CAM in PyNs led to a significant decrease in the number of ChC/PyN synapses and gephyrin puncta per PyN AIS (Tai et al., 2019). L1CAM alone does not sufficiently explain the subcellular specificity of the ChC/PyN AIS innervation, since L1CAM is distributed pan-axonally along the PyN. A cytoskeletal complex of ankyrinG (AnkG) and βIV spectrin at the PyN AIS has been suggested as a model to anchor and cluster L1CAM molecules to promote high-affinity cell adhesion to nearby ChC cartridges (Tai et al., 2019). Supporting this model, disruption of the L1CAM-AnkG-βIV-spectrin complex was shown to reduce the density of L1CAM distribution at the AIS and importantly impair the innervation of AIS by ChC cartridges (Tai et al., 2019). It would be of great interest to identify such molecular

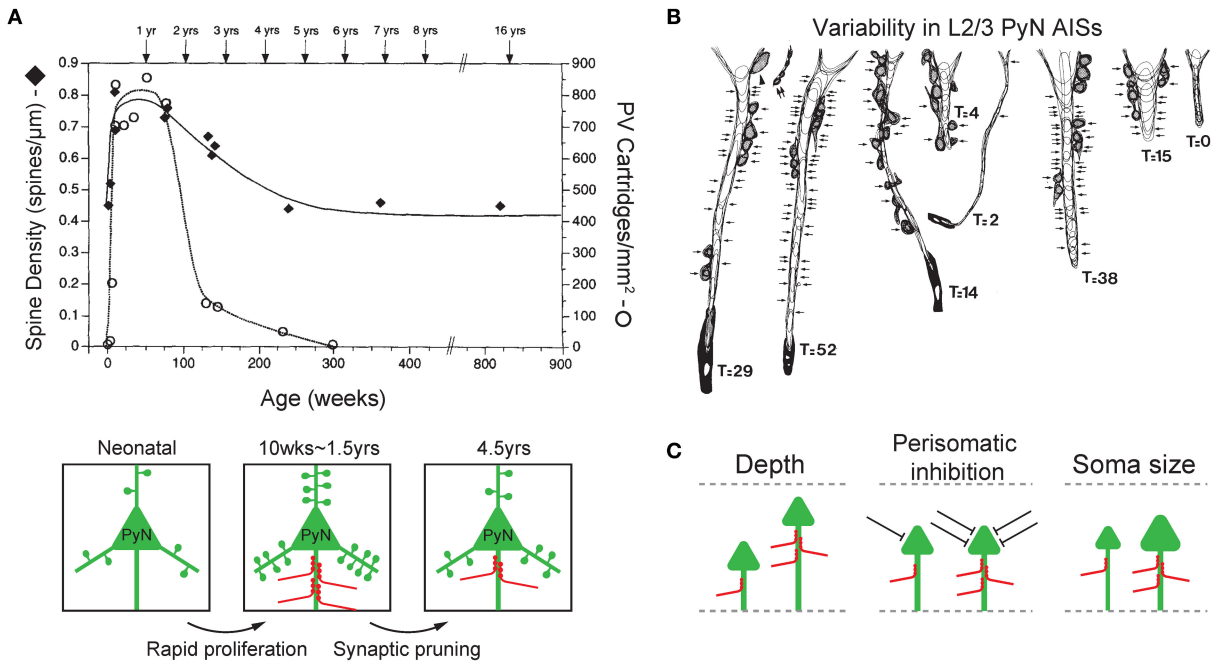

FIGURE 2
Plasticity and variability of axo-axonic synapses. **(A)** Synchronous developmental time course of changes in PyN spine density (filled diamonds) and ChC cartridge density (blank circle) in the L3 monkey prefrontal cortex. Both PyN dendritic spine density and ChC cartridge density rapidly increase during 2–3 post-natal months (rapid proliferation), reach their highest levels at 1.5 years of age, progressively decline until 4.5 years of age (synaptic pruning), then remain stable in early adulthood. Adapted from Anderson et al. (1995). **(B)** Variability in the ChC axon terminals on AISs of L2/3 PyNs of the monkey sensory-motor cortex. Arrows indicate synaptic contacts only on the AIS. *T* indicates the total number of synapses on the AIS (GAD-positive). Adapted from DeFelipe et al. (1985). **(C)** Features of target PyNs correlated with axo-axonic synaptic strength. The cortical depth of PyN soma location (left), the degree of perisomatic inhibition (middle), and the size of PyN soma (i.e. soma area and AIS radius, right) are positively correlated with the strength of ChC inputs to the AIS. Adapted from Schneider-Mizell et al. (2021).

cues that determine the connectomic target preference of ChC axons for future study.

The post-natal development of ChC axons involves an initial stage of the rapid proliferation of new synapses followed by a later stage of removal and refinement of these synapses (Pan-Vazquez et al., 2020; Gour et al., 2021; Figure 2A). In various brain regions of kittens, ChC axons branched more profusely and axon terminals displayed more complex structures when compared to those of adult cats (Somogyi et al., 1982). Specifically in the kitten visual cortex, the rapid proliferation of ChC axons and axo-axonic synaptogenesis was shown to occur up to the age of 7–8 weeks, after which the axon terminations and synaptic boutons became simplified, more prominent, and organized (Somogyi et al., 1982). *In vivo* imaging of ChCs during post-natal development showed that ChC axons rapidly arborized and formed axo-axonic synapses between P12 and P18 (Pan-Vazquez et al., 2020). In that study, they further showed that the plasticity of axo-axonic synapses is reversible and follow homeostatic plasticity rules based on developmental switches in GABAergic polarity of axo-axonic synapses from depolarizing during P12–P18 and to hyperpolarizing in older mice (P40–46). A recent study using three-dimensional electron microscopy revealed that ChC axons exhibit axo-axonic target preference for innervation of the AISs of layer 2/3 PyNs (~60% of ChC axon terminals made contact with the AIS of PyNs) by P14 and develop their full target preference with almost ~90% contact with the AIS of PyNs by P28 (Gour et al., 2021). These studies suggest that ChCs undergo significant plasticity during post-natal development, guided by various molecular and neurophysiological factors (Anderson et al., 1995; Fazzari et al., 2010; Favuzzi et al., 2019), to establish powerful inhibition on the excitatory activity of PyNs.

Interestingly, the time-course of changes in the synaptic density of inhibitory ChC synapses on the PyN AIS parallels that of excitatory synapses by other neurons on PyN dendritic spines (Figure 2A). In the monkey L3 PFC, the dendritic spines of PyNs where excitatory input is received displayed a pattern of rapid proliferation and subsequent simplification during post-natal development. PyN spine density increased rapidly during the first 2–3 post-natal months, remained high until 1.5 years of age, and progressively declined until 4.5 years of age, at which point the spine density stabilized into adulthood (Anderson et al., 1995). The same time-course of development was observed with the synaptic boutons of ChCs in the L3 prefrontal cortex

that contact the AIS of PyNs. Using immunohistochemistry of PV which is found in axon terminals of ChCs, ChC boutons were first observed on 22 post-natal days, and their density substantially increased during the first 3 post-natal months. Much like the spine density of PyNs, ChC bouton density remained at its peak (of 750/mm^2) through 1.5 years of age, then declined over the next year (Anderson et al., 1995). This close temporal parallel between the post-natal developmental pattern of PyN dendritic spines and ChC synaptic boutons is not trivial, given that the time-course of synaptogenesis greatly varies by cell type (DeFelipe et al., 1985; Schneider-Mizell et al., 2021). As such, this suggests that the plasticity of ChC axon terminals may be dependent on the level of excitatory activity of PyNs, which may function to maintain a precise balance between the inhibition exerted by ChC axo-axonic synapses and excitation by dendritic spine synapses of PyNs.

Variability in axo-axonic synaptic strengths

The plasticity of ChC axon terminals and axo-axonic synapses is further demonstrated by the observation that there exists substantial variability in the magnitude of ChC input to PyN AISs (DeFelipe et al., 1985; Schneider-Mizell et al., 2021; Figure 2B). This variability reflects the ability of ChCs to regulate their inhibitory strength based on the characteristics of its target cell, and may have a role in shaping the functional properties of PyNs. Variability in ChC input seems to be dependent on three aspects of the innervated PyNs: laminar depth of the soma, other sources of perisomatic inhibition, and size of soma and AIS (Figure 2C).

Firstly, the laminar depth of the PyN's location is associated with ChC input strength (Figure 2C; left). Deeper PyNs receive weaker ChC inhibition. This correlation has been demonstrated in the monkey sensory-motor cortex (DeFelipe et al., 1985) and the mouse visual cortex (Schneider-Mizell et al., 2021). First, ChC axon terminals in the monkey sensory-motor cortex area 4 were stained with immunohistochemistry for the enzyme GAD which is found in GABAergic axon terminals. Doing so revealed that the AIS of PyNs in cortical layers 2 and 3 were innervated by a greater number of GAD-positive ChC axon terminals when compared to those of L5 (DeFelipe et al., 1985). In a later study of the mouse visual cortex, it was observed that even within cortical layers 2/3, greater cortical depth was associated with less number of ChC axo-axonic synapses onto a single PyN AIS hence a weaker inhibition (Schneider-Mizell et al., 2021). Second, the overall level of perisomatic inhibition, excluding ChC axo-axonic synapses, on PyN was correlated with a greater number of ChC synapses (Schneider-Mizell et al., 2021; Figure 2C; middle). Perisomatic inhibition included inhibitory synapses on the soma and non-ChC AIS synapses. Thirdly, the larger size of PyN, specifically the soma area and the radius of AIS, was associated with greater ChC input (Schneider-Mizell et al., 2021; Figure 2C; right).

That ChC axon terminals undergo significant plasticity during post-natal development and display variability in their synaptic connections to PyN AISs in adult animals supports that there is substantial variance in the strengths of the axo-axonal synapses that connect ChCs to PyNs. This variance in synaptic strength may be functionally relevant to the maintenance and regulation of the activity of PyN populations. Indeed, given the likely role of ChCs in maintaining the E/I balance of PyN populations, ChC axon terminals may demonstrate plasticity in response to varying levels of PyN population activity. Increased PyN excitatory activity may trigger the strengthening of axo-axonal synapses hence increasing levels of inhibition, to restore E/I balance and ultimately preserve the precision of the population output of PyNs. The failure to perform this function may be the underlying basis of neuropsychiatric disorders like schizophrenia, namely thought disorder, in which ChC dysfunction has been implicated.

Chandelier cell functions

Electrophysiological properties of ChCs

ChCs are commonly classified as fast-spiking interneurons by their electrophysiological firing (Veres et al., 2014). Upper L2/3 ChCs of the prefrontal cortex exhibit high-frequency non-adapting firing pattern and a low levels of excitability (Kawaguchi, 1995; Zaitsev et al., 2009) with moderate accommodation (Veres et al., 2014). Paired cell recordings between ChCs and pyramidal neurons in monkey DLPFC revealed that cortical ChCs have a high release probability (González-Burgos et al., 2005). Repetitive stimulation of ChCs produced frequency-dependent depression and the failure rate of ChCs was almost zero. These features indicate that inhibitory inputs from ChCs to PyNs serve as a low-pass filter providing efficient inhibition at the beginning part of the burst. Although ChCs are generally considered fast-spiking, it is noteworthy that electrophysiological properties of ChCs vary between brain regions and different species.

ChCs in different brain regions exhibit electrophysiological heterogeneity with regard to specific membrane properties. For instance, in the neocortex (Povysheva et al., 2013) and hippocampus (Buhl et al., 1994), where the majority of ChC electrophysiological recordings have been done, membranes of ChCs display different input resistance, with neocortical ChCs having a significantly higher input resistance (∼167 MΩ) than hippocampal ChCs (∼73.9 MΩ). Apart from this difference, neocortical and hippocampal ChCs share similar time constants of ∼8 and ∼7.7 ms, similar resting membrane potentials of −65 and −65.1 mV, and similar amplitude of action potentials of

∼60 and ∼64.1 mV, respectively. The greater input resistance of neocortical ChCs indicates either a larger axonal diameter or less number of open membrane channels compared to hippocampal ChCs. These electrophysiological differences, in addition to specific morphological differences such as the more elaborate axonal branching in the hippocampus (Li et al., 1992), may reflect a functional difference in the ways that ChCs of different brain regions uniquely contribute to the neural coding and circuitry of their respective areas.

Although fast-spiking interneurons characterized by their short, fast bursts of action potentials without adaptation do not constitute a homogeneous group, the majority of fast-spiking interneurons express the high-affinity calcium binding protein, parvalbumin (PV) and consist of two morphologically distinct cell types by the horizontal spread of the axonal arborization: basket-cells (BCs) and ChCs (Kawaguchi and Kubota, 1997; Zaitsev et al., 2005). Despite salient differences in morphology between ChCs and BCs, basic electrophysiological properties such as rapid time course, the small amplitude at resting membrane potential, and GABA-A receptor-mediated inhibition do not differ significantly between ChCs and BCs (Gonzalez-Burgos et al., 2005; Povysheva et al., 2013). For example, the functional properties of single IPSPs were qualitatively and quantitatively similar between ChCs and BCs in the monkey prefrontal cortex (Gonzalez-Burgos et al., 2005). However, in the prefrontal cortex, some differences between ChCs and BCs (firing frequency, fast and medium afterhyperpolarization, and depolarizing sag) exist across species and a difference in the first spike latency is species-specific (Woodruff et al., 2009; Povysheva et al., 2013). For example, the firing frequency of ChCs is substantially higher than of BCs in monkeys, rats, and ferrets (Krimer and Goldman-Rakic, 2001; Povysheva et al., 2013). In mouse hippocampus CA3, BCs and ChCs showed different properties (Papp et al., 2013): BCs had a lower threshold for action potential (AP) generation and lower input resistance, narrower AP and afterhyperpolarization than ChCs. BCs fire more frequently than ChCs. Thus, the differences in firing properties between ChCs and PV-BC could result from their morphological differences (Papp et al., 2013) and brain regions and in turn differently contribute to post-synaptic activity during rhythmic network oscillations in a cell-type and brain-region specific manner (Klausberger et al., 2003; Dugladze et al., 2012; Massi et al., 2012).

Excitation and inhibition by ChCs

The axon terminals of ChCs express glutamic acid decarboxylase (GAD) which is responsible for the synthesis of GABA (DeFelipe et al., 1985), and GABA transporter (GAT)-1 which mediates GABA clearance from the synaptic cleft (Inda et al., 2007), indicating the GABAergic nature of ChCs. GABA release from ChCs activates GABA-A receptors at the post-synaptic site in PyNs (Nusser et al., 1996; Gonzalez-Burgos and Lewis, 2008) which results in the opening of chloride ion channels. Since the opening of chlorine channels typically results in the influx of chloride anions across the membrane which hyperpolarizes the post-synaptic membrane (Kaila, 1994), the effect of ChC GABAergic signaling was generally considered as inhibition.

However, several *in vitro* studies have reported that the release of GABA from cortical ChCs evokes excitatory post-synaptic responses (Szabadics et al., 2006; Molnár et al., 2008; Woodruff et al., 2009). Notably, Szabadics et al. (2006) found that PyN AISs were absent of the potassium-chloride cotransporter 2 (KCC2), which regulates the intracellular chloride concentration at the post-synaptic surface by extruding the anion (Payne et al., 1996). The absence of KCC2 at the AIS was proposed as a potential explanation for this phenomenon. The absence of KCC2 at the AIS would reduce the extrusion of intracellular chloride, leading to a reversal of the transmembrane chloride gradient and a depolarized GABA-A reversal potential (Woodruff et al., 2010). The depolarized GABA-A reversal potential would allow GABA-A receptors to mediate depolarizing events upon activation. It is noteworthy that the causal relationship between the lack of KCC2 on the PyN AIS and the depolarizing effect of ChCs has not been directly shown. To add a layer of complexity to GABAergic signaling at the AIS, an *in vitro study* suggested the role of intracellular bicarbonate (HCO_3^-) levels in ensuring the inhibitory effect of the GABAergic input to the AIS of PyN (Jones et al., 2014). The level of intracellular bicarbonate (HCO_3^-) regulates action potential generation in both soma and AIS *via* Kv7/KCNQ channel modulation: local HCO_3^- efflux through GABA-A receptors at the AIS of PyN facilitates local KCNQ channel activity, which in turn greatly reduces action potential probability despite a local depolarizing Cl^- gradient.

In the neocortex, an *ex vivo* study showed that ChCs have depolarizing effects on PyNs under resting membrane potential yet hyperpolarizing effects under fluctuating membrane potential dynamics, suggesting the possibility of a state-dependent, dual function of ChCs (Woodruff et al., 2011). However, in the BLA, ChCs were shown to hyperpolarize PyNs even under resting membrane potential (Veres et al., 2014), similar to other *in vitro* studies in the hippocampus that demonstrated their inhibitory function (Buhl et al., 1994; Glickfeld et al., 2009). Therefore, future studies are needed to determine whether the state-dependent depolarizing effects of ChCs occur in a region-specific manner.

Studies suggesting the excitatory function of ChCs have been conducted in *in vitro* conditions. In *in vivo* studies, evidence for the inhibitory function of ChCs has been prevalent. For example, L2 ChCs in the prelimbic cortex of free-behaving mice have been shown to inhibit the firing of PyNs (Lu et al., 2017). In this study, ChCs of Nkx2.1-CreER mice were virally expressed

with channelrhodopsin-2 (ChR2), and the response of target PyNs was observed using single-unit optrode recording. The optogenetic activation of prelimbic L2 ChCs monosynaptically inhibited the firing of a large number of PyNs. Similar results were reported in the CA1 hippocampus of Unc5b-CreER mice using *in vivo* extracellular recording and calcium imaging methods (Dudok et al., 2021). First, CA1 ChCs were virally expressed with ChR2, and silicone probes were used to record the activity of CA1 units in head-fixed mice during spontaneous running and resting. Optogenetic activation of ChCs resulted in rapid reductions in PyN firing rate, suggesting the inhibitory effect of ChCs. Second, ChCs were expressed with the excitatory opsin ChRmine or inhibitory opsin eNpHR and the entire CA1 neuronal population with GCaMP6f for two-photon calcium imaging. Activation of ChCs through ChRmine reduced the number of transients in PyNs, while inhibition through eNpHR significantly increased transient rates. Therefore, these results collectively suggest that the *in vivo* function of ChCs in adult animals is inhibitory.

Despite the increasing number of *in vivo* studies that have provided an understanding of the function of ChCs in live animals, the question of whether ChC synapses are depolarizing or hyperpolarizing is still not fully understood regarding different post-natal developmental periods and brain states. Developmental considerations may explain the observations of depolarizing effects of GABAergic release by ChCs reported in previous *in vitro* studies (Szabadics et al., 2006; Molnár et al., 2008; Woodruff et al., 2009). GABA is generally thought to be excitatory only during early development until around P7, when the efflux of chloride ions due to an intracellular regulation causes the membrane potential to rise above the threshold (Owens and Kriegstein, 2002; Wang et al., 2016). A recent study showed that GABAergic signaling at the AIS of mouse prefrontal PyNs switches polarity from depolarizing to hyperpolarizing over a protracted periadolescent period based on developmentally changed functions of KCC2 and NKCC1 (sodium potassium chloride cotransporter 1) (Rinetti-Vargas et al., 2017), suggesting changing role of ChCs over post-natal development.

Neuromodulation of ChCs

Cortical brain states can be effectively regulated by neuromodulators such as noradrenaline (NA), acetylcholine (ACh), dopamine, and serotonin. Such neuromodulatory control, which can modulate the activity of cortical GABAergic neurons, plays a critical role in mediating plasticity for circuit wiring and information processing (Yaeger et al., 2019; Steinecke et al., 2022). In the neocortex, NA and ACh are released from afferent axonal fibers predominantly originating from the locus coeruleus and the nucleus basalis of the basal forebrain, respectively. In the rat frontal cortex, NA or α-adrenergic agonist, 6-fluoronorepinephrine, directly affects the activities of most GABAergic cell types by inducing depolarization but not action potential firing in fast-spiking cells including multipolar cells and ChCs (Kawaguchi and Shindou, 1998). Regarding the effect of ACh in the neocortex, activation of muscarinic receptors (mAChRs) generally increases PyN firing *via* direct depolarization and/or enhances the intrinsic excitability of PyNs (Obermayer et al., 2017). Muscarinic 1 receptors are widely expressed on somatodendritic domains of L2/3 and 5 PyNs and INs, where they increase membrane excitability (Ballinger et al., 2016). In contrast, Muscarinic 2 receptors are typically expressed in the pre-synaptic domain where they inhibit ACh release on local inhibitory GABAergic terminals to decrease GABA release (Disney et al., 2006). In the mouse PFC, carbachol, an ACh receptor agonist, potentiated the excitatory synaptic currents onto PV-BCs in L3–6, but not onto PV-BCs and ChCs in the superficial layer (Tikhonova et al., 2018). ACh can regulate the function of perisomatic inhibitory cells by modulating their GABA release (Lawrence, 2008). GABA release in PV-BCs, CCK-BCs, and ChCs is depressed by cholinergic receptor activation (Fukudome et al., 2004; Szabó et al., 2010). Cholinergic receptor activation by carbachol does not significantly depolarize fast-spiking cells (Kawaguchi and Shindou, 1998). Carbachol significantly reduced the amplitude of uIPSCs in PV-BCs and ChCs, and the reduction was restored by M2-type muscarinic receptor-preferring antagonist (Szabó et al., 2010). Furthermore, carbachol changed the short-term dynamics of GABA release: it accelerated the decay of uIPSCs in ChC-PyN pairs but not in fast-spiking BC-PyN pairs. In addition, carbachol significantly suppressed or even eliminated the short-term depression of uIPSCs in fast-spiking BC-PyN and ChC-PyN pairs in a frequency-dependent manner (Szabó et al., 2010). These suggest that ACh can differentially control the impact of perisomatic GABA release from different sources. It appears that the effects of neuromodulators including dopamine and serotonin on ChCs remain elusive. Although electron microscopy revealed that cortical PV-INs receive direct synaptic inputs from dopaminergic axons (Sesack et al., 1998), it is unclear whether dopaminergic axons exhibit distinct projections to PV-BCs and ChCs. An *in vitro* study reported that a ChC in the rat sensorimotor cortex did not respond to serotonin (5-HT) (Foehring et al., 2002). To determine specific functions of cortical ChCs in neural circuits and brain function, systematic future studies on development, brain states, and neuromodulation are needed.

Behavioral function of ChCs

The electrophysiology and connectivity of ChCs have been characterized by many *in vitro* studies, which allowed an understanding of its function of powerfully inhibiting the action potential of PyNs and regulating the population output of PyN

ensembles (Buhl et al., 1994; Veres et al., 2014). With recent advancements in genetic labeling techniques, studies have begun demonstrating the *in vivo* activity of ChCs in various brain areas and its functional relevance in the behavior of live animals.

Role of ChCs in brain oscillations

Brain rhythm indicates highly coordinated neuronal activity underlying cognitive processes. For example, sharp wave-ripple complexes (SWRs), which have been postulated to arise from a synchronous burst of PyN population, are required for memory consolidation (Csicsvari et al., 2000). Diverse features of interneurons allow synaptic inhibition of PyNs at various subcellular compartments and temporal regulation of PyN activities with unique patterns. These interactions between interneurons and networks of PyNs determine brain rhythm oscillations (Klausberger and Somogyi, 2008). Particularly, gamma oscillations (30–80 Hz) are critical for important cognitive functions such as attentional selection (Vinck et al., 2013), working memory operations (Carr et al., 2012), perception (Melloni et al., 2007), conceptual categorization (Engel et al., 2001), and hippocampal functions such as learning and memory (Colgin and Moser, 2010). Disrupted gamma oscillation is associated with cognitive deficits in schizophrenia such as the disorganization of thought (Lewis et al., 2005; Cho et al., 2006). Fast spiking PV-expressing GABAergic interneurons such as PV-BCs and ChCs have been associated with gamma oscillations since they provide strong, phasic, and synchronous inhibition to networks of PyNs *via* their innervation of perisomatic compartments (Bartos et al., 2007; Gonzalez-Burgos and Lewis, 2008; Sohal et al., 2009).

Perisomatic inhibition at gamma frequency plays an important role in determining the spiking timing of PyNs within the theta cycle (Bartos et al., 2007; Gonzalez-Burgos and Lewis, 2008; Sohal et al., 2009). Indeed, both PV-BCs and ChCs have a high discharge probability in the descending phase of the theta when the discharge probability of PyNs is lowest and gamma power is highest (Buzsáki, 2002). However, distinct firing patterns between PV-BCs and ChCs have been reported. In the rat hippocampus CA3, PV-BCs fire at high frequency and are phase-locked to sharp wave ripple oscillation while ChCs preferentially and rhythmically fire around the peak of the theta cycles and increase firing probability at the beginning of the sharp wave episode and become saline at the maximum amplitude and after the sharp wave (Klausberger et al., 2003). Recent studies reported heterogeneous dynamics of ChCs during the sharp wave ripples (Varga et al., 2014; Geiller et al., 2020). In the rat prelimbic cortex, *in vivo* extracellular recording revealed that during DOWN- to UP-state transitions of slow oscillations, when spindle oscillations occur, PV-BCs and PyNs increased their firing rate earlier than ChCs, showing differential coupling to gamma and spindle oscillations between PV-BCs and ChCs (Massi et al., 2012). These suggest different contributions of ChCs and PV-BCs to the temporal organization of PyN network activity.

Temporal coupling of ChCs to theta and spindle oscillations rather than gamma oscillation has been suggested as their contribution to the dynamic selection and control of neuronal ensembles (Massi et al., 2012; Dudok et al., 2021). While PV-BCs are widely accepted to mediate the generation of gamma oscillations (Massi et al., 2012), the role of ChCs in generating gamma oscillations is unclear (Bartos et al., 2007; Tukker et al., 2007). Indeed, the microcircuitry of PyNs and PV-BCs can generate gamma frequency oscillations without the involvement of ChCs, evidenced by an *in vitro* study suggesting that PV-BCs but not ChCs play a central role in the generation of cholinergically induced oscillations in hippocampal slices, one of the most studied *in vitro* models of gamma oscillations (Gulyas et al., 2010). Moreover, ChC activity is more strongly coupled to the theta cycle than the gamma cycle (Klausberger et al., 2003; Klausberger and Somogyi, 2008). One possible explanation for distinct contributions between PV-BCs and ChCs to brain oscillations was that the differential synaptic localization of GABA-A receptor subunits such as α1 and α2 subunits on the somata and AIS domains of post-synaptic PyNs (Nusser et al., 1996) may underlie cell-type specific association with high- or low-frequency oscillations, depending on the IPSC duration based on the kinetics of GABA-A receptor subunit composition. For instance, the kinetics of α2-subunit-containing GABA-A receptors post-synaptic to ChCs appears to be too slow to drive gamma oscillation, which requires a fast decay of the inhibitory post-synaptic current in PyNs (Gonzalez-Burgos and Lewis, 2008). However, paired recording from interneurons and PyNs in the basal nucleus of the amygdala showed that unitary inhibitory post-synaptic currents (uIPSCs) originating from PV-BCs and ChCs are similar in the magnitude of peak amplitude and the decay time constant, but different in the latency measured at unitary connections between interneurons and PyNs (Barsy et al., 2017). A recent study using the face-matched mirror replica immunogold labeling showed similar GABA-A receptor subunit composition in perisomatic synapses made by distinct interneuron types including ChCs, PV-BCs, and CCK-BCs (Kerti-Szigeti and Nusser, 2016), suggesting that ChCs and BCs are likely to have similar post-synaptic regulation. It is noteworthy that paired recordings from interneurons and PyNs revealed a longer decay time of uIPSCs in ChC-PyN pairs than in fast-spiking BC-PyN pairs (Szabó et al., 2010). Different decay kinetics might be due to the spillover of GABA between release sites, which can result from high release probability. Cholinergic receptor agonist carbachol reduced GABA release probability from the terminals without directly altering GABA receptor functions (Behrends and Bruggencate, 1993). Carbachol accelerated the decay of uIPSCs in ChC-PyN pairs but not in fast-spiking BC-PyN pairs (Szabó et al., 2010). Given similar GABA-A receptor subunit composition at

the perisomatic inhibitory synapses (Kerti-Szigeti and Nusser, 2016), different decay kinetics between ChCs and BCs could be due to cholinergic modulation of synaptic inhibition and the cross-talk of neighboring synapses (Szabó et al., 2010), not solely due to distinct GABA-A receptor subunit composition. In addition, an *in vivo* study showed that ChCs significantly increased their firing during arousal which switched the brain states from slow to theta oscillations in the hippocampus and a low-amplitude desynchronized field potential in the prelimbic cortex while BCs and PyNs did not change their firing (Massi et al., 2012). Given arousal is often associated with cholinergic signaling, different modulation by cholinergic receptor activation between ChCs and BCs may result in a distinct contribution to theta oscillation in a state-dependent manner. The anatomical differences between PV-BCs and ChCs can be related to their distinct involvement of brain oscillations. PV-BCs and ChCs have different dendritic arborizations and locations of their soma. They receive spatiotemporally distinct patterns of excitatory synaptic inputs from local PyNs, long-range thalamocortical connection, and neuromodulatory inputs, and in turn form different recurrent feedback excitation and inhibition in a microcircuit (Gonzalez-Burgos and Lewis, 2008; Andrási et al., 2017). The distinct wiring features and output properties between BCs and ChCs may differentiate control of the spike-timing of PyNs (Vereczki et al., 2016). Future study is needed to clarify the functional involvement of ChCs in gamma or theta oscillations during behavior, which is important to understand the impact of ChC dysfunction in cognitive processes.

Role of ChCs in various brain regions

ChC activity in the hippocampus has been shown to be associated with locomotion and whisking behavior and to regulate the creation of hippocampal place fields. In a recent *in vivo* optogenetic study (Dudok et al., 2021; Figure 3A), CA1 hippocampal ChCs of Unc5b-CreER mice were selectively labeled by their expression of Unc5b (a netrin receptor highly specific to ChCs) (Paul et al., 2017) and virally expressed with GCaMP6f for two-photon calcium imaging and all CA1 neurons with jRGECO1a to monitor control activation levels. During voluntary running and resting on a treadmill, ChC activation was maximal during periods of locomotion and exceeded the activation of other CA1 neurons. Furthermore, during periods of rest, transient increases in ChC activity were observed during the onset of whisking movements, with the intensity of transients correlated to the duration of whisking. The presentation of visual or tactile sensory stimuli did not activate ChCs unless accompanied by whisking behavior. These results collectively suggest that hippocampal ChCs activate during locomotion and whisking behavior yet are not affected by sensory stimuli in the absence of movement (Dudok et al., 2021). In the same study, head-fixed mice were allowed to freely explore a cue-rich treadmill while ChCs were photostimulated at a selected location. *In vivo* optogenetic activation of ChCs resulted in the transient disappearance of hippocampal place fields at the selected location while inhibition resulted in the addition of novel place fields that persisted for long periods. Therefore, these results suggest that ChCs have a role in regulating hippocampal place fields, possibly by controlling the activity of hippocampal PyN populations which are widely known to be the neural substrates of place fields (O'Keefe and Nadel, 1978; Figure 3B).

In a recent *in vivo* study, ChC activity in the primary visual cortex (V1) has been shown to be associated with pupillary dilation and locomotion (Schneider-Mizell et al., 2021; Figure 3C). V1 ChCs of Vipr2-IRES2-Cre mice were selectively labeled by their expression of genetic marker Vipr2 and virally expressed with GCaMP6f. Head-fixed mice were exposed to a screen of uniform luminance and allowed to behave spontaneously. ChCs demonstrated seconds-long coordinated activity in which all recorded ChCs were concurrently activated, and these episodes of coordinated activity were strongly correlated with episodes of pupillary dilation during locomotion, which is known to be a proxy for arousal states (McGinley et al., 2015; Reimer et al., 2016). Therefore, these results suggest that coordinated ChC population activity is associated with naturally occurring states of high arousal marked by pupillary dilation during locomotion.

In another *in vivo* study, ChCs in the binocular zone (BZ) of V1 have been shown to play an important developmental role in binocular vision by undergoing massive apoptosis in response to retinal and callosal activity (Wang et al., 2021; Figure 3D). V1 ChCs of Nkx2.1-CreER:Ai14 mice were selectively labeled by tamoxifen administration during pregnancy. The proper developmental elimination of ChCs at the BZ through apoptosis was shown to be mediated by transcallosal inputs from the contralateral visual cortex and pre-vision retinal activity. When the proper elimination of ChCs was prevented by suppressing transcallosal inputs, BZ neurons displayed a significantly reduced responsiveness to stimulation of the ipsilateral eye, resulting in a contralateral eye-dominated V1 and deficient binocular vision, as shown by impaired depth perception. Therefore, these results suggest the crucial role of ChC elimination at the BZ in the proper development of binocular vision.

ChC activity in the basolateral amygdala (BLA) has been shown to increase in response to noxious stimuli (Bienvenu et al., 2012). In an *in vivo* study, the activity of single BLA ChCs of rats was recorded while pinches and electrical shocks were delivered to the contralateral hindpaw. In response to the stimuli, ChCs consistently and dramatically increased their firing rates with short latency, which rapidly adapted and curtailed upon stimulus offset. The BLA is known to cooperate with the hippocampus to regulate the formation of emotional memories (Maren and Fanselow, 1995; Richardson et al., 2004).

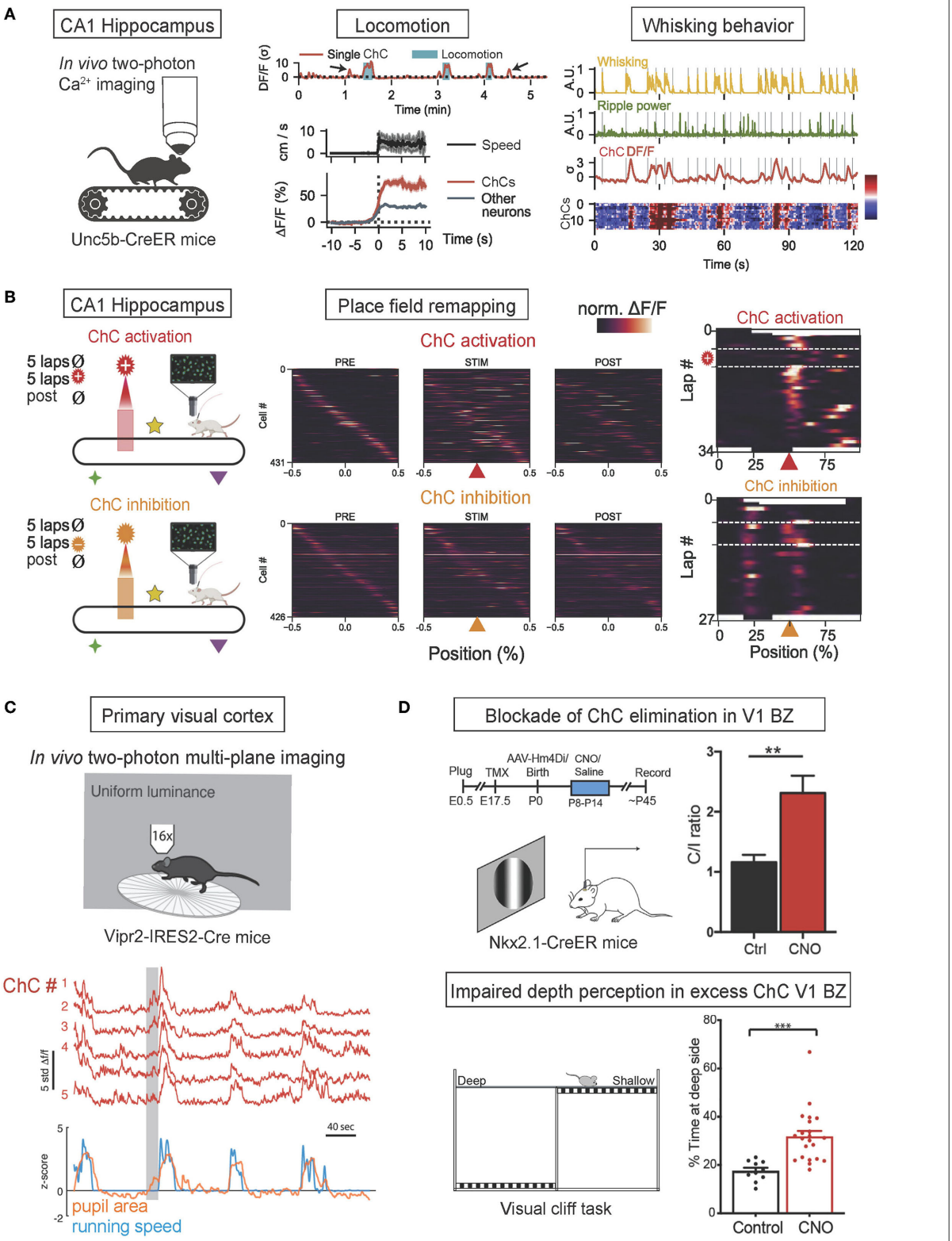

FIGURE 3
In vivo functions of ChCs during behavior. **(A)** *In vivo* two-photon calcium imaging of ChC activity in ChC-specific Unc5b-CreER mice on a treadmill. The increase of ChC activity in the CA1 hippocampus is associated with the onset of locomotion and whisking behavior. The

(Continued)

FIGURE 3 (Continued)
concurrence of increased ChC activation (higher than other neurons) with greater running speed and higher frequency of whisking. Adapted from Dudok et al. (2021). **(B)** Simultaneous two-photon calcium imaging and spatially-locked optogenetic manipulation of CA1 ChCsl. Head-fixed Unc5b-CreER mice were allowed to run on a cue-rich treadmill (PRE), then photostimulation was applied in a fixed spatial location on the treadmill (STIM), and finally, the mice ran with no manipulation (POST). Spatial tuning curves of PyN place cells during PRE, STIM, and POST phases demonstrated that optogenetic ChC activation with ChRmine expression suppressed in-field activity of place cells (top), exhibiting the transient loss of place fields while ChC silencing with eNpHR expression induced novel place fields (bottom). Adapted from Dudok et al. (2021). **(C)** *In vivo* two-photon calcium imaging of ChC activity in ChC-specific Vipr2-IRES-Cre mice. Coordinated activity of ChCs in the V1 in freely behaving mice subjected to a uniform luminance visual stimulus was correlated with increased pupillary dilation during locomotion, a proxy for the state of arousal. Adapted from Schneider-Mizell et al. (2021). **(D)** Blockade of ChC elimination in the V1 binocular zone (BZ) results in deficient binocular vision. Timeline of experiments and neuronal responses in ChC-excess V1 (top). Clozapine-N-oxide (CNO) was applied to the V1 during P8-P14 to block ChC elimination at ∼P30, resulting in excess ChC and shifting contralateral/ipsilateral responses ratio (C/I ratio) in CNO-treated mice. Schematic of visual cliff test for binocularly guided visual behavior (bottom). CNO-treated mice spend more time over at the deep side, suggesting deficits in binocular vision in excess-ChC V1 mice. $^{**}p < 0.01$, $^{***}p < 0.001$. Adapted from Wang et al. (2021).

Therefore, these results suggest that the activity of ChCs is involved in the process of emotional memory formation.

ChC activity in the prelimbic cortex was also shown to increase in response to noxious stimuli (Massi et al., 2012). In an *in vivo* study, the activity of prelimbic ChCs of rats was recorded while their tails were pinched. In response to the stimuli, ChCs increased their firing rates, accompanied by a switch in brain state from slow to theta oscillations. In contrast, the average firing rates of BC and PyN populations in the mPFC were unaffected by the stimuli. These results suggest the inhibitory role of ChCs in counteracting the impact of excitatory inputs from cortical and subcortical areas to allow firing only by the most excited PyNs (Massi et al., 2012).

Role of ChCs in neural coding

By virtue of its strategic, exclusive connectivity onto the AIS of PyNs where the action potential is generated with the highest likelihood after diverse somatodendritic excitatory inputs arrived at the soma, ChCs have been generally thought to exert an effective inhibitory control on PyN outputs (Somogyi, 1977). ChCs effectively inhibit the firing of PyN or delay spike generation by 30 ms if ChC inhibition preceded PyN spiking by no more than 80 ms (Veres et al., 2014).

While PV-basket cell and PyNs connectivity are extensively reciprocal and largely non-selective, ChC-PyNs connectivity is directional and highly selective (Lu et al., 2017). In addition to the difference in connectivity to PyN populations, computational and experimental studies suggested that ChC inhibition effectively controls the threshold for action potential generations in PyNs while BC inhibition controls the suprathreshold discharge (Douglas and Martin, 1990; Veres et al., 2014). It offers a mechanism for ChCs enhancing the signal-to-noise ratio in population activity in which small signals are blocked by ChC inhibition while larger signals are relatively unaffected. Recent *in vivo* studies showed that ChCs fire in synchrony during high arousal states (Dudok et al., 2021; Schneider-Mizell et al., 2021). Given that the AIS of a single PyN receives the summed inhibitions from the afferent axons of multiple ChCs (Tamás and Szabadics, 2004; Veres et al., 2014), the synchronized ChC inputs can efficiently veto action potential generation in PyNs receiving moderate excitatory inputs, leaving out selective PyN activity receiving strong excitatory inputs. Since a single ChC can delay spike generation by 10–30 ms (Veres et al., 2014), ChCs provide the ability to regulate spike timing-dependent plasticity by controlling the precise time of PyN spiking. In addition, activity-dependent plasticity in ChC-PyN connections offers a mechanism to set a threshold of action potential generations as a function of individual neurons' excitability (Grubb and Burrone, 2010; Kuba, 2012; Wefelmeyer et al., 2015). These functions of ChCs may suggest its role in shaping neuronal outputs at the population level and selecting neuronal ensembles to route information flow dynamically.

Properties of synaptic and neuromodulatory inputs to ChCs are also important to understanding the impacts of ChCs on PyN population activity. L2 ChCs exhibit predominant apical L1 dendrites and electrical stimulation of layer 1 recruits ChC-mediated feedforward inhibition on L2/3 PyNs (Woodruff et al., 2011). Major sources of L2 ChCs include sparse local excitatory inputs and more diverse sources from local inhibitory neurons, the thalamic nuclei implicated in working memory and behavioral flexibility (Parnaudeau et al., 2013) such as the mediodorsal, anteromedial, and ventromedial thalamic nuclei, and the cholinergic inputs from the basal forebrain associated with arousal (Jiang et al., 2015; Lu et al., 2017). These inputs innervate the predominant apical layer 1 dendrites of ChCs, providing top-down, highly processed information to ChCs depending on the behavioral state of the animal (Woodruff et al., 2011). Thus, L1 dendritic integrations and feedforward inhibitory control of PyN population in ChCs can be regarded as an important computational unit for providing state-dependent top-down control on the formation and dynamics of neuronal assemblies in cortical networks.

The balance of excitatory and inhibitory inputs received by a neuron plays an important role in neural circuit homeostasis and information processing in cortical networks (Vreeswijk

and Sompolinsky, 1996; Shu et al., 2003; Rubin et al., 2017), and disruption of the balance is strongly associated with pathological and dysfunctional brain states including epilepsy, autism spectrum disorder, and schizophrenia (Yizhar et al., 2011; Denève and Machens, 2016). The excitatory-inhibitory (E/I) balance is referred to as the equal average amounts of depolarizing and hyperpolarizing synaptic membrane currents (Vogels et al., 2011). If a neural network is considered globally balanced, each neuron receives large but approximately equal amounts of excitatory and inhibitory inputs that result in relatively small fluctuations in total synaptic input by canceling each other. Experimental observations suggested that excitation and inhibition are globally balanced in cortical circuits (Shu et al., 2003; Haider, 2006; Iascone et al., 2020).

Given that ChCs are strategically positioned to exert powerful and selective control over outputs of PyN population (Veres et al., 2014; Blazquez-Llorca et al., 2015; Lu et al., 2017), ChCs have been suggested to ultimately contribute to keeping network excitability from going out of control by maintaining proper E/I balance. Indeed, whole-cell *in vivo* recordings revealed that ChCs, which have a low spontaneous firing rate, fire more robustly than other cortical neurons when the overall cortical excitation increases (Zhu et al., 2004). Axon terminals of ChCs are lost at the cortical epileptic foci, suggesting that disruption of ChC function contributes to the hyperexcitability of the network (Ribak, 1985). While the role of ChCs in maintaining global E/I balance serves a homeostatic function in the brain (Figure 4A), it remains elusive how ChCs contribute to dynamic information processing which is highly relevant to healthy cognition and many neuropsychiatric symptoms. Here we review a potential link between ChC and neural coding.

Percepts and memories are thought to be represented in the neuronal population by the activity of PyN ensembles often called excitatory "engrams." The inhibitory engrams have been proposed as "negative images" or "inhibitory representation" for associative memory storage and recall (Barron et al., 2017; Figure 4B). The inhibitory engrams can be constructed in neural networks by E/I balance through homeostatic mechanisms that maintain a balance of depolarizing and hyperpolarizing currents in a neuron despite plastic changes across neurons and synapses. Plasticity of inhibitory synapses has been experimentally and theoretically proposed as a critical mechanism to create the inhibitory engrams that counterbalance new, unbalanced excitatory patterns that arise within neural networks in response to experience (Tao and Poo, 2005; Froemke et al., 2007; Vogels et al., 2011; Hennequin et al., 2017). Such experience-dependent inhibitory synaptic plasticity has been suggested to underlie precise E/I balance in time and space (Hennequin et al., 2017): the E/I balance is said to be tight if excitation and inhibitory inputs to a single neuron balance each other on fast timescales (Vogels et al., 2011; Denève and Machens, 2016) and said to be detailed if spatial patterns of excitation and inhibitory inputs to a single neuron balance each other (Vogels and Abbott, 2009). Previous experimental studies suggest that precise E/I balance provides precision and efficiency in cortical neural coding (Wehr and Zador, 2003; Isaacson and Scanziani, 2011; Zhou and Yu, 2018). Theoretical works have suggested that precise E/I balance confers the ability of neurons to gate multiple signals as a more efficient way to select for relevant features rather than suppressing all irrelevant inputs (Vogels and Abbott, 2009; Ferguson and Gao, 2018), which is consistent with the suggested role of ChC in enhancing the signal-to-noise ratio in that weak signals are blocked by AIS inhibition while strong signals pass relatively unaffected (Douglas and Martin, 1990).

Experimental evidence has suggested that ChCs play a role in controlling cell-by-cell level inhibition within a network. High variability in the number of ChC pre-synaptic inputs on the AIS of PyN has been reported in cats (Fairén and Valverde, 1980), monkeys (DeFelipe et al., 1985), and mice (Wang and Sun, 2012; Veres et al., 2014; Schneider-Mizell et al., 2021). A recent electron-microscopic study suggested that ChCs formed synapses with nearly all PyNs in L2/3 and the strength of ChC synapses adjusted for individual target cells according to cell-specific structural factors: the number of ChC synapses positively correlates with the properties of individual target cells such as the physical size of the cell and the amount of somatic inhibition (Schneider-Mizell et al., 2021), which is consistent with the notion that ChCs may provide a different degree of inhibition across individual cells to match their inputs. Furthermore, previous studies suggest that the plasticity of axo-axonic synapses at the AIS is activity-dependent (Grubb and Burrone, 2010; Kuba et al., 2010; Kuba, 2012). Presynaptic activity regulates intrinsic excitability at AIS and structural tuning of the AIS, which fine-tune neuronal excitability (Kuba et al., 2010; Kuba, 2012). In hippocampal PyNs, the increased neuronal activity causes a distal shift of the AISs, which reduces their excitability (Grubb and Burrone, 2010). In auditory neurons in birds, AISs are short and remote when synaptic inputs are strong while the AISs elongate to increase their excitability when synaptic inputs are deprived (Kuba et al., 2010; Kuba, 2012). Although activity-dependent development of GABAergic synapses has been observed in dendrites of developing brains (Oh et al., 2016; Oh and Smith, 2018), activity-dependent mechanisms for inhibitory synapse plasticity at AIS are not yet clear. However, given the strategic position of ChCs in mediating cell-to-cell level inhibition on PyN populations and activity-dependent plasticity of axo-axonic synapses, structural and functional plasticity of ChC axo-axonic synapses can be of great interest in mediating inhibitory representations and explaining key features of cognition. The potential roles of cortical ChCs in mediating detailed E/I balance may be especially important in high-level executive functions such as working memory, attentional selection, planning, and decision-making, which entail a large capacity for effective and dynamic control of signal flow in the prefrontal circuitry receiving multimodal inputs from various sensory areas, limbic areas, and

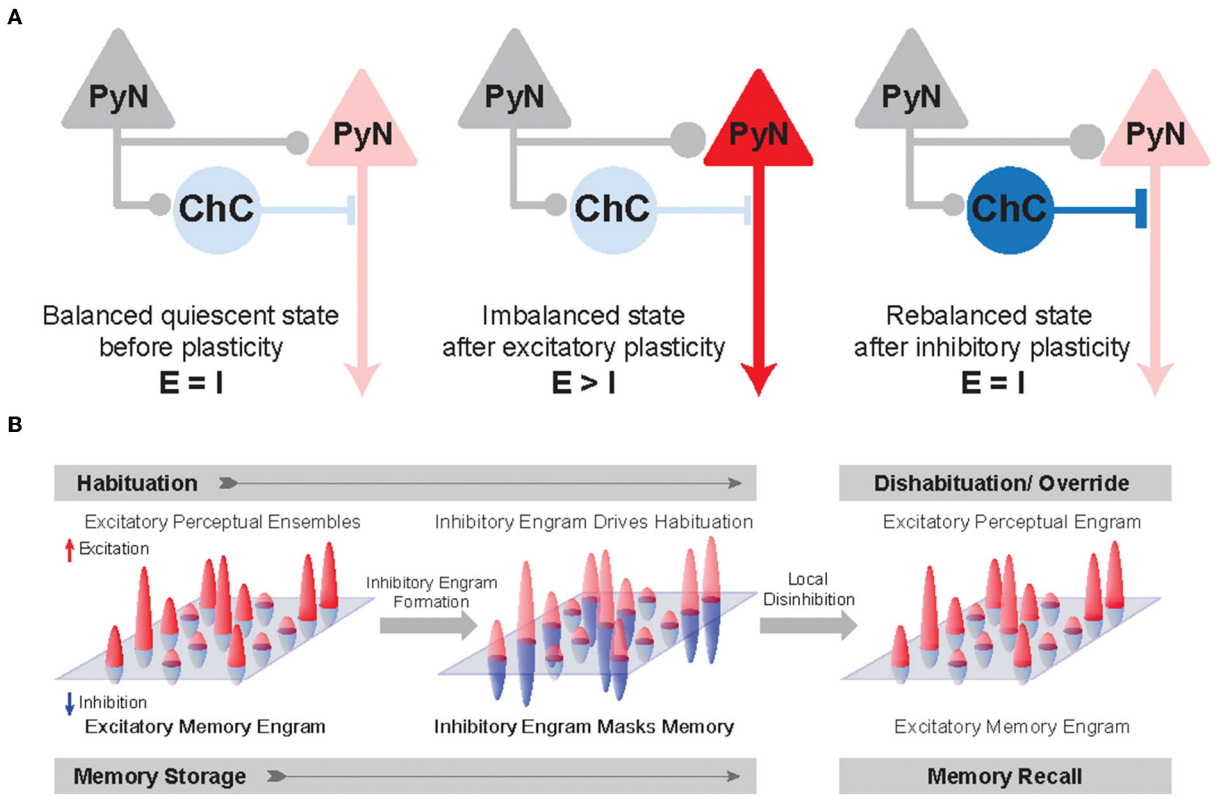

FIGURE 4
Inhibitory synapse plasticity for E/I rebalancing and inhibitory engram formation in perception and memory. **(A)** Schematic circuit diagram showing pre-synaptic PyNs (gray), post-synaptic PyNs (red), and ChCs (blue). The post-synaptic PyN receives balanced excitatory and inhibitory inputs (Balanced quiescent state). The effect of excitatory plasticity between pre- and post-synaptic PyNs initially leads to E/I imbalance (Imbalanced state). Inhibitory plasticity in axo-axonic synapses between ChCs and PyNs can subsequently restore E/I balance following excitatory plasticity (Rebalanced state). **(B)** A hypothetical framework of inhibitory engrams in perception and memory. Positive red and negative blue peaks represent excitatory and inhibitory inputs, respectively, onto an array of post-synaptic PyNs. These peaks constitute excitatory and inhibitory engrams, respectively. Regarding habituation, experiencing novel stimuli result in excitatory perceptual ensembles, but trigger relatively weak or imprecise inhibition. Repeated experiences result in the formation of a matched inhibitory engram that reduces the response and drives behavioral habituation. Regarding the memory process, memory is first encoded as excitatory engrams. Repeated experience results in the formation of matched inhibitory engrams to rebalance the array of post-synaptic PyNs. The formation of these inhibitory memory engrams may occur *via* homeostatic potentiation of inhibition onto post-synaptic PyNs that show increased levels of excitation. Inhibitory engrams allow flexible yet stable memory storage in a latent form for context-appropriate recall, which is hypothesized to occur through focused disinhibition. Adapted from Barron et al. (2017).

neuromodulatory nuclei. Future *in vivo* experiments would be important to examine how ChCs facilitate the precision and efficiency of cortical neural codes.

Schizophrenia and pathophysiology of ChCs

Schizophrenia is a psychiatric disorder that is associated with cognitive symptoms such as delusion, hallucinations, and disorganized thought (Elvevag and Goldberg, 2000; Telles-Correia et al., 2016). Specifically, cognitive dysfunctions in schizophrenia consist of overarching deficits in the ability to adjust thoughts or behaviors in a manner to achieve goals (Cho et al., 2006; Lesh et al., 2011). The dorsolateral prefrontal cortex (DLPFC) is the main site of aberrant electrophysiological activity reflecting neuronal network dysfunction in schizophrenia (Cho et al., 2006; Minzenberg et al., 2009). A reduction in excitation of the L3 DLPFC PyN populations has been known as a salient pathology of schizophrenia (Lewis et al., 2012), indicating a disrupted state of E/I balance. Such dysfunctions in schizophrenia are thought to be related to alterations in the inhibitory circuitry of the PFC resulting from pathological cellular changes of cortical GABAergic interneurons (Tanaka, 2008; Lewis et al., 2012; Selten et al., 2018). Recently, as emerging evidence suggests that disruption in E/I balance and interneuron dysfunction are shared for pathophysiological mechanisms of psychiatric disorders (Yizhar et al., 2011; Xu and

Wong, 2018; Shaw et al., 2020), interest in the contribution of ChCs to proper circuit function in disease has been growing (Wang et al., 2016; Gallo et al., 2020). The neocortical ChC is one of the critical interneuron types that have been closely associated with schizophrenia, since cellular changes in the ChC's molecular composition, GABAergic signaling, and axon terminal structure have been rigorously documented in post-mortem schizophrenic human subjects (Pierri et al., 1999; Volk et al., 2002; Hashimoto et al., 2003, 2008; Rocco et al., 2016, 2017; Schoonover et al., 2020). Given the possibility that ChCs may be the neural substrate of precisely maintaining E/I balance required for proper information flow in the PFC, pathological alterations of ChCs may be directly linked to the cognitive symptoms displayed in schizophrenia. Here we review the current understanding of the molecular and structural alterations of ChCs in schizophrenia.

ChCs were shown to display pre- and post-synaptic molecular alterations suggesting an increase in ChC-mediated inhibition on PyNs. First, the density of GABA transporter type 1 (GAT-1) has been reported to be significantly reduced on the axon terminal cartridges of ChCs in layers 2 to 4 in the DLPFC (Pierri et al., 1999; Volk et al., 2002; Figure 5A). Since GAT-1 is responsible for the clearance of GABA from the synaptic cleft and reduction in GAT-1 function at perisomatic synapses of DLPFC PyNs is known to prolong GABA-A receptor-mediated IPSPs (Gonzalez-Burgos et al., 2009), the effect of pre-synaptic GAT-1 density reduction in layers 2–4 is thought to be an increase in ChC-mediated inhibition on PyNs. Second, the density of GABA-A α2-subunit receptors increased on the post-synaptic AISs of PyNs in supragranular layers of DLPFC in schizophrenia, with the greatest increase shown in L2 (Volk et al., 2002; Figure 5A). Furthermore, the mRNA expression level of GABA-A α2-subunit was 14% higher in L2 of DLPFC in schizophrenia (Beneyto et al., 2011). These post-synaptic alterations of GAT-1 and GABA-A α2-subunit receptors at AISs suggest an increase in ChC-mediated inhibition on PyNs in the DLPFC in schizophrenia. It is noteworthy that these molecular alterations were not shared in other psychiatric disorders such as major depression disorder (Volk et al., 2002), indicating the distinct role of this pathophysiology in schizophrenia.

Given the general classification of ChCs as PV-INs, the specific role of ChCs in schizophrenia was obscured by observations of decreased expression of glutamic acid decarboxylase 67 (GAD67) involved in GABA synthesis in PV-INs in schizophrenia (Hashimoto et al., 2003). However, similar expression levels of GAD67 in ChCs between schizophrenia and healthy subjects (Rocco et al., 2016) differentiate their effect from the effect of GAD67 reduction shown in PV-INs. Indeed, in schizophrenia (Curley et al., 2011), PV-BC synaptic boutons in the DLPFC showed decreased levels of GAD67, suggesting that PV-BC-mediated inhibition is decreased. Thus, these results may suggest that ChCs and PV-BCs contribute to different pathophysiology of the DLPFC in schizophrenia: ChCs exert excessive inhibition on PyNs while PV-BCs may decrease inhibition to compensate for the PyN excitability. In addition, it is noteworthy that L2/3 PyNs in the DLPFC display a reduced density of dendritic spines (Lewis et al., 2012; Glausier and Lewis, 2013), reflecting a reduction in excitatory drive from upstream areas. This dendritic alteration in PyNs may also contribute to disrupted E/I balance within the DLPFC recurrent network of schizophrenia.

ChCs were shown to display structural alterations in their axonal terminals in schizophrenia. A recent study investigated the change in density of ChC cartridges in schizophrenia by taking immunopositivity to vesicular GABA transporter (vGAT) as the accurate measure for true cartridge count (Rocco et al., 2017) since neither vGAT mRNA expression level nor the level of vGAT per individual axonal bouton is affected in the DLPFC of schizophrenia (Rocco et al., 2016). It was shown that the density of ChC cartridges in schizophrenia is significantly increased in L2 of DLPFC while the number of boutons per cartridge is unaffected (Rocco et al., 2017), suggesting that ChCs may innervate a greater number of PyNs and exert greater inhibitory control over PyN populations in schizophrenia. Furthermore, the increase in ChC cartridge density in the L2 DLPFC was specific to those cartridges that expressed calbindin (CB) (Rocco et al., 2017), which is thought to be heterogeneously expressed in ChC cartridges (Rio and DeFelipe, 1997). Future studies will need to investigate the functional role of CB+ ChC cartridges in schizophrenia and the role of CB in regulating the development of ChC cartridges.

The involvement of PV-INs in schizophrenia has been suggested by numerous observations of altered gamma-band oscillations (Figure 5B), which are correlated with working memory load (Howard et al., 2003). Gamma oscillations have been shown to be lower powered in the frontal lobe of schizophrenia patients during cognitive control tasks (Cho et al., 2006). In contrast, more recent evidence has shown that, in medication-naïve, first-episode, chronic schizophrenic patients, gamma-band power is elevated in the resting state (Kikuchi et al., 2011). However, although PV-INs are thought to give rise to gamma oscillations (Bartos et al., 2007; Gonzalez-Burgos and Lewis, 2008; Sohal et al., 2009), the status of ChCs as PV-INs and the involvement of ChCs in gamma oscillations is unclear (Bartos et al., 2007; Tukker et al., 2007). Thus, abnormal gamma oscillations in schizophrenia may not reflect dysfunction of ChCs but that of PV-BCs, which comprise the majority of PV-INs.

Accumulating evidence suggests that ChCs in schizophrenia exert excessive inhibition on PyNs. The dysfunction of ChCs in schizophrenia likely has a contributory role by overly reducing the excitatory activity of PyN ensembles and in turn disrupting E/I balance (Figure 5B). Given that precise E/I balance in PyN ensembles allows for proper precise neural coding and executive cognitive function in the DLPFC, ChCs may have a far more

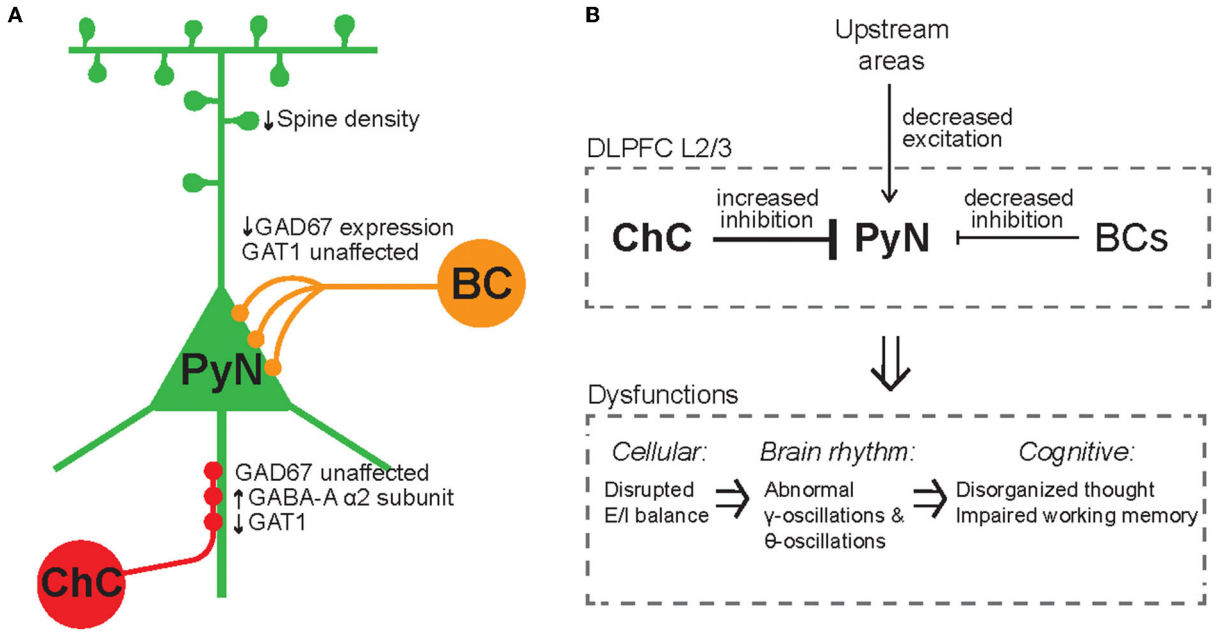

FIGURE 5
Synaptic alterations of ChCs, BCs, and PyNs in schizophrenia. **(A)** Schematic of molecular and cellular alterations of ChCs, BCs, and PyNs in schizophrenia. In ChCs, GAD67 levels in terminals are unaffected, post-synaptic GABA-A α2-subunit receptor density is increased, pre-synaptic GAT1 density is reduced, and ChC cartridge density increases. ChC-related alterations correspond to an increase in inhibition on PyNs. In BCs, GAT67 levels are decreased, suggesting a decrease of BC-mediated inhibition on PyNs. In PyNs, dendritic spine density is reduced, resulting in lower levels of excitatory drive. **(B)** GABAergic interneuron-related pathophysiology in schizophrenia. ChC-related alterations reflect an increased inhibition on PyNs, and PyNs receive lower levels of excitatory drive from upstream areas, resulting in reduced excitability of PyNs and disruption of E/I balance. BC-related alterations reflect a decrease in inhibition on PyNs.

salient role in the cognitive dysfunction of schizophrenia than previously thought.

Summary/conclusion

Despite the diversity of GABAergic interneuron types that are thought to underlie various cortical processes and complex behaviors, the specific role of single-type interneurons remains elusive. Here we reviewed the ChC, a single-type GABAergic interneuron, in regard to the structural and functional roles of ChCs in brain circuit and neural coding and their dysfunction in neuropsychiatric conditions.

The morphology and input/output connectivity features of ChCs contribute to their functional role in neural coding. Cortical ChCs can integrate by receiving excitatory local and long-range input and cholinergic input from the basal forebrain through their apical dendrites in Layer 1 and electrically couple the activity of ChCs *via* gap junction. The iconic chandelier-like axonal arborization of ChCs exclusively innervates the AIS of neighboring PyNs, where ChCs provide efficient inhibitory control to the site of action potential generation. These structural features can provide strategic, temporally-organized inhibitory control of PyN populations based on brain states or tasks.

We reviewed the neuroplasticity of ChC axo-axonic synapses with respect to development, cholinergic modulation, and pre-synaptic molecules, which can regulate their axonal growth. A developmental pattern and a cell-adhesion molecule can regulate the target specificity of axo-axonic synapses. In addition, the parallel time course of axo-axonic synapse density with PyN excitability during development suggests the role of ChC in maintaining E/I balance in the cortical network. The variability in axo-axonic synaptic strengths positively correlates with features of target PyNs including soma location, size, and perisomatic inhibition. Given the remarkable developmental and activity-dependent plasticity of axo-axonic synapses, future studies will need to identify other molecular and neuromodulatory control mechanisms of ChC target specificity and variability of axo-axonic synaptic strengths, which are essential for the proper assembly of the cortical circuit and dynamic information processing, respectively.

ChC function depends on their electrophysiology and post-synaptic responses to their GABAergic signaling. Despite their fast-spiking property, heterogeneity in membrane properties

of ChCs is found across different brain regions such as the neocortex and hippocampus, suggesting their diverse contributions to their embedded network and coding. We compared the electrophysiological features of two fast-spiking cell types, ChCs and PV-BCs, and discussed factors that may contribute to differences in their firing properties. To discern their controversial GABAergic synaptic effect, we examined *in vitro* and *in vivo* evidence of depolarizing and hyperpolarizing effects made by ChC synapses. Although several explanations have been provided for the excitatory effects of ChCs *in vitro*, emerging *in vivo* studies with ChC-specific manipulations have revealed their inhibitory effect in free-behaving adult animals. However, developmental factors and neuromodulation-dependent brain states need to be considered to understand the specific role of ChC synaptic effects. Therefore, systematic future *in vivo* studies using ChC-specific genetic markers across different developmental stages and brain states would clarify the functional features of ChCs in the post-synaptic PyN activity.

As brain rhythms indicate highly coordinated neuronal activity underlying cognitive states and behavior, we compared distinct temporal coupling of ChCs and BCs to gamma and theta oscillations. Factors such as GABA-A receptor subunit composition, state-dependent cholinergic modulation, and distinct wiring features may account for their differential contributions to gamma and theta oscillations and functional implications to PyN network activity. Recent *in vivo* studies of genetically targeting ChCs in various brain regions revealed that the activity of ChCs represents arousal states and displays strong responsiveness to salient stimuli. ChC-specific manipulation showed its direct inhibitory influence on behavioral functions of target neurons. ChC activity may actively process salient information to selectively recruit the most relevant PyN ensembles, which in turn facilitate the corresponding behaviors. The previously enigmatic behavioral functions of ChCs have been gradually unmasked through recent advancements in ChC-specific genetic labeling, optogenetics, and *in vivo* recording techniques. Yet, the active role of ChCs during cognitive tasks has not been demonstrated in the PFC where cognitive deficits are seen in schizophrenia. Future studies will need to investigate the higher-level cognitive functions of ChCs.

We discussed how ChCs shape neuronal outputs at the population level and select neuronal ensembles to route information flow dynamically. Directional and cooperative ChC-PyNs connectivity allows ChC to control the threshold for generating PyN action potentials and regulating the temporal precision of PyN spiking. This enhances the signal-to-noise ratio in PyN population codes and provides the ability to limit temporal windows for spike timing-dependent plasticity, which is necessary for shaping neural codes. Activity-dependent plasticity in ChC-PyN connections offers a mechanism to set a threshold of action potential generations as a function of individual neurons' excitability. Given the importance of E/I balance for neural circuit homeostasis and information processing, theoretical perspectives of experience-dependent plasticity of inhibitory synapses for precise E/I balance will be useful to understand how ChCs may gate multiple signals and facilitate associative memory processes through inhibitory engrams. As an underlying cellular mechanism, we discussed the activity-dependent plasticity of axo-axonic synapses that enables fine-tuned inhibition to match excitability. Thus, cell-to-cell level ChC-mediated inhibition and their activity-dependent plasticity may offer a mechanism for constructing behaviorally relevant inhibitory representations. Future *in vivo* experiments would be important to examine how cortical ChCs facilitate effective and dynamic control of information flow with precision for high-level executive functions during health and disease.

We reviewed the pathophysiological changes of ChCs in schizophrenia. Both molecular and structural alterations of ChCs in schizophrenia exert excessive inhibition on DLPFC PyNs, which may underlie cognitive deficits of schizophrenia such as disorganized thought. PV-BCs in the DLPFC appear to undergo cellular changes in schizophrenia that result in the opposite pathophysiology to ChCs: decreased inhibition of PyNs. ChC-related changes in schizophrenia seem to display laminar-specificity to the superficial layers. Although gamma oscillations have been shown to be altered in schizophrenia, the specific contribution of ChCs to gamma oscillations is unclear. Future studies will need to investigate the differential roles of laminar-specific ChCs and their involvement in altered brain activity.

In conclusion, significant progress in the research of GABAergic interneuron transcriptomic profiles, developmental biology, and functions has allowed us to recognize the association between cell-type specific dysfunction and neural disorders. While emerging evidence suggests that pathophysiological mechanisms of psychiatric disorders include disrupted E/I balance and interneuron dysfunction as shared features, we cannot fully understand diverse dysfunctional cognition or behavior without understanding the specific role of each interneuron type in neural coding. Recent *in vivo* studies with genetic targeting of ChCs have provided insights into the distinctive roles of single-type interneurons in neural computation, dissecting the complex functions of GABAergic interneurons. Future research needs to address how neocortical ChCs adaptively orchestrate dynamic PyN activity *via* axo-axonic synaptic plasticity for information processing during cognitive tasks, and what genetic or molecular factors cause defects in the development and functions of axo-axonic synapses in disease. Such efforts are crucial to specify pathophysiology and design effective therapeutic approaches. Strategy and knowledge gained from ChC studies may be utilized as a benchmark to unveil specific contributions of diverse GABAergic interneurons to circuit

wiring and neural coding in health and disease at single cell-type precision.

Data availability statement

The original contributions presented in the study are included in the article/supplementary material, further inquiries can be directed to the corresponding author.

Author contributions

KJ and YC did literature search and wrote the manuscript draft. KJ, YC, and H-BK edited the manuscript. All authors contributed to the article and approved the submitted version.

Funding

This work was supported by Johns Hopkins School of Medicine (to H-BK) and DP1MH119428 (to H-BK).

Acknowledgments

We thank members of the Kwon Laboratory for helpful discussions.

Conflict of interest

The authors declare that the research was conducted in the absence of any commercial or financial relationships that could be construed as a potential conflict of interest.

Publisher's note

References

Acsády, L., Görcs, T. J., and Freund, T. F. (1996). Different populations of vasoactive intestinal polypeptide-immunoreactive interneurons are specialized to control pyramidal cells or interneurons in the hippocampus. *Neuroscience* 73, 317–334. doi: 10.1016/0306-4522(95)00609-5

Anderson, S. A., Classey, J. D., Condé, F., Lund, J. S., and Lewis, D. A. (1995). Synchronous development of pyramidal neuron dendritic spines and parvalbumin-immunoreactive chandelier neuron axon terminals in layer III of monkey prefrontal cortex. *Neuroscience* 67, 7–22. doi: 10.1016/0306-4522(95)00051-J

Andrási, T., Veres, J. M., Rovira-Esteban, L., Kozma, R., Vikór, A., Gregori, E., et al. (2017). Differential excitatory control of 2 parallel basket cell networks in amygdala microcircuits. *PLoS Biol.* 15, e2001421. doi: 10.1371/journal.pbio.2001421

Ballinger, E. C., Ananth, M., Talmage, D. A., and Role, L. W. (2016). Basal forebrain cholinergic circuits and signaling in cognition and cognitive decline. *Neuron* 91, 1199–1218. doi: 10.1016/j.neuron.2016.09.006

Barron, H. C., Vogels, T. P., Behrens, T. E., and Ramaswami, M. (2017). Inhibitory engrams in perception and memory. *Proc. Natl. Acad. Sci. U.S.A.* 114, 6666–6674. doi: 10.1073/pnas.1701812114

Barsy, B., Szabó, G. G., Andrási, T., Vikór, A., and Hájos, N. (2017). Different output properties of perisomatic region-targeting interneurons in the basal amygdala. *Eur. J. Neurosci.* 45, 548–558. doi: 10.1111/ejn.13498

Bartos, M., Vida, I., and Jonas, P. (2007). Synaptic mechanisms of synchronized gamma oscillations in inhibitory interneuron networks. *Nat. Rev. Neurosci.* 8, 45–56. doi: 10.1038/nrn2044

Behrends, J. C., and Bruggencate, G. (1993). Cholinergic modulation of synaptic inhibition in the guinea pig hippocampus *in vitro*: excitation of GABAergic interneurons and inhibition of GABA-release. *J. Neurophysiol.* 69, 626–629. doi: 10.1152/jn.1993.69.2.626

Beierlein, M., Gibson, J. R., and Connors, B. W. (2000). A network of electrically coupled interneurons drives synchronized inhibition in neocortex. *Nat. Neurosci.* 3, 904–910. doi: 10.1038/78809

Beneyto, M., Abbott, A., Hashimoto, T., and Lewis, D. A. (2011). Lamina-Specific alterations in cortical GABAA receptor subunit expression in schizophrenia. *Cereb. Cortex* 21, 999–1011. doi: 10.1093/cercor/bhq169

BICCN (2021). A multimodal cell census and atlas of the mammalian primary motor cortex. *Nature* 598, 86–102. doi: 10.1038/s41586-021-03950-0

Bienvenu, T. C. M., Busti, D., Magill, P. J., Ferraguti, F., and Capogna, M. (2012). Cell-Type-Specific recruitment of amygdala interneurons to hippocampal theta rhythm and noxious stimuli *in vivo*. *Neuron* 74–20, 1059–1074. doi: 10.1016/j.neuron.2012.04.022

Blatow, M., Rozov, A., Katona, I., Hormuzdi, S. G., Meyer, A. H., Whittington, M. A., et al. (2003). A novel network of multipolar bursting interneurons generates theta frequency oscillations in neocortex. *Neuron* 38, 805–817. doi: 10.1016/S0896-6273(03)00300-3

Blazquez-Llorca, L., Woodruff, A., Inan, M., Anderson, S. A., Yuste, R., DeFelipe, J., et al. (2015). Spatial distribution of neurons innervated by chandelier cells. *Brain Struct. Funct.* 220, 281722834. doi: 10.1007/s00429-014-0828-3

Buhl, E. H., Han, Z. S., Lorinczi, Z., Stezhka, V. V., Karnup, S. V., and Somogyi, P. (1994). Physiological properties of anatomically identified axo-axonic cells in the rat hippocampus. *J. Neurophysiol.* 71, 1289–1307. doi: 10.1152/jn.1994.71.4.1289

Buzsáki, G. (2002). Theta oscillations in the *Hippocampus*. *Neuron* 33, 325–340. doi: 10.1016/S0896-6273(02)00586-X

Carr, M. F., Karlsson, M. P., and Frank, L. M. (2012). Transient slow gamma synchrony underlies hippocampal memory replay. *Neuron* 75, 700–713. doi: 10.1016/j.neuron.2012.06.014

Cauli, B., Porter, J. T., Tsuzuki, K., Lambolez, B., Rossier, J., Quenet, B., et al. (2000). Classification of fusiform neocortical interneurons based on unsupervised clustering. *Proc. Natl. Acad. Sci. U.S.A.* 97, 6144–6149. doi: 10.1073/pnas.97.11.6144

Cho, R. Y., Konecky, R. O., and Carter, C. S. (2006). Impairments in frontal cortical γ synchrony and cognitive control in schizophrenia. *Proc. Natl. Acad. Sci. U.S.A.* 103, 19878–19883. doi: 10.1073/pnas.0609440103

Colgin, L. L., and Moser, E. I. (2010). Gamma oscillations in the hippocampus. *Physiology* 25, 319–329. doi: 10.1152/physiol.00021.2010

Csicsvari, J., Hirase, H., Mamiya, A., and Buzsáki, G. (2000). Ensemble patterns of hippocampal CA3-CA1 neurons during sharp wave–associated population events. *Neuron* 28, 585–594. doi: 10.1016/S0896-6273(00)00135-5

Curley, A. A., Arion, D., Volk, D. W., Asafu-Adjei, J. K., Sampson, A. R., Fish, K. N., et al. (2011). Cortical deficits of glutamic acid decarboxylase 67 expression

in schizophrenia: clinical, protein, and cell type-specific features. *Am. J. Psychiatry* 168, 921–929. doi: 10.1176/appi.ajp.2011.11010052

DeFelipe, J. (1999). Chandelier cells and epilepsy. *Brain* 122, 1807–1822. doi: 10.1093/brain/122.10.1807

DeFelipe, J., Hendry, S. H. C., Jones, E. G., and Schmechel, D. (1985). Variability in the terminations of GABAergic chandelier cell axons on initial segments of pyramidal cell axons in the monkey sensory-motor cortex. *J. Comp. Neurol.* 231, 364–384. doi: 10.1002/cne.902310307

Denève, S., and Machens, C. K. (2016). Efficient codes and balanced networks. *Nat. Neurosci.* 19, 375–382. doi: 10.1038/nn.4243

Disney, A. A., Domakonda, K. V., and Aoki, C. (2006). Differential expression of muscarinic acetylcholine receptors across excitatory and inhibitory cells in visual cortical areas V1 and V2 of the macaque monkey. *J. Comp. Neurol.* 499, 49–63. doi: 10.1002/cne.21096

Douglas, R. J., and Martin, K. A. C. (1990). Control of neuronal output by inhibition at the axon initial segment. *Neural Comput.* 2, 283–292. doi: 10.1162/neco.1990.2.3.283

Dudok, B., Szoboszlay, M., Paul, A., Klein, P. M., Liao, Z., Hwaun, E., et al. (2021). Recruitment and inhibitory action of hippocampal axo-axonic cells during behavior. *Neuron* 109, 3838–3850.e8. doi: 10.1016/j.neuron.2021.09.033

Dugladze, T., Schmitz, D., Whittington, M. A., Vida, I., and Gloveli, T. (2012). Segregation of axonal and somatic activity during fast network oscillations. *Science* 336, 1458–1461. doi: 10.1126/science.1222017

Elvevag, B., and Goldberg, T. E. (2000). Cognitive impairment in schizophrenia is the core of the disorder. *Crit. Rev. Neurobiol.* 14, 21. doi: 10.1615/CritRevNeurobiol.v14.i1.10

Engel, A. K., Fries, P., and Singer, W. (2001). Dynamic predictions: oscillations and synchrony in top–down processing. *Nat. Rev. Neurosci.* 2, 704–716. doi: 10.1038/35094565

Fairén, A., and Valverde, F. (1980). A specialized type of neuron in the visual cortex of cat: a golgi and electron microscope study of chandelier cells. *J. Comp. Neurol.* 194, 761–779. doi: 10.1002/cne.901940405

Favuzzi, E., Deogracias, R., Marques-Smith, A., Maeso, P., Jezequel, J., Exposito-Alonso, D., et al. (2019). Distinct molecular programs regulate synapse specificity in cortical inhibitory circuits. *Science* 363, 413–417. doi: 10.1126/science.aau8977

Fazzari, P., Paternain, A. V., Valiente, M., Pla, R., Luján, R., Lloyd, K., et al. (2010). Control of cortical GABA circuitry development by Nrg1 and ErbB4 signalling. *Nature* 464, 1376–1380. doi: 10.1038/nature08928

Ferguson, B. R., and Gao, W.-J. (2018). PV interneurons: critical regulators of E/I balance for prefrontal cortex-dependent behavior and psychiatric disorders. *Front. Neural Circuit* 12, 37. doi: 10.3389/fncir.2018.00037

Foehring, R. C., Brederode, J. F. M., van Kinney, G. A., and Spain, W. J. (2002). Serotonergic modulation of supragranular neurons in rat sensorimotor cortex. *J. Neurosci.* 22, 8238–8250. doi: 10.1523/JNEUROSCI.22-18-08238.2002

Fogarty, M., Grist, M., Gelman, D., Marin, O., Pachnis, V., and Kessaris, N. (2007). Spatial genetic patterning of the embryonic neuroepithelium generates GABAergic interneuron diversity in the adult cortex. *J. Neurosci.* 27, 10935–10946. doi: 10.1523/JNEUROSCI.1629-07.2007

Froemke, R. C., Merzenich, M. M., and Schreiner, C. E. (2007). A synaptic memory trace for cortical receptive field plasticity. *Nature* 450, 425–429. doi: 10.1038/nature06289

Fukudome, Y., Ohno-Shosaku, T., Matsui, M., Omori, Y., Fukaya, M., Tsubokawa, H., et al. (2004). Two distinct classes of muscarinic action on hippocampal inhibitory synapses: M2-mediated direct suppression and M1/M3-mediated indirect suppression through endocannabinoid signalling. *Eur. J. Neurosci.* 19, 2682–2692. doi: 10.1111/j.0953-816X.2004.03384.x

Gallo, N. B., Paul, A., and Aelst, L. V. (2020). Shedding light on chandelier cell development, connectivity, and contribution to neural disorders. *Trends Neurosci.* 43, 565–580. doi: 10.1016/j.tins.2020.05.003

Geiller, T., Vancura, B., Terada, S., Troullinou, E., Chavlis, S., Tsagkatakis, G., et al. (2020). Large-Scale 3D two-photon imaging of molecularly identified CA1 interneuron dynamics in behaving mice. *Neuron* 108, 968–983.e9. doi: 10.1016/j.neuron.2020.09.013

Glausier, J. R., and Lewis, D. A. (2013). Dendritic spine pathology in schizophrenia. *Neuroscience* 251, 90–107. doi: 10.1016/j.neuroscience.2012.04.044

Glickfeld, L. L., Roberts, J. D., Somogyi, P., and Scanziani, M. (2009). Interneurons hyperpolarize pyramidal cells along their entire somatodendritic axis. *Nat. Neurosci.* 12, 21–23. doi: 10.1038/nn.2230

Gonchar, Y., Wang, Q., and Burkhalter, A. (2008). Multiple distinct subtypes of GABAergic neurons in mouse visual cortex identified by triple immunostaining. *Front. Neuroanat.* 1, 3. doi: 10.3389/neuro.05.003.2007

González-Burgos, G., Krimer, L. S., Povysheva, N. V., Barrionuevo, G., and Lewis, D. A. (2005). Functional properties of fast spiking interneurons and their synaptic connections with pyramidal cells in primate dorsolateral prefrontal cortex. *J. Neurophysiol.* 93, 942–953. doi: 10.1152/jn.00787.2004

Gonzalez-Burgos, G., Kroener, S., Seamans, J. K., Lewis, D. A., and Barrionuevo, G. (2005). Dopaminergic modulation of short-term synaptic plasticity in fast-spiking interneurons of primate dorsolateral prefrontal cortex. *J. Neurophysiol.* 94, 4168–4177. doi: 10.1152/jn.00698.2005

Gonzalez-Burgos, G., and Lewis, D. A. (2008). GABA neurons and the mechanisms of network oscillations: implications for understanding cortical dysfunction in schizophrenia. *Schizophr. Bull.* 34, 944–961. doi: 10.1093/schbul/sbn070

Gonzalez-Burgos, G., Rotaru, D. C., Zaitsev, A. V., Povysheva, N. V., and Lewis, D. A. (2009). GABA transporter GAT1 prevents spillover at proximal and distal GABA synapses onto primate prefrontal cortex neurons. *J. Neurophysiol.* 101, 533–547. doi: 10.1152/jn.91161.2008

Gour, A., Boergens, K. M., Heike, N., Hua, Y., Laserstein, P., Song, K., et al. (2021). Postnatal connectomic development of inhibition in mouse barrel cortex. *Science* 371, ebb4534. doi: 10.1126/science.abb4534

Grosser, S., Barreda, F. J., Beed, P., Schmitz, D., Booker, S. A., and Vida, I. (2021). Parvalbumin interneurons are differentially connected to principal cells in inhibitory feedback microcircuits along the dorsoventral axis of the medial entorhinal cortex. *Eneuro* 8, 1–14. doi: 10.1523/ENEURO.0354-20.2020

Grubb, M. S., and Burrone, J. (2010). Activity-dependent relocation of the axon initial segment fine-tunes neuronal excitability. *Nature* 465, 1070–1074. doi: 10.1038/nature09160

Gulyás, A. I., Miles, R., Sik, A., Tóth, K., Tamamaki, N., and Freund, T. F. (1993). Hippocampal pyramidal cells excite inhibitory neurons through a single release site. *Nature* 366, 683–687. doi: 10.1038/366683a0

Gulyas, A. I., Szabo, G. G., Ulbert, I., Holderith, N., Monyer, H., Erdelyi, F., et al. (2010). Parvalbumin-Containing fast-spiking basket cells generate the field potential oscillations induced by cholinergic receptor activation in the hippocampus. *J. Neurosci.* 30, 15134–15145. doi: 10.1523/JNEUROSCI.4104-10.2010

Haider, B. (2006). Neocortical network activity *in vivo* is generated through a dynamic balance of excitation and inhibition. *J. Neurosci.* 26, 4535–4545. doi: 10.1523/JNEUROSCI.5297-05.2006

Hashimoto, T., Arion, D., Unger, T., Maldonado-Avilés, J. G., Morris, H. M., Volk, D. W., et al. (2008). Alterations in GABA-related transcriptome in the dorsolateral prefrontal cortex of subjects with schizophrenia. *Mol. Psychiatr.* 13, 147–161. doi: 10.1038/sj.mp.4002011

Hashimoto, T., Volk, D. W., Eggan, S. M., Mirnics, K., Pierri, J. N., Sun, Z., et al. (2003). Gene expression deficits in a subclass of GABA neurons in the prefrontal cortex of subjects with schizophrenia. *J. Neurosci.* 23, 6315–6326. doi: 10.1523/JNEUROSCI.23-15-06315.2003

Hennequin, G., Agnes, E. J., and Vogels, T. P. (2017). Inhibitory plasticity: balance, control, and codependence. *Annu. Rev. Neurosci.* 40, 557–579. doi: 10.1146/annurev-neuro-072116-031005

Hensch, T. K., and Fagiolini, M. (2005). Excitatory–inhibitory balance and critical period plasticity in developing visual cortex. *Prog. Brain Res.* 147, 115–124. doi: 10.1016/S0079-6123(04)47009-5

Howard, A., Tamas, G., and Soltesz, I. (2005). Lighting the chandelier: new vistas for axo-axonic cells. *Trends Neurosci.* 28, 310–316. doi: 10.1016/j.tins.2005.04.004

Howard, M. W., Rizzuto, D. S., Caplan, J. B., Madsen, J. R., Lisman, J., Aschenbrenner-Scheibe, R., et al. (2003). Gamma oscillations correlate with working memory load in humans. *Cereb. Cortex* 13, 1369–1374. doi: 10.1093/cercor/bhg084

Iascone, D. M., Li, Y., Sümbül, U., Doron, M., Chen, H., Andreu, V., et al. (2020). Whole-Neuron synaptic mapping reveals spatially precise excitatory/inhibitory balance limiting dendritic and somatic spiking. *Neuron* 106, 566–578.e8. doi: 10.1016/j.neuron.2020.02.015

Inan, M., Blázquez-Llorca, L., Merchán-Pérez, A., Anderson, S. A., DeFelipe, J., and Yuste, R. (2013). Dense and overlapping innervation of pyramidal neurons by chandelier cells. *J. Neurosci.* 33, 1907–1914. doi: 10.1523/JNEUROSCI.4049-12.2013

Inda, M., DeFelipe, J., and Muñoz, A. (2007). The distribution of chandelier cell axon terminals that express the GABA plasma membrane transporter GAT-1 in the human neocortex. *Cereb. Cortex* 17, 2060–2071. doi: 10.1093/cercor/bhl114

Inda, M. C., DeFelipe, J., and Muñoz, A. (2009). Morphology and distribution of chandelier cell axon terminals in the mouse cerebral cortex and claustroamygdaloid complex. *Cereb. Cortex* 19, 41–54. doi: 10.1093/cercor/bhn057

Isaacson, J. S., and Scanziani, M. (2011). How inhibition shapes cortical activity. *Neuron* 72, 231–243. doi: 10.1016/j.neuron.2011.09.027

Jiang, X., Shen, S., Cadwell, C. R., Berens, P., Sinz, F., Ecker, A. S., et al. (2015). Principles of connectivity among morphologically defined cell types in adult neocortex. *Science* 350, aac9462. doi: 10.1126/science.aac9462

Jones, E. G. (1975). Varieties and distribution of non-pyramidal cells in the somatic sensory cortex of the squirrel monkey. *J. Comp. Neurol.* 160, 205–267. doi: 10.1002/cne.901600204

Jones, R. T., Faas, G. C., and Mody, I. (2014). Intracellular bicarbonate regulates action potential generation via KCNQ channel modulation. *J. Neurosci.* 34, 4409–4417. doi: 10.1523/JNEUROSCI.3836-13.2014

Kaila, K. (1994). Ionic basis of GABAA receptor channel function in the nervous system. *Prog. Neurobiol.* 42, 489–537. doi: 10.1016/0301-0082(94)90049-3

Kapfer, C., Glickfeld, L. L., Atallah, B. V., and Scanziani, M. (2007). Supralinear increase of recurrent inhibition during sparse activity in the somatosensory cortex. *Nat. Neurosci.* 10, 743–753. doi: 10.1038/nn1909

Karube, F., Kubota, Y., and Kawaguchi, Y. (2004). Axon branching and synaptic bouton phenotypes in GABAergic nonpyramidal cell subtypes. *J. Neurosci.* 24, 2853–2865. doi: 10.1523/JNEUROSCI.4814-03.2004

Kawaguchi, Y. (1995). Physiological subgroups of nonpyramidal cells with specific morphological characteristics in layer II/III of rat frontal cortex. *J. Neurosci.* 15, 2638–2655. doi: 10.1523/JNEUROSCI.15-04-02638.1995

Kawaguchi, Y., and Kubota, Y. (1997). GABAergic cell subtypes and their synaptic connections in rat frontal cortex. *Cereb. Cortex* 7, 476–486. doi: 10.1093/cercor/7.6.476

Kawaguchi, Y., and Shindou, T. (1998). Noradrenergic excitation and inhibition of GABAergic cell types in rat frontal cortex. *J. Neurosci.* 18, 6963–6976. doi: 10.1523/JNEUROSCI.18-17-06963.1998

Kerti-Szigeti, K., and Nusser, Z. (2016). Similar GABAA receptor subunit composition in somatic and axon initial segment synapses of hippocampal pyramidal cells. *Elife* 5, e18426. doi: 10.7554/eLife.18426.020

Kikuchi, M., Hashimoto, T., Nagasawa, T., Hirosawa, T., Minabe, Y., Yoshimura, M., et al. (2011). Frontal areas contribute to reduced global coordination of resting-state gamma activities in drug-naïve patients with schizophrenia. *Schizophr. Res.* 130, 187–194. doi: 10.1016/j.schres.2011.06.003

Klausberger, T., Magill, P. J., Márton, L. F., Roberts, J. D. B., Cobden, P. M., Buzsáki, G., et al. (2003). Brain-state- and cell-type-specific firing of hippocampal interneurons *in vivo*. *Nature* 421, 844–848. doi: 10.1038/nature01374

Klausberger, T., and Somogyi, P. (2008). Neuronal diversity and temporal dynamics: the unity of hippocampal circuit operations. *Science* 321, 53–57. doi: 10.1126/science.1149381

Krimer, L. S., and Goldman-Rakic, P. S. (2001). Prefrontal microcircuits: membrane properties and excitatory input of local, medium, and wide arbor interneurons. *J. Neurosci.* 21, 3788–3796. doi: 10.1523/JNEUROSCI.21-11-03788.2001

Kuba, H. (2012). Structural tuning and plasticity of the axon initial segment in auditory neurons. *J. Physiol.* 590, 5571–5579. doi: 10.1113/jphysiol.2012.237305

Kuba, H., Oichi, Y., and Ohmori, H. (2010). Presynaptic activity regulates Na+ channel distribution at the axon initial segment. *Nature* 465, 1075–1078. doi: 10.1038/nature09087

Lawrence, J. J. (2008). Cholinergic control of GABA release: emerging parallels between neocortex and hippocampus. *Trends Neurosci.* 31, 317–327. doi: 10.1016/j.tins.2008.03.008

Lee, S., Hjerling-Leffler, J., Zagha, E., Fishell, G., and Rudy, B. (2010). The largest group of superficial neocortical GABAergic interneurons expresses ionotropic serotonin receptors. *J. Neurosci.* 30, 16796–16808. doi: 10.1523/JNEUROSCI.1869-10.2010

Lesh, T. A., Niendam, T. A., Minzenberg, M. J., and Carter, C. S. (2011). Cognitive control deficits in schizophrenia: mechanisms and meaning. *Neuropsychopharmacology* 36, 316–338. doi: 10.1038/npp.2010.156

Lewis, D. A., Curley, A. A., Glausier, J. R., and Volk, D. W. (2012). Cortical parvalbumin interneurons and cognitive dysfunction in schizophrenia. *Trends Neurosci.* 35, 57–67. doi: 10.1016/j.tins.2011.10.004

Lewis, D. A., Hashimoto, T., and Volk, D. W. (2005). Cortical inhibitory neurons and schizophrenia. *Nat. Rev. Neurosci.* 6, 312–324. doi: 10.1038/nrn1648

Lewis, D. A., and Lund, J. S. (1990). Heterogeneity of chandelier neurons in monkey neocortex: corticotropin-releasing factor-and parvalbumin-immunoreactive populations. *J. Comp. Neurol.* 293, 599–615. doi: 10.1002/cne.902930406

Li, X.-G., Somogyi, P., Tepper, J. M., and Buzsáki, G. (1992). Axonal and dendritic arborization of an intracellularly labeled chandelier cell in the CA1 region of rat hippocampus. *Exp. Brain Res.* 90, 519–525. doi: 10.1007/BF00230934

Lu, J., Tucciarone, J., Padilla-Coreano, N., He, M., Gordon, J. A., and Huang, Z. J. (2017). Selective inhibitory control of pyramidal neuron ensembles and cortical subnetworks by chandelier cells. *Nat. Neurosci.* 20, 1377–1383. doi: 10.1038/nn.4624

Lunden, J. W., Durens, M., Phillips, A. W., and Nestor, M. W. (2019). Cortical interneuron function in autism spectrum condition. *Pediatr. Res.* 85, 146–154. doi: 10.1038/s41390-018-0214-6

Ma, Y., Hu, H., Berrebi, A. S., Mathers, P. H., and Agmon, A. (2006). Distinct subtypes of somatostatin-containing neocortical interneurons revealed in transgenic mice. *J. Neurosci.* 26, 5069–5082. doi: 10.1523/JNEUROSCI.0661-06.2006

Maren, S., and Fanselow, M. (1995). Synaptic plasticity in the basolateral amygdala induced by hippocampal formation stimulation *in vivo*. *J. Neurosci.* 15, 7548–7564. doi: 10.1523/JNEUROSCI.15-11-07548.1995

Martin, K. A. C., Somogyi, P., and Whitteridge, D. (1983). Physiological and morphological properties of identified basket cells in the cat's visual cortex. *Exp. Brain Res.* 50, 193–200. doi: 10.1007/BF00239183

Massi, L., Lagler, M., Hartwich, K., Borhegyi, Z., Somogyi, P., and Klausberger, T. (2012). Temporal dynamics of parvalbumin-expressing axo-axonic and basket cells in the rat medial prefrontal cortex *in vivo*. *J. Neurosci.* 32, 16496–16502. doi: 10.1523/JNEUROSCI.3475-12.2012

McDonald, A. J. (1982). Neurons of the lateral and basolateral amygdaloid nuclei: a golgi study in the rat. *J. Comp. Neurol.* 212, 293–312. doi: 10.1002/cne.902120307

McGinley, M. J., David, S. V., and McCormick, D. A. (2015). Cortical membrane potential signature of optimal states for sensory signal detection. *Neuron* 87, 179–192. doi: 10.1016/j.neuron.2015.05.038

Melloni, L., Molina, C., Pena, M., Torres, D., Singer, W., and Rodriguez, E. (2007). Synchronization of neural activity across cortical areas correlates with conscious perception. *J. Neurosci.* 27, 2858–2865. doi: 10.1523/JNEUROSCI.4623-06.2007

Micheva, K. D., Busse, B., Weiler, N. C., O'Rourke, N., and Smith, S. J. (2010). Single-Synapse analysis of a diverse synapse population: proteomic imaging methods and markers. *Neuron* 68, 639–653. doi: 10.1016/j.neuron.2010.09.024

Minzenberg, M. J., Laird, A. R., Thelen, S., Carter, C. S., and Glahn, D. C. (2009). Meta-analysis of 41 functional neuroimaging studies of executive function in schizophrenia. *Arch. Gen. Psychiatry* 66, 811–822. doi: 10.1001/archgenpsychiatry.2009.91

Miyoshi, G., Hjerling-Leffler, J., Karayannis, T., Sousa, V. H., Butt, S. J. B., Battiste, J., et al. (2010). Genetic fate mapping reveals that the caudal ganglionic eminence produces a large and diverse population of superficial cortical interneurons. *J. Neurosci.* 30, 1582–1594. doi: 10.1523/JNEUROSCI.4515-09.2010

Molnár, G., Oláh, S., Komlósi, G., Füle, M., Szabadics, J., Varga, C., et al. (2008). Complex events initiated by individual spikes in the human cerebral cortex. *PLoS Biol.* 6, e222. doi: 10.1371/journal.pbio.0060222

Nusser, Z., Sieghart, W., Benke, D., Fritschy, J. M., and Somogyi, P. (1996). Differential synaptic localization of two major gamma-aminobutyric acid type A receptor alpha subunits on hippocampal pyramidal cells. *Proc. Natl. Acad. Sci. U.S.A.* 93, 11939–11944. doi: 10.1073/pnas.93.21.11939

Obermayer, J., Verhoog, M. B., Luchicchi, A., and Mansvelder, H. D. (2017). Cholinergic modulation of cortical microcircuits is layer-specific: evidence from rodent, monkey and human brain. *Front. Neural Circuit* 11, 100. doi: 10.3389/fncir.2017.00100

Ogawa, Y., and Rasband, M. N. (2008). The functional organization and assembly of the axon initial segment. *Curr. Opin. Neurobiol.* 18, 307–313. doi: 10.1016/j.conb.2008.08.008

Oh, W. C., Lutzu, S., Castillo, P. E., and Kwon, H. B. (2016). *De novo* synaptogenesis induced by GABA in the developing mouse cortex. *Science* 353, 1037–1040. doi: 10.1126/science.aaf5206

Oh, W. C., and Smith, K. R. (2018). Activity-dependent development of GABAergic synapses. *Brain Res.* 1707, 18–26. doi: 10.1016/j.brainres.2018.11.014

O'Keefe, J., and Nadel, L. (1978). *The Hippocampus as a Cognitive Map*. Oxford: Oxford University Press.

Owens, D. F., and Kriegstein, A. R. (2002). Is there more to gaba than synaptic inhibition? *Nat. Rev. Neurosci.* 3, 715–727. doi: 10.1038/nrn919

Pan-Vazquez, A., Wefelmeyer, W., Sabater, V. G., Neves, G., and Burrone, J. (2020). Activity-Dependent plasticity of axo-axonic synapses at the axon initial segment. *Neuron* 106, 265–276.e6. doi: 10.1016/j.neuron.2020.01.037

Papp, O. I., Karlócai, M. R., Tóth, I. E., Freund, T. F., and Hájos, N. (2013). Different input and output properties characterize parvalbumin-positive basket and axo-axonic cells in the hippocampal CA3 subfield. *Hippocampus* 23, 903–918. doi: 10.1002/hipo.22147

Parnaudeau, S., O'Neill, P.-K., Bolkan, S. S., Ward, R. D., Abbas, A. I., Roth, B. L., et al. (2013). Inhibition of mediodorsal thalamus disrupts thalamofrontal connectivity and cognition. *Neuron* 77, 1151–1162. doi: 10.1016/j.neuron.2013.01.038

Paul, A., Crow, M., Raudales, R., He, M., Gillis, J., and Huang, Z. J. (2017). Transcriptional architecture of synaptic communication delineates GABAergic neuron identity. *Cell* 171, 522–539.e20. doi: 10.1016/j.cell.2017.08.032

Payne, J. A., Stevenson, T. J., and Donaldson, L. F. (1996). Molecular characterization of a putative K-Cl cotransporter in rat brain. *J. Biol. Chem.* 271, 16245–16252. doi: 10.1074/jbc.271.27.16245

Peters, A., Proskauer, C. C., and Ribak, C. E. (1982). Chandelier cells in rat visual cortex. *J. Comp. Neurol.* 206, 397–416. doi: 10.1002/cne.902060408

Pfeffer, C. K., Xue, M., He, M., Huang, Z. J., and Scanziani, M. (2013). Inhibition of inhibition in visual cortex: the logic of connections between molecularly distinct interneurons. *Nat. Neurosci.* 16, 1068–1076. doi: 10.1038/nn.3446

Pierri, J. N., Chaudry, A. S., Woo, T.-U. W., and Lewis, D. A. (1999). Alterations in chandelier neuron axon terminals in the prefrontal cortex of schizophrenic subjects. *Am. J. Psychiatry* 156, 1709–1719. doi: 10.1176/ajp.156.11.1709

Povysheva, N. V., Zaitsev, A. V., Gonzalez-Burgos, G., and Lewis, D. A. (2013). Electrophysiological heterogeneity of fast-spiking interneurons: chandelier versus basket cells. *PLoS ONE* 8, e70553. doi: 10.1371/journal.pone.0070553

Reimer, J., McGinley, M. J., Liu, Y., Rodenkirch, C., Wang, Q., McCormick, D. A., et al. (2016). Pupil fluctuations track rapid changes in adrenergic and cholinergic activity in cortex. *Nat. Commun.* 7, 13289. doi: 10.1038/ncomms13289

Ribak, C. E. (1985). Axon terminals of GABAergic chandelier cells are lost at epileptic foci. *Brain Res.* 326, 251–260. doi: 10.1016/0006-8993(85)90034-4

Richardson, M. P., Strange, B. A., and Dolan, R. J. (2004). Encoding of emotional memories depends on amygdala and hippocampus and their interactions. *Nat. Neurosci.* 7, 278–285. doi: 10.1038/nn1190

Rinetti-Vargas, G., Phamluong, K., Ron, D., and Bender, K. J. (2017). Periadolescent maturation of GABAergic hyperpolarization at the axon initial segment. *Cell Rep.* 20, 21–29. doi: 10.1016/j.celrep.2017.06.030

Rio, M. R., and DeFelipe, J. (1997). Colocalization of parvalbumin and calbindin D-28k in neurons including chandelier cells of the human temporal neocortex. *J. Chem. Neuroanat.* 12, 165–173. doi: 10.1016/S0891-0618(96)00191-3

Rocco, B. R., DeDionisio, A. M., Lewis, D. A., and Fish, K. N. (2017). Alterations in a unique class of cortical chandelier cell axon cartridges in schizophrenia. *Biol. Psychiatry* 82, 40–48. doi: 10.1016/j.biopsych.2016.09.018

Rocco, B. R., Lewis, D. A., and Fish, K. N. (2016). Markedly lower glutamic acid decarboxylase 67 protein levels in a subset of boutons in schizophrenia. *Biol. Psychiatry* 79, 1006–1015. doi: 10.1016/j.biopsych.2015.07.022

Rubin, R., Abbott, L. F., and Sompolinsky, H. (2017). Balanced excitation and inhibition are required for high-capacity, noise-robust neuronal selectivity. *Proc. Natl. Acad. Sci. U.S.A.* 114, E9366–E9375. doi: 10.1073/pnas.1705841114

Rudy, B., Fishell, G., Lee, S., and Hjerling-Leffler, J. (2011). Three groups of interneurons account for nearly 100% of neocortical GABAergic neurons. *Dev. Neurobiol.* 71, 45–61. doi: 10.1002/dneu.20853

Schmidt, S., Braak, E., and Braak, H. (1993). Parvalbumin-immunoreactive structures of the adult human entorhinal and transentorhinal region. *Hippocampus* 3, 459–470. doi: 10.1002/hipo.450030407

Schneider-Mizell, C. M., Bodor, A. L., Collman, F., Brittain, D., Bleckert, A., Dorkenwald, S., et al. (2021). Structure and function of axo-axonic inhibition. *Elife* 10, e73783. doi: 10.7554/eLife.73783.sa2

Schoonover, K. E., Dienel, S. J., and Lewis, D. A. (2020). Prefrontal cortical alterations of glutamate and GABA neurotransmission in schizophrenia: insights for rational biomarker development. *Biomark. Neuropsychiatry* 3, 100015. doi: 10.1016/j.bionps.2020.100015

Selten, M., Bokhoven, H., van, and Kasri, N. N. (2018). Inhibitory control of the excitatory/inhibitory balance in psychiatric disorders. *F1000research* 7, 23. doi: 10.12688/f1000research.12155.1

Sesack, S. R., Hawrylak, V. A., Melchitzky, D. S., and Lewis, D. A. (1998). Dopamine innervation of a subclass of local circuit neurons in monkey prefrontal cortex: ultrastructural analysis of tyrosine hydroxylase and parvalbumin immunoreactive structures. *Cereb. Cortex* 8, 614–622. doi: 10.1093/cercor/8.7.614

Shaw, A. D., Knight, L., Freeman, T. C. A., Williams, G. M., Moran, R. J., Friston, K. J., et al. (2020). Oscillatory, computational, and behavioral evidence for impaired GABAergic inhibition in schizophrenia. *Schizophr. Bull.* 46, 345–353. doi: 10.1093/schbul/sbz066

Shu, Y., Hasenstaub, A., and McCormick, D. A. (2003). Turning on and off recurrent balanced cortical activity. *Nature* 423, 288–293. doi: 10.1038/nature01616

Sik, A., Tamamaki, N., and Freund, T. F. (1993). Complete axon arborization of a single CA3 pyramidal cell in the rat hippocampus, and its relationship with postsynaptic parvalbumin-containing interneurons. *Eur. J. Neurosci.* 5, 1719–1728. doi: 10.1111/j.1460-9568.1993.tb00239.x

Sohal, V. S., Zhang, F., Yizhar, O., and Deisseroth, K. (2009). Parvalbumin neurons and gamma rhythms enhance cortical circuit performance. *Nature* 459, 698–702. doi: 10.1038/nature07991

Somogyi, P. (1977). A specific 'axo-axonal' interneuron in the visual cortex of the rat. *Brain Res.* 136, 345–350. doi: 10.1016/0006-8993(77)90808-3

Somogyi, P., Freund, T. F., and Cowey, A. (1982). The axo-axonic interneuron in the cerebral cortex of the rat, cat and monkey. *Neuroscience* 7, 2577–2607. doi: 10.1016/0306-4522(82)90086-0

Somogyi, P., Nunzi, M. G., Gorio, A., and Smith, A. D. (1983). A new type of specific interneuron in the monkey hippocampus forming synapses exclusively with the axon initial segments of pyramidal cells. *Brain Res.* 259, 137–142. doi: 10.1016/0006-8993(83)91076-4

Soriano, E., and Frotscher, M. (1989). A GABAergic axo-axonic cell in the fascia dentata controls the main excitatory hippocampal pathway. *Brain Res.* 503, 170–174. doi: 10.1016/0006-8993(89)91722-8

Steinecke, A., Bolton, M. M., and Taniguchi, H. (2022). Neuromodulatory control of inhibitory network arborization in the developing postnatal neocortex. *Sci. Adv.* 8, eabe7192. doi: 10.1126/sciadv.abe7192

Steinecke, A., Hozhabri, E., Tapanes, S., Ishino, Y., Zeng, H., Kamasawa, N., et al. (2017). Neocortical chandelier cells developmentally shape axonal arbors through reorganization but establish subcellular synapse specificity without refinement. *Eneuro* 4, 1–14. doi: 10.1523/ENEURO.0057-17.2017

Stuart, G. J., and Sakmann, B. (1994). Active propagation of somatic action potentials into neocortical pyramidal cell dendrites. *Nature* 367, 69–72. doi: 10.1038/367069a0

Szabadics, J., Varga, C., Molnár, G., Oláh, S., Barzó, P., and Tamás, G. (2006). Excitatory effect of GABAergic axo-axonic cells in cortical microcircuits. *Science* 311, 233–235. doi: 10.1126/science.1121325

Szabó, G. G., Holderith, N., Gulyás, A. I., Freund, T. F., and Hájos, N. (2010). Distinct synaptic properties of perisomatic inhibitory cell types and their different modulation by cholinergic receptor activation in the CA3 region of the mouse hippocampus. *Euro. J. Neurosci.* 31, 2234–2246. doi: 10.1111/j.1460-9568.2010.07292.x

Szentágothai, J. (1975). The 'module-concept' in cerebral cortex architecture. *Brain Res.* 95, 475–496. doi: 10.1016/0006-8993(75)90122-5

Szentágothai, J., and Arbib, M. A. (1974). Conceptual models of neural organization. *Neurosci. Res. Prog. B* 12, 305–510.

Szoboszlay, M., Lorincz, A., Lanore, F., Vervaeke, K., Silver, R. A., and Nusser, Z. (2016). Functional properties of dendritic gap junctions in cerebellar golgi cells. *Neuron* 90, 1043–1056. doi: 10.1016/j.neuron.2016.03.029

Tai, Y., Gallo, N. B., Wang, M., Yu, J.-R., and Aelst, L. V. (2019). Axo-axonic innervation of neocortical pyramidal neurons by GABAergic chandelier cells requires ankyrinG-associated L1CAM. *Neuron* 102, 358–372.e9. doi: 10.1016/j.neuron.2019.02.009

Tai, Y., Janas, J. A., Wang, C.-L., and Van Aelst, L. (2014). Regulation of chandelier cell cartridge and bouton development via DOCK7-mediated ErbB4 activation. *Cell Rep.* 6, 254–263. doi: 10.1016/j.celrep.2013.12.034

Tamamaki, N., Yanagawa, Y., Tomioka, R., Miyazaki, J., Obata, K., and Kaneko, T. (2003). Green fluorescent protein expression and colocalization with calretinin, parvalbumin, and somatostatin in the GAD67-GFP knock-in mouse. *J. Comp. Neurol.* 467, 60–79. doi: 10.1002/cne.10905

Tamás, G., and Szabadics, J. (2004). Summation of unitary IPSPs elicited by identified axo-axonic interneurons. *Cereb. Cortex* 14, 823–826. doi: 10.1093/cercor/bhh051

Tanaka, S. (2008). Dysfunctional GABAergic inhibition in the prefrontal cortex leading to "psychotic" hyperactivation. *BMC Neurosci.* 9, 41. doi: 10.1186/1471-2202-9-41

Taniguchi, H. (2014). Genetic dissection of GABAergic neural circuits in mouse neocortex. *Front. Cell. Neurosci.* 8, 8. doi: 10.3389/fncel.2014.00008

Taniguchi, H., Lu, J., and Huang, Z. J. (2013). The spatial and temporal origin of chandelier cells in mouse neocortex. *Science* 339, 70–74. doi: 10.1126/science.1227622

Tao, H. W., and Poo, M. (2005). Activity-Dependent matching of excitatory and inhibitory inputs during refinement of visual receptive fields. *Neuron* 45, 829–836. doi: 10.1016/j.neuron.2005.01.046

Tasic, B., Yao, Z., Graybuck, L. T., Smith, K. A., Nguyen, T. N., Bertagnolli, D., et al. (2018). Shared and distinct transcriptomic cell types across neocortical areas. *Nature* 563, 72–78. doi: 10.1038/s41586-018-0654-5

Telles-Correia, D., Moreira, A. L., Marques, J. G., Saraiva, S., Moreira, C. A., Antunes, F., et al. (2016). The proximity between hallucination and delusion dimensions: an observational, analytic, cross-sectional, multicentre study. *Front. Psychol.* 7, 1642. doi: 10.3389/fpsyg.2016.01642

Tikhonova, T. B., Miyamae, T., Gulchina, Y., Lewis, D. A., and Gonzalez-Burgos, G. (2018). Cell type- and layer-specific muscarinic potentiation of excitatory synaptic drive onto parvalbumin neurons in mouse prefrontal cortex. *Eneuro* 5, 1–21. doi: 10.1523/ENEURO.0208-18.2018

Tremblay, R., Lee, S., and Rudy, B. (2016). GABAergic interneurons in the neocortex: From cellular properties to circuits. *Neuron* 91, 260–292. doi: 10.1016/j.neuron.2016.06.033

Tukker, J. J., Fuentealba, P., Hartwich, K., Somogyi, P., and Klausberger, T. (2007). Cell type-specific tuning of hippocampal interneuron firing during gamma oscillations *in vivo*. *J. Neurosci.* 27, 8184–8189. doi: 10.1523/JNEUROSCI.1685-07.2007

Varga, C., Oijala, M., Lish, J., Szabo, G. G., Bezaire, M., Marchionni, I., et al. (2014). Functional fission of parvalbumin interneuron classes during fast network events. *Elife* 3, e04006. doi: 10.7554/eLife.04006.012

Vereczki, V. K., Veres, J. M., Müller, K., Nagy, G. A., Rácz, B., Barsy, B., et al. (2016). Synaptic organization of perisomatic GABAergic inputs onto the principal cells of the mouse basolateral amygdala. *Front. Neuroanat.* 10, 20. doi: 10.3389/fnana.2016.00020

Veres, J. M., Nagy, G. A., Vereczki, V. K., Andrási, T., and Hájos, N. (2014). Strategically positioned inhibitory synapses of axo-axonic cells potently control principal neuron spiking in the basolateral amygdala. *J. Neurosci.* 34, 16194–16206. doi: 10.1523/JNEUROSCI.2232-14.2014

Vinck, M., Womelsdorf, T., Buffalo, E. A., Desimone, R., and Fries, P. (2013). Attentional modulation of cell-class-specific gamma-band synchronization in awake monkey area V4. *Neuron* 80, 1077–1089. doi: 10.1016/j.neuron.2013.08.019

Vogels, T. P., and Abbott, L. F. (2009). Gating multiple signals through detailed balance of excitation and inhibition in spiking networks. *Nat. Neurosci.* 12, 4834491. doi: 10.1038/nn.2276

Vogels, T. P., Sprekeler, H., Zenke, F., Clopath, C., and Gerstner, W. (2011). Inhibitory plasticity balances excitation and inhibition in sensory pathways and memory networks. *Science* 334, 1569–1573. doi: 10.1126/science.1211095

Volk, D. W., Pierri, J. N., Fritschy, J.-M., Auh, S., Sampson, A. R., and Lewis, D. A. (2002). Reciprocal alterations in pre- and postsynaptic inhibitory markers at chandelier cell inputs to pyramidal neurons in schizophrenia. *Cereb. Cortex* 12, 1063–1070. doi: 10.1093/cercor/12.10.1063

Vreeswijk, C., and Sompolinsky, H. (1996). Chaos in Neuronal networks with balanced excitatory and inhibitory activity. *Science* 274, 1724–1726. doi: 10.1126/science.274.5293.1724

Wang, B.-S., Sarria, M. S. B., An, X., He, M., Alam, N. M., Prusky, G. T., et al. (2021). Retinal and callosal activity-dependent chandelier cell elimination shapes binocularity in primary visual cortex. *Neuron* 109, 502–515.e7. doi: 10.1016/j.neuron.2020.11.004

Wang, X., and Sun, Q. (2012). Characterization of axo-axonic synapses in the piriform cortex of *Mus musculus*. *J. Comp. Neurol.* 520, 832–847. doi: 10.1002/cne.22792

Wang, X., Tucciarone, J., Jiang, S., Yin, F., Wang, B.-S., Wang, D., et al. (2019). Genetic single neuron anatomy reveals fine granularity of cortical axo-axonic cells. *Cell Rep.* 26, 3145–3159.e5. doi: 10.1016/j.celrep.2019.02.040

Wang, Y., Toledo-Rodriguez, M., Gupta, A., Wu, C., Silberberg, G., Luo, J., et al. (2004). Anatomical, physiological and molecular properties of martinotti cells in the somatosensory cortex of the juvenile rat. *J. Physiol.* 561, 65–90. doi: 10.1113/jphysiol.2004.073353

Wang, Y., Zhang, P., and Wyskiel, D. R. (2016). Chandelier cells in functional and dysfunctional neural circuits. *Front. Neural Circuit* 10, 33. doi: 10.3389/fncir.2016.00033

Wefelmeyer, W., Cattaert, D., and Burrone, J. (2015). Activity-dependent mismatch between axo-axonic synapses and the axon initial segment controls neuronal output. *Proc. Natl. Acad. Sci. U.S.A.* 112, 9757–9762. doi: 10.1073/pnas.1502902112

Wehr, M., and Zador, A. M. (2003). Balanced inhibition underlies tuning and sharpens spike timing in auditory cortex. *Nature* 426, 4424446. doi: 10.1038/nature02116

Willems, J. G. P., Wadman, W. J., and Cappaert, N. L. M. (2018). Parvalbumin interneuron mediated feedforward inhibition controls signal output in the deep layers of the perirhinal-entorhinal cortex. *Hippocampus* 28, 281–296. doi: 10.1002/hipo.22830

Woodruff, A., Xu, Q., Anderson, S. A., and Yuste, R. (2009). Depolarizing effect of neocortical chandelier neurons. *Front. Neural Circuit* 3, 15. doi: 10.3389/neuro.04.015.2009

Woodruff, A. R., Anderson, S. A., and Yuste, R. (2010). The enigmatic function of chandelier cells. *Front. Neurosci.* 4, 201. doi: 10.3389/fnins.2010.00201

Woodruff, A. R., McGarry, L. M., Vogels, T. P., Inan, M., Anderson, S. A., and Yuste, R. (2011). State-Dependent function of neocortical chandelier cells. *J. Neurosci.* 31, 17872–17886. doi: 10.1523/JNEUROSCI.3894-11.2011

Xu, M., and Wong, A. H. C. (2018). GABAergic inhibitory neurons as therapeutic targets for cognitive impairment in schizophrenia. *Acta Pharmacol. Sin.* 39, 733–753. doi: 10.1038/aps.2017.172

Xu, X., and Callaway, E. M. (2009). Laminar specificity of functional input to distinct types of inhibitory cortical neurons. *J. Neurosci.* 29, 70–85. doi: 10.1523/JNEUROSCI.4104-08.2009

Xu, X., Roby, K. D., and Callaway, E. M. (2006). Mouse cortical inhibitory neuron type that coexpresses somatostatin and calretinin. *J. Comp. Neurol.* 499, 144–160. doi: 10.1002/cne.21101

Yaeger, C. E., Ringach, D. L., and Trachtenberg, J. T. (2019). Neuromodulatory control of localized dendritic spiking in critical period cortex. *Nature* 567, 100–104. doi: 10.1038/s41586-019-0963-3

Yao, Z., Velthoven, C. T. J., van Nguyen, T. N., Goldy, J., Sedeno-Cortes, A. E., Baftizadeh, F., et al. (2021). A taxonomy of transcriptomic cell types across the isocortex and hippocampal formation. *Cell* 184, 3222–3241.e26. doi: 10.1016/j.cell.2021.04.021

Yizhar, O., Fenno, L. E., Prigge, M., Schneider, F., Davidson, T. J., O'Shea, D. J., et al. (2011). Neocortical excitation/inhibition balance in information processing and social dysfunction. *Nature* 477, 171–178. doi: 10.1038/nature10360

Zaitsev, A. V., Gonzalez-Burgos, G., Povysheva, N. V., Kröner, S., Lewis, D. A., and Krimer, L. S. (2005). Localization of calcium-binding proteins in physiologically and morphologically characterized interneurons of monkey dorsolateral prefrontal cortex. *Cereb. Cortex* 15, 1178–1186. doi: 10.1093/cercor/bhh218

Zaitsev, A. V., Povysheva, N. V., Gonzalez-Burgos, G., Rotaru, D., Fish, K. N., Krimer, L. S., et al. (2009). Interneuron diversity in layers 2–3 of monkey prefrontal cortex. *Cereb. Cortex* 19, 1597–1615. doi: 10.1093/cercor/bhn198

Zhou, S., and Yu, Y. (2018). Synaptic E-I balance underlies efficient neural coding. *Front. Neurosci.* 12, 46. doi: 10.3389/fnins.2018.00046

Zhu, Y., Stornetta, R. L., and Zhu, J. J. (2004). Chandelier cells control excessive cortical excitation: characteristics of whisker-evoked synaptic responses of layer 2/3 nonpyramidal and pyramidal neurons. *J. Neurosci.* 24, 5101–5108. doi: 10.1523/JNEUROSCI.0544-04.2004

frontiers | Frontiers in Cellular Neuroscience

TYPE Brief Research Report
PUBLISHED 20 October 2022
DOI 10.3389/fncel.2022.983298

OPEN ACCESS

EDITED BY
Frederic Lanore,
UMR 5297 Institut Interdisciplinaire de Neurosciences (IINS), France

REVIEWED BY
Oliver Kann,
Heidelberg University, Germany
Stewart Alan Anderson,
Perelman School of Medicine, University of Pennsylvania, United States

*CORRESPONDENCE
Daniil P. Aksenov
daksenov@northshore.org

SPECIALTY SECTION
This article was submitted to Cellular Neurophysiology, a section of the journal Frontiers in Cellular Neuroscience

RECEIVED 30 June 2022
ACCEPTED 06 October 2022
PUBLISHED 20 October 2022

CITATION
Aksenov DP, Doubovikov ED, Serdyukova NA, Gascoigne DA, Linsenmeier RA and Drobyshevsky A (2022) Brain tissue oxygen dynamics while mimicking the functional deficiency of interneurons. *Front. Cell. Neurosci.* 16:983298. doi: 10.3389/fncel.2022.983298

Brain tissue oxygen dynamics while mimicking the functional deficiency of interneurons

Daniil P. Aksenov[1,2,3]*, Evan D. Doubovikov[1], Natalya A. Serdyukova[4,5], David A. Gascoigne[1], Robert A. Linsenmeier[4] and Alexander Drobyshevsky[3,5]

[1]Department of Radiology, NorthShore University HealthSystem, Evanston, IL, United States, [2]Department of Anesthesiology, NorthShore University HealthSystem, Evanston, IL, United States, [3]Pritzker School of Medicine, University of Chicago, Chicago, IL, United States, [4]Department of Biomedical Engineering, Northwestern University, Evanston, IL, United States, [5]Department of Pediatrics, NorthShore University HealthSystem, Evanston, IL, United States

The dynamic interaction between excitatory and inhibitory activity in the brain is known as excitatory-inhibitory balance (EIB). A significant shift in EIB toward excitation has been observed in numerous pathological states and diseases, such as autism or epilepsy, where interneurons may be dysfunctional. The consequences of this on neurovascular interactions remains to be elucidated. Specifically, it is not known if there is an elevated metabolic consumption of oxygen due to increased excitatory activity. To investigate this, we administered microinjections of picrotoxin, a gamma aminobutyric acid (GABA) antagonist, to the rabbit cortex in the awake state to mimic the functional deficiency of GABAergic interneurons. This caused an observable shift in EIB toward excitation without the induction of seizures. We used chronically implanted electrodes to measure both neuronal activity and brain tissue oxygen concentrations (PO_2) simultaneously and in the same location. Using a high-frequency recording rate for PO_2, we were able to detect two important phenomena, (1) the shift in EIB led to a change in the power spectra of PO_2 fluctuations, such that higher frequencies (8–15 cycles per minute) were suppressed and (2) there were brief periods (dips with a duration of less than 100 ms associated with neuronal bursts) when PO_2 dropped below 10 mmHg, which we defined as the threshold for hypoxia. The dips were followed by an overshoot, which indicates either a rapid vascular response or decrease in oxygen consumption. Our results point to the essential role of interneurons in brain tissue oxygen regulation in the resting state.

KEYWORDS

GABA, neurovascular unit, neuronal synchronization, cerebral cortex, rabbit, epilepsy, hypersynchronization

Introduction

A shift in excitatory-inhibitory balance (EIB) in the brain toward excitation is a very common clinical and pathophysiological phenomenon, which can present in adulthood or as a result of disturbed development, due to the functional deficiency of inhibitory interneurons (Gascoigne et al., 2021). This phenomenon manifests as neuronal hypersynchronization during the resting state, a process which affects normal neuronal and neurovascular interactions (Staley, 2015; van Vliet and Marchi, 2022). Note, that the term "hypersynchronization" referred to in this study is related to the epileptiform bursts in neuronal activity and is different from other types of synchronization (e.g., to stimulation, during sleep, etc.) (Traub et al., 1993; Behrens et al., 2005; Schneider et al., 2019). The clinical characteristics of a shift in EIB, range from autism (Rubenstein and Merzenich, 2003) to epilepsy (Kaeser and Regehr, 2014), depending on its severity. Typically, this state has a very long duration (months and years) (Berg, 2011; Gascoigne et al., 2021).

The changes to neurovascular interactions that occur as a result of a shift in EIB toward excitation are not well known. From a clinical perspective, the most important question pertains to whether this process leads to localized hypoxia, due to the significantly heightened energy consumption from synchronized neuronal activity. Previous studies have found neurovascular decoupling during synchronized neuronal activity, yet have not been able to report actual hypoxia (Winkler et al., 2012; Prager et al., 2019; Ferlini et al., 2021). Moreover, some studies have even shown increased cerebral blood flow (CBF) and decreased blood oxygenation during seizures (Kreisman et al., 1991; Bahar et al., 2006; Zhao et al., 2009). It should be noted that oxygen levels in these studies decreased slowly (during seconds) and remained within normoxic criteria, whereas clinical hypoxia is typically considered to be below 10–15 mmHg in brain tissue PO_2 assuming the normal PO_2 is 20–40 mmHg (Ougorets and Caronna, 2008; Manole et al., 2014; Farrell et al., 2016). In line with this, an interesting study, which used 1 Hz frequency recordings, reported drops in brain tissue oxygen levels in response to absence seizures of greater than 10 s in duration (Farrell et al., 2018), yet the PO_2 stayed above 15 mmHg during seizures.

In our study, we have utilized an innovative approach which combines simultaneous neuronal/local field potential and high-frequency (20 Hz) brain tissue oxygen recording from the same location. This allows any changes in neuronal activity to be simultaneously linked with brain tissue oxygen. Moreover, our ability to perform localized microinjections (Aksenov et al., 2014) allows us to effectively locally modulate EIB in awake animals, without affecting the state of the whole brain or afferent projections to the area of interest. Using this approach, we mimicked the functional deficiency of GABA-ergic interneurons in the cerebral cortex using the GABA-antagonist, picrotoxin, to elicit the shift in EIB without generating seizures.

Our results indicate that the shift in EIB causes brief but repeated periods of hypoxia in brain tissue. The presence of such hypoxic events suggests similar processes in patients who experience this type of shift in EIB due to functional deficiency of interneurons.

Methods

Subjects and approach justification

We have used awake rabbit models extensively in previous studies for studying behavioral learning as well as for electrophysiology, brain tissue oxygen, and MR measurements (Aksenov et al., 2016, 2020). There is no discomfort or pain connected with the reported experiments. Thus, rabbits are ideal subjects for electrophysiological experiments.

We chose layer IV of the somatosensory cortex for electrode implantation and drug injections because this brain region receives direct projections from the thalamus and represents one of the main components of the thalamocortical circuits (Ramirez et al., 2014; Zhang and Bruno, 2019). The somatosensory cortex has been extensively examined previously in rabbits (Swadlow et al., 1998). We have chosen the GABA-antagonist picrotoxin because the effects of this drug are well characterized and only involve GABA receptors.

Animal preparation

Seven adult female Dutch-belted rabbits (9-months old, 2–3 kg) were used in accordance with the National Institutes of Health guidelines and protocols, and all procedures, were approved by the NorthShore University HealthSystem Research Institute Institutional Animal Care and Use Committee. Rabbits were housed in standard stainless steel cages with water and food *ad lib*. Animals were chronically implanted with electrodes, as reported previously (Aksenov et al., 2015). For this procedure, animals were anesthetized with a mixture of ketamine (60 mg/kg) and xylazine (10 mg/kg). The recording assembly consisted of a silica tube (Polymicro Technologies, Phoenix, AZ, USA) containing a bundle of four 25 μm diameter gold-silver alloy microwires with formvar insulation (California Fine Wire, Grover Beach, CA, USA, alloy 446), and electroplated with a thin layer of gold (Dalic alkaline plating solution; Sifco Chemical, Independence, OH) at the tip so that they could be used as traditional polarographic oxygen electrodes. These electrodes terminated at different levels within a distance of 150–200 μm. The microwires were connected to a small 6-pin connector that was embedded in dental acrylic. A 150 μm Ag/AgCl reference wire was placed between the skull and

dura mater. A 200 μm silica injection cannula was attached to the microdrive. During surgery, lambda was positioned 1.5 mm below bregma and the stereotaxic coordinates were as follows: anterior-posterior was 2 mm dorsal to bregma, medial-lateral was 6 mm from midline, and dorsal-ventral was under visual control. After implantation the electrode assembly was cemented to the skull using dental acrylic and nylon support screws. After recovery from surgery each subject was habituated for at least 3–5 days prior to the experiments and all experiments were performed beginning at least 14 days after surgery. During recordings the rabbits were restrained by means of a cloth sleeve but their head was not fixed to the cradle. The rabbit's docile temperament and tolerance for restraint are ideal for studies performed in the awake state (Aksenov et al., 2019). The electrodes were advanced to layer IV and their location was confirmed using anatomical MR imaging.

Experimental design

Picrotoxin (Sigma Aldrich, 166 μM) was injected after 15 min of baseline recording. This concentration was chosen because it induces neuronal hypersynchronization without actual seizures. The total duration of an experiment was 50 min. We followed a previously described procedure of localized injections (Aksenov et al., 2005). For the control injections, the same protocol was followed as in picrotoxin injections, but a control vehicle (saline) was injected.

All injections (1 μl volume) were delivered through a silica tube/needle connected to a Hamilton syringe using transparent Tygon tubing. The pH level was adjusted for all injections and was 7.2–7.4. Single units were monitored to ensure that the impact of the potential mechanical displacement of tissue by the injected volume (volume effect) was minimized (Aksenov et al., 2014).

Electrophysiological and PO_2 recording

Our design allowed us to use the same electrode to record either single units or PO_2. The multiple unit signals [local field potentials (LFP) were recorded simultaneously] from the microwires were fed through a miniature preamplifier to a multi-channel differential amplifier system (Neuralynx, Inc, USA). The recording and analysis of electrophysiological data has been described previously (Aksenov et al., 2014, 2015). Briefly, the signals were amplified, band-pass–filtered (300 Hz to 3 kHz for single units (SU) and 1–150 Hz for LFP), and digitized (32 kHz/channel) using a Neuralynx data acquisition system. Unit discrimination was performed offline using threshold detection followed by a cluster analysis of individual action potential wave shapes using Neuralynx analysis software. For PO_2 recording the microwire was polarized to −0.7 V with respect to a reference electrode (located between the skull and dura), and the current was measured with a Keithley model 614 electrometer (Keithley Instruments, Cleveland, OH, USA). The initial designation of which wire, was used for either PO_2 or neuronal activity recording, was random. The output voltage from the electrometer was low-pass filtered at 30 Hz, amplified, and digitized at 20 Hz. The chronically implanted PO_2 electrodes were calibrated before implantation. Additionally, to show that our results do not depend on the sampling rate and filters in terms of PO_2 power spectra, we acquired the data at 200 Hz with the low pass filter at 400 Hz in 2 animals.

Electrode locations were confirmed by MRI using a 9.4T imaging spectrometer (BioSpec 94/30USR, Bruker Biospin MRI GmbH) operating at 1H frequency of 400 MHz. The spectrometer was equipped with an actively-shielded gradient coil (BFG-240–150-S-7, Research Resonance, Inc., Billerica, MA, USA). A single-turn, 20mm-diameter circular RF surface coil was used for both transmission and reception. Anatomical images were acquired using a multislice gradient echo pulse sequence with a TR of 1.5 s, a TE of 10 ms, a 30 mm × 30 mm FOV, and a matrix size of 128 × 128, corresponding to an in-plane resolution of 234 μm × 234 μm.

Data processing

Our initial data consisted of PO_2 data sampled at 20 Hz, and LFP and MUA data sampled at 32 kHz. Then we resampled the data to match the sampling frequencies by taking the necessary increments between data points. For our MUA data, we first took the absolute value over the entire time series, then we used a non-overlapping moving average, selecting the window sizes to produce our desired resampled sampling frequency. For our initial analysis, where we compared the time series dynamics of PO_2 against the time series of both MUA and LFP, we resampled our initial data to 20 Hz. For our second stage of analysis, we resampled all our data to 10 Hz. In total, our picrotoxin (PTX) and saline data each consist of seven experiments (one of each per animal). Note that for plotting the LFP spectrogram, we used a sampling rate of 200 Hz. All pre-processing of the data was done using scripts in Matlab, 2017b in the Windows 10 OS. All subsequent analysis (with the exception of the LFP spectrograms, described below) was performed using iPython notebooks (running Python 3) in the Linux OS.

Power spectra analysis

To study how the frequency content of our data changed over time, we used rolling windows to create spectrograms of our PO_2 and LFP data. For PO_2 at a sampling rate of 10 Hz, we created spectrograms using a time window size of 10 min (6,000 time points), with an overlapping window size of

5,999 time points. For each time window, we scaled the power spectra by dividing by the maximum power value across all frequencies, e.g., for the frequency range with the highest power, the scaled power was equal to 1. For LFP under a sampling rate of 200 Hz, we created spectrograms using a time window size of 10.24 s (2,048 time points), with an overlapping window of 1,024 time points. The units for the LFP spectrogram are in dB/Hz (power/frequency). Power spectra diagrams for PO_2 were done in 10-min non-overlapping windows. For this paper, we display only the 0-to-10-min and 30-to-40-min time window for comparative purposes. All power spectra calculations are done using Welch's method (Welch, 1967).

Consumption and synchronization measures

Since it was stated that the normal PO_2 in brain tissue is 20–40 mmHg and the critical level is 10–15 mmHg in patients (Ougorets and Caronna, 2008), we applied a proportion of 0.4 (i.e., 12/30) to our initial baseline level as the critical threshold. This enabled us to analyze the number of dips below "hypoxic" levels, which are called "consumption spikes" here.

Consumption spikes are characterized by sudden dips in PO_2, beyond what can be considered standard fluctuations in oxygen. To identify these abnormalities, we created a new smoothed series, where we applied a moving average smoothing filter over our original PO_2 time series, with a time window of 5 time points (0.5 s). We then created a residual series, which consisted of the differences between the original PO_2 series and the smoothed series. We then normalized the residual series in accordance with a Gaussian distribution. Finally, for this study, we defined the time of increased O_2 consumption by locating all the time points in the normalized residual series which exceeded the value of 5 (i.e., the PO_2 series deviated from the smoothed series by 5 standard deviations). The high threshold of 5 standard deviations ensured a robust barrier to decrease the chance of recording a false positive case of consumption. Similarly, using our MUA series (resampled at 10 Hz, using averaged bins), we denoted the time points of MUA "synchronization," by recording all of the time points which exceeded 5 standard deviations. Finally, we defined the oxygen dip rate and the MUA synchronization rate as the average number of occurrences of consumption spikes and increases in the MUA above the threshold, over a 30 s (300-time point) time window, with an overlapping window of 299 time points.

Statistical analysis

To analyze the change in baseline after injection, we used a paired *t*-test to compare the average PO_2 in the 5 min before injection the average PO_2 during the 5 min after injection. Our next aim was to statistically compare the high frequency component of the PO_2 power spectra before and after the injection of PTX. We defined the high frequency to be between 5 and 15 cycles per minute (cpm). Note that this high frequency range, which is nearly always present in the normal adult resting state, is distinguished from the high frequency consumption dips post PTX injections, which occur at a much higher rate of 10 Hz. Using our maximum value scaled power spectra for PO_2, we calculated the percentage of power over all frequencies within the high frequency range for our specific time windows. This gave us the metric of the proportion of high frequency power for the time windows of 0–10 min and 30–40 min. We then recorded these proportions for those two time windows over all our experiments (PTX and Saline, separately), and used a paired *t*-test to determine if the mean differences in the proportion of power in the high frequency range before and after injection were statistically significant. We also compared the relative amplitude of low frequencies in PO_2, characterized as the frequencies between 1 and 2 cpm, for the first 10-min time window and the 30–40-min time window. We measured the total power within the 1–2 cpm frequency ranges, scaled relative to the total power for the time window, and applied a paired *t*-test to measure the statistical significance of the mean differences between the 0 to 10-min time window and the 30–40-min time window.

To determine the statistical significance of our oxygen dip rate and MUA synchronization measures for our PTX experiments, we calculated *p*-value thresholds in accordance to the null distribution generated by our saline data. The null distribution for the oxygen dip rate was generated by storing all the oxygen dip rate values for the saline data, across all time windows, and across all saline experiments. The null distribution for the MUA synchronization measure was calculated by the same means. We were then able to construct histograms, and use a best-fit beta distribution to approximate the theoretical distribution of our null data for each metric. Using, for example, the theoretical null distribution of the oxygen dip rate, we were able to determine the value of the oxygen dip rate which corresponded to a *p*-value of 1%. Using the null distribution, we were then able to determine the *p*-value thresholds for our oxygen dip rate and MUA synchronization metrics.

Finally, we analyzed the overshoot after the consumption dips by getting the average across all PTX experiments and using a paired t-test between points before and after the dip. Then the point after the dip was subtracted from the point before the dip to get the average difference which represents the overshoot.

Results

Hypoxic dips

Neuronal hypersynchronization events (**Figures 1A,B**) and multiple dips in brain tissue PO_2 were recorded after picrotoxin

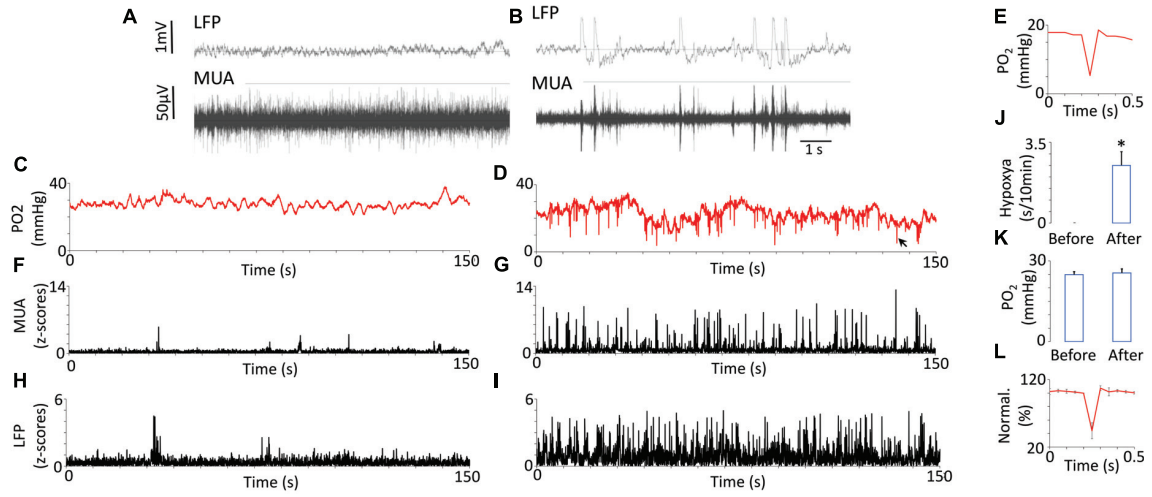

FIGURE 1
Oxygen dynamics in response to neuronal synchronization induced by the injection of picrotoxin. Examples of raw recording of multi-unit activity (MUA) and local field potentials (LFP) before **(A)** and after **(B)** injection of picrotoxin illustrate electrophysiological characteristics of neuronal synchronization (appearance of rhythmic bursts and near-silent periods between them). Fluctuations of brain tissue oxygen (PO_2) before injections were relatively periodical with low magnitude **(C)**. After the injection the magnitude of PO_2 fluctuations increased and regular dips below 10 mmHg appeared **(D)**. Sometimes the dips reached even 5 mmHg while having duration less then 100 ms **(E)**. The black arrow indicates the dip on D which is presented on panel **(E)**. MUA before injection did not have any regular bursts **(F)** but after injection the bursts appeared **(G)**. LFP before **(H)** and after injection **(I)** generally followed the behavior of MUA. Note that dips in PO_2 appeared together with bursts on MUA or LFP. The total duration of hypoxia reached 2 s over 10 min **(J)**. The averaged baseline of PO_2 did not change after the injection ($N = 7$) **(K)**. The error bars represent standard error. The overshoot after the dip is shown on the population data **(L)**. The data was normalized to 100% of the point before the dip. Error bars represent standard deviation for better visibility. Asterisk represents a significant difference ($p < 0.05$).

injections (Figures 1C,D). The occurrences of these dips corresponded to the synchronized bursts in neuronal activity on LFP/MUA (Figures 1F–I), and they were never observed before picrotoxin injection or after an injection of a control vehicle. We did not observe any head motion associated with synchronized bursts of neuronal activity or any seizures. The synchronized LFP bursts had a duration of around 80 ms whereas the dips in PO_2 had durations of approximately 30–40 ms (Figure 1E and Supplementary Figure 1). Based on (Ougorets and Caronna, 2008), we took the threshold critical/hypoxic level to be 10 mmHg. The cumulative duration of dips over 10 min was 2.5 ± 0.72 s (Figure 1J). None of these events were observed before the injection of picrotoxin or after the injection of vehicle and, thus, a two-tailed paired t-test showed significance ($p < 0.013$). The baseline of brain tissue oxygen, measured as the time-average, did not change after picrotoxin injection (24.89 ± 1.1 mmHg before vs. 25.52 ± 1.49 mmHg after, mean ± SEM) (Figure 1K). Supplementary Figure 2 additionally illustrates the relationship between raw data of PO_2 and electrophysiology after injection of picrotoxin.

An overshoot was often observed after the dips (Figure 1E). A two-tailed paired t-test comparing points before and after the dip revealed a significant difference ($p = 0.007$). On average the difference between levels of oxygen which preceded and followed the dip was 1.28 ± 0.21 mmHg (mean ± SEM). Sometimes this difference could reach 4 mmHg. Figure 1L shows group data normalized to the value before the dip.

Power spectra analysis for PO_2 and local field potentials

Looking over the entire duration of the experiment, the injection of PTX had a distinct effect on the overall frequency distribution of PO_2. As the PO_2 spectrograms show (Figures 2A,C), the power at higher frequencies greatly decreased during a certain period after injection (occurring at 15 min). As expected, this decrease in higher frequency fluctuations corresponds with an increase in the delta LFP band power (Figures 2B,D), signifying neuronal hypersynchronization induced by PTX. In contrast, for our control experiment, there is no visible change in the dynamics of the high frequency component of our PO_2 time series (Figure 2E) nor in the power of any particular LFP band (Figure 2F). The rapid increase in the delta band power, with a simultaneous decrease in the high frequency power of PO_2, in contrast to the control case, highlights the link between the onset of neuronal hypersynchronization and a disruption in brain tissue oxygen fluctuations via a shift in PO_2 power spectra toward the lower frequencies.

Figures 2G,H show the power spectra diagrams for two separate PTX experiments. Figure 2I shows the power spectra

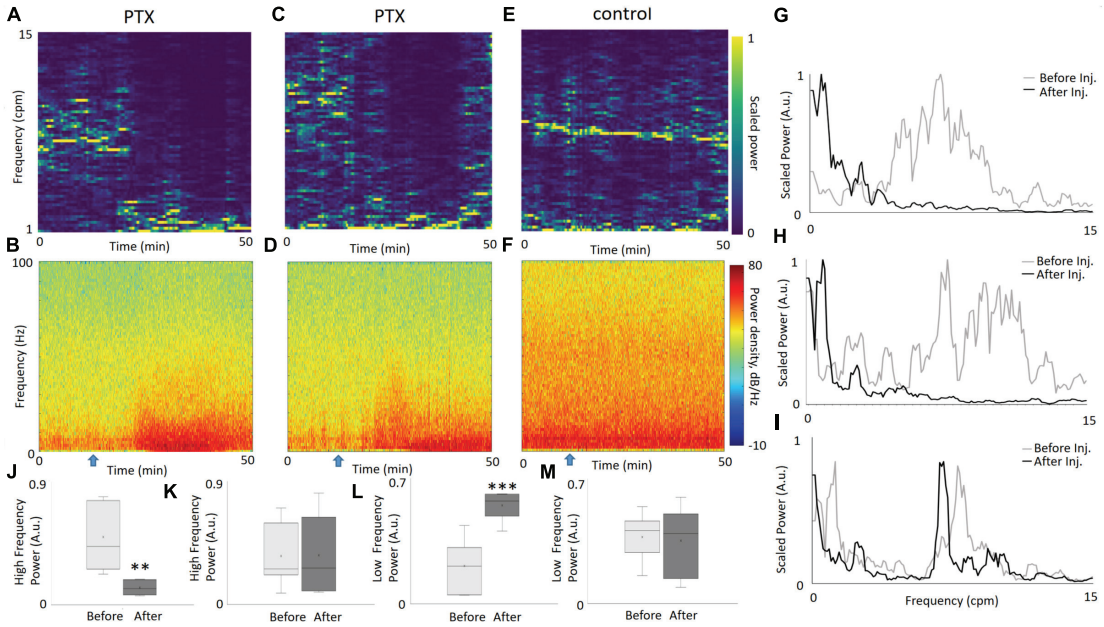

FIGURE 2
The dynamics of PO_2 and LFP, before and after the injection of PTX. PO_2 spectrograms from two illustrative experiments **(A,C)** highlight the change of dominant frequencies from relatively fast (5–15 cpm) to slow (<5cpm) after injection of PTX at the 15 min mark (denoted by a blue arrow). An increase in the power of the delta LFP band, as seen in the LFP spectrograms **(B,D)**, following the injection. Meanwhile, both the PO_2 and LFP spectrogram for the saline experiment show no apparent change in dynamics [**(E,F)**, respectively]. Comparing the power spectral density (PSD) of PO_2 from the first 10 min to a time window between 30 and 40 min, explicitly shows the disappearance of high frequency PO_2 fluctuations for the PTX experiments [**(G,H)**, corresponding to **(A,C)**, respectively], unlike the saline experiment corresponding to panel **(E)**, which displays no visible change **(I)**. We measured the proportion of power within the PSD in the 5–15 cpm frequency ("high frequency") range for periods before and after injection, over all our PTX experiments (N = 7) and display the distribution as a whisker-bar plot **(J)**. A paired t-test confirmed that the difference in proportion of the high frequency component before and after injection is statistically significant (p = 0.002). Similarly, for our saline experiments (N = 7), there was no statistical difference before and after injection **(K)**, confirming the stability of a high frequency PO_2 oscillatory component in the control. We also compared the low frequency (1–2 cpm) amplitude relative to the total power for each time window, graphing a bar-whisker plot for our PTX data **(L)** and our saline data **(M)**. The differences in amplitude are statistically significant (p = 0.0008) before and after injection for our PTX experiments, and not significant for our saline experiments. Two asterisks represent a significant difference $p < 0.01$. Three asterisks represent a significant difference $p < 0.001$.

for the same two time windows for the control experiment. The power shifts from high frequencies to lower frequencies for the PTX experiments, and stays the same for the control experiment. To visualize this phenomenon over all PTX experiments, we calculated the proportion of power contained within the 5-15 cpm frequency range (we denote this as high frequency) for both before and after injection, and graphed the box-whisker plot of their distribution (Figure 2J). We applied the same methodology over our saline experiments, and graphed the resulting box-whisker plots (Figure 2K). A paired t-test confirms that the mean difference of the proportion of high frequency power before and after PTX injection is statistically significant (p = 0.0028), while the control data shows no statistically significant difference before and after saline injection (p = 0.94). Similarly, we calculated the proportion of power within the 1–2 cpm frequency range (denoted as low frequency) for the respective before and after injection time windows for both our PTX experiments (Figure 2L) and saline experiments (Figure 2M). The mean differences in slow frequency amplitudes before and after injection for our PTX experiments was statistically significant (p = 0.0008), while the saline experiments showed no statistical difference. Supplementary Figure 3 illustrates the change in total (not relative) power and indicates that the amplitude of slow frequencies (1–2 cpm) greatly increased after injection of picrotoxin. Supplementary Figure 4 illustrates similar changes in power when a 200Hz sampling frequency was used.

Consumption and synchronization dynamics

Using the same two PTX experiments and control experiment as in Figure 2, we plot the dynamics of the oxygen dip rate alongside with MUA synchronization (Figures 3A–F). The oxygen dip rate is a measure of the average number of consumption spikes over a rolling 30 s window. For our PTX experiments (Figures 3A,C), there is a sudden increase in the oxygen dip rate after 30 min with multiple values crossing the 1% p-value threshold (red line). The control experiment

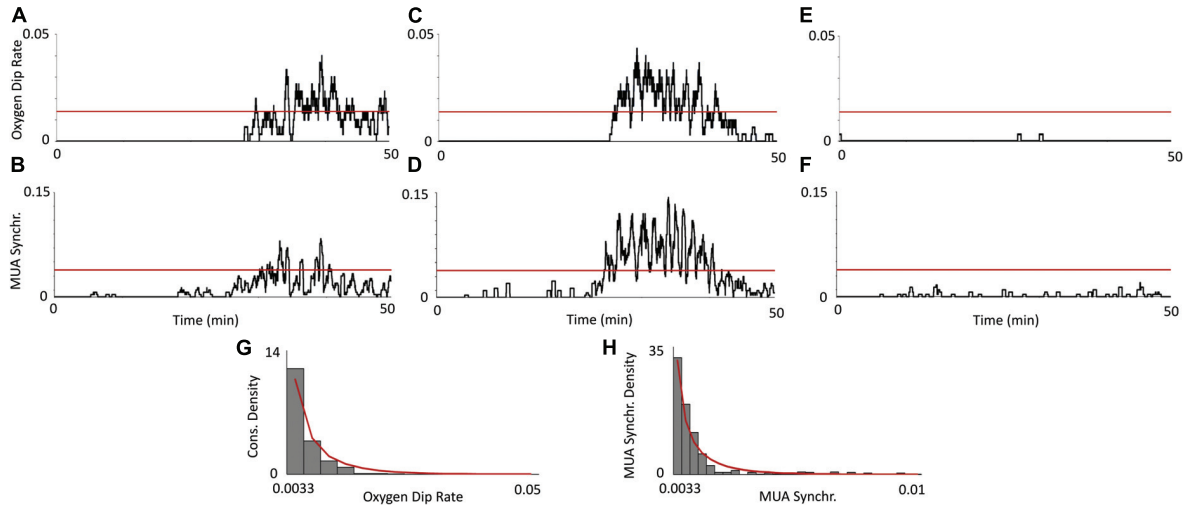

FIGURE 3
Relationship between oxygen consumption and neuronal synchronization. Using the same two PTX experiments from **Figure 2**, a plot of the consumption rate measure **(A,C)**, shows a significant increase in PO_2 consumption past the 30 s mark. This increase in PO_2 consumption corresponds with an increase in MUA activity **(B,D)**, indicating that the consumption spikes are indeed due to an increase in aggregate neuronal activity. The oxygen dip rate and MUA synchronization measure show no statistically significant deviations [**(E,F)**, respectively], indicating that this consumption activity does not occur in the control. The red, horizontal line denotes the threshold value (for each respective measure) at a 1% level of significance, calculated from the distribution of saline experiments. The density plot of the oxygen dip rate and MUA synchronization measures over all saline experiments (N = 7) is plotted [**(G,H)**, respectively]. The bars denote data from our actual recorded control experiments and the red line denotes the best-fit beta distribution.

has a oxygen dip rate of nearly zero over the entire 50-min duration (**Figure 3E**). MUA synchronization measures the average number of significant increases in the absolute value of the original MUA signal. For our PTX experiments, a significant increase in MUA synchronization corresponds to increases in the oxygen dip rate (**Figures 3B,D**), while the control experiment shows no significant increase in the level of MUA synchronization (**Figure 3F**). **Figures 3G,H** show the density plots for the oxygen dip rate and MUA synchronization measures over all saline experiments, respectively. The red line plots the best-fit beta distribution over the recorded data, representing the theoretical distribution used to calculate the p-value threshold. The calibration PO_2 values are shown by **Supplementary Figure 5**.

Discussion

Our results show that pharmacologically mimicking the debilitation of interneurons produced two phenomena at the level of brain tissue oxygen: (1) there was a change in the rate and magnitude of brain tissue oxygen fluctuations and (2) there were short-lasting and severe dips in PO_2. The interaction between these events caused localized hypoxia.

The fluctuation of brain tissue PO_2 in the brain is an important and ever-present process that corresponds to the vasomotion at the level of arterioles (Hudetz et al., 1998; Aalkjaer et al., 2011). These fluctuations are thought to prevent local hypoxia (Tsai and Intaglietta, 1993; Goldman and Popel, 2001; Doubovikov and Aksenov, 2020). In the normal brain, the predominant frequency is around 10 cpm in adults (Manil et al., 1984; Linsenmeier et al., 2016; Aksenov et al., 2018), and this frequency is an indicator of mature neurovascular interactions which allow fast responses to localized increases in neuronal activity (Doubovikov and Aksenov, 2020). Injections of picrotoxin shifted the dominant frequency of oxygen fluctuations toward 1–3 cpm by increasing their magnitude. Interestingly, this slow frequency corresponds to the "neonatal" frequency of oxygen fluctuations where neuronal control over vasomotion is yet to be established and arteriolar vasomotion is spontaneous (Aksenov et al., 2018). Moreover, this slow frequency dominates under general anesthesia (Linsenmeier et al., 2016), when neuronal activity is greatly decreased (Aksenov et al., 2015). Thus, it indicates that the full function of local neuronal networks is required for oxygen fluctuations of higher frequencies (~10 cpm) to dominate. Since picrotoxin causes a "disconnection" not only between interneurons and pyramidal cells but also between interneurons and arterioles (Vaucher et al., 2000), these processes disturb neuronal control of vasomotion, which leads to the observed shift of brain tissue oxygen fluctuations toward lower frequencies.

The other observed phenomenon, short-duration (<100 ms) dips in brain tissue oxygen, is most likely related to elevated energy consumption when neuronal activity is synchronized. An oxygen decrease was also observed during stimulation, which was accompanied by a delayed vascular

response (Uludag, 2008; Watanabe et al., 2013; Freeman and Li, 2016). It is necessary to emphasize that epileptiform neuronal bursts are different from neuronal responses to stimulation: the bursts represent a hypersynchronization of the total neuronal population; they consist of sustained neuronal depolarization with multiple action potentials following each other (Bromfield et al., 2006) and, thus, indicate very fast, brief and massive oxygen consumption, which can be observed even *in vitro* (Ivanov et al., 2015), depending how fast the oxygen electrode can respond. Our results clearly indicated there to be periods of localized hypoxia where the oxygen level was below 10 mmHg, and at times they even dropped to 5 mmHg, indicative of a more severe hypoxic event. Note that there is not a generally accepted level designated as hypoxia, and the values can be different depending on experimental conditions (Kariman et al., 1983; Foster et al., 2005; Kasischke et al., 2011). Overall, our results point to the role of interneurons and GABA in regulating neuronal activity by preventing resting-state neuronal hypersynchronization and the corresponding hypoxia in brain tissue.

It is generally accepted that the vascular response is typically delayed by 2–5 s (Zheng et al., 2002; Masamoto et al., 2003; Aksenov et al., 2015; Cai et al., 2018), which raises the question of what mechanism is responsible for recovery from the short-lasting resting state dips in brain tissue oxygen. Only three processes can possibly explain the recovery: vascular delivery of oxygen, oxygen diffusion from neighboring tissue and a drop in oxygen consumption while maintaining constant oxygen delivery. The role of oxygen diffusion from neighboring tissue can be excluded due to its very slow rate, dependent on an O_2 diffusion coefficient of 1540 $\mu m^2/s$ in the brain (Ganfield et al., 1970). Calculations show that the actual oxygen diffusion rate is 2 μm/50 ms in our case, which is not remotely sufficient to compensate for oxygen loss, taking into account the distances between our tubing/electrodes (150–200 μm). On the other hand, we have observed a small overshoot in dips (**Figure 1**), which directly indicates the role of the vascular response, a drop in the oxygen consumption or some combination of both. Such a quick vascular response is interesting and is possible due to the physiology of the smooth muscle cells of arterioles, because they can relax in less than 50 ms (Nelson et al., 1995; Hall, 2011) and involve fast-acting mediators (Hosford and Gourine, 2019). However, the drop in oxygen consumption is also possibly due to neurons entering a hyperpolarized phase, following the epileptiform burst. Additional studies would be necessary to establish the exact timing difference between LFP spikes and PO_2 dips by recording at higher frequency and to ascertain whether this is a region-dependent effect.

The short duration of hypoxia points to the question of whether it can produce actual damage. Generally speaking, with sufficient severity, hypoxia can lead to the upregulation of reactive oxygen species (ROS) which can rapidly accumulate beyond the protective capacity of the antioxidative system, leading to oxidative stress (Chen et al., 2018). The presence of oxidative stress poses a potential detrimental threat to a range of cell types in the brain, as the excess of ROS has a high propensity to react with and damage macromolecules within cells (e.g., DNA/RNA oxidation, protein oxidation, nitration of tyrosine residues, and lipid peroxidation), leading to the debilitation of the cell (Moreira et al., 2005). Moreover, hypoxic conditions have also been shown to lower intracellular and extracellular pH(Rolett et al., 2000; Yao and Haddad, 2004), phosphocreatine (Rolett et al., 2000), inorganic phosphate (Nioka et al., 1990; Rolett et al., 2000), lactate (Sarrafzadeh et al., 2003), as well as NADH (Rolett et al., 2000; Shetty et al., 2014). The combination of these consequences to the biochemical environment of affected cells can significantly impair their normal functioning and are associated with subsequent neuroapoptosis. However, it is difficult to suggest such dramatic changes to be present during the short duration of hypoxia we observed in this study, because the results of previous studies are predominantly based on measurements taken minutes after the onset of ischemia. On the other hand, processes related to oxidative stress are very fast and can take place within milliseconds. For example, it has been shown that a significant burst of local ROS occurs within 2 s of a mitochondrial permeability transition event, which, in turn, could have immediate consequences for the local cellular homeostasis (Zorov et al., 2000). Although it is difficult to compare the relative effects of these smaller, harmful events to hypoxia under longer durations, the repetitive nature of the short-lasting hypoxia due to the debilitation of interneurons can potentially have an accumulating effect. Our data suggest that over the course of 10 min, there will be an accumulated 2 s of hypoxic conditions (**Figure 1**). Moreover, considering this effect can persist for years in humans, the number of such short hypoxic events can be tremendous.

Finally, we would like to emphasize that due to the short duration of the reported hypoxic events, not all methods can be used to record and observe them. It seems that the task of recording brain tissue oxygen requires a minimum of a 20 Hz sampling rate. This excludes methods, such as functional MRI, that do not have sufficient temporal resolution. However, subclinical local neuronal hypersynchronization can be visible on EEG directly (depending on the size of epileptogenic zone) and indirectly (where slow bands (e.g., delta) prevail locally during the awake resting state).

We conclude that excitatory-inhibitory imbalance and long-lasting resting state neuronal hypersynchronization is a potentially dangerous phenomenon because of the multiple events of local hypoxia. In summary, we have shown the importance of interneurons in maintaining both physiological levels of neuronal activity and oxygen homeostasis. Interneurons are involved in regulating oxygen delivery through brain tissue oxygen fluctuations and oxygen consumption via restricting synchronized neuronal activity in resting state.

Data availability statement

The raw data supporting the conclusions of this article will be made available by the authors, without undue reservation.

Ethics statement

The animal study was reviewed and approved by NorthShore University HealthSystem Research Institute Institutional Animal Care and Use Committee.

Author contributions

DA: conceptualization, project administration, and resources. ED, DA, and NS: formal analysis. DA and AD: funding acquisition and supervision. NS and DA: data acquisition. DA and RL: methodology. ED: software. DA, ED, and DG: roles/writing—original draft. NS, RL, and AD: writing—review and editing. All authors contributed to the article and approved the submitted version.

Funding

This work was supported by R01GM112715 (National Institute of General Medical Sciences), R01NS107383 (National Institute of Neurological Disorders and Stroke), and R01NS119251 (National Institute of Neurological Disorders and Stroke).

Conflict of interest

The authors declare that the research was conducted in the absence of any commercial or financial relationships that could be construed as a potential conflict of interest.

Publisher's note

All claims expressed in this article are solely those of the authors and do not necessarily represent those of their affiliated organizations, or those of the publisher, the editors and the reviewers. Any product that may be evaluated in this article, or claim that may be made by its manufacturer, is not guaranteed or endorsed by the publisher.

Supplementary material

The Supplementary Material for this article can be found online at: https://www.frontiersin.org/articles/10.3389/fncel.2022.983298/full#supplementary-material

References

Aalkjaer, C., Boedtkjer, D., and Matchkov, V. (2011). Vasomotion - what is currently thought? *Acta Physiol. (Oxf)* 202, 253–269. doi: 10.1111/j.1748-1716.2011.02320.x

Aksenov, D. P., Dmitriev, A. V., Miller, M. J., Wyrwicz, A. M., and Linsenmeier, R. A. (2018). Brain tissue oxygen regulation in awake and anesthetized neonates. *Neuropharmacology* 135, 368–375. doi: 10.1016/j.neuropharm.2018.03.030

Aksenov, D. P., Li, L., Iordanescu, G., Miller, M. J., and Wyrwicz, A. M. (2014). Volume effect of localized injection in functional MRI and electrophysiology. *Magn. Reson. Med.* 72, 1170–1175. doi: 10.1002/mrm.24996

Aksenov, D. P., Li, L., Miller, M. J., and Wyrwicz, A. M. (2016). Blood oxygenation level dependent signal and neuronal adaptation to optogenetic and sensory stimulation in somatosensory cortex in awake animals. *Eur. J. Neurosci.* 44, 2722–2729. doi: 10.1111/ejn.13384

Aksenov, D. P., Li, L., Miller, M. J., and Wyrwicz, A. M. (2019). Role of the inhibitory system in shaping the BOLD fMRI response. *Neuroimage* 201:116034. doi: 10.1016/j.neuroimage.2019.116034

Aksenov, D. P., Li, L., Miller, M. J., Iordanescu, G., and Wyrwicz, A. M. (2015). Effects of anesthesia on BOLD signal and neuronal activity in the somatosensory cortex. *J. Cereb. Blood Flow Metab.* 35, 1819–1826. doi: 10.1038/jcbfm.2015.130

Aksenov, D. P., Serdyukova, N. A., Bloedel, J. R., and Bracha, V. (2005). Glutamate neurotransmission in the cerebellar interposed nuclei: Involvement in classically conditioned eyeblinks and neuronal activity. *J. Neurophysiol.* 93, 44–52. doi: 10.1152/jn.00586.2004

Aksenov, D. P., Venkatasubramanian, P. N., Miller, M. J., Dixon, C. J., Li, L., and Wyrwicz, A. M. (2020). Effects of neonatal isoflurane anesthesia exposure on learning-specific and sensory systems in adults. *Sci. Rep.* 10:13832. doi: 10.1038/s41598-020-70818-0

Bahar, S., Suh, M., Zhao, M., and Schwartz, T. H. (2006). Intrinsic optical signal imaging of neocortical seizures: The 'epileptic dip'. *Neuroreport* 17, 499–503.

Behrens, C. J., van den Boom, L. P., de Hoz, L., Friedman, A., and Heinemann, U. (2005). Induction of sharp wave-ripple complexes in vitro and reorganization of hippocampal networks. *Nat. Neurosci.* 8, 1560–1567. doi: 10.1038/nn1571

Berg, A. T. (2011). Epilepsy, cognition, and behavior: The clinical picture. *Epilepsia* 52 Suppl 1, 7–12. doi: 10.1111/j.1528-1167.2010.02905.x

Bromfield, E. B., Cavazos, J. E., and Sirven, J. (2006). *An introduction to epilepsy*. Chicago: American Epilepsy Society.

Cai, C., Fordsmann, J. C., Jensen, S. H., Gesslein, B., Lønstrup, M., Hald, B. O., et al. (2018). Stimulation-induced increases in cerebral blood flow and local capillary vasoconstriction depend on conducted vascular responses. *Proc. Natl. Acad. Sci. U.S.A.* 115, E5796–E5804. doi: 10.1073/pnas.1707702115

Chen, R., Lai, U. H., Zhu, L., Singh, A., Ahmed, M., and Forsyth, N. R. (2018). Reactive oxygen species formation in the brain at different oxygen levels: The role of hypoxia inducible factors. *Front. Cell Dev. Biol.* 6:132. doi: 10.3389/fcell.2018.00132

Doubovikov, E. D., and Aksenov, D. P. (2020). Oscillations and concentration dynamics of brain tissue oxygen in neonates and adults. *J. Comput. Neurosci.* 48, 21–26. doi: 10.1007/s10827-019-00736-2

Farrell, J. S., Gaxiola-Valdez, I., Wolff, M. D., David, L. S., Dika, H. I., Geeraert, B. L., et al. (2016). Postictal behavioural impairments are due to a severe prolonged hypoperfusion/hypoxia event that is COX-2 dependent. *Elife* 5, e19352.

Farrell, J. S., Greba, Q., Snutch, T. P., Howland, J. G., and Teskey, G. C. (2018). Fast oxygen dynamics as a potential biomarker for epilepsy. *Sci. Rep.* 8:17935. doi: 10.1038/s41598-018-36287-2

Ferlini, L., Su, F., Creteur, J., Taccone, F. S., and Gaspard, N. (2021). Cerebral and systemic hemodynamic effect of recurring seizures. *Sci. Rep.* 11:22209. doi: 10.1038/s41598-021-01704-6

Foster, K. A., Beaver, C. J., and Turner, D. A. (2005). Interaction between tissue oxygen tension and NADH imaging during synaptic stimulation and hypoxia in rat hippocampal slices. *Neuroscience* 132, 645–657. doi: 10.1016/j.neuroscience.2005.01.040

Freeman, R. D., and Li, B. (2016). Neural-metabolic coupling in the central visual pathway. *Philos. Trans. R. Soc. Lond B Biol. Sci.* 371:20150357. doi: 10.1098/rstb.2015.0357

Ganfield, R. A., Nair, P., and Whalen, W. J. (1970). Mass transfer, storage, and utilization of O2 in cat cerebral cortex. *Am. J. Physiol.* 219, 814–821. doi: 10.1152/ajplegacy.1970.219.3.814

Gascoigne, D. A., Serdyukova, N. A., and Aksenov, D. P. (2021). Early development of the GABAergic system and the Associated Risks of Neonatal Anesthesia. *Int. J. Mol. Sci.* 22:12951. doi: 10.3390/ijms222312951

Goldman, D., and Popel, A. S. (2001). A computational study of the effect of vasomotion on oxygen transport from capillary networks. *J. Theor. Biol.* 209, 189–199. doi: 10.1006/jtbi.2000.2254

Hall, J. E. (2011). *Guyton and hall textbook of medical physiology*. Philadelphia: Saunders Elsevier.

Hosford, P. S., and Gourine, A. V. (2019). What is the key mediator of the neurovascular coupling response? *Neurosci. Biobehav. Rev.* 96, 174–181. doi: 10.1016/j.neubiorev.2018.11.011

Hudetz, A. G., Biswal, B. B., Shen, H., Lauer, K. K., and Kampine, J. P. (1998). Spontaneous fluctuations in cerebral oxygen supply. An introduction. *Adv. Exp. Med. Biol.* 454, 551–559.

Ivanov, A. I., Bernard, C., and Turner, D. A. (2015). Metabolic responses differentiate between interictal, ictal and persistent epileptiform activity in intact, immature hippocampus in vitro. *Neurobiol. Dis.* 75, 1–14.

Kaeser, P. S., and Regehr, W. G. (2014). Molecular mechanisms for synchronous, asynchronous, and spontaneous neurotransmitter release. *Annu. Rev. Physiol.* 76, 333–363. doi: 10.1146/annurev-physiol-021113-170338

Kariman, K., Hempel, F. G., and Jobsis, F. F. (1983). In vivo comparison of cytochrome aa3 redox state and tissue PO2 in transient anoxia. *J. Appl. Physiol. Respir. Environ. Exerc. Physiol.* 55, 1057–1063. doi: 10.1152/jappl.1983.55.4.1057

Kasischke, K. A., Lambert, E. M., Panepento, B., Sun, A., Gelbard, H. A., Burgess, R. W., et al. (2011). Two-photon NADH imaging exposes boundaries of oxygen diffusion in cortical vascular supply regions. *J. Cereb. Blood Flow Metab.* 31, 68–81. doi: 10.1038/jcbfm.2010.158

Kreisman, N. R., Magee, J. C., and Brizzee, B. L. (1991). Relative hypoperfusion in rat cerebral cortex during recurrent seizures. *J. Cereb. Blood Flow Metab.* 11, 77–87. doi: 10.1038/jcbfm.1991.9

Linsenmeier, R. A., Aksenov, D. P., Faber, H. M., Makar, P., and Wyrwicz, A. M. (2016). Spontaneous fluctuations of PO2 in the rabbit somatosensory cortex. *Adv. Exp. Med. Biol.* 876, 311–317. doi: 10.1007/978-1-4939-3023-4_39

Manil, J., Bourgain, R. H., Van Waeyenberge, M., Colin, F., Blockeel, E., De Mey, B., et al. (1984). Properties of the spontaneous fluctuations in cortical oxygen pressure. *Adv. Exp. Med. Biol.* 169, 231–239. doi: 10.1007/978-1-4684-1188-1_17

Manole, M. D., Kochanek, P. M., Bayır, H., Alexander, H., Dezfulian, C., Fink, E. L., et al. (2014). Brain tissue oxygen monitoring identifies cortical hypoxia and thalamic hyperoxia after experimental cardiac arrest in rats. *Pediatr. Res.* 75, 295–301. doi: 10.1038/pr.2013.220

Masamoto, K., Omura, T., Takizawa, N., Kobayashi, H., Katura, T., Maki, A., et al. (2003). Biphasic changes in tissue partial pressure of oxygen closely related to localized neural activity in guinea pig auditory cortex. *J. Cereb. Blood Flow Metab.* 23, 1075–1084. doi: 10.1097/01.WCB.0000084248.20114.B3

Moreira, P. I., Smith, M. A., Zhu, X., Nunomura, A., Castellani, R. J., and Perry, G. (2005). Oxidative stress and neurodegeneration. *Ann. N. Y. Acad. Sci.* 1043, 545–552. doi: 10.1196/annals.1333.062

Nelson, M. T., Cheng, H., Rubart, M., Santana, L. F., Bonev, A. D., Knot, H. J., et al. (1995). Relaxation of arterial smooth muscle by calcium sparks. *Science* 270, 633–637. doi: 10.1126/science.270.5236.633

Nioka, S., Chance, B., Smith, D. S., Mayevsky, A., Reilly, M. P., Alter, C., et al. (1990). Cerebral energy metabolism and oxygen state during hypoxia in neonate and adult dogs. *Pediatr. Res.* 28, 54–62. doi: 10.1203/00006450-199007000-00013

Ougorets, I., and Caronna, J. J. (2008). *Critical care medicine ch. Coma*. Amsterdam: Elsevier Inc, 1309–1328.

Prager, O., Kamintsky, L., Hasam-Henderson, L. A., Schoknecht, K., Wuntke, V., Papageorgiou, I., et al. (2019). Seizure-induced microvascular injury is associated with impaired neurovascular coupling and blood-brain barrier dysfunction. *Epilepsia* 60, 322–336. doi: 10.1111/epi.14631

Ramirez, A., Pnevmatikakis, E. A., Merel, J., Paninski, L., Miller, K. D., and Bruno, R. M. (2014). Spatiotemporal receptive fields of barrel cortex revealed by reverse correlation of synaptic input. *Nat. Neurosci.* 17, 866–875. doi: 10.1038/nn.3720

Rolett, E. L., Azzawi, A., Liu, K. J., Yongbi, M. N., Swartz, H. M., and Dunn, J. F. (2000). Critical oxygen tension in rat brain: A combined (31)P-NMR and EPR oximetry study. *Am. J. Physiol. Regul. Integr. Comp. Physiol.* 279, R9–R16. doi: 10.1152/ajpregu.2000.279.1.R9

Rubenstein, J. L., and Merzenich, M. M. (2003). Model of autism: Increased ratio of excitation/inhibition in key neural systems. *Genes Brain Behav.* 2, 255–267. doi: 10.1034/j.1601-183x.2003.00037.x

Sarrafzadeh, A. S., Kiening, K. L., Callsen, T. A., and Unterberg, A. W. (2003). Metabolic changes during impending and manifest cerebral hypoxia in traumatic brain injury. *Br. J. Neurosurg.* 17, 340–346. doi: 10.1080/02688690310001601234

Schneider, J., Berndt, N., Papageorgiou, I. E., Maurer, J., Bulik, S., Both, M., et al. (2019). Local oxygen homeostasis during various neuronal network activity states in the mouse hippocampus. *J. Cereb. Blood Flow Metab.* 39, 859–873. doi: 10.1177/0271678X17740091

Shetty, P. K., Galeffi, F., and Turner, D. A. (2014). Nicotinamide pre-treatment ameliorates NAD(H) hyperoxidation and improves neuronal function after severe hypoxia. *Neurobiol. Dis.* 62, 469–478. doi: 10.1016/j.nbd.2013.10.025

Staley, K. (2015). Molecular mechanisms of epilepsy. *Nat. Neurosci.* 18, 367–372. doi: 10.1038/nn.3947

Swadlow, H., Beloozerova, I., and Sirota, M. (1998). Sharp, local synchrony among putative feed-forward inhibitory interneurons of rabbit somatosensory cortex. *J. Neurophysiol.* 79, 567–582.

Traub, R. D., Miles, R., and Jefferys, J. G. (1993). Synaptic and intrinsic conductances shape picrotoxin-induced synchronized after-discharges in the guinea-pig hippocampal slice. *J. Physiol.* 461, 525–547. doi: 10.1113/jphysiol.1993.sp019527

Tsai, A. G., and Intaglietta, M. (1993). Evidence of flowmotion induced changes in local tissue oxygenation. *Int. J. Microcirc. Clin. Exp.* 12, 75–88.

Uludag, K. (2008). Transient and sustained BOLD responses to sustained visual stimulation. *Magn. Reson. Imaging* 26, 863–869. doi: 10.1016/j.mri.2008.01.049

van Vliet, E. A., and Marchi, N. (2022). Neurovascular unit dysfunction as a mechanism of seizures and epilepsy during aging. *Epilepsia* 63, 1297–1313. doi: 10.1111/epi.17210

Vaucher, E., Tong, X. K., Cholet, N., Lantin, S., and Hamel, E. (2000). GABA neurons provide a rich input to microvessels but not nitric oxide neurons in the rat cerebral cortex: A means for direct regulation of local cerebral blood flow. *J. Comp. Neurol.* 421, 161–171.

Watanabe, M., Bartels, A., Macke, J. H., Murayama, Y., and Logothetis, N. K. (2013). Temporal jitter of the BOLD signal reveals a reliable initial dip and improved spatial resolution. *Curr. Biol.* 23, 2146–2150. doi: 10.1016/j.cub.2013.08.057

Welch, P. (1967). The use of the fast Fourier transform for the estimation of power spectra: A method based on time averaging over short, modified periodograms. *IEEE Trans. Audio Electroacoust.* 15, 70–73.

Winkler, M. K., Chassidim, Y., Lublinsky, S., Revankar, G. S., Major, S., Kang, E. J., et al. (2012). Impaired neurovascular coupling to ictal epileptic activity and spreading depolarization in a patient with subarachnoid hemorrhage: Possible link to blood-brain barrier dysfunction. *Epilepsia* 53 Suppl, 22–30. doi: 10.1111/j.1528-1167.2012.03699.x

Yao, H., and Haddad, G. G. (2004). Calcium and pH homeostasis in neurons during hypoxia and ischemia. *Cell Calcium* 36, 247–255. doi: 10.1016/j.ceca.2004.02.013

Zhang, W., and Bruno, R. M. (2019). High-order thalamic inputs to primary somatosensory cortex are stronger and longer lasting than cortical inputs. *Elife* 8:e44158. doi: 10.7554/eLife.44158

Zhao, M., Ma, H., Suh, M., and Schwartz, T. H. (2009). Spatiotemporal dynamics of perfusion and oximetry during ictal discharges in the rat neocortex. *J. Neurosci.* 29, 2814–2823. doi: 10.1523/JNEUROSCI.4667-08.2009

Zheng, Y., Martindale, J., Johnston, D., Jones, M., Berwick, J., and Mayhew, J. (2002). A model of the hemodynamic response and oxygen delivery to brain. *Neuroimage* 16, 617–637. doi: 10.1006/nimg.2002.1078

Zorov, D. B., Filburn, C. R., Klotz, L. O., Zweier, J. L., and Sollott, S. J. (2000). Reactive oxygen species (ROS)-induced ROS release: A new phenomenon accompanying induction of the mitochondrial permeability transition in cardiac myocytes. *J. Exp. Med.* 192, 1001–1014. doi: 10.1084/jem.192.7.1001

frontiers | Frontiers in Cellular Neuroscience

TYPE Review
PUBLISHED 05 May 2023
DOI 10.3389/fncel.2023.1188574

OPEN ACCESS

EDITED BY
Frederic Lanore,
UMR 5297 Institut Interdisciplinaire de Neurosciences (IINS), France

REVIEWED BY
Fabrice Ango,
Université de Montpellier, France
Giordano Lippi,
The Scripps Research Institute, United States

*CORRESPONDENCE
Jochen Winterer
✉ jochen.winterer@hest.ethz.ch

RECEIVED 17 March 2023
ACCEPTED 20 April 2023
PUBLISHED 05 May 2023

CITATION
Kołosowska KA, Schratt G and Winterer J (2023) microRNA-dependent regulation of gene expression in GABAergic interneurons.
Front. Cell. Neurosci. 17:1188574.
doi: 10.3389/fncel.2023.1188574

microRNA-dependent regulation of gene expression in GABAergic interneurons

Karolina Anna Kołosowska[1], Gerhard Schratt[2] and Jochen Winterer[2]*

[1]Department of Neurochemistry, Institute of Psychiatry and Neurology, Warsaw, Poland, [2]Lab of Systems Neuroscience, Department of Health Science and Technology, Institute for Neuroscience, Swiss Federal Institute of Technology ETH, Zurich, Switzerland

Information processing within neuronal circuits relies on their proper development and a balanced interplay between principal and local inhibitory interneurons within those circuits. Gamma-aminobutyric acid (GABA)ergic inhibitory interneurons are a remarkably heterogeneous population, comprising subclasses based on their morphological, electrophysiological, and molecular features, with differential connectivity and activity patterns. microRNA (miRNA)-dependent post-transcriptional control of gene expression represents an important regulatory mechanism for neuronal development and plasticity. miRNAs are a large group of small non-coding RNAs (21–24 nucleotides) acting as negative regulators of mRNA translation and stability. However, while miRNA-dependent gene regulation in principal neurons has been described heretofore in several studies, an understanding of the role of miRNAs in inhibitory interneurons is only beginning to emerge. Recent research demonstrated that miRNAs are differentially expressed in interneuron subclasses, are vitally important for migration, maturation, and survival of interneurons during embryonic development and are crucial for cognitive function and memory formation. In this review, we discuss recent progress in understanding miRNA-dependent regulation of gene expression in interneuron development and function. We aim to shed light onto mechanisms by which miRNAs in GABAergic interneurons contribute to sculpting neuronal circuits, and how their dysregulation may underlie the emergence of numerous neurodevelopmental and neuropsychiatric disorders.

KEYWORDS

microRNA, interneurons, neural circuits, neurodevelopment, neuropsychiatric disorders

Introduction

Cortical information processing depends on intricately and dynamically interconnected neuronal circuits composed of (1) glutamatergic excitatory neurons (or principal neurons), and (2) γ-aminobutyric acid (GABA)ergic inhibitory interneurons (INs) (Wood et al., 2017; Swanson and Maffei, 2019). GABAergic INs are a highly heterogeneous neuronal population that can be further divided into distinct subtypes based on morphology, molecular markers, electrophysiological properties, and connectivity (Ascoli et al., 2008; Lim et al., 2018; Mihaljević et al., 2019). Whilst principal neurons signal within and among various brain

regions, the majority of cortical GABAergic INs are considered to project mainly locally (but see descriptions of long-range projecting GABAergic INs (Jinno et al., 2007; Caputi et al., 2013). In this manner they control local network activity by gating information flow and contributing to sculpting network dynamics (Teppola et al., 2019). Examples of such functions include the maintenance of excitatory and inhibitory (E/I) balance, the generation and synchronization of cortical rhythms, as well as the modulation of cortical circuit plasticity (Tremblay et al., 2016; Fishell and Kepecs, 2020).

The generation and integration of the accurate number and IN subtype during relevant developmental time windows underlies the proper functioning of neural circuitry. A large amount of evidence indicates that the expression of particular genetic programmes confers structural and functional IN diversity, which becomes evident after IN precursors become postmitotic (Shi et al., 2021; Bugeon et al., 2022). Subsequently, during migration and final position settling, extrinsic local cues shape subtype identity of cortical INs, thereby determining morphology and corollary their connectivity patterns (Guo and Anton, 2014; Peyre et al., 2015; Mayer et al., 2018; Mi et al., 2018; Fishell and Kepecs, 2020). Moreover, it has been demonstrated, that INs can change their molecular profile based on their engagement in local circuits (Donato et al., 2013; Dehorter et al., 2015, 2017). Consequently, disturbances in IN development and mature function are reflected in their misspecification and misplacement, in alterations of their morphology and connectivity as well as in their inability to change and adapt their gene expression profile in context-specific brain activity (Volk et al., 2015; Dienel and Lewis, 2019; Mukherjee et al., 2019; Iannone and De Marco García, 2021). In line with the importance of INs for circuit function, developmental disturbances, or disruptions of mature IN function have emerged as pathophysiological substrates implicated in neurodevelopmental and neuropsychiatric disorders, such as schizophrenia, depression, epilepsy, and autism spectrum disorders (Brown et al., 2015; Nelson and Valakh, 2015; Del Pino et al., 2018; Selten et al., 2018; Juric-Sekhar and Hevner, 2019; Mukherjee et al., 2019).

Post-transcriptional mechanisms play critical roles in the control of gene expression during neuronal development and function. Compared to transcriptional regulation, post-transcriptional control of gene expression allows for faster responses to environmental cues, and in addition is not restricted to the nucleus. Recently, a group of small, non-coding RNAs, known as microRNAs (miRNAs), has been highlighted as a vital and ubiquitous layer of post-transcriptional control of gene expression. miRNAs base-pair to complementary sequences in their target mRNA molecules and inhibit their translation or promote degradation (Bartel, 2018). miRNAs are particularly abundant in the brain, where they contribute to proteomic diversity across regions and are important mediators of synaptic plasticity (Schratt et al., 2006; Schratt, 2009; Aksoy-Aksel et al., 2014; Ye et al., 2016). Numerous studies have shown their fundamental involvement at different stages of neuronal development and in the control of mature neuronal functions (Kosik, 2006; Fineberg et al., 2009; McNeill and Van Vactor, 2012; Zahr et al., 2019; Zolboot et al., 2021; Chan et al., 2022). Their expression and activity are often dysregulated in pathological states resulting in a shift of the cellular and extracellular miRNA patterns. Therefore, miRNA profiling along with the analysis of their target signaling pathways has emerged as a promising approach to study the pathogenesis of many diseases (Chen et al., 2010; Geekiyanage et al., 2012; Bencurova et al., 2017; Paul et al., 2018; Figueiredo et al., 2022; Khan and Saraya, 2022; Wei and Shetty, 2022).

Notwithstanding the considerable amount of knowledge on the role of miRNA in pyramidal neuron development and plasticity, little is known on how miRNAs govern fundamental aspects of cortical inhibition. There are a few studies pinpointing the importance of miRNA regulation in GABAergic IN development and mature functions. In this review, we assemble and arrange recent data regarding miRNA-dependent gene regulation of GABAergic IN activity, with the aim to shed light onto mechanisms by which miRNA-dependent control of gene expression in INs contributes to sculpting brain circuit dynamics. We propose that elucidating miRNA-associated signaling networks may offer a powerful platform for understanding mechanisms leading to impairments of cortical INs in neurodevelopmental and neuropsychiatric disorders, such as schizophrenia and autism (Tu et al., 2018; Lim et al., 2021).

microRNAs as gene expression regulators

miRNAs constitute a subclass of small (approximately 19–24 nucleotides in length), single-stranded non-coding RNAs that regulate post-transcriptional gene expression by repressing translation or promoting degradation of their target mRNAs. The early 1990s discovery of the first two miRNAs, lin-4 and let-7, involved in the regulation of the nematode *Caenorhabditis elegans* development, has attracted significant interest and marked a crucial milestone in molecular neurobiology by introducing a new level for controlling gene expression (Lee et al., 1993; Wightman et al., 1993). Subsequently, a growing number of miRNAs have been successively identified through various computational and experimental methods in species ranging from plants to humans. In 2002, miRBase, a miRNA registry was launched to serve as the main online repository for information regarding all potential miRNA sequences, nomenclature, classification, and target prediction (Griffiths-Jones, 2004). The most recent release of miRBase (v22) contains 48 860 mature miRNA sequences from 271 organisms. More than 2,500 mature miRNAs have been discovered in the human genome (Kozomara et al., 2019) and the expression of up to 60% of human protein-coding genes is predicted to be modulated by miRNAs (Friedman et al., 2009; Akhtar et al., 2016).

Most miRNAs are deployed over the genome and transcribed as individual genes, while some of them are clustered and co-expressed as polycistronic units under the control of the same promoter (Truscott et al., 2016). According to their genomic location, which determines their transcriptional regulation, miRNAs can be classified into intragenic and intergenic miRNAs (Liu et al., 2019). Intragenic miRNAs are positioned within protein-coding or non-coding genes (so called host genes) at different gene regions and are supposed to be co-transcribed with their host genes by Polymerase II (Liu et al., 2019). Conversely, intergenic miRNAs are inserted between genes and transcribed from their own Polymerase II/III promoters (Liu et al., 2019). miRNAs are first transcribed as long primary transcripts, which then undergo a

series of sequential processes leading to the generation of mature miRNA (Lee et al., 2002, 2004; Bartel, 2004; Denli et al., 2004; Lund et al., 2004; Okamura et al., 2004; Okada et al., 2009; Ha and Kim, 2014; O'Brien et al., 2018; Medley et al., 2021; Ergin and Çetinkaya, 2022). For a more detailed description of the biogenesis of miRNAs see **Figure 1**. In addition to the canonical pathway of miRNA biogenesis, various alternative mechanisms that may omit some of the canonical steps (so called non-canonical biogenesis pathways) can produce miRNAs (Yang and Lai, 2011; Cipolla, 2014; Ha and Kim, 2014; Stavast and Erkeland, 2019) and have been shown to be involved in different human diseases, including cancer (reviewed by Liu et al., 2019).

Target specificity of the miRNA-induced silencing complex (miRISC) is determined by the sequence complementarity between the miRNA strand and the target mRNA. The sequence primarily involved in miRNA–mRNA recognition—the "seed" region—is usually composed of 6–8 nucleotides of the 5′ region of the miRNA (Chen et al., 2008; Bartel, 2009). Due to the small size of the "seed" region and the length of 3′ UTRs, miRNAs may have hundreds of mRNA targets, and any given target may be under the control of numerous miRNAs (Friedman et al., 2009). The target mRNA may be "deactivated" by one or more of the following processes: (1) endonucleolytic cleavage of the mRNA strand, (2) destabilization of the mRNA through shortening of its poly(A) tail and decapping, followed by exonucleolytic cleavage, and (3) less efficient translation into proteins on ribosomes (Fabian et al., 2010). However, endonucleolytic cleavage happens only in the rare case of perfect complementarity between miRNAs and their target mRNA. Otherwise, there is usually a combination of degradation and translational inhibition. The degree by which each of these mechanisms contributes to silencing of mRNAs is variable and not easily deduced from the geometry of the miRNA/mRNA pair.

miRNAs in the neuron

miRNAs are present in many mammalian cell types and in various biological fluids within cells (e.g., peripheral blood mononuclear cells, PBMCs), or in the form of exosomes and as extracellular circulating miRNAs (Lagos-Quintana et al., 2002; Kriegel et al., 2013). They are highly abundant in the brain, where they significantly contribute to the functional proteomic diversity across cells and regions. miRNA interactions with their target mRNAs depend not only on sequence complementarity, but also on spatial proximity, which contributes to efficient regulation of local protein synthesis (Jansen, 2001; Martin and Ephrussi, 2009). miRNAs are highly abundant in dendrites and axons (Martin and Zukin, 2006; Kye et al., 2007; Schratt, 2009). While regulation of transcription is spatially restricted to the nucleus, miRNAs may fine-tune protein synthesis in remote subcellular compartments such as synapses (Dubes et al., 2019). The local repertoire of mRNAs preserves protein homeostasis for physiological processes and in response to intracellular and environmental cues (Das et al., 2021), and miRNA biogenesis and function themselves are subject to activity-dependent regulation (Aksoy-Aksel et al., 2014; Sambandan et al., 2017; Zampa et al., 2018). As a result, each synapse may be autonomously altered in structure and function during synaptic plasticity processes (Martin and Zukin, 2006). Furthermore, the miRNA biogenesis machinery is not restricted to the soma. For example, specific pre-miRNAs can be transported into the synapto-dendritic compartment (Bicker et al., 2013) and cleaved at the synapse to mature miRNAs (Lugli et al., 2008, Sambandan et al., 2017). Accordingly, both Dicer and the Argonaute protein eiF2c, a core component of the miRISC, are found in post-synaptic densities of dendritic spines (Lugli et al., 2005). Taken together, specific miRNAs have been established as key modulators of brain-specific signaling pathways associated with neuronal stem cell self-renewal, cell fate determination, neuronal and glial cell differentiation and proliferation, neurite growth, neurogenesis, synapse development and plasticity (Kosik, 2006; Schratt et al., 2006; Lugli et al., 2008; Fiore et al., 2009; Schratt, 2009; Siegel et al., 2009; Gao, 2010; Shi et al., 2010; Perruisseau-Carrier et al., 2011; de Chevigny et al., 2012; Wakabayashi et al., 2014; Stappert et al., 2015; Bielefeld et al., 2017; Chen et al., 2018; Zampa et al., 2018).

The multimodal diversity of GABAergic interneurons

Conventional classification uses various features to describe and categorize cortical INs (Ascoli et al., 2008). IN subtypes are placed in distinct subgroups according to morphological characteristics, intrinsic electrophysiological properties, as well as connectivity and protein expression patterns (Ascoli et al., 2008; Lee et al., 2010; Kepecs and Fishell, 2014; Tremblay et al., 2016; Tasic et al., 2018; Mihaljević et al., 2019). Recent developments in single cell transcriptomics added a new layer of complexity to IN classification (Tasic et al., 2016, 2018; Gouwens et al., 2019, 2020; Miyoshi, 2019). Gouwens et al. (2020) distinguished 28 types of cortical INs with congruent morphoelectrical and transcriptomic characteristics (so called met-types). Hierarchical clustering of IN properties revealed five major IN categories which were complementary, non-overlapping and designated by the expression of specific molecular markers: the calcium binding protein parvalbumin (PV), the neuropeptide somatostatin (Sst), the vasoactive intestinal peptide (VIP), the lysosomal-associated membrane protein family member 5 (LAMP5), and synuclein gamma (SNCG); the latter two subclasses mainly representing neurogliaform INs and cholecystokinin (CCK) INs, respectively. These categories overlap to a great extent with the cardinal IN subclasses distinguished according to their developmental and spatiotemporal origin in the medial or caudal ganglionic eminence (MGE or CGE, respectively), as described below (Fishell and Kepecs, 2020; Gouwens et al., 2020). Interestingly, the classification of met-types not only recapitulates the distinction of cardinal IN cell types based on developmental origin, but also reveals a layer-specific axon innervation pattern as a defining feature that distinguishes different met-types (Kawaguchi and Kubota, 1997; Klausberger and Somogyi, 2008; DeFelipe et al., 2013; Gouwens et al., 2020). In other words, the axonal projection pattern separates transcriptomic IN subtypes and in this manner implicates a functional differentiation according to their projection pattern. One consequence of this diversity in axonal arborisation is a functional compartmentalization of inhibition (Lovett-Barron et al., 2012; Royer et al., 2012; Fishell and Kepecs, 2020;

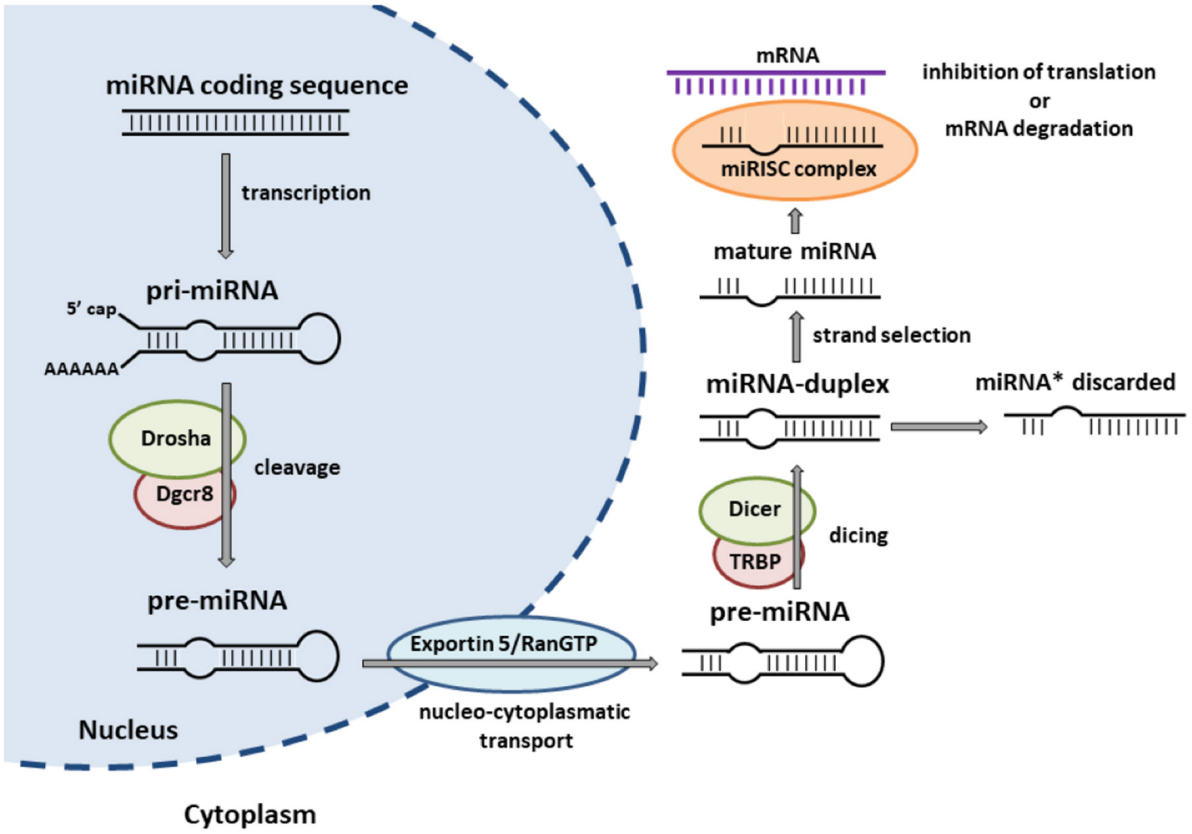

FIGURE 1
Canonical miRNA biogenesis pathway. miRNAs are initially transcribed by RNA Polymerase II/III into long primary transcripts (pri-miRNAs) that typically include a poly(A) tail and secondary hairpin structure. The pri-miRNA is subsequently cleaved by the microprocessor complex, containing the endonuclease Drosha and its partner protein Dgcr8/Pasha to the stem-loop precursor miRNA (pre-miRNA), which is then exported to the cytoplasm by exportin 5/RanGTP complex. In the cytoplasm, another RNase III enzyme, Dicer/TRBP, cuts the hairpin structure of the pre-miRNA to a miRNA duplex. One strand of the miRNA duplex is selectively incorporated into the miRNA-induced silencing complex (miRISC) and identified as the "miRNA" or "guide" strand. The other strand (originally named as "miRNA*") is often not incorporated into a functional miRISC and subsequently degraded in the cytoplasm. Within the miRISC, miRNAs bind to complementary sequences of target mRNAs to repress their translation or induce their degradation. Adapted from Winter et al. (2009).

Bloss et al., 2016). However, the implications of a granular differentiation among transcriptomic IN subtypes warrants further investigation, especially as recent observations indicate that, e.g., PV INs display a form of plasticity where they can adapt their molecular profile, intrinsic properties and connectivity pattern to changes in the local circuitry (Donato et al., 2013; Caroni, 2015; Dehorter et al., 2015). On a broader level, differentiation upon axonal projection patterns segregates IN into four major classes: (1) INs that project onto the soma of pyramidal neurons (PV INs), (2) INs that project onto the axon initial segment of pyramidal neurons (axo-axonic cells, or chandelier cells, also PV expressing), and (3) INs that project onto the dendrites of pyramidal neurons (Sst INs); finally, a fourth class consists of INs that project onto other INs (VIP INs). One interpretation of this diversity in axonal patterning is a division of labor of highly specialized inhibitory synapses (Huang et al., 2007; Klausberger and Somogyi, 2008; Fishell and Kepecs, 2020). For the remainder of this review, we will use this classification scheme as a guideline to relate miRNA-dependent control of gene expression in different IN classes to cortical inhibition. A short characteristic of major IN subclasses is presented in Figure 2.

Differences in interneurons across species

There are major differences between rodents and primates in the proportion of glutamatergic principal cells and GABAergic INs, as well as among IN subtypes (Jones, 2009). The relation of pyramidal neurons vs. INs is approximately 2:1 in humans as compared to 5:1 in mice. Nearly 50% of GABA INs in rodents express PV, while approximately 20% are VIP immunoreactive. In primates, only around 20% of GABAergic INs are PV positive. Since IN subtypes integrate within cortical circuits in distinct manners, these dissimilarities are expected to differentially impact local and global network functioning. In contrast to rodents, in

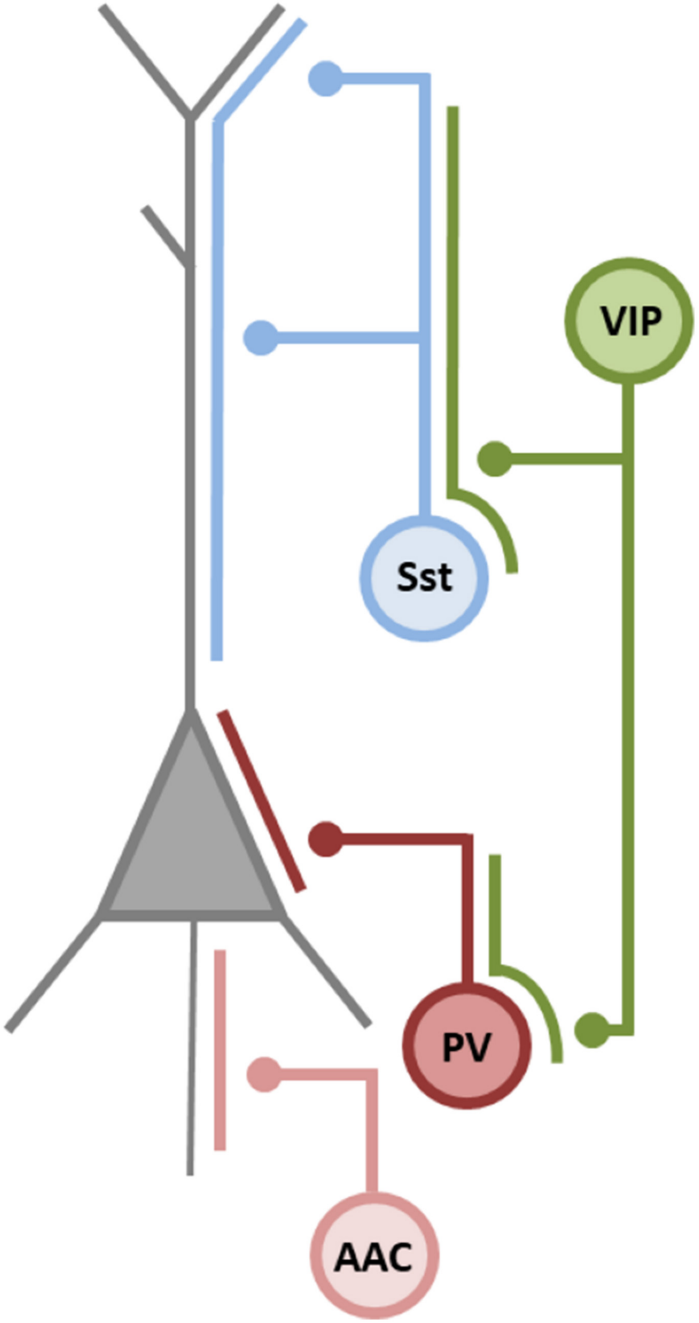

FIGURE 2
GABAergic interneuron overview. Cardinal classes of cortical IN differ in their morphology, neurochemical content, intrinsic electrophysiological properties and pattern of connectivity. For detailed description we refer to recent, excellent reviews on the classification and function of inhibitory INs (Tasic et al., 2016, 2018; Gouwens et al., 2019, 2020; Miyoshi, 2019). Parvalbumin (PV) INs synapse mainly on the somatic and perisomatic compartment of pyramidal cells, thereby controlling the spike generation in pyramidal cells. They are the major source of feedforward inhibition (Pouille and Scanziani, 2001; Freund, 2003; Mallet et al., 2005; Woodruff et al., 2009; Hu et al., 2014) and due to their divergent axonal targeting, they are able to synchronize large groups of postsynaptic neurons (Pouille and Scanziani, 2001; Ferguson and Gao, 2018; Yang and Sun, 2018; Missonnier et al., 2020). Consequently, they play pivotal roles in the generation and regulation of cortical rhythms, i.e., hippocampal theta rhythms, sharp wave ripples, and especially γ oscillations (Pouille and Scanziani, 2001; Sohal et al., 2009). Chandelier cells, or axo-axonic cells (AACs) are also PV expressing INs. They innervate the axon initial segment providing inhibition onto the spike initiation zone of pyramidal cells (Woodruff et al., 2009, but see Szabadics et al., 2006). Recently, it has been shown that AACs are active during heightened arousal and theta states (Dudok et al., 2021; Schneider-Mizell et al., 2021), thereby controlling CA1 pyramidal neurons outside of their place fields. Somatostatin (Sst) INs target the dendrites of pyramidal neurons (Kawaguchi and Kubota, 1996, 1997; Wang et al., 2004). Sst IN regulation of principal cell dendrites is critical for spine reorganization. Consequently, they play an important role in memory and learning processes (Chen et al., 2015; Honoré et al., 2021). Sst INs impact local circuits *via* feedback or lateral inhibition and have been shown to support cortical oscillations (Attinger et al., 2017; Muñoz et al., 2017; Obermayer et al., 2018). Vasoactive intestinal peptide (VIP) INs constitute the fourth major class of INs, comprising roughly 15% of all INs. VIP INs preferentially target other INs, mainly Sst, and, to a lesser degree, PV INs, thereby providing disinhibitory control over principal neurons (Rudy et al., 2011; Pi et al., 2013; Rhomberg et al., 2018). Thus, they constitute an important component of cortical disinhibitory circuits playing a role in gain control during sensory discrimination (Pi et al., 2013), and in cortical plasticity (Fu et al., 2015). Adapted from Fishell and Kepecs (2020).

the fetal human forebrain two independent lineages of cortical INs have been distinguished (Letinic et al., 2002; Zecevic et al., 2011). While the subcortical ganglionic eminence (GE) is the primary source of rodent INs, the developmental origin of neocortical GABAergic INs in humans and non-human primates is still under debate. However, recent studies suggest that the majority of primate neocortical GABAergic INs may originate from GEs of the ventral telencephalon, similarly to rodents (Petanjek et al., 2009; Ma et al., 2013; Yu et al., 2021). Moreover, while the neurogenesis period varies within the GE subregions and across species, major IN classes and their migratory routes are evolutionarily ancient and remain well conserved (López-Bendito et al., 2008).

Development of GABAergic cortical interneurons

Fate-mapping experiments revealed that cardinal IN types can be predicted based on their spatiotemporal origin, at the time when IN become postmitotic (Nery et al., 2002; Xu et al., 2003; Taniguchi et al., 2013; Mayer et al., 2018; Fishell and Kepecs, 2020). The precursors of cardinal GABAergic IN subgroups are primarily generated in the subpallidum in the ventral telencephalon (Wonders and Anderson, 2006; Batista-Brito and Fishell, 2009; Corbin and Butt, 2011). In rodents, neurogenesis and proliferation of GABAergic INs precursors occurs in the MGE and CGE and to a lesser extent in the preoptic area (POA), a subregion of the hypothalamus (Wonders and Anderson, 2006; Batista-Brito and Fishell, 2009; Gelman et al., 2009; Gelman and Marín, 2010; Corbin and Butt, 2011; Sultan et al., 2013). Each of these areas generates distinct IN subtypes depending on specific gene regulatory networks implemented by spatially and temporally restricted transcription factor activity (Kessaris et al., 2014). Collectively, MGE and CGE constitute the embryonic source of > 90% of GABAergic INs in the murine cerebral cortex (Wonders and Anderson, 2006; Batista-Brito and Fishell, 2009). MGE-derived INs are the major source of cardinal PV and Sst INs (Marín and Rubenstein, 2001; Xu et al., 2003; Butt et al., 2005; Wonders and Anderson, 2006; Fogarty et al., 2007; Miyoshi et al., 2010; Bandler et al., 2017) and their specification is mediated by numerous transcription factors including the Dlx family, the Nkx2 family, Lhx6, and Sox6 (Wonders and Anderson, 2006; Fogarty et al., 2007; Huang et al., 2007; Butt et al., 2008; Batista-Brito and Fishell, 2009). CGE-derived INs express the transcription factors Sp8, COUP-TF2, Prox1, and Pax6, resulting in IN subpopulations that closely overlap with the cardinal subgroup of VIP cells and other smaller cardinal subgroups (Pleasure et al., 2000; Xu et al., 2003; Butt et al., 2005; Lee et al., 2010; Miyoshi et al., 2015; Tremblay et al., 2016; Lim et al., 2018; Fishell and Kepecs, 2020). Upon their generation, postmitotic cortical INs migrate tangentially from the subpallium along the subventricular and marginal zone to the cortical plate, switch their migration pattern and travel radially into the developing cortical plate to finally reach their destination in the postnatal cortex (Faux et al., 2012; Wamsley and Fishell, 2017). Like IN generation and cardinal specification, migration and settling are complex processes regulated by an intricate network of various motogens, chemoattractants, transcription factors, and neurotransmitters (Marín and Rubenstein, 2001; De Marco García et al., 2011; Wamsley and Fishell, 2017; Lim et al., 2018). These developmental programs are regulated not only by intrinsic IN activity, but also by the forming immature neuronal circuits (Hurni et al., 2017; Bugeon et al., 2021). In addition, the early excitatory nature of GABA adds another layer of complexity to the multidimensional processes governing IN laminar positioning and integration within cortical circuits (Ben-Ari, 2007). Taken together, during migration and settling interaction of developing INs with extrinsic local cues promotes additional functional subtype diversity and finally shape IN morphology to establish their local connectivity pattern.

miRNA significance for GABAergic interneuron development

Deep miRNA sequencing during cortical IN differentiation of human induced pluripotent stem cells (hiPSCs) revealed dynamic alterations of miRNA profiles across different stages of development (Tu et al., 2018). Specific miRNA expression patterns were observed at four time points: D0, D11, D25, D80, representing hiPSCs, neuron progenitor cells, immature neurons, and mature neurons, respectively. The generated miRNomes at D0 and D11 and those generated at D25 and D80 clustered together. While the miRNA-302 family, miRNA-372, and miRNA-367 were specifically highly expressed at the hiPSCs stage, the let-7 family, miRNA-9, and miRNA-124 were enriched in mature INs. Interestingly, the -3p and -5p forms were not always expressed consistently during neuronal differentiation, indicating that miRNA strand switching might affect developmental processes as well. Thus, dynamic changes of miRNA patterns reflect a complex regulatory mechanism governing distinct stages of neuronal differentiation as well as the emergence of final cortical IN cell types.

Tuncdemir et al. (2015) examined the impact of miRNA depletion (by means of Dicer knockout) in MGE-derived IN proliferation, migration, and differentiation by removing Dicer from MGE-progenitors as well as post-mitotic MGE-derived INs in mice. The loss of miRNAs impacted neither proliferation nor the initiation of migration. However, miRNAs were essential for the transition from tangential to radial migration and the subsequent survival and maturation of cortical INs, resulting in a profound reduction of cortical INs at postnatal day 21 (Tuncdemir et al., 2015). Furthermore, almost 50% of the fate-mapped neurons lost their cardinal signature (PV or Sst) and showed defects in their morphology. Interestingly, despite the reduction of INs at postnatal day 21, a precocious expression of Sst, neuropeptide Y (NPY) and glutamic acid decarboxylase 65 (GAD65) was observed in E15.5 Dicer mutant animals, indicative of a miRNA-dependent expression of specific IN markers. Finally, the transcription factors Lhx6, Sox6, and Satb1 were not changed in Dicer-mutant mice, arguing that miRNA-dependent mechanisms do not act through the previously demonstrated transcription factor networks in MGE-derived IN specification (Batista-Brito et al., 2009; Lee et al., 2010; Tremblay et al., 2016; Lim et al., 2018). Taken together, these results indicate that miRNA-dependent gene expression can regulate migration, maturation and specification of cortical INs, adding another regulatory layer to the previously described transcription factor programs.

The conditional removal of Dicer in postmitotic VIP INs in mice resulted in a progressive loss of VIP INs in adulthood, despite normal migration and maturation (Qiu et al., 2020). Before significant cell loss of VIP INs in superficial layers of the somatosensory and motor cortices, VIP INs displayed profound changes in intrinsic and synaptic properties. VIP INs had broader action potential (AP) half-width and smaller AP amplitudes. Furthermore, the frequency of miniature excitatory postsynaptic currents (mEPSCs) as well as miniature inhibitory postsynaptic currents (mIPSCs) was reduced. Concomitant to these changes, pyramidal neurons were affected as well: they displayed increased mIPSC frequencies and amplitudes as well as increased mEPSC frequencies. Surprisingly, behavioral testing revealed an improved spatial working memory and motor coordination performance (Qiu et al., 2020). In a follow-up study, Wu et al. (2022), characterized the effect of Dicer ablation in postmitotic VIP INs in the olfactory bulb. They observed disrupted odor processing and discrimination in mutant mice, as well as disturbed beta oscillations and theta coherence between the olfactory bulb (OB) and the anterior piriform cortex (Wu et al., 2022). Importantly, the Dicer ablation restricted to the olfactory bulb VIP INs recapitulated the behavioral and electrophysiological results of the global knockout (Wu et al., 2022).

Conditional deletion of Dgcr8, a part of the canonical microprocessor complex, in postmitotic cortical pyramidal neurons ($Dgcr8^{fl/fl}$ mice, crossed to Nex-Cre mice) induced a profound reduction of their soma size and a loss of dendritic complexity in the cortex of mice resulting in an overall reduction of brain size in these animals (Hsu et al., 2012). These findings were recapitulated, when knocking out Dicer in $Dicer^{fl/fl}$;Nex-Cre mice (Hong et al., 2013). However, in contrast to the deletion of Dicer, knocking out Dgcr8 was accompanied by a selective reduction of the PV IN population and perisomatic inhibitory synapses (Hsu et al., 2012). This non-cell autonomous effect was attributed to a disrupted brain-derived neurotrophic factor (BDNF)/tropomyosin receptor kinase B (TrkB) signaling pathway in $Dgcr8^{fl/fl}$; Cre mice. Alternations in the number and function of PV IN population have been frequently observed in schizophrenia (Ferguson and Gao, 2018). More specifically, schizophrenia has been linked to deficits in the excitatory recruitment of PV INs in the ventral hippocampus and medial prefrontal cortex (mPFC) (Gonzalez-Burgos et al., 2015; Glausier and Lewis, 2018; Dienel and Lewis, 2019). Interestingly, Dgcr8 haploinsufficiency contributes to neurological, behavioral, and anatomical phenotypes of the 22q11 Deletion Syndrome (22q11DS), that encompasses DiGeorge syndrome, velo-cardio-facial syndrome and conotruncal anomaly face syndrome (Schofield et al., 2011). 0.6–2% of schizophrenia cases have been attributed to the 22q11DS microdeletion and approximately 30% of individuals with 22q11DS develop some type of schizophrenia in adolescence or adulthood (Green et al., 2009; Sellier et al., 2014). Consequently, 22q11DS has been proposed to represent a genetic subtype of schizophrenia (Bassett and Chow, 1999; Liu et al., 2002). Dgcr8 haploinsufficient mice (Dgcr8 ±) displayed reduced expression of miRNAs in the brain and showed cognitive deficits, along with altered electrical properties of layer 5 pyramidal neurons in the mPFC, decreased complexity of basal dendrites, and reduced excitatory synaptic transmission (Schofield et al., 2011). In an 22q11.2DS mouse model for schizophrenia (Lgdel ± mice), Mukherjee et al. (2019) observed a chronic PV plasticity state with reduced PV and glutamate decarboxylase 67 (GAD67) expression. In these mice, bidirectional PV plasticity and therefore the molecular, synaptic, and intrinsic adaptation of PV INs to changing levels of neural activity is disrupted, indicative of a maladjustment of PV INs to an excitatory recruitment deficit. Consequently, Lgdel ± mice displayed profound network and cognitive dysfunctions with reduced high-gamma oscillatory activity in the mPFC as well as behavioral deficits e.g., in conspecific and in object interaction. However, if and how Dgcr8 haploinsufficiency and consequently dysregulation in the post-transcriptional control of miRNA expression is implicated in the phenotypic changes in Lgdel ± mice, remains to be determined.

miRNA "signature" for subtypes of GABAergic interneurons

Recent advances in genomic profiling have allowed to identify specific miRNA patterns across various cell types and tissues, some of which also displayed changes in expression patterns upon altered physiological states and in response to environmental cues (Weber et al., 2010; Kriegel et al., 2013; van Spronsen et al., 2013; Londin et al., 2015; Kuosmanen et al., 2017). To a considerable extent, the identity and activity of neuronal subpopulations can be determined by their gene expression profile, which in principle also includes miRNA expression patterns (Nelson et al., 2006; Hobert, 2008; He et al., 2012). In this manner, a systematic analysis of miRNA profiles in distinct IN subtypes would represent a first step toward establishing a link between cell phenotypes, miRNA expression and finally their contribution to neuronal circuit dynamics.

Using miRNA tagging and affinity-purification (miRAP) targeted to cell types through the Cre-loxP binary system, He et al. (2012) revealed distinct miRNA profiles in glutamatergic neurons and in subtypes of GABAergic INs in the neocortex and cerebellum of mice. miRNA profiles of neurons expressing GAD65, PV, and Sst clustered more closely together as compared to glutamatergic neurons. Moreover, they clustered together with Purkinje cells, a class of GABAergic inhibitory neurons in the cerebellum, implying that miRNA profiles are specific for neuron subtypes that share the neurotransmitter phenotype as well as a common developmental origin (He et al., 2012). When comparing PV and Sst subpopulations, 125 out of 511 detected miRNAs were differentially expressed. For example, miRNA-133b was significantly enriched in the PV cells, while miRNA-187 was more abundant in Sst cells (He et al., 2012). Along these lines, transcriptional profiling of PV immunoreactive neurons isolated postmortem from layer 3 of the superior temporal gyrus from schizophrenic patients revealed a differential expression for 15 miRNAs (hsa-miRNA-151-3p, hsa-miRNA-338-5p, hsa-miRNA-106a, hsa-miRNA-197, hsa-miRNA-342-3p, hsa-miRNA-518f, hsa-miRNA-1274b, hsa-miRNA-151-3p, hsa-miRNA-195, hsa-miRNA-197, hsa-miRNA-218, hsa-miRNA-342-3p, hsa-miRNA-34a, hsa-miRNA-361-5p, hsa-miRNA-520c-3p). The subsequent analysis of the predicted miRNA targets revealed elements of signaling pathways that overlap with those found to be unbalanced in schizophrenia (Pietersen et al., 2014).

Taken together, these data suggest that PV IN network disruptions may be at least partially mediated by gene network

dysregulations due to altered expression of a rather small number of miRNAs (Pietersen et al., 2014) and that differentially expressed miRNAs might serve as a "signature" for GABAergic IN subtypes and regulate different subtype-specific functions.

Olfactory bulb interneurons

The OB is regarded as an independent developmental domain (López-Mascaraque and de Castro, 2002) and provides an example where particular miRNAs have been shown to determine distinct developmental trajectories (Zolboot et al., 2021), rendering OB INs an attractive model to study cell type- and context-dependent miRNA regulation of signaling pathways. The mammalian OB contains two IN subpopulations of different spatiotemporal origin: INs generated during embryogenesis and the early postnatal period from local OB progenitor cells, and INs deriving from subventricular adult progenitors during the early postnatal period and adulthood (Vergaño-Vera et al., 2006; Alonso et al., 2012). These two subgroups present distinct morphological and physiological characteristics and are thought to play different roles in odor discrimination. Interestingly, miRNA-125, the mammalian homolog of lin-4 linked to regulation of neuronal differentiation and synaptic function (Sokol et al., 2008), is expressed only in OB INs from the subventricular zone. Sponging miRNA-125 resulted in enhanced dendritic morphogenesis and increased activation upon odor stimulation in adult born OB INs, indicative of an instructive role for miRNA-125 in the integration of adult born INs into OB circuitry (Akerblom et al., 2014).

In OB INs, not only developmental but also activity dependent regulation of gene expression is controlled by miRNAs. Sustained exposure of sibling larvae to kin odorants induces changes in neurotransmitter expression from GABA to dopamine (DA) in *Xenopus* accessory olfactory bulb (AOB) INs, accompanied by behavioral preference for kin odorants (Dulcis et al., 2017). Vice versa, prolonged exposure of sibling larvae to non-kin odorants drives a DA-to-GABA shift in AOB neurons paralleled by an aversion-to-attraction shift in social preference toward the same non-kin odorants. By means of small RNA sequencing and functional interrogation, miRNA-375 and miRNA-200b were identified as key regulators mediating changes in DA vs. GABA expression. miRNA-375 was shown to inhibit the transcription factor Pax6, a main determinant of the dopaminergic phenotype in AOB (Ninkovic et al., 2010), whereas inhibition of miRNA-200b increased both Pax6 and Bcl11b mRNA levels in the AOB resulting in a reduction of GABAergic neurons and an increase in the DA neuron population (Dulcis et al., 2017).

miRNA regulation of GABAergic interneuron function in physiology and pathology

miRNA-138-5p

miRNA-138-5p has been shown to be involved in dendritic spine morphogenesis in cultured hippocampal pyramidal neurons (Siegel et al., 2009). However, recently a pivotal role for miRNA-138-5p in the regulation of PV inhibitory synaptic transmission in the mouse hippocampus has been reported (Daswani et al., 2022). miRNA-138-5p inactivation specifically in INs by viral injection of sponge transcripts or by Cre-mediated expression of sponge transcripts restricted to PV INs resulted in an increased frequency of mIPSC in murine CA1 pyramidal neurons. Sponge transcripts sequester endogenous miRNA, thereby leading to miRNA inactivation and the de-repression of cognate target genes (Ebert and Sharp, 2010). At the behavioral level, miRNA-138-5p inactivation was accompanied by short-term memory deficits (Daswani et al., 2022). Moreover, genes found to be upregulated in the hippocampus of miRNA-138-5p sponge expressing mice significantly overlapped with genes that were also unbalanced in schizophrenic patients. Specifically, the receptor tyrosine kinase ErbB4 was upregulated upon miRNA-138-5p sponging and subsequently validated as a direct miRNA-138-5p target (Daswani et al., 2022). ErbB4 is predominantly expressed in PV INs (Vullhorst et al., 2009; Neddens and Buonanno, 2010; Skirzewski et al., 2018). Neuregulins and their receptor ErbB4 are critical for the assembly of PV IN circuitry including their migration, axon and dendrite development, and synapse formation (Mei and Nave, 2014), and have been identified as schizophrenia susceptibility genes (Bennett, 2009; Banerjee et al., 2010; Neddens et al., 2011; Joshi et al., 2014; Mei and Nave, 2014). ErbB4 has been found in the axons, as well as on the postsynaptic side of PV INs at afferent excitatory and inhibitory inputs (Fazzari et al., 2010). Recently, it has been demonstrated that ErbB4 plays an important role in the local translation of synaptic genes (Bernard et al., 2022) and that ErbB4 is instructive for the induction of bidirectional PV plasticity in the mPFC (Chen et al., 2022). Finally, alterations in neuregulin1 (NRG1)-ErbB4 signaling have been demonstrated to alter memory performance. However, depending on the model, ablating ErbB4 in PV INs of hippocampal CA1 either enhance (Tian et al., 2017) or impair (Robinson et al., 2022) spatial and working memory performance.

Taken together, these observations indicate that the regulation of PV INs by miR-138-5p and its downstream target ErbB4 is critically involved in the homeostasis of mature hippocampal PV IN microcircuits. Furthermore, disturbances of miRNA regulation in PV INs induces short-term memory deficits in mice reminiscent to cognitive impairments frequently observed in patients suffering from schizophrenia (Del Pino et al., 2013).

miRNA-137

miRNA-137, a brain-enriched miRNA, has been shown to be involved in neurogenesis, dendritic morphogenesis and synaptic plasticity (Szulwach et al., 2010; Chen et al., 2012), and has been identified as a candidate gene for the etiology of schizophrenia, bipolar disorder, and autism spectrum disorders (Devanna and Vernes, 2014; Yin et al., 2014; Abdolmaleky et al., 2021). In the PFC and the blood of redox dysregulated mice [glutamate-cysteine ligase modifier subunit (Gclm)-KO mice], oxidative stress was associated with an elevated miRNA-137 level, a decrease in

cytochrome c oxidase subunit 6A2 (COX6A2) and mitophagy markers, an accumulation of damaged mitochondria, and disturbed PV IN function (Khadimallah et al., 2022). In early psychosis patients, corresponding changes were detected, i.e., an increase in exosomal miRNA-137, a decrease in COX6A2 and mitophagy markers in the plasma and a concomitant reduction of γ oscillatory activity in the EEG (Khadimallah et al., 2022). Consequently, inhibition of miRNA-137 in the cortex of Gclm-KO mice reversed the alterations in PV network and the decrease in COX6A2, indicative for an involvement of the miRNA-137/COX6A2 pathway in cortical PV IN circuit impairments typically observed in schizophrenia.

miRNA-181a-5p

Mild traumatic brain injury (mTBI) can result in a permanent impairment of learning and memory. Within the dentate gyrus (DG) of the hippocampus, the hilar subregion is particularly sensitive to mTBI and disruption of hilar IN inhibitory input has been linked to cognitive deficits following mTBI (Hicks et al., 1993). In a mouse model of mTBI, miRNA-181a-5p antagomir injected intracerebroventricularly prior to closed-skull cortical impact reduced neuronal miRNA-181a levels, restored deficits in novel object recognition and increased PV expression in hilar INs (Griffiths et al., 2019). Furthermore, these changes were associated with a decrease in the mTBI-related DG hyperactivity. PV is known to buffer calcium influx in PV INs (Schwaller et al., 2002) and thereby might be involved in calcium-mediated excitotoxicity. By reinstating PV expression, miRNA-181a-5p antagomir could alleviate the imbalance between excitation and inhibition in the DG due to mTBI (Griffiths et al., 2019). Interestingly, the level of miRNA-181a-5p was also increased in the hippocampus of post-status epileptic rats (Ren et al., 2016; Kong et al., 2020). Moreover, inhibition of miRNA-181a-5p *via* miRNA-181a antagomir led to seizure suppression and evoked a neuroprotective response *via* sirtuin 1 upregulation (Kong et al., 2020), and caspase-3 activation involved in neuronal apoptosis (Ren et al., 2016). However, the role of miRNA-181a-5p regulation of PV IN function and its contribution to the excitatory-inhibitory balance warrants further investigation.

miRNA-24

The transcription factor Sox6 is crucial for subtype determination of MGE-derived postmitotic INs by suppression of PV IN specification while inducing specification of Sst INs (Batista-Brito et al., 2009; Kelsom and Lu, 2013; Hu et al., 2017). Gestational and lactational exposure to three endocrine disrupting chemicals (EDCs) in rats resulted in a sex-specific impairment of hippocampus-dependent behaviors and alternations in expression patterns of particular IN subtypes. Male, but not female offspring exposed to EDCs displayed learning and memory deficits accompanied by a decrease in miRNA-24 level, upregulation of mRNA for transcription factor Sox6, Sox11, Pou2f2/Oct2, Pou3f2/Brn2, and downregulation of mRNA for PV in the hippocampus (Lichtensteiger et al., 2021). Individual Sox6 mRNA levels correlated inversely with miRNA-24 and PV mRNA expression. Moreover, mRNAs for NRG1 and its receptor ErbB4 were upregulated upon exposure to EDCs in male hippocampal INs, indicating that sex differences add an additional layer of post-transcriptional control of gene expression by miRNAs in PV INs.

miRNA-218

The early postnatal period is a crucial time window regarding ultimate morphological differentiation and the proper integration of cortical INs within local networks. Recently, miRNA-218 has been demonstrated to regulate multiple aspects of neural circuit development in the early postnatal period (Taylor et al., 2022). Transient inhibition of miRNA-218 in the dorsal hippocampus in early postnatal life resulted in the disruption of early depolarizing GABAergic signaling, structural defects in dendritic spines in CA1, and increased intrinsic membrane excitability in CA3 pyramidal neurons resulting in a heightened hippocampal network activity and a predisposition to seizures. Previous work has shown that miRNA-218 is implicated in embryonic motor neuron development (Amin et al., 2015, 2021; Thiebes et al., 2015; Reichenstein et al., 2019), in homeostatic plasticity (Rocchi et al., 2019), in stress related responses (Torres-Berrío et al., 2020; Schell et al., 2022; Yoshino et al., 2022), as well as in regulating contextual and spatial memory processes (Lu et al., 2021). Surprisingly, transcriptional profiling revealed that the upregulated genes upon miRNA-218 inhibition were more enriched in INs as compared to pyramidal neurons (Taylor et al., 2022). Consequently, conditional knockout of miRNA-218 in INs, but not pyramidal neurons, was sufficient to recapitulate the effects on hippocampal network assembly. Taken together, these results suggest that miRNA-218 regulates IN function in early postnatal life, thereby coordinating hippocampal network assembly to establish proper E/I balance in the adult.

miRNA-134

miRNA-134, one of the best-studied miRNAs in the brain, is highly activity-dependent and has been shown to regulate dendrite growth and dendritic spine formation in rat hippocampal pyramidal neurons (Schratt et al., 2006; Fiore et al., 2009; Bicker et al., 2014; Bahlakeh et al., 2021). Although its function in excitatory neurons has been well documented, using a ratiometric miRNA sensor Chai et al. (2013) surprisingly detected an activity-dependent upregulation of miRNA-134 in cortical INs that were immunoreactive for Sst or calretinin (CR), but not in pyramidal neurons. In Sst INs, miRNA-134 interacted directly with the mRNA encoding the palmitoylation enzyme DHHC9, which in turn regulated the proper membrane targeting of H-Ras. H-Ras has been implicated in multiple forms

of plasticity in the developing visual cortex (Arendt et al., 2004; Kaneko et al., 2010). However, how H-Ras regulates Sst IN function is currently not known and warrants further investigation.

Other miRNAs

Low GABAergic tone is increasingly implicated in the etiology of stress-related disorders (Ma et al., 2016; Zhang et al., 2017; Fogaça and Duman, 2019; Ma et al., 2019; Perlman et al., 2021). In the cortex of mice that underwent chronic unpredictable mild stress (CUMS), upregulation of several miRNAs was observed (miRNA-15b-5p, miRNA-144-3p, miRNA-582-5p and miRNA-879-5p). Stressed mice displayed impairments in GABA synthesis, reuptake, and release, indicative of an impairment in GABAergic signaling. Transcriptional profiling revealed a downregulation of GAD67, vesicular GABA transporter (VGAT) and GABA transporter type 3 (GAT-3) mRNAs which were subsequently shown to be negatively regulated by the upregulated miRNAs (Ma et al., 2016). Recent evidence from human postmortem and animal studies suggests a relatively selective vulnerability of Sst INs in depressive disorder, while changes in other INs seem to be less pronounced (Tripp et al., 2011; Lin and Sibille, 2015; Fee et al., 2017). However, to characterize the role of individual miRNAs and their target mRNAs in this specific IN subtype further investigation is required.

Conclusion and future directions

The significance of post-transcriptional regulation of gene expression by miRNAs in the central nervous system (CNS) is mirrored by a growing number of studies linking dysregulation of miRNA pathways to various neurodevelopmental and neuropsychiatric disorders. While an important role for miRNAs in regulating the development and function of GABAergic INs is beginning to emerge, it is apparent that a more detailed characterization of individual miRNAs and their target mRNAs in specific IN types is needed. This line of research has the potential not only to increase our fundamental knowledge of the consequences of miRNA regulation of GABAergic INs, but also the mechanistic understanding of neuropsychiatric disorders with recognized GABAergic dysfunctions like schizophrenia, autism spectrum and affective disorders.

Genetic programs underlying IN development are orchestrated by both transcriptional and post-transcriptional regulation. Data presented in this review indicate that the phenotypic and physiological features of IN subtypes depend not only on developmental spatiotemporal patterning of transcription factor activity and environmental cues, but also on miRNA expression and function (Strobl-Mazzulla et al., 2012; Tuncdemir et al., 2015; Dulcis et al., 2017). Furthermore, the interactions between gene expression, inductive events and miRNA activity not only determine IN developmental pathways but also impact mature network organization (Lichtensteiger et al., 2021; Taylor et al., 2022). In this manner, miRNAs are important elements of the gene regulatory network contributing to IN specification (Strobl-Mazzulla et al., 2012; Dulcis et al., 2017), as well as to the modification of network assemblies during critical developmental periods (Lichtensteiger et al., 2021; Taylor et al., 2022).

In addition, INs display remarkable plasticity features in an experience-dependent and behaviorally specific manner. They can adapt their molecular profile, their intrinsic and synaptic properties to changing levels of neuronal activity (Donato et al., 2013; Dehorter et al., 2015, 2017). However, there is a gap of knowledge in linking gene expression programs of INs to circuit modification mechanistically. miRNA-dependent post-transcriptional regulation of gene expression might be a prominent candidate to fill this gap as miRNA-dependent regulation of central aspects of principal neuron development and plasticity has been demonstrated (Schratt et al., 2006; Siegel et al., 2009; McNeill and Van Vactor, 2012; Aksoy-Aksel et al., 2014). Daswani et al. (2022) observed developmentally independent modifications in PV IN microcircuitry due to miRNA-138-5p inhibition in a cell type-specific manner. However, if these changes are plastic, i.e., if they are modified bidirectionally and in an activity-dependent manner, remains to be determined. Despite these first observations, the precise contribution of miRNAs to PV IN plasticity and to possible plasticity features of other IN subtypes remains elusive.

An essential step toward understanding the regulatory role of miRNAs in GABAergic INs is an extensive portrayal of miRNome profiles in a cell type-specific manner, in the relevant developmental trajectories as well as in mature microcircuitry. Obviously, this poses major technical challenges, particularly due to the high heterogeneity of GABAergic INs. Recent progress in sequencing technologies has provided a first step toward the analysis of differential miRNA expression, thus allowing to discriminate between neurons and glia cells (Colin et al., 2009), brain regions (Bak et al., 2008; Minami et al., 2014) as well as cell types (He et al., 2012). However, single-cell small RNA sequencing techniques and consequently a finer granularity of analysis are only beginning to emerge (Smith and Hutvagner, 2022). Moreover, a fine-grain analysis of the role of specific miRNAs in a cell type-specific manner is complicated by the pleotropic ability of single miRNAs to regulate multiple biological pathways. Therefore, a more comprehensive characterization of the miRNome-targetome interactions is required (Keaveney et al., 2020). The recognition of the biological relevance of a particular miRNA and its targeted molecular pathways will foreseeably be facilitated by advances in bioinformatics, transcriptomics, proteomics and other "omics" approaches. Together with elaborate molecular tools such as antagomirs, "sponges", miRNA mimics and precursors, as well as cell type-specific Cre-driver transgenic mouse lines that are intended to silence or overexpress miRNAs, the path to reveal distinct miRNA-dependent biological processes in a cell type-specific manner is set (Issler and Chen, 2015). Finally, a comprehensive knowledge of the role of miRNAs in GABAergic INs may be instrumental in elucidating the molecular basis of many CNS diseases with recognized GABAergic dysfunction. As neuronal miRNAs are responsive to environmental changes and are actively secreted by cells, they may additionally constitute useful diagnostic and prognostic biomarkers for the respective disease (van den Berg et al., 2020; Tsermpini et al., 2022).

Author contributions

JW and KK: conception and design. KK: literature search. KK, GS, and JW: wrote the manuscript. All authors contributed to the article and approved the submitted version.

Funding

KK was supported by a research fellowship from the National Science Centre in Poland (No. 2018/28/C/NZ7/00240). Open access funding by ETH Zurich.

Acknowledgments

We would like to apologize to colleagues whose work is not cited due to space constraints. We thank Michael Soutschek, Theofanis Karayannis, and Roberto Fiore for their comments on the manuscript.

Conflict of interest

The authors declare that the research was conducted in the absence of any commercial or financial relationships that could be construed as a potential conflict of interest.

Publisher's note

References

Abdolmaleky, H., Zhou, J., and Thiagalingam, S. (2021). Cataloging recent advances in epigenetic alterations in major mental disorders and autism. *Epigenomics* 13, 1231–1245. doi: 10.2217/epi-2021-0074

Akerblom, M., Petri, R., Sachdeva, R., Klussendorf, T., Mattsson, B., Gentner, B., et al. (2014). microRNA-125 distinguishes developmentally generated and adult-born olfactory bulb interneurons. *Development* 141, 1580–1588. doi: 10.1242/dev.101659

Akhtar, M., Micolucci, L., Islam, M., Olivieri, F., and Procopio, A. (2016). Bioinformatic tools for microRNA dissection. *Nucleic Acids Res.* 44, 24–44. doi: 10.1093/nar/gkv1221

Aksoy-Aksel, A., Zampa, F., and Schratt, G. (2014). MicroRNAs and synaptic plasticity–a mutual relationship. *Philos. Trans. R. Soc. Lond. B Biol. Sci.* 369:20130515. doi: 10.1098/rstb.2013.0515

Alonso, M., Lepousez, G., Sebastien, W., Bardy, C., Gabellec, M., Torquet, N., et al. (2012). Activation of adult-born neurons facilitates learning and memory. *Nat. Neurosci.* 15, 897–904. doi: 10.1038/nn.3108

Amin, N., Bai, G., Klug, J., Bonanomi, D., Pankratz, M., Gifford, W., et al. (2015). Loss of motoneuron-specific microRNA-218 causes systemic neuromuscular failure. *Science* 350, 1525–1529. doi: 10.1126/science.aad2509

Amin, N., Senturk, G., Costaguta, G., Driscoll, S., O'Leary, B., Bonanomi, D., et al. (2021). A hidden threshold in motor neuron gene networks revealed by modulation of miR-218 dose. *Neuron* 109, 3252.e6–3267.e6. doi: 10.1016/j.neuron.2021.07.028

Arendt, T., Gärtner, U., Seeger, G., Barmashenko, G., Palm, K., Mittmann, T., et al. (2004). Neuronal activation of Ras regulates synaptic connectivity. *Eur. J. Neurosci.* 19, 2953–2966. doi: 10.1111/j.0953-816X.2004.03409.x

Ascoli, G., Alonso-Nanclares, L., Anderson, S., Barrionuevo, G., Benavides-Piccione, R., Burkhalter, A., et al. (2008). Petilla terminology: Nomenclature of features of GABAergic interneurons of the cerebral cortex. *Nat. Rev. Neurosci.* 9, 557–568. doi: 10.1038/nrn2402

Attinger, A., Wang, B., and Keller, G. (2017). Visuomotor coupling shapes the functional development of mouse visual cortex. *Cell* 169, 1291.e14–1302.e14. doi: 10.1016/j.cell.2017.05.023

Bahlakeh, G., Gorji, A., Soltani, H., and Ghadiri, T. (2021). MicroRNA alterations in neuropathologic cognitive disorders with an emphasis on dementia: Lessons from animal models. *J. Cell Physiol.* 236, 806–823. doi: 10.1002/jcp.29908

Bak, M., Silahtaroglu, A., Møller, M., Christensen, M., Rath, M., Skryabin, B., et al. (2008). MicroRNA expression in the adult mouse central nervous system. *RNA* 14, 432–444. doi: 10.1261/rna.783108

Bandler, R., Mayer, C., and Fishell, G. (2017). Cortical interneuron specification: The juncture of genes, time and geometry. *Curr. Opin. Neurobiol.* 42, 17–24. doi: 10.1016/j.conb.2016.10.003

Banerjee, A., Macdonald, M., Borgmann-Winter, K., and Hahn, C. (2010). Neuregulin 1-erbB4 pathway in schizophrenia: From genes to an interactome. *Brain Res. Bull.* 83, 132–139. doi: 10.1016/j.brainresbull.2010.04.011

Bartel, D. (2004). MicroRNAs: Genomics, biogenesis, mechanism, and function. *Cell* 116, 281–297. doi: 10.1016/s0092-8674(04)00045-5

Bartel, D. (2009). MicroRNAs: Target recognition and regulatory functions. *Cell* 136, 215–233. doi: 10.1016/j.cell.2009.01.002

Bartel, D. (2018). Metazoan MicroRNAs. *Cell* 173, 20–51. doi: 10.1016/j.cell.2018.03.006

Bassett, A., and Chow, E. (1999). 22q11 deletion syndrome: A genetic subtype of schizophrenia. *Biol. Psychiatry* 46, 882–891. doi: 10.1016/s0006-3223(99)00114-6

Batista-Brito, R., and Fishell, G. (2009). The developmental integration of cortical interneurons into a functional network. *Curr. Top. Dev. Biol.* 87, 81–118. doi: 10.1016/S0070-2153(09)01203-4

Batista-Brito, R., Rossignol, E., Hjerling-Leffler, J., Denaxa, M., Wegner, M., Lefebvre, V., et al. (2009). The cell-intrinsic requirement of Sox6 for cortical interneuron development. *Neuron* 63, 466–481. doi: 10.1016/j.neuron.2009.08.005

Ben-Ari, Y. (2007). GABA excites and sculpts immature neurons well before delivery: Modulation by GABA of the development of ventricular progenitor cells. *Epilepsy Curr.* 7, 167–169. doi: 10.1111/j.1535-7511.2007.00214.x

Bencurova, P., Baloun, J., Musilova, K., Radova, L., Tichy, B., Pail, M., et al. (2017). MicroRNA and mesial temporal lobe epilepsy with hippocampal sclerosis: Whole miRNome profiling of human hippocampus. *Epilepsia* 58, 1782–1793. doi: 10.1111/epi.13870

Bennett, M. (2009). Positive and negative symptoms in schizophrenia: The NMDA receptor hypofunction hypothesis, neuregulin/ErbB4 and synapse regression. *Aust. N. Z. J. Psychiatry* 43, 711–721. doi: 10.1080/00048670903001943

Bernard, C., Exposito-Alonso, D., Selten, M., Sanalidou, S., Hanusz-Godoy, A., Aguilera, A., et al. (2022). Cortical wiring by synapse type-specific control of local protein synthesis. *Science* 378:eabm7466. doi: 10.1126/science.abm7466

Bicker, S., Khudayberdiev, S., Weiß, K., Zocher, K., Baumeister, S., and Schratt, G. (2013). The DEAH-box helicase DHX36 mediates dendritic localization of the neuronal precursor-microRNA-134. *Genes Dev.* 27, 991–996. doi: 10.1101/gad.211243.112

Bicker, S., Lackinger, M., Weiß, K., and Schratt, G. (2014). MicroRNA-132, –134, and –138: A microRNA troika rules in neuronal dendrites. *Cell Mol. Life Sci.* 71, 3987–4005. doi: 10.1007/s00018-014-1671-7

Bielefeld, P., Mooney, C., Henshall, D., and Fitzsimons, C. (2017). miRNA-mediated regulation of adult hippocampal neurogenesis; implications for epilepsy. *Brain Plast.* 3, 43–59. doi: 10.3233/BPL-160036

Bloss, E., Cembrowski, M., Karsh, B., Colonell, J., Fetter, R., and Spruston, N. (2016). Structured dendritic inhibition supports branch-selective integration in CA1 pyramidal cells. *Neuron* 89, 1016–1030. doi: 10.1016/j.neuron.2016.01.029

Brown, J., Ramikie, T., Schmidt, M., Báldi, R., Garbett, K., Everheart, M., et al. (2015). Inhibition of parvalbumin-expressing interneurons results in complex behavioral changes. *Mol. Psychiatry* 20, 1499–1507. doi: 10.1038/mp.2014.192

Bugeon, S., Duffield, J., Dipoppa, M., Ritoux, A., Prankerd, I., Nicoloutsopoulos, D., et al. (2022). A transcriptomic axis predicts state modulation of cortical interneurons. *Nature* 607, 330–338. doi: 10.1038/s41586-022-04915-7

Bugeon, S., Haubold, C., Ryzynski, A., Cremer, H., and Platel, J. (2021). Intrinsic neuronal activity during migration controls the recruitment of specific interneuron subtypes in the postnatal mouse olfactory bulb. *J. Neurosci.* 41, 2630–2644. doi: 10.1523/JNEUROSCI.1960-20.2021

Butt, S., Fuccillo, M., Nery, S., Noctor, S., Kriegstein, A., Corbin, J., et al. (2005). The temporal and spatial origins of cortical interneurons predict their physiological subtype. *Neuron* 48, 591–604. doi: 10.1016/j.neuron.2005.09.034

Butt, S., Sousa, V., Fuccillo, M., Hjerling-Leffler, J., Miyoshi, G., Kimura, S., et al. (2008). The requirement of Nkx2-1 in the temporal specification of cortical interneuron subtypes. *Neuron* 59, 722–732. doi: 10.1016/j.neuron.2008.07.031

Caputi, A., Melzer, S., Michael, M., and Monyer, H. (2013). The long and short of GABAergic neurons. *Curr. Opin. Neurobiol.* 23, 179–186. doi: 10.1016/j.conb.2013.01.021

Caroni, P. (2015). Inhibitory microcircuit modules in hippocampal learning. *Curr. Opin. Neurobiol.* 35, 66–73. doi: 10.1016/j.conb.2015.06.010

Chai, S., Cambronne, X., Eichhorn, S., and Goodman, R. (2013). MicroRNA-134 activity in somatostatin interneurons regulates H-Ras localization by repressing the palmitoylation enzyme, DHHC9. *Proc. Natl. Acad. Sci. U.S.A.* 110, 17898–17903. doi: 10.1073/pnas.1317528110

Chan, J., Sánchez-Vidaña, D., Anoopkumar-Dukie, S., Li, Y., and Benson Wui-Man, L. (2022). RNA-binding protein signaling in adult neurogenesis. *Front. Cell Dev. Biol.* 10:982549. doi: 10.3389/fcell.2022.982549

Chen, D., Hu, S., Wu, Z., Liu, J., and Li, S. (2018). The role of MiR-132 in regulating neural stem cell proliferation, differentiation and neuronal maturation. *Cell Physiol. Biochem.* 47, 2319–2330. doi: 10.1159/000491543

Chen, F., Xu, Y., Shi, K., Zhang, Z., Xie, Z., Wu, H., et al. (2022). Multi-omics study reveals associations among neurotransmitter, extracellular vesicle-derived microRNA and psychiatric comorbidities during heroin and methamphetamine withdrawal. *Biomed. Pharmacother.* 155:113685. doi: 10.1016/j.biopha.2022.113685

Chen, H., Qian, K., Tang, Z., Xing, B., Chen, H., Liu, N., et al. (2010). Bioinformatics and microarray analysis of microRNA expression profiles of murine embryonic stem cells, neural stem cells induced from ESCs and isolated from E8.5 mouse neural tube. *Neurol. Res.* 32, 603–613. doi: 10.1179/174313209X455691

Chen, K., Song, F., Calin, G., Wei, Q., Hao, X., and Zhang, W. (2008). Polymorphisms in microRNA targets: A gold mine for molecular epidemiology. *Carcinogenesis* 29, 1306–1311. doi: 10.1093/carcin/bgn116

Chen, L., Wang, X., Wang, H., Li, Y., Yan, W., Han, L., et al. (2012). miR-137 is frequently down-regulated in glioblastoma and is a negative regulator of cox-2. *Eur. J. Cancer* 48, 3104–3111. doi: 10.1016/j.ejca.2012.02.007

Chen, S., Kim, A., Peters, A., and Komiyama, T. (2015). Subtype-specific plasticity of inhibitory circuits in motor cortex during motor learning. *Nat. Neurosci.* 18, 1109–1115. doi: 10.1038/nn.4049

Cipolla, G. (2014). A non-canonical landscape of the microRNA system. *Front. Genet.* 5:337. doi: 10.3389/fgene.2014.00337

Colin, A., Faideau, M., Dufour, N., Auregan, G., Hassig, R., Andrieu, T., et al. (2009). Engineered lentiviral vector targeting astrocytes in vivo. *Glia* 57, 667–679. doi: 10.1002/glia.20795

Corbin, J., and Butt, S. (2011). Developmental mechanisms for the generation of telencephalic interneurons. *Dev. Neurobiol.* 71, 710–732. doi: 10.1002/dneu.20890

Das, S., Vera, M., Gandin, V., Singer, R., and Tutucci, E. (2021). Intracellular mRNA transport and localized translation. *Nat. Rev. Mol. Cell Biol.* 22, 483–504. doi: 10.1038/s41580-021-00356-8

Daswani, R., Gilardi, C., Soutschek, M., Nanda, P., Weiss, K., Bicker, S., et al. (2022). MicroRNA-138 controls hippocampal interneuron function and short-term memory in mice. *Elife* 11, e74056. doi: 10.7554/eLife.74056

de Chevigny, A., Coré, N., Follert, P., Gaudin, M., Barbry, P., Béclin, C., et al. (2012). miR-7a regulation of Pax6 controls spatial origin of forebrain dopaminergic neurons. *Nat. Neurosci.* 15, 1120–1126. doi: 10.1038/nn.3142

De Marco García, N., Karayannis, T., and Fishell, G. (2011). Neuronal activity is required for the development of specific cortical interneuron subtypes. *Nature* 472, 351–355. doi: 10.1038/nature09865

DeFelipe, J., López-Cruz, P., Benavides-Piccione, R., Bielza, C., Larrañaga, P., Anderson, S., et al. (2013). New insights into the classification and nomenclature of cortical GABAergic interneurons. *Nat. Rev. Neurosci.* 14, 202–216. doi: 10.1038/nrn3444

Dehorter, N., Ciceri, G., Bartolini, G., Lim, L., del Pino, I., and Marín, O. (2015). Tuning of fast-spiking interneuron properties by an activity-dependent transcriptional switch. *Science* 349, 1216–1220. doi: 10.1126/science.aab3415

Dehorter, N., Marichal, N., Marín, O., and Berninger, B. (2017). Tuning neural circuits by turning the interneuron knob. *Curr. Opin. Neurobiol.* 42, 144–151. doi: 10.1016/j.conb.2016.12.009

Del Pino, I., García-Frigola, C., Dehorter, N., Brotons-Mas, J., Alvarez-Salvado, E., Martínez de Lagrán, M., et al. (2013). Erbb4 deletion from fast-spiking interneurons causes schizophrenia-like phenotypes. *Neuron* 79, 1152–1168. doi: 10.1016/j.neuron.2013.07.010

Del Pino, I., Rico, B., and Marín, O. (2018). Neural circuit dysfunction in mouse models of neurodevelopmental disorders. *Curr. Opin. Neurobiol.* 48, 174–182. doi: 10.1016/j.conb.2017.12.013

Denli, A., Tops, B., Plasterk, R., Ketting, R., and Hannon, G. (2004). Processing of primary microRNAs by the Microprocessor complex. *Nature* 432, 231–235. doi: 10.1038/nature03049

Devanna, P., and Vernes, S. (2014). A direct molecular link between the autism candidate gene RORa and the schizophrenia candidate MIR137. *Sci. Rep.* 4:3994. doi: 10.1038/srep03994

Dienel, S., and Lewis, D. (2019). Alterations in cortical interneurons and cognitive function in schizophrenia. *Neurobiol. Dis.* 131:104208. doi: 10.1016/j.nbd.2018.06.020

Donato, F., Rompani, S., and Caroni, P. (2013). Parvalbumin-expressing basket-cell network plasticity induced by experience regulates adult learning. *Nature* 504, 272–276. doi: 10.1038/nature12866

Dubes, S., Favereaux, A., Thoumine, O., and Letellier, M. (2019). miRNA-dependent control of homeostatic plasticity in neurons. *Front. Cell Neurosci.* 13:536. doi: 10.3389/fncel.2019.00536

Dudok, B., Szoboszlay, M., Paul, A., Klein, P., Liao, Z., Hwaun, E., et al. (2021). Recruitment and inhibitory action of hippocampal axo-axonic cells during behavior. *Neuron* 109, 3838.e8–3850.e8. doi: 10.1016/j.neuron.2021.09.033

Dulcis, D., Lippi, G., Stark, C., Do, L., Berg, D., and Spitzer, N. (2017). Neurotransmitter switching regulated by miRNAs controls changes in social preference. *Neuron* 95, 1319.e5–1333.e5. doi: 10.1016/j.neuron.2017.08.023

Ebert, M., and Sharp, P. (2010). MicroRNA sponges: Progress and possibilities. *RNA* 16, 2043–2050. doi: 10.1261/rna.2414110

Ergin, K., and Çetinkaya, R. (2022). Regulation of MicroRNAs. *Methods Mol. Biol.* 2257, 1–32. doi: 10.1007/978-1-0716-1170-8_1

Fabian, M., Sonenberg, N., and Filipowicz, W. (2010). Regulation of mRNA translation and stability by microRNAs. *Annu. Rev. Biochem.* 79, 351–379. doi: 10.1146/annurev-biochem-060308-103103

Faux, C., Rakic, S., Andrews, W., and Britto, J. (2012). Neurons on the move: Migration and lamination of cortical interneurons. *Neurosignals* 20, 168–189. doi: 10.1159/000334489

Fazzari, P., Paternain, A., Valiente, M., Pla, R., Luján, R., Lloyd, K., et al. (2010). Control of cortical GABA circuitry development by Nrg1 and ErbB4 signalling. *Nature* 464, 1376–1380. doi: 10.1038/nature08928

Fee, C., Banasr, M., and Sibille, E. (2017). Somatostatin-positive gamma-aminobutyric acid interneuron deficits in depression: Cortical microcircuit and therapeutic perspectives. *Biol. Psychiatry* 82, 549–559. doi: 10.1016/j.biopsych.2017.05.024

Ferguson, B., and Gao, W. (2018). PV interneurons: Critical regulators of E/I balance for prefrontal cortex-dependent behavior and psychiatric disorders. *Front. Neural Circuits* 12:37. doi: 10.3389/fncir.2018.00037

Figueiredo, R., Adão, R., Leite-Moreira, A., Mâncio, J., and Brás-Silva, C. (2022). Candidate microRNAs as prognostic biomarkers in heart failure: A systematic review. *Rev. Port Cardiol.* 41, 865–885. doi: 10.1016/j.repc.2021.03.020

Fineberg, S., Kosik, K., and Davidson, B. (2009). MicroRNAs potentiate neural development. *Neuron* 64, 303–309. doi: 10.1016/j.neuron.2009.10.020

Fiore, R., Khudayberdiev, S., Christensen, M., Siegel, G., Flavell, S., Kim, T., et al. (2009). Mef2-mediated transcription of the miR379-410 cluster regulates activity-dependent dendritogenesis by fine-tuning Pumilio2 protein levels. *EMBO J.* 28, 697–710. doi: 10.1038/emboj.2009.10

Fishell, G., and Kepecs, A. (2020). Interneuron Types as Attractors and Controllers. *Annu. Rev. Neurosci.* 43, 1–30. doi: 10.1146/annurev-neuro-070918-050421

Fogaça, M., and Duman, R. (2019). Cortical GABAergic dysfunction in stress and depression: New insights for therapeutic interventions. *Front. Cell Neurosci.* 13:87. doi: 10.3389/fncel.2019.00087

Fogarty, M., Grist, M., Gelman, D., Marín, O., Pachnis, V., and Kessaris, N. (2007). Spatial genetic patterning of the embryonic neuroepithelium generates GABAergic interneuron diversity in the adult cortex. *J. Neurosci.* 27, 10935–10946. doi: 10.1523/JNEUROSCI.1629-07.2007

Freund, T. (2003). Interneuron diversity series: Rhythm and mood in perisomatic inhibition. *Trends Neurosci.* 26, 489–495. doi: 10.1016/S0166-2236(03)00227-3

Friedman, R., Farh, K., Burge, C., and Bartel, D. (2009). Most mammalian mRNAs are conserved targets of microRNAs. *Genome Res.* 19, 92–105. doi: 10.1101/gr.082701.108

Fu, Y., Kaneko, M., Tang, Y., Alvarez-Buylla, A., and Stryker, M. (2015). A cortical disinhibitory circuit for enhancing adult plasticity. *Elife* 4:e05558. doi: 10.7554/eLife.05558

Gao, F. (2010). Context-dependent functions of specific microRNAs in neuronal development. *Neural Dev.* 5:25. doi: 10.1186/1749-8104-5-25

Geekiyanage, H., Jicha, G., Nelson, P., and Chan, C. (2012). Blood serum miRNA: Non-invasive biomarkers for Alzheimer's disease. *Exp. Neurol.* 235, 491–496. doi: 10.1016/j.expneurol.2011.11.026

Gelman, D., and Marín, O. (2010). Generation of interneuron diversity in the mouse cerebral cortex. *Eur. J. Neurosci.* 31, 2136–2141. doi: 10.1111/j.1460-9568.2010.07267.x

Gelman, D., Martini, F., Nóbrega-Pereira, S., Pierani, A., Kessaris, N., and Marín, O. (2009). The embryonic preoptic area is a novel source of cortical GABAergic interneurons. *J. Neurosci.* 29, 9380–9389. doi: 10.1523/JNEUROSCI.0604-09.2009

Glausier, J., and Lewis, D. (2018). Mapping pathologic circuitry in schizophrenia. *Handb. Clin. Neurol.* 150, 389–417. doi: 10.1016/B978-0-444-63639-3.00025-6

Gonzalez-Burgos, G., Cho, R., and Lewis, D. (2015). Alterations in cortical network oscillations and parvalbumin neurons in schizophrenia. *Biol. Psychiatry* 77, 1031–1040. doi: 10.1016/j.biopsych.2015.03.010

Gouwens, N., Sorensen, S., Baftizadeh, F., Budzillo, A., Lee, B., Jarsky, T., et al. (2020). Integrated morphoelectric and transcriptomic classification of cortical GABAergic cells. *Cell* 183, 935.e19–953.e19. doi: 10.1016/j.cell.2020.09.057

Gouwens, N., Sorensen, S., Berg, J., Lee, C., Jarsky, T., Ting, J., et al. (2019). Classification of electrophysiological and morphological neuron types in the mouse visual cortex. *Nat. Neurosci.* 22, 1182–1195. doi: 10.1038/s41593-019-0417-0

Green, T., Gothelf, D., Glaser, B., Debbane, M., Frisch, A., Kotler, M., et al. (2009). Psychiatric disorders and intellectual functioning throughout development in velocardiofacial (22q11.2 deletion) syndrome. *J. Am. Acad. Child Adolesc. Psychiatry* 48, 1060–1068. doi: 10.1097/CHI.0b013e3181b76683

Griffiths, B., Sahbaie, P., Rao, A., Arvola, O., Xu, L., Liang, D., et al. (2019). Pre-treatment with microRNA-181a antagomir prevents loss of parvalbumin expression and preserves novel object recognition following mild traumatic brain injury. *Neuromol. Med.* 21, 170–181. doi: 10.1007/s12017-019-08532-y

Griffiths-Jones, S. (2004). The microRNA Registry. *Nucleic Acids Res.* 2, D109–D111. doi: 10.1093/nar/gkh023

Guo, J., and Anton, E. (2014). Decision making during interneuron migration in the developing cerebral cortex. *Trends Cell Biol.* 24, 342–351. doi: 10.1016/j.tcb.2013.12.001

Ha, M., and Kim, V. (2014). Regulation of microRNA biogenesis. *Nat. Rev. Mol. Cell Biol.* 15, 509–524. doi: 10.1038/nrm3838

He, M., Liu, Y., Wang, X., Zhang, M., Hannon, G., and Huang, Z. (2012). Cell-type-based analysis of microRNA profiles in the mouse brain. *Neuron* 73, 35–48. doi: 10.1016/j.neuron.2011.11.010

Hicks, R., Smith, D., Lowenstein, D., Saint Marie, R., and McIntosh, T. (1993). Mild experimental brain injury in the rat induces cognitive deficits associated with regional neuronal loss in the hippocampus. *J. Neurotrauma* 10, 405–414. doi: 10.1089/neu.1993.10.405

Hobert, O. (2008). Gene regulation by transcription factors and microRNAs. *Science* 319, 1785–1786. doi: 10.1126/science.1151651

Hong, J., Zhang, H., Kawase-Koga, Y., and Sun, T. (2013). MicroRNA function is required for neurite outgrowth of mature neurons in the mouse postnatal cerebral cortex. *Front. Cell Neurosci.* 7:151. doi: 10.3389/fncel.2013.00151

Honoré, E., Khlaifia, A., Bosson, A., and Lacaille, J. (2021). Hippocampal somatostatin interneurons, Long-term synaptic plasticity and memory. *Front. Neural Circuits* 15:687558. doi: 10.3389/fncir.2021.687558

Hsu, R., Schofield, C., Dela Cruz, C., Jones-Davis, D., Blelloch, R., and Ullian, E. (2012). Loss of microRNAs in pyramidal neurons leads to specific changes in inhibitory synaptic transmission in the prefrontal cortex. *Mol. Cell Neurosci.* 50, 283–292. doi: 10.1016/j.mcn.2012.06.002

Hu, H., Gan, J., and Jonas, P. (2014). Interneurons. Fast-spiking, parvalbumin? GABAergic interneurons: From cellular design to microcircuit function. *Science* 345:1255263. doi: 10.1126/science.1255263

Hu, J., Vogt, D., Lindtner, S., Sandberg, M., Silberberg, S., and Rubenstein, J. (2017). Coup-TF1 and Coup-TF2 control subtype and laminar identity of MGE-derived neocortical interneurons. *Development* 144, 2837–2851. doi: 10.1242/dev.150664

Huang, Z., Di Cristo, G., and Ango, F. (2007). Development of GABA innervation in the cerebral and cerebellar cortices. *Nat. Rev. Neurosci.* 8, 673–686. doi: 10.1038/nrn2188

Hurni, N., Kolodziejczak, M., Tomasello, U., Badia, J., Jacobshagen, M., Prados, J., et al. (2017). Transient cell-intrinsic activity regulates the migration and laminar positioning of cortical projection neurons. *Cereb. Cortex* 27, 3052–3063. doi: 10.1093/cercor/bhx059

Iannone, A., and De Marco García, N. (2021). The emergence of network activity patterns in the somatosensory cortex – an early window to autism spectrum disorders. *Neuroscience* 466, 298–309. doi: 10.1016/j.neuroscience.2021.04.005

Issler, O., and Chen, A. (2015). Determining the role of microRNAs in psychiatric disorders. *Nat. Rev. Neurosci.* 16, 201–212. doi: 10.1038/nrn3879

Jansen, R. (2001). mRNA localization: Message on the move. *Nat. Rev. Mol. Cell Biol.* 2, 247–256. doi: 10.1038/35067016

Jinno, S., Klausberger, T., Marton, L., Dalezios, Y., Roberts, J., Fuentealba, P., et al. (2007). Neuronal diversity in GABAergic long-range projections from the hippocampus. *J. Neurosci.* 27, 8790–8804. doi: 10.1523/JNEUROSCI.1847-07.2007

Jones, E. (2009). The origins of cortical interneurons: Mouse versus monkey and human. *Cereb. Cortex* 19, 1953–1956. doi: 10.1093/cercor/bhp088

Joshi, D., Fullerton, J., and Weickert, C. (2014). Elevated ErbB4 mRNA is related to interneuron deficit in prefrontal cortex in schizophrenia. *J. Psychiatr. Res.* 53, 125–132. doi: 10.1016/j.jpsychires.2014.02.014

Juric-Sekhar, G., and Hevner, R. (2019). Malformations of cerebral cortex development: Molecules and mechanisms. *Annu. Rev. Pathol.* 14, 293–318. doi: 10.1146/annurev-pathmechdis-012418-012927

Kaneko, M., Cheetham, C., Lee, Y., Silva, A., Stryker, M., and Fox, K. (2010). Constitutively active H-ras accelerates multiple forms of plasticity in developing visual cortex. *Proc. Natl. Acad. Sci. U.S.A.* 107, 19026–19031. doi: 10.1073/pnas.1013866107

Kawaguchi, Y., and Kubota, Y. (1996). Physiological and morphological identification of somatostatin- or vasoactive intestinal polypeptide-containing cells among GABAergic cell subtypes in rat frontal cortex. *J. Neurosci.* 16, 2701–2715. doi: 10.1523/JNEUROSCI.16-08-02701.1996

Kawaguchi, Y., and Kubota, Y. (1997). GABAergic cell subtypes and their synaptic connections in rat frontal cortex. *Cereb. Cortex* 7, 476–486. doi: 10.1093/cercor/7.6.476

Keaveney, M., Rahsepar, B., Tseng, H., Fernandez, F., Mount, R., Ta, T., et al. (2020). CaMKIIα-positive interneurons identified via a microRNA-based viral gene targeting strategy. *J. Neurosci.* 40, 9576–9588. doi: 10.1523/JNEUROSCI.2570-19.2020

Kelsom, C., and Lu, W. (2013). Development and specification of GABAergic cortical interneurons. *Cell Biosci.* 3:19. doi: 10.1186/2045-3701-3-19

Kepecs, A., and Fishell, G. (2014). Interneuron cell types are fit to function. *Nature* 505, 318–326. doi: 10.1038/nature12983

Kessaris, N., Magno, L., Rubin, A., and Oliveira, M. (2014). Genetic programs controlling cortical interneuron fate. *Curr. Opin. Neurobiol.* 26, 79–87. doi: 10.1016/j.conb.2013.12.012

Khadimallah, I., Jenni, R., Cabungcal, J., Cleusix, M., Fournier, M., Beard, E., et al. (2022). Mitochondrial, exosomal miR137-COX6A2 and gamma synchrony as biomarkers of parvalbumin interneurons, psychopathology, and neurocognition in schizophrenia. *Mol. Psychiatry* 27, 1192–1204. doi: 10.1038/s41380-021-01313-9

Khan, I., and Saraya, A. (2022). Circulating MicroRNAs as noninvasive diagnostic and prognostic biomarkers in pancreatic cancer: A review. *J. Gastrointest Cancer* [Epub ahead of print]. doi: 10.1007/s12029-022-00877-1

Klausberger, T., and Somogyi, P. (2008). Neuronal diversity and temporal dynamics: The unity of hippocampal circuit operations. *Science* 321, 53–57. doi: 10.1126/science.1149381

Kong, H., Wang, H., Zhuo, Z., Li, Z., Tian, P., Wu, J., et al. (2020). Inhibition of miR-181a-5p reduces astrocyte and microglia activation and oxidative stress by activating SIRT1 in immature rats with epilepsy. *Lab. Invest.* 100, 1223–1237. doi: 10.1038/s41374-020-0444-1

Kosik, K. (2006). The neuronal microRNA system. *Nat. Rev. Neurosci.* 7, 911–920. doi: 10.1038/nrn2037

Kozomara, A., Birgaoanu, M., and Griffiths-Jones, S. (2019). miRBase: From microRNA sequences to function. *Nucleic Acids Res.* 47, D155–D162. doi: 10.1093/nar/gky1141

Kriegel, A., Liu, Y., Liu, P., Baker, M., Hodges, M., Hua, X., et al. (2013). Characteristics of microRNAs enriched in specific cell types and primary tissue types in solid organs. *Physiol. Genomics* 45, 1144–1156. doi: 10.1152/physiolgenomics.00090.2013

Kuosmanen, S., Kansanen, E., Sihvola, V., and Levonen, A. (2017). MicroRNA profiling reveals distinct profiles for tissue-derived and cultured endothelial cells. *Sci. Rep.* 7:10943. doi: 10.1038/s41598-017-11487-4

Kye, M., Liu, T., Levy, S., Xu, N., Groves, B., Bonneau, R., et al. (2007). Somatodendritic microRNAs identified by laser capture and multiplex RT-PCR. *RNA* 13, 1224–1234. doi: 10.1261/rna.480407

Lagos-Quintana, M., Rauhut, R., Yalcin, A., Meyer, J., Lendeckel, W., and Tuschl, T. (2002). Identification of tissue-specific microRNAs from mouse. *Curr. Biol.* 12, 735–739. doi: 10.1016/s0960-9822(02)00809-6

Lee, R., Feinbaum, R., and Ambros, V. (1993). The C. elegans heterochronic gene lin-4 encodes small RNAs with antisense complementarity to lin-14. *Cell* 75, 843–854. doi: 10.1016/0092-8674(93)90529-Y

Lee, S., Hjerling-Leffler, J., Zagha, E., Fishell, G., and Rudy, B. (2010). The largest group of superficial neocortical GABAergic interneurons expresses ionotropic serotonin receptors. *J. Neurosci.* 30, 16796–16808. doi: 10.1523/JNEUROSCI.1869-10.2010

Lee, Y., Jeon, K., Lee, J., Kim, S., and Kim, V. (2002). MicroRNA maturation: Stepwise processing and subcellular localization. *EMBO J.* 21, 4663–4670. doi: 10.1093/emboj/cdf476

Lee, Y., Kim, M., Han, J., Yeom, K., Lee, S., Baek, S., et al. (2004). MicroRNA genes are transcribed by RNA polymerase II. *EMBO J.* 23, 4051–4060. doi: 10.1038/sj.emboj.7600385

Letinic, K., Zoncu, R., and Rakic, P. (2002). Origin of GABAergic neurons in the human neocortex. *Nature* 417, 645–649. doi: 10.1038/nature00779

Lichtensteiger, W., Bassetti-Gaille, C., Rehrauer, H., Georgijevic, J., Tresguerres, J., and Schlumpf, M. (2021). Converging effects of three different endocrine disrupters on sox and pou gene expression in developing rat hippocampus: Possible role of microRNA in sex differences. *Front. Genet.* 12:718796. doi: 10.3389/fgene.2021.718796

Lim, L., Mi, D., Llorca, A., and Marín, O. (2018). Development and functional diversification of cortical interneurons. *Neuron* 100, 294–313. doi: 10.1016/j.neuron.2018.10.009

Lim, Y., Beane-Ebel, J., Tanaka, Y., Ning, B., Husted, C., Henderson, D., et al. (2021). Exploration of alcohol use disorder-associated brain miRNA-mRNA regulatory networks. *Transl. Psychiatry* 11:504. doi: 10.1038/s41398-021-01635-w

Lin, L., and Sibille, E. (2015). Somatostatin, neuronal vulnerability and behavioral emotionality. *Mol. Psychiatry* 20, 377–387. doi: 10.1038/mp.2014.184

Liu, B., Shyr, Y., Cai, J., and Liu, Q. (2019). Interplay between miRNAs and host genes and their role in cancer. *Brief Funct. Genomics* 18, 255–266. doi: 10.1093/bfgp/elz002

Liu, H., Abecasis, G., Heath, S., Knowles, A., Demars, S., Chen, Y., et al. (2002). Genetic variation in the 22q11 locus and susceptibility to schizophrenia. *Proc. Natl. Acad. Sci. U.S.A.* 99, 16859–16864. doi: 10.1073/pnas.232186099

Londin, E., Loher, P., Telonis, A., Quann, K., Clark, P., Jing, Y., et al. (2015). Analysis of 13 cell types reveals evidence for the expression of numerous novel primate- and tissue-specific microRNAs. *Proc. Natl. Acad. Sci. U.S.A.* 112, E1106–E1115. doi: 10.1073/pnas.1420955112

López-Bendito, G., Sánchez-Alcañiz, J., Pla, R., Borrell, V., Picó, E., Valdeolmillos, M., et al. (2008). Chemokine signaling controls intracortical migration and final distribution of GABAergic interneurons. *J. Neurosci.* 28, 1613–1624. doi: 10.1523/JNEUROSCI.4651-07.2008

López-Mascaraque, L., and de Castro, F. (2002). The olfactory bulb as an independent developmental domain. *Cell. Death Differ.* 9, 1279–1286. doi: 10.1038/sj.cdd.4401076

Lovett-Barron, M., Turi, G., Kaifosh, P., Lee, P., Bolze, F., Sun, X., et al. (2012). Regulation of neuronal input transformations by tunable dendritic inhibition. *Nat. Neurosci.* 15, 423–430, S1–S3. doi: 10.1038/nn.3024

Lu, S., Fu, C., Liang, L., Yang, B., Shen, W., Wang, Q., et al. (2021). miR-218-2 regulates cognitive functions in the hippocampus through complement component 3-dependent modulation of synaptic vesicle release. *Proc. Natl. Acad. Sci. U.S.A.* 118:e2021770118. doi: 10.1073/pnas.2021770118

Lugli, G., Larson, J., Martone, M., Jones, Y., and Smalheiser, N. (2005). Dicer and eIF2c are enriched at postsynaptic densities in adult mouse brain and are modified by neuronal activity in a calpain-dependent manner. *J. Neurochem.* 94, 896–905. doi: 10.1111/j.1471-4159.2005.03224.x

Lugli, G., Torvik, V., Larson, J., and Smalheiser, N. (2008). Expression of microRNAs and their precursors in synaptic fractions of adult mouse forebrain. *J. Neurochem.* 106, 650–661. doi: 10.1111/j.1471-4159.2008.05413.x

Lund, E., Güttinger, S., Calado, A., Dahlberg, J., and Kutay, U. (2004). Nuclear export of microRNA precursors. *Science* 303, 95–98. doi: 10.1126/science.1090599

Ma, K., Xu, A., Cui, S., Sun, M., Xue, Y., and Wang, J. (2016). Impaired GABA synthesis, uptake and release are associated with depression-like behaviors induced by chronic mild stress. *Transl. Psychiatry* 6:e910. doi: 10.1038/tp.2016.181

Ma, K., Zhang, H., Wang, S., Wang, H., Wang, Y., Liu, J., et al. (2019). The molecular mechanism underlying GABAergic dysfunction in nucleus accumbens of depression-like behaviours in mice. *J. Cell. Mol. Med.* 23, 7021–7028. doi: 10.1111/jcmm.14596

Ma, T., Wang, C., Wang, L., Zhou, X., Tian, M., Zhang, Q., et al. (2013). Subcortical origins of human and monkey neocortical interneurons. *Nat. Neurosci.* 16, 1588–1597. doi: 10.1038/nn.3536

Mallet, N., Le Moine, C., Charpier, S., and Gonon, F. (2005). Feedforward inhibition of projection neurons by fast-spiking GABA interneurons in the rat striatum in vivo. *J. Neurosci.* 25, 3857–3869. doi: 10.1523/JNEUROSCI.5027-04.2005

Marín, O., and Rubenstein, J. (2001). A long, remarkable journey: Tangential migration in the telencephalon. *Nat. Rev. Neurosci.* 2, 780–790. doi: 10.1038/35097509

Martin, K., and Ephrussi, A. (2009). mRNA localization: Gene expression in the spatial dimension. *Cell* 136, 719–730. doi: 10.1016/j.cell.2009.01.044

Martin, K., and Zukin, R. S. (2006). RNA trafficking and local protein synthesis in dendrites: An overview. *J. Neurosci.* 26, 7131–7134. doi: 10.1523/JNEUROSCI.1801-06.2006

Mayer, C., Hafemeister, C., Bandler, R., Machold, R., Batista Brito, R., Jaglin, X., et al. (2018). Developmental diversification of cortical inhibitory interneurons. *Nature* 555, 457–462. doi: 10.1038/nature25999

McNeill, E., and Van Vactor, D. (2012). MicroRNAs shape the neuronal landscape. *Neuron* 75, 363–379. doi: 10.1016/j.neuron.2012.07.005

Medley, J., Panzade, G., and Zinovyeva, A. (2021). microRNA strand selection: Unwinding the rules. *Wiley Interdiscip Rev. RNA* 12:e1627. doi: 10.1002/wrna.1627

Mei, L., and Nave, K. (2014). Neuregulin-ERBB signaling in the nervous system and neuropsychiatric diseases. *Neuron* 83, 27–49. doi: 10.1016/j.neuron.2014.06.007

Mi, D., Li, Z., Lim, L., Li, M., Moissidis, M., Yang, Y., et al. (2018). Early emergence of cortical interneuron diversity in the mouse embryo. *Science* 360, 81–85. doi: 10.1126/science.aar6821

Mihaljević, B., Benavides-Piccione, R., Bielza, C., Larrañaga, P., and DeFelipe, J. (2019). Classification of GABAergic interneurons by leading neuroscientists. *Sci. Data* 6:221. doi: 10.1038/s41597-019-0246-8

Minami, K., Uehara, T., Morikawa, Y., Omura, K., Kanki, M., Horinouchi, A., et al. (2014). miRNA expression atlas in male rat. *Sci. Data* 1:140005. doi: 10.1038/sdata.2014.5

Missonnier, P., Prévot, A., Herrmann, F., Ventura, J., Padée, A., and Merlo, M. (2020). Disruption of gamma-delta relationship related to working memory deficits in first-episode psychosis. *J. Neural Transm. (Vienna)* 127, 103–115. doi: 10.1007/s00702-019-02126-5

Miyoshi, G. (2019). Elucidating the developmental trajectories of GABAergic cortical interneuron subtypes. *Neurosci. Res.* 138, 26–32. doi: 10.1016/j.neures.2018.09.012

Miyoshi, G., Hjerling-Leffler, J., Karayannis, T., Sousa, V., Butt, S., Battiste, J., et al. (2010). Genetic fate mapping reveals that the caudal ganglionic eminence produces a large and diverse population of superficial cortical interneurons. *J. Neurosci.* 30, 1582–1594. doi: 10.1523/JNEUROSCI.4515-09.2010

Miyoshi, G., Young, A., Petros, T., Karayannis, T., McKenzie Chang, M., Lavado, A., et al. (2015). Prox1 regulates the subtype-specific development of caudal ganglionic eminence-derived GABAergic cortical interneurons. *J. Neurosci.* 35, 12869–12889. doi: 10.1523/JNEUROSCI.1164-15.2015

Mukherjee, A., Carvalho, F., Eliez, S., and Caroni, P. (2019). Long-lasting rescue of network and cognitive dysfunction in a genetic schizophrenia model. *Cell* 178, 1387.e14–1402.e14. doi: 10.1016/j.cell.2019.07.023

Muñoz, W., Tremblay, R., Levenstein, D., and Rudy, B. (2017). Layer-specific modulation of neocortical dendritic inhibition during active wakefulness. *Science* 355, 954–959. doi: 10.1126/science.aag2599

Neddens, J., and Buonanno, A. (2010). Selective populations of hippocampal interneurons express ErbB4 and their number and distribution is altered in ErbB4 knockout mice. *Hippocampus* 20, 724–744. doi: 10.1002/hipo.20675

Neddens, J., Fish, K., Tricoire, L., Vullhorst, D., Shamir, A., Chung, W., et al. (2011). Conserved interneuron-specific ErbB4 expression in frontal cortex of rodents, monkeys, and humans: Implications for schizophrenia. *Biol. Psychiatry* 70, 636–645. doi: 10.1016/j.biopsych.2011.04.016

Nelson, P., Baldwin, D., Kloosterman, W., Kauppinen, S., Plasterk, R., and Mourelatos, Z. (2006). RAKE and LNA-ISH reveal microRNA expression and localization in archival human brain. *RNA* 12, 187–191. doi: 10.1261/rna.2258506

Nelson, S., and Valakh, V. (2015). Excitatory/inhibitory balance and circuit homeostasis in autism spectrum disorders. *Neuron* 87, 684–698. doi: 10.1016/j.neuron.2015.07.033

Nery, S., Fishell, G., and Corbin, J. (2002). The caudal ganglionic eminence is a source of distinct cortical and subcortical cell populations. *Nat. Neurosci.* 5, 1279–1287. doi: 10.1038/nn971

Ninkovic, J., Pinto, L., Petricca, S., Lepier, A., Sun, J., Rieger, M., et al. (2010). The transcription factor Pax6 regulates survival of dopaminergic olfactory bulb neurons via crystallin αA. *Neuron* 68, 682–694. doi: 10.1016/j.neuron.2010.09.030

Obermayer, J., Heistek, T., Kerkhofs, A., Goriounova, N., Kroon, T., Baayen, J., et al. (2018). Lateral inhibition by Martinotti interneurons is facilitated by cholinergic inputs in human and mouse neocortex. *Nat. Commun.* 9:4101. doi: 10.1038/s41467-018-06628-w

O'Brien, J., Hayder, H., Zayed, Y., and Peng, C. (2018). Overview of MicroRNA biogenesis, mechanisms of actions, and circulation. *Front. Endocrinol. (Lausanne)* 9:402. doi: 10.3389/fendo.2018.00402

Okada, C., Yamashita, E., Lee, S., Shibata, S., Katahira, J., Nakagawa, A., et al. (2009). A high-resolution structure of the pre-microRNA nuclear export machinery. *Science* 326, 1275–1279. doi: 10.1126/science.1178705

Okamura, K., Ishizuka, A., Siomi, H., and Siomi, M. (2004). Distinct roles for argonaute proteins in small RNA-directed RNA cleavage pathways. *Genes Dev.* 18, 1655–1666. doi: 10.1101/gad.1210204

Paul, P., Chakraborty, A., Sarkar, D., Langthasa, M., Rahman, M., Bari, M., et al. (2018). Interplay between miRNAs and human diseases. *J. Cell Physiol.* 233, 2007–2018. doi: 10.1002/jcp.25854

Perlman, G., Tanti, A., and Mechawar, N. (2021). Parvalbumin interneuron alterations in stress-related mood disorders: A systematic review. *Neurobiol. Stress* 15:100380. doi: 10.1016/j.ynstr.2021.100380

Perruisseau-Carrier, C., Jurga, M., Forraz, N., and McGuckin, C. (2011). miRNAs stem cell reprogramming for neuronal induction and differentiation. *Mol. Neurobiol.* 43, 215–227. doi: 10.1007/s12035-011-8179-z

Petanjek, Z., Berger, B., and Esclapez, M. (2009). Origins of cortical GABAergic neurons in the cynomolgus monkey. *Cereb. Cortex* 19, 249–262. doi: 10.1093/cercor/bhn078

Peyre, E., Silva, C., and Nguyen, L. (2015). Crosstalk between intracellular and extracellular signals regulating interneuron production, migration and integration into the cortex. *Front. Cell Neurosci.* 9:129. doi: 10.3389/fncel.2015.00129

Pi, H., Hangya, B., Kvitsiani, D., Sanders, J., Huang, Z., and Kepecs, A. (2013). Cortical interneurons that specialize in disinhibitory control. *Nature* 503, 521–524. doi: 10.1038/nature12676

Pietersen, C., Mauney, S., Kim, S., Passeri, E., Lim, M., Rooney, R., et al. (2014). Molecular profiles of parvalbumin-immunoreactive neurons in the superior temporal cortex in schizophrenia. *J. Neurogenet.* 28, 70–85. doi: 10.3109/01677063.2013.878339

Pleasure, S., Anderson, S., Hevner, R., Bagri, A., Marin, O., Lowenstein, D., et al. (2000). Cell migration from the ganglionic eminences is required for the development of hippocampal GABAergic interneurons. *Neuron* 28, 727–740. doi: 10.1016/S0896-6273(00)00149-5

Pouille, F., and Scanziani, M. (2001). Enforcement of temporal fidelity in pyramidal cells by somatic feed-forward inhibition. *Science* 293, 1159–1163. doi: 10.1126/science.1060342

Qiu, F., Mao, X., Liu, P., Wu, J., Zhang, Y., Sun, D., et al. (2020). microRNA deficiency in VIP+ interneurons leads to cortical circuit dysfunction. *Cereb. Cortex* 30, 2229–2249. doi: 10.1093/cercor/bhz236

Reichenstein, I., Eitan, C., Diaz-Garcia, S., Haim, G., Magen, I., Siany, A., et al. (2019). Human genetics and neuropathology suggest a link between miR-218 and amyotrophic lateral sclerosis pathophysiology. *Sci. Transl. Med.* 11:eaav5264. doi: 10.1126/scitranslmed.aav5264

Ren, L., Zhu, R., and Li, X. (2016). Silencing miR-181a produces neuroprotection against hippocampus neuron cell apoptosis post-status epilepticus in a rat model and in children with temporal lobe epilepsy. *Genet. Mol. Res.* 15, 1–11. doi: 10.4238/gmr.15017798

Rhomberg, T., Rovira-Esteban, L., Vikór, A., Paradiso, E., Kremser, C., Nagy-Pál, P., et al. (2018). Vasoactive intestinal polypeptide-immunoreactive interneurons within circuits of the mouse basolateral amygdala. *J. Neurosci.* 38, 6983–7003. doi: 10.1523/JNEUROSCI.2063-17.2018

Robinson, H., Tan, Z., Santiago-Marrero, I., Arzola, E., Dong, T., Xiong, W., et al. (2022). Neuregulin 1 and ErbB4 kinase actively regulate sharp wave ripples in the hippocampus. *J. Neurosci.* 42, 390–404. doi: 10.1523/JNEUROSCI.1022-21.2021

Rocchi, A., Moretti, D., Lignani, G., Colombo, E., Scholz-Starke, J., Baldelli, P., et al. (2019). Neurite-enriched MicroRNA-218 stimulates translation of the GluA2 subunit and increases excitatory synaptic strength. *Mol. Neurobiol.* 56, 5701–5714. doi: 10.1007/s12035-019-1492-7

Royer, S., Zemelman, B., Losonczy, A., Kim, J., Chance, F., Magee, J., et al. (2012). Control of timing, rate and bursts of hippocampal place cells by dendritic and somatic inhibition. *Nat. Neurosci.* 15, 769–775. doi: 10.1038/nn.3077

Rudy, B., Fishell, G., Lee, S., and Hjerling-Leffler, J. (2011). Three groups of interneurons account for nearly 100% of neocortical GABAergic neurons. *Dev. Neurobiol.* 71, 45–61. doi: 10.1002/dneu.20853

Sambandan, S., Akbalik, G., Kochen, L., Rinne, J., Kahlstatt, J., Glock, C., et al. (2017). Activity-dependent spatially localized miRNA maturation in neuronal dendrites. *Science* 355, 634–637. doi: 10.1126/science.aaf8995

Schell, G., Roy, B., Prall, K., and Dwivedi, Y. (2022). miR-218: A stress-responsive epigenetic modifier. *Noncoding RNA* 8:55. doi: 10.3390/ncrna8040055

Schneider-Mizell, C., Bodor, A., Collman, F., Brittain, D., Bleckert, A., Dorkenwald, S., et al. (2021). Structure and function of axo-axonic inhibition. *Elife* 10:e73783. doi: 10.7554/eLife.73783

Schofield, C., Hsu, R., Barker, A., Gertz, C., Blelloch, R., and Ullian, E. (2011). Monoallelic deletion of the microRNA biogenesis gene Dgcr8 produces deficits in the development of excitatory synaptic transmission in the prefrontal cortex. *Neural Dev.* 6:11. doi: 10.1186/1749-8104-6-11

Schratt, G. (2009). microRNAs at the synapse. *Nat. Rev. Neurosci.* 10, 842–849. doi: 10.1038/nrn2763

Schratt, G., Tuebing, F., Nigh, E., Kane, C., Sabatini, M., Kiebler, M., et al. (2006). A brain-specific microRNA regulates dendritic spine development. *Nature* 439, 283–289. doi: 10.1038/nature04367

Schwaller, B., Meyer, M., and Schiffmann, S. (2002). 'New' functions for 'old' proteins: The role of the calcium-binding proteins calbindin D-28k, calretinin and parvalbumin, in cerebellar physiology. Studies with knockout mice. *Cerebellum* 1, 241–258. doi: 10.1080/147342202320883551

Sellier, C., Hwang, V., Dandekar, R., Durbin-Johnson, B., Charlet-Berguerand, N., Ander, B., et al. (2014). Decreased DGCR8 expression and miRNA dysregulation in individuals with 22q11.2 deletion syndrome. *PLoS One* 9:e103884. doi: 10.1371/journal.pone.0103884

Selten, M., van Bokhoven, H., and Nadif Kasri, N. (2018). Inhibitory control of the excitatory/inhibitory balance in psychiatric disorders. *F1000Res* 7:23. doi: 10.12688/f1000research.12155.1

Shi, Y., Wang, M., Mi, D., Lu, T., Wang, B., Dong, H., et al. (2021). Mouse and human share conserved transcriptional programs for interneuron development. *Science* 374:eabj6641. doi: 10.1126/science.abj6641

Shi, Y., Zhao, X., Hsieh, J., Wichterle, H., Impey, S., Banerjee, S., et al. (2010). MicroRNA regulation of neural stem cells and neurogenesis. *J. Neurosci.* 30, 14931–14936. doi: 10.1523/JNEUROSCI.4280-10.2010

Siegel, G., Obernosterer, G., Fiore, R., Oehmen, M., Bicker, S., Christensen, M., et al. (2009). A functional screen implicates microRNA-138-dependent regulation of the depalmitoylation enzyme APT1 in dendritic spine morphogenesis. *Nat. Cell Biol.* 11, 705–716. doi: 10.1038/ncb1876

Skirzewski, M., Karavanova, I., Shamir, A., Erben, L., Garcia-Olivares, J., Shin, J., et al. (2018). ErbB4 signaling in dopaminergic axonal projections increases extracellular dopamine levels and regulates spatial/working memory behaviors. *Mol. Psychiatry* 23, 2227–2237. doi: 10.1038/mp.2017.132

Smith, C., and Hutvagner, G. (2022). A comparative analysis of single cell small RNA sequencing data reveals heterogeneous isomiR expression and regulation. *Sci. Rep.* 12:2834. doi: 10.1038/s41598-022-06876-3

Sohal, V., Zhang, F., Yizhar, O., and Deisseroth, K. (2009). Parvalbumin neurons and gamma rhythms enhance cortical circuit performance. *Nature* 459, 698–702. doi: 10.1038/nature07991

Sokol, N., Xu, P., Jan, Y., and Ambros, V. (2008). Drosophila let-7 microRNA is required for remodeling of the neuromusculature during metamorphosis. *Genes Dev.* 22, 1591–1596. doi: 10.1101/gad.1671708

Stappert, L., Roese-Koerner, B., and Brüstle, O. (2015). The role of microRNAs in human neural stem cells, neuronal differentiation and subtype specification. *Cell Tissue Res.* 359, 47–64. doi: 10.1007/s00441-014-1981-y

Stavast, C., and Erkeland, S. (2019). The non-canonical aspects of MicroRNAs: Many roads to gene regulation. *Cells* 8:1465. doi: 10.3390/cells8111465

Strobl-Mazzulla, P., Marini, M., and Buzzi, A. (2012). Epigenetic landscape and miRNA involvement during neural crest development. *Dev. Dyn.* 241, 1849–1856. doi: 10.1002/dvdy.23868

Sultan, K., Brown, K., and Shi, S. (2013). Production and organization of neocortical interneurons. *Front. Cell Neurosci.* 7:221. doi: 10.3389/fncel.2013.00221

Swanson, O., and Maffei, A. (2019). From hiring to firing: Activation of inhibitory neurons and their recruitment in behavior. *Front. Mol. Neurosci.* 12:168. doi: 10.3389/fnmol.2019.00168

Szabadics, J., Varga, C., Molnár, G., Oláh, S., Barzó, P., and Tamás, G. (2006). Excitatory effect of GABAergic axo-axonic cells in cortical microcircuits. *Science* 311, 233–235. doi: 10.1126/science.1121325

Szulwach, K., Li, X., Smrt, R., Li, Y., Luo, Y., Lin, L., et al. (2010). Cross talk between microRNA and epigenetic regulation in adult neurogenesis. *J. Cell Biol.* 189, 127–141. doi: 10.1083/jcb.200908151

Taniguchi, H., Lu, J., and Huang, Z. (2013). The spatial and temporal origin of chandelier cells in mouse neocortex. *Science* 339, 70–74. doi: 10.1126/science.1227622

Tasic, B., Menon, V., Nguyen, T., Kim, T., Jarsky, T., Yao, Z., et al. (2016). Adult mouse cortical cell taxonomy revealed by single cell transcriptomics. *Nat. Neurosci.* 19, 335–346. doi: 10.1038/nn.4216

Tasic, B., Yao, Z., Graybuck, L., Smith, K., Nguyen, T., Bertagnolli, D., et al. (2018). Shared and distinct transcriptomic cell types across neocortical areas. *Nature* 563, 72–78. doi: 10.1038/s41586-018-0654-5

Taylor, S., Kobayashi, M., Vilella, A., Tiwari, D., Zolboot, N., Hartzell, A., et al. (2022). MicroRNA-218 instructs proper assembly of hippocampal networks. *bioRxiv [Preprint]*. Available online at: https://doi.org/10.1101/2022.08.24.505085 (Accessed August 25, 2022).

Teppola, H., Aćimović, J., and Linne, M. (2019). Unique features of network bursts emerge from the complex interplay of excitatory and inhibitory receptors in rat neocortical networks. *Front. Cell Neurosci.* 13:377. doi: 10.3389/fncel.2019.00377

Thiebes, K., Nam, H., Cambronne, X., Shen, R., Glasgow, S., Cho, H., et al. (2015). miR-218 is essential to establish motor neuron fate as a downstream effector of Isl1-Lhx3. *Nat. Commun.* 6:7718. doi: 10.1038/ncomms8718

Tian, J., Geng, F., Gao, F., Chen, Y., Liu, J., Wu, J., et al. (2017). Down-regulation of Neuregulin1/ErbB4 signaling in the hippocampus is critical for learning and memory. *Mol. Neurobiol.* 54, 3976–3987. doi: 10.1007/s12035-016-9956-5

Torres-Berrío, A., Nouel, D., Cuesta, S., Parise, E., Restrepo-Lozano, J., Larochelle, P., et al. (2020). MiR-218: A molecular switch and potential biomarker of susceptibility to stress. *Mol. Psychiatry* 25, 951–964. doi: 10.1038/s41380-019-0421-5

Tremblay, R., Lee, S., and Rudy, B. (2016). GABAergic Interneurons in the Neocortex: From Cellular Properties to Circuits. *Neuron* 91, 260–292. doi: 10.1016/j.neuron.2016.06.033

Tripp, A., Kota, R., Lewis, D., and Sibille, E. (2011). Reduced somatostatin in subgenual anterior cingulate cortex in major depression. *Neurobiol. Dis.* 42, 116–124.

Truscott, M., Islam, A., and Frolov, M. (2016). Novel regulation and functional interaction of polycistronic miRNAs. *RNA* 22, 129–138. doi: 10.1261/rna.053264.115

Tsermpini, E., Kalogirou, C., Kyriakopoulos, G., Patrinos, G., and Stathopoulos, C. (2022). miRNAs as potential diagnostic biomarkers and pharmacogenomic indicators in psychiatric disorders. *Pharmacogenomics J.* 22, 211–222. doi: 10.1038/s41397-022-00283-7

Tu, J., Cao, D., Li, L., Cheung, H., and Chan, W. (2018). MicroRNA profiling during directed differentiation of cortical interneurons from human-induced pluripotent stem cells. *FEBS Open Bio* 8, 502–512. doi: 10.1002/2211-5463.12377

Tuncdemir, S., Fishell, G., and Batista-Brito, R. (2015). miRNAs are essential for the survival and maturation of cortical interneurons. *Cereb. Cortex* 25, 1842–1857. doi: 10.1093/cercor/bht426

van den Berg, M., Krauskopf, J., Ramaekers, J., Kleinjans, J., Prickaerts, J., and Briedé, J. (2020). Circulating microRNAs as potential biomarkers for psychiatric and neurodegenerative disorders. *Prog. Neurobiol.* 185:101732. doi: 10.1016/j.pneurobio.2019.101732

van Spronsen, M., van Battum, E., Kuijpers, M., Vangoor, V., Rietman, M., Pothof, J., et al. (2013). Developmental and activity-dependent miRNA expression profiling in primary hippocampal neuron cultures. *PLoS One* 8:e74907. doi: 10.1371/journal.pone.0074907

Vergaño-Vera, E., Yusta-Boyo, M., de Castro, F., Bernad, A., de Pablo, F., and Vicario-Abejón, C. (2006). Generation of GABAergic and dopaminergic interneurons from endogenous embryonic olfactory bulb precursor cells. *Development* 133, 4367–4379. doi: 10.1242/dev.02601

Volk, D., Chitrapu, A., Edelson, J., and Lewis, D. (2015). Chemokine receptors and cortical interneuron dysfunction in schizophrenia. *Schizophr. Res.* 167, 12–17. doi: 10.1016/j.schres.2014.10.031

Vullhorst, D., Neddens, J., Karavanova, I., Tricoire, L., Petralia, R., McBain, C., et al. (2009). Selective expression of ErbB4 in interneurons, but not pyramidal cells, of the rodent hippocampus. *J. Neurosci.* 29, 12255–12264. doi: 10.1523/JNEUROSCI.2454-09.2009

Wakabayashi, T., Hidaka, R., Fujimaki, S., Asashima, M., and Kuwabara, T. (2014). MicroRNAs and epigenetics in adult neurogenesis. *Adv. Genet.* 86, 27–44. doi: 10.1016/B978-0-12-800222-3.00002-4

Wamsley, B., and Fishell, G. (2017). Genetic and activity-dependent mechanisms underlying interneuron diversity. *Nat. Rev. Neurosci.* 18, 299–309. doi: 10.1038/nrn.2017.30

Wang, Y., Toledo-Rodriguez, M., Gupta, A., Wu, C., Silberberg, G., Luo, J., et al. (2004). Anatomical, physiological and molecular properties of Martinotti cells in the somatosensory cortex of the juvenile rat. *J. Physiol.* 561, 65–90. doi: 10.1113/jphysiol.2004.073353

Weber, J., Baxter, D., Zhang, S., Huang, D., Huang, K., Lee, M., et al. (2010). The microRNA spectrum in 12 body fluids. *Clin. Chem.* 56, 1733–1741. doi: 10.1373/clinchem.2010.147405

Wei, Z., and Shetty, A. (2022). Can mild cognitive impairment and Alzheimer's disease be diagnosed by monitoring a miRNA triad in the blood? *Aging Cell.* 21:e13627.

Wightman, B., Ha, I., and Ruvkun, G. (1993). Posttranscriptional regulation of the heterochronic gene lin-14 by lin-4 mediates temporal pattern formation in C. elegans. *Cell* 75, 855–862. doi: 10.1016/0092-8674(93)90530-4

Winter, J., Jung, S., Keller, S., Gregory, R., and Diederichs, S. (2009). Many roads to maturity: microRNA biogenesis pathways and their regulation. *Nat. Cell Biol.* 11, 228–234. doi: 10.1038/ncb0309-228

Wonders, C., and Anderson, S. (2006). The origin and specification of cortical interneurons. *Nat. Rev. Neurosci.* 7, 687–696. doi: 10.1038/nrn1954

Wood, K., Blackwell, J., and Geffen, M. (2017). Cortical inhibitory interneurons control sensory processing. *Curr. Opin. Neurobiol.* 46, 200–207. doi: 10.1016/j.conb.2017.08.018

Woodruff, A., Xu, Q., Anderson, S., and Yuste, R. (2009). Depolarizing effect of neocortical chandelier neurons. *Front. Neural. Circuits* 3:15. doi: 10.3389/neuro.04.015.2009

Wu, J., Liu, P., Mao, X., Qiu, F., Gong, L., Wu, J., et al. (2022). Ablation of microRNAs in VIP+ interneurons impairs olfactory discrimination and decreases neural activity in the olfactory bulb. *Acta Physiol. (Oxf)* 234:e13767. doi: 10.1111/apha.13767

Xu, Q., de la Cruz, E., and Anderson, S. (2003). Cortical interneuron fate determination: Diverse sources for distinct subtypes? *Cereb. Cortex* 13, 670–676. doi: 10.1093/cercor/13.6.670

Yang, J., and Lai, E. (2011). Alternative miRNA biogenesis pathways and the interpretation of core miRNA pathway mutants. *Mol. Cell* 43, 892–903. doi: 10.1016/j.molcel.2011.07.024

Yang, W., and Sun, Q. (2018). Circuit-specific and neuronal subcellular-wide E-I balance in cortical pyramidal cells. *Sci. Rep.* 8:3971. doi: 10.1038/s41598-018-22314-9

Ye, Y., Xu, H., Su, X., and He, X. (2016). Role of MicroRNA in governing synaptic plasticity. *Neural Plast.* 2016:4959523. doi: 10.1155/2016/4959523

Yin, J., Lin, J., Luo, X., Chen, Y., Li, Z., Ma, G., et al. (2014). miR-137: A new player in schizophrenia. *Int. J. Mol. Sci.* 15, 3262–3271. doi: 10.3390/ijms15023262

Yoshino, Y., Roy, B., and Dwivedi, Y. (2022). Corticosterone-mediated regulation and functions of miR-218-5p in rat brain. *Sci. Rep.* 12:194. doi: 10.1038/s41598-021-03863-y

Yu, Y., Zeng, Z., Xie, D., Chen, R., Sha, Y., Huang, S., et al. (2021). Interneuron origin and molecular diversity in the human fetal brain. *Nat. Neurosci.* 24, 1745–1756. doi: 10.1038/s41593-021-00940-3

Zahr, S., Kaplan, D., and Miller, F. (2019). Translating neural stem cells to neurons in the mammalian brain. *Cell Death Differ.* 26, 2495–2512. doi: 10.1038/s41418-019-0411-9

Zampa, F., Bicker, S., and Schratt, G. (2018). Activity-Dependent Pre-miR-134 dendritic localization is required for hippocampal neuron dendritogenesis. *Front. Mol. Neurosci.* 11:171. doi: 10.3389/fnmol.2018.00171

Zecevic, N., Hu, F., and Jakovcevski, I. (2011). Interneurons in the developing human neocortex. *Dev. Neurobiol.* 71, 18–33. doi: 10.1002/dneu.20812

Zhang, C., Liu, X., and Yuan, T. (2017). Somatostatin-positive GABAergic interneuron: New targets for depression. *Mol. Psychiatry* 22, 790–791. doi: 10.1038/mp.2017.11

Zolboot, N., Du, J., Zampa, F., and Lippi, G. (2021). MicroRNAs instruct and maintain cell type diversity in the nervous system. *Front. Mol. Neurosci.* 14:646072. doi: 10.3389/fnmol.2021.646072

frontiers | Frontiers in Cellular Neuroscience

TYPE Systematic Review
PUBLISHED 26 June 2023
DOI 10.3389/fncel.2023.1212202

OPEN ACCESS

EDITED BY
Dominique Debanne,
INSERM U1072 Neurobiologie des canaux Ioniques et de la Synapse, France

REVIEWED BY
Rocco Pizzarelli,
European Brain Research Institute, Italy
Nikolai Cyril Dembrow,
University of Washington, United States
Ludovic Tricoire,
Sorbonne Universités, France

*CORRESPONDENCE
Thomas C. M. Bienvenu
✉ thomas.bienvenu@u-bordeaux.fr

†These authors have contributed equally to this work

RECEIVED 25 April 2023
ACCEPTED 09 June 2023
PUBLISHED 26 June 2023

CITATION
Vivien J, El Azraoui A, Lheraux C, Lanore F, Aouizerate B, Herry C, Humeau Y and Bienvenu TCM (2023) Axo-axonic cells in neuropsychiatric disorders: a systematic review. *Front. Cell. Neurosci.* 17:1212202. doi: 10.3389/fncel.2023.1212202

Axo-axonic cells in neuropsychiatric disorders: a systematic review

Juliette Vivien[1†], Anass El Azraoui[1,2†], Cloé Lheraux[1], Frederic Lanore[3], Bruno Aouizerate[1,3,4], Cyril Herry[1], Yann Humeau[2] and Thomas C. M. Bienvenu[1,3*]

[1]Université de Bordeaux, Inserm Neurocentre Magendie U1215, Bordeaux, France, [2]Univ Bordeaux, CNRS, Interdisciplinary Institute for Neuroscience, IINS, UMR 5297, Bordeaux, France, [3]Centre Hospitalier Charles Perrens, Inserm Neurocentre Magendie U1215, Bordeaux, France, [4]INRAE, Bordeaux INP, NutriNeuro, UMR 1286, Bordeaux, France

Imbalance between excitation and inhibition in the cerebral cortex is one of the main theories in neuropsychiatric disorder pathophysiology. Cortical inhibition is finely regulated by a variety of highly specialized GABAergic interneuron types, which are thought to organize neural network activities. Among interneurons, axo-axonic cells are unique in making synapses with the axon initial segment of pyramidal neurons. Alterations of axo-axonic cells have been proposed to be implicated in disorders including epilepsy, schizophrenia and autism spectrum disorder. However, evidence for the alteration of axo-axonic cells in disease has only been examined in narrative reviews. By performing a systematic review of studies investigating axo-axonic cells and axo-axonic communication in epilepsy, schizophrenia and autism spectrum disorder, we outline convergent findings and discrepancies in the literature. Overall, the implication of axo-axonic cells in neuropsychiatric disorders might have been overstated. Additional work is needed to assess initial, mostly indirect findings, and to unravel how defects in axo-axonic cells translates to cortical dysregulation and, in turn, to pathological states.

KEYWORDS

interneuron, chandelier cell, epilepsy, schizophrenia, autism

Introduction

Imbalance between synaptic excitation and inhibition in cortical regions (including neocortex and hippocampus) is a key feature of many brain disorders (Marin, 2012; Sohal and Rubenstein, 2019). Activities of cortical neuron assemblies are coordinated by brain rhythms of various frequencies which are known to be critical for cognitive, emotional and motor function (Buzsaki and Draguhn, 2004). Throughout the brain, inhibition provided by GABAergic interneurons orchestrate cortical oscillations (Roux and Buzsaki, 2015). Lack of pyramidal neuron inhibition results in global hyperexcitability and highly synchronous discharges, which are hallmarks of epilepsy (EPI). Beyond hyperexcitability, dysregulation of oscillatory activities may result in more subtle alterations in cortical functions. Basal and sensory-evoked oscillatory rhythms have been found to be altered in schizophrenia (SCZ) and autism spectrum disorders (ASD; Simon and Wallace, 2016; Hunt et al., 2017). As inhibition is critical for cortical oscillations (Roux and Buzsaki, 2015), these findings collectively point toward a central implication of interneuron functional alterations in neuropsychiatric disorders (Marin, 2012; Sohal and Rubenstein, 2019).

In cortex, inhibition is provided by distinct types of GABAergic cells, with extensive diversity in structure reflected in specialized functions. Indeed, by receiving different

synaptic inputs and by targeting distinct functional domains along somato-dendritic arborizations of pyramidal cells, distinct GABAergic interneuron types are thought to play highly specific roles in organizing cortical network activities (e.g., Kepecs and Fishell, 2014). Perisomatic inhibition is mainly provided by interneurons which typically emit short-duration action potentials at high frequencies and express the calcium binding protein parvalbumin (PV). PV+ interneurons are powerful inhibitors of principal neurons and regulate fast (>30 Hz) brain rhythms, such as gamma oscillations (30–80 Hz; Cardin et al., 2009; Sohal et al., 2009). This, added to their expression of disease-related genes, has led to the hypothesis that PV+ interneuron dysfunction may be implicated in neuropsychiatric disorders (reviewed in Marin, 2012).

The PV+ interneuron class has been further divided into two main types: basket cells, which axon make synapses with cell bodies and proximal dendrites of pyramidal neurons, and axo-axonic cells (AACs), which axonal boutons exclusively innervate the axon initial segment (AIS) of pyramidal neurons (Somogyi, 1977). Axo-axonic terminals are organized in vertical clusters ("cartridges"), hence the alternative name of "Chandelier cells" for AACs. This typical morphology is the most distinctive characteristic of AACs at the cellular level. In addition, PV is a classical (albeit non-selective) marker of AACs (but PV- AACs are found in cortex, e.g., Taniguchi et al., 2013). In addition, Human AACs may express calbindin (CB), which has been found to be associated (del Rio and DeFelipe, 1997), or mutually exclusive with PV (Wittner et al., 2002). At the electron microscopic level, AACs make symmetrical synapses with the axon initial segment (identified by cisternal organelles, dense undercoating, bundled microtubules). Accordingly, axo-axonic terminals contain the molecular machinery for GABA release, including glutamic acid decarboxylase (GAD), membrane GABA transporters (GAT-1) and vesicular GABA transporters (VGAT; Jung et al., 2022). At the postsynaptic level, AISs are organized by scaffold proteins with Ankyrin-G playing a decisive role (Gallo et al., 2020). AISs synapses are enriched in α2 subunit-containing $GABA_A$-Rs (Nusser et al., 1996), although a quantitative freeze-fracture replica study found equal levels of α1 and α2 subunits (Kerti-Szigeti and Nusser, 2016). These morphological and molecular features are classically used to study AACs, including in the studies reviewed in this article.

Because action potentials are generated at the AIS, AACs have long been speculated to exert powerful control on pyramidal neurons activities, and to play a key role in regulating network excitability and neuronal assemblies. Being sole inhibitors at the AIS and showing disease-related changes, AACs might represent a cortical Achille's heel. Indeed, the potential role of AACs in network physiology has been mirrored by studies of cortical AACs in disease, pointing toward abnormalities at AACs' cell bodies and synapses in postmortem samples of patients suffering from EPI (DeFelipe et al., 1993), SCZ (Woo et al., 1998) or, more recently, ASD (Ariza et al., 2018). AACs and their implication in disease have attracted a lot of interest, as previously summarized (Wang et al., 2016; Gallo et al., 2020; Juarez and Martinez Cerdeno, 2022). However, no previous work has reviewed *systematically* the studies linking AACs to brain disorders. The aim of this article is to provide a systematic review of articles documenting AACs' implication in neuropsychiatric disorders (EPI, SCZ, and ASD), for scientists and clinicians studying those disorders, and to help design future studies on robust experimental grounds.

Methods

The systematic review followed PRISMA guidelines. Two independent electronic databases (Pubmed and Web of Science) were searched until July 2021 for articles dealing with AACs in EPI, SCZ and ASD with the following search terms: ≪(chandelier cell OR axo axonic) AND epilep*≫, ≪(chandelier cell OR axo axonic) AND schizophrenia≫, ≪(chandelier cell OR axo axonic) AND autism≫, respectively. Duplicates were removed, and titles and abstracts were screened for inclusion. Full texts were obtained and examined if articles potentially corresponded to eligibility criteria. Two investigators (AEA and JV) screened the literature. In case of a disagreement, individual articles were studied by all the authors, until consensus was reached. Full articles matching inclusion criteria were studied and summarized by the authors. Additional articles found by cross-referencing were also examined and included when indicated.

Eligibility was defined by the following criteria, which were defined prior to the selection of articles:

Inclusion criteria

Articles investigating AACs' modifications in EPI, SCZ, ASD in brain tissue from patients (including case reports), or in animal models of those disorders (*in vivo* and/or *in vitro*) were included for analysis.

Exclusion criteria

Articles written in languages other than English, review articles, and studies giving no specific results on AACs were excluded from the final analysis. Articles lacking an unambiguous (e.g., morphological) identification of AACs or their synaptic compartments at AISs were thus excluded. Likewise, studies lacking a characterization of potential AACs' alterations were excluded. All exclusions were documented and reasons for exclusions are reported.

Results

A total of 200 articles were screened after duplicates removal (EPI 109, SCZ 77, ASD 14). Thirty-two articles were included in the final analysis (EPI 16, SCZ 13, ASD 3). The screening steps are illustrated in the corresponding flowcharts (Figures 1–3; see also Supplementary material). The results concerning AACs are summarized in Tables 1–3.

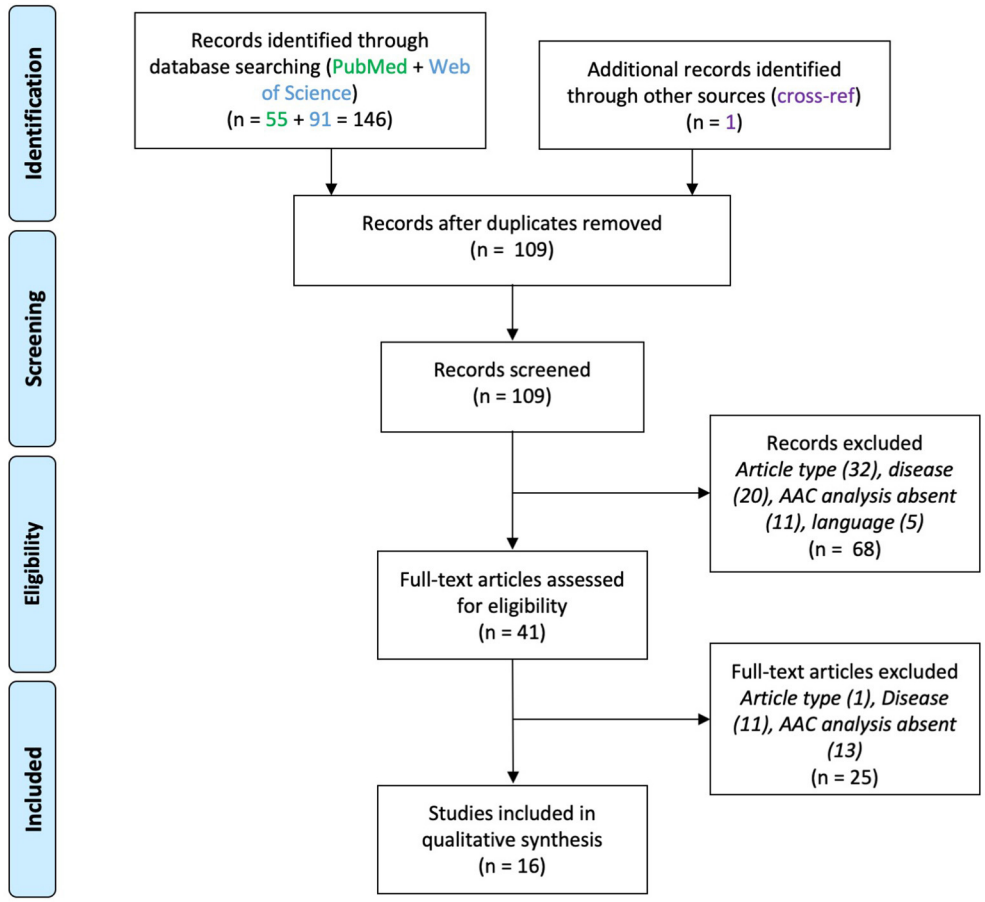

FIGURE 1
PRISMA flowchart for studies on axo-axonic cells in epilepsy.

Epilepsy

Sixteen papers were included (Figure 1). These studies used either human brain samples from patients affected by medically intractable epilepsy ($n = 11$) or from animal models of epilepsy ($n = 5$). Neocortical and hippocampal alterations in AACs were reported, which are divided below for clarity. Results are summarized in Table 1.

Neocortex

In the neocortex, a loss of PV+ AACs' cartridges has been reported in the anterior temporal lobe of epileptic patients, with some samples displaying pathological cytoarchitectures (DeFelipe et al., 1993; Marco et al., 1996). The decrease in PV+ AACs' cartridges has also been observed in dysplastic samples from patients suffering from EPI secondary to focal cortical dysplasia (Alonso-Nanclares et al., 2005). In a case report of a young patient with cortical dysplasia, a decrease in PV immunoreactivity was described (Ferrer et al., 1992), suggesting that the decreased density of cartridges observed in the previous studies may correspond to a decrease in PV levels. This finding was associated with abnormal morphologies of the remaining PV+ cells, including the observation of an enlarged AAC (Ferrer et al., 1992). Ferrer and colleagues also reported hypertrophic PV+ cartridges in a patient suffering from diffuse hypoxic encephalopathy associated with focal seizures (Ferrer et al., 1994). A case report of a patient suffering from seizures secondary to a temporal lobe astrocytoma also described a decrease in PV immunoreactivity and numbers of AAC boutons in the peri-tumoral tissue (Marco et al., 1997), in line with other findings. Altogether, these studies reported a decrease in PV+ AACs' cartridges and an abnormal morphology of the remaining AACs. However, these results were only qualitative with no quantification of this apparent loss, which may also correspond to a decrease in PV expression. Despite the lack of quantification, these findings are consistent with previous experimental work showing degeneration of axonal boutons contacting the AIS at epileptic foci in the somatosensory cortex in a monkey model of focal epilepsy following intracerebral administration of alumina gel (Ribak, 1985).

Hippocampus

Studies on the human hippocampus of patients with EPI or animal models of temporal lobe EPI reported different

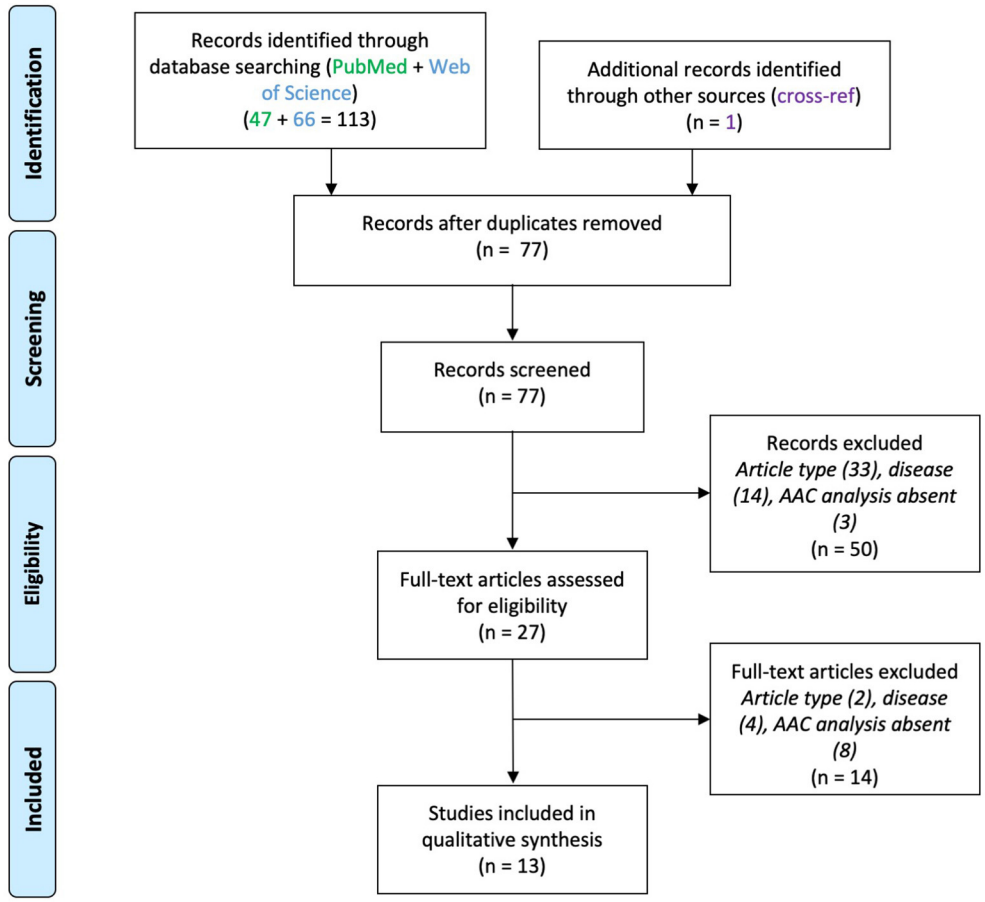

FIGURE 2
PRISMA flowchart for studies on axo-axonic cells in schizophrenia.

alterations depending on the subregion studied and on the level of hippocampal sclerosis.

Cornu Ammonis

Wittner et al. (2005) found no change in synaptic coverage of pyramidal cells' AIS in human non-sclerotic Cornu Ammonis (CA) fields, in contrast to their somatic innervation. In sclerotic CA, these authors observed a decreased synaptic coverage of degenerating AISs, and a lack of AAC terminal staining for PV, suggesting a degeneration of AACs' cartridges. In the healthy (del Rio and DeFelipe, 1997) and mildly sclerotic CA1 region (Wittner et al., 2002), the AIS of pyramidal cells are innervated by CB-labeled boutons, which disappear in strongly sclerotic tissue, where pyramidal cells cannot be seen (Wittner et al., 2002). Similarly, in sclerotic hippocampal samples, a global loss of PV+ terminals has been described, with some PV+ cartridges remaining, of hypertrophic appearance (Arellano et al., 2004). These results collectively point toward a deficit in AAC innervation of pyramidal cells paralleling principal neuron degeneration in hippocampal sclerosis.

In the non-sclerotic Cornu Ammonis (CA), a study in rats reported that PV+ AAC boutons contacting pyramidal cells' AIS were intact and therefore resisted to kainic acid-induced seizures, in contrast to alterations in axo-somatic basket profiles (Best et al., 1994). On the contrary, in a rat model of chronic epilepsy through injection of pilocarpine, a decrease in the synaptic coverage of AIS has been observed (Dinocourt et al., 2003).

Finally, in a single physiological study using a model of interictal epileptiform discharge in CA3 slices of mice, AACs undergo increase in their firing with epileptiform discharges, suggesting an active role of AACs in generating epileptiform activity (Karlócai et al., 2014).

Dentate gyrus

In the sclerotic dentate gyrus (DG) of patients with temporal lobe EPI, the morphological "complexity" of PV+ and CB+ AACs' cartridges has been found to be increased, with more boutons and axonal rows per cartridge (Arellano et al., 2004). This increased complexity of AACs' cartridges could explain the findings of increased synaptic coverage of granule cells' AIS in epileptic patients (Wittner et al., 2001). Interestingly, the increase in AACs' cartridge complexity appeared to parallel the severity of sclerosis in the human DG (Wittner et al., 2001). The most recent work on human brain tissue found that the density of AACs' PV+ boutons is preserved in epileptic DG without sclerosis, and decreased in sclerosis (Alhourani et al., 2020). However, the density of VGAT+/GAD67+ boutons (i.e., putative axo-axonic terminals) was similar to controls in both cases

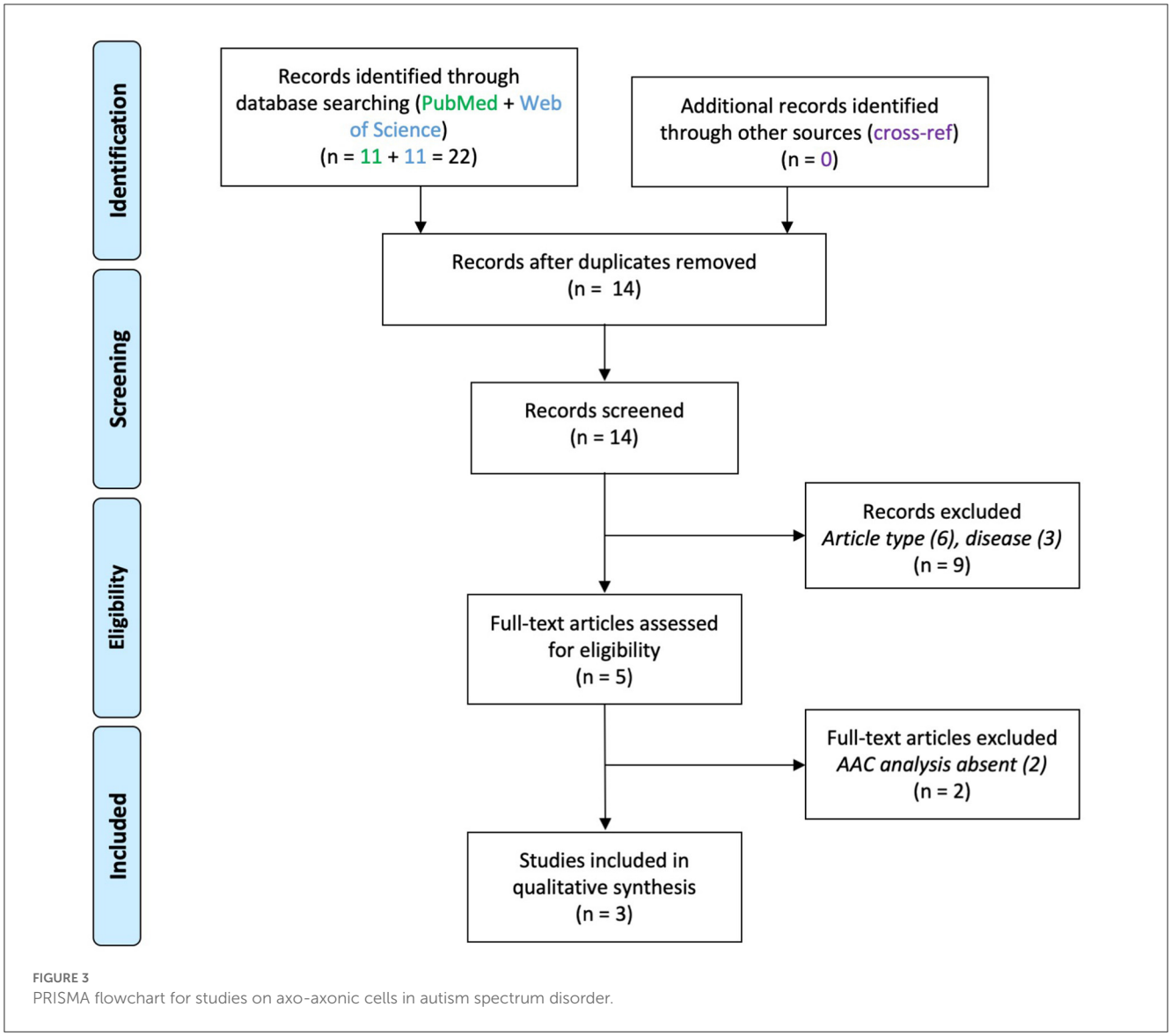

FIGURE 3
PRISMA flowchart for studies on axo-axonic cells in autism spectrum disorder.

(Alhourani et al., 2020), suggesting that AACs' terminals might be preserved, and PV expression decreased. In addition, GAD67 and VGAT expression levels were increased in AACs' terminals in sclerotic tissue, suggestive of a compensatory mechanism. Finally, axo-axonic boutons were found intact in DG in EPI modeled with either perforant-path electric stimulation or kainic acid administration to induce seizures in rats (Sloviter et al., 2003).

Overall, these findings indicate that the DG and the CA region follow opposite directions in hippocampal sclerosis, with reduced AIS synaptic coverage in CA, and preserved innervation by more complex cartridges of surviving DG granule cells. On the other hand, AACs appear to be preserved in the non-sclerotic hippocampus. A general finding in human studies is the reduced level of PV expression in histologically abnormal tissue.

Schizophrenia

Thirteen papers were included (Figure 2), which reported molecular and functional alterations in AACs associated with SCZ (Table 2). Eight of them were post-mortem brain tissue analysis using immuno-histochemistry. The remaining five used animal models of SCZ.

Post-mortem studies

Except for one study (Konopaske et al., 2006), all post-mortem studies were performed on the prefrontal cortex (PFC), which activity is altered in SCZ (Minzenberg et al., 2009). All reported pre- and/or post-synaptic alterations of AACs to pyramidal cell connections, albeit with conflicting conclusions.

TABLE 1 Summary of studies on axo-axonic cells in epilepsy.

References	Model(s)	Population characteristics (ratio M:F; age range)	Area(s) studied	Methods	Variable(s) studied	Main findings	Comments
Ribak (1985)	Monkey Alumina gel-injected monkeys(intracortical or sub-arachoid)	Three adult monkeys (*Macaca mulatta* & *M. fascicularis*)	Sensorimotor cortex, layers 2, 3 and 5	Electron microscopy	Number of AACs boutons contacting the AIS	Decreased number of AACs boutons at the level of the AIS (from 10 to 15 terminals per AIS in control hemisphere to 0–3 in epileptic loci).	Semi-quantitative study (only ranges provided). Age and gender of monkeys not known.
Best et al. (1994)	KA-lesioned Wistar rats (ICV injections)	Juvenile rats (Wistar, 180 g), all male. 15 M injected and 5 M; age-matched controls.	Hippocampus (CA1)	PV IHC, light and electron microscopy	Distribution of PV+ axonal boutons 3 days, 1, 2, 4 weeks and 3 months.	No degenerating PV+ AAC boutons at the AIS of pyramidal cells in KA-treated hemispheres, at any time point vs. almost total loss of PV+ perisomatic innervation.	Qualitative study, small sample size.
Sloviter et al. (2003)	Perforant path electrically-stimulated and KA-lesioned rats (IV)	Young adult rats (Sprague-Dawley, 250–400 g), all male: (PP-stimulation $n = 4$; KA: $n = 2$)	Hippocampus (Dentate gyrus)	Electron microscopy	Degeneration of AAC boutons at days 4 and 7 post PP stimulation or 10 post-KA injection	No degeneration of axo-axonic boutons in kainic acid treated rats, nor in PP-stimulated rats.	Qualitative study, with exclusive use of degenerating axonal profiles as a marker of AAC loss/damage.
Dinocourt et al. (2003)	Pilocarpine-treated rats (IP injection)	Young adult rats (Wistar, 200–290 g), all males (pilocarpine: $n = 10$ M; seven for light microscopy, three for electron microscopy vs. three matched controls)	Hippocampus (CA1 stratum oriens)	Light (with PV and SOM IHC) and electron microscopy.	Density of AACs boutons contacting the AIS of pyramidal cells at 3 months post-treatment	Decrease in synaptic density and synaptic coverage at the AIS in CA1 pyramidal cells, of pilocarpine treated rats (both of 63%). And 34% decrease in number of PV-expressing, somatostatin-negative (putative AAC) in str. oriens compared to controls.	Limited cohort for the electron microscopic study of synapses at the AIS (three controls + three pilocarpine-treated)
Karlócai et al. (2014)	High potassium-treated brain slices of mice (epileptic discharges).	Juvenile mice (P19–P40), wild type (CD1 and BL6 strains) and transgenic (PV-eGFP) of both genders	Hippocampus (CA3)	Local field potential combined with intracellular recording (loose-patch, whole-cell) followed by anatomical identification of the recorded neurons	AAC firing around and during epileptiform events, compared to sharp wave ripples.	Increase in firing rates during epileptiform events, compared to spontaneously occurring sharp wave-ripples.	*In vitro* model without *in vivo* measurements.
Ferrer et al. (1992)	Surgical resection tissue in a patient suffering from drug-resistant epilepsy due to cortical dysplasia	1F; 14-year-old (cortical dysplasia)	Peri-rolandic region (primary motor and primary somatosensory cortices)	PV IHC	Morphology of PV+ AACs in dysplastic tissue	PV immunoreactivity is decreased in areas of tissue necrosis whereas neighboring dysplastic areas display abnormal populations of very-large PV+ AACs.	Qualitative, single-case study, of a particular condition (dysplasia). Only one abnormal AAC described in the body of the article.

(Continued)

10.3389/fncel.2023.1212202

TABLE 1 (Continued)

References	Model(s)	Population characteristics (ratio M:F; age range)	Area(s) studied	Methods	Variable(s) studied	Main findings	Comments
DeFelipe et al. (1993)	Peri-lesional surgical resection tissue from drug-resistant patients with TLE	2:3; 12–34 yrs (intractable TLE)	BA20, 21 and 38	EcoG. PV IHC. Light and electron microscopy	Density of PV+ AAC cartridges in epilepsy	Heterogeneous patterns, with 2/4 patterns showing a global loss of PV+ axon and 1/4 showing a specific loss of PV+ AAC cartridges (uncorrelated with the EcoG spiking profile).	Qualitative study (no quantification, no control). Quantification of AAC terminals only in pattern "A" ("normal"). Only PV+ AACs were studied.
Ferrer et al. (1994)	Surgical resection tissue from patients affected by different forms of epilepsy	17:13; 9–50 yrs one diffuse hypoxic encephalopathy, nine neoplasms, two focal cortical dysplasia, one with subcortical ectopic neuronal nests, one with focal disorder of migration, two cavernous angiomas, 12 temporal lobe epilepsy with mesial sclerosis, two cryptogenic epilepsy	Various epileptic foci including frontal and temporal regions.	PV IHC; light microscopy	Density and morphology of PV+ axons	Increase in number and size of PV+ AACs cartridges in some discrete areas (hypertrophic cartridges) in the only case for which AACs analysis is reported, of diffuse hypoxic encephalopathy.	Qualitative study without controls, epilepsy is associated with another disorder. Result about AAC is from only one patient. Only PV+ AACs are studied.
Marco et al. (1996)	Peri-lesional surgical resection tissue from patients with TLE (±tumors)	6:3; 13–44 (epileptic without brain tumor); 2:2; 18–30 (epileptic with brain tumors); 2 M; 70–91 (controls)	BA20, 21, and 38	EcoG. PV IHC	Density of PV immunostaining and PV+ AAC cartridges	Heterogeneous patterns, with 2/4 patterns showing a global loss of PV+ axon and 1/4 showing a specific loss of PV+ AAC cartridges (both uncorrelated with the EcoG profile). NB: AAC alterations present in 5/9 samples of TLE without tumor, and 4/4 of TLE with tumor)	Qualitative study. Only 2 controls (older). Only PV+ AACs are studied.
Marco et al. (1997)	Peri-lesional surgical resection tissue from one patient with secondary TLE (astrocytoma)	1F; 30-year-old (epilepsy and brain tumor); tissue sections from various controls	BA38	PV IHC. Light and electron microscopy.	PV+ cells and axon terminals. Synapses at the AIS.	Decreased in AACs' cartridges density. Decreased number of synapses at the AIS accompanied by an increased gliosis.	Qualitative study. Case report from an epileptic patient with a brain tumor, who underwent radiotherapy and previous surgical treatments.
Wittner et al. (2001)	Surgical resection tissue from patients with TLE (with hippocampal sclerosis)	14:9; 17–56 (intractable TLE with 3 degrees of sclerosis); 3:3; 37–56 (controls)	Hippocampus (dentate gyrus)	PV IHC. Light and electron microscopy	Number of PV+ boutons contacting the AIS (LM) and synaptic density at the AIS (EM).	Increased density of synapses at the AIS of granule cells, following degrees of hippocampal sclerosis. NB: loss or decrease of PV immunoreactivity at light and electron microscopic levels.	Semi-quantitative study (no statistical analysis).
Wittner et al. (2002)	Surgical resection tissue from patients with TLE (hippocampal sclerosis)	14:9; 17–56 (intractable TLE with mild—6 samples- or strong sclerosis—17 samples-); 3:3; 37–56 (controls)	Hippocampus (CA1)	CB IHC. Light and electron microscopy	Subcellular target distribution of CB-positive axon terminals	The proportion of AISs among the target elements of CB+ terminals considerably decreased or even disappeared in the strongly sclerotic cases.	Same cohort as Wittner et al. (2001).

(Continued)

10.3389/fncel.2023.1212202

TABLE 1 (Continued)

References	Model(s)	Population characteristics (ratio M:F; age range)	Area(s) studied	Methods	Variable(s) studied	Main findings	Comments
Arellano et al. (2004)	Surgical resection tissue from patients with TLE	8:6; 17–50 (TLE with hippocampal sclerosis); 3 M; 23–63 (controls)	Hippocampus (dentate gyrus, CA, subiculum)	GAT1, CB, PV, NeuN and PSA-NCAM IHC; light microscopy	Morphology and density of AAC cartridges.	Increased complexity of cartridges on surviving granule cells (dentate gyrus) and pyramidal cells (CA). No difference in subiculum. NB: general reduction in CB & PV immunoreactivity.	Qualitative study. Regional heterogeneity within individual samples and across patients
Alonso-Nanclares et al. (2005)	Surgical resection tissue from patients with focal cortical dysplasia	1:2; 3.5–24 (focal cortical dysplasia); 3 M; 24–37 epileptic patients with hippocampal sclerosis (controls)	Different location depending on the site of lesion (parietal lobe, fronto-insular cortex or inferior frontal gyrus)	PV IHC. Light and electron microscopy	PV+ axon terminals.	Decreased density of PV+ cartridges and/or of immunoreactivity in cartridges on giant neurons. Decrease in axo-axonic innervation is accompanied by an increase in axo-somatic innervation.	Qualitative study. Epilepsy associated with FCD. Only three patients with the youngest being 3.5 years old. Regional heterogeneity within individual samples and across patients. Controls also suffer from seizures, with hippocampal sclerosis. Only PV+ AACs are studied. No electron microscopic report of axon initial segment innervation.
Wittner et al. (2005)	Biopsy brain tissues from patients with TLE	17:15; 14–56 (TLE; four grades: mild cell loss, patchy cell loss, sclerosis, gliosis); 4:3; 37–56 (controls)	Hippocampus (CA1)	PV IHC. Light and electron microscopy.	PV+ cells and axons density (LM); synaptic coverage of AIS (EM)	No significant difference in AIS synaptic innervation (EM, presynapses containing or not PV). Decreased synaptic coverage of degenerating AISs. Severe PV+ cell loss in patchy hippocampal cell loss and sclerosis cases, with no axonal staining for PV in the sclerotic CA1. No difference in cases of mild cell loss.	Observation of degenerating AISs limited to two cases (qualitative observation). Same control group as Wittner et al. (2001, 2002), except one case.
Alhourani et al. (2020)	Biopsy brain tissues from Patients with TLE	3:2; 37–49 (intractable TLE); 3:2, 36–50 (matched controls)	Hippocampus (dentate gyrus)	IHC: VGAT, PV, GAD65 and GAD67. Quantitative fluorescent confocal microscopy	Density of AAC boutons (vGAT+/GAD67+/ GAD65-) and GAD67/vGAT/ PV protein levels in these boutons.	No change in VGAT+/GAD67+ bouton density Decreased PV+/VGAT+ bouton density in the sclerotic group (92%); no difference between non-sclerotic and control samples Increased levels of GAD67 and vGAT is in the sclerotic group compared to both groups (GAD67: vs. control: +482%; vs. non-sclerotic: +212%; vGAT: +400–500%).	Quantitative study Matched controls No report of density of VGAT+/GAD67+ boutons per tissue volume (only normalized by total neuron number)

BA, Brodmann area; CA, *Cornu Ammonis* (hippocampal region); CB, calbindin; ECoG, electrocorticography; EGFP, enhanced green fluorescent protein; EM, electron microscopy; GAD(65, 67), glutamic acid decarboxylase (65/67 kDa isoforms); GAT1, GABA transporter type1; ICV, intracerebroventricular (injection); IHC, immunohistochemistry (also used here for immunofluorescence for simplicity); IP, intraperitoneal (injection); IV, intravenous (injection); KA, kainic acid; LM, light microscopy; NeuN, neuronal nuclei (marker); PSA-NCAM, polysialylated form of neural cell adhesion molecule; PV, parvalbumin; SOM, somatostatin; TLE, temporal lobe epilepsy; VGAT, vesicular GABA transporter.

10.3389/fncel.2023.1212202

TABLE 2 Summary of studies on axo-axonic cells in schizophrenia.

References	Model(s)	Population characteristics (ratio M:F; age)	Area(s) studied	Methods	Variable(s) studied	Main findings	Comments
Woo et al. (1998)	post-mortem human brains from patients with SCZ	10:5; 53.6 ± 13.0 (SD; SCZ), 10:5; 53.7 ± 12.4 (psychiatric controls); 10:5; 53.9 ± 13.8 (non-psychiatric controls)	BA9 and BA46, all layers	GAT-1 and calretinin IHC, light microscopy	Density of GAT-1+ cartridges	The density of GAT-1+ cartridges is decreased by 40% in SCZ vs. both control conditions. No variation in the mean density of GAT-1+ boutons nor in calretinin-IR boutons in layers 2-3a of BA9.	No variation in mean cartridge length, nor in PFC volume. Subjects treated with antipsychotics without SCZ had higher cartridge densities than in subjects with SCZ
Pierri et al. (1999)	Post-mortem human brains from patients with SCZ	20:10; 51.6 ± 13.0 (SCZ), 20:10; 51.6 ± 13.3 (psychiatric controls); 20:10; 52.1 ± 13.8 (non-psychiatric controls)	BA46, layers 2–3a, 3b—4, and 6	GAT-1 IHC, light microscopy	Density of GAT-1+ cartridges	The density of GAT-1+ cartridges is decreased in SCZ: - layers 2–3a 27% (vs. both controls) - layer 3b—4: 31.5 and 19.4% (vs healthy and psychiatric controls, respectively) - layer 6 (not statistically significant)	No variation in mean cartridge length, nor in PFC volume/cortical thickness. Higher cartridge density in patients treated with antipsychotic medication and increased cartridge density following haloperidol treatment in macaque.
Kalus et al. (1999)	Post-mortem human brains from patients with SCZ	3:2; 60.2 ± 20.6 (SCZ) 3:2; 66.0 ± 23.6 (non-psychiatric controls)	BA24c, layers 5 and 6	PV IHC, light microscopy	Density of PV+ cartridges	The density of PV+ cartridges is *increased* in SCZ by 59% in layers 5 and 6 of the ACC.	Small cohort. Only study focused on the deep layers (layer 5 in particular) and on the ACC
Volk et al. (2002)	Post-mortem human brains from patients with SCZ	9:5; 53 ± 8 (SCZ), 9:5; 53 ± 8 (MDD controls); 9:5; 52 ± 9 (non-psychiatric controls)	BA46, layers 2–3a	GABA-A Rα2 IHC, light microscopy	Density of α2-labeled AIS	The mean number of α2-labeled AIS is increased by 113% in SCZ. The densities of GAT-1+ cartridges and of α2-labeled AIS are inversely correlated.	Same cohort and techniques as Pierri et al. (1999). No variation in mean AIS length, nor in PFC volume. No effect of medication in the SCZ group.
Konopaske et al. (2006)	Post-mortem human brains from patients with SCZ	6:8; 48.3 ± 8.8 (SCZ), 6:8; 48.1 ± 7.1 (non-psychiatric controls)	BA42 (associative auditory cortex), layers 2–3a and 6	GAT-1 IHC, light microscopy	Density of GAT-1+ cartridges	No statistically significant (9.8%) decrease in the density of GAT-1+ cartridges in the auditory cortex.	Subjects drawn from the cohort and techniques of Pierri et al. (1999). No verification of variation in cartridge length or cortical volume
Cruz et al. (2009)	Post-mortem human brains from patients with SCZ	9:5, 52.6 ± 8.5 (SCZ); 9:5, 52.4 ± 8.6; (control with no mental disorder) 9:5, 53.0 ± 7.6 (MDD)	BA46, layers 2-3a and 6	Ankyrin G and βIV spectrin IHC	Density of ankyrin-G+ AIS and βIV-spectrin+ AIS in SCZ	decreased density of ankyrin-G+ AIS by 19 and 15% in superficial in cortical layers 2/3a in SCZ compared to control and MDD groups, respectively, but not in the deep (L6) cortical layer. No differences for βIV spectrin.	Same cohort and techniques as Pierri et al. (1999) and Volk et al. (2002). No variation in mean AIS length, nor in cortical volume.

(Continued)

10.3389/fncel.2023.1212202

TABLE 2 (Continued)

References	Model(s)	Population characteristics (ratio M:F; age)	Area(s) studied	Methods	Variable(s) studied	Main findings	Comments
Rocco et al. (2016)	Post-mortem human brains from patients with SCZ	14:6; 45 ± 7 (SCZ), 14:6; 46 ± 9 (non-psychiatric controls)	BA9, layers 2–6	VGAT and GAD67 IHC, light microscopy	VGAT and GAD67 protein levels in interneurons boutons	VGAT and GAD67 protein levels in VGAT+ AAC boutons do not differ between SCZ and controls, in contrast to other interneurons.	The total number of VGAT+ cartridges or AAC boutons in each group is not reported (but see Rocco et al., 2017). No statistically significant effect of antipsychotic medication on the global result.
Rocco et al. (2017)	Post-mortem human brains from patients with SCZ	14:6; 45 ± 7 (SCZ), 14:6; 46 ± 9 (non-psychiatric controls)	BA9, layers 2–6	CB, GAD67 and VGAT IHC, light microscopy	Density of VGAT+ and VGAT+/CB+ cartridges	Higher density of VGAT+ cartridges (+21%) in layer 2-superficial layer 3 of SCZ vs. control PFC. Accounted for by a 2.7 increase in CB+/VGAT+ cartridge density in layer 2. No difference in deeper layers in VGAT+/CB+, VGAT+/CB- cartridge density, or VGAT levels in AAC terminals	Same cohort and techniques as in Rocco et al. (2016). No statistically significant effect of antipsychotic medication on the global result. No measurement of GAT1 as a replication of previous results. No assessment of variations in cartridge length or cortical volume.
Morrow et al. (2007)	PCP-treated monkey	4:0; adults (PCP-treated) 4:0; adults (controls).	Walker's area 46 (homologous to BA46), all layers	PV IHC, light microscopy	Number of PV+ cartridges across the cortex	Decreased number of PV+ axo-axonic structures by about 40% in layers 2/3 of PCP-treated monkeys. No change in spatial distribution across layers. No change in numbers or distributions of PV+ and CR+ cells.	A decrease in PV expression cannot be excluded. The exact age of monkeys is unknown.
Bloomfield et al. (2008)	Isolation-reared rats	IHC: 4:0M; 20-week (socially reared); 3:0; 20-week (isolation reared) PPI testing only: males (*n* unknown), P84 for both	mPFC (anterior cingulate, prelimbic and infralimbic)	GAT-1 IHC, PPI testing	Total number of GAT-1+ cartridges and PPI	Reduced number of GAT-1+ cartridges by 36% in the ventral prelimbic cortex of isolation reared rats. No difference in other mPFC divisions (anterior cingulate, dorsal prelimbic, infralimbic).	A decrease in GAT-1 expression cannot be excluded. No measure of cortical volume, no verification of cartridge length. No direct link established between behavioral and morphological findings
Del Pino et al. (2013)	Mutant mouse model (conditional ErbB4 mutants = Lhx6-Cre; Erbb4 F/F mice)	IHC and biochemistry: P30 mice. For *in vitro* electrophysiology: P20-22 mice. For *in vivo* electrophysiology on anesthetized mice: P2-3-month male mice (number not specified).	Hippocampus and PFC	vGluT1, GABA-A Rα2, ankyrin-G IHC. *in vitro* and *in vivo* electrophysiological recordings + behavioral assays (activity cages, elevated-plus maze,	Impact of a conditional ErbB4 KO in PV interneurons on AAC's morphology and function, and on behavior	The soma and dendrites of neocortical AACs lacking Erbb4 receive significantly less VGlut1+ terminals than control cells. The density of boutons in AACs cartridges and of GABAAa2 clusters at AIS is decreased. Mutant mice showed synaptic defects in particular increased	Extensive study which analyzed from the molecular to behavioral impact of the mutation. The manipulation of ErbB4 is not specific for AAC, also affecting basket cells. Missing details regarding animals gender and age.

(Continued)

10.3389/fncel.2023.1212202

TABLE 2 (Continued)

References	Model(s)	Population characteristics (ratio M:F; age)	Area(s) studied	Methods	Variable(s) studied	Main findings	Comments
				Y maze, marble burying, three-chambered social test, nesting, PPI)		excitability (PV+ fast-spiking neurons and pyramidal cells), abnormal synchrony, increased oscillatory activity- increased locomotor activity, abnormal emotional responses, impaired social behavior and impaired cognitive function.	
Yang et al. (2019)	Mutant mouse models (cKO mice = Nkx2.1CreER;erbb4$^{-/-}$ and ErbB4 knockdown mice = Nkx2.1CreER;LSL-Flpo with Flp-dependent shRNA targeting ErbB4 in mPFC	*In vitro* electrophysiology: P21-30 or 2 weeks following AAV injections (made at P45-50). 2–3-month-old males for behavior testing. P30 for western blot.	mPFC, layers 2/3	PV, ErbB4, vGluT1 and ankyrin G IHC + *in vitro* electrophysiology + behavioral assays (open field, elevated-plus maze, PPI test, automated radial arm maze, three-chamber social interaction test)	Impact of ErbB4 KO in mPFC AACs on their morphology and functions	Immunohistochemistry: cKO : decrease in the density of AACs' boutons on AISs, decreased density of vGluT1+ boutons on AAC somata; knock-down: no data. Electrophysiology: cKO: decreased frequency and amplitude of mEPSCs in AACs, decreased amplitude of mIPSCs in pyramidal neurons; knock-down: decreased frequency and amplitude of mEPSCs in AACs, decreased frequency of mIPSCs in pyramidal neurons. Behavior: cKO: impaired PPI, hyperactivity, working memory deficits normalized by an agonist of $GABA_A$-Rα2 receptors agonist; knock-down: impaired working memory, impaired social novelty recognition (no effect on PPI/locomotion).	The gender or the number of mice for each experiment is unknown.
Fujikawa et al. (2021)	Intraperitoneal Ketamine injections (daily for 7 days) in wild type (C57BL/6J) mice; control= saline	Not reported	Dorsal hippocampus	SATB1, PV, NPY, SST, (HNK-1) glycan (Cat-315 antibody) IHC	Density of PV+ cells and cell types relative to Cat-315 expression	Decreased density of Cat-315-AACs and no change in Cat-315+ AACs in the ketamine group. Decreased density of Cat-315+/PV+ neurons in stratum oriens and stratum pyramidale; no change in Cat-315-/PV+ neuron density; increased Cat-315+/PV- density in the ketamine group (primary result).	Age of the mice unknown Many cell types affected by ketamine in various ways No causal links established in ketamine/Cat-135/interneuron type interactions.

AAC, axo-axonic cell; AAV, adeno-associated virus; ACC, anterior cingulate cortex; AIS, axon initial segment; BA, Brodmann area; cKO, conditional knockout; eGFP, enhanced green fluorescent protein; Errb4, Erb-B2 receptor tyrosine kinase 4; GABAR, gamma-aminobutyric acid receptor; GAT-1, GABA transporter 1; HNK-1, human natural killer-1 (glycan); H-S, hippocampo-septal projection interneurons; IHC, immunohistochemistry (also used here for immunofluorescence for simplicity); MDD, major depressive disorder; mPFC, medial prefrontal cortex; NPY, neuropeptide Y; O-LM, oriens-lacunosum moleculare (interneuron); PCP, phencyclidine; PPI, pre-pulse inhibition; PV, parvalbumin; Px, postnatal age, in days; SATB1, special AT-rich sequence-binding protein-1; SCZ, schizophrenia; SD, standard deviation; SOM/SST, somatostatin; VGLUT1, vesicular glutamate transporter 1.

10.3389/fncel.2023.1212202

TABLE 3 Summary of studies on axo-axonic cells in autism spectrum disorders.

References	Model	Population characteristics (ratio M:F; age range)	Area(s) studied	Methods	Variable(s) studied	Main findings	Comments
Ariza et al. (2018)	Post-mortem human brain tissue from ASD patients	10:0; 7–48 (ASD; 9:1; 6–56 (control)	BA9, BA46, BA47	PV and VVA IHC	Percentage of AACs (defined as PV+/VVA−) among the total number of cells	Decreased percentage of PV+ AACs in ASD, by 65.1% in BA46, by 39.1% in BA47 and by 40% in BA9	Except for one control case, subjects were all males. Only PV+ AACs were studied. Data are expressed in percentages to avoid the introduction of error due to differential tissue shrinkage, but no information about the total number of neurons is provided.
Hong et al. (2020)	Post-mortem human brain tissue from ASD patients	19:1; 6–56 (ASD); 19:1; 7–56 (control)	BA9, BA46, BA47 (layers 3 and 5)	GABA-A Rα2 and neurofilament IHC	Percent area of AIS occupied by GABA-A Rα2 in ASD brain tissue	The percent area of GABA-A Rα2 staining in pyramidal cells AIS is decreased in layer 3 by 61% in BA9 and by 54% in BA47 in ASD (no difference in layer 5). No difference in BA46.	Manual delineation of AIS, but blinding of phenotype.
Amina et al. (2021)	Post-mortem human brain tissue from ASD patients	11:0; 7–23 (ASD); 7:4; 7–24 (control)	BA9, BA46, BA47	GAT-1 IHC	Number of GAT-1+ cartridges per defined area (3 mm band from pia to white matter)	Decrease in the total number of GAT1+ cartridges in ASD	The definition of areas analyzed is not normalized by area: potential confounding factor if surface was decreased in ASD samples.

AAC, axo-axonic cell; ASD, autism spectrum disorder; BA, Brodmann area; GABA-A R, type A GABA receptor; GAT-1, GABA transporter 1; PV, parvalbumin; VVA, Vicia villosa agglutinin.

Pre-synaptic alterations

The number of axo-axonic boutons and cartridges has been reported to be altered to various degrees in SCZ. The first article of this kind reported a 40% decrease in the density of GAT-1+ AACs' cartridges in SCZ compared to controls (Woo et al., 1998). This decrease later appeared to concern mainly layers 2–3 of the PFC in patients with SCZ, compared to controls (Pierri et al., 1999). It was then interpreted as reflecting either a decrease in cartridge density or reduced levels of GAT-1. Interestingly, this alteration displayed some degree of specificity for the PFC, since using the same approach, no significant decrease in GAT-1+ AACs' cartridges was found in the auditory cortex (Konopaske et al., 2006), and an increased density of PV+ AACs' cartridges was reported in layer 5/6 of the anterior cingulate cortex of patients with SCZ (Kalus et al., 1999). In contrast to bouton density, the expression levels of presynaptic proteins including GAD67 or VGAT were found to be preserved in SCZ subjects (Rocco et al., 2016).

In fact, the group that reported reduced PFC axo-axonic innervation in SCZ (Woo et al., 1998; Pierri et al., 1999) recently found that the number of axo-axonic boutons was unaltered in SCZ, using VGAT (instead of GAT-1) as a presynaptic marker (Rocco et al., 2017). Moreover, the density of AACs' CB+ cartridges is increased in layer 2 of PFC (Rocco et al., 2017), with no change in CB-negative cartridges density or VGAT expression levels in SCZ. Therefore, the suspected defect in AACs' cartridges (Woo et al., 1998; Pierri et al., 1999) likely reflected a decreased expression of GAT-1. Importantly, these findings did not appear to be a consequence of gender status, nicotine use, benzodiazepines and/or sodium valproate, antidepressants, or antipsychotics when accounted for in statistical analyses (Rocco et al., 2016, 2017).

Post-synaptic alterations

The density of AISs expressing the $GABA_A$ receptor α2 subunit ($GABA_A$-Rα2) is increased in PFC from patients with SCZ, and negatively correlated with the numbers of GAT-1+ AACs' cartridges (Volk et al., 2002). This result was interpreted as a compensatory mechanism, with increased $GABA_A$-R α2 expression balancing a reduced number of GABAergic terminals- and in turn a likely reduced release of GABA. However, as Lewis and collaborators later showed, the number of GABAergic terminals was preserved (Rocco et al., 2017). Finally, a decrease in the density of Ankyrin-G+ AISs in the absence of β-spectrin+ (another AIS scaffold) has been reported in the PFC of patients with SCZ (Cruz et al., 2009). This result suggests a decreased expression of Ankyrin-G at AISs in SCZ, and potential defects in function since Ankyrin-G is a key scaffold protein for axo-axonic synapses at the AIS (Tai et al., 2019). Overall, evidence is limited regarding the involvement of AACs' postsynaptic changes in SCZ.

Animal models of schizophrenia

Studies on animal models of SCZ have provided evidence for structural alterations in AACs and for links between structural findings and functional or behavioral deficits.

Regarding structural studies, a monkey model of SCZ generated with repeated treatments with phencyclidine displayed a 40% decrease in the number of prefrontal PV+ axo-axonic structures (Morrow et al., 2007). In the isolation-reared rat model of SCZ, no

global differences in the total number of GAT-1+ cartridges were found in the rat PFC, but a local decrease by 36% was identified in the ventral prelimbic region relative to control (Bloomfield et al., 2008). Lastly, in a ketamine model of SCZ in mice, interneurons were studied with regards to the presence of perineuronal nets detected with the marker Cat-315; (Fujikawa et al., 2021). The number of Cat-315–/PV+ AACs (identified with PV expression in the absence of neuropeptide Y or SATB1 expression) were fewer in ketamine-treated mice compared to controls, while Cat-315+/PV+ AACs were not affected (Fujikawa et al., 2021).

More direct evidence of AAC implication in SCZ has been provided by the conditional KO of *ERBB4* (a SCZ risk-gene) in medial ganglionic eminence-derived interneurons (comprising PV+ cells) in mice (Del Pino et al., 2013). Among synaptic defects, Del Pino et al. found a decreased density of PV+ axo-axonic boutons and a decreased density of $GABA_A$-R α2 clusters at the AIS contrary to human post-mortem results of Volk et al. (2002). AACs also received fewer excitatory synapses, as measured anatomically and physiologically with reduced miniature excitatory postsynaptic currents frequencies *in vitro*. These defects were accompanied by global increase in excitability, both of PV+ interneurons and of pyramidal cells *in vitro*. *In vivo*, this resulted in more frequent population spike occurrence in the DG, increased hippocampal oscillation power and decreased synchrony between brain regions (Del Pino et al., 2013). The latter oscillatory pattern is reminiscent of abnormalities found in SCZ (Hunt et al., 2017). Furthermore, mutant mice showed behavioral impairments consisting of increased locomotor activity, reduced anxiety, impaired working memory and reduced social interactions (Del Pino et al., 2013). However, the behavioral analysis lacked specificity for AACs. With the implementation of a novel mouse line to target selectively AACs by temporal tagging of Nkx2.1-expressing progenitors (Nkx2.1CreER; He et al., 2016), these results were confirmed by performing KO of *ERBB4* selectively in AACs (Yang et al., 2019). The density of AACs was preserved, while the density of their synaptic boutons contacting the AIS was decreased. AACs also received less glutamatergic innervation (Yang et al., 2019), in agreement with previous findings on MGE-derived interneurons (Del Pino et al., 2013). Consistently, the frequency of miniature inhibitory postsynaptic currents was reduced in pyramidal neurons. Behaviorally, mice displayed increased locomotor activity, reduced paired-pulse inhibition, impaired working memory and altered social behavior (Yang et al., 2019), in line with the previous study (Del Pino et al., 2013). Behavioral deficits were rescued by systemic or intra-PFC infusion of the partial GABA-A Rα2 agonist L-838417 (Yang et al., 2019). These results were recapitulated in the Nkx2.1CreER conditional knock-down of *ERBB4* in AACs restricted to the PFC, suggesting the results were not the consequence of developmental compensatory mechanisms, and that prefrontal AACs might be implicated in schizophrenia (Yang et al., 2019).

Overall, these results are consistent in showing that pyramidal neurons innervation by AACs is reduced in animal models of SCZ, and that such alterations might directly underlie pathological phenotypes via reduced functional inhibition at the AIS and perturbed brain rhythms.

Autism spectrum disorders

Three articles were found which reported on AACs in ASD (Figure 3), studying post-mortem tissue from PFC (Table 3).

To distinguish between PV+ AACs and PV+ basket cells, Ariza and colleagues used double immunohistochemical labeling of PV and *Vicia Villosa* lectin and the PV+/VVA– phenotype as a proxy for AACs (Ariza et al., 2018). They found a 40–65% decrease in the absolute number of PV+ AACs while the number of PV+ basket cells was not significantly reduced (Ariza et al., 2018). The absolute number of GAT-1+ cartridges was found to be decreased by 40–60% across prefrontal areas by the same group (Amina et al., 2021). This result may support the hypothesis that prefrontal AACs' density is reduced in ASD as opposed to PV or GAT-1 immunoreactivity.

Post-synaptic alterations were also reported for AACs, with a reduction in the AIS surface covered by GAB_AA-Rα2 subunits in upper cortical layers of samples from patients with ASD (Hong et al., 2020). This result suggests that presynaptic loss of AACs is not compensated for by an increase in postsynaptic expression of $GABA_A$-Rs in ASD.

Discussion

The aim of this work was to provide a systematic review of AACs' alterations in neuropsychiatric disorders. Namely, articles on AACs in EPI, SCZ and ASD were studied. Review of the 32 articles relevant to this topic point to alterations in AAC to AIS synapses in brain disorders (summarized in Figure 4). Previous articles have reviewed AACs' function, and have debated their implication in disease, including recent publications (Wang et al., 2016; Gallo et al., 2020; Juarez and Martinez Cerdeno, 2022; Jung et al., 2022). However, to the best of our knowledge, none of the previous reviews has followed a systematic procedure, precluding a thorough analysis of AAC dysfunction in disease. Our review article thus provides a comprehensive summary of AACs in three main neuropsychiatric disorders, in a systematic format, for the first time. Below, we briefly summarize and articulate the main findings, before discussing their limitations and suggesting some perspectives.

Main findings

Overall the systematic review of AACs' implication in EPI, SCZ, and ASD revealed some consistency, but also many contradictory findings, especially in human tissue.

In EPI, there appears to be region-specific alterations. In hippocampus, defects vary depending on the region, and with the amount of sclerosis severity. A consistent finding is reported in the sclerotic CA, with PV+ and CB+ AACs' cartridges displaying decreased density and PV expression levels, while no clear phenotype emerged from studies in non-sclerotic tissue. On the contrary, in the epileptic DG, AACs seem to be preserved, and display increased arborization complexity paralleling sclerosis. In contrast, an earlier study reported a qualitative decrease of GAT-1

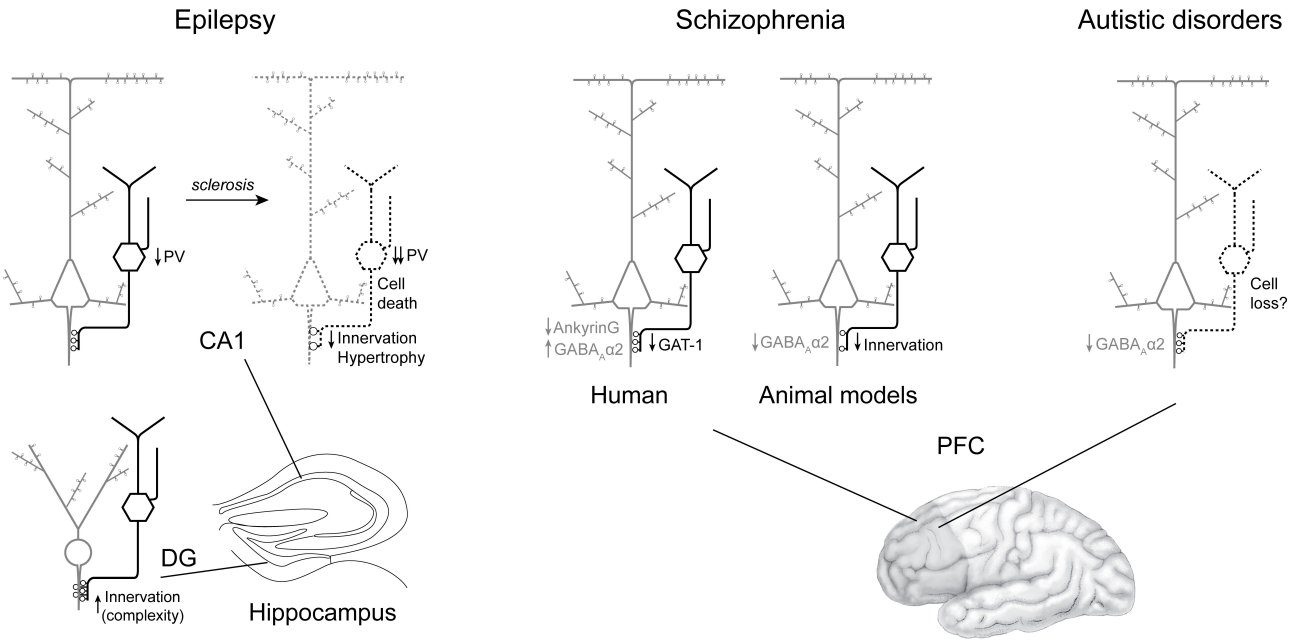

FIGURE 4
Summary of axo-axonic cells alterations consistently found in epilepsy, schizophrenia and autism spectrum disorder. In epilepsy **(left)** without sclerosis, AACs are spared in both CA1 (with reduced PV expression) and dentate gyrus (with findings of increased axo-axonic cartridge complexity). In the sclerotic CA1, PV expression, axo-axonic cell density and axo-axonic innervation appear altered, paralleling pyramidal cell loss. In brain samples from patients with schizophrenia **(middle)**, the density of AACs seems preserved, while in their synaptic boutons, GAT-1 is downregulated. At the postsynaptic level, there are more GABA$_A$-Rα2 clusters. In contrast, in animal models, axo-axonic innervation is reduced along with GABA$_A$-Rα2 cluster density. In ASD **(right)**, preliminary evidence point toward a reduced density of GABA$_A$-Rα2 clusters, and a possible AAC loss.

immunoreactivity in the DG, including at the border between the granule cell layer and the subgranular hilus, where AISs are located (Sayin et al., 2003). Surgical samples have been reported to be heterogeneous within and across subjects of individual studies (e.g., Arellano et al., 2004), reflecting biological variability, rather than differences in techniques applied for fixation or tissue processing. Thus, it is likely that the small sample sizes and heterogeneity in the subjects analyzed may partly account for the general lack of consistency in the studies reviewed here. The loss of AACs in the sclerotic tissue might contribute to pathological activities by loss of inhibition, or by GABAergic excitation in this condition (e.g., Hristova et al., 2021, but see Krook-Magnuson et al., 2013), but could also merely reflect a global cell loss, proportional to pyramidal cell death. Intriguingly, alterations in AACs did not mirror epileptiform activities, when the latter were recorded in patients before surgical removal of the samples subsequently analyzed (DeFelipe et al., 1993; Marco et al., 1997). This suggests that AACs might not play an active role in epileptogenesis.

In SCZ, initial studies pointed to the loss of AACs' cartridges in human tissue. However, complementary analyses revealed that AACs' terminals were preserved, indicating that initial findings reflected the inability to detect molecular markers in axo-axonic boutons because of low expression levels (Rocco et al., 2017). In contrast, the density of CB-expressing cartridges may be increased (Rocco et al., 2017) in superficial layers of the PFC in SCZ, the meaning of which is uncertain. Expression of postsynaptic GABA$_A$-Rα2, on the other hand, may be increased, the causes and consequences of which also remain to be established. Paradoxically, in animal models, consistent reductions of AIS innervation by AACs were found, along with decreased GABA$_A$-Rα2 expression postsynaptically and decreased glutamatergic innervation presynaptically (Del Pino et al., 2013; Wang et al., 2016). Notably, one of the hypothesis on the onset of schizophrenia is a decrease of NMDA transmission, which implicate PV+ interneurons (e.g., Gawande et al., 2023), and perhaps AACs. In the animal model of *ERBB4* KO in AACs, cognitive alterations were improved by a GABA$_A$-Rα2 agonist (Yang et al., 2019). Interestingly, in an open label trial, the GABA$_A$-Rα2-3 selective agonist MK-0777 improved cognitive function in patients with SCZ (Lewis et al., 2008). However, a subsequent randomized controlled trial failed to demonstrate any benefit (Buchanan et al., 2011). There are many potential explanations to these discrepancies between human and animal studies. For instance, the animal models employed by these authors relied on monogenetic alterations that may not reflect the full and complex spectrum of polygenic alterations found in schizophrenia (Trubetskoy et al., 2022). To date, it remains unclear how AACs are altered in SCZ, and what could be the direct contribution of these alterations to clinical symptoms.

Research on AACs' implication in ASD is still recent, and only three articles were found in the inclusion period, reporting a reduced number of AAC somata and cartridges (Ariza et al., 2018; Amina et al., 2021) and a decrease in postsynaptic GABA$_A$-Rα2 at the AIS in the PFC of subjects with ASD (Hong et al., 2020). The indirect detection of AACs and cartridges using molecular markers as proxies calls for caution, as exemplified by the case of SCZ (and see below). The decreased density of GABA$_A$-Rα2 at the AIS (Hong et al., 2020) is also in contrast with findings in SCZ (Volk et al.,

2002), with unknown functional consequences. Despite the paucity of the literature, these initial results suggest a potential implication of the axo-axonic synapse in ASD pathophysiology.

It is intriguing that EPI, SCZ and ASD implicate overlapping brain regions, which contain relatively high densities of AACs (Inda et al., 2009). Those disorders are linked to neurodevelopmental abnormalities, while AACs have a peculiar, late developmental pattern compared with other interneurons (Taniguchi et al., 2013). Moreover, AACs undergo structural and functional maturation until young adulthood (Rinetti-Vargas et al., 2017; Steinecke et al., 2017), a period at risk of SCZ or EPI occurrence. Comorbid EPI and psychotic disorders or ASD, are highly prevalent in clinical populations (Clancy et al., 2014; Tye et al., 2018). As a result, one may speculate that common pathophysiological principles may be at stake and implicate AACs. To test this hypothesis, it would be interesting to investigate alterations of AACs in brain samples from subjects with comorbid disorders. Moreover, animal studies suggest that AACs might be implicated in other neurodevelopmental disorders. Prenatal exposure to cocaine results in decreased density of AAC cartridges in the PFC (Morrow et al., 2003). In a mouse model of Down syndrome, AACs displayed aberrant innervation of AIS with increased number of cartridges, cartridge length, bouton size and amount of GABAergic inhibition in electrophysiological recording (Liu et al., 2023). Human counterparts of these findings are currently lacking. In summary, AACs may bear common and direct pathogenic factors across EPI, SCZ and ASD, but the focus of the review on this topic may also artificially inflate this hypothesis.

Limitations and perspectives

The first main limitation is the result of indirect strategies to study AACs in human brain samples. Most of the histological methods applied to human tissue have so far relied on molecular markers, be it to infer the density of AACs to pyramidal cells synapses, or to evaluate the density of AACs. Clear limitations of this strategy are highlighted in the following examples. First, in SCZ, the reduction of GAT-1+ cartridges later appeared to reflect a reduction in protein levels rather than the loss of AACs (Rocco et al., 2017). Second, PV+ cartridges have been widely used as a proxy for axo-axonic synapses in EPI studies. However, the same studies consistently reported a global reduction of PV immunoreactivity in epileptic tissue (Wittner et al., 2001; Arellano et al., 2004), which might have contributed to the observation of reduced AAC cartridges density. Moreover, a significant number of AACs may be devoid of PV in the healthy brain (Taniguchi et al., 2013; Tasic et al., 2018). The case of increased CB+ axo-axonic cartridges density in SCZ (Rocco et al., 2017) or in EPI (Arellano et al., 2004) is intriguing in this context. Third, in an ASD study, the absence of perineuronal nets around PV+ cells was used to identify AACs (Ariza et al., 2018), while perineuronal nets have been extensively found around hippocampal AACs (Fujikawa et al., 2021). Alterations in molecular content of AACs may indeed be the consequence of compensatory or even confounding factors, including pharmacological treatments. In addition, most Human studies were published by one or two research groups in each disorder, calling for replication studies.

The second main limitation in knowledge is the lack of experimental evidence to causally link structure and function. Indeed, most of the articles reviewed here were reports of histopathological studies in Human, which are, by essence, correlative and cannot provide mechanisms. Animal models are instrumental to understand pathogenesis and suggest causal links between cellular alterations and symptoms. However, only very few studies were found on this topic, and data is still lacking at all levels: cells (synaptic transmission), network (assemblies, oscillations), and behavior. We have highlighted three important functional studies (Konopaske et al., 2006; Del Pino et al., 2013; Yang et al., 2019), also showing discrepancies in histological findings with human data. Animal models will thus need to be cross validated with Human data in order to improve translation. One interesting pathway is the reduced density of $GABA_A$-Rα2 at the AIS, as suggested by animal studies in SCZ (Del Pino et al., 2013, but see Volk et al., 2002) and clinical samples in ASD (Hong et al., 2020). In addition, reduced levels of $GABA_A$-Rα2 at the AIS (possibly from AACs) induce greater seizure susceptibility in mice (Hines et al., 2018). $GABA_A$-Rs containing the α2 subunit show fast activation and slow deactivation kinetics (Lavoie et al., 1997). Therefore, the loss of this postsynaptic partner of AACs might induce a strong hyperexcitability in principal neurons. Until recently, AACs studies have been limited by the lack of specific genetic markers. Using single-cell RNA sequencing, such markers have been identified, including PTHLH, Uncb5 and Vipr2 (Paul et al., 2017; Tasic et al., 2018). As a result of these discoveries, genetic targeting of cortical AACs is now accessible in animal models using Nkx2.1CreER (He et al., 2016) or Vipr2-Cre mouse lines (Tasic et al., 2018) for the neocortex, or using Unc5b-2A-CreER mice for the hippocampus (Dudok et al., 2021). It is beyond the scope of this work to extensively review this, but recent work have started to unravel AACs functions in physiological conditions using these transgenic animals (e.g., Lu et al., 2017; Dudok et al., 2021; Schneider-Mizell et al., 2021; Jung et al., 2023; Seignette et al., 2023). These showed that AACs only weakly inhibited principal neurons' firing, suggesting that alterations of AACs in disease might not result in gross excitation/inhibition imbalance. In fact, AACs seem to ensure excitation homeostasis in cortical networks (Pan-Vazquez et al., 2020), a loss of which may have dramatic consequences on cortical function (e.g., overexcitation, increased local synchrony and reduced interregional coordination).

Direct examination of AACs is warranted, and may rely on complementary approaches. Detailed reconstructions of AACs at the cellular and ultrastructural levels following Golgi staining or semi-automated electron microcopy (e.g., Schneider-Mizell et al., 2021) would provide invaluable information. The study by Wittner et al. (2005) is noteworthy as being the only one in this review that systematically examined AIS innervation at the electron microscopic level regardless of PV content. Recently identified molecular markers of AACs will also prove useful in identifying AACs in human tissue (e.g., Alhourani et al., 2020). Moreover, targeting AACs with novel transgenic mouse lines represent an opportunity to directly evaluate whether a genetic mutation implicates AACs in generating a pathological phenotype (as in Yang et al., 2019). Targeting AACs for recording and opto- or chemo-genetic manipulations could also be implemented to study their implications in disease models constructed with non-genetic

interventions (e.g., pharmacological, lesional). These experiments are expected to provide key evidence to causally link axo-axonic cells to brain disorders.

Conclusion

Although observations made in brain tissue from human subjects and in animal models indicate that axo-axonic cells may be altered in epilepsy, schizophrenia, and autism spectrum disorders, the literature is limited and mainly inconsistent, precluding clear conclusions to be drawn.

By joining clinical research and refined preclinical models, we hope that the coming years will bring significant clarification and progress in the field of AACs in disease.

Data availability statement

The original contributions presented in the study are included in the article/Supplementary material, further inquiries can be directed to the corresponding author.

Author contributions

JV and AE: literature search and screening. JV, AE, and TB: article selection. JV, AE, CL, and TB: literature synthesis. JV, AE, CL, FL, BA, CH, YH, and TB: manuscript writing and revisions. TB: supervision of the project. All authors contributed to the article and approved the submitted version.

Funding

This work was funded by Fondation Bettencourt Schueller with a CCA Inserm-Bettencourt grant to TB (R20005GS). AE and CL benefited from the help of the Bordeaux Neurocampus Graduate Program, managed by the French National Research Agency reference ANR-17-EURE-0028.

Acknowledgments

We would like to dedicate this article to our mentor, Dr. Marco Capogna, who tragically passed away during the preparation of this manuscript.

Conflict of interest

The authors declare that the research was conducted in the absence of any commercial or financial relationships that could be construed as a potential conflict of interest.

Publisher's note

All claims expressed in this article are solely those of the authors and do not necessarily represent those of their affiliated organizations, or those of the publisher, the editors and the reviewers. Any product that may be evaluated in this article, or claim that may be made by its manufacturer, is not guaranteed or endorsed by the publisher.

Supplementary material

The Supplementary Material for this article can be found online at: https://www.frontiersin.org/articles/10.3389/fncel.2023.1212202/full#supplementary-material

References

Alhourani, A., Fish, K. N., Wozny, T. A., Sudhakar, V., Hamilton, R. L., and Richardson, R. M. (2020). GABA bouton subpopulations in the human dentate gyrus are differentially altered in mesial temporal lobe epilepsy. *J. Neurophysiol.* 123, 392–406. doi: 10.1152/jn.00523.2018

Alonso-Nanclares, L., Garbelli, R., Sola, R. G., Pastor, J., Tassi, L., Spreafico, R., et al. (2005). Microanatomy of the dysplastic neocortex from epileptic patients. *Brain* 128, 158–173. doi: 10.1093/brain/awh331

Amina, S., Falcone, C., Hong, T., Wolf-Ochoa, M. W., Vakilzadeh, G., Allen, E., et al. (2021). Chandelier cartridge density is reduced in the prefrontal cortex in autism. *Cereb. Cortex* 31, 2944–2951. doi: 10.1093/cercor/bhaa402

Arellano, J. I., Munoz, A., Ballesteros-Yanez, I., Sola, R. G., and DeFelipe, J. (2004). Histopathology and reorganization of chandelier cells in the human epileptic sclerotic hippocampus. *Brain* 127, 45–64. doi: 10.1093/brain/awh004

Ariza, J., Rogers, H., Hashemi, E., Noctor, S. C., and Martinez-Cerdeno, V. (2018). The number of chandelier and basket cells are differentially decreased in prefrontal cortex in autism. *Cereb. Cortex* 28, 411–420. doi: 10.1093/cercor/bhw349

Best, N., Mitchell, J., and Wheal, H. V. (1994). Ultrastructure of parvalbumin-immunoreactive neurons in the CA1 area of the rat hippocampus following a kainic acid injection. *Acta Neuropathol.* 87, 187–195. doi: 10.1007/BF00296189

Bloomfield, C., French, S. J., Jones, D. N., Reavill, C., Southam, E., Cilia, J., et al. (2008). Chandelier cartridges in the prefrontal cortex are reduced in isolation reared rats. *Synapse* 62, 628–631. doi: 10.1002/syn.20521

Buchanan, R. W., Keefe, R. S., Lieberman, J. A., Barch, D. M., Csernansky, J. G., Goff, D. C., et al. (2011). A randomized clinical trial of MK-0777 for the treatment of cognitive impairments in people with schizophrenia. *Biol. Psychiatry* 69, 442–449. doi: 10.1016/j.biopsych.2010.09.052

Buzsaki, G., and Draguhn, A. (2004). Neuronal oscillations in cortical networks. *Science* 304, 1926–1929. doi: 10.1126/science.1099745

Cardin, J. A., Carlen, M., Meletis, K., Knoblich, U., Zhang, F., Deisseroth, K., et al. (2009). Driving fast-spiking cells induces gamma rhythm and controls sensory responses. *Nature* 459, 663–667. doi: 10.1038/nature08002

Clancy, M. J., Clarke, M. C., Connor, D. J., Cannon, M., and Cotter, D. R. (2014). The prevalence of psychosis in epilepsy; a systematic review and meta-analysis. *BMC Psychiatry* 14, 75. doi: 10.1186/1471-244X-14-75

Cruz, D. A., Weaver, C. L., Lovallo, E. M., Melchitzky, D. S., and Lewis, D. A. (2009). Selective alterations in postsynaptic markers of chandelier cell inputs to cortical pyramidal neurons in subjects with schizophrenia. *Neuropsychopharmacology* 34, 2112–2124. doi: 10.1038/npp.2009.36

DeFelipe, J., Garcia Sola, R., Marco, P., del Rio, M. R., Pulido, P., and Ramon y Cajal, S. (1993). Selective changes in the microorganization of the human epileptogenic neocortex revealed by parvalbumin immunoreactivity. *Cereb. Cortex* 3, 39–48. doi: 10.1093/cercor/3.1.39

Del Pino, I., Garcia-Frigola, C., Dehorter, N., Brotons-Mas, J. R., Alvarez-Salvado, E., Martinez de Lagran, M., et al. (2013). Erbb4 deletion from fast-spiking

interneurons causes schizophrenia-like phenotypes. *Neuron* 79, 1152–1168. doi: 10.1016/j.neuron.2013.07.010

del Rio, M. R., and DeFelipe, J. (1997). Colocalization of parvalbumin and calbindin D-28k in neurons including chandelier cells of the human temporal neocortex. *J. Chem. Neuroanat.* 12, 165–173. doi: 10.1016/S0891-0618(96)00191-3

Dinocourt, C., Petanjek, Z., Freund, T. F., Ben-Ari, Y., and Esclapez, M. (2003). Loss of interneurons innervating pyramidal cell dendrites and axon initial segments in the CA1 region of the hippocampus following pilocarpine-induced seizures. *J. Comp. Neurol.* 459, 407–425. doi: 10.1002/cne.10622

Dudok, B., Szoboszlay, M., Paul, A., Klein, P. M., Liao, Z., Hwaun, E., et al. (2021). Recruitment and inhibitory action of hippocampal axo-axonic cells during behavior. *Neuron* 109, 3838–3850 e3838. doi: 10.1016/j.neuron.2021.09.033

Ferrer, I., Oliver, B., Russi, A., Casas, R., and Rivera, R. (1994). Parvalbumin and calbindin-D28k immunocytochemistry in human neocortical epileptic foci. *J. Neurol. Sci.* 123, 18–25. doi: 10.1016/0022-510X(94)90198-8

Ferrer, I., Pineda, M., Tallada, M., Oliver, B., Russi, A., Oller, L., et al. (1992). Abnormal local-circuit neurons in epilepsia partialis continua associated with focal cortical dysplasia. *Acta Neuropathol.* 83, 647–652. doi: 10.1007/BF00299415

Fujikawa, R., Yamada, J., and Jinno, S. (2021). Subclass imbalance of parvalbumin-expressing GABAergic neurons in the hippocampus of a mouse ketamine model for schizophrenia, with reference to perineuronal nets. *Schizophr. Res.* 229, 80–93. doi: 10.1016/j.schres.2020.11.016

Gallo, N. B., Paul, A., and Van Aelst, L. (2020). Shedding light on chandelier cell development, connectivity, and contribution to neural disorders. *Trends Neurosci.* 43, 565–580. doi: 10.1016/j.tins.2020.05.003

Gawande, D. Y., Narasimhan, K. K, S., Shelkar, G. P., Pavuluri, R., Stessman, H. A. F., and Dravid, S. M. (2023). GluN2D subunit in parvalbumin interneurons regulates prefrontal cortex feedforward inhibitory circuit and molecular networks relevant to schizophrenia. *Biol. Psychiatry*. doi: 10.1016/j.biopsych.2023.03.020. [Epub ahead of print].

He, M., Tucciarone, J., Lee, S., Nigro, M. J., Kim, Y., Levine, J. M., et al. (2016). Strategies and tools for combinatorial targeting of GABAergic neurons in mouse cerebral cortex. *Neuron* 92, 555. doi: 10.1016/j.neuron.2016.08.021

Hines, R. M., Maric, H. M., Hines, D. J., Modgil, A., Panzanelli, P., Nakamura, Y., et al. (2018). Developmental seizures and mortality result from reducing GABA(A) receptor alpha2-subunit interaction with collybistin. *Nat. Commun.* 9, 3130. doi: 10.1038/s41467-018-05481-1

Hong, T., Falcone, C., Dufour, B., Amina, S., Castro, R. P., Regalado, J., et al. (2020). GABA(A)Ralpha2 is decreased in the axon initial segment of pyramidal cells in specific areas of the prefrontal cortex in autism. *Neuroscience* 437, 76–86. doi: 10.1016/j.neuroscience.2020.04.025

Hristova, K., Martinez-Gonzalez, C., Watson, T. C., Codadu, N. K., Hashemi, K., Kind, P. C., et al. (2021). Medial septal GABAergic neurons reduce seizure duration upon optogenetic closed-loop stimulation. *Brain* 144, 1576–1589. doi: 10.1093/brain/awab042

Hunt, M. J., Kopell, N. J., Traub, R. D., and Whittington, M. A. (2017). Aberrant network activity in schizophrenia. *Trends Neurosci.* 40, 371–382. doi: 10.1016/j.tins.2017.04.003

Inda, M. C., DeFelipe, J., and Munoz, A. (2009). Morphology and distribution of chandelier cell axon terminals in the mouse cerebral cortex and claustroamygdaloid complex. *Cereb. Cortex* 19, 41–54. doi: 10.1093/cercor/bhn057

Juarez, P., and Martinez Cerdeno, V. (2022). Parvalbumin and parvalbumin chandelier interneurons in autism and other psychiatric disorders. *Front. Psychiatry* 13, 913550. doi: 10.3389/fpsyt.2022.913550

Jung, K., Chang, M., Steinecke, A., Berke, B., Choi, Y., Oisi, Y., et al. (2023). An adaptive behavioral control motif mediated by cortical axo-axonic inhibition. *Biorxiv*. doi: 10.1101/2023.03.10.531767. Available online at: https://www.biorxiv.org/about/FAQ

Jung, K., Choi, Y., and Kwon, H. B. (2022). Cortical control of chandelier cells in neural codes. *Front. Cell. Neurosci.* 16, 992409. doi: 10.3389/fncel.2022.992409

Kalus, P., Senitz, D., Lauer, M., and Beckmann, H. (1999). Inhibitory cartridge synapses in the anterior cingulate cortex of schizophrenics. *J. Neural Transm.* 106, 763–771. doi: 10.1007/s007020050197

Karlócai, M. R., Kohus, Z., Kali, S., Ulbert, I., Szabo, G., Mate, Z., et al. (2014). Physiological sharp wave-ripples and interictal events *in vitro*: what's the difference? *Brain* 137, 463–485. doi: 10.1093/brain/awt348

Kepecs, A., and Fishell, G. (2014). Interneuron cell types are fit to function. *Nature* 505, 318–326. doi: 10.1038/nature12983

Kerti-Szigeti, K., and Nusser, Z. (2016). Similar GABAA receptor subunit composition in somatic and axon initial segment synapses of hippocampal pyramidal cells. *Elife* 5. doi: 10.7554/eLife.18426.020

Konopaske, G. T., Sweet, R. A., Wu, Q., Sampson, A., and Lewis, D. A. (2006). Regional specificity of chandelier neuron axon terminal alterations in schizophrenia. *Neuroscience* 138, 189–196. doi: 10.1016/j.neuroscience.2005.10.070

Krook-Magnuson, E., Armstrong, C., Oijala, M., and Soltesz, I. (2013). On-demand optogenetic control of spontaneous seizures in temporal lobe epilepsy. *Nat. Commun.* 4, 1376. doi: 10.1038/ncomms2376

Lavoie, A. M., Tingey, J. J., Harrison, N. L., Pritchett, D. B., and Twyman, R. E. (1997). Activation and deactivation rates of recombinant GABA(A) receptor channels are dependent on alpha-subunit isoform. *Biophys. J.* 73, 2518–2526. doi: 10.1016/S0006-3495(97)78280-8

Lewis, D. A., Cho, R. Y., Carter, C. S., Eklund, K., Forster, S., Kelly, M. A., et al. (2008). Subunit-selective modulation of GABA type A receptor neurotransmission and cognition in schizophrenia. *Am. J. Psychiatry* 165, 1585–1593. doi: 10.1176/appi.ajp.2008.08030395

Liu, H., Caballero-Floran, R. N., Hergenreder, T., Yang, T., Hull, J. M., Pan, G., et al. (2023). DSCAM gene triplication causes excessive GABAergic synapses in the neocortex in Down syndrome mouse models. *PLoS Biol.* 21, e3002078. doi: 10.1371/journal.pbio.3002078

Lu, J., Tucciarone, J., Padilla-Coreano, N., He, M., Gordon, J. A., and Huang, Z. J. (2017). Selective inhibitory control of pyramidal neuron ensembles and cortical subnetworks by chandelier cells. *Nat. Neurosci.* 20, 1377–1383. doi: 10.1038/nn.4624

Marco, P., Sola, R. G., Pulido, P., Alijarde, M. T., Sanchez, A., Ramon y Cajal, S., et al. (1996). Inhibitory neurons in the human epileptogenic temporal neocortex. An immunocytochemical study. Brain 119 (Pt 4), 1327–1347. doi: 10.1093/brain/119.4.1327

Marco, P., Sola, R. G., Ramon y Cajal, S., and DeFelipe, J. (1997). Loss of inhibitory synapses on the soma and axon initial segment of pyramidal cells in human epileptic peritumoural neocortex: implications for epilepsy. *Brain Res. Bull.* 44, 47–66. doi: 10.1016/S0361-9230(97)00090-7

Marin, O. (2012). Interneuron dysfunction in psychiatric disorders. *Nat. Rev. Neurosci.* 13, 107–120. doi: 10.1038/nrn3155

Minzenberg, M. J., Laird, A. R., Thelen, S., Carter, C. S., and Glahn, D. C. (2009). Meta-analysis of 41 functional neuroimaging studies of executive function in schizophrenia. *Arch. Gen. Psychiatry* 66, 811–822. doi: 10.1001/archgenpsychiatry.2009.91

Morrow, B. A., Elsworth, J. D., and Roth, R. H. (2003). Axo-axonic structures in the medial prefrontal cortex of the rat: reduction by prenatal exposure to cocaine. *J. Neurosci.* 23, 5227–5234. doi: 10.1523/JNEUROSCI.23-12-05227.2003

Morrow, B. A., Elsworth, J. D., and Roth, R. H. (2007). Repeated phencyclidine in monkeys results in loss of parvalbumin-containing axo-axonic projections in the prefrontal cortex. *Psychopharmacology* 192, 283–290. doi: 10.1007/s00213-007-0708-0

Nusser, Z., Sieghart, W., Benke, D., Fritschy, J. M., and Somogyi, P. (1996). Differential synaptic localization of two major gamma-aminobutyric acid type A receptor alpha subunits on hippocampal pyramidal cells. *Proc. Natl. Acad. Sci. U. S. A.* 93, 11939–11944. doi: 10.1073/pnas.93.21.11939

Pan-Vazquez, A., Wefelmeyer, W., Gonzalez Sabater, V., Neves, G., and Burrone, J. (2020). Activity-dependent plasticity of axo-axonic synapses at the axon initial segment. *Neuron* 10,6 265–276 e266. doi: 10.1016/j.neuron.2020.01.037

Paul, A., Crow, M., Raudales, R., He, M., Gillis, J., and Huang, Z. J. (2017). Transcriptional architecture of synaptic communication delineates GABAergic neuron identity. *Cell* 171, 522–539 e520. doi: 10.1016/j.cell.2017.08.032

Pierri, J. N., Chaudry, A. S., Woo, T. U., and Lewis, D. A. (1999). Alterations in chandelier neuron axon terminals in the prefrontal cortex of schizophrenic subjects. *Am. J. Psychiatry* 156, 1709–1719. doi: 10.1176/ajp.156.11.1709

Ribak, C. E. (1985). Axon terminals of GABAergic chandelier cells are lost at epileptic foci. *Brain Res.* 326, 251–260. doi: 10.1016/0006-8993(85)90034-4

Rinetti-Vargas, G., Phamluong, K., Ron, D., and Bender, K. J. (2017). Periadolescent maturation of GABAergic hyperpolarization at the axon initial segment. *Cell Rep.* 20, 21–29. doi: 10.1016/j.celrep.2017.06.030

Rocco, B. R., DeDionisio, A. M., Lewis, D. A., and Fish, K. N. (2017). Alterations in a unique class of cortical chandelier cell axon cartridges in schizophrenia. *Biol. Psychiatry* 82, 40–48. doi: 10.1016/j.biopsych.2016.09.018

Rocco, B. R., Lewis, D. A., and Fish, K. N. (2016). Markedly lower glutamic acid decarboxylase 67 protein levels in a subset of boutons in schizophrenia. *Biol. Psychiatry* 79, 1006–1015. doi: 10.1016/j.biopsych.2015.07.022

Roux, L., and Buzsaki, G. (2015). Tasks for inhibitory interneurons in intact brain circuits. *Neuropharmacology* 88, 10–23. doi: 10.1016/j.neuropharm.2014.09.011

Sayin, U., Osting, S., Hagen, J., Rutecki, P., and Sutula, T. (2003). Spontaneous seizures and loss of axo-axonic and axo-somatic inhibition induced by repeated brief seizures in kindled rats. *J. Neurosci.* 23, 2759–2768. doi: 10.1523/JNEUROSCI.23-07-02759.2003

Schneider-Mizell, C. M., Bodor, A. L., Collman, F., Brittain, D., Bleckert, A., Dorkenwald, S., et al. (2021). Structure and function of axo-axonic inhibition. *Elife* 10. doi: 10.7554/eLife.73783.sa2

Seignette, K., Jamann, N., Papale, P., Terra, H., Porneso, R. P. O., de Kraker, L., et al. (2023). Visuomotor experience induces functional and structural plasticity of chandelier cells. *Biorxiv*. doi: 10.1101/2023.04.21.537780. Available online at: https://www.biorxiv.org/about/FAQ

Simon, D. M., and Wallace, M. T. (2016). Dysfunction of sensory oscillations in autism spectrum disorder. *Neurosci. Biobehav. Rev.* 68, 848–861. doi: 10.1016/j.neubiorev.2016.07.016

Sloviter, R. S., Zappone, C. A., Harvey, B. D., Bumanglag, A. V., Bender, R. A., and Frotscher, M. (2003). "Dormant basket cell" hypothesis revisited: relative vulnerabilities of dentate gyrus mossy cells and inhibitory interneurons after hippocampal status epilepticus in the rat. *J. Comp. Neurol.* 459, 44–76. doi: 10.1002/cne.10630

Sohal, V. S., and Rubenstein, J.L. R. (2019). Excitation-inhibition balance as a framework for investigating mechanisms in neuropsychiatric disorders. *Mol. Psychiatry* 24, 1248–1257. doi: 10.1038/s41380-019-0426-0

Sohal, V. S., Zhang, F., Yizhar, O., and Deisseroth, K. (2009). Parvalbumin neurons and gamma rhythms enhance cortical circuit performance. *Nature* 459, 698–702. doi: 10.1038/nature07991

Somogyi, P. (1977). A specific 'axo-axonal' interneuron in the visual cortex of the rat. *Brain Res.* 136, 345–350. doi: 10.1016/0006-8993(77)90808-3

Steinecke, A., Hozhabri, E., Tapanes, S., Ishino, Y., Zeng, H., Kamasawa, N., et al. (2017). Neocortical chandelier cells developmentally shape axonal arbors through reorganization but establish subcellular synapse specificity without refinement. *eNeuro* 4. doi: 10.1523/ENEURO.0057-17.2017

Tai, Y., Gallo, N. B., Wang, M., Yu, J. R., and Van Aelst, L. (2019). Axo-axonic innervation of neocortical pyramidal neurons by GABAergic chandelier cells requires ankyrinG-associated L1CAM. *Neuron* 102, 358–372 e359. doi: 10.1016/j.neuron.2019.02.009

Taniguchi, H., Lu, J., and Huang, Z. J. (2013). The spatial and temporal origin of chandelier cells in mouse neocortex. *Science* 339, 70–74. doi: 10.1126/science.1227622

Tasic, B., Yao, Z., Graybuck, L. T., Smith, K. A., Nguyen, T. N., Bertagnolli, D., et al. (2018). Shared and distinct transcriptomic cell types across neocortical areas. *Nature* 563, 72–78. doi: 10.1038/s41586-018-0654-5

Trubetskoy, V., Pardinas, A. F., Qi, T., Panagiotaropoulou, G., Awasthi, S., Bigdeli, T. B., et al. (2022). Mapping genomic loci implicates genes and synaptic biology in schizophrenia. *Nature* 604, 502–508. doi: 10.1038/s41586-022-04434-5

Tye, C., Runicles, A. K., Whitehouse, A. J. O., and Alvares, G. A. (2018). Characterizing the interplay between autism spectrum disorder and comorbid medical conditions: an integrative review. *Front. Psychiatry* 9, 751. doi: 10.3389/fpsyt.2018.00751

Volk, D. W., Pierri, J. N., Fritschy, J. M., Auh, S., Sampson, A. R., and Lewis, D. A. (2002). Reciprocal alterations in pre- and postsynaptic inhibitory markers at chandelier cell inputs to pyramidal neurons in schizophrenia. *Cereb. Cortex* 12, 1063–1070. doi: 10.1093/cercor/12.10.1063

Wang, Y., Zhang, P., and Wyskiel, D. R. (2016). Chandelier cells in functional and dysfunctional neural circuits. *Front. Neural Circ.* 10, 33. doi: 10.3389/fncir.2016.00033

Wittner, L., Eross, L., Czirjak, S., Halasz, P., Freund, T. F., and Magloczky, Z. (2005). Surviving CA1 pyramidal cells receive intact perisomatic inhibitory input in the human epileptic hippocampus. *Brain* 128, 138–152. doi: 10.1093/brain/awh339

Wittner, L., Eross, L., Szabo, Z., Toth, S., Czirjak, S., Halasz, P., et al. (2002). Synaptic reorganization of calbindin-positive neurons in the human hippocampal CA1 region in temporal lobe epilepsy. *Neuroscience* 115, 961–978. doi: 10.1016/S0306-4522(02)00264-6

Wittner, L., Magloczky, Z., Borhegyi, Z., Halasz, P., Toth, S., Eross, L., et al. (2001). Preservation of perisomatic inhibitory input of granule cells in the epileptic human dentate gyrus. *Neuroscience* 108, 587–600. doi: 10.1016/S0306-4522(01)00446-8

Woo, T. U., Whitehead, R. E., Melchitzky, D. S., and Lewis, D. A. (1998). A subclass of prefrontal gamma-aminobutyric acid axon terminals are selectively altered in schizophrenia. *Proc. Natl. Acad. Sci. U. S. A.* 95, 5341–5346. doi: 10.1073/pnas.95.9.5341

Yang, J. M., Shen, C. J., Chen, X. J., Kong, Y., Liu, Y. S., Li, X. W., et al. (2019). erbb4 deficits in chandelier cells of the medial prefrontal cortex confer cognitive dysfunctions: implications for schizophrenia. *Cereb. Cortex* 29, 4334–4346. doi: 10.1093/cercor/bhy316

frontiers | Frontiers in Cellular Neuroscience

TYPE Original Research
PUBLISHED 20 July 2023
DOI 10.3389/fncel.2023.1146278

OPEN ACCESS

EDITED BY
Norbert Hajos,
Indiana University Bloomington, United States

REVIEWED BY
Sam A. Booker,
The University of Edinburgh, United Kingdom
Joanna Urban Ciecko,
Polish Academy of Sciences, Poland

*CORRESPONDENCE
Irene Han-Juo Cheng
✉ ihjcheng@nycu.edu.tw
Cheng-Di Chiu
✉ cdchiu@mail.cmu.edu.tw

†These authors have contributed equally to this work and share first authorship

RECEIVED 17 January 2023
ACCEPTED 14 June 2023
PUBLISHED 20 July 2023

CITATION
Huang T-H, Lin Y-S, Hsiao C-W, Wang L-Y, Ajibola MI, Abdulmajeed WI, Lin Y-L, Li Y-J, Chen C-Y, Lien C-C, Chiu C-D and Cheng IH-J (2023) Differential expression of $GABA_A$ receptor subunits δ and α6 mediates tonic inhibition in parvalbumin and somatostatin interneurons in the mouse hippocampus. *Front. Cell. Neurosci.* 17:1146278. doi: 10.3389/fncel.2023.1146278

Differential expression of $GABA_A$ receptor subunits δ and α6 mediates tonic inhibition in parvalbumin and somatostatin interneurons in the mouse hippocampus

Tzu-Hsuan Huang[1†], Yi-Sian Lin[2,3†], Chiao-Wan Hsiao[1,4†], Liang-Yun Wang[2], Musa Iyiola Ajibola[5,6], Wahab Imam Abdulmajeed[5,6,7], Yu-Ling Lin[5], Yu-Jui Li[5], Cho-Yi Chen[2,8], Cheng-Chang Lien[4,5,6,8], Cheng-Di Chiu[9,10,11,12]* and Irene Han-Juo Cheng[1,4,8]*

[1]Institute of Brain Science, National Yang Ming Chiao Tung University, Taipei, Taiwan, [2]Institute of Biomedical Informatics, National Yang Ming Chiao Tung University, Taipei, Taiwan, [3]Program in Genetics and Genomics, Baylor College of Medicine, Houston, TX, United States, [4]Program in Molecular Medicine, National Yang Ming Chiao Tung University and Academia Sinica, Taipei, Taiwan, [5]Institute of Neuroscience, National Yang Ming Chiao Tung University, Taipei, Taiwan, [6]Taiwan International Graduate Program in Interdisciplinary Neuroscience, College of Life Sciences, National Yang Ming Chiao Tung University and Academia Sinica, Taipei, Taiwan, [7]Department of Physiology, Faculty of Basic Medical Sciences, College of Health Sciences, University of Ilorin, Ilorin, Nigeria, [8]Brain Research Center, National Yang Ming Chiao Tung University, Taipei, Taiwan, [9]Department of Neurosurgery, China Medical University Hospital, Taichung, Taiwan, [10]Spine Center, China Medical University Hospital, Taichung, Taiwan, [11]Graduate Institute of Biomedical Science, China Medical University, Taichung, Taiwan, [12]School of Medicine, China Medical University, Taichung, Taiwan

Inhibitory γ-aminobutyric acid (GABA)-ergic interneurons mediate inhibition in neuronal circuitry and support normal brain function. Consequently, dysregulation of inhibition is implicated in various brain disorders. Parvalbumin (PV) and somatostatin (SST) interneurons, the two major types of GABAergic inhibitory interneurons in the hippocampus, exhibit distinct morpho-physiological properties and coordinate information processing and memory formation. However, the molecular mechanisms underlying the specialized properties of PV and SST interneurons remain unclear. This study aimed to compare the transcriptomic differences between these two classes of interneurons in the hippocampus using the ribosome tagging approach. The results revealed distinct expressions of genes such as voltage-gated ion channels and $GABA_A$ receptor subunits between PV and SST interneurons. *Gabrd* and *Gabra6* were identified as contributors to the contrasting tonic GABAergic inhibition observed in PV and SST interneurons. Moreover, some of the differentially expressed genes were associated with schizophrenia and epilepsy. In conclusion, our results provide molecular insights into the distinct roles of PV and SST interneurons in health and disease.

KEYWORDS

tonic inhibition, somatostatin (SST), parvalbumin (PV), RiboTag, $GABA_A$ receptor, GABRD, RNA-seq

1. Introduction

Excitatory and inhibitory neurons form the foundation of neuronal networks and coordinate neuronal activities under physiological conditions. Despite constituting only 10–20% of total neurons, local-circuit γ-aminobutyric acid (GABA) inhibitory neurons, also known as GABAergic interneurons, play vital roles in maintaining the balance of excitation-inhibition within neuronal circuits. Consequently, dysfunction of inhibition is associated with various brain disorders (Belelli et al., 2009; Baroncelli et al., 2011; Ruden et al., 2021; Song et al., 2021; Yang et al., 2022). GABAergic interneurons release GABA to regulate neuronal excitability through either phasic or tonic inhibition (Szabadics et al., 2007; Brickley and Mody, 2012). Phasic inhibition is mediated by synaptic GABA receptors, whereas tonic inhibition is generated by extrasynaptic GABA receptors (Farrant and Nusser, 2005). These two modes of inhibition are mediated by $GABA_A$ receptors composed of different subunits (Prenosil et al., 2006; Lee and Maguire, 2014).

Parvalbumin (PV)- and somatostatin (SST)-expressing interneurons are the two major classes of GABAergic interneurons. They have distinct morphological features, synaptic connectivity, and physiological properties (Hu et al., 2014; Lee et al., 2016; Booker and Vida, 2018). Morphologically, PV interneurons, including basket cells and axon-axonic cells, selectively project their axons to perisomatic regions of target neurons. On the other hand, SST interneurons, which comprise multiple cell subtypes, preferentially target their dendritic domains (Lee et al., 2016; Booker and Vida, 2018). Therefore, PV interneurons selectively control spike generation by strategically positioning synapses near the axon initial segments, whereas SST interneurons regulate synaptic plasticity by tuning dendritic membrane potential (Miles et al., 1996; Klausberger and Somogyi, 2008; Kepecs and Fishell, 2014). Under physiological conditions, PV and SST interneurons coordinate and synchronize network activities through distinct spatial and temporal domains (Kepecs and Fishell, 2014). PV and SST interneurons fire at different phases during neuronal synchronization. For instance, PV interneurons fire preferentially at the descending phase of theta oscillations, whereas SST interneurons fire rhythmically at the trough phase of theta cycles (Klausberger et al., 2003). Moreover, PV interneurons promote the synchronization of spike times when instantaneous firing rates are low (<12 Hz), whereas SST interneurons preferentially promote the synchronization of spike times when instantaneous firing rates are high (>12 Hz) (Jang et al., 2020). PV interneurons exhibit characteristics of fast-spiking neurons, whereas SST interneurons display traits of non-fast-spiking neurons (Lee et al., 2016). PV interneurons are characterized by low input resistance, fast membrane time constant, and depressing excitatory inputs (Jonas et al., 2004; Hu et al., 2014). In contrast, SST interneurons possess high input resistance, slow membrane time constant, and facilitate excitatory inputs (Pouille and Scanziani, 2004). Thus, PV and SST interneurons manifest distinguishable spike probabilities upon repetitive excitation (Pouille and Scanziani, 2004; Kapfer et al., 2007; Silberberg and Markram, 2007; Silberberg, 2008). PV interneurons are primarily activated during the initial phase of excitation inputs, whereas SST interneurons are preferentially recruited during the late phase of repetitive excitation (Pouille and Scanziani, 2004).

γ-aminobutyric acid exerts powerful inhibition on neuronal excitability by activating fast ionotropic $GABA_A$ and slow metabotropic $GABA_B$ receptors. Stimulation of the $GABA_B$ receptor causes a prolonged decrease in neuronal excitability via the inhibition of adenylyl cyclase and voltage-gated Ca^{2+} channels as well as the opening of G protein-coupled inward-rectifying potassium channels (Mannoury la Cour et al., 2008). $GABA_A$ receptors are heteropentameric chloride channels assembled by various combinations of 19 subunits (Sigel and Steinmann, 2012). Different subunit compositions determine their electrophysiological properties, cell surface distribution, and pharmacological response (Farrant and Nusser, 2005). The δ subunit is one of the most relevant subunits that mediate a slow constant inhibitory current called tonic inhibition and is expressed in most brain regions (Arslan, 2021; Sun et al., 2022). The human transcriptomic dataset from the Allen Brain Institute indicates that the expression of the δ subunit of $GABA_AR$ (*Gabrd*) in PV interneurons is higher than that in other interneurons, such as SST and vasoactive intestinal polypeptide interneurons (Field et al., 2021). Thus, tonic inhibition can differentially modulate the excitability of neuron subtypes (Glykys et al., 2008; Lee and Maguire, 2014; Bryson et al., 2020).

Gene expression dictates cellular functions. Recent advances in cell type-specific gene profiling techniques have yielded valuable insights into the physiological functions of a cell type. Conventionally, microfluidic or magnetic bead-based cell sorting is used to isolate the defined cell type from dissociated tissues (Haimon et al., 2018). Owing to the morphological complexity and relatively low abundance of GABAergic inhibitory interneurons, these standard cell dissociation and isolation protocols may not be as effective in capturing the mRNA of inhibitory interneurons. Moreover, extensive cell isolation procedures can damage mature neurons and potentially modify gene expression. Cell type-specific ribosome tagging (RiboTag) followed by RNA sequencing (RNA-seq) provides an alternative method to analyze the transcriptome of sparse cells in mouse brains without disruptive cell isolation.

Previous studies have applied RiboTag to cortical inhibitory interneurons (Mardinly et al., 2016; Huntley et al., 2020). This study aimed to understand the functional differences between PV and SST cells in the mouse hippocampus. To achieve this, we employed the RiboTag method to isolate cell type-specific mRNA transcripts *in vivo*. Subsequently, RNA sequencing was performed to compare the differentially expressed genes between PV and SST interneurons in the hippocampus. To validate the significance of these findings, potential genes and pathways of interest were confirmed through additional techniques such as real-time quantitative polymerase chain reaction (RT-qPCR), immunofluorescence staining, and electrophysiology. Our findings indicate that the upregulation of *Gabrd* and *Gabra6* potentially contributes to the contrasting tonic GABAergic inhibition observed between PV and SST interneurons. Moreover, some differentially expressed genes identified in our analysis have been linked to conditions such as schizophrenia and epilepsy.

2. Materials and methods

2.1. Animals

For cell-type specific expression of HA-tagged ribosomes in PV or SST interneurons, the RiboTag mice (B6N.129-*Rpl22*$^{tm1.1Psam}$/J, JAX® Strain # 011029) were crossed with either PV-Cre driver mice (B6;129P2-*Pvalb*$^{tm1(cre)Arbr}$/J, JAX® Strain # 008069) or SST-Cre driver mice (B6N.Cg-*Sst*$^{tm2.1(cre)Zjh}$/J, JAX® Strain # 13044) (Figure 1A). The RiboTag mouse line carries an Rpl22 allele fused to Cre-induced hemagglutinin (HA) (RPL22^{HA}) that facilitates the isolation of ribosome-bound mRNA specifically from Cre + cells by immunoprecipitation (Sanz et al., 2009). For electrophysiology recording, the Ai14 reporter mice [B6.Cg-Gt(ROSA)26Sor$^{tm14(CAG-tdTomato)Hze}$/J, JAX® Strain # 007914] were crossed with either PV-Cre or SST-Cre driver mice. Mice were housed in groups of 2–5 in a standard cage under a 12-h light-dark cycle at 25°C and 60% humidity and provided food and water *ad libitum*. The detailed information for mice used in each experiment is listed in Supplementary Table 3. This study was approved by the Institutional Animal Care and Use Committee (IACUC) of the National Yang Ming Chiao Tung University. This study followed all applicable international, national, and institutional guidelines for the care and use of animals.

2.2. Genotyping

A 2-mm mouse tail was cut and incubated with 50 μl 1X DNA isolation buffer (25 mM NaOH and 0.2 mM EDTA) at 98°C for 1 h. The lysate was neutralized with 50 μl 40 mM Tris-HCl (pH 5.5) and spun down. Then, 1 μl of the supernatant was taken as the DNA template for PCR amplification by using a PCR dye master mix (ADPMX02D-100; Arrowtech, USA or SA-PB10.44-05; PCR Biosystems, USA) according to the manufacturer's instructions. The PV-Cre allele was amplified with the forward primer 5′-CAGAGCAGGCATGGTGACTA-3′ and reverse primer

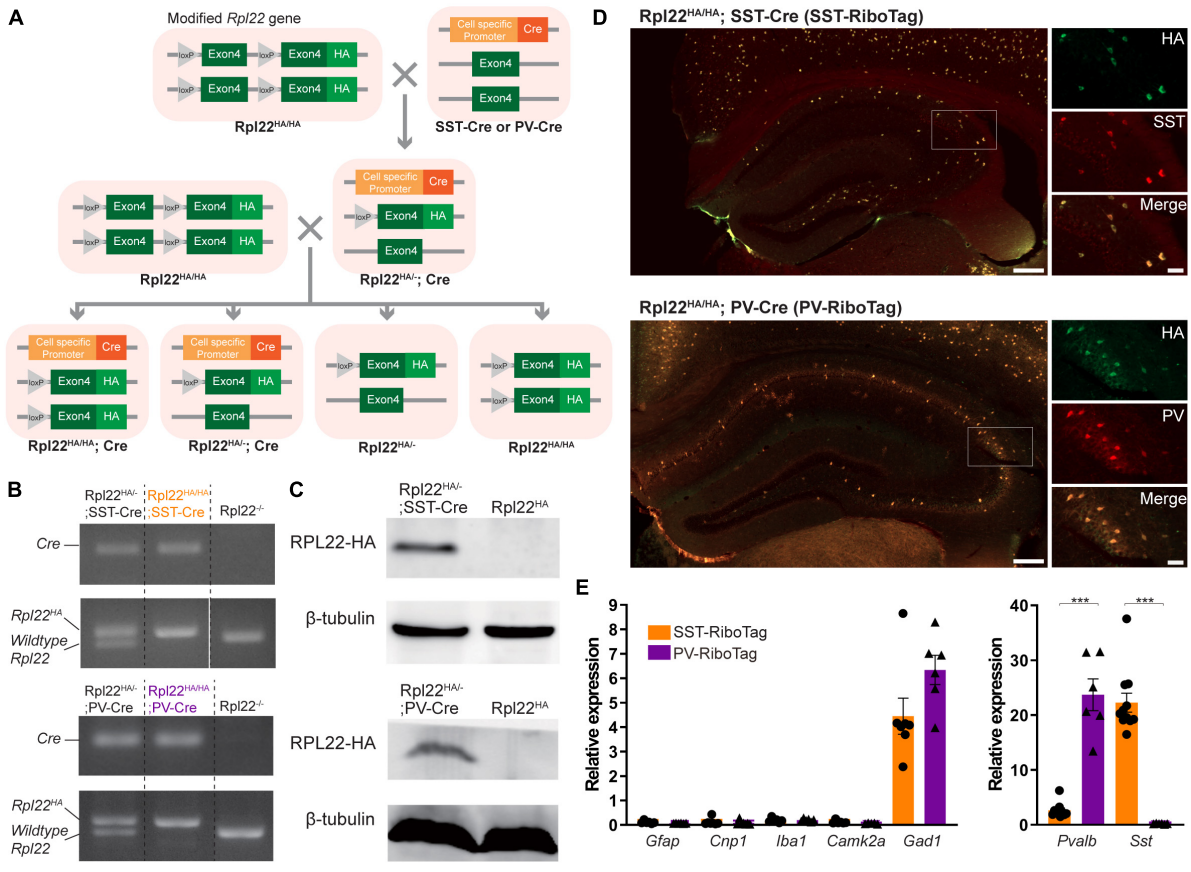

FIGURE 1
Cell type-specific expressions of Rpl22-HA (RiboTag) in hippocampal SST and PV neurons. **(A)** The breeding strategy for generating Rpl22$^{HA/HA}$; PV-Cre (PV-RiboTag) or Rpl22$^{HA/HA}$; SST-Cre (SST-RiboTag) mice. **(B)** Representative PCR genotyping images with primers recognizing Cre and Rpl22 alleles. **(C)** Immunoblotting using HA antibody indicating Rpl22-HA expression in the hippocampus of PV-RiboTag or SST-RiboTag mice. **(D)** Representative immunofluorescence images demonstrate that HA-expressing cells (green) are colocalized with either SST or PV cells (red). The scale bars represent 200 (left) μm and 50 (right) μm. **(E)** RT-qPCR measurement of mRNA levels of markers for astrocyte (*Gfap*) (SST-RiboTag, n = 6; Rpl22^{HA}; PV-RiboTag, n = 6), oligodendrocytes (*Cnp1*) (SST-RiboTag, n = 7; PV-RiboTag, n = 7), microglia (*Iba1*) (SST-RiboTag, n = 6; PV-RiboTag, n = 6), pyramidal neuron (*Camk2a*) (SST-RiboTag, n = 6; PV-RiboTag, n = 5), GABAergic inhibitory interneuron (*Gad1*) (SST-RiboTag, n = 7; PV-RiboTag, n = 6), PV cell (*Pvalb*) (SST-RiboTag, n = 7; PV-RiboTag, n = 6), and SST cell (*Sst*) (SST-RiboTag, n = 11; PV-RiboTag, n = 6) in ribosome-bound mRNA isolated from PV-RiboTag (purple) and SST-RiboTag mice (orange). Data are presented as the mean ± SEM and analyzed using the Mann–Whitney test. ***p < 0.001. The detailed mice age, gender and the statistical analysis results were listed in Supplementary Table 3.

5′-AGTACCAAGCAGGCAGGAGA-3′. The SST-Cre allele was amplified with the forward primer 5′-TGGTTTGTCCAAACTC ATCAA-3′ and reverse primer 5′-GGGCCAGGAGTTAAGG AAGA-3′. The Rpl22^{HA} allele was amplified with the forward primer 5′-GGGAGGCTTGCTGGATATG-3′ and the reverse primer 5′-TTTCCAGACACAGGCTAAGTACAC-3′. PCR was performed under the touchdown cycling protocol suggested by the Jackson Laboratory. All PCR products were analyzed by electrophoresis on 3% agarose gel. The size of the PCR product was 100 bp for the PV-Cre allele, 200 bp for the SST-Cre allele, 260 bp for the wild-type Rpl22 allele, and 290 bp for the Rpl22^{HA} allele.

2.3. HA-tagged ribosome immunoprecipitation and RNA extraction

Mice were executed by cervical dislocation without euthanasia. The hippocampi from either Rpl22^{HA};PV-Cre (PV-RiboTag) or Rpl22^{HA};SST-Cre (SST-RiboTag) mice were dissected and homogenized in 500 μl polysome buffer (50 mM Tris-HCl, pH 7.4, 12 mM $MgCl_2$, 100 mM KCl, 1 mM DTT, 1% NP40, 200 U/ml ribonuclease inhibitor, 0.5 mg/ml heparin, 100 μg/ml cycloheximide, and 10 μl/ml Protease inhibitor cocktail) using a bead-based tissue homogenizer (Bullet Blender®; Next Advance, Inc.). The lysate was centrifuged at 4°C at 16,000 × *g* for 10 min, and 30 μl of supernatant was collected as an input for validation. The remaining supernatant was incubated with the anti-HA antibody at 4°C for 4 h with rotary agitation. Pre-washed protein G beads were added to the antibody homogenate and incubated overnight at 4°C with rotary agitation. After 12 h, the samples were washed three times with high-salt buffer (50 mM Tris-HCl, pH 7.4, 12 mM $MgCl_2$, 300 mM KCl, 1 mM DTT, 1% NP40, 100 U/ml Ribonuclease inhibitor, 100 μg/ml cycloheximide, 5 μl/ml protease inhibitor cocktail). Lysis buffer (Qiagen RLT buffer containing 2-Mercaptoethanol) was added to the beads and input samples. Total RNA was purified using the Qiagen RNeasy Micro kit (Cat. No. 74004; Qiagen) according to the manufacturer's instructions and quantified with a Qubit fluorometer. Information for all chemicals and antibodies is listed in **Supplementary Tables 1, 2**.

2.4. Immunoblotting

The immunoprecipitation (IP) and input samples were incubated with SDS sample buffer (87.5 mM Tris-HCl, 1% SDS, 30% glycerol, 0.6 M DTT, and 180 μM bromophenol blue, pH 6.8) at 95°C for 10 min. Proteins were separated by 15% Tris-glycine SDS-polyacrylamide gel electrophoresis and transferred to nitrocellulose membranes. After blocking in casein blocking buffer, the membranes were probed with rabbit anti-HA (1:1000; ab9110; Abcam) and mouse anti-beta tubulin (1:2000; ab7751; Abcam) antibodies. The membranes were washed in Tris-buffered saline Tween and probed with horseradish peroxidase-conjugated anti-mouse IgG (1:1000; Jackson ImmunoResearch) and anti-rabbit IgG Trueblot® (1:1000; Rockland). Proteins signals were developed by using a chemiluminescent substrate ECL detection system (Millipore) and imaged with a luminescence camera system (LAS4000; Fujifilm). Information for all chemicals and antibodies is listed in **Supplementary Tables 1, 2**.

2.5. Immunofluorescence staining

Somatostatin-RiboTag mice and PV-RiboTag mice were euthanized by intraperitoneal administration of urethane (1,500 mg/kg), followed by perfusion with normal saline and 4% paraformaldehyde through the myocardial vascular system. The brains were fixed in 4% paraformaldehyde/PBS for 20 h and then embedded with 30% sucrose overnight. The embedded brains were frozen in an optimal cutting temperature medium (Tissue-Tek® O.C.T. Compound, 4583, SAKURA) and sliced coronally at a 30-μm thickness in −20°C Cryostat (Thermo Cryostar NX70). The brain slices were washed three times with 1X PBS, permeabilized in 0.5% Triton X-100/PBS, and blocked with 10% blocking buffer (0.1% Triton X-100, 10% fetal bovine serum, 3% bovine serum albumin, and 0.1% sodium azide in PBS). The slices were then incubated with primary antibodies against HA (1:1000; GTX115044; GeneTex or 1:200; MMS-101R; Biolegend), GABRD (1:200; PA5-77408; Invitrogen), GABRA6 (1:200; NB300-196; Novus) SST (1:100; MAB354; Millipore), and PV (1:1000; MAB1572; Millipore) overnight at 4°C; washed three times with 1X PBS. Afterward, they were washed three times with 1X PBS, followed by a 2-h incubation at room temperature with the respective secondary antibodies: anti-rabbit Alexa 488 (1:500), anti-rabbit Alexa 594 (1:500), anti-mouse Alexa 488 (1:500), anti-mouse Alexa 594 (1:500) and anti-rat Alexa 594 (1:1000). Finally, the slices were mounted using VECTASHIELD® mounting medium (Vector Laboratories). Images were captured by fluorescence microscopy (Olympus BX63 and Zeiss Apotome.2); 120 HA-positive cells in the hippocampus were enrolled in 1 mouse sample, and the average integration ratio of GABRD or GABRA6 overlap HA signals were quantified by MetaMorph Premier analysis software. Information for chemicals and antibodies is listed in **Supplementary Tables 1, 2**.

2.6. RT-qPCR

The purified RNA was generated into cDNA using an oligo-dT primer and SuperScript II reverse transcriptase (ERT12925K; Lucigen). The level of specific mRNA was analyzed using specific primer pairs (listed in **Supplementary Table 4**). Samples were mixed with 2X qPCRBIO SyGreen Blue Mix HI-ROX (PB20.16-01, PCR Biosystems) and analyzed on the StepOnePlus real-time PCR system. Quantitative polymerase chain reaction (qPCR) was carried out under the following conditions: an initial denaturation step at 95°C for 3 min, 40 cycles of denaturation at 95°C for 30 s, and annealing/extension at 60°C for 30 s. The *Gapdh* gene was used as an internal control. Normalized mRNA levels were quantified using the $2^{--\Delta\Delta Ct}$ method.

2.7. RNA sequencing

The purified RNA samples were treated with DNase I to remove DNA contamination before subjecting for library preparation. The RNA quality was tested using the Agilent 2100 Bioanalyzer (Agilent Technologies, Inc., Santa Clara, CA, USA). Samples with an RNA integrity number (RIN) greater than 6.6 were subjected

to RNA sequencing library preparation. For samples with total RNA < 10 ng, the RNA sequencing libraries were prepared using the Switching Mechanism At the 5′ end of RNA Template (SMART)-Seq Stranded Kit (Takara Bio USA, Inc., San Jose, CA, USA), which incorporated SMART cDNA synthesis technology and preserved the strand orientation of the original RNA. For samples with total RNA > 100 ng, the RNA sequencing libraries were prepared using Illumina TruSeq Stranded mRNA Sample Preparation Kit (Illumina Inc., USA) which produced directional RNA-seq libraries. The RNA libraries were quantified by qPCR, and the quality was assessed with the 2100 Bioanalyzer HS DNA Kit. The RNA libraries were sequenced on a NextSeq550 (Illumina, Inc., San Diego, CA, USA) by paired-end sequencing with a 75-bp read length to a minimum depth of 30–70 million reads. The low quality of bases (<Q20), the first 12 bases, and adapters were trimmed from the dataset. The reads were mapped to Genome Reference Consortium Mouse Build 38 (GRCm38/mm10) and run RNA-seq analysis by CLC Genomics Workbench (QIAGEN, Germany). Expression levels were measured in transcripts per million (TPM), and the expression level for a gene was calculated as the sum of the TPM values of its isoforms.

2.8. Differential expression analysis

Differential gene expression was analyzed using DESeq2 v1.32.0 (Love et al., 2014). Genes with low counts (sum < 10 in each sample) were filtered out. The design formula was to compare the difference in gene expression between two cell types while controlling for batch effect. The cutoff for differentially expressed genes (DEGs) was |log2foldchange| > 1 and an adjusted $P < 0.05$ (Benjamini-Hochberg method). Results were visualized with a volcano plot generated using the EnhancedVolcano v1.10.0[1] and Pretty Heatmap (pheatmap v1.0.12).

2.9. Functional enrichment analysis

Differentially expressed genes were subjected to functional enrichment characterization with the biological process (BP) of Gene Ontology (GO) (Release 2021-09-01) and pathways in the Kyoto Encyclopedia of Genes and Genomes (KEGG) (Release 100.0) using clusterProfiler v4.0.5 (Wu et al., 2021). Over-representation tests were used to identify significant GO terms and KEGG pathways, and the significance threshold was set at a *P*-value of <0.05. Results were visualized with treeplots using the Enrichplot v1.12.3. The Ward.D method was used to cluster enriched terms. A set of succinct representative words were manually assigned for each cluster.

2.10. Disease gene sets

Enriched schizophrenia and epilepsy-related gene sets were extracted from the web server "Enrichr" (Chen et al., 2013; Kuleshov et al., 2016) using DEGs as input (results downloaded on Oct 6, 2021). Only overlapping DEGs were shown on the heatmap.

2.11. Virus and stereotaxic surgery

To specifically label PV neurons in the dentate gyrus (DG), we injected AAV5-hSyn-DIO-mCherry or AAV1-hDlx-DIO-tdtomato virus into PV-Cre mice. In the stereotaxic surgery, mice were deeply anesthetized with isoflurane (4% induction, 1.5–2% maintenance in O_2; Halocarbon Laboratories, North Augusta, SC, USA) and placed in a stereotaxic injection frame (IVM-3000; Scientifica, Uckfield, UK). During all surgical procedures, mice were kept on a heating pad (Physiological Biological Temperature Controller TMP-5b, Supertech Instruments, Budapest, Hungary) to maintain their surface body temperatures at 34°C. After securing the head with ear bars, 75% ethanol was used to sterilize the surgical area, and the eyes were protected using an ophthalmic gel. The injections were performed using the following stereotaxic coordinates: 3.5 mm posterior from bregma, 2.8 mm lateral from the midline on both sides, 3 and 3.2 mm ventral from the cortical surface. For viral injections, we bilaterally injected 0.3 μL of the viral solution into each location, using a 10-μL NanoFil syringe and a 34-G beveled metal needle (World Precision Instruments, Sarasota, FL, USA). The flow rate (0.1 μL/min) was controlled with a nanopump controller (KD Scientific, Holliston, MA, USA). After viral injection, the needle was raised 0.1 mm above the injection site for an additional 10 min to allow the virus to diffuse before being withdrawn slowly. After withdrawing the needle, the incision was closed by suturing, and the mice were returned to their home cage for recovery.

2.12. Brain slice preparation for electrophysiology

Transverse acute brain slices (300-μm thick) containing the hippocampus were cut from SST-Cre; Ai14, PV-Cre; Ai14 mice using a vibratome (DTK-1000; Dosaka, Kyoto, Japan). The mice were anesthetized using isoflurane and rapidly decapitated. The brains were quickly removed and transferred to an ice-cold oxygenated (95% O_2 and 5% CO_2) sucrose cutting solution containing (in mM): 87 NaCl, 25 $NaHCO_3$, 1.25 $NaH2PO_4$, 2.5 KCl, 10 glucose, 75 sucrose, 0.5 $CaCl_2$, and 7 $MgCl_2$. After sectioning, the slices were recovered at 34°C for 30 min in a holding chamber filled with an oxygenated sucrose solution and then transferred to room temperature (22–24°C) for further experiments.

2.13. Patch clamp recording

For the whole-cell recordings, individual slices were transferred to a submerged chamber and were continuously perfused with oxygenated artificial cerebrospinal fluid (ACSF) containing the following (in mM): 125 NaCl, 25 $NaHCO_3$, 1.25 NaH_2PO_4, 2.5 KCl, 25 glucose, 2 $CaCl_2$, and 1 $MgCl_2$. The tdTomato or mCherry expressing cells in the DG were visualized in the brain slices using epifluorescence. Then, the cells were

1 https://github.com/kevinblighe/EnhancedVolcano

recorded under an infrared differential interference contrast or infrared Dodt gradient contrast microscope (IR-DIC or IR-DGC, BX51WI, Olympus) equipped with an LED source (590 nm, LED4D162, controlled by DC4104 driver, Thorlabs, NJ, USA). Whole-cell patch-clamp recordings were performed at 22–24°C using Axopatch 200B amplifier or Multiclamp 700B amplifier (Molecular Devices, Sunnyvale, CA, USA). The recording electrode pipettes (2–7 MΩ) pulled from borosilicate glass tubing (outer diameter, 1.5 mm; inner diameter, 0.86 mm; Harvard Apparatus) were filled with a high-Cl^- internal solution containing the following (in mM): 15 K-gluconate, 140 KCl, 0.1 EGTA, 2 $MgCl_2$, 4 Na_2ATP, 10 HEPES, 0.5 Na_3GTP, and 0.4% biocytin (w/v, Life Technologies, Grand Island, NY, USA). $GABA_AR$-mediated currents were blocked with the GABA type A receptor ($GABA_AR$) antagonist SR95531 (10 μM), while δ-$GABA_AR$-mediated currents were induced with the δ-GABA type A receptor (δ-$GABA_AR$) agonist THIP (10 μM, MedChemExpress). Phasic and tonic GABA currents were recorded using a high Cl^- internal solution at a holding potential of −70 mV in voltage-clamp in the presence of kynurenic acid (Kyn, 2 mM), a blocker for ionotropic glutamatergic receptors.

Data were analyzed using Clampfit 10.3 (Molecular Devices, CA, USA). The amplitude of tonic inhibition was analyzed as the difference between the holding currents measured before and after the application of either the $GABA_AR$ antagonist SR95531 (10 μM) or the δ-$GABA_AR$ agonist THIP (10 μM). The holding current was calculated from average values of the 5-s epoch, without obvious spontaneous synaptic events, taken in three different segments before and after bath application of either 10 μM SR95531 or 10 μM THIP as previously described (Song et al., 2011; Gupta et al., 2012). Briefly, the magnitude of tonic GABA current was calculated by plotting all-point histograms of relevant 5-s segments of data. These data were fit to Gaussian equations, constraining fits to values two bins more negative than the peak. This ensured that the tail of higher-amplitude values representing spontaneous inhibitory postsynaptic currents (sIPSCs) did not influence the fit (Santhakumar et al., 2006, 2010). The peak value was designated as the average value of the holding currents. The current density was calculated by dividing the tonic GABA current by cell capacitance. The input resistance was measured by the ratio of a steady-state voltage response (last 100 ms of a 1-s pulse) versus a 10 pA hyperpolarizing current pulse injected (Liu et al., 2014; Ajibola et al., 2021). The signals were recorded using Multiclamp 700B amplifiers (Molecular Devices); filtered at 4 kHz; and sampled at 10 kHz using a digitizer (Digidata 1440A, Molecular Devices), which was controlled using the pCLAMP version_10.3 (Molecular Devices).

2.14. Statistical analysis

The differences in qPCR and immunofluorescence staining experiments between SST-RiboTag and PV-RiboTag mice were presented as the mean ± SEM and analyzed using the Mann-Whitney test. The detailed statistical results were listed in **Supplementary Table 3**. For RNA-seq analysis, DESeq2 (v1.32.0) was used with SST-RiboTag $n = 5$ and PV-RiboTag $n = 7$. Raw read counts were normalized with library size. Normalized counts were compared pairwise between groups and analyzed by Wald test. B-H adjusted p-value and log2 fold change were used to determine DEGs. Please see **Supplementary Tables 5–9** for the Bioinformatic analysis statistics.

3. Results

3.1. Ribosome tagging isolates mRNA from PV and SST interneurons

Parvalbumin and SST interneurons are physiologically and anatomically distinct populations. To compare their differences at the molecular level, we employed the RiboTag approach to determine the transcriptome of PV and SST interneurons in the mouse hippocampus. The RiboTag mice were crossed with either PV-Cre or SST-Cre mice to drive the cell-type specific expression of HA-tagged ribosomes in either PV or SST interneurons (**Figure 1A**). The genotypes of $Rpl22^{HA/HA}$; SST-Cre and $Rpl22^{HA/HA}$; PV-Cre mice as determined by PCR are shown in **Figure 1B**. In the hippocampus, RPL22-HA protein was expressed only in the presence of Cre, as indicated by immunoblotting results (**Figure 1C**). The cell type-specific expression of HA-tagged ribosomes was confirmed by double immunoreactivities against HA with either PV or SST. All mice used in this study were $Rpl22^{HA/HA}$ and indicated as SST-RiboTag and PV-RiboTag in the following text.

Hemagglutinin tag was only presented in either PV or SST interneurons in the hippocampus of SST-RiboTag or PV-RiboTag mice, respectively (**Figure 1D**). To check the enrichment of mRNAs from PV or SST interneurons, HA-tagged ribosomes were immunoprecipitated with an anti-HA antibody, and the ribosome-bound mRNAs were purified. Ribosome-bound mRNAs from both genotypes contained markers for GABAergic inhibitory interneurons (*Gad1*), and not all types of glia cells (*Gfap*, *Cnp1*, *Iba1*) and pyramidal neurons (*Camk2a*) (**Figure 1E**). *Sst* or *Pvalb* are the markers for these two types of interneurons. In ribosome-bound RNAs, *Sst* and *Pvalb* were highly enriched in SST- and PV-RiboTag mice, respectively (**Figure 1E**). These results indicated the specificity of the RiboTag approach to isolate mRNA from PV or SST inhibitory interneurons.

3.2. Voltage-gated ion channels are differentially expressed between PV and SST interneurons

To profile cell type-specific gene expression, we purified the total mRNA (input) and immunoprecipitated HA-tagged ribosome-bound mRNA (IP) from SST-RiboTag or PV-RiboTag mice (**Figure 2A**). The RIN of samples used for RNA-seq ranged from 6.6 to 9.0 (**Figure 2B**). The principal component analysis (PCA) plot of mRNA profiles revealed three clusters from SST-RiboTag IP samples (orange ▲), PV-RiboTag IP samples (purple ▲), and input samples from both genotypes (○). The inputs from SST-RiboTag mice were undisguisable from those from PV-RiboTag mice (**Figure 2C**). Although mRNA from SST and PV

10.3389/fncel.2023.1146278

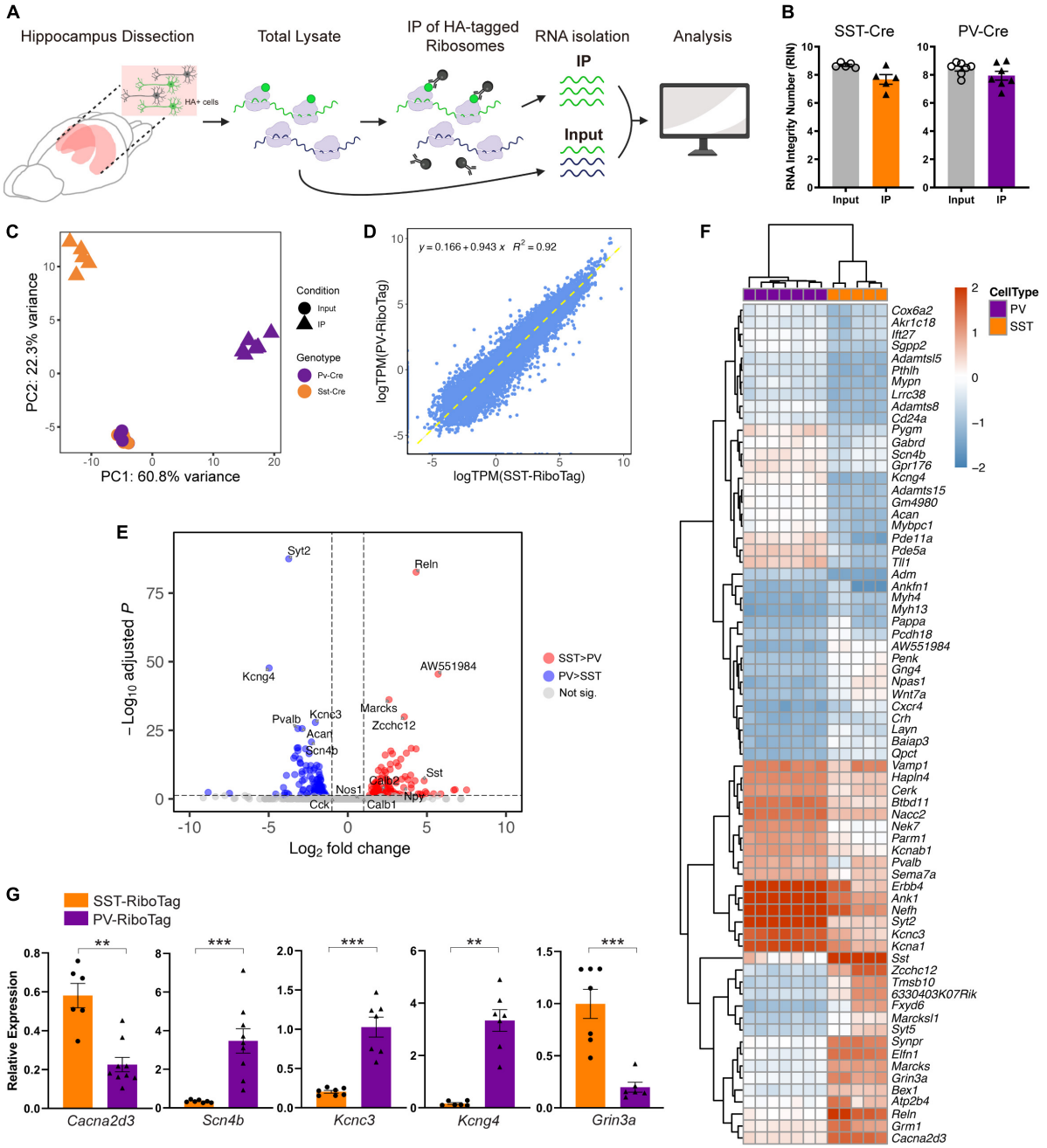

FIGURE 2
Differential gene expression profiles of PV and SST interneurons. **(A)** Workflow for the isolation of total RNA and cell type-specific RNA in the hippocampus. **(B)** RNA integrity number (RIN) of input and IP samples of PV-RiboTag (purple) and SST-RiboTag mice (orange). **(C)** Principal component analysis of 10 SST-Cre samples (5 IP-input pairs) and 14 PV-Cre samples (7 IP-input pairs). **(D)** Correlation between expression (TPM) of SST-IP and of PV-IP. **(E)** The volcano plot shows DEGs between SST and PV interneurons. Red dots indicate genes with significantly higher expression in SST interneurons than in PV interneurons. Blue dots represent genes with significantly higher expression in PV interneurons than in SST interneurons. Top DEGs (adjusted $P < 10^{-20}$) and known markers for SST or PV interneurons are labeled. **(F)** Heatmap showing the top 70 DEGs between SST and PV interneurons ranked by adjusted *P*. **(G)** RT-qPCR quantification of mRNA expression of markers for selected DEGs: *Kcnc3* (SST-RiboTag, $n = 7$; PV-RiboTag, $n = 7$), *Kcng4* (SST-RiboTag, $n = 6$; PV-RiboTag, $n = 7$), *Cacna2d3* (SST-RiboTag, $n = 6$; PV-RiboTag, $n = 9$), *Scn4b* (SST-RiboTag, $n = 7$; PV-RiboTag, $n = 9$), *Grin3a* (SST-RiboTag, $n = 7$; PV-RiboTag, $n = 6$) in IP samples of PV-RiboTag (purple) and SST-RiboTag mice (orange). Data are presented as the mean ± SEM and analyzed using the Mann–Whitney test. ***$p < 0.001$, **$p < 0.01$. The detailed mice age, gender and the statistical analysis results were listed in **Supplementary Table 3**.

interneurons can be separated on the PCA plot, its expression correlation was high ($R^2 = 0.92$). A few points were distributed above or below the diagonal line, indicating that genes were expressed differentially between these two cell types (**Figure 2D**). In differential expression analysis, 106 DEGs were upregulated in SST interneurons, whereas 105 DEGs were upregulated in PV interneurons (|log2FoldChange| > 1; adjusted-*P* < 0.05) (**Supplementary Table 5**).

Among the upregulated genes in SST interneurons, *Reln* and *AW551984* showed the most significant differential expression. For genes that were upregulated in PV interneurons, *Syt2*, a marker for a subgroup of PV-expressing basket cells in the mouse hippocampus (Garcia-Junco-Clemente et al., 2010), reached the most significant expression level (**Figure 2E**). The top 70 most significant DEGs between SST and PV interneurons are highlighted in **Figure 2F**. SST interneurons were enriched with genes encoding auxiliary subunits of voltage-gated calcium channels (VGCCs), including *Cacna2d3*, *Cacng4*, and *Cacng5*. In contrast, the voltage-gated sodium channel gene *Scn4b* and a set of voltage-gated potassium channel genes (*Kcng4*, *Kcnab1*, *Kcnc3*, and *Kcna1*) were preferentially expressed in PV interneurons. An independent group of mice was used for RT-qPCR to confirm the RNA-Seq results. Genes that encode voltage-gated ion channels (*Cacna2d3*, *Scn4b*, *Kcnc3*, *Kcng4*, and *Grin3a*) all have significant differences between PV and SST interneurons (**Figure 2G**).

3.3. DEGs between PV and SST interneurons are enriched in synaptic transmission functions

To gain insight into the biological processes involved in SST and PV interneurons, we performed GO enrichment analyses for the DEGs. Genes with significantly higher expression in SST interneurons were enriched in GO categories of synaptic transmission, both glutamatergic and GABAergic. In addition, several clusters of genes related to amine-, cocaine-, behavior-, and G-protein-coupled receptor-related processes were also upregulated in SST interneurons (**Figure 3A**; **Supplementary Table 6**). Meanwhile, genes with significantly higher expression in PV interneurons were enriched in GO categories associated with potassium ion transport, transporter activity, and neurotransmitter release (**Figure 3B**; **Supplementary Table 7**). KEGG pathway enrichment analysis showed that the DEGs between SST and PV interneurons, regardless of direction, were enriched in neuroactive ligand-receptor interaction, drug addiction, GABAergic synapse, and several cardio-related pathways (**Figure 3C**; **Supplementary Table 8**).

3.4. $GABA_A$ receptor genes are differentially expressed between PV and SST interneurons

Synaptic dynamics are different between PV interneuron-principal neuron and SST interneuron-principal neuron connections (Klausberger and Somogyi, 2008; Kepecs and Fishell, 2014; Liu et al., 2014). Compared to interneuron-principal synapses, less is known about interneuron-interneuron synapses. Here, we further depicted the differential expression of the GABAergic synapse pathway in SST and PV interneurons in the KEGG (**Figure 4A**). Notably, $GABA_A$-, $GABA_B$-, and $GABA_C$-receptors encoding genes that showed higher expression in PV interneurons outnumbered those in SST interneurons. In contrast, the genes expression for VGCCs were greater in SST interneurons than in PV interneurons. A heatmap for gene expression of GABA receptor subunits in SST and PV interneurons is shown in **Figure 4B**. Among these subunits, *Gabrd* and *Gabra6* both encoded $GABA_A$ receptor subunits. RNA-seq data showed that the mRNA levels of both *Gabrd* and *Gabra6* were significantly higher in PV interneurons than in SST interneurons (**Figure 4C**). Increases in these two mRNAs were confirmed in the RT-qPCR analysis from the independent group of animals (**Figure 4D**).

3.5. PV interneurons exhibit larger tonic inhibition than do SST interneurons

To confirm that the protein levels of the $GABA_A$ receptor subunit GABRD and GABRA6 were higher in hippocampal PV interneurons, immunofluorescence co-staining against HA and GABRD was performed. The HA signal in green was used to represent the PV or SST interneurons in PV-RiboTag or SST-RiboTag mice, while the GABRD signal was depicted in red (**Figure 5A**). The average fluorescence intensity of GABRD in PV interneurons was significantly higher than that in SST interneurons (**Figure 5B**). Similarly, double staining GABRA6 (green) with HA (red) showed that GABRA6 is co-localized more with PV interneurons than with SST interneurons (**Figures 5C, D**). Taking the above results together, the relative GABRD and GABRA6 protein levels in PV or SST interneurons are consistent with mRNA findings using the RiboTag approach. The *Gabrd* gene encodes the δ-subunit of $GABA_A$ receptors associated with extrasynaptic activity, which mediates tonic inhibition in CA1 and CA3 pyramidal cells, DG granule cells, and molecular layer interneurons (Glykys et al., 2008). While GABRA6 is expressed predominantly in cerebellar granule cells, the function of GABRA6 in the hippocampus is currently unknown. Previous studies had demonstrated that the δ subunit partners principally with the α6 subunit, δ and α6 subunits co-assemble and are necessary for tonic inhibition (Santhakumar et al., 2006). Therefore, the differential expression of GABRD and GABRA6 might contribute to the difference in tonic inhibitory currents between hippocampal PV and SST interneurons.

To determine the tonic $GABA_A$R-mediated currents in these two types of interneurons, whole-cell recordings were made on SST and PV interneurons identified using SST-Cre; Ai14 and PV-Cre; Ai14 reporter mice, respectively (**Figures 5E, F**). The recordings were made in the presence of an ionotropic glutamate receptor blocker (2 mM Kyn). After recording inhibitory currents at the basal level, a $GABA_A$R antagonist (10 μM SR95531) was added to abolish the phasic $GABA_A$R-mediated sIPSCs and tonic (or sustained) $GABA_A$R-mediated currents. The degree of inhibition of tonic $GABA_A$R-mediated current was quantified by the shift of the baseline (**Figures 5E, F**, traces). Compared to the SST interneurons, the PV interneurons showed a prominent shift in the baseline current (**Figures 5E, F**, traces; SST: 68 ± 12.8 pA to 59 ± 10.4 pA; $n = 7$ cells; PV: 45 ± 9.0 pA to 22.5 ± 8.5 pA; $n = 7$ cells). Overall, the magnitude of tonic GABA currents recorded from the PV interneurons was significantly larger than that of SST interneurons (**Figure 5G**, PV interneurons, 22.5 ± 2.3 pA, $n = 7$ cells, 5 mice; SST interneurons, 9.1 ± 2.3 pA; $n = 7$ cells, 5 mice; Mann-Whitney test; $p = 0.0175$, $U = 6.0$). Moreover, the tonic current density was also significantly larger in PV interneurons (0.33 ± 0.04 pA/pF) than in

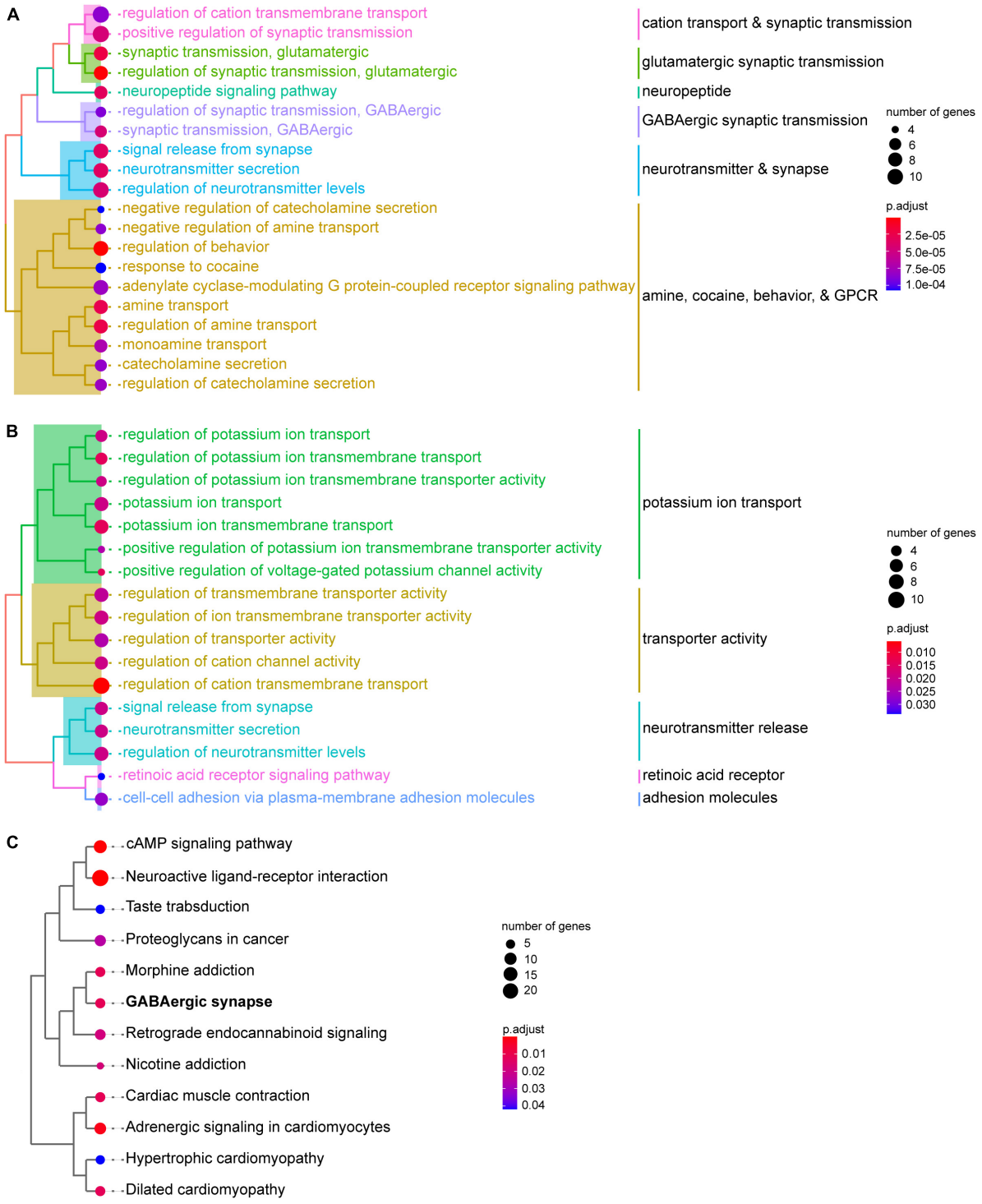

FIGURE 3
Functional enrichment analysis of PV and SST interneurons. **(A)** GO biological process enrichment shows the functions of genes with significantly higher expression in SST interneurons than in PV interneurons. **(B)** GO biological process enrichment shows functions of with significantly higher expression in PV interneurons than in SST interneurons. **(C)** KEGG pathway enrichment analysis of DEGs between SST and PV interneurons. GO terms or KEGG pathways are clustered using the ward.D method. The size of the circle represents the number of hit DEGs in each gene set. The color bar indicates the significance of enrichment.

SST interneurons (0.14 ± 0.05 pA/pF) (Figure 5H, Mann-Whitney test; $p = 0.0262$, $U = 7.0$).

To further compare the tonic δ-GABA$_A$R-mediated currents between SST and PV interneurons, whole-cell patch-clamp recordings were made on SST and PV interneurons (Figures 5I, J) in the presence of an ionotropic glutamate receptor blocker (2 mM; Kyn). After recording basal level inhibitory currents, a δ-GABA$_A$R agonist (10 μM; THIP) was applied to induce the

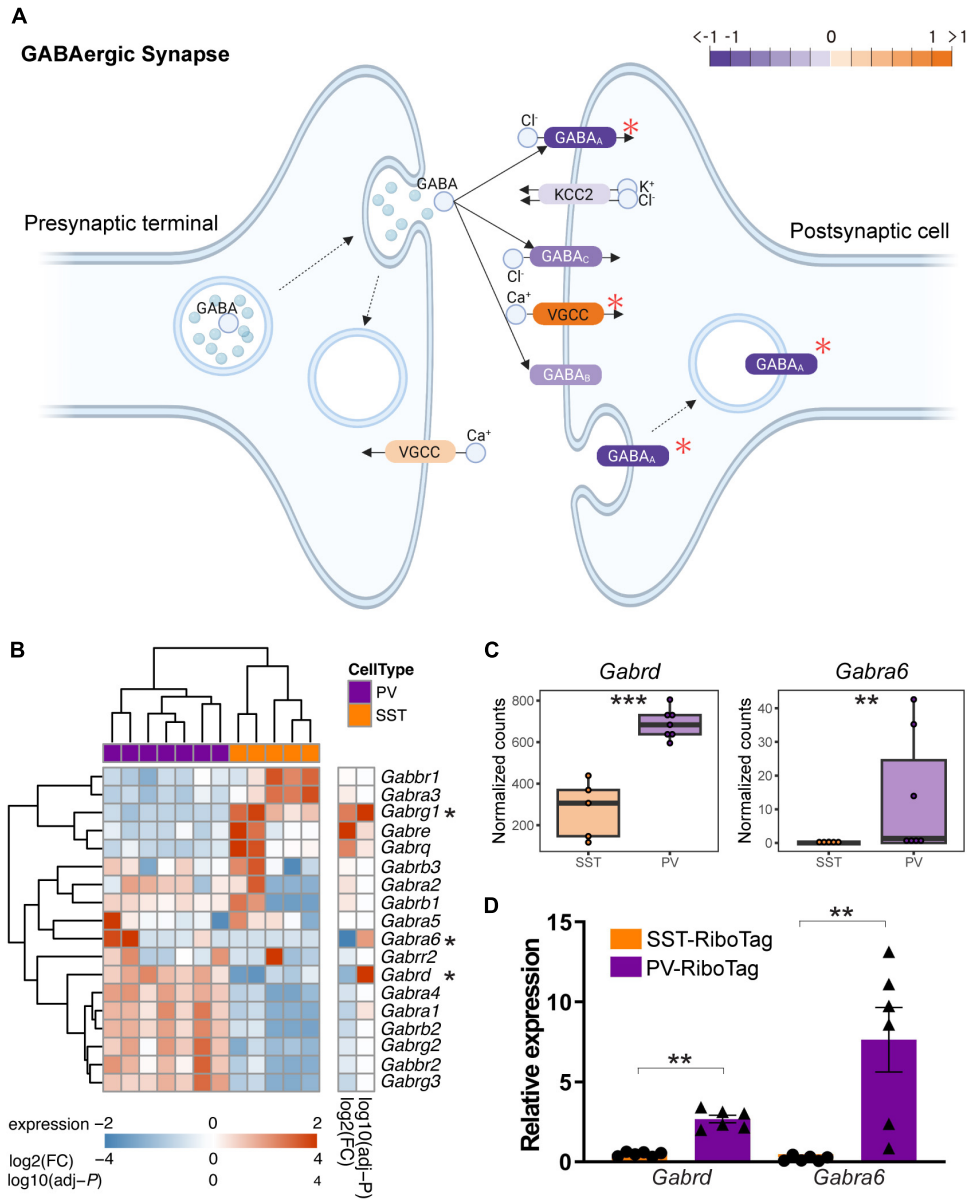

FIGURE 4
The difference in GABA receptor gene expression between PV and SST interneurons. **(A)** Modified KEGG Pathview showing the expression of SST and PV interneurons in the KEGG pathway "GABAergic synapse." The orange indicates higher expression in SST interneurons, and the purple indicates higher expression in PV interneurons. The red asterisk indicates the gene with significant differential expression between SST and PV interneurons. **(B)** Heatmap showing the expression of GABA receptor-encoding genes in SST and PV interneurons. The asterisk indicates significant differential expression between SST and PV interneurons. The color bar shows variance stabilizing transformed expression, log2(fold change), and log10(adjusted *P*). **(C)** Boxplot showing the expression (normalized counts) of *Gabrd* and *Gabra6* in SST and PV interneurons in RNA-seq data. ***adjusted $P < 0.001$, **adjusted $P < 0.01$ in differential expression analysis. **(D)** RT-qPCR quantification of mRNA expression of markers for *Gabrd* and *Gabra6* in independent IP samples of PV-RiboTag (purple, $n = 6$) and SST-RiboTag mice (orange, $n = 6$). Data are presented as the mean ± SEM and analyzed using the Mann–Whitney test. **$p < 0.01$.

δ-GABA$_A$R-mediated tonic inhibitory currents. The degree of enhancement of δ-GABA$_A$R-mediated tonic inhibitory current was quantified by the shift of the baseline (Figures 5I, J, traces). Compared to the SST interneurons, the PV interneurons showed a prominent shift in the baseline current (Figures 5I, J, traces; SST: −56.0 ± 6.4 pA to −99.1 ± 12.1 pA, $n = 8$ cells; PV: −12.2 ± 4.1 pA to −102.0 ± 12.1 pA, $n = 5$ cells). Overall, the magnitude of δ-GABA$_A$R-mediated tonic inhibitory currents recorded from the PV interneurons was significantly larger than that of SST interneurons (Figure 5K; SST: 43.1 ± 16.1 pA, $n = 8$ cells from 2 mice; PV: 89.7 ± 17.9 pA, $n = 5$ cells from 3 mice; Mann-Whitney test, $U = 6$, $p = 0.0451$). Moreover, the tonic inhibitory current density was also significantly larger in PV interneurons than in SST interneurons (Figure 5L, SST: 0.39 ± 0.14 pA/pF, $n = 8$ cells from 2 mice; PV: 0.92 ± 0.13 pA/pF $n = 5$ from 3 mice; Mann-Whitney test, $U = 6$, $p = 0.0451$). Collectively, the result demonstrated that PV interneurons exhibit larger δ-GABA$_A$R-mediated tonic inhibitory currents than SST interneurons in the hippocampal DG.

10.3389/fncel.2023.1146278

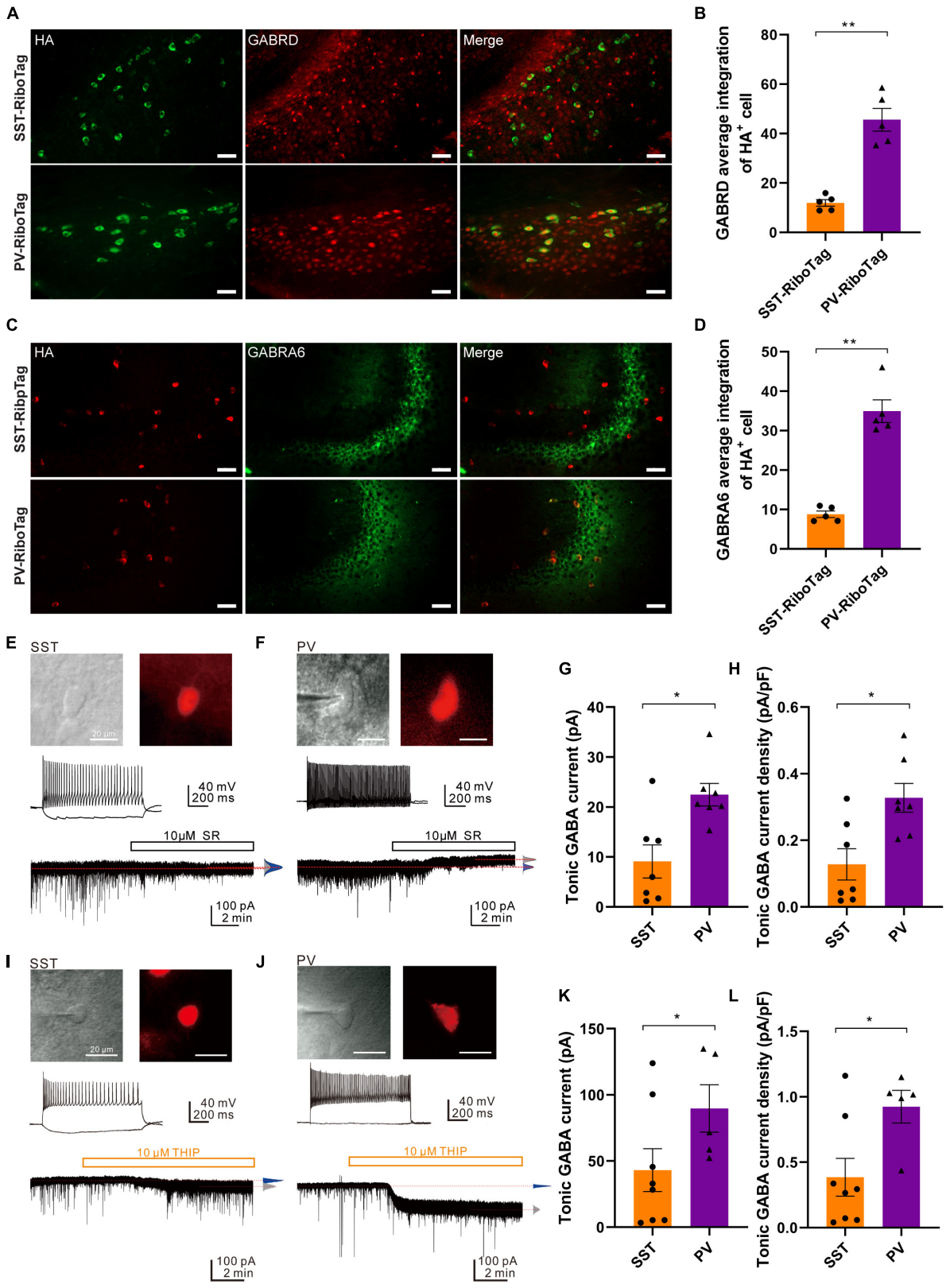

FIGURE 5

$GABA_AR$ subunits (GABRD and GABRA6) expression and tonic $GABA_AR$-mediated currents in the SST and PV interneurons. **(A)** The co-immunofluorescence staining results of HA (green, left panel) and GABRD (red, middle panel) expression and the overlay images (right panel) in the hippocampal DG from SST-RiboTag (upper panel) and PV-RiboTag (lower panel) mice. Scale bar, 50 μm. **(B)** Quantification of GABRD average integration within HA-positive cells in the hippocampus. n = 5 SST-RiboTag mice (3-month-old, 3 males, 2 females); n = 5 PV-RiboTag mice (3-month-old, 3 males, 2 females). $^{**}p < 0.01$. The GABRD-HA integration ratios were quantified and calculated by MetaMorph Premier analysis software; each dot in the graph represented the average results of 120 HA + cells from 1 mouse. Data are presented as the mean ± SEM and

(Continued)

FIGURE 5 (Continued)
analyzed by the Mann–Whitney test. **(C)** The co-immunofluorescence staining results of HA (red, left panel) and GABRA6 (green, middle panel) expression and the overlay images (right panel) in the hippocampus from SST-RiboTag (upper panel) and PV-RiboTag (lower panel) mice. Scale bar, 50 μm. **(D)** Quantification of GABRA6 average integration within HA-positive cells in the hippocampus. n = 5 SST-RiboTag mice (3-month-old, 3 males, 2 females); n = 5 PV-RiboTag mice (3-month-old, 3 males, 2 females). $^{**}p < 0.01$. The GABRA6-HA integration ratios were quantified and calculated by MetaMorph Premier analysis software; each dot in the graph represented the average results of 120 HA-positive cells from 1 mouse. Data are presented as the mean ± SEM and analyzed by the Mann–Whitney test. **(E)** IR-DIC and epifluorescence images showing an SST interneuron in the DG of an SST-Cre; Ai14 mouse brain. Scale bar, 20 μm. (top). The non-fast-spiking firing pattern of an SST interneuron (middle). Representative trace showing small tonic $GABA_A$R-mediated current in the same neuron (V_{hold} = −70 mV) blocked by 10 μM SR95531 in the presence of 2 mM Kyn (bottom). **(F)** IR-DIC and epifluorescence images showing a PV interneuron in the DG of a PV-Cre; Ai14 mouse brain. Scale bar, 20 μm (top). The typical fast-spiking firing pattern of the PV interneuron (middle). Representative trace showing tonic $GABA_A$R-mediated current in the neuron (V_{hold} = −70 mV) blocked by 10 μM SR95531 in the presence of 2 mM Kyn. Red dashed lines indicate Gaussian means (bottom). **(G)** Summary plot of the tonic GABA current obtained from SST- and PV-expressing interneurons in the DG. SST cells; n = 7 from 5 mice; PV cells, n = 7 from 5 mice; Mann–Whitney test, U = 6.0, p = 0.0175. Data are presented as the mean ± SEM. **(H)** Summary plot of the tonic current density (pA/pF) obtained from SST and PV interneurons in the DG. SST cells: n = 7 from 5 mice; PV cells: n = 7 from 5 mice. Mann-Whitney test, U = 7.0, $^{*}p$ = 0.0262. Data are presented as the mean ± SEM. **(I)** IR-DIC and epifluorescence images showing an SST interneuron in the DG of an SST-Cre; Ai14 mouse brain. Scale bar, 20 μm (top). The non-fast-spiking firing pattern of an SST interneuron (middle). Representative trace showing tonic δ-$GABA_A$R-mediated current in the SST cell (V_{hold} = −70 mV) induced by 10 μM THIP in the presence of 2 mM Kyn. Red dashed lines indicate Gaussian means (bottom). **(J)** IR-DIC and epifluorescence images showing a PV interneuron in the DG of a mCherry-expressing PV-Cre mouse brain. Scale bar, 20 μm (top). The typical fast-spiking firing pattern of the PV interneuron (middle). Representative trace showing tonic δ-$GABA_A$R-mediated current in the PV cell (V_{hold} = −70 mV) induced by 10 μM THIP in the presence of 2 mM Kyn. Red dashed lines indicate Gaussian means (bottom). **(K)** Summary plot of the tonic GABA current (pA) obtained from SST and PV interneurons in the DG (SST cells: 43.1 ± 16.1 pA, n = 8 cells from 2 mice; PV cells: 89.7 ± 17.9 pA, n = 5 cells from 3 mice; Mann–Whitney test, U = 6, $^{*}p$ = 0.0451). **(L)** Summary plot of the tonic current density (pA/pF) obtained from SST and PV interneurons in the DG (SST cells: 0.39 ± 0.14 pA/pF, n = 8 cells from 2 mice; PV cells: 0.92 ± 0.13 pA/pF n = 5 from 3 mice; Mann–Whitney test, U = 6, $^{*}p$ = 0.0451).

3.6. DEGs between PV and SST interneurons are associated with schizophrenia and epilepsy

Finally, going beyond their physiological functions, we delved into exploring potential disease-associated DEGs between PV and SST interneurons. Dysfunction of PV or SST interneurons has been implicated in the development of schizophrenia and temporal lobe epilepsy (Tallent and Qiu, 2008; Drexel et al., 2017). Our study revealed a strong association between the DEGs of PV and SST interneurons and pathways related to schizophrenia. Specifically, the analysis identified 29 DEGs between PV and SST interneurons that were involved in schizophrenia-related pathways (**Figure 6A**). In addition, 24 DEGs between PV and SST interneurons overlapped with epilepsy-related pathways (**Figure 6B**). There were 8 DEGs (*Ldoc1*, *Nefh*, *Parm1*, *Ptpro*, *Pvalb*, *Spp1*, *Synpr*, *Vamp1*) shared by the schizophrenia and epilepsy gene sets (**Figure 6C**), suggesting a common molecular basis between the two disorders.

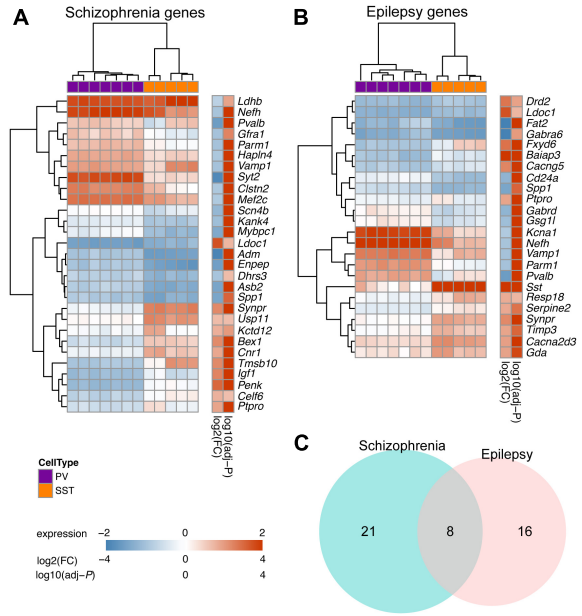

FIGURE 6
Overlapping DEGs between PV and SST interneurons with disease-related genes for schizophrenia and epilepsy. **(A)** Heatmap showing the top DEGs between SST and PV interneurons (adjusted-$P < 10^{-5}$ in Enrichr enrichment analysis) in schizophrenia-associated gene sets. **(B)** Top DEGs between SST and PV interneurons (adjusted-$P < 0.05$ in Enrichr enrichment analysis) in epilepsy-associated gene sets. For panels **(A,B)**, the Color bar shows variance stabilizing transformed expression, log2(fold change), and log10(adjusted P). **(C)** Venn diagram showing overlap of DEGs within schizophrenia-associated gene sets and epilepsy-associated gene sets.

4. Discussion

4.1. Main findings

The molecular mechanisms underlying the specialized properties of PV and SST interneurons are yet to be clarified to date. In this study, SST interneurons exhibited increased expression of various voltage-gated Ca^{2+} channels, whereas PV interneurons showed heightened expression of Na^{+} and K^{+} channels. In addition, both mRNA and protein levels of the $GABA_A$ receptor δ and α6 subunits were higher in the PV interneurons than in SST interneurons. These two subunits of the $GABA_A$ receptor are predominantly found extrasynaptically and contribute to tonic inhibition (Santhakumar et al., 2006; Tong et al., 2015), in agreement with the larger tonic currents recorded in PV interneurons than those in SST interneurons. Compared to gain control by phasic inhibition, tonic inhibition

of PV interneurons can offset their output in response to input (Mitchell and Silver, 2003). Finally, the transcriptomic analysis revealed numerous DEGs associated with schizophrenia and epilepsy, providing a foundation for future studies of these genes.

4.2. Comparison of RiboTag and other methods

Specific cell-type transcriptomics is primarily conducted using single-cell sequencing, which isolates mRNA from single cells using droplet microfluidic-based technology (Hwang et al., 2018) or the patch-seq approach (Lipovsek et al., 2021). The advantages of microfluidic technology are high throughput, small sample volume, and low cross-contamination (Brouzes et al., 2009; Hwang et al., 2018). However, isolating the cells from the physiological tissue context requires mechanical processing and enzymatic digestion, which increases the risk of artifacts and introduces a bias toward subpopulations (Halldorsson et al., 2015; Haimon et al., 2018). The sequencing data from cell types with complicated morphology and low abundance may be harder to be acquired. Patch-seq collects mRNA after electrophysiological recordings and morphological reconstruction of the same cells. The major advantage of this technique is that it enables the study of the transcriptome, anatomical position, electrical properties, and morphological structure of a single neuron. However, a main limitation is a very low throughput due to the requirement of interdisciplinary skills that take years to master (Lipovsek et al., 2021). Another limitation is the possibility of contamination because the pipette may pick up debris RNA from the extracellular space while reaching the target cell (Cadwell et al., 2017).

The RiboTag method allows us to robustly collect mRNA from specific subtypes of interneurons in tissue extracts. Compared with other approaches, the RiboTag method is more appropriate for simultaneously comparing transcriptomes of one specific cell type in multiple mice after behavioral tests or drug treatment. Furthermore, comparing the mRNA between whole tissue (input) and specific cell type (IP) from the same mouse provides baseline information on the experimental animal (Lesiak et al., 2015). However, one of the limitations of the RiboTag method is its inability to detect non-coding RNAs (ncRNAs), which do not bind to ribosomes. Two types of ncRNAs, micro RNAs, and long non-coding RNAs, have been implicated in regulating brain development, homeostasis, neurodegeneration, and plasticity. For example, the Evf-2 lncRNA is vital for GABAergic neuron development by regulating gene expression (Wei et al., 2018). Another limitation of the RiboTag method is the lack of information on the sub-population of interneurons. Interneurons expressing the same molecular marker may have different electrophysiological properties (Markram et al., 2015; Tremblay et al., 2016; Zeng and Sanes, 2017). Given that this approach collects all the mRNA from cell expression of the same Cre recombinase, information on the interneuron subtype cannot be acquired.

4.3. The comparison and limitation of this study

The PV and SST interneurons follow a similar developmental organization in the hippocampus and cortex (Yao et al., 2021). To determine the regional similarities or differences in gene expression in PV and SST interneurons, we compared the DEGs in our study to those identified in the mouse cortex (Huntley et al., 2020). The overlapping up- and down-regulated genes in the two studies were provided in **Supplementary Table 9**. Notably, *Reln*, a gene that generally co-expressed with SST interneurons (Pohlkamp et al., 2014), was significantly up-regulated in SST interneurons in both the mouse hippocampus and cortex. On the other hand, *Syt2* was significantly up-regulated in PV interneurons in the hippocampus and cortex. Several ion channel genes were also expressed in the cortex, such as *Cacna2d3*, *Cacng4*, and *Cacng5* in SST interneurons, and *Kcng4* and *Kcnc3* in PV interneurons. However, *Scn4b*, *Kcnab1*, and *Kcna1* were not up-regulated in PV interneurons in the cortex.

Although *Sst* and *Pvalb* have been utilized as markers for SST and PV interneurons, respectively, it is worth noting that their expression is not exclusive to their respective cell types. SST or PV interneurons can be further divided into subtypes using single-cell RNA-seq. In the mouse cortex and hippocampus, a small fraction of SST interneurons expresses *Pvalb*, while a small fraction of PV interneurons expresses *Sst* (Gouwens et al., 2020; Yao et al., 2021). This co-expression is also reported in Allen Brain Map Transcriptomics Explorer (modified in **Supplementary Figure 1A**). Indeed, our data revealed a low level of *Pvalb* expression in SST interneurons (**Figure 1E**; **Supplementary Figure 1B**), suggesting that a subtype of *Pvalb*-expressing SST interneurons was immunoprecipitated with the RiboTag approach. The co-expression could be a confounding factor to our transcriptome analysis. However, it is important to acknowledge that the PV-Cre and SST-Cre lines employed in this study are widely used in various interneuron investigations (Zou et al., 2016; Drexel et al., 2017; Gouwens et al., 2020; Jang et al., 2020; Udakis et al., 2020; Morales et al., 2021; Asgarihafshejani et al., 2022; Drexel et al., 2022). Therefore, our findings can offer valuable molecular insights for the utilization of these lines.

This study has additional limitations, as it does not account for the transcriptomic variations between PV and SST interneurons in specific hippocampal subregions, such as CA1 and DG, where these neurons may display distinct transcriptomic profiles in response to various conditions like diseases or behavioral paradigms. PV and SST interneurons show different morphological, molecular, and electrophysiological properties across the hippocampal subregions (Botcher et al., 2014). Furthermore, PV and SST interneurons are involved in different memory types. For example, CA1 PV interneurons are crucial for spatial working memory (Murray et al., 2011), whereas CA1 SST interneurons control contextual fear memory and regulate object location memory (Lovett-Barron et al., 2014; Asgarihafshejani et al., 2022; Honore and Lacaille, 2022). DG PV interneurons modulate anxiety, social interaction, and memory extinction (Zou et al., 2016); nevertheless, DG SST interneurons are required for contextual and spatial overlapping memories (Morales et al., 2021). In the future, it is imperative to

consider the hippocampal subregional heterogeneity of PV and SST interneurons to investigate their role in neuropsychiatric disorders or learning and memory.

4.4. Dysregulation of interneuron gene expression in schizophrenia and epilepsy

Schizophrenia and epilepsy are two brain disorders associated with the dysfunction of interneurons. In schizophrenia, the impaired excitatory-inhibitory (E-I) balance and reduced oscillatory activity result from decreased GABAergic signaling due to hypoexcitability of PV interneurons (Lodge et al., 2009; Lewis et al., 2012). Similarly, various forms of epilepsy, such as temporal lobe epilepsy, SCN8A epileptic encephalopathy, and Dravet syndrome, are associated with an imbalanced E-I ratio arising from dysfunction in SST and PV interneurons (Tai et al., 2014; Wengert et al., 2021; Drexel et al., 2022). Although the pathophysiology mechanisms of these neuropsychiatric disorders are not clearly understood, insights into the gene expression profiles of PV or SST interneurons can provide valuable indications.

Between SST and PV transcriptomes, we identified 29 and 24 DEGs overlapping with gene sets involving schizophrenia and epilepsy, respectively. The voltage-gated sodium channel β subunit 4 (*Scn4b)* is expressed higher in PV interneuron and serves as a marker in the dorsolateral prefrontal cortex for schizophrenia (Guillozet-Bongaarts et al., 2014). Schizophrenia is associated with reduced excitability of PV interneurons. It is of interest to investigate the potential correlation between the higher *Scn4b* expression and the hypoexcitability in PV interneurons, and how they underlie the schizophrenia phenotype. Furthermore, *Cacna2d3*, a gene encoding voltage-dependent calcium channel subunit α2/δ3, has been implicated as a candidate gene for epilepsy (Peng et al., 2021). Besides, impairment in dendritic inhibition, rather than somatic inhibition, has been observed in various in several forms of epilepsy (Cossart et al., 2001; Wittner et al., 2001; Wittner et al., 2005; Sanjay et al., 2015). SST interneurons play a role in dendritic inhibition, contributing to the regulation of Ca^{2+} signaling, while PV interneurons primarily regulate hippocampal network oscillations through perisomatic inhibition (Udakis et al., 2020). Future studies will be required to test if the reduced expression of *Cacna2d3* in SST interneurons leads to decreased dendritic inhibition, which in turn to epileptic features. Moreover, we detected eight genes associated with both schizophrenia and epilepsy that were differentially expressed between SST and PV interneurons, thus providing further direction for their roles in these diseases.

This article highlights *Gabrd*, a gene implicated in both schizophrenia and epilepsy. The link between differential tonic inhibition in SST and PV interneurons suggests that the $GABA_A$ receptor δ subunit may be a possible target for schizophrenia/epilepsy drugs. Another $GABA_A$ receptor examined in our study, *Gabra6*, is predominantly expressed in the cerebellum under physiological conditions. In the hippocampus, it is associated with stress-induced depressive behaviors (Yang et al., 2016). Mutations in *Gabra6* have also been identified in patients with idiopathic generalized epilepsy (Riaz et al., 2021), and its single-nucleotide polymorphism is associated with schizophrenia (Gong et al., 2013). In our study, the mRNA and protein level of *Gabra6* was higher in hippocampal PV interneurons than in SST interneurons under physiological conditions. Because our experiments were conducted under normal physiological conditions, further studies using disease models are required to confirm the relationship between these gene expressions and disease development.

In conclusion, this study demonstrates the feasibility of employing the RiboTag-seq approach for investigating gene expression profiles specific to different cell types. The results reveal the molecular signatures that may be involved in the physiological functions of particular interneuron types and provide valuable insights into their implications in brain disorders.

Data availability statement

The datasets presented in this study are deposited in the online repositories. The names of the repository/repositories and accession number(s) can be found below: https://dataverse.lib.nycu.edu.tw/dataset.xhtml?persistentId=doi:10.57770/U1BJQ8, NYCU Dataverse.

Ethics statement

The animal study was reviewed and approved by the Institutional Animal Care and Use Committee (IACUC) of the National Yang Ming Chiao Tung University.

Author contributions

C-YC, C-CL, C-DC, and IC contributed to the conception and design of the study, edited, and revised the manuscript. T-HH, C-WH, and MA performed the experiments. Y-SL, L-YW, and C-YC analyzed the RNA-seq data. T-HH, Y-SL, and C-WH wrote the first draft of the manuscript. All authors read and approved the submitted version.

Funding

This work was supported by the Ministry of Science and Technology, Taiwan (Grant Nos. MOST 111-2321-B-A49-005, MOST 111-2320-B-A49-305, MOST 109-2320-B-010-015-MY3, MOST 111-2320-B-A49-009-MY3, MOST 111-2636-E-A49-006, and MOST 111-2221-E-A49-130-MY3), NSTC 112-2321-B-A49-009, in part by the National Health Research Institutes, Taiwan (Grant No. NHRI-EX 111-11135NI), and by the China Medical University and Hospital (Grant No. DMR-111-097).

Acknowledgments

We thank the Genomics Center for Clinical and Biotechnological Applications of National Core Facility for

Biopharmaceuticals, Taiwan (MOST 109-2740-B-010-002) for sequencing. We also thank the support from the Brain Research Center, National Yang Ming Chiao Tung University, from the Featured Areas Research Center Program within the framework of the Higher Education Sprout Project by the Ministry of Education (MOE) in Taiwan.

Conflict of interest

The authors declare that the research was conducted in the absence of any commercial or financial relationships that could be construed as a potential conflict of interest.

Publisher's note

All claims expressed in this article are solely those of the authors and do not necessarily represent those of their affiliated organizations, or those of the publisher, the editors and the reviewers. Any product that may be evaluated in this article, or claim that may be made by its manufacturer, is not guaranteed or endorsed by the publisher.

Supplementary material

The Supplementary Material for this article can be found online at: https://www.frontiersin.org/articles/10.3389/fncel.2023.1146278/full#supplementary-material

SUPPLEMENTARY TABLE 1
Chemicals and products list.

SUPPLEMENTARY TABLE 2
Antibodies used in this study.

SUPPLEMENTARY TABLE 3
List of mice information in this study.

SUPPLEMENTARY TABLE 4
Primer list for RT-qPCR.

SUPPLEMENTARY TABLE 5
List of differentially expressed genes (DEGs) between SST and PV interneurons.

SUPPLEMENTARY TABLE 6
List of enriched GO terms for up-regulated genes in SST interneurons.

SUPPLEMENTARY TABLE 7
List of enriched GO terms for up-regulated genes in PV interneurons.

SUPPLEMENTARY TABLE 8
List of enriched KEGG pathways for DEGs between SST and PV interneurons.

SUPPLEMENTARY TABLE 9
List of shared DEGs in this study and Huntley et al., 2020.

References

Ajibola, M. I., Wu, J. W., Abdulmajeed, W. I., and Lien, C. C. (2021). Hypothalamic glutamate/GABA cotransmission modulates hippocampal circuits and supports long-term potentiation. *J. Neurosci.* 41, 8181–8196. doi: 10.1523/JNEUROSCI.0410-21.2021

Arslan, A. (2021). Extrasynaptic delta-subunit containing GABA(A) receptors. *J. Integr. Neurosci.* 20, 173–184. doi: 10.31083/j.jin.2021.01.284

Asgarihafshejani, A., Honore, E., Michon, F. X., Laplante, I., and Lacaille, J. C. (2022). Long-term potentiation at pyramidal cell to somatostatin interneuron synapses controls hippocampal network plasticity and memory. *iScience* 25:104259. doi: 10.1016/j.isci.2022.104259

Baroncelli, L., Braschi, C., Spolidoro, M., Begenisic, T., Maffei, L., and Sale, A. (2011). Brain plasticity and disease: A matter of inhibition. *Neural Plast.* 2011:286073. doi: 10.1155/2011/286073

Belelli, D., Harrison, N. L., Maguire, J., Macdonald, R. L., Walker, M. C., and Cope, D. W. (2009). Extrasynaptic GABAA receptors: Form, pharmacology, and function. *J. Neurosci.* 29, 12757–12763. doi: 10.1523/JNEUROSCI.3340-09.2009

Booker, S. A., and Vida, I. (2018). Morphological diversity and connectivity of hippocampal interneurons. *Cell Tissue Res.* 373, 619–641. doi: 10.1007/s00441-018-2882-2

Botcher, N. A., Falck, J. E., Thomson, A. M., and Mercer, A. (2014). Distribution of interneurons in the CA2 region of the rat hippocampus. *Front. Neuroanat.* 8:104. doi: 10.3389/fnana.2014.00104

Brickley, S. G., and Mody, I. (2012). Extrasynaptic GABA(A) receptors: Their function in the CNS and implications for disease. *Neuron* 73, 23–34. doi: 10.1016/j.neuron.2011.12.012

Brouzes, E., Medkova, M., Savenelli, N., Marran, D., Twardowski, M., Hutchison, J. B., et al. (2009). Droplet microfluidic technology for single-cell high-throughput screening. *Proc. Natl. Acad. Sci. U.S.A.* 106, 14195–14200. doi: 10.1073/pnas.0903542106

Bryson, A., Hatch, R. J., Zandt, B. J., Rossert, C., Berkovic, S. F., Reid, C. A., et al. (2020). GABA-mediated tonic inhibition differentially modulates gain in functional subtypes of cortical interneurons. *Proc. Natl. Acad. Sci. U.S.A.* 117, 3192–3202. doi: 10.1073/pnas.1906369117

Cadwell, C. R., Sandberg, R., Jiang, X., and Tolias, A. S. (2017). Q&A: Using Patch-seq to profile single cells. *BMC Biol.* 15:58. doi: 10.1186/s12915-017-0396-0

Chen, E. Y., Tan, C. M., Kou, Y., Duan, Q., Wang, Z., Meirelles, G. V., et al. (2013). Enrichr: Interactive and collaborative HTML5 gene list enrichment analysis tool. *BMC Bioinformatics* 14:128. doi: 10.1186/1471-2105-14-128

Cossart, R., Dinocourt, C., Hirsch, J. C., Merchan-Perez, A., De Felipe, J., Ben-Ari, Y., et al. (2001). Dendritic but not somatic GABAergic inhibition is decreased in experimental epilepsy. *Nat. Neurosci.* 4, 52–62.

Drexel, M., Rahimi, S., and Sperk, G. (2022). Silencing of hippocampal somatostatin interneurons induces recurrent spontaneous limbic seizures in mice. *Neuroscience* 487, 155–165. doi: 10.1016/j.neuroscience.2022.02.007

Drexel, M., Romanov, R. A., Wood, J., Weger, S., Heilbronn, R., Wulff, P., et al. (2017). Selective silencing of hippocampal Parvalbumin interneurons induces development of recurrent spontaneous limbic seizures in mice. *J. Neurosci.* 37, 8166–8179. doi: 10.1523/JNEUROSCI.3456-16.2017

Farrant, M., and Nusser, Z. (2005). Variations on an inhibitory theme: Phasic and tonic activation of GABA(A) receptors. *Nat. Rev. Neurosci.* 6, 215–229. doi: 10.1038/nrn1625

Field, M. I, Lukacs, P., Hunter, E., Stacey, R., Plaha, P., Livermore, L., et al. (2021). Tonic GABAA receptor-mediated currents of human cortical GABAergic interneurons vary amongst cell types. *J. Neurosci.* 41, 9702–9719. doi: 10.1523/JNEUROSCI.0175-21.2021

Garcia-Junco-Clemente, P., Cantero, G., Gomez-Sanchez, L., Linares-Clemente, P., Martinez-Lopez, J. A., Lujan, R., et al. (2010). Cysteine string protein-alpha prevents activity-dependent degeneration in GABAergic synapses. *J. Neurosci.* 30, 7377–7391. doi: 10.1523/JNEUROSCI.0924-10.2010

Glykys, J., Mann, E. O., and Mody, I. (2008). Which GABA(A) receptor subunits are necessary for tonic inhibition in the hippocampus? *J. Neurosci.* 28, 1421–1426.

Gong, Y., Wu, C. N., Xu, J., Feng, G., Xing, Q. H., Fu, W., et al. (2013). Polymorphisms in microRNA target sites influence susceptibility to schizophrenia by altering the binding of miRNAs to their targets. *Eur. Neuropsychopharmacol.* 23, 1182–1189. doi: 10.1016/j.euroneuro.2012.12.002

Gouwens, N. W., Sorensen, S. A., Baftizadeh, F., Budzillo, A., Lee, B. R., Jarsky, T., et al. (2020). Integrated morphoelectric and transcriptomic classification of cortical GABAergic cells. *Cell* 183, 935–953.e19.

Guillozet-Bongaarts, A. L., Hyde, T. M., Dalley, R. A., Hawrylycz, M. J., Henry, A., Hof, P. R., et al. (2014). Altered gene expression in the dorsolateral prefrontal cortex of individuals with schizophrenia. *Mol. Psychiatry* 19, 478–485.

Gupta, A., Elgammal, F. S., Proddutur, A., Shah, S., and Santhakumar, V. (2012). Decrease in tonic inhibition contributes to increase in dentate semilunar granule cell excitability after brain injury. *J. Neurosci.* 32, 2523–2537. doi: 10.1523/JNEUROSCI.4141-11.2012

Haimon, Z., Volaski, A., Orthgiess, J., Boura-Halfon, S., Varol, D., Shemer, A., et al. (2018). Re-evaluating microglia expression profiles using RiboTag and cell isolation strategies. *Nat. Immunol.* 19, 636–644. doi: 10.1038/s41590-018-0110-6

Halldorsson, S., Lucumi, E., Gomez-Sjoberg, R., and Fleming, R. M. T. (2015). Advantages and challenges of microfluidic cell culture in polydimethylsiloxane devices. *Biosens. Bioelectron.* 63, 218–231.

Honore, E., and Lacaille, J. C. (2022). Object location learning in mice requires hippocampal somatostatin interneuron activity and is facilitated by mTORC1-mediated long-term potentiation of their excitatory synapses. *Mol. Brain* 15:101. doi: 10.1186/s13041-022-00988-7

Hu, H., Gan, J., and Jonas, P. (2014). Interneurons. Fast-spiking, parvalbumin(+) GABAergic interneurons: From cellular design to microcircuit function. *Science* 345:1255263.

Huntley, M. A., Srinivasan, K., Friedman, B. A., Wang, T. M., Yee, A. X., Wang, Y., et al. (2020). Genome-wide analysis of differential gene expression and splicing in excitatory neurons and interneuron subtypes. *J. Neurosci.* 40, 958–973. doi: 10.1523/JNEUROSCI.1615-19.2019

Hwang, B., Lee, J. H., and Bang, D. (2018). Single-cell RNA sequencing technologies and bioinformatics pipelines. *Exp. Mol. Med.* 50, 1–14.

Jang, H. J., Chung, H., Rowland, J. M., Richards, B. A., Kohl, M. M., and Kwag, J. (2020). Distinct roles of parvalbumin and somatostatin interneurons in gating the synchronization of spike times in the neocortex. *Sci. Adv.* 6:eaay5333. doi: 10.1126/sciadv.aay5333

Jonas, P., Bischofberger, J., Fricker, D., and Miles, R. (2004). Interneuron Diversity series: Fast in, fast out–temporal and spatial signal processing in hippocampal interneurons. *Trends Neurosci.* 27, 30–40. doi: 10.1016/j.tins.2003.10.010

Kapfer, C., Glickfeld, L. L., Atallah, B. V., and Scanziani, M. (2007). Supralinear increase of recurrent inhibition during sparse activity in the somatosensory cortex. *Nat. Neurosci.* 10, 743–753. doi: 10.1038/nn1909

Kepecs, A., and Fishell, G. (2014). Interneuron cell types are fit to function. *Nature* 505, 318–326.

Klausberger, T., and Somogyi, P. (2008). Neuronal diversity and temporal dynamics: The unity of hippocampal circuit operations. *Science* 321, 53–57. doi: 10.1126/science.1149381

Klausberger, T., Magill, P. J., Marton, L. F., Roberts, J. D., Cobden, P. M., Buzsaki, G., et al. (2003). Brain-state- and cell-type-specific firing of hippocampal interneurons in vivo. *Nature* 421, 844–848. doi: 10.1038/nature01374

Kuleshov, M. V., Jones, M. R., Rouillard, A. D., Fernandez, N. F., Duan, Q., Wang, Z., et al. (2016). Enrichr: A comprehensive gene set enrichment analysis web server 2016 update. *Nucleic Acids Res.* 44, W90–W97. doi: 10.1093/nar/gkw377

Lee, C. T., Kao, M. H., Hou, W. H., Wei, Y. T., Chen, C. L., and Lien, C. C. (2016). Causal evidence for the role of specific GABAergic interneuron types in entorhinal recruitment of dentate granule cells. *Sci. Rep.* 6:36885. doi: 10.1038/srep36885

Lee, V., and Maguire, J. (2014). The impact of tonic GABAA receptor-mediated inhibition on neuronal excitability varies across brain region and cell type. *Front. Neural Circuits* 8:3. doi: 10.3389/fncir.2014.00003

Lesiak, A. J., Brodsky, M., and Neumaier, J. F. (2015). RiboTag is a flexible tool for measuring the translational state of targeted cells in heterogeneous cell cultures. *BioTechniques* 58, 308–317. doi: 10.2144/000114299

Lewis, D. A., Curley, A. A., Glausier, J. R., and Volk, D. W. (2012). Cortical parvalbumin interneurons and cognitive dysfunction in schizophrenia. *Trends Neurosci.* 35, 57–67.

Lipovsek, M., Bardy, C., Cadwell, C. R., Hadley, K., Kobak, D., and Tripathy, S. J. (2021). Patch-seq: Past, present, and future. *J. Neurosci.* 41, 937–946.

Liu, Y. C., Cheng, J. K., and Lien, C. C. (2014). Rapid dynamic changes of dendritic inhibition in the dentate gyrus by presynaptic activity patterns. *J. Neurosci.* 34, 1344–1357. doi: 10.1523/JNEUROSCI.2566-13.2014

Lodge, D. J., Behrens, M. M., and Grace, A. A. (2009). A loss of parvalbumin-containing interneurons is associated with diminished oscillatory activity in an animal model of schizophrenia. *J. Neurosci.* 29, 2344–2354. doi: 10.1523/JNEUROSCI.5419-08.2009

Love, M. I., Huber, W., and Anders, S. (2014). Moderated estimation of fold change and dispersion for RNA-seq data with DESeq2. *Genome Biol.* 15:550. doi: 10.1186/s13059-014-0550-8

Lovett-Barron, M., Kaifosh, P., Kheirbek, M. A., Danielson, N., Zaremba, J. D., Reardon, T. R., et al. (2014). Dendritic inhibition in the hippocampus supports fear learning. *Science* 343, 857–863.

Mannoury la Cour, C., Herbelles, C., Pasteau, V., de Nanteuil, G., and Millan, M. J. (2008). Influence of positive allosteric modulators on GABA(B) receptor coupling in rat brain: A scintillation proximity assay characterisation of G protein subtypes. *J. Neurochem.* 105, 308–323. doi: 10.1111/j.1471-4159.2007.05131.x

Mardinly, A. R., Spiegel, I., Patrizi, A., Centofante, E., Bazinet, J. E., Tzeng, C. P., et al. (2016). Sensory experience regulates cortical inhibition by inducing IGF1 in VIP neurons. *Nature* 531, 371–375. doi: 10.1038/nature17187

Markram, H., Muller, E., Ramaswamy, S., Reimann, M. W., Abdellah, M., Sanchez, C. A., et al. (2015). Reconstruction and simulation of neocortical microcircuitry. *Cell* 163, 456–492.

Miles, R., Toth, K., Gulyas, A. I., Hajos, N., and Freund, T. F. (1996). Differences between somatic and dendritic inhibition in the hippocampus. *Neuron* 16, 815–823.

Mitchell, S. J., and Silver, R. A. (2003). Shunting inhibition modulates neuronal gain during synaptic excitation. *Neuron* 38, 433–445.

Morales, C., Morici, J. F., Espinosa, N., Sacson, A., Lara-Vasquez, A., Garcia-Perez, M. A., et al. (2021). Dentate gyrus somatostatin cells are required for contextual discrimination during episodic memory encoding. *Cereb. Cortex* 31, 1046–1059. doi: 10.1093/cercor/bhaa273

Murray, A. J., Sauer, J. F., Riedel, G., McClure, C., Ansel, L., Cheyne, L., et al. (2011). Parvalbumin-positive CA1 interneurons are required for spatial working but not for reference memory. *Nat. Neurosci.* 14, 297–299. doi: 10.1038/nn.2751

Peng, J., Zhou, Y., and Wang, K. (2021). Multiplex gene and phenotype network to characterize shared genetic pathways of epilepsy and autism. *Sci. Rep.* 11:952. doi: 10.1038/s41598-020-78654-y

Pohlkamp, T., David, C., Cauli, B., Gallopin, T., Bouche, E., Karagiannis, A., et al. (2014). Characterization and distribution of Reelin-positive interneuron subtypes in the rat barrel cortex. *Cereb. Cortex* 24, 3046–3058. doi: 10.1093/cercor/bht161

Pouille, F., and Scanziani, M. (2004). Routing of spike series by dynamic circuits in the hippocampus. *Nature* 429, 717–723. doi: 10.1038/nature02615

Prenosil, G. A., Schneider Gasser, E. M., Rudolph, U., Keist, R., Fritschy, J. M., and Vogt, K. E. (2006). Specific subtypes of GABAA receptors mediate phasic and tonic forms of inhibition in hippocampal pyramidal neurons. *J. Neurophysiol.* 96, 846–857. doi: 10.1152/jn.01199.2005

Riaz, M., Abbasi, M. H., Sheikh, N., Saleem, T., and Virk, A. O. (2021). GABRA1 and GABRA6 gene mutations in idiopathic generalized epilepsy patients. *Seizure* 93, 88–94. doi: 10.1016/j.seizure.2021.10.013

Ruden, J. B., Dugan, L. L., and Konradi, C. (2021). Parvalbumin interneuron vulnerability and brain disorders. *Neuropsychopharmacology* 46, 279–287.

Sanjay, M., Neymotin, S. A., and Krothapalli, S. B. (2015). Impaired dendritic inhibition leads to epileptic activity in a computer model of CA3. *Hippocampus* 25, 1336–1350. doi: 10.1002/hipo.22440

Santhakumar, V., Hanchar, H. J., Wallner, M., Olsen, R. W., and Otis, T. S. (2006). Contributions of the GABAA receptor alpha6 subunit to phasic and tonic inhibition revealed by a naturally occurring polymorphism in the alpha6 gene. *J. Neurosci.* 26, 3357–3364. doi: 10.1523/JNEUROSCI.4799-05.2006

Santhakumar, V., Jones, R. T., and Mody, I. (2010). Developmental regulation and neuroprotective effects of striatal tonic GABAA currents. *Neuroscience* 167, 644–655. doi: 10.1016/j.neuroscience.2010.02.048

Sanz, E., Yang, L., Su, T., Morris, D. R., McKnight, G. S., and Amieux, P. S. (2009). Cell-type-specific isolation of ribosome-associated mRNA from complex tissues. *Proc. Natl. Acad. Sci. U.S.A.* 106, 13939–13944. doi: 10.1073/pnas.0907143106

Sigel, E., and Steinmann, M. E. (2012). Structure, function, and modulation of GABA(A) receptors. *J. Biol. Chem.* 287, 40224–40231.

Silberberg, G. (2008). Polysynaptic subcircuits in the neocortex: Spatial and temporal diversity. *Curr. Opin. Neurobiol.* 18, 332–337. doi: 10.1016/j.conb.2008.08.009

Silberberg, G., and Markram, H. (2007). Disynaptic inhibition between neocortical pyramidal cells mediated by Martinotti cells. *Neuron* 53, 735–746.

Song, I., Savtchenko, L., and Semyanov, A. (2011). Tonic excitation or inhibition is set by GABA(A) conductance in hippocampal interneurons. *Nat. Commun.* 2:376.

Song, Y. H., Yoon, J., and Lee, S. H. (2021). The role of neuropeptide somatostatin in the brain and its application in treating neurological disorders. *Exp. Mol. Med.* 53, 328–338.

Sun, Y., Peng, Z., Wei, X., Zhang, N., Huang, C. S., Wallner, M., et al. (2022). Virally-induced expression of GABA(A) receptor delta subunits following their pathological loss reveals their role in regulating GABA(A) receptor assembly. *Prog. Neurobiol.* 218:102337. doi: 10.1016/j.pneurobio.2022.102337

Szabadics, J., Tamas, G., and Soltesz, I. (2007). Different transmitter transients underlie presynaptic cell type specificity of GABAA,slow and GABAA, fast. *Proc. Natl. Acad. Sci. U.S.A.* 104, 14831–14836. doi: 10.1073/pnas.0707204104

Tai, C., Abe, Y., Westenbroek, R. E., Scheuer, T., and Catterall, W. A. (2014). Impaired excitability of somatostatin- and parvalbumin-expressing cortical interneurons in a mouse model of Dravet syndrome. *Proc. Natl. Acad. Sci. U.S.A.* 111, E3139–E3148. doi: 10.1073/pnas.1411131111

Tallent, M. K., and Qiu, C. (2008). Somatostatin: An endogenous antiepileptic. *Mol. Cell. Endocrinol.* 286, 96–103.

Tong, X., Peng, Z., Zhang, N., Cetina, Y., Huang, C. S., Wallner, M., et al. (2015). Ectopic expression of α6 and δ $GABA_A$ receptor subunits in hilar somatostatin

neurons increases tonic inhibition and alters network activity in the dentate gyrus. *J. Neurosci.* 35, 16142–16158.

Tremblay, R., Lee, S., and Rudy, B. (2016). GABAergic interneurons in the neocortex: From cellular properties to circuits. *Neuron* 91, 260–292.

Udakis, M., Pedrosa, V., Chamberlain, S. E. L., Clopath, C., and Mellor, J. R. (2020). Interneuron-specific plasticity at parvalbumin and somatostatin inhibitory synapses onto CA1 pyramidal neurons shapes hippocampal output. *Nat. Commun.* 11:4395. doi: 10.1038/s41467-020-18074-8

Wei, C. W., Luo, T., Zou, S. S., and Wu, A. S. (2018). The role of long noncoding RNAs in central nervous system and neurodegenerative diseases. *Front. Behav. Neurosci.* 12:175. doi: 10.3389/fnbeh.2018.00175

Wengert, E. R., Miralles, R. M., Wedgwood, K. C. A., Wagley, P. K., Strohm, S. M., Panchal, P. S., et al. (2021). Somatostatin-positive interneurons contribute to seizures in SCN8A epileptic encephalopathy. *J. Neurosci.* 41, 9257–9273. doi: 10.1523/JNEUROSCI.0718-21.2021

Wittner, L., Eross, L., Czirjak, S., Halasz, P., Freund, T. F., and Magloczky, Z. (2005). Surviving CA1 pyramidal cells receive intact perisomatic inhibitory input in the human epileptic hippocampus. *Brain* 128, 138–152. doi: 10.1093/brain/awh339

Wittner, L., Magloczky, Z., Borhegyi, Z., Halasz, P., Toth, S., Eross, L., et al. (2001). Preservation of perisomatic inhibitory input of granule cells in the epileptic human dentate gyrus. *Neuroscience* 108, 587–600. doi: 10.1016/s0306-4522(01)00446-8

Wu, T., Hu, E., Xu, S., Chen, M., Guo, P., Dai, Z., et al. (2021). clusterProfiler 4.0: A universal enrichment tool for interpreting omics data. *Innovation (Camb.)* 2:100141. doi: 10.1016/j.xinn.2021.100141

Yang, J., Yang, X., and Tang, K. (2022). Interneuron development and dysfunction. *FEBS J.* 289, 2318–2336.

Yang, L., Xu, T., Zhang, K., Wei, Z., Li, X., Huang, M., et al. (2016). The essential role of hippocampal alpha6 subunit-containing GABAA receptors in maternal separation stress-induced adolescent depressive behaviors. *Behav. Brain Res.* 313, 135–143. doi: 10.1016/j.bbr.2016.07.002

Yao, Z., van Velthoven, C. T. J., Nguyen, T. N., Goldy, J., Sedeno-Cortes, A. E., Baftizadeh, F., et al. (2021). A taxonomy of transcriptomic cell types across the isocortex and hippocampal formation. *Cell* 184, 3222–3241.e26.

Zeng, H., and Sanes, J. R. (2017). Neuronal cell-type classification: Challenges, opportunities and the path forward. *Nat. Rev. Neurosci.* 18, 530–546. doi: 10.1038/nrn.2017.85

Zou, D., Chen, L., Deng, D., Jiang, D., Dong, F., McSweeney, C., et al. (2016). DREADD in parvalbumin interneurons of the dentate gyrus modulates anxiety, social interaction and memory extinction. *Curr. Mol. Med.* 16, 91–102. doi: 10.2174/1566524016666151222150024

frontiers | Frontiers in Cellular Neuroscience

TYPE Original Research
PUBLISHED 05 September 2023
DOI 10.3389/fncel.2023.1120338

OPEN ACCESS

EDITED BY
Alexei Morozov,
Virginia Tech, United States

REVIEWED BY
David Mott,
University of South Carolina, United States
Bart Christiaan Jongbloets,
Utrecht University, Netherlands
Ingrid Ehrlich,
University of Stuttgart, Germany

*CORRESPONDENCE
Judit M. Veres
✉ veres@koki.hu
Norbert Hajos
✉ nhajos@iu.edu

†These authors have contributed equally to this work

RECEIVED 09 December 2022
ACCEPTED 22 August 2023
PUBLISHED 05 September 2023

CITATION
Veres JM, Fekete Z, Müller K, Andrasi T, Rovira-Esteban L, Barabas B, Papp OI and Hajos N (2023) Fear learning and aversive stimuli differentially change excitatory synaptic transmission in perisomatic inhibitory cells of the basal amygdala.
Front. Cell. Neurosci. 17:1120338.
doi: 10.3389/fncel.2023.1120338

Fear learning and aversive stimuli differentially change excitatory synaptic transmission in perisomatic inhibitory cells of the basal amygdala

Judit M. Veres[1*†], Zsuzsanna Fekete[1,2†], Kinga Müller[1,2], Tibor Andrasi[1], Laura Rovira-Esteban[1], Bence Barabas[1,2], Orsolya I. Papp[1] and Norbert Hajos[1,3,4*]

[1]Laboratory of Network Neurophysiology, ELRN Institute of Experimental Medicine, Budapest, Hungary, [2]János Szentágothai School of Neurosciences, Semmelweis University, Budapest, Hungary, [3]The Linda and Jack Gill Center for Molecular Bioscience, Indiana University Bloomington, Bloomington, IN, United States, [4]Program in Neuroscience, Department of Psychological and Brain Sciences, Indiana University Bloomington, Bloomington, IN, United States

Inhibitory circuits in the basal amygdala (BA) have been shown to play a crucial role in associative fear learning. How the excitatory synaptic inputs received by BA GABAergic interneurons are influenced by memory formation, a network parameter that may contribute to learning processes, is still largely unknown. Here, we investigated the features of excitatory synaptic transmission received by the three types of perisomatic inhibitory interneurons upon cue-dependent fear conditioning and aversive stimulus and tone presentations without association. Acute slices were prepared from transgenic mice: one group received tone presentation only (conditioned stimulus, CS group), the second group was challenged by mild electrical shocks unpaired with the CS (unsigned unconditioned stimulus, unsigned US group) and the third group was presented with the CS paired with the US (signed US group). We found that excitatory synaptic inputs (miniature excitatory postsynaptic currents, mEPSCs) recorded in distinct interneuron types in the BA showed plastic changes with different patterns. Parvalbumin (PV) basket cells in the unsigned US and signed US group received mEPSCs with reduced amplitude and rate in comparison to the only CS group. Coupling the US and CS in the signed US group caused a slight increase in the amplitude of the events in comparison to the unsigned US group, where the association of CS and US does not take place. Excitatory synaptic inputs onto cholecystokinin (CCK) basket cells showed a markedly different change from PV basket cells in these behavioral paradigms: only the decay time was significantly faster in the unsigned US group compared to the only CS group, whereas the amplitude of mEPSCs increased in the signed US group compared to the only CS group. Excitatory synaptic inputs received by PV axo-axonic cells showed the least difference in the three behavioral paradigm: the only significant change was that the rate of mEPSCs increased in the signed US group when compared to the only CS group. These results collectively show that associative learning and aversive stimuli unpaired with CS cause different changes in excitatory synaptic transmission in BA perisomatic interneuron types, supporting the hypothesis that they play distinct roles in the BA network operations upon pain information processing and fear memory formation.

KEYWORDS

interneurons, GABA, fear conditioning, associative learning, excitation

Introduction

Pavlovian fear conditioning is one of the most used behavioral paradigms, which serves as a model to study the basic cellular and circuit mechanisms underlying associated learning in neural networks. In this paradigm, an aversive stimulus (unconditioned stimulus, US) is presented together with a cue (conditioned stimulus, CS), resulting in a formed association between these signals wherein the animal learns that the cue (i.e., the CS) predicts the US. Previous studies have shown that the amygdala plays a central role in associative fear learning, and proposed that the association of CS and US takes place in the lateral nucleus of the amygdala (LA) (Romanski et al., 1993; Fanselow and Kim, 1994; Pape and Pare, 2010). Recent studies indicate that the link between the cue and aversive stimuli may even take place in the thalamus (Barsy et al., 2020), the association then being transmitted to the LA. The LA, after processing the information in conjunction with other inputs, passes it to the basal amygdala (BA). However, recent findings also imply that the BA has a direct role in fear memory processes (Herry et al., 2008; Amano et al., 2011; Jasnow et al., 2013).

Similar to other cortical areas, the BA networks are composed of glutamatergic excitatory principal neurons and GABAergic inhibitory interneurons (Vereczki et al., 2021). Although it is known that interneurons are necessary for appropriate and balanced cortical network functions, there is no evidence so far that excitatory synaptic inputs received by interneurons show plastic changes upon fear memory formation in the BA (Lucas et al., 2016; Polepalli et al., 2020; He et al., 2021). Interneurons in the BA show high diversity in their neurochemical content, electrophysiological properties and target distributions, which endow them with distinct roles in the network functions (Hajos, 2021). Among the many interneuron types, those which target the cell body, proximal dendrites and axon initial segment can control the activity of principal neurons the most efficiently (Miles et al., 1996). These interneurons, named perisomatic-region targeting interneurons (PTIs), are composed of three main types. Axo-axonic cells (AAC) often express parvalbumin (Vereczki et al., 2021) and target the axon initial segments of principal neurons (Somogyi, 1977; McDonald et al., 2002; Veres et al., 2014), whereas two types of basket cells contact somata and proximal dendrites: parvalbumin (PVBC) and cholecystokinin (CCKBC) containing basket cells (Freund and Katona, 2007). Based on the position of their inhibitory input onto principal neurons, PTIs can very effectively inhibit and delay cell firing (Cobb et al., 1995; Woodruff and Sah, 2007; Veres et al., 2014, 2017). Thus, PTIs can tightly control the activity of the BA networks and are potentially crucial regulators of CS-US association, however the role of distinct PTI types requires clarification. There is evidence that simultaneously manipulating all PV containing cells in the LA and BA can interfere with cue-dependent fear learning in the amygdala (Wolff et al., 2014), but how AACs and PVBCs in the BA contribute to this memory process is unknown. *In vivo* recordings suggest that the US elicits high firing activity in AACs, while PVBCs show heterogenous response: some are excited while others inhibited by aversive stimuli (Bienvenu et al., 2012; Krabbe et al., 2019). Due to the lack of appropriate tools for monitoring CCKBC activity *in vivo*, it is still unknown how their firing changes upon CS-US association. As inhibitory control of principal neuron firing by PTIs is very effective (Veres et al., 2014, 2017), any change in excitatory synaptic inputs on these GABAergic cell types can potently alter the activity of the local networks as well as the BA output.

To reveal the changes in the properties of excitatory synaptic inputs on PTIs upon fear learning, we recorded miniature excitatory postsynaptic currents (mEPSC) from identified AACs, PVBCs, and CCKBCs in acute slices prepared from three groups of mice that experienced different behavioral protocols using a tone as CS and a mild electrical shock as US. One group experienced CS only, another group received independent random CS and US (unsigned US group), and the third group was presented with CS co-terminating with US (signed US group). As fear memory formation was only observed in the signed US group, with this approach we could compare the effects of fear memory formation on the excitatory synaptic transmission received by PTIs with those obtained upon the presentation of sensory inputs (auditory and noxious stimuli).

Our results showed that the excitatory synaptic inputs on all PTI types underwent changes in response to aversive stimuli, while formation of fear association caused only minor further modifications in their properties. The different alterations in mEPSC characteristics in distinct PTI types suggest that these cells fulfill different roles during aversive information processing in BA network function and fear memory formation.

Materials and methods

Experimental animals

All experiments were approved by the Committee for the Scientific Ethics of Animal Research (22.1/360/3/2011) and were performed according to the guidelines of the institutional ethical code and the Hungarian Act of Animal Care and Experimentation (1998; XXVIII, section 243/1998, renewed in 40/2013) in accordance with the European Directive 86/609/CEE and modified according to the Directives 2010/63/EU. Transgenic or double-transgenic male mice (6–15 weeks old) expressing eGFP under the control of the Pvalb promoter (BAC-PV-eGFP, $n = 19$, Meyer et al., 2002), expressing DsRed under the Cck promoter (BAC-CCK-DsRed, $n = 16$, Mate et al., 2013), or expressing both eGFP and DsRed controlled by Pvalb and Cck promoters, respectively, were used ($n = 4$). Mice were housed in groups of 4–6 in the animal facility on a 12 h light/dark cycle under controlled temperature (26.5°C). Four days before the experiments, mice were kept individually to avoid cross-influence of stress levels in behavioral experiments.

Behavioral tests

Cue-dependent fear conditioning consisted of a chamber with black dotted white background, slightly curved walls, metal rod floor,

white illumination and was cleaned with 70% ethanol (context A). First, mice were allowed to habituate to this context for 5 min at Zeitgeber time (ZT) 2–3 h, then returned to their home cage. After 1 h, mice were transferred back to context A, where, after a 120 s-long acclimation period, three different protocols were used. (1) only CS group ($n = 14$): CS (7.5 kHz sound for 20 s) was presented 7 times without US (with 110 ± 23 s intervals; mean ± SD); (2) unsigned US group ($n = 12$): 7 CS and 7 US (mild electrical shocks, 2 mA for 1 s) were presented randomly [with 111 ± 21 s intervals for CS and 110 ± 33 s intervals for US (mean ± SD)]; (3) signed US group ($n = 13$): 20 s-long CS presentations were co-terminated with the 1 s-long US, pairs repeated 7 times at random intervals (110 ± 23 s; mean ± SD). On the next day at ZT 1–2 h, for testing cued fear expression, after a 120 s-long acclimation, mice were subjected to a 20 s-long CS in a novel context (context B: square chamber with white background, paper floor, red illumination, cleaned with 1% acetic acid). Freezing (as an index of fear) was *post hoc* measured manually on video recordings with an in-house software (H 77, courtesy of Prof. József Haller, Institute of Experimental Medicine, Budapest, Hungary) by trained observers blind to the animal treatment. Freezing was defined as no visible movement of the body except that required for respiration. Freezing levels are expressed as a percentage (duration of freezing within the CS/total time of the CS or duration of freezing during baseline/total time of the baseline, respectively).

Slice preparation

Immediately after the fear expression test, mice were transferred to the anesthetizing chamber and deeply anesthetized with isoflurane and decapitated for acute slice preparation. The brain was quickly removed and placed into ice-cold solution containing (in mM): 252 sucrose, 2.5 KCl, 26 $NaHCO_3$, 0.5 $CaCl_2$, 5 $MgCl_2$, 1.25 NaH_2PO_4, 10 glucose, bubbled with 95% O_2/ 5% CO_2 (carbogen gas). Horizontal slices of 200-µm thickness containing the BA were prepared with a Leica VT1200S vibratome and kept in an interface-type holding chamber filled with artificial cerebrospinal fluid (ACSF) at 36°C that gradually cooled down to room temperature. ACSF contained the following (in mM): 126 NaCl, 2.5 KCl, 1.25 NaH_2PO_4, 2 $MgCl_2$, 2 $CaCl_2$, 26 $NaHCO_3$, and 10 glucose, bubbled with carbogen gas.

Electrophysiological recordings

After at least 1 h incubation, slices were transferred to a submerged type recording chamber perfused with ACSF (32–34°C) containing 0.5 µM tetrodotoxin (TTX, Hello Bio) and 100 µM picrotoxin (Sigma-Aldrich) with the flow rate of approximately 2–2.5 mL/min. Recordings were performed under visual guidance using differential interference contrast microscopy (Olympus BX61W or Nikon FN-1) with a 40x objective. Neurons expressing eGFP or DsRed were visualized with the aid of a mercury arc lamp and detected with a CCD camera (Hamamatsu Photonics or Andor Zyla). Patch pipettes (4–7 MΩ) for whole-cell recordings were pulled from borosilicate capillaries with inner filament (thin walled, OD 1.5) using a DMZ-Universal Puller (Zeitz Instruments) or using a P1000 pipette puller (Sutter Instruments). The internal solution contained (in mM): 110 K-gluconate, 4 NaCl, 2 Mg-ATP, 20 HEPES, 0.1 EGTA, 0.3 GTP (sodium salt), 10 phosphocreatine, 0.2% biocytin, and 0.1 spermine adjusted to pH 7.3 using KOH, with an osmolarity of 290 mOsm/L. Neurons were recorded in whole-cell mode at a holding potential of −65 mV with 9–15 MΩ series resistance (Rs mean ± SD, in MΩ: PVBC only CS: 11.29 ± 1.30, unsigned US: 11.23 ± 1.76, signed US: 10.49 ± 0.81; CCKBC only CS: 10.85 ± 1.71, unsigned US: 10.24 ± 1.23, signed US: 10.28 ± 1.53; AAC only CS: 11.63 ± 1.80, unsigned US: 11.30 ± 1.58, signed US: 11.29 ± 1.08). Recordings were performed with a Multiclamp 700B amplifier (Molecular Devices), low-pass filtered at 3 kHz, digitized at 10–50 kHz, and not corrected for junction potential. Data acquisition software EVAN 1.3 (courtesy of Professor Istvan Mody, Department of Neurology and Physiology, University of California, Los Angeles, CA) or Clampex 10.4 (Molecular Devices) were used for recordings. mEPSC analysis was performed on the recordings obtained between 5 and 10 min after establishing whole cell configuration. During the analyzed time period (30–120 s) series resistance did not change more than 10%. During the offline analysis with Clampfit 10.4, individual miniature events were detected automatically, followed by visual inspection of each detected event and those missed by the algorithm. Only events with peak amplitude higher than 10 pA were considered as mEPSCs. Peak amplitude and inter-event interval of mEPSCs were measured in Clampfit 10.4 (n = approximately 200 consecutive events/neuron) and analyzed with Origin 2021. Statistical analysis was performed on the pooled datasets in each group. mEPSC kinetics were analyzed on the average trace of approximately 150 selected events. 10–90% of rise time was measured with Clampfit 10.4, the decay time constant (tau) was calculated by fitting an exponential curve on the average trace in Origin 2021.

Immunostainings for identification of the recorded cells

After the recordings, slices were fixed overnight in 4% paraformaldehyde (PFA) in 0.1 M phosphate buffer (PB, pH 7.4). Biocytin-filled recorded cells were visualized with Alexa488-conjugated streptavidin (1:10.000, Molecular Probes). For CCKBC identification, immunostaining using guinea pig anti-CB1 (1,1,000; Frontier Institute, CB1-GP-Af530) or rabbit anti-CB1 (1,1,000, Cayman chemical, # 10006590), visualized either with Alexa405-coupled donkey anti-guinea pig secondary antibody (1:500, Jackson) or Alexa647-coupled donkey anti-rabbit secondary antibody (1,500, Jackson) was performed on biocytin-filled DsRed+ cells, and only those with CB1 receptor expression on their axonal boutons were included in the study. To distinguish PVBCs and AACs, immunostaining against calbindin was performed in biocytin-filled eGFP+ cells (rabbit anti-calbindin 1:3000 (Swant, CB-38a) or chicken anti-calbindin, 1:1000 (SYSY #214006), revealed with Cy3-coupled donkey-anti rabbit or chicken secondary antibodies, respectively, 1:500, Jackson). Interneurons with calbindin expression in their somata and/or axon terminals were considered BCs (Vereczki et al., 2016). AACs were defined if they showed no immunoreactivity for calbindin and displayed characteristic cartridges of terminals surrounding putative axon initial segments (AISs), that were visualized with Ankyrin G staining in case for 7 AACs (rabbit-anti Ankyrin G, 1:100, Santa Cruz sc-28,561, visualized with Cy3-coupled donkey anti-rabbit antibody, Jackson) (Gulyás et al., 2010; Veres et al.,

2014). Confocal images were taken using a Nikon C2 microscope using CFI Super Plan Fluor 20X objective (N.A. 0.45; z step size: 1 µm, xy: 0.31 µm/pixel) and CFI Plan Apo VC60X Oil objective for higher magnification (N.A. 1.40; z step size: 0.13 µm, xy: 0.08 µm/pixel).

Statistical analysis

As data showed non-normal distribution according to the Shapiro–Wilk test, Kruskal– Wallis ANOVA (K-W ANOVA) with *post hoc* Dunn's test was used. The relationship between mEPSC properties and freezing levels was tested with Pearson's r correlation and ANOVA. All statistics were performed using OriginPro 2018 and Origin 2021.

Results

Separation of the effects of fear memory formation and sensory inputs

To distinguish between the effects of fear memory formation and the CS/US presentations on the excitatory synaptic inputs of BA PTIs, three different behavioral paradigms were used (Figure 1A). First, to test the behavioral consequences of the CS presentation, mice were subjected to the CS (tones) without the US (shocks, Figure 1A$_2$, only CS group, black). As expected, these mice showed no elevated freezing levels upon the CS demonstration the next day in a different context (Figure 1B, black). Then, to test the effects of CS and US without association, tones and shocks were presented randomly during conditioning (Figure 1A$_2$, unsigned US group, red). In this group, the delivery of the US was not signed by the CS, therefore, the association between CS and US did not form, as demonstrated by the lack of freezing upon the cue presentation the next day (Figure 1B, red). In contrast, when tones were co-terminated with mild electrical shocks, i.e., the oncoming US was signed by a CS (Figure 1A$_2$, signed US group, blue), the fear memory was formed. The results of the CS-US association were clear when the next day the CS presentation alone induced significant freezing in a different context (Figure 1B cue, K-W ANOVA $p = 3\times10^{-6}$), while there was no difference during the baseline period (Figure 1B baseline, K-W ANOVA $p = 0.29$). Thus, in line with previous findings, pairing a CS with a US results in lasting changes in neuronal networks, assessed at the behavioral level (Ledoux, 2003). Importantly, there was no difference in the cue evoked freezing levels of BAC-PV-eGFP and BAC-CCK-DsRed mice in the unsigned US and signed US group (Mann–Whitney test, $p = 0.78$ and $p = 0.69$, respectively), indicating that distinct BAC insertion in the two mouse lines does not compromise the fear memory porcesses. Our experimental design, therefore, allows the separation of the consequences of fear memory formation from those caused by the sensory signals via *ex vivo* investigations using the three mouse groups.

Excitatory synaptic inputs in PVBCs are reduced upon the US presentation

To test whether excitatory synaptic inputs in different PTI types are capable of plastic changes, acute brain slices containing the amygdala were prepared immediately after cued fear testing. PV neurons in the BA were visually targeted based on their eGFP expression and their calbindin content was confirmed *post hoc* (Figures 2A, B). Calbindin is a

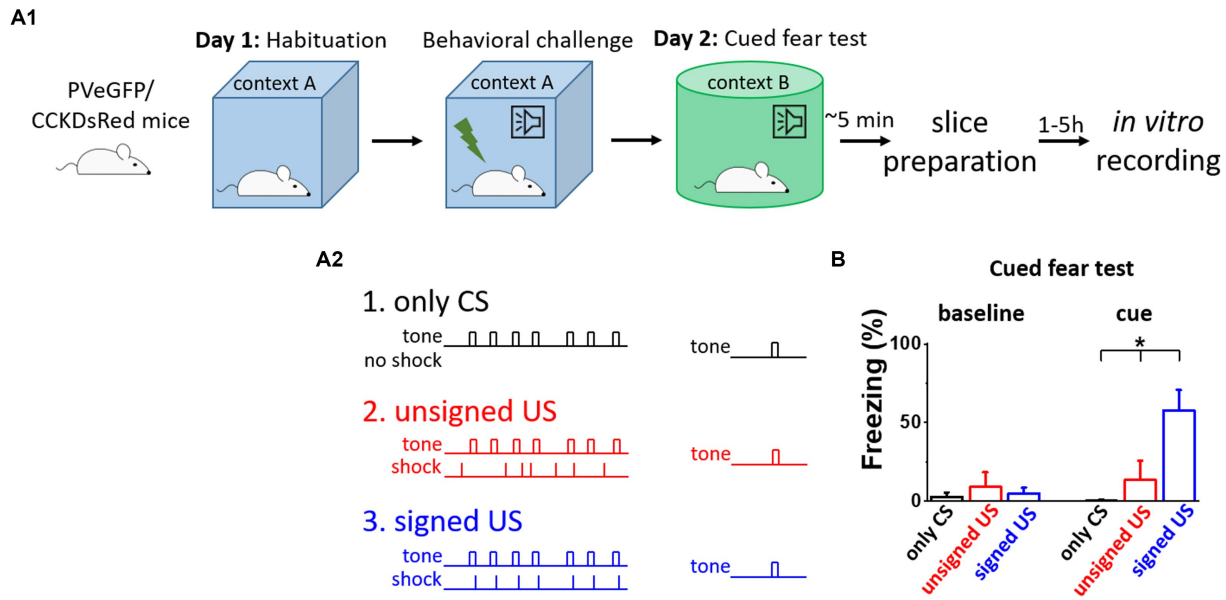

FIGURE 1
Fear memory effectively formed upon signed US presentation, but not in other conditions. **(A$_1$)** Experimental design. **(A$_2$)** The three mouse groups with different combinations of CS (tone) and US (shock) presentation. **(B)** Freezing tested on the consecutive day was elevated only in the signed US group, therefore the other two conditioning paradigms can serve as assessments of the effects of the sensory inputs on the network. Asterisk indicates significant difference (K-W ANOVA $p = 3\times10^{-6}$, only CS vs. unsigned US $p = 0.39$, only CS vs. signed US $p = 2\times10^{-6}$, unsigned US vs. signed US $p = 0.003$). Box represents mean, whiskers SEM. Only CS group $n = 14$, unsigned US group $n = 12$, signed US group $n = 13$.

neurochemical marker for PVBCs in the rodent amygdala that separates these interneurons from PV AACs (Bienvenu et al., 2012; Vereczki et al., 2016). mEPSCs were recorded in whole-cell patch-clamp mode in the presence of 0.5 µM tetrodotoxin (TTX, voltage-gated Na^+ channel blocker) and 100 µM picrotoxin ($GABA_A$ receptor antagonist) in slices from the three behavioral groups challenged differently (Figure 2C; Tables 1, 2). To evaluate the changes in the properties of synaptic inputs in PVBCs mEPSC parameters recorded from all cells were pooled in each group separately and analyzed (Figure 2D). The distribution of mEPSC amplitudes in PVBCs sampled in the three groups showed significant differences (Figure 2D, K-W ANOVA $p = 1\times10^{-16}$); we found a 11% decrease in mEPSC amplitudes in the unsigned group when compared to the only CS group (Dunn's test $p = 6\times10^{-17}$) and a 5% decrease when we compared the signed US to the only CS group (Dunn's test $p = 0.025$). Interestingly, there was a significant increase (7%) in this mEPSC feature in PVBCs if we compared those that were recorded in the unsigned and signed US groups (Dunn's test $p = 1\times10^{-6}$). This observation implies that the US itself can elicit changes in mEPSC peak amplitudes in PVBCs, but the associated learning subsides those changes. When we compared the inter-event intervals (IEI) of mEPSCs (Figure 2E) we found significant changes among groups (K-W ANOVA $p = 3\times10^{-22}$). When compared to the only CS group, the unsigned US presentation led to a 26% (Dunn's test $p = 2\times10^{-17}$) increase in IEIs (i.e., reduced the rate), and the signed US group also showed a 23% increase (Dunn's test $p = 2\times10^{-17}$). There was no difference in mEPSC rates in the unsigned and signed US group (Dunn's test $p = 0.3$), implying that the effect of CS and US association on this mEPSC characteristic is indistinguishable from those that are caused by the independent presentation of CS and US. Rise time and decay kinetics of mEPSCs were not different in the three paradigms (Table 2, K-W ANOVA $p = 0.758$ and $p = 0.598$, respectively). Taken together, these results suggest that the US presentation decreases mEPSC amplitudes and their occurrence in PVBCs, but fear memory formation may cause a slighter reduction in the amplitude of their excitatory synaptic inputs in comparison to CS presentation only.

Increased amplitude and decreased decay time constant of mEPSCs in CCKBCs upon US presentation

Next, we assessed whether the excitatory synaptic inputs in the other main basket cell type, CCKBCs, are also capable of plastic changes in our paradigms. To selectively record from these cells, a CCK-DsRed mouse strain was used (Mate et al., 2013; Rovira-Esteban et al., 2017) to visually target CCKBCs based on their DsRed content (Figures 3A, B;

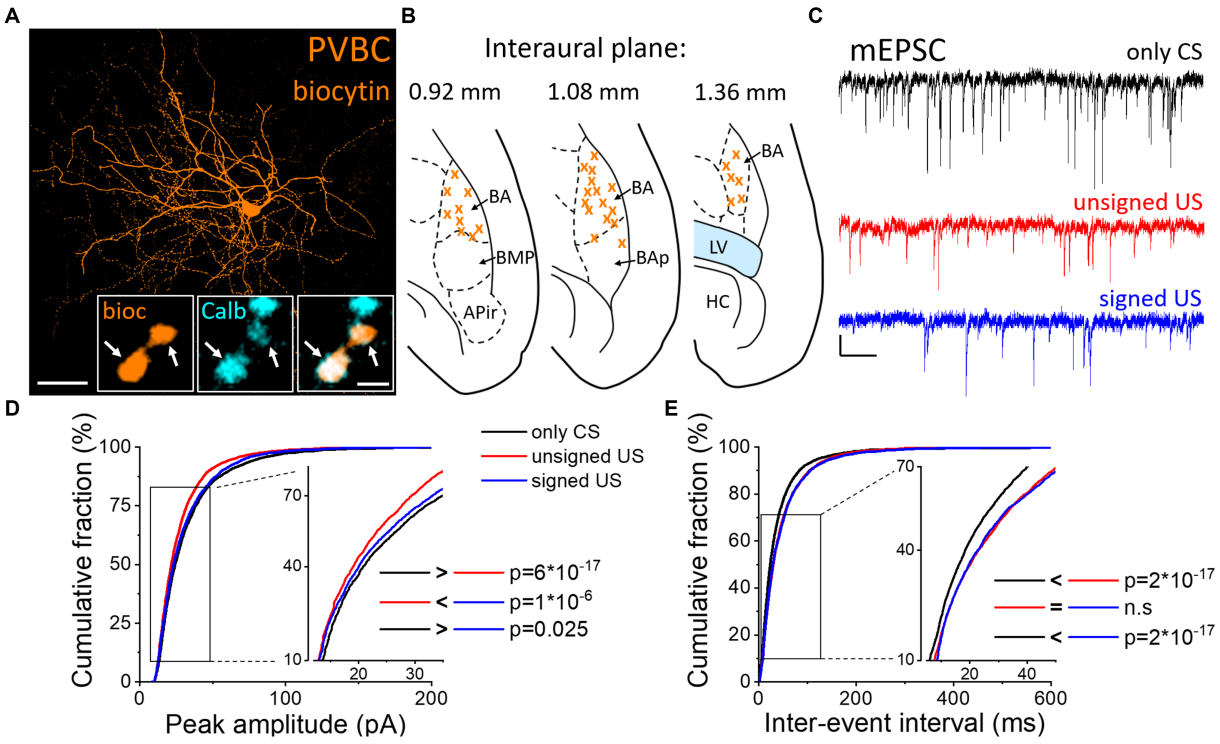

FIGURE 2
Differences in mEPSC properties in PVBCs recorded in slices prepared from the three groups of mice. **(A)** Maximum z intensity projection image of a biocytin-filled PVBC. Inset: Axon terminals of PVBCs (orange) are immunopositive for calbindin (Calb, cyan), a neurochemical marker that distinguishes PVBCs from AACs in the BA. Arrows indicate colocalization. Scales: 50 µm and 1 µm (inset). **(B)** Position (orange x) of the recorded PVBC depicted on schematic drawings representing horizontal brain sections [based on Paxinos (2012)]. Out of the 50 recorded cells, only 30 randomly selected interneurons are shown for clarity. APir: piriform amygdalar area, BA: basal amygdala, BAp: posterior part of the basal amygdala, BMP: basomedial amygdala, posterior part, HC: hippocampus, LV: lateral ventricle. **(C)** Representative traces of miniature excitatory postsynaptic current (mEPSC) recordings in the presence of 0.5 µM tetrodotoxin (TTX) and 100 µM picrotoxin in the three groups. Scales: 20 pA (y) and 100 ms (x). **(D,E)** Cumulative distribution of mEPSC peak amplitudes **(D)** and inter-event intervals **(E)**; data pooled from all cells in each group. Graphs in inserts are plotted using a normal probability Y axis. *p* values show the result of K-W ANOVA *post hoc* Dunn's tests (see details in Table 1). n.s., non-significant difference.

TABLE 1 Data and statistical analysis of mEPSC amplitude and inter-event interval in the recorded PTIs.

Cell type	Variable	Group	Cell number (mouse number)	Value (median ± IQ range)	Group comparison *p* value (K-W ANOVA)	Paired comparison	*p* value (Dunn's test)	Change
PVBC	Peak amplitude (pA) (Figure 2D)	Only CS	17 (7)	24.35 ± 21.41	$1*10^{-16}$	Only CS vs. unsigned US	$6*10^{-17}$	11% ↓
		Unsigned US	17 (6)	21.66 ± 16.55		Only CS vs. signed US	0.0251	5% ↓
		Signed US	16 (7)	23.11 ± 20.85		Unsigned US vs. signed US	$1*10^{-6}$	7% ↑
	IEI (ms) (Figure 2E)	Only CS	17 (7)	23.70 ± 34.90	$3*10^{-22}$	Only CS vs. unsigned US	$2*10^{-17}$	26% ↑
		Unsigned US	17 (6)	30.00 ± 43.60		Only CS vs. signed US	$2*10^{-17}$	23% ↑
		Signed US	16 (7)	29.24 ± 44.55		Unsigned US vs. signed US	1	–
CCKBC	Peak amplitude (pA) (Figure 3D)	Only CS	23 (6)	17.13 ± 7.12	0.001	Only CS vs. unsigned US	0.124	–
		Unsigned US	24 (6)	17.32 ± 7.67		Only CS vs. signed US	$9*10^{-4}$	3% ↑
		Signed US	21 (6)	17.58 ± 7.96		Unsigned US vs. signed US	0.303	–
	IEI (ms) (Figure 3E)	Only CS	23 (6)	83.31 ± 137.0	0.175			
		Unsigned US	24 (6)	85.35 ± 144.75				
		Signed US	21 (6)	83.75 ± 131.30				
AAC	Peak amplitude (pA) (Figure 4D)	Only CS	20 (7)	18.06 ± 10.51	0.406			
		Unsigned US	14 (5)	17.76 ± 10.64				
		Signed US	21 (7)	18.19 ± 11.17				
	IEI (ms) (Figure 4E)	Only CS	20 (7)	58.75 ± 104.00	0.031	Only CS vs. unsigned US	1	–
		Unsigned US	14 (5)	56.45 ± 96.73		Only CS vs. signed US	0.026	7% ↓
		Signed US	21 (7)	54.45 ± 90.50		Unsigned US vs. signed US	0.465	–

Vereczki et al., 2016). After recordings, CB1 content of axon terminals was confirmed with immunolabeling (Figure 3A insets). mEPSCs were recorded (Figure 3C; Tables 1, 2) and analyzed by the same methods as in PVBCs described above. The evaluation of changes in mEPSC characteristics recorded in CCKBCs showed a difference in their peak amplitudes (Figure 3D, K-W ANOVA $p = 0.001$). There was a slight (3%) but significant increase in mEPSC peak amplitudes in the signed US groups when compared to the only CS controls (Dunn's test $p = 2\times10^{-17}$). However, there was no significant difference between the only CS vs. unsigned US (Dunn's test $p = 0.12$) and unsigned US vs. signed US comparisons (Dunn's test $p = 0.30$). Interestingly, we could not find any difference in the IEI of mEPSCs (Figure 3E, K-W ANOVA $p = 0.175$). Regarding the kinetic properties of mEPSCs (Table 2), the rise time was not different in the three paradigms (K-W ANOVA $p = 0.895$), however, there was a significant 17% decrease in the decay time constant when we compared the only CS group to the unsigned US group (Dunn's test $p = 0.004$). Taken together, these results show that the fear learning increases the amplitude of mEPSC and the unsigned US accelerates the mEPSC decaying phase in the CCKBC population.

Excitatory synaptic inputs in AACs change only upon fear memory formation

Besides the two basket cell types, AACs are the third PTI type that are capable to efficiently control the spiking activity of principal neurons (Veres et al., 2014). Therefore, any change in the excitatory synaptic inputs of AACs as a consequence of fear conditioning could be pivotal in the accomplishment of their functions. AACs were targeted in the BA based on their eGFP content in PV-eGFP animals

TABLE 2 Data and statistical analysis of mEPSC kinetic features recorded in PTIs.

Cell type	Variable	Group	Cell number (mouse number)	Value (median ± IQ range)	Group comparison p value (K-W ANOVA)	Paired comparison	*p* value (Dunn's test)	Change
PVBC	Rise time 10–90% (ms)	Only CS	17 (7)	0.28 ± 0.07	0.758	Only CS vs. unsigned US		
		Unsigned US	17 (6)	0.31 ± 0.06		Only CS vs. signed US		
		Signed US	16 (7)	0.34 ± 0.09		Unsigned US vs. signed US		
	Decay time constant (ms)	Only CS	17 (7)	0.94 ± 0.38	0.598	Only CS vs. unsigned US		
		Unsigned US	17 (6)	1.01 ± 0.40		Only CS vs. signed US		
		Signed US	16 (7)	1.06 ± 0.4		Unsigned US vs. signed US		
CCKBC	Rise time 10–90% (ms)	Only CS	23 (6)	0.60 ± 0.20	0.895	Only CS vs. unsigned US		
		Unsigned US	24 (6)	0.61 ± 0.09		Only CS vs. signed US		
		Signed US	21 (6)	0.60 ± 0.11		Unsigned US vs. signed US		
	Decay time constant (ms)	Only CS	23 (6)	1.91 ± 0.58	0.006	Only CS vs. unsigned US	0.004	17% ↓
		Unsigned US	24 (6)	1.57 ± 0.41		Only CS vs. signed US	0.375	–
		Signed US	21 (6)	1.80 ± 0.46		Unsigned US vs. signed US	0.352	–
AAC	Rise time 10–90% (ms)	Only CS	20 (7)	0.26 ± 0.09	0.230	Only CS vs. unsigned US		
		Unsigned US	14 (5)	0.33 ± 0.08		Only CS vs. signed US		
		Signed US	21 (7)	0.32 ± 0.09		Unsigned US vs. signed US		
	Decay time constant (ms)	Only CS	20 (7)	0.84 ± 0.20	0.289	Only CS vs. unsigned US		
		Unsigned US	14 (5)	0.93 ± 0.18		Only CS vs. signed US		
		Signed US	21 (7)	0.91 ± 0.24		Unsigned US vs. signed US		

and were separated *post hoc* from PVBCs based on their characteristic axonal cartridges formed around axon initial segments that can be visualized by Ankyrin-G staining (Figures 4A, B) and the absence of calbindin immunolabeling in their somata and axon terminals. mEPSCs were recorded (Figure 4C; Tables 1, 2) and analyzed as described above. Unlike basket cells, excitatory synaptic inputs in AACs did not show change in their amplitude (Figure 4D, K-W ANOVA $p = 0.406$), however, there was a slight but significant change in the rate of mEPSCs ((Figure 4E, K-W ANOVA $p = 0.031$): in the signed US group the rate of mEPSCs were 7% higher than in the only CS group (Dunn's test $p = 0.026$). Rise time and decay kinetics of mEPSCs were not different in the three paradigms (Table 2, K-W ANOVA $p = 0.23$ and $p = 0.289$, respectively). Taken together, our data indicate that there is a unique increase in mEPSC rates in AACs upon signed US presentation that was not present in any other PTI type.

Fear learning strength does not correlate with mEPSC properties

As the strength of fear memory learning can be variable among individual mice, assessed by the time spent in freezing, we asked the

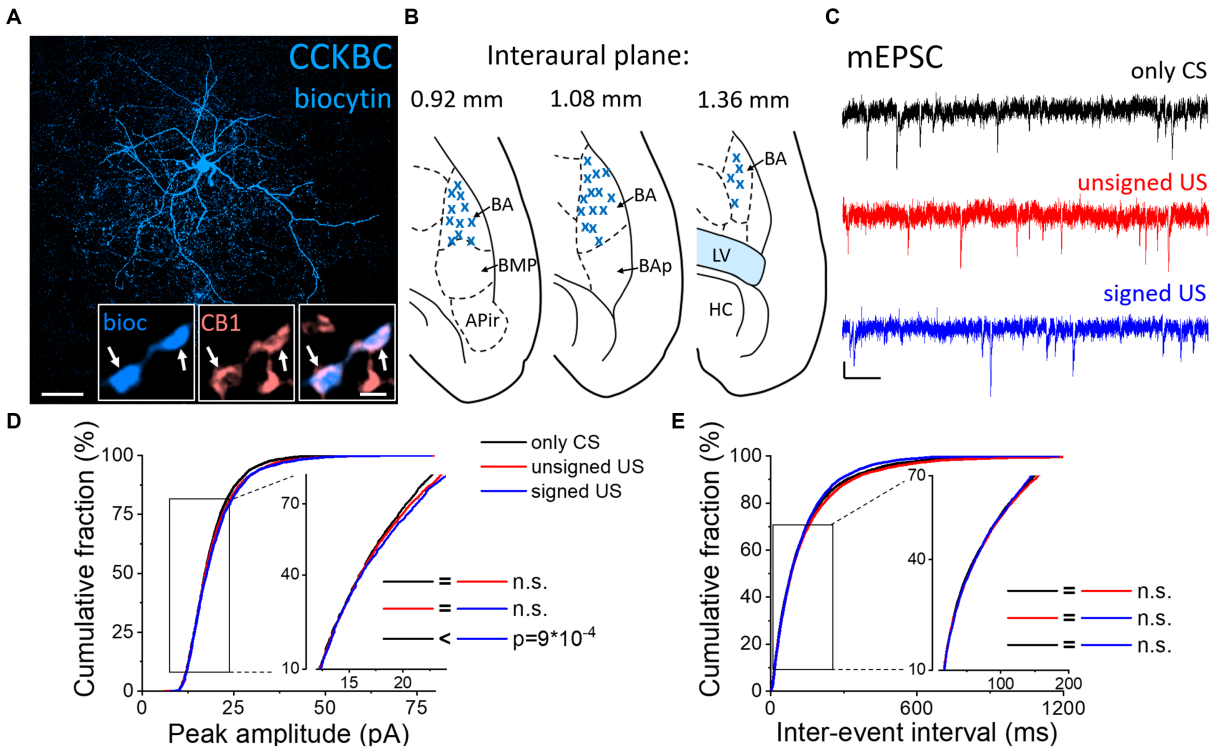

FIGURE 3
Increased amplitude of mEPSCs in CCKBCs upon US presentation **(A)** Maximum z intensity projection image of a biocytin-filled CCKBC. Inset: Axon terminals of same CCKBC (blue) are immunopositive for type one cannabinoid receptors (CB1, pink). Arrows indicate colocalization. Scales: 50 µm and 1 µm (inset). **(B)** Position (blue x) of the recorded CCKBC depicted on schematic drawings representing horizontal brain sections [based on Paxinos (2012)]. Out of the 68 recorded cells, only 30 randomly selected interneurons are shown for clarity. APir: piriform amygdalar area, BA: basal amygdala, BAp: posterior part of the basal amygdala, BMP: basomedial amygdala, posterior part, HC: hippocampus, LV: lateral ventricle. **(C)** Representative traces of miniature excitatory postsynaptic current (mEPSC) recordings in the presence of 0.5 µM TTX and 100 µM picrotoxin from the three groups. Scales: 10 pA (y) and 100 ms (x). **(D,E)** Cumulative distribution of mEPSC peak amplitudes **(D)** and inter-event intervals **(E)**; data pooled from all cells in each group. Graphs in inserts are plotted using a normal probability Y axis. *p* values show the result of K-W ANOVA *post hoc* Dunn's tests (see details in Table 1). n.s., non-significant difference.

question whether the variability in freezing is reflected in the excitatory inputs of PTIs in the BA. Therefore, we compared the electrophysiological properties of mEPSCs in PTIs recorded from mice with different freezing levels upon cue presentation on the test day, as a proxy for the strength of fear learning (Figure 5). We correlated the peak amplitude, IEI, rise time and decay time constant of mEPSCs in PVBCs (Figure 5A), CCKBCs (Figure 5B) and AACs (Figure 5C), in each behavioral paradigm (only CS, unsigned US and signed US groups). We found that none of the groups showed a significant linear correlation with the freezing level of the animal ($p > 0.05$), suggesting that the level of behavioral output induced by fear learning in the individuals is not reflected in the properties of excitatory inputs at the single cell level.

Discussion

In this study, we revealed cell type-specific changes in the properties of excitatory synaptic transmission in PTIs upon unsigned aversive stimulus presentation and fear memory formation in comparison to tone presentation only in the BA (Figure 6). Both the peak amplitude and rate of mEPSCs in PVBCs decreased in the unsigned and signed US paradigm when compared to the only CS group, though a smaller decrease could be observed in the amplitude of mEPSCs when the unsigned US and CS only groups were compared. AACs received excitatory synaptic inputs with shorter inter-event intervals (i.e., the mEPSC rate increased) when the US was paired to the CS compared to the only CS group. These results suggest that although these two PTI types show similarities in their PV expression and features in the membrane voltage responses (Barsy et al., 2017), their excitatory synaptic inputs are modified distinctly by fear learning, implying the different roles of PVBCs and AACs in network function. In contrast to PVBCs and AACs, CCKBCs were the only cell type showing any change in mEPSC kinetics (in decay time constant) after unpaired US protocol, with no further modification after fear memory formation. Also, in sharp contrast to PVBCs, there was a slight but significant increase in mEPSC amplitudes in the fear association paradigm when we compared it to the only CS group. Such opposite change in the synaptic transmission observed between CCKBCs and PVBCs is exemplified in multiple instances. For example, nitric oxide originating from the postsynaptic pyramidal neurons reduces the inhibitory transmission from the axon terminals of CCKBCs (Makara et al., 2007), but increases transmission at the output synapses of PVBCs (Lourenco et al., 2014). Thus, opposite alterations in CCKBC and PVBC characteristics under various circumstances may be a general rule in cortical circuits.

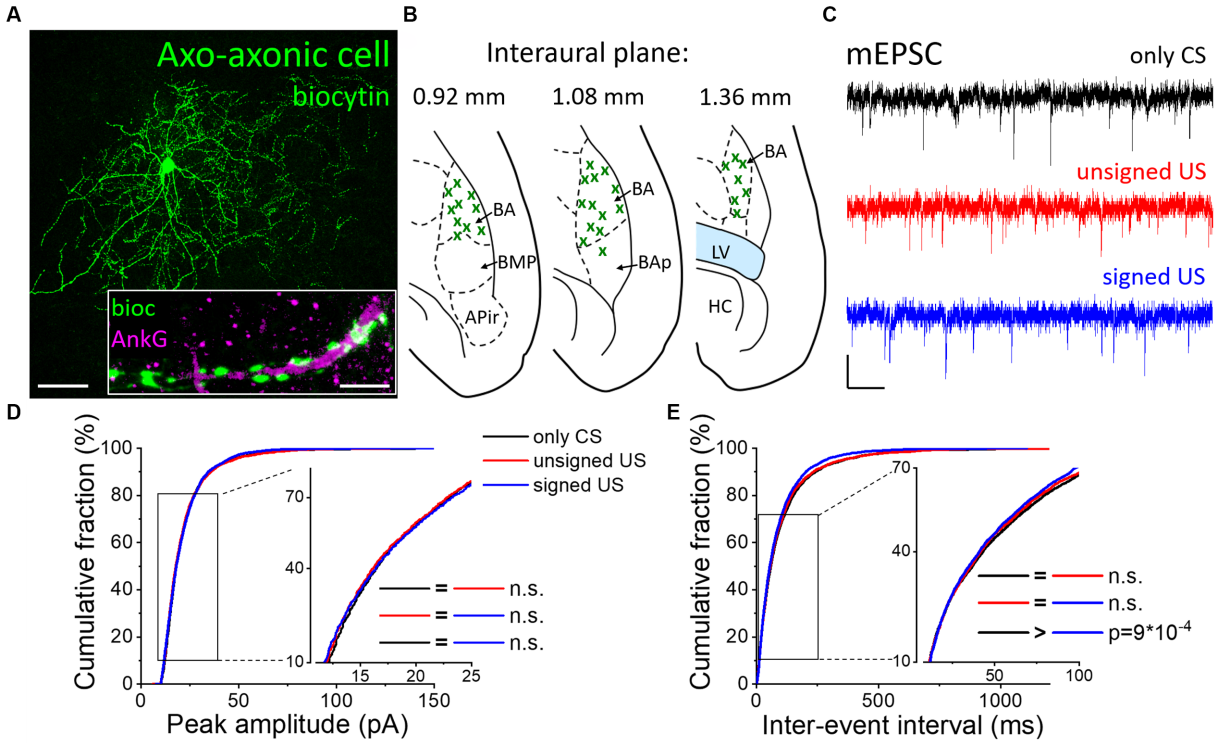

FIGURE 4
Excitatory synaptic inputs in AACs change only upon the signed US presentation. **(A)** Maximum z intensity projection image of a biocytin-filled AAC. Inset: Axon terminals of the same AAC (green) form a characteristic cartridge along an Ankyrin-G (magenta) labeled axon initial segment. Scales: 50 μm and 5 μm (inset). **(B)** Position (green x) of each recorded AAC depicted on schematic drawings representing horizontal brain sections [based on Paxinos (2012)]. Out of the 55 recorded cells, only 30 randomly selected interneurons are shown for clarity. APir: piriform amygdalar area, BA: basal amygdala, BAp: posterior part of the basal amygdala, BMP: basomedial amygdala, posterior part, HC: hippocampus, LV: lateral ventricle. **(C)** Representative traces of miniature excitatory postsynaptic current (mEPSC) recordings in the presence of 0.5 μM TTX and 100 μM picrotoxin obtained in AACs sampled from the three groups. Scales: 10 pA (y) and 100 ms (x). **(D,E)** Cumulative distribution of mEPSC peak amplitudes **(D)** and inter-event intervals **(E)**; data pooled from all cells in each group. Graphs in inserts are plotted using a normal probability Y axis. *p* values show the result of K-W ANOVA *post hoc* Dunn's tests (see details in Table 1). n.s., non-significant difference.

It has been shown that activity of interneurons changes in response to both the CS and US (Krabbe et al., 2019), therefore, in order to dissect their role in processing aversive stimuli versus fear memory formation, it is important to use a control group that was exposed to the auditory stimulus (only CS group), instead of using naïve mice as controls. To separate the effects of aversive stimuli and fear memory formation, we used the unsigned US group as an additional reference where the noxious stimulus could not be predicted by the presentation of the CS. With the use of these two groups, we demonstrated that excitatory synaptic inputs of all PTI types in the BA were modified in response to the aversive stimuli. Notably, CCKBCs were the only PTI type that showed a change in the kinetic properties of their excitatory synaptic inputs in the unsigned group, a finding that may imply a unique alteration in the excitatory input of CCKBCs after exposure to aversive stimuli. The faster decay of mEPSCs may be related to the changes in subunit composition of ionotropic glutamate receptors mediating the synaptic communication between the excitatory cells and CCKBCs. Such changes in kinetics upon environmental challenges have been described recently (Shultz et al., 2022). Our findings that mEPSC amplitudes are increased in the signed US group when compared to the only CS group may suggest that increasing excitation on CCKBCs can lead to a more potent recruitment of these interneurons upon learning. This elevated recruitment may cause an increased synaptic inhibition in the principal neuron populations that can be overcome only by those highly active, presumably coding, principal neurons that are able to trigger depolarization induced suppression of inhibition (DSI) at their GABAergic inputs from CCKBCs (Pitler and Alger, 1992; Wilson and Nicoll, 2001; Zhu and Lovinger, 2005; Losonczy et al., 2010), while the synaptic inhibition on the non-coding cells remains intact. This process, therefore, may be an efficient mechanism to improve the signal-to-noise ratio in BA networks during aversive stimulus processing (Grewe et al., 2017). Alternatively, the change in the excitatory synaptic transmission received by CCKBCs could reflect their crucial role in stress responses evoked by the unpredictable noxious stimuli, a paradigm that serves also as a stress model (Matuszewich et al., 2007). Notably, it has been previously shown that PVBCs and CCKBCs form independent, parallel inhibitory networks in the BA (Andrasi et al., 2017), a circuit motif that also supports their divergent functions in amygdala operations.

Although the extent of the changes in mEPSC properties in BA PTIs may seem a rather small, it has to be kept in mind that both PV and CCK interneurons receive thousands of glutamatergic inputs (Gulyas et al., 1999; Matyas et al., 2004) of which only a small portion is expected to be altered upon associative learning or noxious stimulus processing. This assumption is based on the observations that PTIs

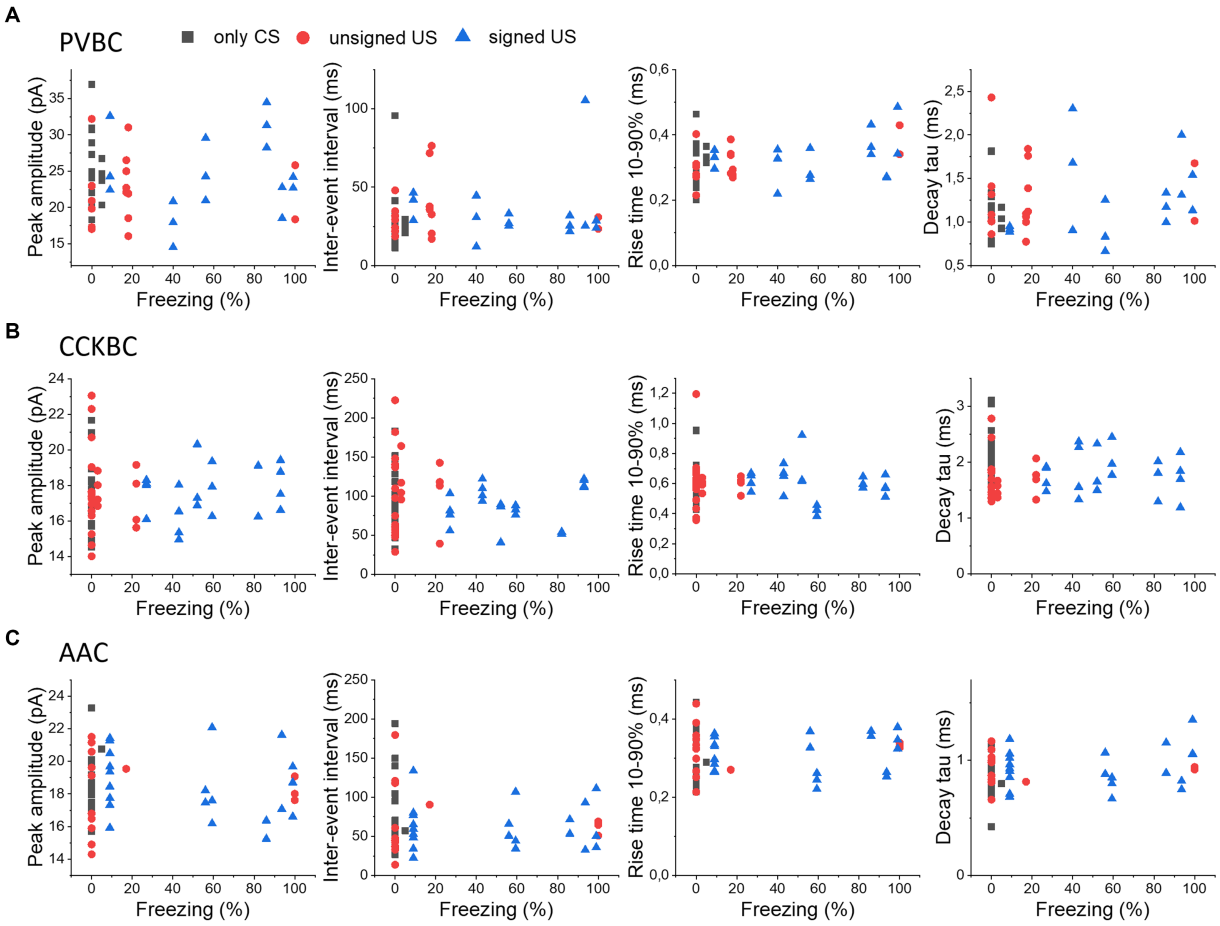

FIGURE 5
No correlation in the properties of mEPSCs in PTIs and the expression of fear levels. The median values of peak amplitude, inter-event interval, rise time 10–90% and decay time constant (tau) of mEPSCs for each cell are shown as a function of the freezing levels upon cue presentation in PVBCs **(A)**, CCKBCs **(B)**, and AACs **(C)**.

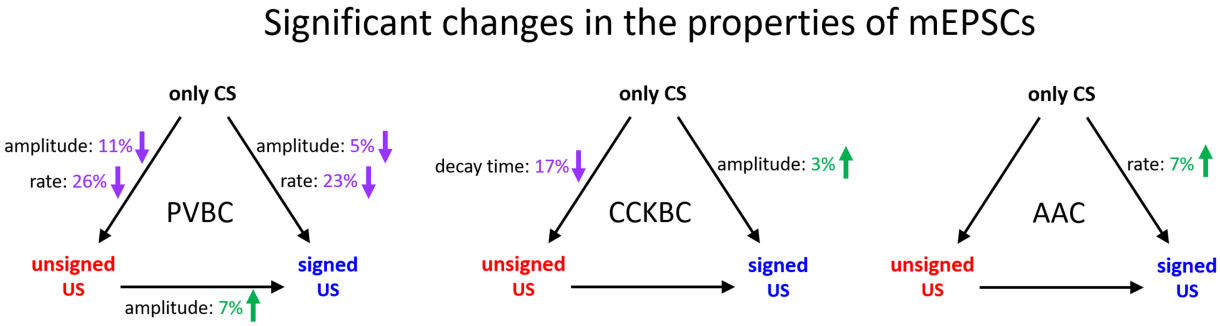

FIGURE 6
Summary of significant changes in the properties of excitatory synaptic inputs of PTIs in the BA in the three behavioral paradigm. Black arrows indicate the compared pairs, only the significant changes in mEPSC amplitude, rate and decay time are shown and are expressed in % values. Green numbers and upward arrows indicate increase, purple numbers and downward arrows indicate decrease. For the exact tests and significance values see Tables 1, 2.

receive excitatory inputs from their neighbor principal neurons (Andrasi et al., 2017), a portion of which is engaged in memory processes or pain processing does not exceed typically 10–15% (Trouche et al., 2013; Senn et al., 2014; Grewe et al., 2017; Corder et al., 2019). In addition, interneurons are innervated also by extra-amygdalar excitatory afferents, e.g., from the thalamus (Krabbe et al., 2019). Although their ratio is unknown within the glutamatergic synapses received by distinct GABAergic cell types in the BA at

present, these inputs may also undergo plastic changes upon fear learning (Barsy et al., 2020), thus, they can also contribute to the observed changes in this study. Moreover, not all GABAergic interneurons within a population have been found to participate in these neural processes (Bienvenu et al., 2012; Wolff et al., 2014; Krabbe et al., 2019). Thus, in a randomly sampled interneuron pool, the contribution of the excitatory inputs that underwent plastic changes in our circumstances to the entire population may be rather limited.

A previous study compared the changes of synaptic inputs on PV interneurons in the LA and BA after fear learning and found that the rate of mEPSCs in PV interneurons is changed only in the LA but not in the BA (Lucas et al., 2016). However, in that study PVBCs and AACs were not distinguished. As the excitatory synaptic inputs of these GABAergic cell types underwent different alterations after learning in the BA (Figure 6), pooling of their data may mask the changes observed between the mEPSC properties recorded in PVBCs and PV AACs. What could be the mechanisms underlying the observed decrease in mEPSC amplitudes in PVBCs upon the US presentation? Our previous study showed that excitatory synaptic inputs on PVBCs and AACs can undergo LTD in a CB1 receptor-dependent manner in the hippocampus (Peterfi et al., 2012) a mechanism that might explain the US-induced decrease in the amplitude of excitatory synaptic inputs observed in PVBCs. However, the increased mEPSC rate in AACs in the signed US group in comparison to the only CS group indicates that synaptic mechanisms underlying the changes in mEPSC properties observed in PVBCs and AACs during the different challenges are necessarily distinct.

The basolateral amygdala is thought to play a central role in fear memory processes, and PTIs in this region are crucial in regulating BA networks due to their powerful capacity to control principal neuron functions (Veres et al., 2014, 2017). Previous studies have highlighted cell type specific roles of interneurons by reporting specific responses to aversive stimuli and firing during oscillations (Bienvenu et al., 2012; Manko et al., 2012; Krabbe et al., 2019), unique sensitivity to neuromodulators (Bocchio et al., 2016; Fu et al., 2022; Mineur et al., 2022), and behavior-induced, target specific output changes (Trouche et al., 2013). Our study extends this knowledge to the level of their excitatory input by showing PTI type specific differences upon aversive stimulus processing and fear memory formation, which will help us to understand how different types of interneurons in the BA network function in health and disease.

Data availability statement

The raw data supporting the conclusions of this article will be made available by the authors, without undue reservation.

Ethics statement

The animal study was approved by the Animal Committee of the Institute of Experimental Medicine, Budapest, Hungary. The study was conducted in accordance with the local legislation and institutional requirements.

Author contributions

JV: acquisition of data, analysis and interpretation of data, drafting the article. ZF, KM, TA, and LR-E: acquisition of data. OP and BB: acquisition of data, analysis and interpretation of data. NH: conception and design, analysis and interpretation of data, drafting the article. All authors contributed to the article and approved the submitted version.

Funding

This work was supported by National Research, Development and Innovation Office (K131893 and RRF-2.3.1-21-2022-00011) and Hungarian Brain Research Program (2017-1.2.1-NKP-2017-00002).

Acknowledgments

We are grateful to Erzsébet Gregori and Éva Krizsán for their excellent technical assistance. We also thank László Barna, the Nikon Microscopy Center at the Institute of Experimental Medicine, Nikon Austria GmbH, and Auro-Science Consulting, Ltd., for kindly providing microscopy support.

Conflict of interest

The authors declare that the research was conducted in the absence of any commercial or financial relationships that could be construed as a potential conflict of interest.

Publisher's note

References

Amano, T., Duvarci, S., Popa, D., and Pare, D. (2011). The fear circuit revisited: contributions of the basal amygdala nuclei to conditioned fear. *J. Neurosci.* 31, 15481–15489. doi: 10.1523/JNEUROSCI.3410-11.2011

Andrasi, T., Veres, J. M., Rovira-Esteban, L., Kozma, R., Vikor, A., Gregori, E., et al. (2017). Differential excitatory control of 2 parallel basket cell networks in amygdala microcircuits. *PLoS Biol.* 15:e2001421. doi: 10.1371/journal.pbio.2001421

Barsy, B., Kocsis, K., Magyar, A., Babiczky, A., Szabo, M., Veres, J. M., et al. (2020). Associative and plastic thalamic signaling to the lateral amygdala controls fear behavior. *Nat. Neurosci.* 23, 625–637. doi: 10.1038/s41593-020-0620-z

Barsy, B., Szabo, G. G., Andrasi, T., Vikor, A., and Hajos, N. (2017). Different output properties of perisomatic region-targeting interneurons in the basal amygdala. *Eur. J. Neurosci.* 45, 548–558. doi: 10.1111/ejn.13498

Bienvenu, T. C., Busti, D., Magill, P. J., Ferraguti, F., and Capogna, M. (2012). Cell-type-specific recruitment of amygdala interneurons to hippocampal theta rhythm and noxious stimuli in vivo. *Neuron* 74, 1059–1074. doi: 10.1016/j.neuron.2012.04.022

Bocchio, M., Mchugh, S. B., Bannerman, D. M., Sharp, T., and Capogna, M. (2016). Serotonin, amygdala and fear: assembling the puzzle. *Front. Neural Circuits* 10:24. doi: 10.3389/fncir.2016.00024

Cobb, S. R., Buhl, E. H., Halasy, K., Paulsen, O., and Somogyi, P. (1995). Synchronization of neuronal activity in hippocampus by individual GABAergic interneurons. *Nature* 378, 75–78. doi: 10.1038/378075a0

Corder, G., Ahanonu, B., Grewe, B. F., Wang, D., Schnitzer, M. J., and Scherrer, G. (2019). An amygdalar neural ensemble that encodes the unpleasantness of pain. *Science* 363, 276–281. doi: 10.1126/science.aap8586

Fanselow, M. S., and Kim, J. J. (1994). Acquisition of contextual Pavlovian fear conditioning is blocked by application of an NMDA receptor antagonist D,L-2-amino-5-phosphonovaleric acid to the basolateral amygdala. *Behav. Neurosci.* 108, 210–212. doi: 10.1037/0735-7044.108.1.210

Freund, T. F., and Katona, I. (2007). Perisomatic inhibition. *Neuron* 56, 33–42. doi: 10.1016/j.neuron.2007.09.012

Fu, X., Teboul, E., Weiss, G. L., Antonoudiou, P., Borkar, C. D., Fadok, J. P., et al. (2022). Gq neuromodulation of BLA parvalbumin interneurons induces burst firing and mediates fear-associated network and behavioral state transition in mice. *Nat. Commun.* 13:1290. doi: 10.1038/s41467-022-28928-y

Grewe, B. F., Grundemann, J., Kitch, L. J., Lecoq, J. A., Parker, J. G., Marshall, J. D., et al. (2017). Neural ensemble dynamics underlying a long-term associative memory. *Nature* 543, 670–675. doi: 10.1038/nature21682

Gulyas, A. I., Megias, M., Emri, Z., and Freund, T. F. (1999). Total number and ratio of excitatory and inhibitory synapses converging onto single interneurons of different types in the CA1 area of the rat hippocampus. *J. Neurosci. Off. J. Soc. Neurosci.* 19, 10082–10097. doi: 10.1523/JNEUROSCI.19-22-10082.1999

Gulyás, A. I., Szabó, G. G., Ulbert, I., Holderith, N., Monyer, H., Erdélyi, F., et al. (2010). Parvalbumin-containing fast-spiking basket cells generate the field potential oscillations induced by cholinergic receptor activation in the hippocampus. *J. Neurosci.* 30, 15134–15145. doi: 10.1523/JNEUROSCI.4104-10.2010

Hajos, N. (2021). Interneuron types and their circuits in the basolateral amygdala. *Front. Neural Circuits* 15:687257. doi: 10.3389/fncir.2021.687257

He, X., Li, J., Zhou, G., Yang, J., Mckenzie, S., Li, Y., et al. (2021). Gating of hippocampal rhythms and memory by synaptic plasticity in inhibitory interneurons. *Neuron* 109:1013. doi: 10.1016/j.neuron.2021.01.014

Herry, C., Ciocchi, S., Senn, V., Demmou, L., Muller, C., and Luthi, A. (2008). Switching on and off fear by distinct neuronal circuits. *Nature* 454, 600–606. doi: 10.1038/nature07166

Jasnow, A. M., Ehrlich, D. E., Choi, D. C., Dabrowska, J., Bowers, M. E., Mccullough, K. M., et al. (2013). Thy1-expressing neurons in the basolateral amygdala may mediate fear inhibition. *J. Neurosci.* 33, 10396–10404. doi: 10.1523/JNEUROSCI.5539-12.2013

Krabbe, S., Paradiso, E., D'aquin, S., Bitterman, Y., Courtin, J., Xu, C., et al. (2019). Adaptive disinhibitory gating by VIP interneurons permits associative learning. *Nat. Neurosci.* 22, 1834–1843. doi: 10.1038/s41593-019-0508-y

Ledoux, J. (2003). The emotional brain, fear, and the amygdala. *Cell. Mol. Neurobiol.* 23, 727–738. doi: 10.1023/A:1025048802629

Losonczy, A., Zemelman, B. V., Vaziri, A., and Magee, J. C. (2010). Network mechanisms of theta related neuronal activity in hippocampal CA1 pyramidal neurons. *Nat. Neurosci.* 13, 967–972. doi: 10.1038/nn.2597

Lourenco, J., Pacioni, S., Rebola, N., Van Woerden, G. M., Marinelli, S., Digregorio, D., et al. (2014). Non-associative potentiation of perisomatic inhibition alters the temporal coding of neocortical layer 5 pyramidal neurons. *PLoS Biol.* 12:e1001903. doi: 10.1371/journal.pbio.1001903

Lucas, E. K., Jegarl, A. M., Morishita, H., and Clem, R. L. (2016). Multimodal and site-specific plasticity of amygdala parvalbumin interneurons after fear learning. *Neuron* 91, 629–643. doi: 10.1016/j.neuron.2016.06.032

Makara, J. K., Katona, I., Nyiri, G., Nemeth, B., Ledent, C., Watanabe, M., et al. (2007). Involvement of nitric oxide in depolarization-induced suppression of inhibition in hippocampal pyramidal cells during activation of cholinergic receptors. *J. Neurosci.* 27, 10211–10222. doi: 10.1523/JNEUROSCI.2104-07.2007

Manko, M., Bienvenu, T. C., Dalezios, Y., and Capogna, M. (2012). Neurogliaform cells of amygdala: a source of slow phasic inhibition in the basolateral complex. *J. Physiol.* 590, 5611–5627. doi: 10.1113/jphysiol.2012.236745

Mate, Z., Poles, M. Z., Szabo, G., Bagyanszki, M., Talapka, P., Fekete, E., et al. (2013). Spatiotemporal expression pattern of DsRedT3/CCK gene construct during postnatal development of myenteric plexus in transgenic mice. *Cell Tissue Res.* 352, 199–206. doi: 10.1007/s00441-013-1552-7

Matuszewich, L., Karney, J. J., Carter, S. R., Janasik, S. P., O'Brien, J. L., and Friedman, R. D. (2007). The delayed effects of chronic unpredictable stress on anxiety measures. *Physiol. Behav.* 90, 674–681. doi: 10.1016/j.physbeh.2006.12.006

Matyas, F., Freund, T. F., and Gulyas, A. I. (2004). Convergence of excitatory and inhibitory inputs onto CCK-containing basket cells in the CA1 area of the rat hippocampus. *Eur. J. Neurosci.* 19, 1243–1256. doi: 10.1111/j.1460-9568.2004.03225.x

Mcdonald, A. J., Muller, J. F., and Mascagni, F. (2002). GABAergic innervation of alpha type ii calcium/calmodulin-dependent protein kinase immunoreactive pyramidal neurons in the rat basolateral amygdala. *J. Comp. Neurol.* 446, 199–218. doi: 10.1002/cne.10204

Meyer, A. H., Katona, I., Blatow, M., Rozov, A., and Monyer, H. (2002). In vivo labeling of parvalbumin-positive interneurons and analysis of electrical coupling in identified neurons. *J. Neurosci.* 22, 7055–7064. doi: 10.1523/JNEUROSCI.22-16-07055.2002

Miles, R., Toth, K., Gulyás, A. I., Hajos, N., and Freund, T. F. (1996). Differences between somatic and dendritic inhibition in the hippocampus. *Neuron* 16, 815–823. doi: 10.1016/S0896-6273(00)80101-4

Mineur, Y. S., Mose, T. N., Maibom, K. L., Pittenger, S. T., Soares, A. R., Wu, H., et al. (2022). Ach signaling modulates activity of the GABAergic signaling network in the basolateral amygdala and behavior in stress-relevant paradigms. *Mol. Psychiatry* 27, 4918–4927. doi: 10.1038/s41380-022-01749-7

Pape, H. C., and Pare, D. (2010). Plastic synaptic networks of the amygdala for the acquisition, expression, and extinction of conditioned fear. *Physiol. Rev.* 90, 419–463. doi: 10.1152/physrev.00037.2009

Paxinos, G. (2012). *Paxinos and Franklin's the mouse brain in stereotaxic coordinates*, San Diego, Academic Press.

Peterfi, Z., Urban, G. M., Papp, O. I., Nemeth, B., Monyer, H., Szabo, G., et al. (2012). Endocannabinoid-mediated long-term depression of afferent excitatory synapses in hippocampal pyramidal cells and GABAergic interneurons. *J. Neurosci.* 32, 14448–14463. doi: 10.1523/JNEUROSCI.1676-12.2012

Pitler, T. A., and Alger, B. E. (1992). Postsynaptic spike firing reduces synaptic GABAA responses in hippocampal pyramidal cells. *J. Neurosci.* 12, 4122–4132. doi: 10.1523/JNEUROSCI.12-10-04122.1992

Polepalli, J. S., Gooch, H., and Sah, P. (2020). Diversity of interneurons in the lateral and basal amygdala. *Npj Sci. Learn.* 5:10. doi: 10.1038/s41539-020-0071-z

Romanski, L. M., Clugnet, M. C., Bordi, F., and Ledoux, J. E. (1993). Somatosensory and auditory convergence in the lateral nucleus of the amygdala. *Behav. Neurosci.* 107, 444–450. doi: 10.1037/0735-7044.107.3.444

Rovira-Esteban, L., Peterfi, Z., Vikor, A., Mate, Z., Szabo, G., and Hajos, N. (2017). Morphological and physiological properties of CCK/CB1R-expressing interneurons in the basal amygdala. *Brain Struct. Funct.* 222, 3543–3565. doi: 10.1007/s00429-017-1417-z

Senn, V., Wolff, S. B., Herry, C., Grenier, F., Ehrlich, I., Grundemann, J., et al. (2014). Long-range connectivity defines behavioral specificity of amygdala neurons. *Neuron* 81, 428–437. doi: 10.1016/j.neuron.2013.11.006

Shultz, B., Farkash, A., Collins, B., Mohammadmirzaei, N., and Knox, D. (2022). Fear learning-induced changes in AMPAR and NMDAR expression in the fear circuit. *Learn. Mem.* 29, 83–92. doi: 10.1101/lm.053525.121

Somogyi, P. (1977). A specific 'axo-axonal' interneuron in the visual cortex of the rat. *Brain Res.* 136, 345–350. doi: 10.1016/0006-8993(77)90808-3

Trouche, S., Sasaki, J. M., Tu, T., and Reijmers, L. G. (2013). Fear extinction causes target-specific remodeling of perisomatic inhibitory synapses. *Neuron* 80, 1054–1065. doi: 10.1016/j.neuron.2013.07.047

Vereczki, V. K., Müller, K., Krizsán, E., Máté, Z., Fekete, Z., Rovira-Esteban, L., et al. (2021). Total number and ratio of GABAergic neuron types in the mouse lateral and basal amygdala. *bioRxiv* 41, 4575–4595. doi: 10.1523/JNEUROSCI.2700-20.2021

Vereczki, V. K., Veres, J. M., Muller, K., Nagy, G. A., Racz, B., Barsy, B., et al. (2016). Synaptic organization of perisomatic GABAergic inputs onto the principal cells of the mouse basolateral amygdala. *Front. Neuroanat.* 10:20. doi: 10.3389/fnana.2016.00020

Veres, J. M., Nagy, G. A., and Hajos, N. (2017). Perisomatic GABAergic synapses of basket cells effectively control principal neuron activity in amygdala networks. *eLife* 6:e20721. doi: 10.7554/eLife.20721

Veres, J. M., Nagy, G. A., Vereczki, V. K., Andrasi, T., and Hajos, N. (2014). Strategically positioned inhibitory synapses of axo-axonic cells potently control principal neuron spiking in the basolateral amygdala. *J. Neurosci. Off. J. Soc. Neurosci.* 34, 16194–16206. doi: 10.1523/JNEUROSCI.2232-14.2014

Wilson, R. I., and Nicoll, R. A. (2001). Endogenous cannabinoids mediate retrograde signalling at hippocampal synapses. *Nature* 410, 588–592. doi: 10.1038/35069076

Wolff, S. B., Grundemann, J., Tovote, P., Krabbe, S., Jacobson, G. A., Muller, C., et al. (2014). Amygdala interneuron subtypes control fear learning through disinhibition. *Nature* 509, 453–458. doi: 10.1038/nature13258

Woodruff, A. R., and Sah, P. (2007). Inhibition and synchronization of basal amygdala principal neuron spiking by parvalbumin-positive interneurons. *J. Neurophysiol.* 98, 2956–2961. doi: 10.1152/jn.00739.2007

Zhu, P. J., and Lovinger, D. M. (2005). Retrograde endocannabinoid signaling in a postsynaptic neuron/synaptic bouton preparation from basolateral amygdala. *J. Neurosci.* 25, 6199–6207. doi: 10.1523/JNEUROSCI.1148-05.2005

10.3389/fncel.2023.1120338

Glossary

AAC	axo-axonic cell
ACSF	artificial cerebrospinal fluid
AnkG	Ankyrin G
APir	piriform amygdalar area
BA	basal amygdala
BAp	posterior part of the basal amygdala
BC	basket cell
BMP	basomedial amygdala, posterior part
Calb	calbindin
CB1	type 1 cannabinoid receptor
CCK	cholecystokinin
CS	conditioned stimulus
DSI	depolarization induced suppression of inhibition
eGFP	enhanced green fluorescent protein
GABA	gamma-amino butyric acid
HC	hippocampus
IEI	inter-event interval
LA	lateral amygdala
LTD	long-term depression
LTP	long-term potentiation
LV	lateral ventricle
mEPSC	miniature excitatory postsynaptic potential
PB	phosphate buffer
PFA	paraformaldehyde
PTI	perisomatic region targeting interneuron
PV	parvalbumin
TTX	tetrodotoxin
US	unconditioned stimulus
ZT	Zeitgeber time

frontiers | Frontiers in Cellular Neuroscience

TYPE Brief Research Report
PUBLISHED 01 February 2024
DOI 10.3389/fncel.2024.1254460

OPEN ACCESS

EDITED BY
Thomas Claude Bienvenu,
Université de Bordeaux, France

REVIEWED BY
Edward Mann,
University of Oxford, United Kingdom
Isabel Del Pino,
Spanish National Research Council (CSIC), Spain
András Szőnyi,
Institute of Experimental Medicine (MTA), Hungary

*CORRESPONDENCE
Wen-Hsien Hou
✉ wen-hsien.hou@biomed.au.dk

†Deceased

RECEIVED 07 July 2023
ACCEPTED 09 January 2024
PUBLISHED 01 February 2024

CITATION
Ozsvár A, Sieburg MC, Sietam MD, Hou W-H and Capogna M (2024) A combinatory genetic strategy for targeting neurogliaform neurons in the mouse basolateral amygdala. *Front. Cell. Neurosci.* 18:1254460. doi: 10.3389/fncel.2024.1254460

A combinatory genetic strategy for targeting neurogliaform neurons in the mouse basolateral amygdala

Attila Ozsvár[1,2], Meike Claudia Sieburg[1,3], Monica Dahlstrup Sietam[1,3], Wen-Hsien Hou[1,3]* and Marco Capogna[1,3,4†]

[1]Department of Biomedicine, Aarhus University, Aarhus, Denmark, [2]Department of Clinical Medicine, Aarhus University, Aarhus, Denmark, [3]Danish Research Institute of Translational Neuroscience - DANDRITE, Aarhus University, Aarhus, Denmark, [4]Center for Proteins in Memory (PROMEMO), Danish National Research Foundation, Aarhus University, Aarhus, Denmark

The mouse basolateral amygdala (BLA) contains various GABAergic interneuron subpopulations, which have distinctive roles in the neuronal microcircuit controlling numerous behavioral functions. In mice, roughly 15% of the BLA GABAergic interneurons express neuropeptide Y (NPY), a reasonably characteristic marker for neurogliaform cells (NGFCs) in cortical-like brain structures. However, genetically labeled putative NPY-expressing interneurons in the BLA yield a mixture of interneuron subtypes besides NGFCs. Thus, selective molecular markers are lacking for genetically accessing NGFCs in the BLA. Here, we validated the NGFC-specific labeling with a molecular marker, neuron-derived neurotrophic factor (NDNF), in the mouse BLA, as such specificity has been demonstrated in the neocortex and hippocampus. We characterized genetically defined NDNF-expressing (NDNF+) GABAergic interneurons in the mouse BLA by combining the Ndnf-IRES2-dgCre-D transgenic mouse line with viral labeling, immunohistochemical staining, and *in vitro* electrophysiology. We found that BLA NDNF+ GABAergic cells mainly expressed NGFC neurochemical markers NPY and reelin (Reln) and exhibited small round soma and dense axonal arborization. Whole-cell patch clamp recordings indicated that most NDNF+ interneurons showed late spiking and moderate firing adaptation. Moreover, ~81% of BLA NDNF+ cells generated retroaxonal action potential after current injections or optogenetic stimulations, frequently developing into persistent barrage firing. Optogenetic activation of the BLA NDNF+ cell population yielded both $GABA_A$- and $GABA_B$ receptor-mediated currents onto BLA pyramidal neurons (PNs). We demonstrate a combinatory strategy combining the NDNF-cre mouse line with viral transfection to specifically target adult mouse BLA NGFCs and further explore their functional and behavioral roles.

KEYWORDS

basolateral amygdala (BLA), GABAergic interneurons, neurogliaform cell, neuron-derived neurotrophic factor (NDNF), retroaxonal barrage firing, optogenetics

Introduction

The amygdala is an evolutionarily conserved brain structure located deeply in the temporal lobe (Janak and Tye, 2015). In rodents, the amygdala can anatomically be divided into the basolateral and the central sectors (Pitkänen et al., 1997; LeDoux, 2007). The basolateral amygdala complex (BLA) is critical for processing information related to reward, valence, and emotional behaviors such as fear and anxiety (LeDoux, 2012; Calhoon and Tye, 2015). The central sector comprises the central amygdala and intercalated cell masses, which are thalamic-like structures comprising local- and long-range projecting GABAergic interneurons (Capogna, 2014). The central amygdala is key to diverse behaviors such as anxiety, reinforcement, social interaction, and survival actions such as fear expression and cataplexy (Pape and Pare, 2010; Janak and Tye, 2015; Mahoney et al., 2017; Moscarello and Penzo, 2022).

The BLA receives major afferents from the sensory thalamus and cortices, ventral hippocampus, medial prefrontal cortex, nucleus accumbens, and extended amygdala regions (Ledoux, 2000; Duvarci and Pare, 2014). It is a cortical-like structure comprising 80% excitatory glutamatergic PNs and 20% inhibitory GABAergic interneurons (Pape and Pare, 2010; Hájos, 2021; Vereczki et al., 2021). The latter population comprises heterogeneous clusters characterized by morpho-electrophysiological and neurochemical properties and subcellular targeting areas of the postsynaptic cells (Hájos, 2021; Vereczki et al., 2021). The activity of PNs is shaped by phasic and tonic inhibitions generated by diverse GABAergic interneuron populations (Farrant and Nusser, 2005; Ehrlich et al., 2009; Wolff et al., 2014). Phasic inhibition onto PNs can either originate from perisomatic areas (Veres et al., 2014, 2017) or dendritic areas (Krabbe et al., 2018; d'Aquin et al., 2022), while tonic inhibition tunes the offset control of PN spike probability through extrasynaptic GABAA- and GABAB receptors (Mańko et al., 2012).

One major source of tonically released GABA in BLA is the activation of neurogliaform cells (NGFCs, Mańko et al., 2012; Rovira-Esteban et al., 2019). In the mouse BLA, NGFCs represent about 15% of the total GABAergic interneuron populations (Vereczki et al., 2021). Similar to observations made in the hippocampus and neocortex, BLA NGFCs have small, spherical soma and short, repeatedly branching dendrites primarily confined in the dense axonal arborization (Mańko et al., 2012; Overstreet-Wadiche and McBain, 2015). Despite the relatively small occupied volume of the axonal arborization, its presynaptic bouton density is noticeably high along the axon processes (Oláh et al., 2009; Ozsvár et al., 2021). Such a unique structural feature promotes unparalleled signaling capability to reach not only postsynaptic GABAAR but reliably activate extrasynaptic GABAAR as well as GABABR, triggering a biphasic mixture of fast and slow inhibition on target neurons (Tamás et al., 2003; Mańko et al., 2012).

Consistent with results from other cortical-like structures, NGFCs in the mouse BLA mainly express neuropeptide Y (NPY) and low levels of cholecystokinin (CCK) and somatostatin (Sst, Mańko et al., 2012; Rovira-Esteban et al., 2019; Vereczki et al., 2021). Such complex molecular profiling makes it challenging to isolate NGFCs from other BLA interneuron types by approaches based on classical interneuron molecular markers (Rovira-Esteban et al., 2019; Hájos, 2021; Vereczki et al., 2021). Although the BLA interneuron types have been more extensively characterized in the last decade (Capogna, 2014; Wolff et al., 2014; Vereczki et al., 2021), no available combination of techniques has made it possible to target NGFCs in the mouse BLA selectively. Hence, how BLA NGFCs contribute to the circuit operation and their vulnerability to behavioral disorders remain unknown. Recent studies have described a genetic marker named neuron-derived neurotrophic factor (NDNF) to effectively target NGFCs in the neocortex and hippocampus (Kuang et al., 2010; Tasic et al., 2016; Abs et al., 2018; Mercier et al., 2022). This study proposes and validates a strategy to selectively identify BLA NGFCs in mice by combining the Ndnf-IRES2-dgCre-D mouse line with GABAergic enhancer mdlx-dependent viral transfection.

Materials and methods

Experimental animal model and subject details

The Ndnf-IRES2-dgCre-D mice (hereafter NDNF-cre, Tasic et al., 2016) were purchased from the Jackson laboratory (stock #028536) and bred in the animal facility of Aarhus University. All mice were bred onto the C57BL/6J genetic background. Mice of both sexes (postnatal 8–13 weeks) were used for the experiments. Mice were given food and water *ad libitum* and group-housed on a 12 h light/dark cycle. All animal experiments were performed according to standard ethical guidelines and were approved by the Danish National Animal Experiment Committee (Permission Nos. 2017–15–0201–01201 and 2023-15-0201-01417).

Viral vectors

For labeling NDNF+ GABAergic neurons in the mouse BLA, we injected ssAAV-DJ/2-mDlx-HBB-chI-dlox-EGFP(rev)-dlox-WPRE-bGHp(A) (6 × 10^12 vector genomes/ml, v241-Dj, VVF Zurich, Switzerland). In a subset of experiments, ssAAV-DJ/2-mDlx-HBB-chI-dlox-hChR2(H134R)-mCherry(rev)-dlox-WPRE-bGHp(A) (6 × 10^12 vector genomes/ml, v317-Dj, VVF Zurich, Switzerland) was used for optogenetic assisted target cell mapping.

Stereotaxic injection

Mice (NDNF-cre, n = 25, 6–10 weeks old) were anesthetized using FMM: a mix of 0.05 mg/ml Fentanyl (0.05 mg/kg, Hameln), 5 mg/ml Midazolam (5 mg/kg, Hameln) and 1 mg/ml Medetomidine (0.5 mg/kg, VM Pharma). Mice were placed onto the stereotaxic frame (Kopf instruments) and maintained at a constant body temperature (34–36°C). A midline scalp incision (~0.8 cm) was made, and small craniotomies were made to target BLA bilaterally (coordinates from bregma: AP: −1.47 mm, ML: ± 3.4 mm, DV: −4.45, −4.7 mm). Coordinates were normalized to a bregma-lambda distance of 4.21 mm. A total of 250 nl/site of viruses were injected through a glass capillary (Harvard

Apparatus) by pulses of the Picospritzer III (Parker Hannifin). The pipette was raised 0.1 mm for an additional 10 min to minimize the upward flow of viral solution and was slowly withdrawn. After the viral injection, the incision was closed by suturing. Mice were given an antidote mix of 0.4 mg/ml Naloxone (1.2 mg/kg, B. Braun), 5 mg/ml Atipamelozone Hydrochloride (Revertor; 2.5 mg/kg, Vibrac AG), and 0.5 mg/ml Flumazenil (0.5 mg/kg, Sintetica).

Acute brain slice preparation and patch-clamp recording

Mice were anesthetized with isoflurane (Zoetis) and decapitated. The brains were removed, and 300 μm-thick coronal sections were prepared by a vibratome (Leica) using ice-cold sucrose-based artificial cerebrospinal fluid solution (ACSF, Ozsvár et al., 2021) containing (in mM) 84 NaCl, 25 NaHCO3, 1 NaH2PO4, 2.5 KCl, 25 glucose, 75 sucrose, 0.5 CaCl2, and 4 MgCl2. Slices were recovered in an oxygenated (95% O2 and 5% CO2) chamber containing sucrose and saline at 34°C for 30 min and then kept at 18°C. During the experiment, slices were transferred to a submerged chamber and perfused with oxygenated ACSF containing (in mM) 130 NaCl, 24 NaHCO3, 1 NaH2PO4, 4 KCl, 10 glucose, 1.3 CaCl2, and 0.9 MgCl2. A pE-300 (CoolLED) was used in a subset of experiments to provide optogenetic stimulations (1 mW). 10 μM gabazine (Tocris Bioscience) and 10 μM CGP-55845 (Tocris Bioscience) were added to the ACSF to isolate $GABA_AR$ and $GABA_BR$-dependent responses.

The recorded cells' epifluorescence expression and soma location were visually confirmed and selected under an infrared differential interference contrast (IR-DIC) CCD camera (Scientifica). Whole-cell patch-clamp recordings were made with a Multiclamp 700B amplifier (Molecular Devices). Recording electrodes (3–6 MΩ) were pulled from borosilicate glasses (outer diameter, 1.5 mm; 0.32 mm wall thickness; Harvard Apparatus) and filled with internal solution containing (in mM): 126 K-gluconate, 4 KCl, 4 Mg-ATP, 10 HEPES, 10 phosphocreatine, 0.3 Na-GTP, with or without 0.2 % biocytin (Thermo Fisher Scientific) with pH adjusted to 7.3 with KOH. The series resistance (Rs) was compensated to 70–80% in the voltage-clamp configuration. The data were discarded if Rs > 20 MΩ or Rs change > 20% throughout the recording. Signals were low-pass filtered at 4 kHz (four-pole Bessel) and sampled at 10 kHz using a digitizer (Digidata 1440A; Molecular Devices).

Immunohistochemistry (IHC)

For characterizing the molecular identities of the eGFP+ cells, virally injected NDNF-cre mice were anesthetized by FMM injection (I.P.) and perfused with ice-cold PBS plus heparin (50 mg/ml) followed by 4% PFA. Fixed brains were removed, post-fixed in 4% PFA for 1 h, and stored in 0.1M PBS. Brains were sliced into 60 or 100 μm coronal sections using a vibratome (Leica 1000S, Leica). Collected brain slices were washed with PBS and blocked in a buffer containing 10% normal donkey serum (NDS), 10% normal goat serum (NGS), 1% bovine serum albumin (BSA), and 0.5% PBST for 6 hr at 4°C. After blocking, slices were incubated with primary antibodies: Chicken Anti-GFP (1:1000, ab13970, Abcam), Rabbit Anti-NPY (1:3000, #22940, ImmunoStar), Rabbit Anti-Reln (1:1000, ab230820, Abcam) or Mouse Anti-Reln (1:1000, MAB5364, Merck) diluted in a solution containing: 1% NDS,1% GDS, 3% BSA, and 0.5% PBST for 48 hr at 4°C. After washing with 0.5% PBST, slices were incubated with secondary antibodies: Alexa 488 Donkey Anti-Chicken (1:400, AB_2340375, JacksonImmuno), Alexa 568 Donkey Anti-Rabbit (1:400, A10042, Invitrogen) diluted in antibody solution ON at 4°C. Slices were washed in 0.5% PBST and mounted onto gelatin-coated slides with DAPI-containing mounting medium (FluoromountG, Vectashield) and coverslipped. Images were taken as tile z-stacks under a 20× objective by an IX83 (Olympus) spinning-disk confocal microscope at 5 μm step size.

Morphological recovery of biocytin-filled cells

During recordings, eGFP+ neurons (n = 21 cells) were filled with biocytin (0.2%). After ∼15 min of recording, slices were fixed overnight with 4% PFA in PBS (0.1 M, pH 7.3). After washing with Alexa594-conjugated streptavidin (2 μl/ml; Invitrogen) in PBS containing 0.3% PBST for 2 hr at 4°C. After washing, slices were mounted onto gelatin-coated slides with DAPI-containing mounting medium (FluoromountG, Vectashield) and coverslipped.

Recovered neurons (12/21 cells) were examined by an LSM 980 Airyscan 2 (Zeiss) confocal microscope using a 40× 1.4 NA oil immersion objective. The morphology of the cells was reconstructed from a stack of 120–202 images per cell. Image stacks belonging to a single cell were imported into the Neuromantic 1.7.5 software (Myatt et al., 2012) for 3D reconstruction.

Data analysis and statistics

The electrophysiological data were recorded with pCLAMP 10.6 software (Molecular Devices). The electrophysiological recordings were analyzed by custom-written Matlab scripts (MathWorks). The properties of action potentials (APs) were analyzed from the first suprathreshold voltage responses triggered by depolarizing current injection steps (1 s). The AP peak, width, and afterhyperpolarization (AHP) amplitude were calculated from the onset point of the AP. The AP onset was determined by the projection of the intersection of two linear fits. The first line was fitted to the baseline 2 ms window, and the second line was fitted to the 5–30% of the rising phase of the AP. The rate of depolarization was measured as the linear fit of the trace 1 ms before the onset. The spike latency was calculated on rheobase traces with at least two APs by measuring the delay between the first AP onset time. The input resistance (Rin) was determined from the slope of a linear fit to the subthreshold voltage responses vs. current injection, where stimulating current ranged from −110pA to +30pA. The membrane time constant (τ) was calculated by fitting a single exponential to the voltage response from −110 pA current injection. The membrane capacitance was calculated as τ/Rin. The adaptation index was calculated as the

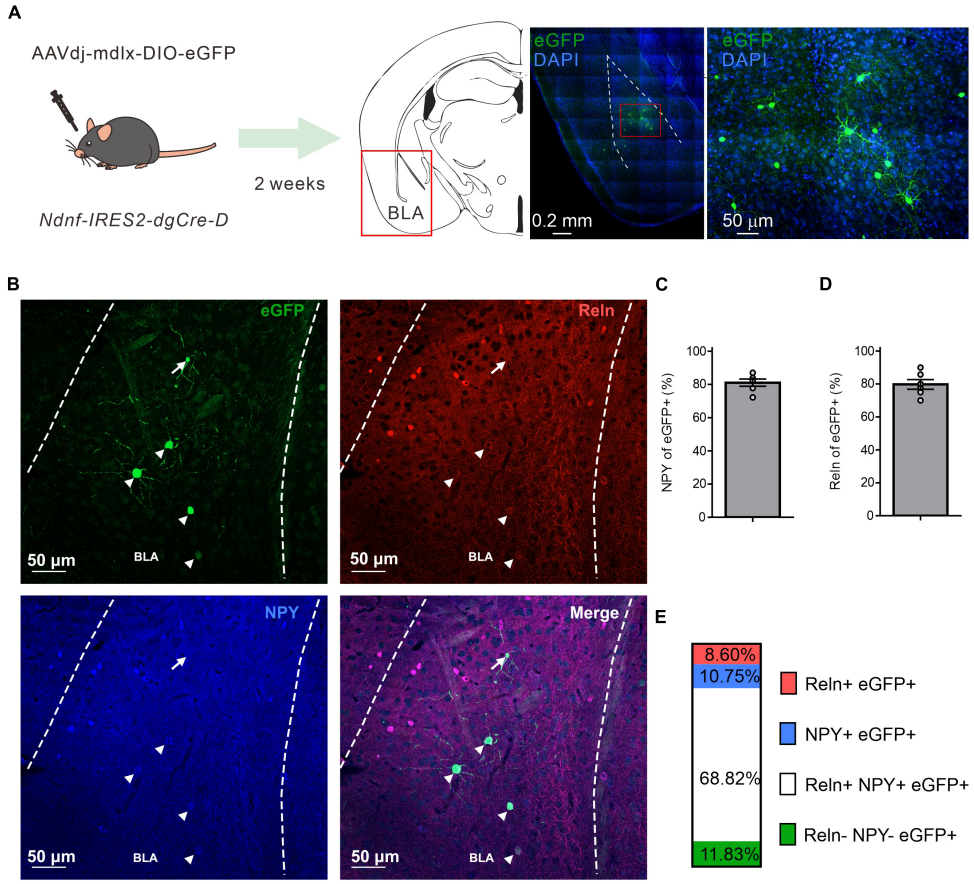

FIGURE 1
NDNF-expressing (NDNF+) GABAergic neurons in the mouse BLA. **(A)** Left, the scheme of genetic strategy; middle, a representative tile image of the amygdala region with eGFP amplification and DAPI staining; right, an enlarged view from the indicated red rectangular area from the middle image. **(B)** Confocal immunofluorescence micrographs showing amplified eGFP, NPY, and Reln expressions in the BLA. Arrowheads indicate triple immunopositive neurons, while the arrow depicts an eGFP-only cell. **(C)** Quantification bar graph of eGFP colocalization with NPY or **(D)** Reln (n = 6 sections, 3 mice, mean ± SEM). **(E)** Quantification bar graph of eGFP colocalization with NPY and Reln (n = 6 sections, 2 mice).

ratio of the first and last inter-spike interval, measured at the first suprathreshold voltage response. For the analysis of the retroaxonal barrage firing data, APs were detected by their peak. Statistic tests were performed and plotted using Prism 6.0 (GraphPad Software). The data distributions were examined by the d'Agostino-Pearson normality test. Statistical significance was tested by the Mann-Whitney U (MWU) test or Wilcoxon signed-rank (WSR) test, and the significance level (p) indicated. Data were presented as mean ± the standard error of the mean (SEM) unless otherwise stated. Significance levels were set at $p < 0.05$. ** denotes $p < 0.01$, *** denotes $p < 0.001$.

Results

NDNF+ GABAergic neurons in the mouse BLA

As NDNF has been proposed as an NGFC-specific genetic marker in the mouse neocortex and hippocampus (Abs et al., 2018; Tasic et al., 2018; Mercier et al., 2022), we aimed to determine if the NDNF-cre mouse line could be used to identify the NGFCs in other cortical-like structures such as BLA. Since there is a likelihood of a low-level Cre expression in PNs during development of the NDNF-cre mouse line (Guo et al., 2021; Mercier et al., 2022), we injected a recombinant adeno-associated viral vector rAAVdj-mdlx-DIO-eGFP carrying an enhanced green fluorescence protein driven by mdlx enhancer (Dimidschstein et al., 2016) in the BLA of NDNF-cre mice (**Figure 1A**). Two weeks later, we examined the eGFP expression pattern and found that the combinatory strategy yielded a sparse labeling pattern (10 - 30 cells per 100-µm section, **Figure 1A**). We further tested if the eGFP+ cells within the BLA expressed classical NGFC markers such as NPY and Reelin (Reln) by double and triple IHC (**Figure 1B**). We observed that most BLA eGFP+ cells express either NPY (81.02 ± 2.15%; **Figure 1C**) or Reln (79.75 ± 2.96%; **Figure 1D**) in double IHC experiments. In a subset of triple IHC experiments, we found that most BLA eGFP+ cells coexpress Reln and NPY (68.83%, **Figure 1E**), and only a minor fraction of cells that are negative to both NPY and Reln (11.82%, **Figure 1E**). Moreover, we did not observe eGFP+ cells with PN-like morphology. These results indicate that the BLA cells labeled by this combinatorial strategy are likely GABAergic interneurons and correspond to

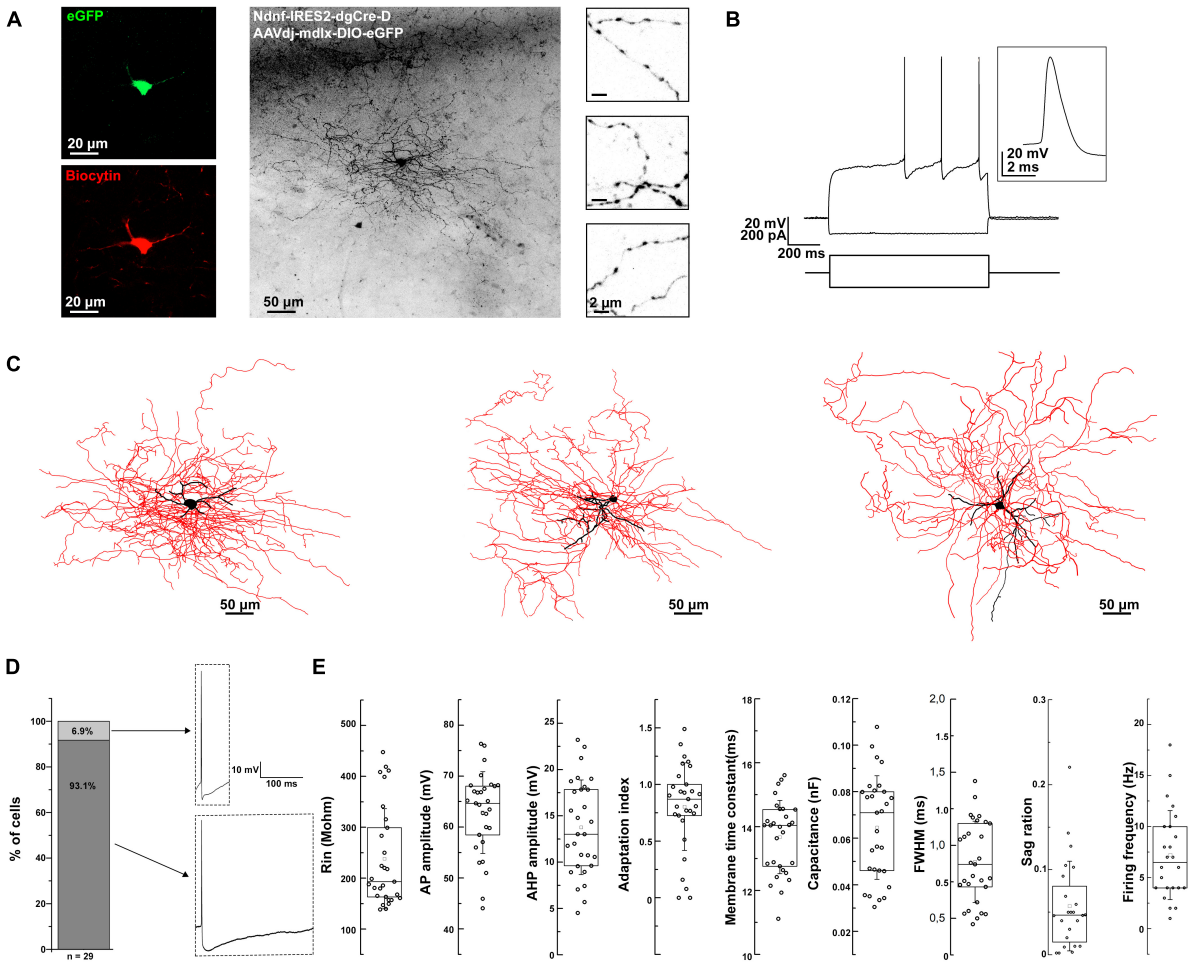

FIGURE 2
Morpho-electrophysiological property characterization of BLA NDNF+ GABAergic cells. **(A)** Confocal image stacks of a biocytin-labeled eGFP+ cell in the BLA of an NDNF-cre mouse. Confocal immunofluorescence micrographs showing immunohistochemically amplified eGFP and biocytin signals. On the right side, high-magnification insets show axonal segments with dense boutons. Scale bars, 20, 50, and 2 µm. **(B)** Passive and active electrophysiological responses from the same eGFP+ cell. Voltage responses to long-pulse current injections (−110 pA and +170 pA, 1 s). Inset, a single AP evoked by a short current pulse (+180 pA, 2 ms) recorded from the same cell. **(C)** Three-dimensional reconstruction of the same cell (left), and two additional reconstructions from separate experiments (middle and right). Black color represents the soma and dendrites, while red represents the axon. Scale bars 50 µm. **(D)** Left, a bar graph indicating that only a small fraction of BLA NDNF+ GABAergic interneurons exhibit non-NGFC AP properties such as sharp AHP peak and fast repolarization kinetics (n = 2 out of 29 cells). Right, representative APs from non-NGFC-like (top) and NGFC-like cells (bottom). **(E)** Box plots representing the different passive and active electrophysiological parameters from all recorded BLA NDNF+ GABAergic interneurons (n = 29 cells, n = 21 mice). For the boxplots, boxes represent the interquartile range, small squares at the center represent the mean, horizontal lines indicate the median, and whiskers show the SD.

one major uniform cell population with similar neurochemical identities.

Morpho-electrophysiological characterization of BLA NDNF+ GABAergic cells

Next, we wondered if the physiological and morphological properties of the virally labeled BLA NDNF+ GABAergic interneurons mainly corresponded to NGFCs. We performed whole-cell recordings from acute mouse brain slices and biocytin-assisted *post-hoc* morphological identification. The recorded neurons had small round or elongated somata, fine, short dendrites, and extensively branching axonal processes containing numerous varicosities (Figures 2A–C).

In terms of electrical properties, the vast majority of the recorded eGFP+ cells exhibited characteristic features such as a slow depolarizing ramp and following late spiking phenomenon similar to previously described BLA NGFCs (Figure 2B; Mańko et al., 2012). These cells had relatively low input resistance and fast membrane time constant. The action potentials (APs) were relatively broad, followed by a pronounced AHP (Figure 2D). The firing patterns were mostly moderately adapting during suprathreshold depolarization, with a relatively low firing frequency. Upon hyperpolarizing current injection, the recorded cells displayed a small sag ratio, indicating low/lack of h-current (Figure 2E and Table 1). Only a minor fraction of the recorded cells exhibited sharp AHP

TABLE 1 Summary of passive and active membrane properties of recorded BLA NDNF-GFP+ interneurons.

Parameters	Mean ± SEM (n = 29 cells)
Rin (MΩ)	238.21 ± 18.28
AP width (ms)	0.88 ± 0.05
AP amplitude (mV)	62.87 ± 1.49
AHP amplitude (mV)	13.77 ± 0.95
AP adaptation index	0.8 ± 0.072
Membrane time constant (ms)	13.67 ± 0.21
Cm (nF)	0.065 ± 0.004
Sag ratio	0.07 ± 0.01
Firing frequency (Hz)	6.9 ± 0.77

AHP, afterhyperpolarization; AP, action potential; Cm, membrane capacitance; Rin, input resistance.

peak and fast repolarization kinetics, compared to the vast majority displaying remarkably slow repolarization kinetics (Figure 2D). In conclusion, the electrophysiological features of the virally labeled BLA NDNF+ GABAergic interneurons resemble remarkably similar features to previously described BLA NGFCs.

Retroaxonal barrage firing in BLA NDNF+ GABAergic interneurons

NGFCs in the neocortex and hippocampus exhibit persistent firing upon continuous depolarization (Suzuki et al., 2014; Chittajallu et al., 2020). We tested whether BLA NGFCs exhibited similar persistent firing properties in some experiments. We prepared acute brain slices and performed whole-cell patch-clamp recordings from virally labeled NDNF+ cells in BLA using NDNF-cre mice injected with AAVdj-mdlx-DIO-eGFP (Figure 3A). The persistent firing was induced using repetitive positive current injection steps (+300 pA, 1 s, Figure 3B). We induced the barrage firing in 13 of 17 tested cells. Phase plots revealed that triggered APs and retro-axonal firing action potentials (rAPs) had two components: an initial component represented spiking in the axon and a second component that overlapped with the current-evoked spikes, indicative of a somato-dendritic spike following the initial, axonally initiated spike (Figure 3C). Further analysis revealed distinct characteristics in the subthreshold rate of depolarization and the AP threshold of rAPs compared to spikes evoked by somatic current injection (Rózsa et al., 2023). The rAPs during the persistent firing showed a lower subthreshold rate of depolarization compared to APs during repetitive current injection steps (0.99 ± 0.65 vs. 1.9 ± 0.67 mV/ms, mean ± SD, WSR-test, $p < 0.001$; $n = 8$ cells, Figures 3D, E). During persistent firing, the rAPs exhibited a more hyperpolarized AP threshold than somatic APs (population: −58.3 ± 2.34 vs. −42.13 ± 2.43 mV, WSR-test, $p < 0.001$, Figure 3F). The subthreshold rate of depolarization and threshold of the APs proved to reliably separate the somatic and axon-initiated APs (Figure 3G).

Functional assessment of BLA NDNF+ GABAergic cells by optogenetic

NGFCs have been reported in different brain areas to provide distinctive biphasic $GABA_AR$ and $GABA_BR$-mediated synaptic inhibition with slow kinetics on target cells (Price et al., 2005; Mańko et al., 2012). To confirm the synaptic output of BLA NDNF+ cells, we expressed Channelrhodopsin-2 (ChR2) in BLA NDNF+ cells by injecting AAVdj-mdlx-DIO-ChR2-mCherry in the BLA of NDNF-cre mice (Figure 4A). After 3–4 weeks, we first tested the ChR2 expression by performing whole-cell recordings on the epifluorescence-identified mCherry+ cells (Figure 4B). The mCherry+ cells also demonstrated similar NGFC-like morphology as previously presented, and brief light pulse trains (5 ms, 10 Hz) reliably triggered APs in mCherry+ cells (3 of 3 tested cells, $n = 2$ mice; Figures 4B–E).

After confirming successful optogenetic control over the BLA NDNF+ cell population, we performed whole-cell recordings on BLA PNs to test the potential synaptic connection. We found slow IPSCs were elicited in BLA PNs upon single pulse or 10 Hz pulse trains (10 of 10 cells, $n = 5$ mice; Figures 4F–H). In a subset of experiments, we further blocked $GABA_AR$ using gabazine (10 μM), which effectively abolished the fast component of the light-evoked PSCs, and the remaining slow outward component can be further abolished by subsequent application of selective $GABA_BR$ antagonist, CGP-55845 (10 μM, Figure 4H). No inward current was observed after the blockade of GABAAR- and GABABR-mediated IPSCs (3 of 3 cells, $n = 2$ mice; Figure 4H). These results demonstrate the optogenetic activation of BLA NDNF cell populations produces both $GABA_AR$- and $GABA_BR$-mediated IPSCs. Lastly, we tested if the barrage firing of BLA NDNF+ cells can be induced by optogenetic activation. In 4 out of 4 ChR2 expressing NDNF+ cells under cell-attached configuration, the optogenetic stimulation triggered the retroaxonal barrage firing (0.6 Hz, 1 s; Figure 4I).

Discussion

The key obstacles to understanding amygdala function include the diversity of cell types, the complex connectivity, and its role in behavior. In the past decade, the advanced knowledge of developmental genetic profiling has made systematic screening and dissecting of amygdala cell types possible (Huang, 2014; Fishell and Kepecs, 2019). Here, we report an approach for specifically targeting the neurogliaform cells in the mouse BLA by combining viral transfection and the NDNF-cre transgenic mouse line.

Our results indicate that a precise Cre-mediated genetic recombination could facilitate cell type investigation in the brain. The mdlx enhancer may prevent the leaky expression of Cre in the excitatory neurons of NDNF-cre mice reported in the hippocampus (Guo et al., 2021; Mercier et al., 2022). In this study, we did not detect BLA eGFP+ cells with PN-like morphology (Figures 1, 2), nor did we observe any signature of evoked putative postsynaptic glutamatergic responses from recorded BLA PNs by optogenetic activating virally labeled BLA NDNF+ cells (Figure 4H). We also do not record any ChR2-mediated photocurrent directly from BLA PNs ($n = 10$ cells from 5 mice). These results suggest absent

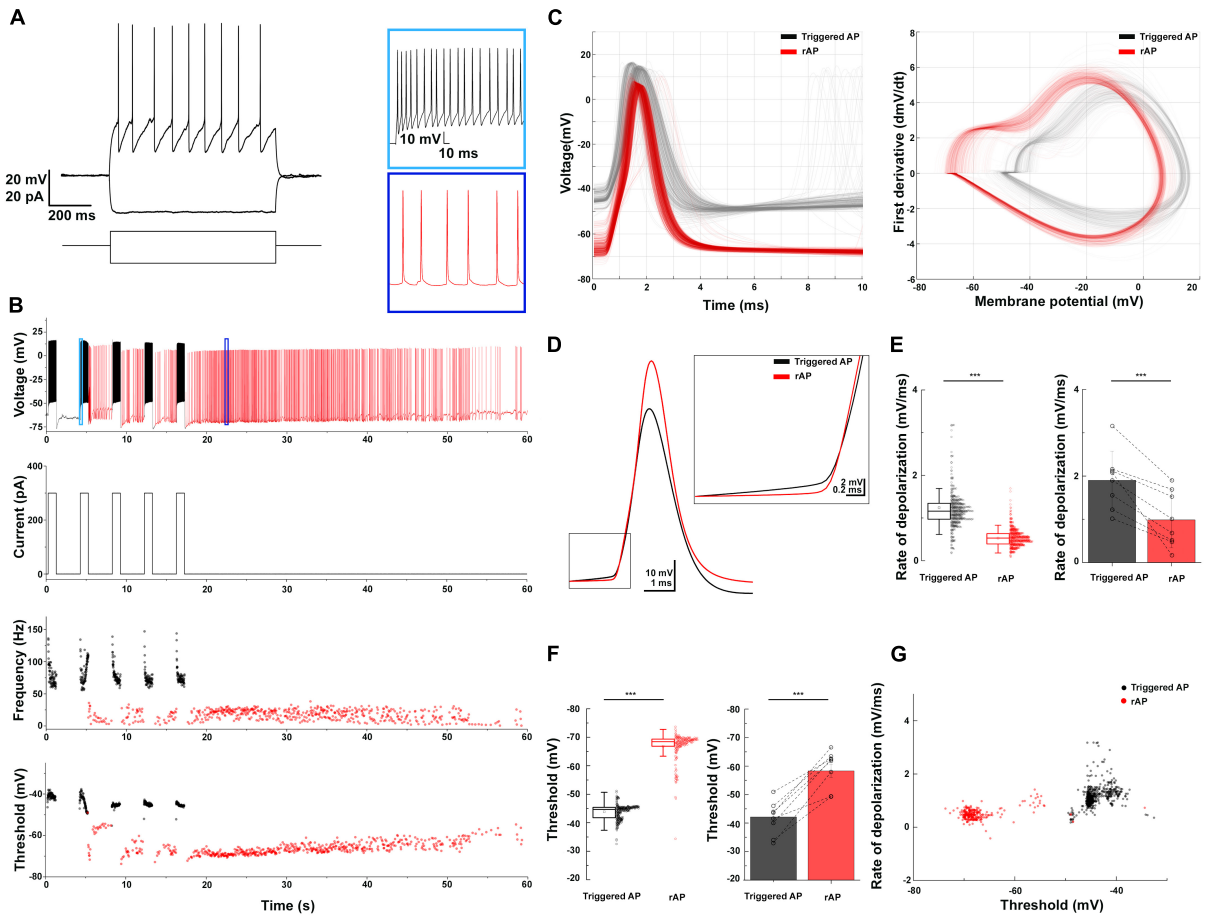

FIGURE 3
Retroaxonal barrage firing in BLA NDNF+ GABAergic neurons. **(A)** The representative firing pattern of a recorded NDNF+ interneuron in the BLA. **(B)** The induced retroaxonal barrage firing after repetitive suprathreshold current injection (+300 pA, 1 s). Light and dark blue boxes show enlarged sections of triggered and retroaxonal barrage firing patterns. The current injection protocol is indicated below. Scatter plots show the frequency and AP threshold throughout the stimulation and retroaxonal barrage firing period from a single cell. Current injection-triggered APs are presented in black, and spontaneous rAPs are depicted in red. **(C)** Triggered APs and rAPs recorded from the single cell shown on panel **(B)**. Left, superimposed triggered APs (black) and rAPs (red). Right, phase plot of triggered APs (black) and rAPs (red). **(D)** Averaged traces of the triggered AP (black) and rAP (red) from a single cell show distinct rates of depolarization before the AP onset. **(E)** Left, a box plot of the triggered APs vs. rAPs depolarization rate values from a single cell (1.22 ± 0.71 vs. 0.5 ± 0.21 mV/ms, mean ± SD, MWU-test, $p < 0.001$); Right, a bar plot shows the population average (1.9 ± 0.67 vs. 0.99 ± 0.65 mV/ms, mean ± SD, WSR-test, $p < 0.001$; $n = 8$ cells). **(F)** Left, a box plot of the triggered APs vs. rAPs threshold values from a single cell (−43.84 ± 2.59 mV vs. −66.85 ± 4.87 mV, mean ± SD, MWU-test, $p < 0.001$); Right, a bar plot shows the population average (−42.13 ± 2.43 mV vs. −58.3 ± 2.34 mV, mean ± SD, WSR-test, $p < 0.001$). For the boxplots, boxes represent the interquartile range, small squares at the center represent the mean, horizontal lines indicate the median, and whiskers show the SD. **(G)** A 2D scatter plot showing clear segregation of triggered APs and rAPs using AP threshold and rate of depolarization from a single cell.

/undetectable Cre expression or Cre-dependent recombination occurred in BLA PNs. Other alternative approaches, such as restricting the active time window of Cre recombinase using tamoxifen-inducible Cre, may also be applied to enhance the target cell selectivity (Cre-ERT2, see Abs et al., 2018).

NGFCs in different brain areas express NDNF (Tasic et al., 2016; Abs et al., 2018; Poorthuis et al., 2018; Mercier et al., 2022). In this study, the vast majority of BLA NDNF+ cells showed similar passive and active electrophysiological properties to previously reported BLA NGFCs (**Figure 2E** and **Table 1**; Mańko et al., 2012; Vereczki et al., 2021). However, a small fraction of the cases exhibit sharper AHP and faster repolarization (**Figure 2D**). Since we were unable to recover the anatomical features of these few cells, it remains unknown whether there are electrophysiological heterogenous NDNF+ cells or result from unspecific labeling.

NDNF is highly enriched in the superficial layer of the neocortex and does not largely overlap with major interneuron neurochemical markers such as parvalbumin, Sst, and vasoactive intestinal peptide (Abs et al., 2018; Schuman et al., 2019). Nevertheless, the potential heterogeneity of NDNF+ GABAergic interneuron populations has also been described in the mouse somatosensory cortex as NDNF expression can be detected in GABAergic canopy cells, which are functionally distinct from NGFCs (Schuman et al., 2019). Furthermore, in non-cortical-like brain structures, such as lateral habenula, NDNF expression fails to selectively label NGFCs (Webster et al., 2021), while NGFCs derived from MGE and CGE show distinct molecular properties (Tricoire et al., 2010, 2011; Overstreet-Wadiche and McBain, 2015; Niquille et al., 2018). Further investigation is thus required to determine whether the combinatory strategy presented in this

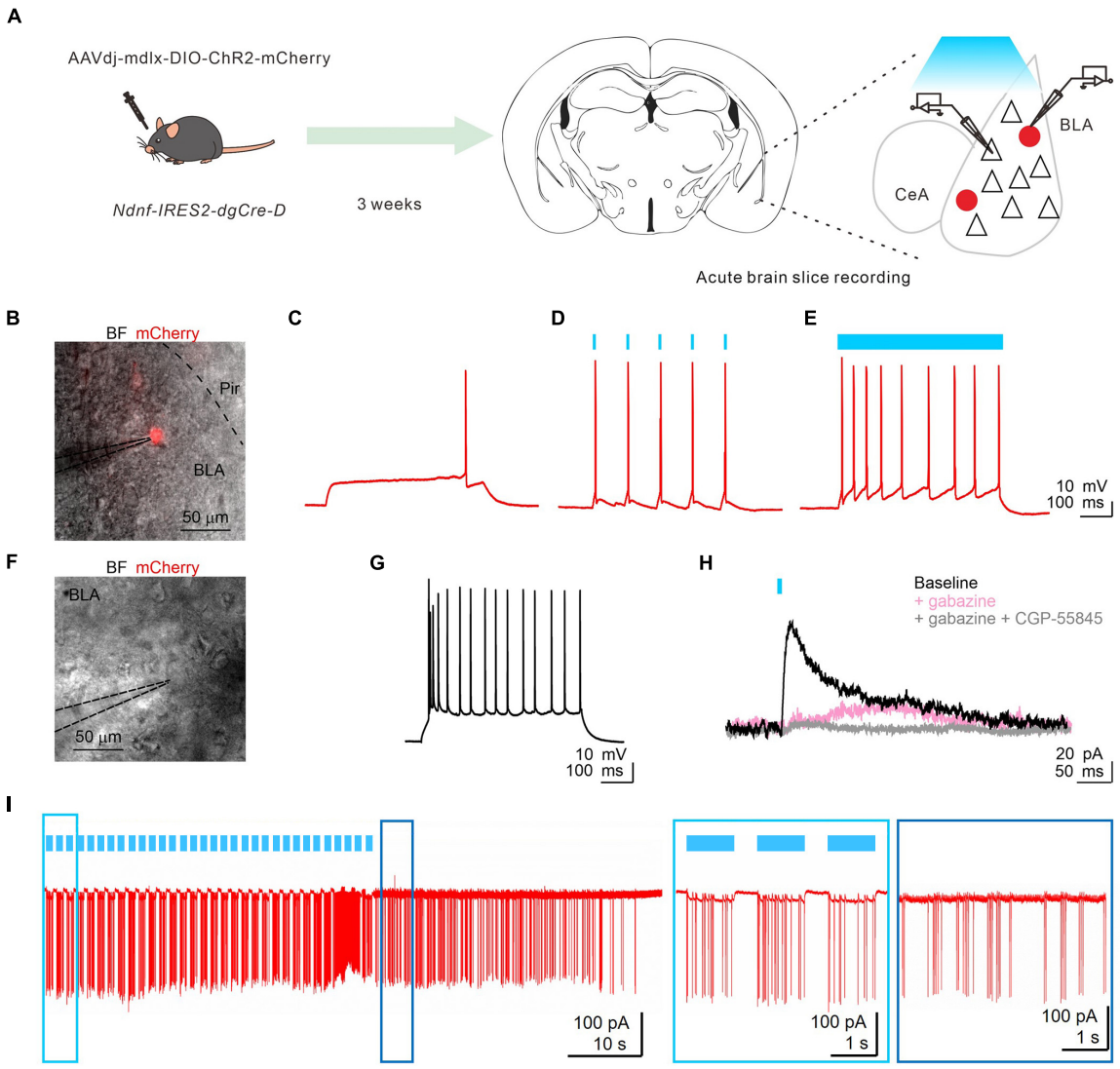

FIGURE 4
Functional assessment of BLA NDNF+ GABAergic cells by optogenetic. **(A)** The experimental paradigm. **(B)** An overlay image of bright field (BF) and red fluorescence signal of a representative recorded BLA mCherry+ neuron. **(C)** The rheobase response upon current injection (+80 pA, 1 s). **(D)** The membrane responses of the recorded neuron are shown on panel **(C)** upon short (10 Hz, 5 ms, 5 pulses) and **(E)** long pulse (1 s) photostimulation. **(F)** An overlay image of BF and red fluorescence signal of a representative recorded BLA mCherry(-) PN. **(G)** The firing pattern of the PN is shown on panel **(F)** upon a current injection step (+100 pA, 1 s). **(H)** PN responses to 10-Hz light pulse trains under voltage clamp configuration. Photostimulation (single pulses, 5 ms, 0.016 Hz) evoked outward currents at −60 mV (black), which could be partly blocked by bath application of GABAAR antagonist, gabazine (gabazine, 10 µM, pink). The residual slow outward current was eliminated by applying selective $GABA_BR$ antagonist, CGP-55845 (gray, n = 3 of 3 tested cells, n = 2 mice). No light-evoked inward currents were observed from recorded PNs throughout the optogenetic assessment (n = 10 cells, n = 5 mice). **(I)** Optogenetic induction of retroaxonal barrage firing with repetitive blue light stimulation (1 s, 0.6 Hz) when recording from ChR2 expressing NDNF+ neurons in the cell-attached configuration. Light and dark blue boxes show enlarged sections of triggered and retroaxonal barrage firing patterns. CeA, central amygdala; Pir, piriform cortex.

study covers the entire BLA NGFC population. Moreover, a small fraction of BLA NDNF+ cells do not express NPY nor Reln; therefore, it remains unclear whether NDNF+ cells in the BLA form a homogenous population or compose a range of NGFC types, as has been comprehensively delineated in the neocortex (Gomez et al., 2023).

Retroaxonal barrage firing is a conserved feature reported in neocortical and hippocampal areas across species. This phenomenon has predominantly been observed in NGFCs (Suzuki et al., 2014; Wang et al., 2015; Chittajallu et al., 2020; Rózsa et al., 2023). We found that 81% (n = 21) of BLA NGFCs exhibited persistent firing properties, indicating a high susceptibility to integrate prolonged activity in the local microcircuit. Furthermore, we validated the feasibility of eliciting persistent firing by optogenetic activation, proposing a potential application to investigate the role of BLA NGFCs' persistent firing activity in behaviors. Persistent activity of NGFCs in the BLA could be a compensatory internal mechanism that suppresses local activity and prevents overexcitation (Suzuki et al., 2014). However, it is well-reported that NGFC synapses pose strong short-term use-dependent depression; hence, the functional relevance and effectiveness of synaptic inhibition are arguable (Tamás et al., 2003;

Karayannis et al., 2010). In the BLA, ∼80% of NDNF+ GABAergic interneurons co-express NPY (**Figures 1C, E**). Therefore, the potential release of vasoactive substances or other molecules such as insulin (Molnár et al., 2014) during persistent firing may serve a regulatory role in fine-tuning energy and oxygen supplies in the micro-environment by increased network activity (Taube and Bassett, 2003; Thompson et al., 2003; Echagarruga et al., 2020). However, the exact mechanisms of barrage firing, the physiological entrainment of BLA NDNF+ interneuron's persistent firing, and its behavioral relevance under possible pathophysiological conditions deserve further investigation.

When examining the synaptic output of BLA NDNF+ GABAergic interneurons using optogenetics, we confirmed the characteristic slow inhibition from postsynaptic PNs, a feature of NGFCs described earlier (Tamás et al., 2003; Szabadics et al., 2007; Oláh et al., 2009; Mańko et al., 2012; Rovira-Esteban et al., 2019). Indeed, optogenetic activation is sufficient to recruit postsynaptic $GABA_BR$ in addition to the $GABA_AR$ on the target cells, contrary to any other known BLA interneuron types (**Figure 4H**; Woodruff and Sah, 2007; Vereczki et al., 2021).

Tonic inhibition plays a significant role in regulating the overall excitability and information processing of the brain circuitry (Marowsky et al., 2012). Such inhibition may serve as the offset control by suppressing spontaneous activity of PNs and enhancing the signal-to-noise ratio of incoming stimuli (Häusser and Clark, 1997; Semyanov et al., 2004; Krook-Magnuson and Huntsman, 2005). This fine-tuning helps to shape the population activity and facilitates the precision of temporal association of distinct salient inputs within the amygdala. A decrease in tonic inhibition can lead to hyperexcitability and altered network dynamics, which may contribute to pathological conditions like anxiety disorders or epilepsy (Fritsch et al., 2009; Tasan et al., 2011; Babaev et al., 2018). In the central amygdala, extrasynaptic inhibition is tightly linked to anxiety levels (Lange et al., 2014; Botta et al., 2015). However, the dynamics of BLA tonic inhibition in different behaviors and their causal relationships remain poorly understood. Since NGFCs are considered one of the major contributors to slow-phasic and tonic GABA release in several brain regions, including BLA (Capogna, 2011, 2014; Hájos, 2021), selective manipulation of BLA NGFC activity may help to elucidate the role of BLA tonic inhibition in distinct behaviors by future optogenetic and chemogenetic interrogations.

Data availability statement

The original contributions presented in this study are included in this article/supplementary material, further inquiries can be directed to the corresponding author.

Ethics statement

All animal experiments were performed according to standard ethical guidelines and were approved by the Danish National Animal Experiment Committee (Permission Nos. 2017-15-0201-01201 and 2023-15-0201-01417).

Author contributions

AO: Conceptualization, Data curation, Formal analysis, Investigation, Methodology, Software, Validation, Visualization, Writing – original draft, Writing – review and editing. MCS: Conceptualization, Investigation, Methodology, Writing – review and editing. MDS: Investigation, Methodology, Writing – review and editing, Funding acquisition. W-HH: Conceptualization, Data curation, Formal analysis, Investigation, Methodology, Project administration, Software, Supervision, Validation, Visualization, Writing – original draft, Writing – review and editing. MC: Conceptualization, Funding acquisition, Investigation, Project administration, Supervision, Writing – original draft.

Funding

The author(s) declare financial support was received for the research, authorship, and/or publication of this article. This study was supported by the Independent Research Fund Denmark (DFF-37741 and DFF-29161 to MC) and the Lundbeck Foundation (R325-2019-1490 to MC and R249-2017-1614 to MDS).

Acknowledgments

We thank the Viral Vector Facility (VVF) of the Neuroscience Center Zurich (ZNZ) for producing the viral vectors used in this study. We also acknowledge the AU Bioimaging Core Facility and the Department of Molecular Biology and Genetics Bioimaging facility for using the equipment and the daily support from animal facilities at the Department of Biomedicine, Aarhus University. We also thank Dr. Kai-Yi Wang and all the members of Marco Capogna's lab for their comments and feedback on the manuscript.

Conflict of interest

The authors declare that the research was conducted in the absence of any commercial or financial relationships that could be construed as a potential conflict of interest.

Publisher's note

References

Abs, E., Poorthuis, R. B., Apelblat, D., Muhammad, K., Pardi, M. B., and Enke, L. (2018). Learning-related plasticity in dendrite-targeting layer 1 interneurons. *Neuron* 100, 684–699.e6. doi: 10.1016/j.neuron.2018.09.001

Babaev, O., Piletti Chatain, C., and Krueger-Burg, D. (2018). Inhibition in the amygdala anxiety circuitry. *Exp. Mol. Med.* 50, 1–6.

Botta, P., Demmou, L., Kasugai, Y., Markovic, M., Xu, C., and Fadok, J. P. (2015). Regulating anxiety with extrasynaptic inhibition. *Nat. Neurosci.* 18, 1493–1500.

Calhoon, G. G., and Tye, K. M. (2015). Resolving the neural circuits of anxiety. *Nat. Neurosci.* 18, 1394–1404.

Capogna, M. (2011). Neurogliaform cells and other interneurons of stratum lacunosum-moleculare gate entorhinal-hippocampal dialogue. *J. Physiol.* 589, 1875–1883. doi: 10.1113/jphysiol.2010.201004

Capogna, M. (2014). GABAergic cell type diversity in the basolateral amygdala. *Curr. Opin. Neurobiol.* 26, 110–116.

Chittajallu, R., Auville, K., Mahadevan, V., Lai, M., Hunt, S., and Calvigioni, D. (2020). Activity-dependent tuning of intrinsic excitability in mouse and human neurogliaform cells. *ELife* 9:e57571. doi: 10.7554/eLife.57571

d'Aquin, S., Szonyi, A., Mahn, M., Krabbe, S., Gründemann, J., and Lüthi, A. (2022). Compartmentalized dendritic plasticity during associative learning. *Science* 376:eabf7052.

Dimidschstein, J., Chen, Q., Tremblay, R., Rogers, S. L., Saldi, G. A., and Guo, L. (2016). A viral strategy for targeting and manipulating interneurons across vertebrate species. *Nat. Neurosci.* 19, 1743–1749.

Duvarci, S., and Pare, D. (2014). Amygdala microcircuits controlling learned fear. *Neuron* 82, 966–980. doi: 10.1016/j.neuron.2014.04.042

Echagarruga, C. T., Gheres, K. W., Norwood, J. N., and Drew, P. J. (2020). nNOS-expressing interneurons control basal and behaviorally evoked arterial dilation in somatosensory cortex of mice. *ELife* 9:e60533. doi: 10.7554/eLife.60533

Ehrlich, I., Humeau, Y., Grenier, F., Ciocchi, S., Herry, C., and Lüthi, A. (2009). Amygdala inhibitory circuits and the control of fear memory. *Neuron* 62, 757–771.

Farrant, M., and Nusser, Z. (2005). Variations on an inhibitory theme: phasic and tonic activation of GABA a receptors. *Nat. Rev. Neurosci.* 6, 215–229. doi: 10.1038/nrn1625

Fishell, G., and Kepecs, A. (2019). Interneuron types as attractors and controllers. *Annu. Rev. Neurosci.* 43, 1–30.

Fritsch, B., Qashu, F., Figueiredo, T. H., Aroniadou-Anderjaska, V., Rogawski, M. A., and Braga, M. F. M. (2009). Pathological alterations in GABAergic interneurons and reduced tonic inhibition in the basolateral amygdala during epileptogenesis. *Neuroscience* 163, 415–429. doi: 10.1016/j.neuroscience.2009.06.034

Gomez, L., Cadilhac, C., Prados, J., Mule, N., Jabaudon, D., and Dayer, A. (2023). Developmental emergence of cortical neurogliaform cell diversity. *Development* 150:dev201830.

Guo, J., Oliveros, H. C., Oh, S. J., Liang, B., Li, Y., and Kavalali, E. T. (2021). Stratum lacunosum-moleculare interneurons of the hippocampus coordinate memory encoding and retrieval. *bioRxiv [Preprint]* doi: 10.1101/2021.06.11.448103

Hájos, N. (2021). Interneuron types and their circuits in the Basolateral Amygdala. *Front. Neural Circuits* 15:687257. doi: 10.3389/fncir.2021.687257

Häusser, M., and Clark, B. A. (1997). Tonic synaptic inhibition modulates neuronal output pattern and spatiotemporal synaptic integration. *Neuron* 19, 665–678. doi: 10.1016/s0896-6273(00)80379-7

Huang, Z. J. (2014). Toward a genetic dissection of cortical circuits in the mouse. *Neuron* 83, 1284–1302. doi: 10.1016/j.neuron.2014.08.041

Janak, P. H., and Tye, K. M. (2015). From circuits to behaviour in the amygdala. *Nature* 517, 284–292.

Karayannis, T., Elfant, D., Huerta-Ocampo, I., Teki, S., Scott, R. S., and Rusakov, D. A. (2010). Slow GABA transient and receptor desensitization shape synaptic responses evoked by hippocampal neurogliaform cells. *J. Neurosci.* 30, 9898–9909. doi: 10.1523/JNEUROSCI.5883-09.2010

Krabbe, S., Gründemann, J., and Lüthi, A. (2018). Amygdala inhibitory circuits regulate associative fear conditioning. *Biol. Psychiatry* 83, 800–809.

Krook-Magnuson, E. I., and Huntsman, M. M. (2005). Excitability of cortical neurons depends upon a powerful tonic conductance in inhibitory networks. *Thalamus Relat. Syst.* 3, 115–120. doi: 10.1017/S1472928807000192

Kuang, X. L., Zhao, X. M., Xu, H. F., Shi, Y. Y., Deng, J. B., and Sun, G. T. (2010). Spatio-temporal expression of a novel neuron-derived neurotrophic factor (NDNF) in mouse brains during development. *BMC Neurosci.* 11:137. doi: 10.1186/1471-2202-11-137

Lange, M. D., Jüngling, K., Paulukat, L., Vieler, M., Gaburro, S., Sosulina, L., et al. (2014). Glutamic acid decarboxylase 65: a link between GABAergic synaptic plasticity in the lateral amygdala and conditioned fear generalization. *Neuropsychopharmacology* 39, 2211–2220. doi: 10.1038/npp.2014.72

LeDoux, J. (2007). The amygdala. *Curr. Biol.* 17, R868–R874. doi: 10.1016/j.cub.2007.08.005

LeDoux, J. (2012). Rethinking the emotional brain. *Neuron* 73, 653–676.

Ledoux, J. E. (2000). Emotion circuits in the brain. *Annu. Rev. Neurosci.* 23, 155–184.

Mahoney, C. E., Agostinelli, L. J., Brooks, J. N. K., Lowell, B. B., and Scammell, T. E. (2017). GABAergic neurons of the central amygdala promote cataplexy. *J. Neurosci.* 37, 3995–4006.

Mańko, M., Bienvenu, T. C. M., Dalezios, Y., and Capogna, M. (2012). Neurogliaform cells of amygdala: a source of slow phasic inhibition in the basolateral complex. *J. Physiol.* 590, 5611–5627. doi: 10.1113/jphysiol.2012.236745

Marowsky, A., Rudolph, U., Fritschy, J. M., and Arand, M. (2012). Tonic inhibition in principal cells of the amygdala: a central role for α3 subunit-containing GABA A receptors. *J. Neurosci.* 32, 8611–8619.

Mercier, M. S., Magloire, V., Cornford, J. H., and Kullmann, D. M. (2022). Long-term potentiation in neurogliaform interneurons modulates excitation-inhibition balance in the temporoammonic pathway. *J. Physiol.* 600, 4001–4017. doi: 10.1113/JP282753

Molnár, G., Faragó, N., Kocsis, ÁK., Rózsa, M., Lovas, S., and Boldog, E. (2014). GABAergic neurogliaform cells represent local sources of insulin in the cerebral cortex. *J. Neurosci.* 34, 1133–1137. doi: 10.1523/JNEUROSCI.4082-13.2014

Moscarello, J. M., and Penzo, M. A. (2022). The central nucleus of the amygdala and the construction of defensive modes across the threat-imminence continuum. *Nat. Neurosci.* 25, 999–1008. doi: 10.1038/s41593-022-01130-5

Myatt, D. R., Hadlington, T., Ascoli, G. A., and Nasuto, S. J. (2012). Neuromantic - from semi-manual to semi-automatic reconstruction of neuron morphology. *Front. Neuroinformatics* 6:4. doi: 10.3389/fninf.2012.00004

Niquille, M., Limoni, G., Markopoulos, F., Cadilhac, C., Prados, J., Holtmaat, A., et al. (2018). Neurogliaform cortical interneurons derive from cells in the preoptic area. *ELife* 7:e32017. doi: 10.7554/eLife.32017

Oláh, S., Füle, M., Komlósi, G., Varga, C., Báldi, R., Barzó, P., et al. (2009). Regulation of cortical microcircuits by unitary GABA-mediated volume transmission. *Nature* 461, 1278–1281. doi: 10.1038/nature08503

Overstreet-Wadiche, L., and McBain, C. J. (2015). Neurogliaform cells in cortical circuits. *Nat. Rev. Neurosci.* 16, 458–468.

Ozsvár, A., Komlósi, G., Oláh, G., Baka, J., Molnár, G., and Tamás, G. (2021). Predominantly linear summation of metabotropic postsynaptic potentials follows coactivation of neurogliaform interneurons. *ELife* 10:e65634. doi: 10.7554/eLife.65634

Pape, H.-C., and Pare, D. (2010). Plastic synaptic networks of the amygdala for the acquisition, expression, and extinction of conditioned fear. *Physiol. Rev.* 90, 419–463.

Pitkänen, A., Savander, V., and LeDoux, J. E. (1997). Organization of intra-amygdaloid circuitries in the rat: an emerging framework for understanding functions of the amygdala. *Trends Neurosci.* 20, 517–523. doi: 10.1016/s0166-2236(97)01125-9

Poorthuis, R. B., Muhammad, K., Wang, M., Verhoog, M. B., Junek, S., Wrana, A., et al. (2018). Rapid neuromodulation of layer 1 interneurons in human neocortex. *Cell Rep.* 23, 951–958. doi: 10.1016/j.celrep.2018.03.111

Price, C. J., Cauli, B., Kovacs, E. R., Kulik, A., Lambolez, B., Shigemoto, R., et al. (2005). Neurogliaform neurons form a novel inhibitory network in the hippocampal CA1 area. *J. Neurosci.* 25, 6775–6786. doi: 10.1523/JNEUROSCI.1135-05.2005

Rovira-Esteban, L., Gunduz-Cinar, O., Bukalo, O., Limoges, A., Brockway, E., and Müller, K. (2019). Excitation of diverse classes of cholecystokinin interneurons in the basal amygdala facilitates fear extinction. *ENeuro* 6:ENEURO.0220-19.2019. doi: 10.1523/ENEURO.0220-19.2019

Rózsa, M., Tóth, M., Oláh, G., Baka, J., Lákovics, R., Barzó, P., et al. (2023). Temporal disparity of action potentials triggered in axon initial segments and distal axons in the neocortex. *Sci. Adv.* 9:eade4511. doi: 10.1126/sciadv.ade4511

Schuman, B., Machold, R., Hashikawa, Y., Fuzik, J., Fishell, G., and Rudy, B. (2019). Four unique interneuron populations reside in neocortical layer 1. *J. Neurosci.* 39, 1613–1618. doi: 10.1523/JNEUROSCI.1613-18.2018

Semyanov, A., Walker, M. C., Kullmann, D. M., and Silver, R. A. (2004). Tonically active GABAA receptors: modulating gain and maintaining the tone. *Trends Neurosci.* 27, 262–269.

Suzuki, N., Tang, C. S. M., and Bekkers, J. M. (2014). Persistent barrage firing in cortical interneurons can be induced in vivo and may be important for the suppression of epileptiform activity. *Front. Cellular Neurosci.* 8:76. doi: 10.3389/fncel.2014.00076

Szabadics, J., Tamás, G., and Soltesz, I. (2007). Different transmitter transients underlie presynaptic cell type specificity of GABAA,slow and GABAA, fast. *Proc. Natl. Acad. Sci. U S A.* 104, 14831–14836. doi: 10.1073/pnas.0707204104

Tamás, G., Lörincz, A., Simon, A., and Szabadics, J. (2003). Identified sources and targets of slow inhibition in the neocortex. *Science* 299, 1902–1905. doi: 10.1126/science.1082053

Tasan, R. O., Bukovac, A., Peterschmitt, Y. N., Sartori, S. B., Landgraf, R., Singewald, N., et al. (2011). Altered GABA transmission in a mouse model of increased trait anxiety. *Neuroscience* 183, 71–80. doi: 10.1016/j.neuroscience.2011.03.051

Tasic, B., Menon, V., Nguyen, T. N., Kim, T. K., Jarsky, T., and Yao, Z. (2016). Adult mouse cortical cell taxonomy revealed by single cell transcriptomics. *Nat. Neurosci.* 19, 335–346.

Tasic, B., Yao, Z., Graybuck, L. T., Smith, K. A., Nguyen, T. N., and Bertagnolli, D. (2018). Shared and distinct transcriptomic cell types across neocortical areas. *Nature* 563, 72–78. doi: 10.1038/s41586-018-0654-5

Taube, J. S., and Bassett, J. P. (2003). Persistent neural activity in head direction cells. *Cereb. Cortex* 13, 1162–1172.

Thompson, J. K., Peterson, M. R., and Freeman, R. D. (2003). Single-neuron activity and tissue oxygenation in the cerebral cortex. *Science* 299, 1070–1073.

Tricoire, L., Pelkey, K. A., Daw, M. I., Sousa, V. H., Miyoshi, G., and Jeffries, B. (2010). Common origins of hippocampal ivy and nitric oxide synthase expressing neurogliaform cells. *J. Neurosci.* 30, 2165–2176. doi: 10.1523/JNEUROSCI.5123-09.2010

Tricoire, L., Pelkey, K. A., Erkkila, B. E., Jeffries, B. W., Yuan, X., and McBain, C. J. (2011). A blueprint for the spatiotemporal origins of mouse hippocampal interneuron diversity. *J. Neurosci.* 31, 10948–10970. doi: 10.1523/JNEUROSCI.0323-11.2011

Vereczki, V. K., Müller, K., Krizsán, É, Máté, Z., Fekete, Z., and Rovira-Esteban, L. (2021). Total number and ratio of GABAergic neuron types in the mouse lateral and basal amygdala. *J. Neurosci.* 41, 4575–4595. doi: 10.1523/JNEUROSCI.2700-20.2021

Veres, J. M., Nagy, G. A., and Hájos, N. (2017). Perisomatic GABAergic synapses of basket cells effectively control principal neuron activity in amygdala networks. *eLife* 6:e20721. doi: 10.7554/eLife.20721

Veres, J. M., Nagy, G. A., Vereczki, V. K., Andrási, T., and Hájos, N. (2014). Strategically positioned inhibitory synapses of axo-axonic cells potently control principal neuron spiking in the basolateral amygdala. *J. Neurosci.* 34, 16194–16206. doi: 10.1523/JNEUROSCI.2232-14.2014

Wang, B., Yin, L., Zou, X., Ye, M., Liu, Y., and He, T. (2015). A subtype of inhibitory interneuron with intrinsic persistent activity in human and monkey neocortex. *Cell Rep.* 10, 1450–1458. doi: 10.1016/j.celrep.2015.02.018

Webster, J. F., Vroman, R., Beerens, S., Sakata, S., and Wozny, C. (2021). NDNF is selectively expressed by neocortical, but not habenular neurogliaform cells. *Eur. J. Neurosci.* 53, 3561–3575. doi: 10.1111/ejn.15237

Wolff, S. B. E., Gründemann, J., Tovote, P., Krabbe, S., Jacobson, G. A., and Müller, C. (2014). Amygdala interneuron subtypes control fear learning through disinhibition. *Nature* 509, 453–458.

Woodruff, A. R., and Sah, P. (2007). Networks of parvalbumin-positive interneurons in the basolateral amygdala. *J. Neurosci.* 27, 553–563.

Frontiers in
Cellular Neuroscience

Leading research in cellular mechanisms underlying brain function and development

Part of the world's most cited neuroscience journal series that advances our understanding of the cellular mechanisms underlying cell function in the nervous system across all species.

Discover the latest Research Topics

See more →

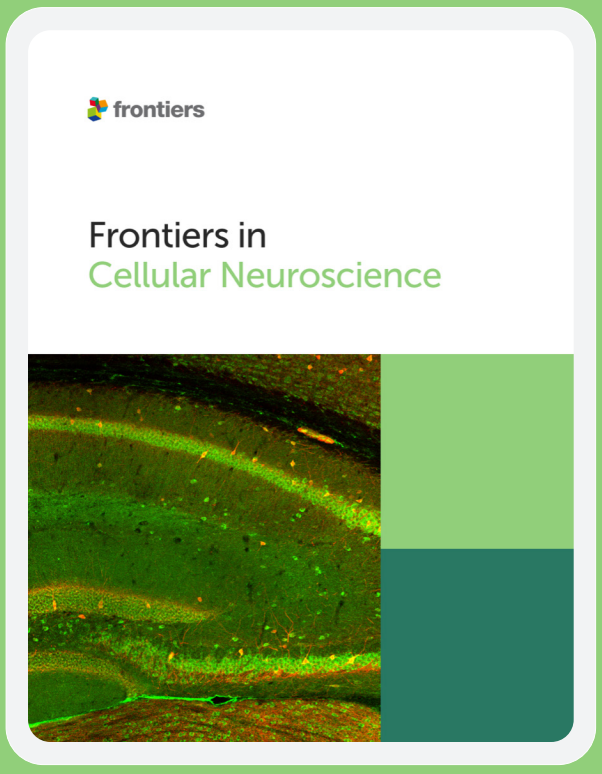

Frontiers

Avenue du Tribunal-Fédéral 34
1005 Lausanne, Switzerland
frontiersin.org

Contact us

+41 (0)21 510 17 00
frontiersin.org/about/contact